Fatigue of HNBR - Effects of formulation and thermal aging

Kubat Narynbek Ulu

UNIVERSITE BRETAGNE SCIENCES LOIRE POUR L'INGENIEUR

CENTRALE NANTES

THESE DE DOCTORAT DE

L'ÉCOLE CENTRALE DE NANTES
COMUE UNIVERSITE BRETAGNE LOIRE

ECOLE DOCTORALE N° 602
Sciences pour l'Ingénieur
Spécialité : Génie mécanique

Par
Kubat NARYNBEK ULU

FATIGUE OF HNBR - EFFECTS OF FORMULATION AND THERMAL AGING

Thèse présentée et soutenue à Nantes, le 6 avril 2018
Unité de recherche : Institut de Recherche en Génie Civil et Mécanique (GeM - CNRS 6183)

Rapporteurs avant soutenance :

Florian Lacroix	Maître de Conférences HDR, LaMé, Polytech Tours
Nicolas Saintier	Professeur des Universités, I2M, Arts Métiers ParisTech, Bordeaux

Composition du Jury :

Président :	Moussa Nait-Abdelaziz	Professeur des Universités, LML, Polytech'Lille
Examinateurs :	Florian Lacroix	Maître de Conférences HDR, LaMé, Polytech Tours
	Nicolas Saintier	Professeur des Universités, I2M, Arts Métiers ParisTech, Bordeaux
	Pierre-Antoine Albouy	Directeur de Recherche CNRS, LPS, Université de Paris Sud
	Anne-Sophie Béranger	Responsable Pôle Mécanique & Simulation, LRCCP
	Michael Johlitz	Privatdozent, Universität der Bundeswehr München
Dir. de thèse :	Bertrand Huneau	Maître de Conférences HDR, GeM, Ecole Centrale de Nantes
Co-dir. de thèse :	Erwan Verron	Professeur des Universités, GeM, Ecole Centrale de Nantes

Acknowledgements

The brevity of the following in no way reflects the enormous amount of gratitude I want to express to everyone mentioned here.

First, I would like to thank Florian Lacroix and Nicolas Saintier for accepting to act as reviewers of the present thesis. It has been a great pleasure to receive your reviews and I sincerely believe that your insights, comments, and questions have improved my PhD defence. Additionally, I would like to thank Florian Lacroix for taking part in the CST of this thesis. Likewise, I would like to thank Moussa Nait-Abdelaziz for presiding and Michael Johlitz for being part of the jury. I felt honored to present my work in front of the experts of the field; a special thank you to Pierre-Antoine Albouy for being part of the jury and, of course, for your extensive consultations on strain-induced crystallization, without which this part of the thesis would probably not have existed.

My sincere gratitude also extends to Anne-Sophie Béranger and Patrick Heuillet for supervising the industrial part of the project. I would like to thank you for your invaluable input and expertise and for being understanding, flexible, and resourceful throughout the thesis. I sincerely believe that achieving balance between industrial needs and scientific pursuit has been in large part to your dedicated leadership.

Certainly, the completion of this thesis is thanks in large part to my supervisors, Bertrand Huneau and Erwan Verron. I feel tremendously fortunate to have started my scientific adventure under your guidance as you have constantly challenged, supported and believed in me since the start of my master's work. I am deeply grateful for the trust you have put in me, in allowing me to work with such independence and letting me explore different avenues of interest. I will always remember your input in my career and personality: Erwan, for your way of thinking and presenting ideas (you have made me a better writer and presenter); Bertrand, for your meticulous attention to detail, work ethic, and dedication to science (in the most troublesome circumstances). Once again, thank you to both of you.

I would like to continue by acknowledging Ivanna for her work done as an intern, especially for the experimental work completed despite all the problems; and, a special thanks to Pierrick and Franck for all the invaluable support at the CRED. I would like to especially thank the SM Team - Adrien, Michel, Thomas B., Thomas C., Marie, Clement, Anne-Sophie, and Alice - for all the valuable input, discussions, and feedback. This gratitude also extends to the great PMM team of GeM, and to my (former) colleagues at LRCCP for all the provided assistance - Stéphane, Mai, Nyhal, Jerome, Laurence, Sylvie, and Pierre, who was instrumental in starting this project. At ECN, I'd like to thank Nicolas, the best tennis partner; Santi, Victor, Tauno, Oleg, and all others for being great football teammates; you all have helped to keep me sane during this thesis. Of course, a special thank you to all my friends in France, and especially Petar, Abdou, Stan, Roxana, Alex for all the wonderful evenings, discussions, and support.

Last, but most importantly, I cannot express enough gratitude to all my relatives and family. Without their support this would not have been possible. To my incredible parents, who have facilitated my interest in knowledge, and who have served as

ideal role models throughout my life. To my brilliant sister, for the invaluable career advice and who has always been my biggest cheerleader. And, of course, to my lovely girlfriend and now wife, who has been so supportive, patient, insightful, and helpful all this time.

Contents

List of Figures

List of Tables

Chapter 1

General Introduction

Hydrogenated nitrile butadiene rubber (HNBR) is a family of high performance elastomers. Depending on its formulation, HNBR possesses specific material properties: excellent resistance to oil (and other industrial solvents) in addition to heat resistance. After being initially used in the automotive industry, it has found a wide range of applications in oil and gas, aerospace, and other demanding industries. In regards to its application, durability - and more specifically fatigue - of HNBR is an important property; and, at present, there is an industrial need to design tools that include formulation selection and prediction of fatigue lifetimes of HNBR products. Moreover, as these are utilized in high temperature environments, it is important to consider the effects of thermo-oxidative aging on fatigue.

From a scientific perspective, there is a lack of extensive studies on fatigue resistance of HNBR, and complete absence of such on the effects of formulation and thermal aging. This direction of research also poses an interesting and a more general scientific perspective since the interaction or coupling between fatigue and aging, both mechanically weakening phenomena, is not completely understood in elastomers.

This PhD thesis, carried out within the industrial framework of CIFRE (Convention for Industrial Training and Research - from French), is a collaboration between GeM (Research Institute in Civil and Mechanical Engineering - from French) of the Ecole Centrale de Nantes and LRCCP (Rubber and Plastics Research and Testing Laboratory - from French), a company specialized in research, testing and consulting services in the field of polymers. This collaborative project focuses on two main objectives:

I. Analyze the effects of formulation - namely acrylonitrile content, percent hydrogenation, and of composite HNBR - on fatigue resistance;

II. Investigate the interaction between thermal aging and fatigue;

And a supplementary objective:

III. Study the presence of strain-induced crystallization (SIC) and its effects on mechanical properties of HNBR.

The manuscript is divided into four chapters, in addition to the present introduction and the general conclusion as the last chapter. This work is structured so that each

chapter focuses on a specific topic of research and each contains sections on state of the art, experimental methods, and results; a summary is proposed at the end of each chapter.

Chapter 2 focuses on HNBR and its mechanical properties, which are to serve as foundation for subsequent investigation of fatigue and thermal aging. First, mechanical characterization of HNBR is introduced. Mechanical response, applications, and manufacturing of HNBR are presented; the relative scarcity of publicly available literature devoted to mechanical response of filled HNBR, as well as the effects of formulation will be highlighted. Moreover, the details of chemical composition of HNBR are also presented in Section 2.1. Subsequently, Section 2.2 presents the formulation of the six blends investigated in the present work. The latter parts of the chapter consist of the investigation of mechanical properties and the effects of formulation; quasi-static, dynamic, and other mechanical properties are explored. Furthermore, an extensive investigation of strain-induced crystallization is performed, providing novel results and insights into the mechanical response of HNBR.

Chapter 3 is devoted to experimental methods used in fatigue life testing of elastomers. It begins with a state of the art of the methods utilized in industry and academia, along with the difficulties encountered during their application; such complexities result in several limitations. These limitations are then addressed by the development of a novel approach in true stress controlled fatigue testing of elastomers. From this perspective, HNBR, with its complex mechanical response, is a useful tool to highlight the limitations of conventional fatigue life testing approaches; it is thus used to validate our method. Moreover, a requirement for introduction of statistical approaches in fatigue life analysis of elastomeric materials is discussed. Existing approaches are analyzed, and novel powerful methods, borrowed from medical sciences, are presented and then applied.

Chapter 4 investigates the effects of formulation on fatigue life of HNBR. It starts with a concise state of the art of the fatigue phenomenon in elastomers; the lack of available literature on fatigue resistance of HNBR is highlighted with a detailed discussion of available studies. Furthermore, Chapter 4 applies the true stress control method of Chapter 3 to study the effects of acrylonitrile content, percent hydrogenation, and of a composite blend on fatigue life of HNBR. These fatigue life results are supplemented by fatigue crack propagation experiments. Finally, damage analysis, with aid of optical and scanning electron microscopy, is carried out to describe fatigue damage mechanisms of HNBR.

Chapter 5 presents the latest results of the thesis, where the effects of thermal aging on fatigue life of HNBR are investigated. A state of the art on general effects of thermal aging as well as its effects on fatigue of elastomers is presented. Two additional sets of fatigue life tests are carried out to study the effects of preliminary thermal aging on fatigue as well as of simultaneous fatigue and aging. Fatigue life results from Chapter 4 are first compared to fatigue life tests at high temperature, where effects of aging are to be observed. Second, the same results are compared with fatigue life tests carried out on pre-aged specimens. At last, a discussion on the connections between the three tests is proposed.

The results of the whole work are lastly laid out in the general conclusion, along with remaining open questions, paving the way for future perspectives.

Finally, an extensive, self-contained French summary of all results is given at the end of the manuscript in Appendix A.

Chapter 2

HNBR and Its Mechanical Properties

Chapter Highlights

- HNBR is a high performance elastomer with high resistance to heat and industrial solvents;
- State of the art for general mechanical properties of HNBR - lack of literature specific to the effects of formulation in filled HNBR;
- HNBR has relatively high stiffness and strength at room temperature; at 120 °C, higher percent hydrogenation and greater ACN content contributes to better preservation of mechanical properties;
- T_g of HNBR varies from around -40 °C to around -20 °C depending on formulation;
- Presence of SIC increases with acrylonitrile content; relationship between stress-strain-crystallinity established for first time in HNBR;
- Significant inelastic response is observed: Mullins effect, residual strain, and permanent set.

Introduction

Investigating the mechanical properties of HNBR is not only required for the subsequent fatigue and aging studies of the present thesis, but is also motivated by a lack of publicly available information. Hence, the goal of the present chapter is twofold: to present the state of the art on the subject, and to experimentally determine the mechanical properties of the HNBR blends used in this study. First, a general overview of HNBR and its physico-chemical properties is followed by a review of published data concerning some of its mechanical properties. Second, performed experiments are presented; they concern uniaxial quasi-static tensile response, small strain viscoelasticity, the Mullins effect, hardness, residual strain and permanent set. To improve the understanding of the mechanical response, the chapter also covers the phenomenon of strain-induced crystallization (SIC) and its effects on macroscopic properties.

Contents

2.1 State of the Art

2.1.1 Introduction to HNBR

Industrial needs

With increasing economic, safety, and environmental concerns, synthetic elastomers are being extensively adopted across a wide range of industries. Their major characteristics include tensile strength, ability to bear large strain, hardness, ozone resistance, *etc.* Some of the requirements for such elastomers are resistance to heat, oils, and industrial solvents. In this context of synthetic elastomers, HNBR is a high-performance synthetic elastomer based on nitrile butadiene rubber (NBR). HNBR has relatively high mechanical properties as compared to many other synthetic elastomers (Wrana et al. 2001). Currently, HNBR is mostly used in automotive industry for production of belts, hoses, vibration dampers, and seals (Hashimoto et al. 1998; Tao et al. 2005). However, it also has found application in oil field exploration and processing, military, aerospace, ship building, and other performance demanding industries (Hashimoto et al. 1998; Wrana et al. 2001; Tao et al. 2005).

Its widespread use is explained by its, compared to other synthetic elastomers, high resistance to petroleum solvents with good aging and heat resistance (Tao et al. 2005). Figure 2.1-1 classifies various elastomers in terms of oil and heat resistances. Oil resistance in the figure is measured as the resistance after 70 h swelling in IPM

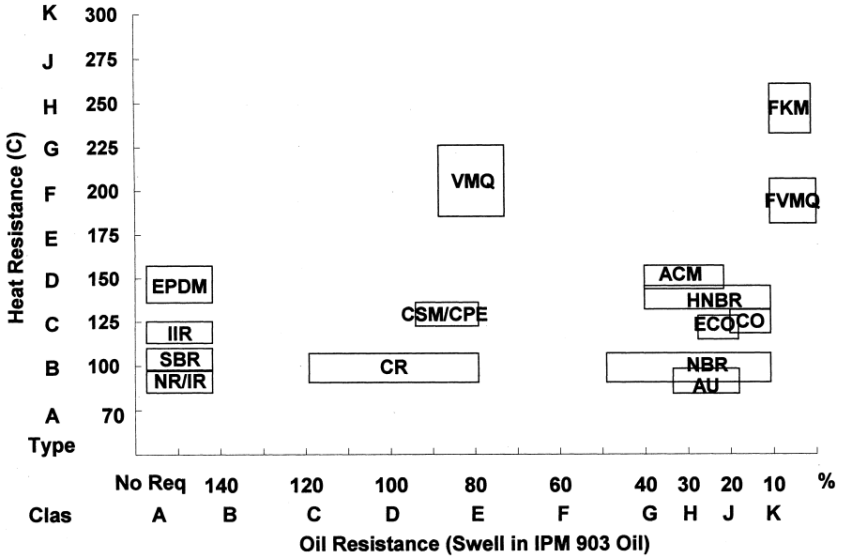

Figure 2.1-1 – ASTM D2000 classification of common elastomers (Tao et al. 2005).

903 oil, and heat resistance is defined as the change in various mechanical properties (±30% of tensile strength, 50% of stretch at break, ±15% of hardness) after thermal aging at the indicated temperature. Moreover, the abrasion resistance of HNBR is better compared to other oil-resistant elastomers, such as NBR, epichlorohydrin-ethylene oxide co-polymers (ECO), fluorocarbons (FKM), and polyacrylate (ACM) as seen in Figure 2.1-2 (Keller 2012). Additionally, HNBR has a median mass-to-volume cost (relative cost to fill a mold cavity) compared to other oil resistant

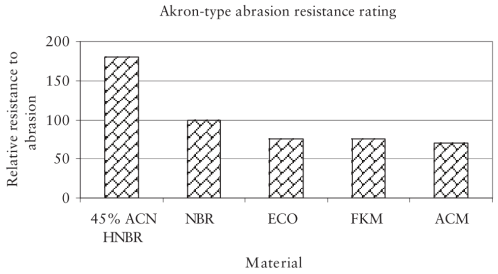

Figure 2.1-2 – Comparison of abrasion resistance of various elastomers with NBR as a reference (Keller 2012).

elastomers (Table 2.1-1). In applications where high strength and abrasion resistance are required, HNBR is preferable to ACM and AEM at higher cost (Keller 2012).

Table 2.1-1 – Commercial comparison of oil resistant elastomers.

Polymer	Cost of compound ($)	lb-vol cost ($)	Operating temperature limit (°C)
NBR	1.00	1.22	100
ACM	2.30	3.04	150
AEM	2.40	3.17	150
HNBR	**10.40**	**12.69**	**150**
FVMQ	23.00	35.19	200
FKM	16	29.76	250

Manufacturing process

Zeon and *Arlanxeo* are two major manufacturers of HNBR sold under the respective *Zetpol* and *Therban* trademark names. There are no unified grades for HNBR and each manufacturer adopts its own classification, but HNBR is generally split into two grades: low temperature (LT) and high temperature (HT). HNBR is primarily classified by acrylonitrile content, followed by degree of hydrogenation, Mooney viscosity, polymerization temperature, stabilizer, third monomer, and appearance of the product (Keller 2012).

Improvement of characteristics of HNBR over NBR in terms of heat, chemical and environmental resistance, and abrasion is achieved by a high saturation level of double carbon-carbon bonds in polymer chains, which are removed by a selective hydrogenation reaction in HNBR. As shown in Figure 2.1-3, the manufacturing process involves dissolution of NBR (emulsion polymerized) in a solvent and its selective catalytic (usually noble metals such as rhenium, palladium, and platinum) hydrogenation (Hashimoto et al. 1998). Selective hydrogenation is necessary in order to prevent hydrogenation of the cyano-groups, which are responsible for the heat and chemical resistance (Sawada 1993).

As in other elastomers, cross-linking (or vulcanization) greatly improves the mechanical properties of HNBR. Peroxide, sulfur cured systems, and phenol resin are mostly utilized as cross-linking agents (Hashimoto et al. 1998; Tao et al. 2005; Osaka et al. 2013). Peroxide can be used for all grades of HNBR (note that only peroxide can be used for fully saturated HNBR). On the contrary, sulfur cured systems are limited to 3-10 wt.-% unsaturation because they require unsaturated double bonds

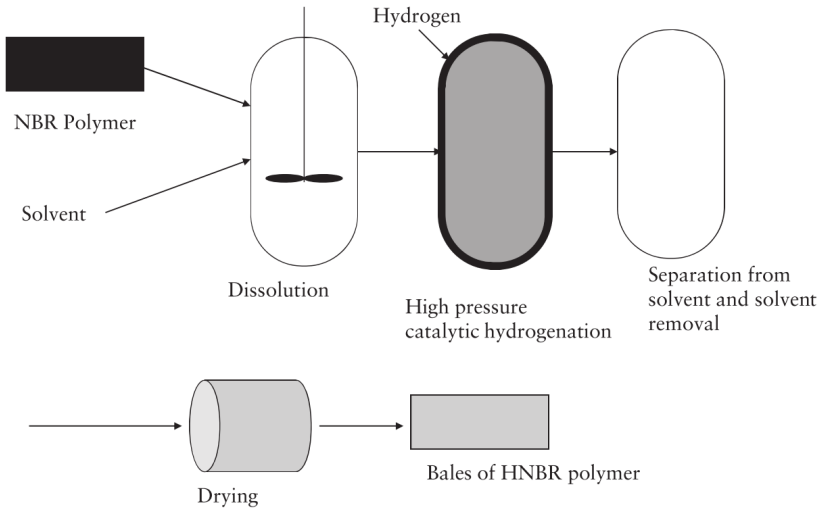

Figure 2.1-3 – Schematic of the manufacturing process of HNBR from NBR (Klingender 1989).

in the main polymer chain for vulcanization to occur (Wrana et al. 2001; Tao et al. 2005). Furthermore, phenolic resin is also used for vulcanization of HNBR (Osaka et al. 2013).

Similarly to standard rubbers, fillers are added to HNBR to improve its characteristics. For example, carbon black is used to improve physical and mechanical properties; various carbon black grades are chosen to achieve desired balance of physical properties and compound cost (Tao et al. 2005). Moreover, other additives such as plasticizers are added to reduce viscosity, control volume, and improve low temperature properties. Antioxidants and antiozonants are also added to HNBR blends to improve their resistance to oxidation and ozone attack, even though HNBR has better characteristics compared to NBR (Keller 2012). A study by *Zeon* has established that combination of 4,4'-Bis (alpha, alpha-dimethylbenzyl) and Zinc 2-mercaptotoluimidazole (each at 1.5 phr) offers the best protection against oxidation in many applications (Lanxess n.d.[b]).

Physico-chemical properties

HNBR is a tetra-polymer containing butadiene, ethylene (by hydrogenation of 1,4-butadeine), propylene (by hydrogenation of 1,2-butadiene), and acrylonitrile (ACN). Its molecular formula is

$$[(C_4H_6)_x(C_4H_8)_y(C_3H_3N)_z]_n,$$

and its molecular structure of HNBR is shown in Figure 2.1-4. Likewise as in NBR, the acrylonitrile group (ACN) provides chemical resistance (to oil and other industrial solvents) and, additionally, leads to better strength characteristics (Hayashi et al. 1991). The ACN content by weight of commercial grade HNBR varies from 17 to 50 percent. The ethylene chain functions to provide excellent elasticity, heat resistance, chemical stability, and ozone resistance (Nakagawa et al. 1992), and also better cold temperature performance (Sawada 1993). Additionally, if required, a

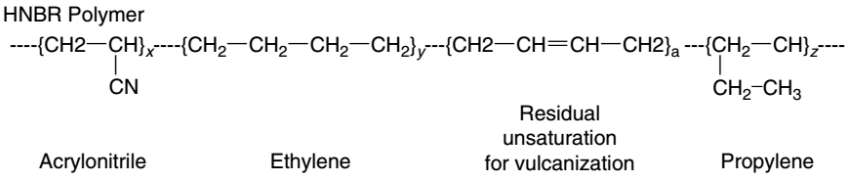

Figure 2.1-4 – Molecular structure of HNBR (Klingender 1989).

small amount of residual double bonds are present in order to facilitate vulcanization (Keller 2012). Percent hydrogenation goes up to 99.9%, which is equivalent to an iodine number[1]of 4. Finally, the propylene group (or vinyl as some authors refer to it) reduces crystallinity and enhances elasticity (Hayashi et al. 1991).

The glass transition temperature (T_g) of HNBR ranges from −70 °C to about −15 °C (Sawada 1993). Consequently, the operating temperature is in range from −40 °C to 170 °C for various grades of HNBR. Moreover, successful use of HNBR has been reported up to temperatures of 180 °C to 200 °C for short term oil applications (Hashimoto et al. 1998; Tao et al. 2005; Keller 2012). In general, the glass transition temperature increases with increasing ACN content; the effect of hydrogenation is less straightforward as illustrated in Figure 2.1-5.

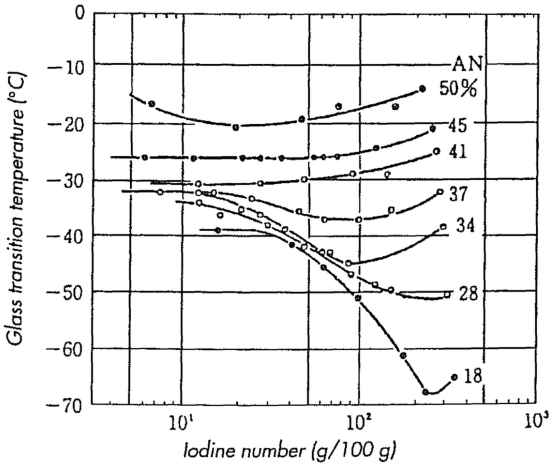

Figure 2.1-5 – Glass transition temperature with respect to iodine number (inverse of percent hydrogenation) and ACN content (Sawada 1993).

The Mooney viscosity of HNBR ranges from 57 to 137 Mooney units (Tao et al. 2005; Lanxess 2010); as percent hydrogenation of HNBR increases, so does the Mooney viscosity (Sawada 1993).

Presence of SIC is reported for HNBR similar to natural rubber, for which the phenomenon is widely studied. Studies of SIC in HNBR are discussed in detail in Section 2.1.3).

[1]Iodine number is a measurement of unsaturation and indicates the mass of iodine in grams that is consumed by 100 grams by a substance. Hence, as the iodine number increases, the number of unsaturated double carbon bonds increases (Thomas 2000).

2.1.2 Mechanical properties

There are few explicit published studies that discuss mechanical behavior of HNBR and especially the effect of acrylonitrile and hydrogenation. An exhaustive bibliographic research has been carried out, and findings relevant to the present work are presented is the following sections.

Quasi-static behavior

One of the primary interests is the uniaxial stress-strain response of HNBR. As shown in Figure 2.1-6(a), with increasing hydrogenation from 88% to 92%, the tensile

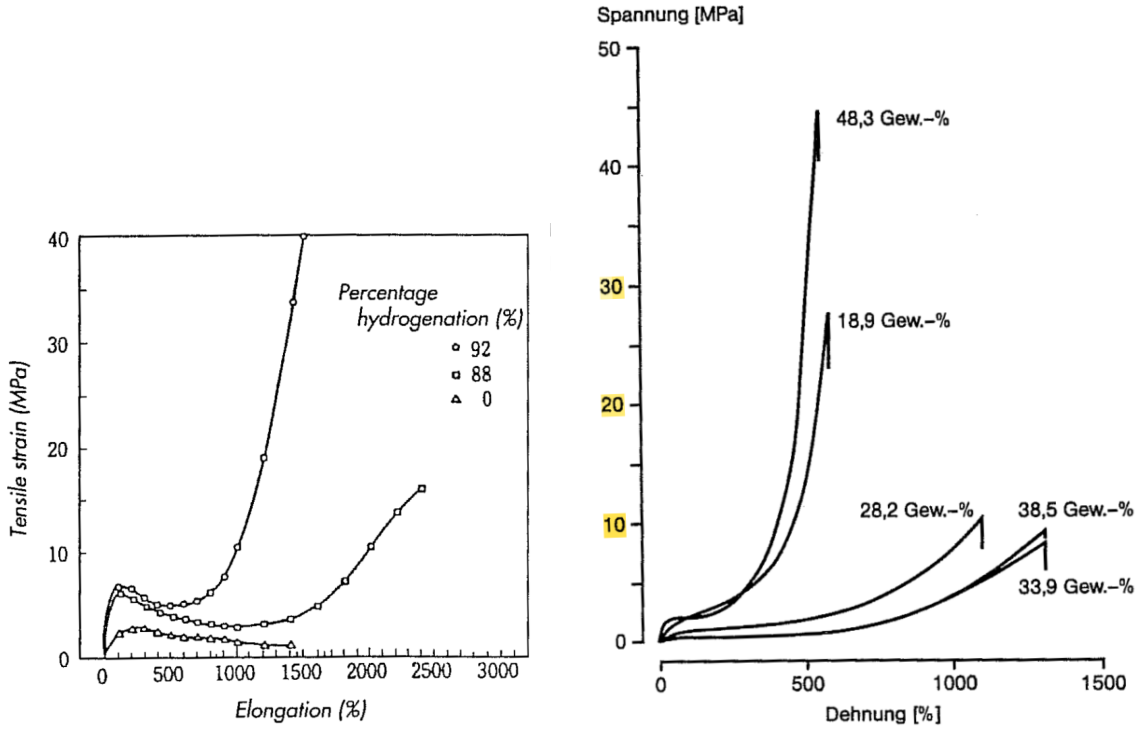

(a) Effect of hydrogenation (Sawada 1993). **(b)** Effect of ACN (Obrecht et al. 1986).

Figure 2.1-6 – Stress-strain response of HNBR with varying percent hydrogenation and ACN content.

strength (σ_f) of unfilled HNBR at room temperature increases from 15 MPa to 40 MPa; moreover, elongation at break (ϵ_f) decreases from 2500% to 1400% (Sawada 1993). This is primarily attributed to the influence of strain-induced crystallization (SIC), the details of which are discussed further in sub-section 2.1.3. In comparison, NBR (0 percent hydrogenation), which does not undergo SIC, has considerably lower strength: its tensile strength is 2 MPa and its elongation at break is 1450%. Similarly, investigating the effects of ACN content, Obrecht et al. (1986) measured uniaxial tensile response of filled and unfilled HNBR at room temperature. The true stress-strain curves of unfilled HNBR blends are shown in Figure 2.1-6(b). The mechanical response does not have a clear trend with ACN content. For example, stiffness and tensile strength are high for HNBR with 18 wt.-% ACN; they are the lowest around 33.9-38.5 wt.-% of ACN for unfilled HNBR; and, finally, they

then increase for ACN content of 48.3 wt.-%. The effect of ACN content is inverse for strain at break. The relationship of stiffness is summarized in Figure 2.1-7; moreover, the figure includes those of filled HNBR and the yield strength of NBR. It is interesting that for carbon black filled HNBR, stiffness has a clear trend as it

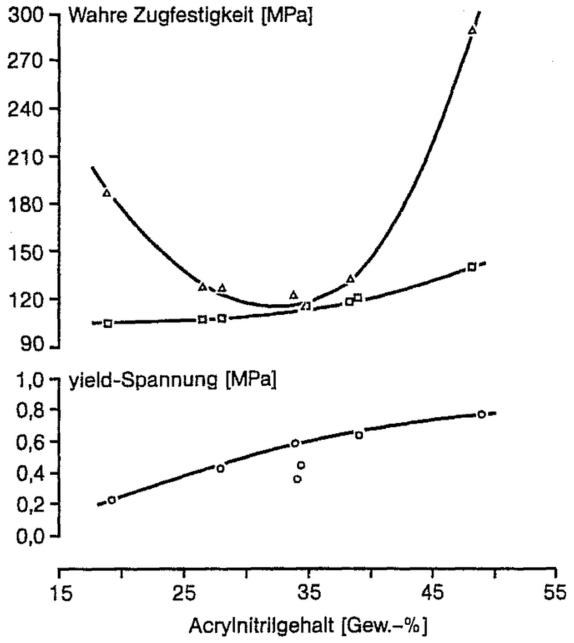

Figure 2.1-7 – True tensile strength of HNBR and yield strength of NBR with respect to ACN content; ▷ – unfilled HNBR; □ – CB filled HNBR; ○ – NBR (Obrecht et al. 1986).

increases with greater ACN content.

Other factors also affect the stress-strain response of HNBR. The addition of fillers, most commonly of carbon black (CB), affects the mechanical properties of HNBR as with other rubbers. Thavamani and Bhowmick (1992) report that with increase of carbon black filler (N110) from 0 to 50 phr, HNBR (44 wt.-% ACN and 91% hydrogenation) becomes more *brittle*:

- The tensile modulus at 300% elongation and the tensile strength of HNBR increase greater amount of CB (ranging from 0 to 50 phr);
- In contrast, the elongation at break decreases with increased carbon black content up to 30 phr and remains constant up to 50 phr.

Similarly, the effects of different types of carbon blacks and their amount (from 25 to 75 phr) on HNBR properties (36 wt.-% ACN and 96% hydrogenation) has been investigated by one of the manufacturers of HNBR (Lanxess n.d.[a]);

and their findings also correspond to those of Thavamani and Bhowmick (1992).

In terms of cross-linking, Keller (2012) found that for HNBR (N330 carbon black filled, 36 wt.-% ACN and 91% hydrogenation), in general, tensile modulus increases and elongation at break decreases with greater amount (in phr) of peroxide, which is most commonly used for HNBR vulcanization. Moreover, Osaka et al. (2013) studied the effect of phenol resin cross-linked HNBR (36 wt.-% ACN, 96 percent hydrogenation) and compared it to peroxide cross-linked HNBR. It is reported that

phenol resin cross-linked HNBR has increased stiffness, rigidity, and elongation to break as compared to peroxide cross-linked HNBR. Moreover, presence of SIC is reduced, while at the same time allowing for longer elongation (up to 2000% strain).

Dynamic behavior

Dynamic properties of elastomers are classically investigated by dynamic mechanical analysis (DMA), which consists in prescribing sinusoidal mechanical loading conditions and measuring the response in strain, as shown in Figure 2.1-8. Depending on

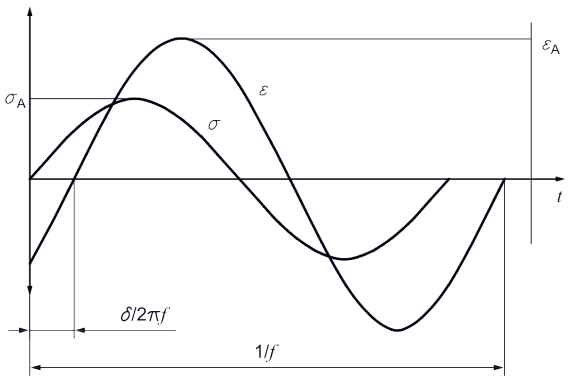

Figure 2.1-8 – Prescribed sinusoidal stress (σ) and measured strain (ϵ) with a phase shift (δ) (NF EN ISO 6721-1 2011).

the type of loading conditions (uniaxial tension-compression or shear), the dynamic elastic modulus (E^*) or dynamic shear modulus (G^*) is measured. Moreover, the corresponding phase difference between stress and strain expresses the viscoelasticity of the material (Ferry 1980). Dynamic shear modulus is given by

$$G^* = G' + iG'', \tag{2.1-1}$$

where G' and G'' are the storage and loss moduli, respectively, given by

$$G' = \frac{\sigma_0}{\epsilon_0}\cos(\delta), \tag{2.1-2}$$

$$G'' = \frac{\sigma_0}{\epsilon_0}\sin(\delta). \tag{2.1-3}$$

Finally, the phase angle is defined as

$$\tan\delta = \frac{G''}{G'}. \tag{2.1-4}$$

In uniaxial tension-compression, E^*E, E', and E'' can be similarly defined.

There are no specific studies devoted to the effects of acrylonitrile content or percent hydrogenation on dynamic properties of HNBR. However, one can refer to an extensive work carried out by Thavamani and Bhowmick (1992) on the influence of some chemical parameters: the effects of cross-link density, curing system, filler and resin were examined on HNBR with 44 wt.-% ACN, and 91% hydrogenation. It has been found that the T_g in 50 phr CB-filled HNBR is not influenced by the cross-link

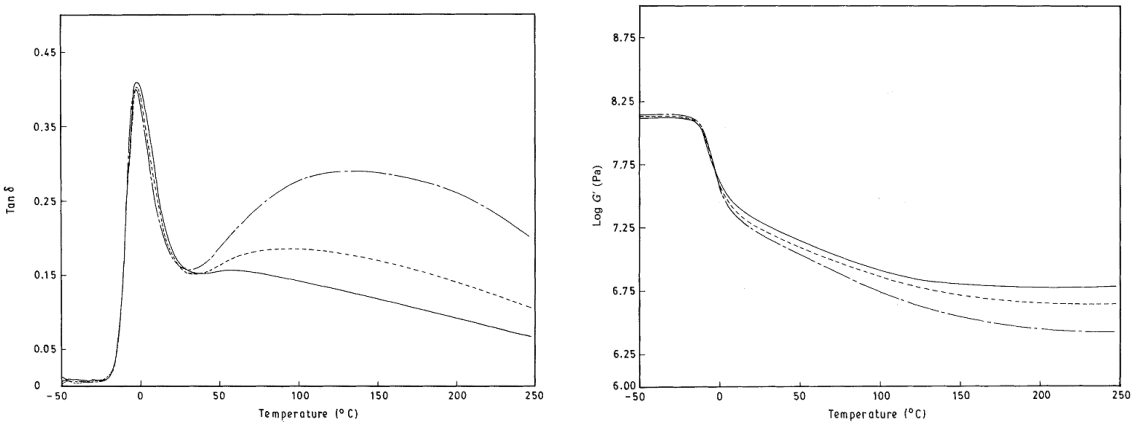

(a) Phase angle ($\tan\delta$). **(b)** Storage modulus.

Figure 2.1-9 – Effect of cross-link density (D1— > D2- - > D3–•–) on DMA response (Thavamani and Bhowmick 1992).

density because prolonged cross-linking process does not alter the chemical nature of the polymer (Figure 2.1-9). However, there are differences in the plateau zone: as cross-link density decreases, more free ends and untrapped entanglements are present in the network, which lead to more relaxation and slippage at high temperatures.

Finally, the effect of the amount of carbon black was examined as shown in Figure 2.1-10. The phase angle peak decreases with increased amount of CB. In the plateau region, the phase angle decreases with increased amount of CB. As expected, the storage modulus also increases with increased amount of CB.

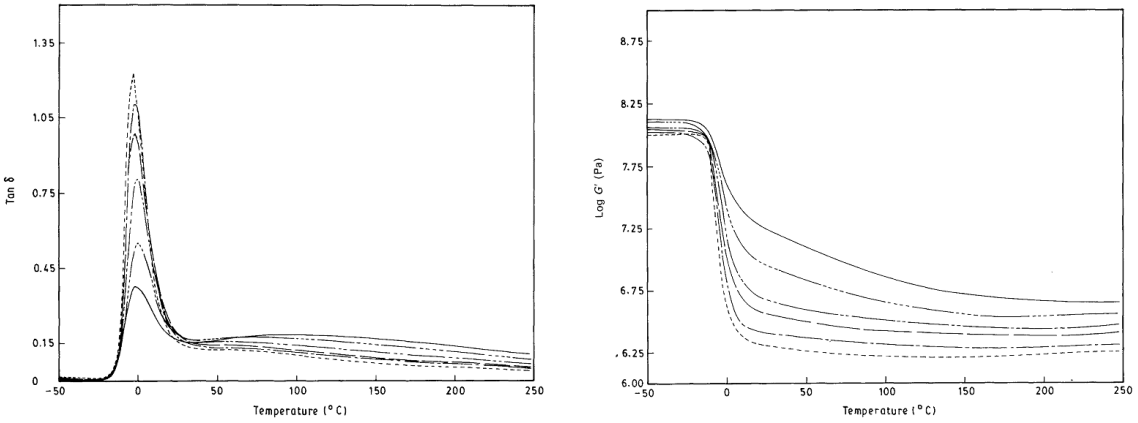

(a) Phase angle ($\tan\delta$). **(b)** Storage modulus.

Figure 2.1-10 – Effect of varying amounts of carbon black filler (0 phr - - -, 10 phr –•–, 20 phr – –, 30 phr –••–, 40 phr –•••–, 50 phr —) on DMA response (Thavamani and Bhowmick 1992).

Other mechanical properties

In addition to investigation of the stress-strain response of HNBR, Obrecht et al. (1986) measured plastic residual strain of carbon black filled HNBR (Figure 2.1-11).

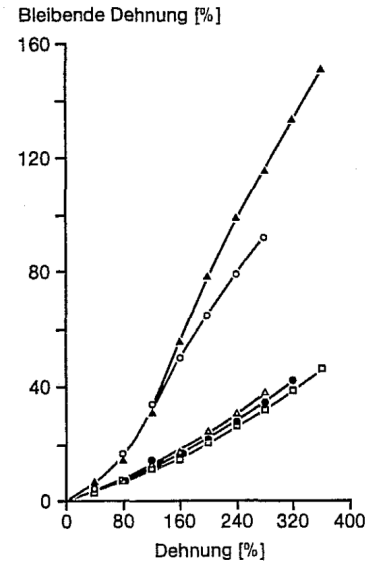

(a) Residual strain of carbon black filled HNBR with respect to initial elongation; wt.-% of ACN: ○ – 18.9; ▷ – 28.2; □ – 34.9; ● – 39.0; ▲ – 48.3

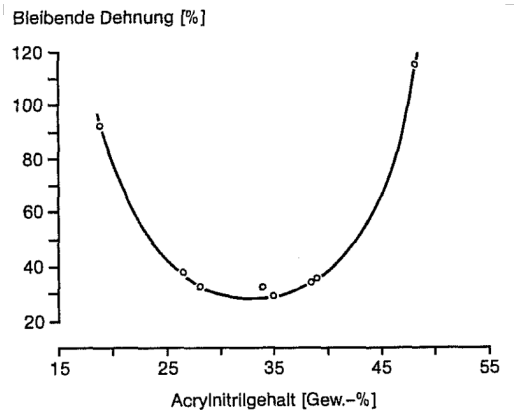

(b) Residual strain with respect to ACN content after 280% initial elongation.

Figure 2.1-11 – Effect of ACN on residual strain of filled HNBR (Obrecht et al. 1986).

This behavior, as evident by the shape of Figure 2.1-11(b), is very similar to the tensile strength of unfilled HNBR (Fig. 2.1-7). To explain it, Obrecht *et al.* argue that local crystalline structures (occurring due to SIC for HNBR with 18.9 wt.-% and 48.3 wt.-% of ACN) melt with delay during unloading, therefore causing higher residual strain.

On the other hand, Sawada (1993) reports that compression set becomes greater with increasing percent hydrogenation; the difference with respect to NBR is observed when percent hydrogenation is greater than 80%. Moreover, the effects of carbon black on compression set of HNBR (36 wt.-% ACN and 96% hydrogenation) was also investigated by (Lanxess n.d.[a]); it was found that, overall, the compression set increases with the greater amount of practically all types of carbon black . Finally, compression set is also affected by the cross-linking process (Keller 2012): in general, compression set (measured by ASTM D395, Method B, 70h at 150 °C) of HNBR (N330 carbon black filled, Zetpol 2020 - 36 wt.-% ACN and 91% hydrogenation) decreases with greater amounts of co-agent and the peroxide agent.

As for hardness of HNBR, it is influenced by carbon black amount and type as for other elastomers. Figure 2.1-12 features the hardness of HNBR (36 wt.-% ACN and 96% hydrogenation) with respect to different types and amount of carbon black (Lanxess n.d.[a]). Similar to the tensile strength, hardness increases with carbon black amount for all types of carbon black. And in general, it decreases with increase in size of carbon black particles. Moreover, Keller (2012) investigated Shore A hardness of HNBR (N330 carbon black filled, Zetpol 2020 - 36 wt.-% ACN and 91% hydrogenation) with respect to recipes containing different amounts of peroxide cross-linking agent. It is reported that, in general, the hardness increases with greater amount of the peroxide agent.

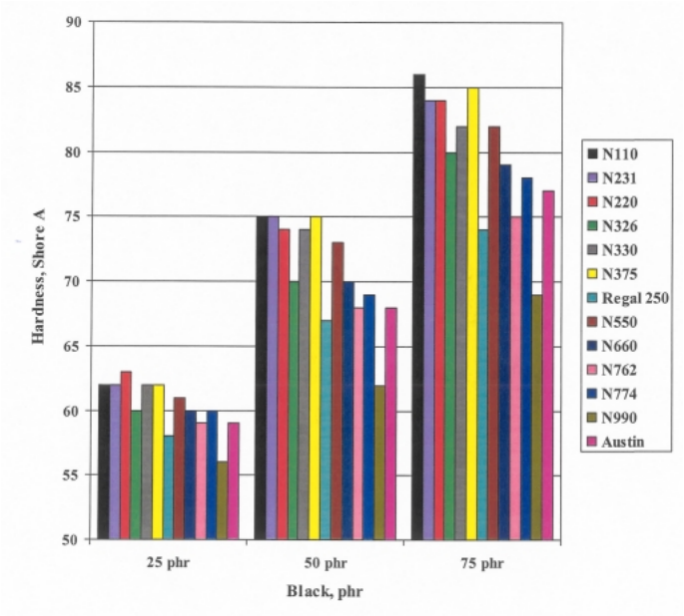

Figure 2.1-12 – Shore A hardness of HNBR (36 wt.-% ACN and 96% hydrogenation) with respect to carbon black type and content (Lanxess n.d.[a]).

Mullins effect

Finally, due to the fact that the HNBR blends used in this study are carbon black filled, a study on the Mullins effect is required. There are no direct studies on this topic specific to HNBR, thus a general discussion is presented. Since the seminal work by Mullins (1969), it has been widely reported that a filled virgin elastomer undergoes significant softening during the first initial loading cycles of cyclic tests, and that the material response after that stabilizes and becomes repeatable. Hence, this large-strain stress softening mechanism is referred to as the Mullins effect. As shown in Figure 2.1-13, when an elastomer is repeatedly stretched for a specific distance from an unstressed state and then equally unloaded, after each successive cycle, the stress decreases for the same strain level. The Mullins effect can reappear after the initial cycles, if the material is subjected to a higher and new maximum loading Diani et al. (2009). In addition to stress softening, inelastic strain is observed after each successive unloading. In Figure 2.1-13, the measured strain does not equal to zero in an unstressed state (F or σ=0). As a consequence, at zero displacement, one can observe a compressive force for massive specimens or buckling for thin specimens.

Theoretically, the Mullins effect is characterized by difference of stress during loading and unloading of the material to a specific strain. As such, on repeated loading, the reloading stress path follows the unloading path of the previous cycle as long as the maximum applied strain is not exceeded. Experimentally, the response is more complex. Under cyclic loading, softening occurs principally during the first couple of cycles. However, the reloading path does not follow the previous unloading path as in the ideal case.

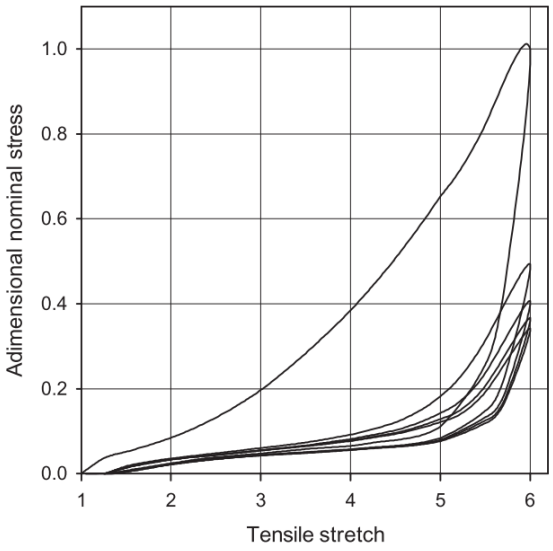

Figure 2.1-13 – Experimental example of the Mullins effect (Chagnon et al. 2004).

2.1.3 Strain-induced crystallization

SIC of rubbers, especially that of natural rubber, has been comprehensive: extensive reviews by Tosaka (2007) and Huneau (2011) for the works published until 2010; in the following years, there are notable works of Albouy et al. (2012), Brüning et al. (2012), Candau et al. (2012), Candau et al. (2015a), and Candau et al. (2015b), and Rublon et al. (2013) among others. In brief, natural rubber is an amorphous solid at room temperature and small strain. However, as first discovered by Katz in 1925, natural rubber polymer chains arrange in a more ordered state under large strain (Katz 1925), and with the help of wide angle X-ray diffraction (WAXD), it is possible to identify diffraction patterns. SIC is a transition in local regions from amorphous state to one with phases of high local crystallinity; large strain induces crystallization by altering the free energy differential between rubbery and crystalline phases. A sketch of this phenomenon is proposed in Figure 2.1-14, upon elongation of the adjacent polymer chains, crystalline regions are formed, where the elongated chains act as nuclei of crystallites (Tosaka et al. 2004).

From a practical point of view, strain-induced crystallization is of great interest because it improves the mechanical properties of elastomers, especially tensile stiffness at large stretch ratios and fatigue resistance (Lindley 1973; Young 1986; Gent and Zhang 2002; Trabelsi et al. 2003; Saintier et al. 2011; Beurrot-Borgarino et al. 2013; Rublon et al. 2014; Candau et al. 2015a). In general, as shown in Figure 2.1-15, there is a crystallization onset (λ_C) at around $\lambda \approx 4$ upon loading for unfilled natural rubber ; upon unloading, crystallization melting (λ_M) is shifted to around $\lambda \approx 3$. Meanwhile, it is obvious that the stiffness of NR increases significantly after λ_C. Moreover, presence of fillers reduces the thresholds for onset and melting of SIC, with $\lambda_C = 2$ and $\lambda_M = 1.8$ in the given example. Additionally, these thresholds are affected by both strain-rate and temperature (Candau et al. 2015b).

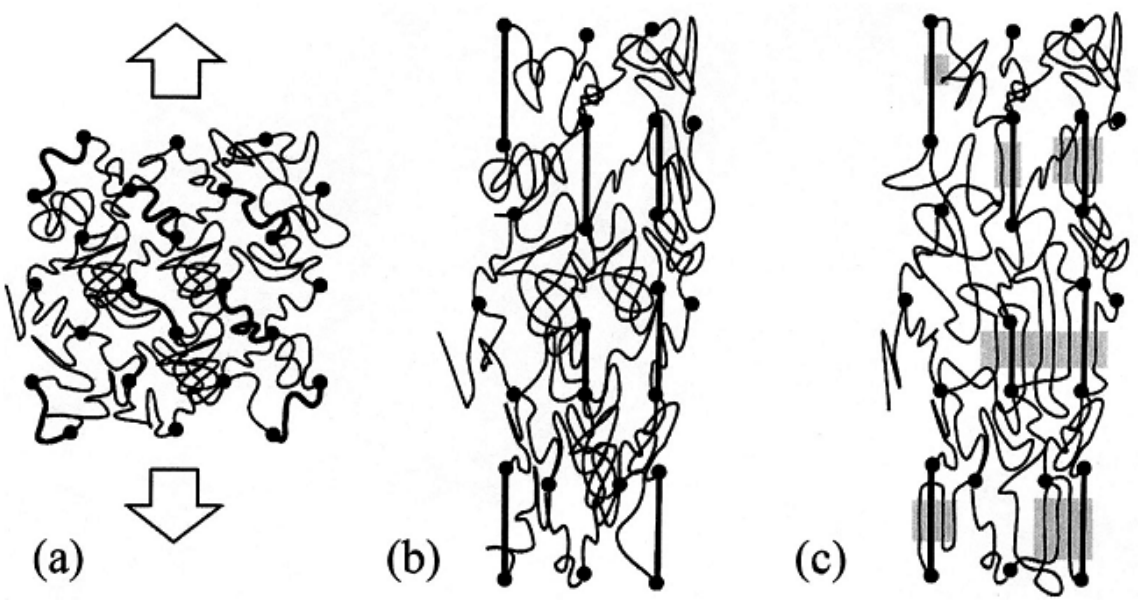

Figure 2.1-14 – Crystallization model of cross-linked NR: a) before deformation; b) after deformation, just before onset of SIC; c) fully stretched chains with crystallites (shaded parts) (Tosaka et al. 2004).

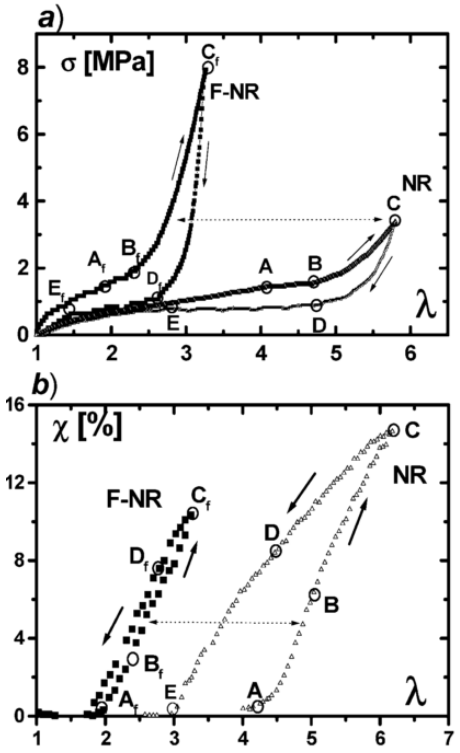

Figure 2.1-15 – a) Stress-strain curves and b) Crystallinity measured during the mechanical cycle of unfilled and filled NR at room temperature (Trabelsi et al. 2003)

.

SIC in HNBR

As mentioned earlier, HNBR, manufactured by hydrogenation of NBR, is said to crystallize under strain; whereas, NBR does not. Sawada (1993) suggests that hydrogenation affects the distribution of acrylonitrile and butadiene and, thus contributes to SIC. In general, HNBR tends to undergo strain-induced crystallization for increasing hydrogenation (Kubo et al. 1987; Sawada 1993). Moreover, ACN content influences the presence of SIC, when it is approximately greater than 35 wt.-% (Obrecht et al. 1986; Braun et al. 1992; Sawada 1993). Severe and White (2000) suggests that at 50 mole percent acrylonitrile, an alternating repeating chemical structure takes place. Presence of SIC has also been reported for lower ACN content: Sawada (1993) reports a general value of less than 30 wt.-%, whereas Obrecht et al. (1986) points the presence of SIC for HNBR with 18.9 wt.-%

In stretched HNBR samples, X-ray diffraction patterns were observed by Obrecht et al. (1986), Braun et al. (1992), Severe and White (2000), among others. The diffraction is caused by the local crystalline structures that are formed due to SIC. Braun et al. (1992) hypothesized that SIC occurs possibly due to polymer chains with a fairly regularly alternating co-monomer sequence (ethylene and acrylonitrile units in almost equal amount), which is inherited from NBR (Braun et al. 1992). Moreover, the authors detected SIC in HNBR (48 wt.-% ACN, hydrogenation percent not specified, not cross-linked) for 100% strain ($\lambda = 2$) in experiments conducted at room temperature. The corresponding patterns occur upon incidence of SIC and the crystallinity increases with stretch as shown in Figure 2.1-16(a). Upon unloading, diffraction peaks are not as intense as at the maximum, however indicating that crystallinity is still present (see Figure 2.1-16(b)). Braun et al. (1992) deter-

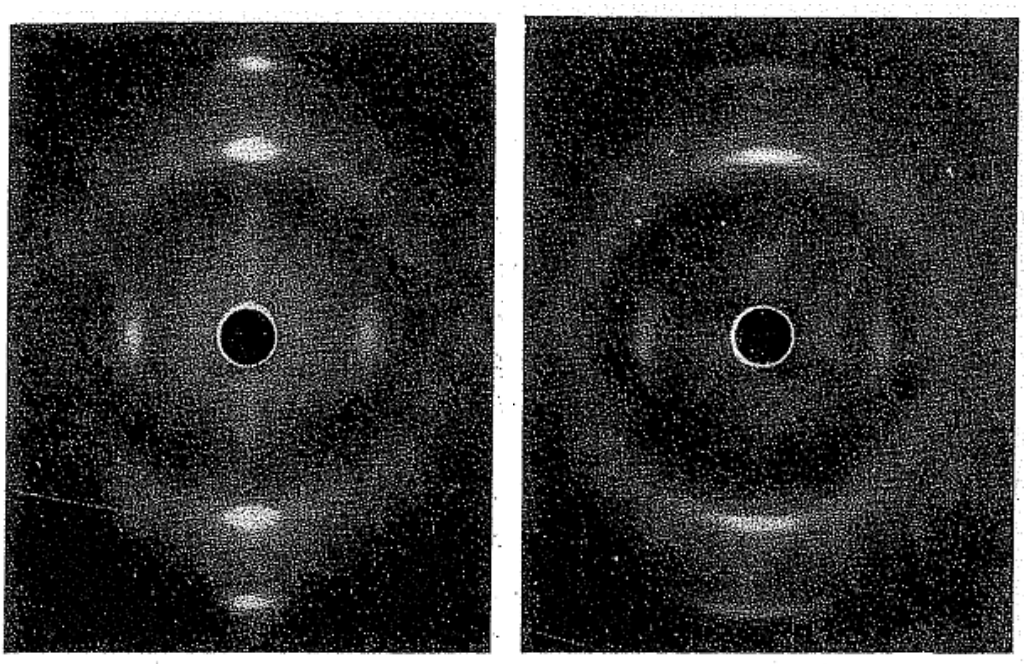

(a) Loading to $\lambda = 700\%$. **(b)** Unloading to $\lambda = 300\%$.

Figure 2.1-16 – X-ray diffraction pattern of HNBR (Braun et al. 1992); horizontal direction of loading.

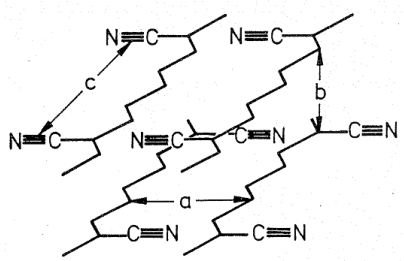

Figure 2.1-17 – Unit cell of HNBR (48 wt.-% ACN) (Braun et al. 1992).

mined the peaks to correspond to three distances defining the unit cell: $a = 0.5$ nm; $b = 0.36$ nm; and $c = 0.77$ nm; Figure 2.1-17 shows the corresponding unit cell of HNBR. In the stretching direction, c corresponds to the extended length of butylene-acrylonitrile. Lengths a and b are perpendicular to the stretching direction with the length a being longer due to the arrangement of the CN group. Similarly, Severe and White (2000) found these distances to be $a = 0.51$ nm, $b = 0.36$ nm, and $c = 0.75$ nm, and also argued that length c can be attributed to the theoretical length of the bonds of a repeating structural unit of HNBR.

Moreover, Braun et al. (1992) investigated the influence of temperature on the incidence of SIC as shown in Figure 2.1-18. Crystallization occurs at relatively small

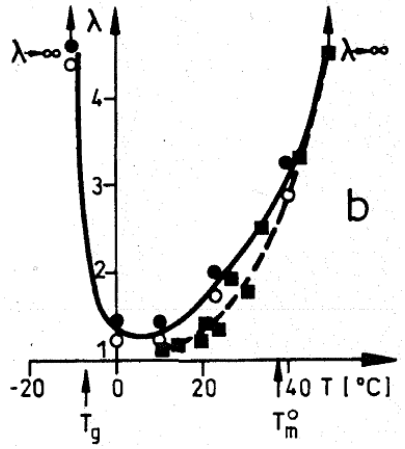

Figure 2.1-18 – Onset of strain-induced crystallization in HNBR (48 wt.-% ACN) measured by □ – cloud point determination, • – small DSC, and ○ – no endotherm DSC (Braun et al. 1992).

stretches between the glass transition temperature, T_g, and room temperature. Below T_g, strain-induced crystallization does not occur and the structure is amorphous due to restricted mobility. At higher temperatures, the material tends to remain amorphous due to excessive flow during deformation and, therefore, it becomes significantly difficult to achieve SIC. Finally, for temperatures greater than 50 °C, SIC does not occur.

Bielinski et al. (1998) studied the effect of iodination treatment on the degree of crystallinity of HNBR (33 wt.-% ACN, 99% hydrogenation). The incidence of SIC is reduced with iodination treatment even though it increases the stiffness of HNBR. In another study, Osaka et al. (2013) investigated the effects of phenol cross-linking on SIC in HNBR (36 wt.-% ACN, 96% hydrogenation). The authors report that,

upon onset of SIC at 650% stretch, the pattern is more apparent in peroxide as compared to phenol cross-linked HNBR. This is attributed to the more spatially homogeneous network structure of phenol cross-linked HNBR, which leads to less oriented chains in the stretching direction as compared with peroxide cross-linked HNBR.

There are no explicit studies on the impact of SIC on the mechanical properties of HNBR. From stress-strain curves one can infer that, due to SIC, HNBR behaves as NR: there is some hysteresis and there is a characteristic plateau region followed by significant modulus increase for very large strain a stress *plateau* (Braun et al. 1992; Sawada 1993). Braun et al. (1992) observed λ_C at ≈ 2 for not cross-linked HNBR with 48 wt.-%. Moreover, during unloading a permanent set is observed which differs from other crystallizing elastomers (Braun et al. 1992). Finally, there is no clear relationship between the stress-strain relationship and the amount of crystallinity during loading or unloading of HNBR as, for example, is shown for natural rubber in Fig. 2.1-15. At most, some studies present X-ray diffraction patterns for one (Obrecht et al. 1986; Severe and White 2000) or two (Braun et al. 1992; Osaka et al. 2013) stretch ratios.

2.2 Presentation of the HNBR Blends of the Study

The HNBR blends have been chosen with the following criteria:

- three blends with different hydrogenation of 91%, 96%, and 99% at a constant 36 wt.-% ACN,
- three blends with different ACN contents of 24 wt.-%, 36 wt.-%, and 44 wt.-% at a constant 96% percent hydrogenation,
- and finally, a composite blend of two HNBR with ACN content of 24 wt.-% and 44 wt.-% for an average of 36 wt.-% ACN.

HNBR with 36wt.-% ACN and 96% hydrogenation is thus chosen as a reference, to which other blends are to be compared.

For clarity, the following naming convention is used throughout this work

$$\mathbf{A}(acn\ \%)\mathbf{H}(hydrogenation\ \%). \tag{2.2-1}$$

In this thesis, to aid with visualization of results, the materials have been color-coded (in some cases, actual colors are darker to allow printing in black and white); same colors are used in presentation of results of different blends, where applicable. These and the corresponding names are summarized in Figure 2.2-1.

	ACN content (wt. - %)			
% Hydrogenation	24	36	44	22 & 44 (avg 36)
>99		A36H99		
96	A24H96	A36H96	A44H96	A44-24
91		A36H91		

Figure 2.2-1 – Naming (and color) convention for investigated HNBR blends.

The formulations of the six blends of HNBR are chosen to closely mimic those of industrial applications; they are presented in Table 2.2-1. All blends are cross-linked with peroxide. They contain 70 phr of N772 carbon black fillers. Moreover, an accelerant (MgO), a plasticizer, and antioxidants (labeled as *Protector 1* and *Protector 2*) are utilized.

Table 2.2-1 – Formulations of investigated HNBR blends.

Naming convention	**A44H96**	**A36H96**	**A24H96**	**A44-24**	**A36H99**	**A36H91**
% hydrogenation	96	96	96	96	>99.5	91
ACN content %	44.2	36.2	24	36 average	36.2	36.2
			Amount (phr)			
HNBR 44/96	100			60		
HNBR 36/96		100				
HNBR 24/96			100	40		
HNBR 36/99					100	
HNBR 36/91						100
Carbon black (N772)	70	70	70	70	70	70
Plasticizer	5	5	5	5	5	5
MgO	3	3	3	3	3	3
Protector 1	1	1	1	1	1	1
Protector 2	1,5	1,5	1,5	1,5	1,5	1,5
Peroxide	7	7	7	7	7	7

2.3 Experimental Methods

2.3.1 Quasi-static tensile response

Uniaxial tensile tests have been performed at *GeM*. These are carried out using an electro-mechanical testing machine *Instron 5584* equipped with a 500 N load cell to characterize true (Cauchy) stress vs. strain response of the six blends. Dumbbell specimens with dimensions shown in Figure 2.3-1 are used for testing. The middle

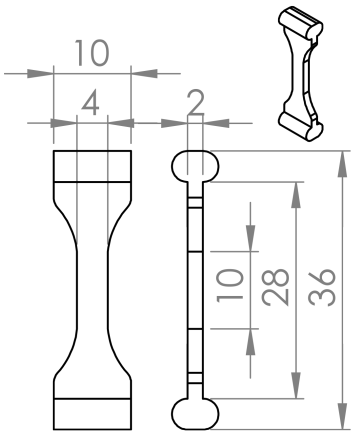

Figure 2.3-1 – Dimensions (in mm) of the dumbbell specimens.

section of the specimen with a gauge length of 10 mm is subjected to uniaxial tensile loading conditions ($\sigma_{22} = \sigma_{33} = 0$, the direction-1 being the tensile direction). Beads at the ends of the specimens are designed to avoid slipping within the machine grips. The specimens are cut using a die from compression molded strips, shown in Figure 2.3-2.

At least 3 specimens are tested for each material. The loading rate is set to 1 mm/s and experiments are conducted until failure. Tests are performed at both room temperature (nominally 23 °C) and 120 °C with a use of a heating chamber. For the latter tests, the specimens are held at temperature inside the heating chamber for 15 min to achieve a uniform temperature inside the specimen.

Both axial and transverse strain are measured with digital image correlation (DIC). Initially for each blend, front and side of the specimen are captured to verify the isotropic response of the material, i.e. $\lambda_2 = \lambda_3$. A strip with a nominal width of 2 mm is painted along the perimeter of the middle section perpendicular to the specimen length, as shown in Figure 2.3-3. A high resolution camera (29 MP) captures photographs of the specimen over the duration of the experiment with a shutter speed ranging from 2 to 4 Hz. A script in *Python* programming language and *OpenCV* library is implemented to measure the dimensions of a polygon in each view as the material deforms (note that for some images such measurements had to be made manually). Finally, stretch ratios for the three orthogonal principal strain directions are recorded. The stretch ratio is generally defined as

$$\lambda = l/l_0, \tag{2.3-1}$$

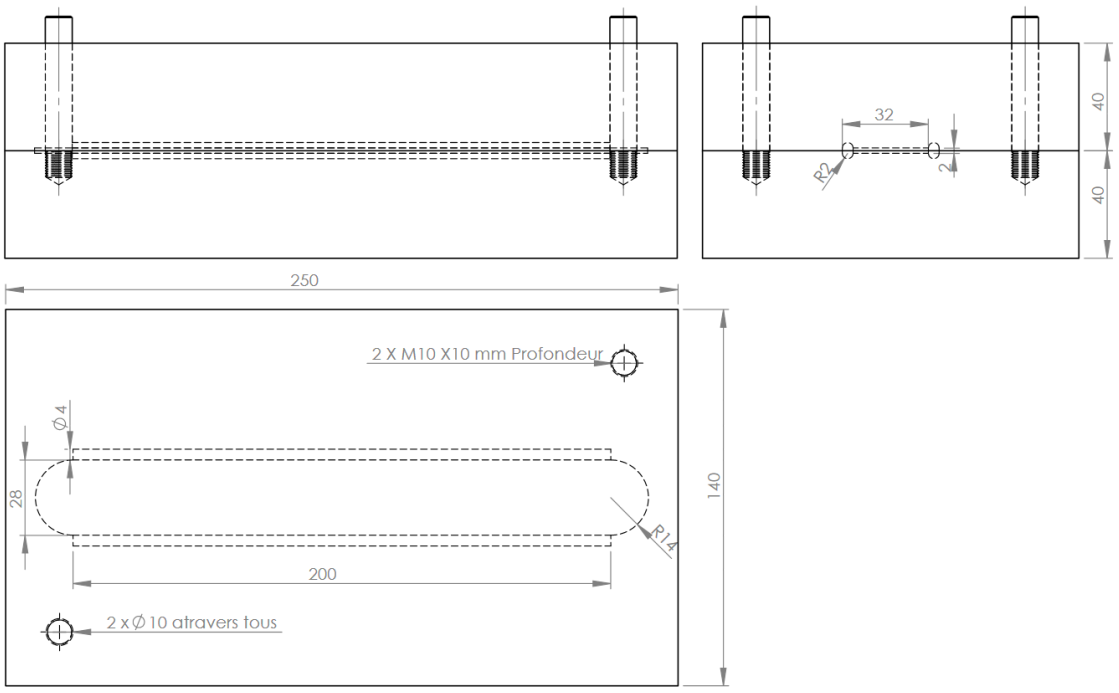

Figure 2.3-2 – Schematic of the mold used to manufacture material strips.

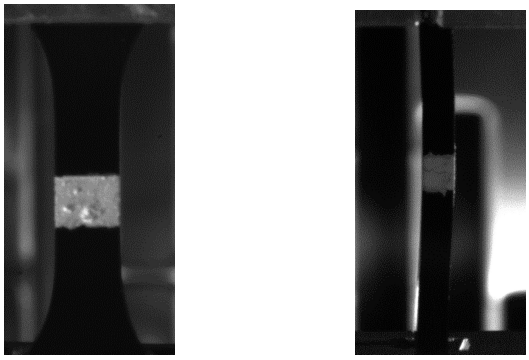

(a) Front view; λ_1 and λ_2 are measured.

(b) Side view; λ_3 is measured.

Figure 2.3-3 – Example of specimen preparation for strain measurements.

where l and l_0 are the deformed and original lengths respectively.

With the measurements of the force F from the load cell, the true (Cauchy) stress is given by

$$\sigma = F/S, \tag{2.3-2}$$

where S is the deformed cross-section area, and is calculated from the initial cross-section area S_0 of the specimen (averaged over three measurements in the gauge length) and the transverse strains (λ_2 and λ_3):

$$S = S_0 \lambda_2 \lambda_3. \tag{2.3-3}$$

2.3.2 Dynamic response

Dynamic Mechanical Analysis

Standard DMA experiments have been carried out at *LRCCP* on *MetraVib DMA+ 450* testing machine in accordance with internal norms of *LRCCP* based on NF EN ISO 6721-1 (2011). Strips with dimensions 4 mm-width and 2 mm-thickness are cut from the same compression molded sheets of the six blends. Pure-shear loading conditions with sinusoidal amplitude of $\pm$ 2 µm are considered. Temperature sweep is performed from $-50\,°C$ to $120\,°C$ and is performed at 3 frequencies - 1, 10, and 100 Hz. Finally, G^* is determined with measurements of G' and G'', and calculation of $\tan(\delta)$. The glass transition temperature (T_g) is determined by locating the peak on the $\tan(\delta)$ vs. temperature curve.

2.3.3 Other mechanical properties

Mullins effect

To investigate the Mullins effect, qualitatively, in the six HNBR blends, the specimen geometry depicted in Fig. 2.3-1 is subjected to cyclic loading conditions. These experiments have been carried out at *GeM*. They are carried out at $120\,°C$. For each blend, a specimen is linearly loaded and unloaded on *Instron 5584* testing machine for 10 cycles from $u = 0$ mm to a displacement corresponding roughly to 60% of the maximum stretch measured during tensile tests outlined in Section 2.3.1. As a remark, the loading ratio or the R-ratio (R) is given by:

$$R_P = \frac{P_{\min}}{P_{\max}}, \tag{2.3-4}$$

where $P_{\min}$ and $P_{\max}$ are the minimum and maximum loading parameters respectively. In present cycling loading, R-ratio in terms of displacement (R_u) equals to zero in terms of displacement ($R_u = u_{\min}/u_{\max}$). For ease of comparison, the true stress endured by each blend is adimensionalized

$$\sigma_{\text{adim}} = \frac{\sigma}{\sigma_{\max\,-\text{cycle 1}}}, \tag{2.3-5}$$

where σ is the measured true stress and $\sigma_{\max\,-\text{cycle 1}}$ is the maximum true stress measured during the first cycle for each blend.

Residual strain and permanent set

These tests have been performed at *GeM*. A sinusoidal displacement is prescribed with the *Instron E10000* electric testing machine, where the maximum displacement is equivalent to $\lambda = 2.15$, $R_u = 0$, and the frequency is set to 1 Hz. The temperature is increased from room temperature (nominally $20\,°C$) and up to $120\,°C$. The length of specimens tested is measured after 1000 cycles, where *residual strain* is the specimen length measured right after unloading and *permanent set* is the specimen length measured after 1 week, *i.e.* the recovery of the material.

To measure global residual strain (ϵ_{res}), first, the machine is instructed to stop the action of the actuator as zero force measurement is reached during unloading of the 1000^{th} cycle. Then, the displacement of the actuator (u_a) is recorded. The specimen length upon unloading is then considered to be

$$L_{t=0} = L_0 + u_a, \tag{2.3-6}$$

with reference specimen length (L_0),actuator displacement (u_a), and index $t = 0$ indicating measurement made right after unloading. Thus, the global residual strain is

$$\epsilon_{res} = \frac{L_{t=0} - L_0}{L_0} = \frac{u_a}{L_0} \tag{2.3-7}$$

An average of at least 3 specimens is recorded.

Measurement of global permanent strain (ϵ_{p}) is done with a caliper after 1 week of recovery at room temperature.

Hardness

Shore-A (indentation) hardness is measured with table mounted instruments at room temperature at *LRCCP*. Tests are carried out according to ISO 7619-1 (2010) standard on "Determination of indentation hardness". For a duration of 3 s, a frustum cone (inner radius - 0.79 mm, outer diameter - 1.25 mm, angle - 35°) on an end of steel rod that makes an indentation on a 2 mm sheet of each blend. Five measurements are performed at intervals of at least 6 mm and an average is recorded.

2.3.4 Strain-induced crystallization

In-situ tensile testing

In order to precisely determine the relationship between strain-induced crystallization (SIC), stretch ratio, and stress, *in-situ* tensile tests are performed simultaneously with capturing of X-ray diffraction patterns.

Since it appears that ACN content plays an important role in presence of SIC, three blends with different ACN content (A44H96, A36H96, and A24H96) are considered. Additionally, two new blends, UF44 and UF36, specifically prepared for these experiments are introduced; they are identical to A44H96 and A36H96 respectively, except that they do not contain carbon black fillers. These unfilled HNBR blends are chosen to better isolate presence of SIC by eliminating the dispersive effects of CB on X-ray diffraction patterns.

These experiments were performed in collaboration with P.-A. Albouy at the *LPS-Orsay* laboratory of the Paris-Sud university. As such, the experimental setup and data analysis is closely based on Albouy et al. (2012), Vieyres et al. (2013), Zaghdoudi et al. (2015), and Imbernon et al. (2016). The rotating anode X-ray generator has a focus size of $0.2 \times 0.2\,\text{mm}^2$, 40 kV, and 40 mA. Its copper anode K_a radiation of 0.1542 nm is selected by a doubly curved graphite monochromator. Two tensile actuators are mounted next to the X-ray generator so that each specimen

is located at the focal point to ensure maximum intensity in the diffraction pattern. The movement of actuators is symmetric, ensuring that the focus is always on the same area of the specimen. A load cell, attached to one of the actuators, measures the applied force. High temperature tests are performed with a use of a poly-carbonate enclosure, equipped with a Kapton window for X-ray exit. The diffraction patterns are recorded with an indirect illumination CDD sensor and an exposure time ranging from 4 to 10 s. Additionally, a camera is used to track and measure the transverse strain of the specimen. A photograph of the experimental setup is shown in Figure 2.3-4.

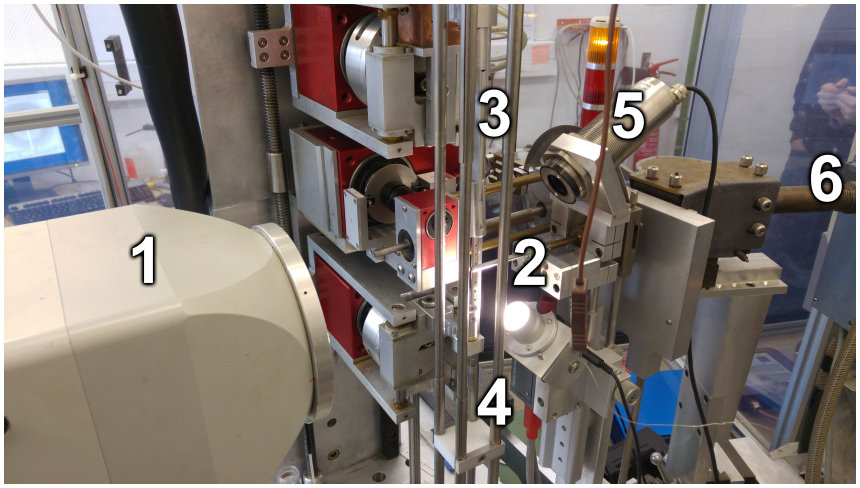

Figure 2.3-4 – Schematic of the experimental setup, where: 1) CDD sensor, 2) X-ray exit, 3) upper actuator, 4) lower actuator, 5) camera, 6) X-ray generator.

The same specimens used for tensile testing (Fig. 2.3-1) are utilized. They are stretched at 20 mm/s up to 160 mm and then fully unloaded. Tests are carried out at room temperature (21 °C) and at 90 °C for carbon black filled blends.

Data processing

As mentioned earlier, the analysis of captured diffraction patterns is carried out on the basis of the method presented in Albouy et al. (2012), Vieyres et al. (2013), and Zaghdoudi et al. (2015). This data analysis has been slightly modified and implemented in a standalone *Python* script with the use of *NumPy* package; the details are presented in Section 2.5.

As a starting point in terms of raw data, a diffraction pattern, shown in Figure 2.3-5(a) (and its geometric schematic representation shown in Figure 2.3-5(b)), occurs due to the anisotropy induced by strain-induced crystallization. Intensity at each pixel is directly proportional to the number of electrons for crystalline and amorphous phases (not specific to specimen geometry and to orientation of both phases) (Kakudo and Kasai 1972). Thus, an angular scan around the azimuthal angle ϕ within the amorphous ring (indicated by the blue region highlighted in Fig. 2.3-5(a)) is carried out to obtain a curve of diffracted intensities as a function of angle ϕ (Wang and Yeh 1978). As such, each peak is specific to a crystalline plane (*hkl* index [200]) and the remaining background represents the amorphous contribution. This

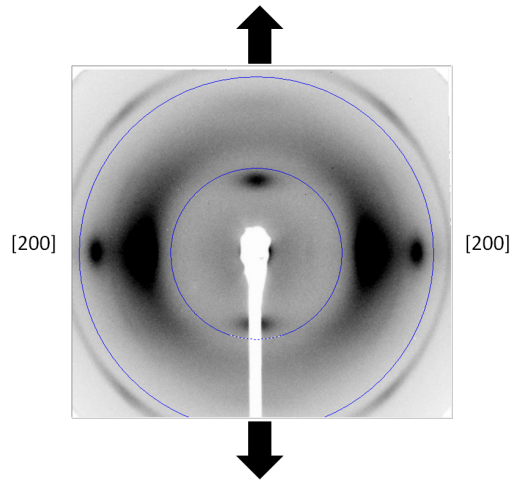

(a) Representative diffraction pattern in HNBR and the region used for an angular scan with crystallographic indexation; arrows indicate stretching direction.

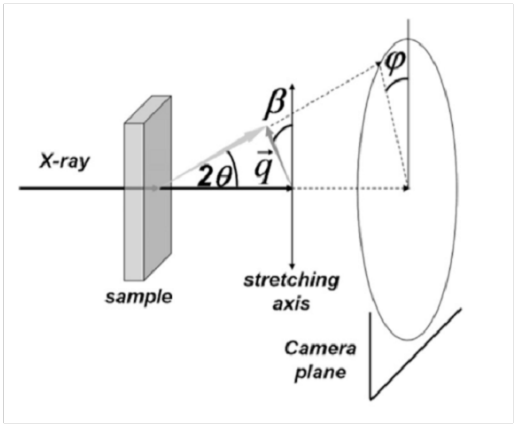

(b) Schematic representation of the scattering geometry; taken from Albouy et al. (2014).

Figure 2.3-5 – Example of raw data and schematic representation of X-ray diffraction patterns.

amorphous contribution includes scattering due to presence of air which is finally subtracted from the intensity curve by recording a reference spectra without specimen. Moreover, since only a specific region of the diffraction pattern is selected, this type of analysis produces results that are indicative and not absolute (Albouy et al. 2012).

The peak deconvolution is performed, first, by adjusting the amorphous contribution with

$$I_{\text{am}}(\phi) = A + B\cos^2(\phi) + C\cos^4(\phi), \tag{2.3-8}$$

and, second, by modelling the crystalline contribution by the Pearson VII function

$$I_{\text{crys}}(\phi) = I_{\max}\frac{w^{2\mu}}{\left[w^2 + \left(2^{\frac{1}{\mu}} - 1\right)(\phi - \phi_0)^2\right]^{\mu}}, \tag{2.3-9}$$

where $I_{\max}$ is the intensity, w is a value affecting the width of a peak, and μ determines the shape of the distribution ($\mu = 1$ corresponds to a Lorentzian distribution and $\mu > 10$ leads to an approximated Gaussian one). Thus, the total intensity is

$$I_{\text{tot}}(\phi) = I_{\text{am}}(\phi) + I_{\text{crys}}(\phi). \tag{2.3-10}$$

Finally, the χ_C is defined as

$$\chi_C = \frac{\int_0^{2\pi} I_{\text{crys}}(\phi)d\phi}{\int_0^{2\pi} I_{\text{crys}}(\phi)d\phi + \int_0^{2\pi} I_{\text{am}}(\phi)d\phi}. \tag{2.3-11}$$

2.4 Mechanical Behavior of Different Blends of HNBR

2.4.1 Quasi-static tensile behavior

At room temperature

Uniaxial stress-strain responses of blends are in shown in Figure 2.4-1.

The relative dispersion in each measurement for each test is as expected for many reasons, among which are imprecision in specimen measurement or calibration of equipment, the presence of flaws/defects in some specimens, *etc.* Responses of blends A44H96 (Figure 2.4-1(a)), **A36H96** (Figure 2.4-1(c)), and A36H91 (Figure 2.4-1(f)) have small variance for roughly $\sigma < 70$ MPa, but tend to diverge for higher stresses. On the other hand, responses of remaining blends, A24H96 (Figure 2.4-1(b)), A44-24 (Figure 2.4-1(d)), and A36H99 ((Figure 2.4-1(e)) have slight variance throughout the whole stress range. Overall, it is acceptable to use the average curves (with error bars) to compare the blends.

Both stretch and stress at break (λ_f and σ_f respectively), as well as tensile modulus at 10 MPa $E_{10\text{ MPa}}$ (taken as a numerical derivative) are summarized in Table 2.4-1. In terms of overall stress-strain response, one can observe a point of inflection

Table 2.4-1 – Stress and strain at break, and tensile moduli of the six HNBR blends at room temperature.

Blend	λ_f	σ_f (MPa)	E_{10MPa} (MPa)
A36H96	$5.21^{+0.29}_{-0.24}$	$93.66^{+11.35}_{-4.44}$	20.41
A44H96	$5.28^{+0.10}_{-0.21}$	$100.45^{+6.90}_{-4.85}$	21.77
A24H96	$5.02^{+0.11}_{-0.16}$	$82.21^{+8.01}_{-4.41}$	19.31
A36H99	$5.75^{+0.21}_{-0.39}$	$91.57^{+4.50}_{-9.96}$	18.05
A36H91	$5.05^{+0.10}_{-0.11}$	$98.61^{+7.20}_{-2.68}$	20.99
A44-24	$4.78^{+0.14}_{-0.16}$	$87.53^{+4.10}_{-5.03}$	22.80

(change in concavity) in all stress-strain responses as the stretch ratio approaches λ_f. Classically, it points to presence of plasticity and perhaps can be attributed to changes in specimen geometry in the wide sections near the grips, whereas the middle section (the narrowest) experiences the largest stress. As a remark, all specimens failures occurred in this middle section.

Now, after the general introduction of results, one can discuss the effects of the formulation. First, the effect of ACN content on tensile response is shown in Figure 2.4-2. There is a clear trend: as the ACN content increases, all three properties increase (λ_f, σ_f, and $E_{10\text{ MPa}}$). However, the difference between **A36H96** and A44H96 is not so significant as there is some overlap between some of the measured stress-strain responses. In general, these results agree in trend and in magnitude with the results obtained by Obrecht et al. (1986) shown in Fig. 2.1-6(b).

Second, the effect of percent hydrogenation is presented in Figure 2.4-3. Here, the

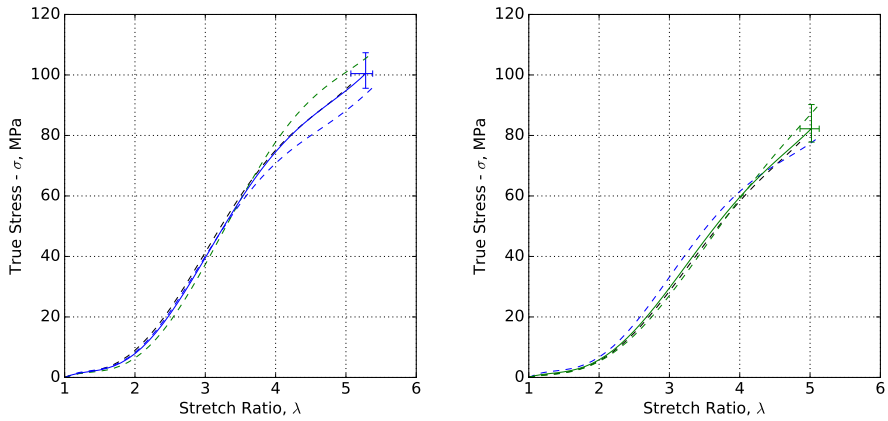

(a) A44H96.

(b) A24H96.

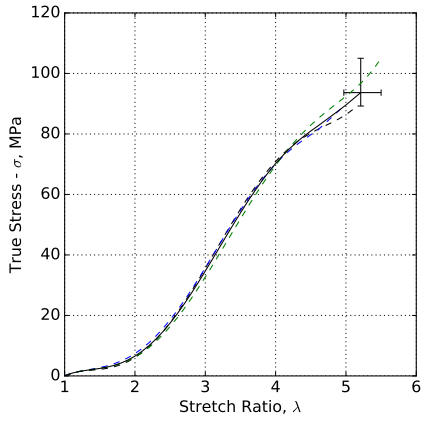

(c) A36H96.

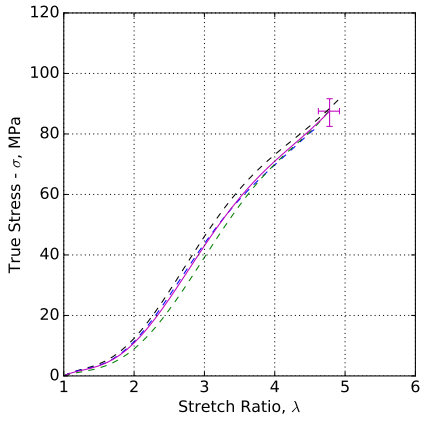

(d) A44-24.

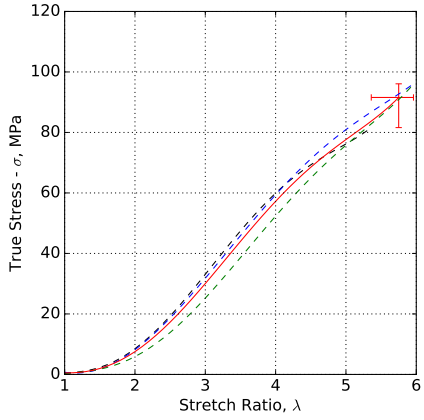

(e) A36H99.

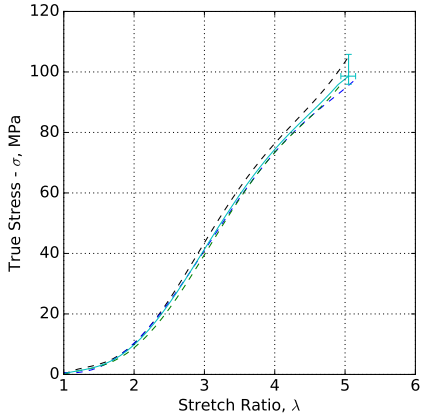

(f) A36H91.

Figure 2.4-1 – Stress-strain response of six HNBR blends at room temperature; dashed line represent individual tests and solid - the corresponding average. End points correspond to the maximum and minimum intervals for stress and stretch at break

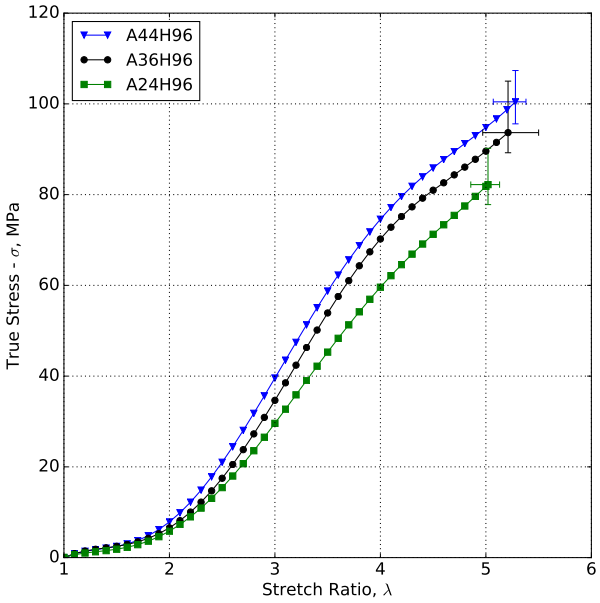

Figure 2.4-2 – Effect of ACN content on stress-strain response of HNBR at room temperature.

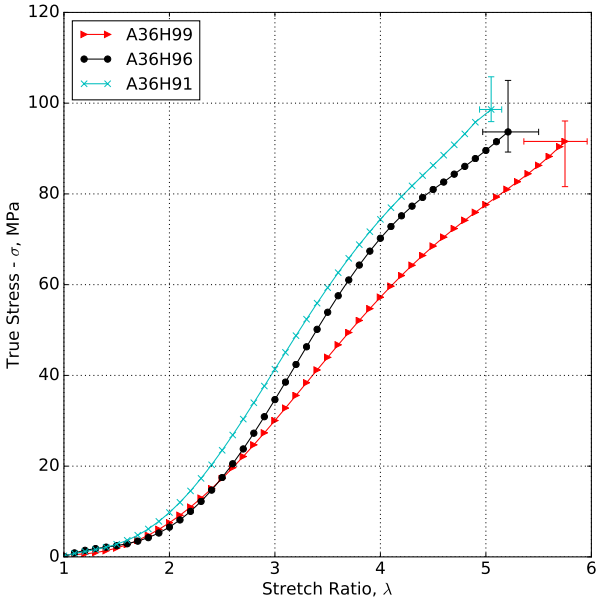

Figure 2.4-3 – Effect of hydrogenation on stress-strain response of HNBR at room temperature.

trend is also clear: HNBR becomes more "ductile" as percent hydrogenation increases, since λ_f increases while both σ_f and $E_{10\,\mathrm{MPa}}$ decrease. It is interesting to refer to Fig. 2.1-6(a) (Sawada 1993), who reported that with increasing hydrogenation from 88% and to 92%, the tensile strength and modulus of unfilled HNBR increase and stretch at break decreases. Unfortunately, there are no such studies for

filled HNBR, however it could be assumed that the "brittle" response of HNBR has a maximum around 91% to 92% hydrogenation.

Finally, the effect of combining two HNBR blends of 24 wt.-% and 44 wt.-% ACN content for an average of 36 wt.-% is shown in Figure 2.4-4 with comparison to **A36H96** and both base blends - A44H96 and A24H96. It is interesting to note

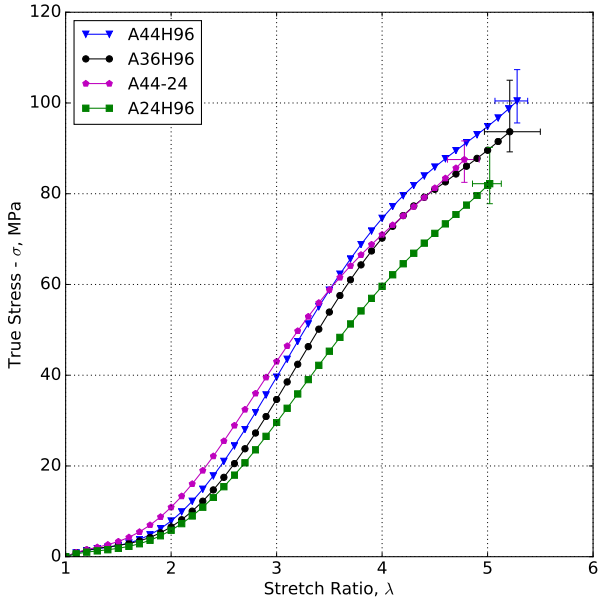

Figure 2.4-4 – Effect of blending of 24 wt.-% and 44 wt.-% ACN HNBR blends for an average of 36 wt.-% on stress-strain response of HNBR at room temperature.

that A44-24 has the highest stiffness of all blends at 10 MPa and lowest strain at break. The stress at break is roughly in-between A44H96 and A24H96, but lower of **A36H96**. Except for higher stiffness, it is not clear what advantages are brought by blending of these two formulations.

At high temperature

A second set of experiments is carried out at 120 °C to investigate the effects of temperature (without thermal aging). Similar to Fig. 2.4-1, Figure 2.4-5 shows the stress-strain responses of the six blends. Both stress and strain at break, as well as the tensile modulus at 10 MPa are show in Table 2.4-2. As expected, there is a significant effect of temperature as evident by decreases in tensile modulus, elongation and stress at break for all blends. There is no publicly available literature on the temperature effects, but one can make a comparison of values of each blend with respect to room temperature by calculating the percent difference with respect to room temperature

$$\Delta_{\%} = 100\% * \frac{V_{120} - V_{\text{room}}}{V_{\text{room}}}, \tag{2.4-1}$$

where V stands for any value; for stretch ratio, as its value starts from 1, $V^{\lambda} = \lambda - 1$. Results are summarized in Table 2.4-3.

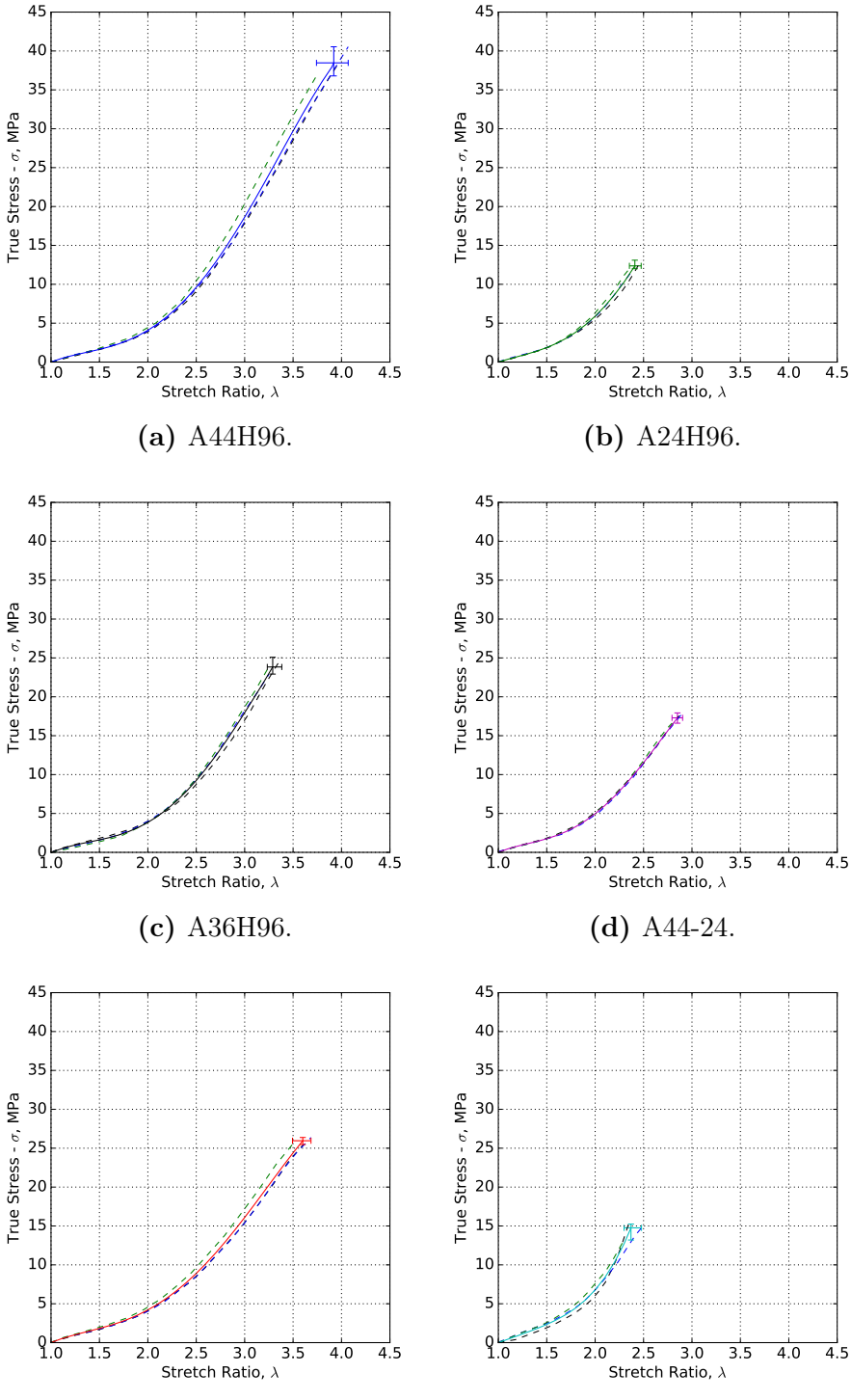

(a) A44H96. **(b)** A24H96.

(c) A36H96. **(d)** A44-24.

(e) A36H99. **(f)** A36H91.

Figure 2.4-5 – Stress-strain response of six HNBR blends at 120 °C; dashed line represent individual tests and solid - the corresponding average.

Table 2.4-2 – Stress and strain at break, and tensile moduli of the six HNBR blends at 120 °C.

Blend	λ_f	σ_f (MPa)	E_{10MPa} (MPa)
A36H96	$3.29^{+0.09}_{-0.06}$	$23.84^{+1.25}_{-0.92}$	15.70
A44H96	$3.92^{+0.15}_{-0.18}$	$38.47^{+2.07}_{-1.68}$	15.45
A24H96	$2.41^{+0.07}_{-0.06}$	$12.37^{+0.73}_{-0.37}$	18.79
A36H99	$3.60^{+0.09}_{-0.11}$	$25.96^{+0.42}_{-0.49}$	13.11
A36H91	$2.37^{+0.11}_{-0.07}$	$14.76^{+0.49}_{-1.56}$	24.20
A44-24	$2.85^{+0.05}_{-0.06}$	$17.29^{+0.64}_{-0.69}$	15.47

Table 2.4-3 – Percent difference of stress and strain at break, and tensile moduli of the six HNBR blends at 120 °C with respect to room temperature.

	$\Delta_{\%}$ (%)		
Blend	λ_f	σ_f (MPa)	E_{10MPa} (MPa)
A36H96	-44.61%	-74.55%	-23.06%
A44H96	-31.78%	-61.70%	-29.02%
A24H96	-64.93%	-84.95%	-2.69%
A36H99	-45.26%	-71.65%	-27.39%
A36H91	-66.17%	-85.03%	15.28%
A44-24	-51.06%	-80.25%	-32.17%

Furthermore, Figure 2.4-6 shows the effect of temperature for HNBR with different ACN content. The trend remains the same for stretch and stress at break, where both increase with ACN content. However, the tensile modulus of A24H96 remains almost the same at 120 °C, while those of **A36H96** and A44H96 decrease by 23% and 29% respectively. A24H96 has the highest tensile modulus, but also the greatest loss of values for stretch and strain at break, which points to the "embrittlement" of the material. This is perhaps indicative of the fact that lower ACN (< 25 wt.-% content) HNBR are mostly used where better low temperature performance is required (Hayashi et al. 1991; Keller 2012; Lanxess n.d.[b]). Overall, it can be said that higher the ACN content, the better are the mechanical properties at high temperatures.

Similarly, the overall trends remain the same for different percentages of hydrogenation in HNBR as shown in Figure 2.4-7. It is clear that additional hydrogenation, which improves heat resistance, is beneficial for retaining of mechanical properties. A36H91, the blend with the lowest hydrogenation, is very sensitive to temperature: it has around 66% drop in stretch at break and an 85% drop in stress at break. At the same time, it is the only blend with increasing modulus at high temperature (by around 15%), thus making it the most "brittle" material at 120 °C. On the other hand, **A36H96** and A36H99 have realitvely similar moduli at 120 °C for low stretch ratios.

Finally, the overall trends also remain similar for composite of 24 wt.-% and 44 wt.-% ACN HNBR blends for an average of 36 wt.-% of HNBR as shown in Figure 2.4-8. In terms of high temperature performance, the composite of A24H96 and A44H96 is roughly in between the two blends. With regards to the loss of properties (Tab. 2.4-3), stress and stretch at break losses are in the same order of magnitude as those of A24H96; on the other hand, the decrease in modulus is the highest of all tested

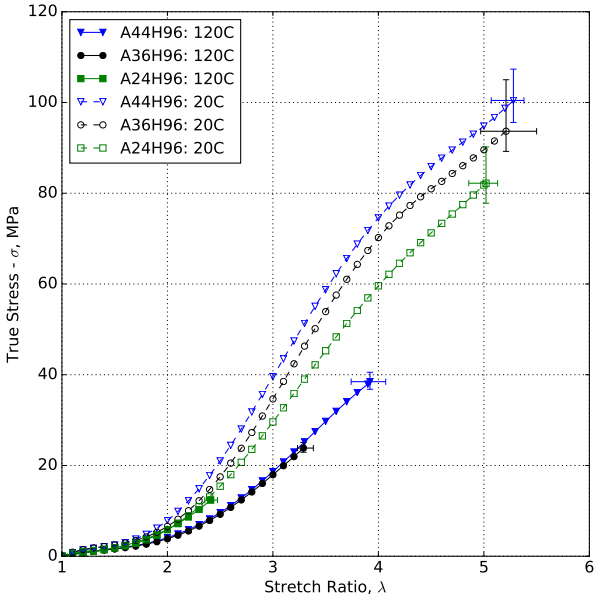

Figure 2.4-6 – Effect of temperature and ACN content on stress-strain response of HNBR.

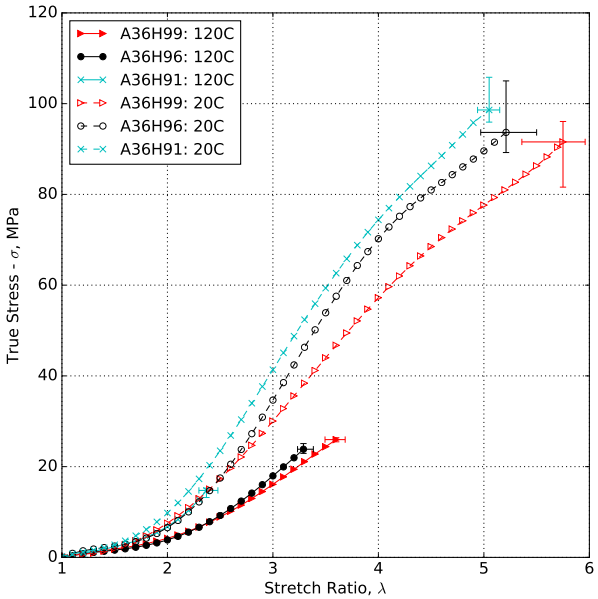

Figure 2.4-7 – Effect of temperature and percent hydrogenation on stress-strain response of HNBR.

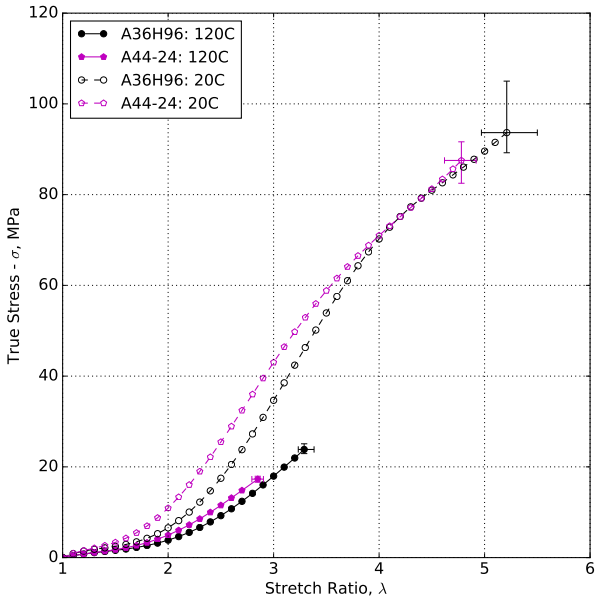

Figure 2.4-8 – Effect of temperature of composite with 24 wt.-% and 44 wt.-% ACN for an average of 36 wt.-% on stress-strain response of HNBR.

blends. To conclude: in terms of tensile response, this composite does not bring many advantages for use at high temperatures.

2.4.2 Dynamic behavior

DMA results with varying frequency for different amounts of ACN content, percent hydrogenation, and that of the composite A44-24 are shown in Figures 2.4-9, 2.4-10, and 2.4-11, respectively. For all blends, one can identify three phases: glassy for the lowest temperatures, rubbery for the highest temperatures, and the transition from glassy to rubbery states. In this last phase, starting from around $-50\,°C$ to around $10\,°C$, a significant drop in the storage modulus is observed as well as peaks in the loss modulus and $tan(\delta)$. As temperature increases up to $120\,°C$, both moduli continuously decrease almost at the same rate for all six blends such that $tan(\delta)$ appears more or less constant. As expected, there is a right-shift as the frequency is increased from 1 Hz to 10 Hz and to 100 Hz; similarly, an increase in the peaks of loss moduli is observed (and therefore in $tan(\delta)$).

Investigating the effect of ACN content specifically, Fig. 2.4-9 shows that the difference in relative stiffness (in the small strain range) of the blends is large in the glassy region and the difference is less pronounced in the rubbery region. Overall, ACN content has a greater effect on dynamic characteristics of HNBR as compared to varying percent hydrogenation as shown in Fig. 2.4-10. Moreover, for composite of 24 wt.-% and 44 wt.-% ACN for an average of 36 wt.-%, the $tan(\delta)$ curve does not exhibit a clear peak (it is broad with several points of inflection), but appears to admit characteristics of those of A24H96 and A44H96. Thus, this is indicative of somewhat a non-homogeneous mixing of the two ACN blends at the microscopic

scale (Thavamani and Bhowmick 1992).

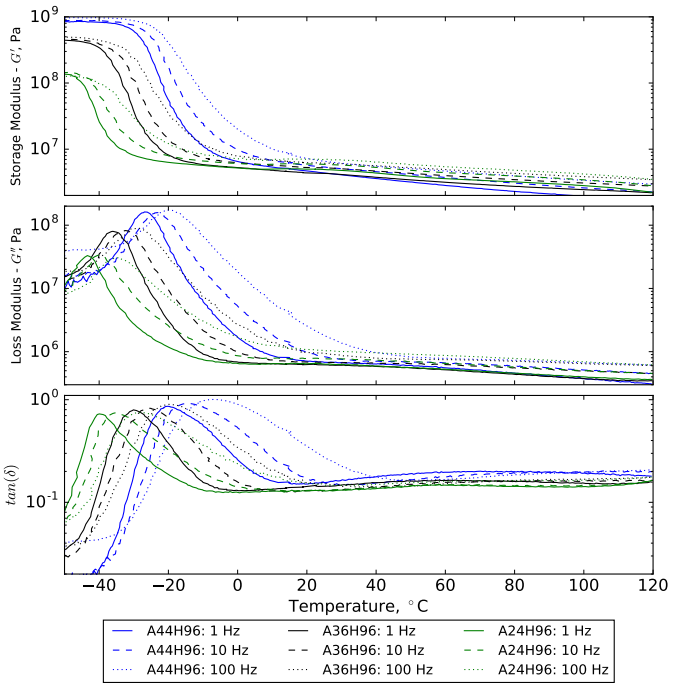

Figure 2.4-9 – Effect of ACN content on DMA results: storage and loss moduli, and tan(δ).

Finally, the T_g is extracted from the peaks of tan(δ) curves of each blend and summarized in Figure 2.4-12. For all blends, higher frequency increases T_g. Figure 2.4-12(a) shows that the difference in T_g with varying ACN content is around 10 °C and increases with greater ACN content. These findings closely match the results of Sawada (1993) (see Fig. 2.1-5). A24H96 has the lowest T_g, which is again - similar to the conclusions of quasi-static tests of the previous section - indicative of the low temperature applications of low ACN content HNBR blends. It should be noted that, as testing or operational temperature decreases towards T_g and enters a rubbery-to-glassy transition temperature region, the mechanical behavior is highly viscous as indicated by the loss moduli in Figs. 2.4-9-2.4-11.

In terms of percent hydrogenation, there is no clear trend as shown in Figure 2.4-12(c). At each frequency, A36H96 has the lowest glass transition temperature followed by A36H91 and then A36H99. In fact, these results also agree with those obtained by Sawada (1993), in which for HNBR blends with ACN content less that 41 wt.-%, there are minima close to full hydrogenation followed by an increase for fully hydrogenated HNBR.

As for the composite HNBR blend, T_g of A44-24 is closer to A44H96 than to A24H96, which could be indicative of the fact that it contains 60 phr of 44 wt.-% ACN grade of HNBR with respect to 40 phr of 24 wt.-% grade.

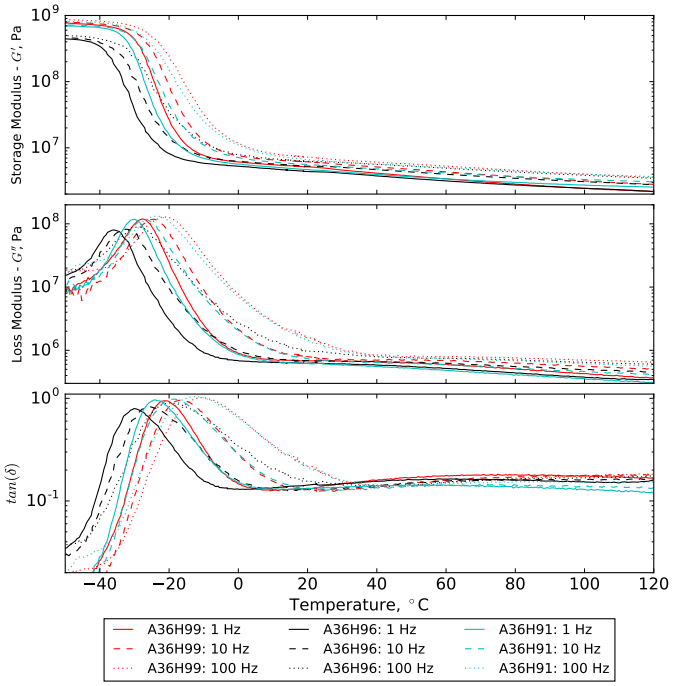

Figure 2.4-10 – Effect of hydrogenation on DMA on DMA results: storage and loss moduli, and tan(δ).

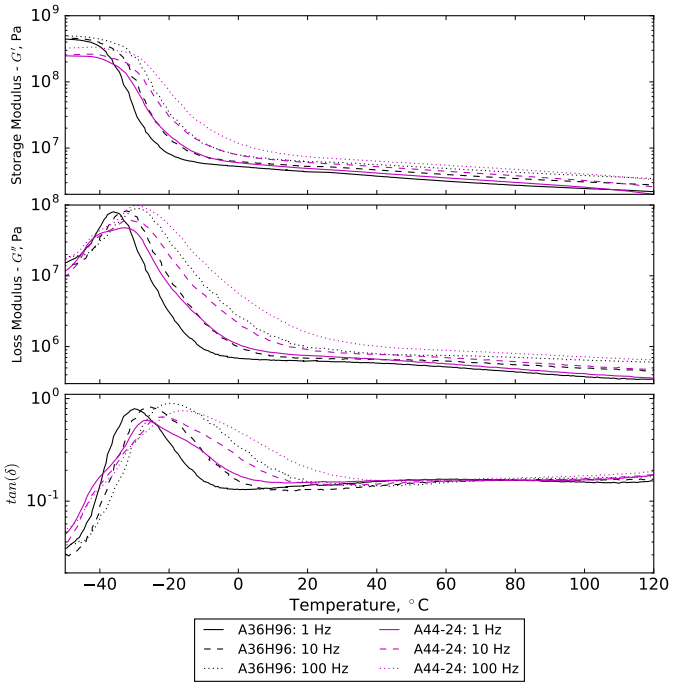

Figure 2.4-11 – DMA results of composite A44-24 of HNBR; storage and loss moduli, and tan(δ).

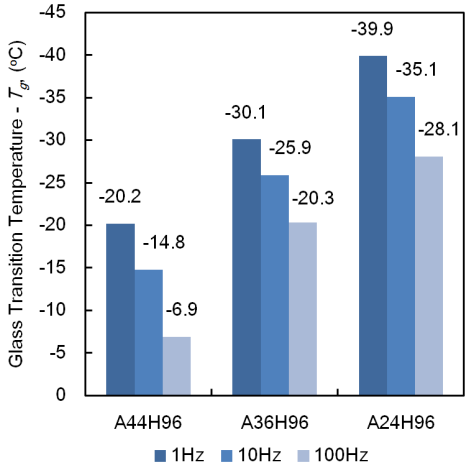

(a) Effect of ACN content.

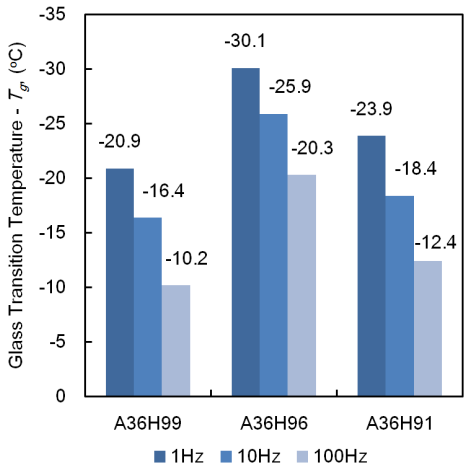

(b) Effect of hydrogenation.

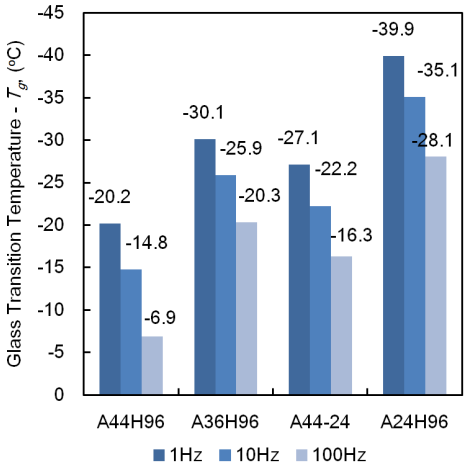

(c) Composite A44-24.

Figure 2.4-12 – Glass transition temperature (T_g) of HNBR blends measured by tan(δ) peaks with effects of frequency.

2.4.3 Other mechanical properties

Investigation of the Mullins effect

A qualitative investigation of the Mullins effect is carried out and the results are shown in Figure 2.4-13. All blends exhibit stress-softening over repeated loading. The cyclic loading is also characterized by the presence of hysteresis, which is the largest during the first cycle. The relative softening is presented in Table 2.4-4. The corresponding results can be separated into two groups. One group contains

Table 2.4-4 – Stress softening due to the Mullins effect for six blends of HNBR at 120 °C.

Blend	$\sigma_{\textbf{cycle 2}}/\sigma_{\max-\textbf{cycle 1}}$	$\sigma_{\textbf{cycle 10}}/\sigma_{\max-\textbf{cycle 1}}$
A36H96	88%	65%
A44H96	71%	39%
A24H96	90%	71%
A36H99	81%	61%
A36H91	99%	88%
A44-24	96%	90%

blends A24H96, A36H91, and A44-24, which have "brittle" behavior characterized by relatively small stress and stretch at break, and high modulus. For these blends, the drop in stiffness is not significant. The second group contains the remaining blends ranked by increasing stress-softening: **A36H96**, A36H99, and A44H96. At this point, it is important to note that the prescribed stretch ratio (around 60% of λ_f) differs for each blend and, more generally, for the two groups: it is up to $\lambda \approx 2.1$ for the first group, and the blends of the second group are stretched from $\lambda \approx 2.4$ up to $\lambda \approx 3.3$ for A44H96, which in turn exhibits the largest stress-softening. The exists a certain dependence of the stress-softening observed during the Mullins effect on the applied stretch; stress-softening increases with increased stretch (Diani et al. 2009). Perhaps then, with present six blends, one can consider just the effect of strain. Considering that all six blends are equally filled with 70 phr of carbon black (as there is consensus that presence of it - or other fillers - contributes to presence of the Mullins effect), an assumption is made that all blends theoretically exhibit similar amount of stress-softening. Hence, the values presented in Tab. 2.4-4 are plotted with respect to the maximum prescribed stretch ratio for all blends in Figure 2.4-14. There is a linear relationship between the maximum prescribed stretch and the amount of softening observed after 2 and 10 cycles; there is a relative goodness of fit with r^2= 0.96 and r^2 = 0.92 after 2 and 10 cycles respectively. A similar result has been observed by Mars and Fatemi (2004b).

Moreover, upon unloading, the stretch ratio (λ) does not equal to one for all blends, *i.e.* there are specimens that do not return to the reference state. This is usually referred to as the *residual strain* and it increases with each cycle, the largest increase corresponding to the first cycle for all blends. Furthermore, the magnitude of the residual strain does not appear to correlate to the amount of stress-softening. This phenomenon, along with permanent set, are further discussed in Section 2.4.3.

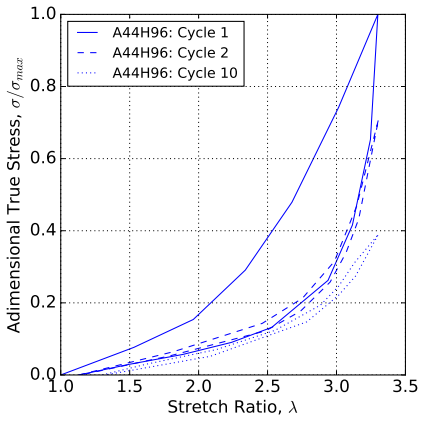

(a) A44H96.

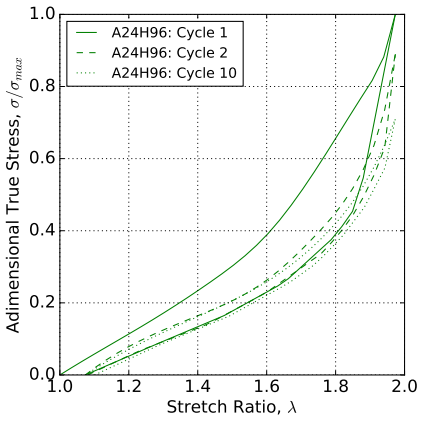

(b) A24H96.

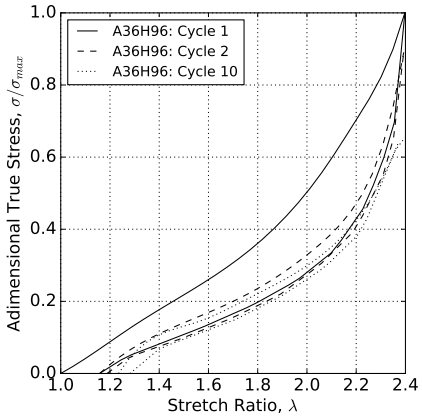

(c) A36H96.

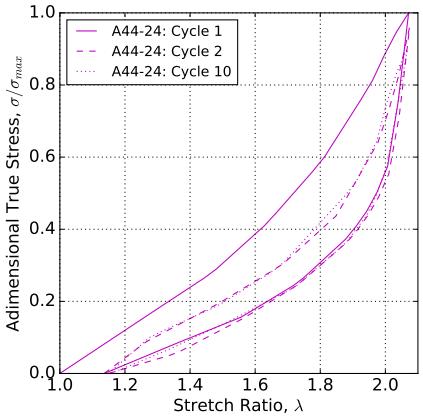

(d) A44-24.

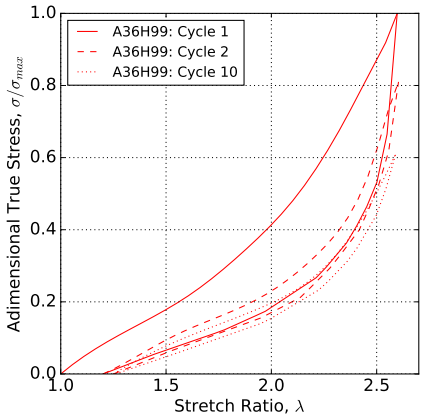

(e) A36H99.

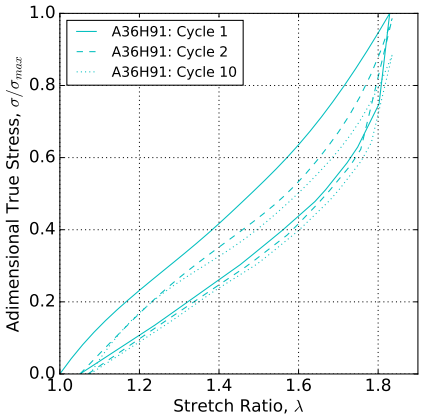

(f) A36H91.

Figure 2.4-13 – Cyclic loading of six HNBR blends at 120 °C. Curves correspond to the 1st, 2nd, and 10th cycles.

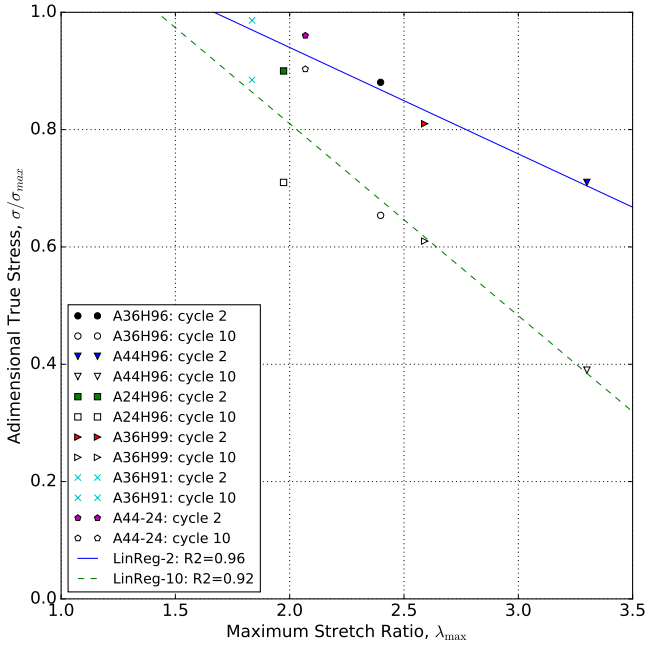

Figure 2.4-14 – Relationship between the Mullins effect and maximum prescribed stretch ratio.

Residual strain and permanent set

As mentioned earlier, residual strain (ϵ_{res}) is a measurement of the global strain, as opposed to the local given by λ; it is calculated as

$$\epsilon_{\text{res}} = \frac{L_{t=0} - L_0}{L_0}, \tag{2.4-2}$$

where $L_{t=0}$ is the specimen length measured immediately after the unloading (there is no relaxation time) and L_0 is the original specimen length (36 mm nominally). On the other hand, permanent set (ϵ_{p}) is

$$\epsilon_{\text{p}} = \frac{L_{t=1\text{ w}} - L_0}{L_0}, \tag{2.4-3}$$

where $L_{t=1\text{ w}}$ is the specimen length measured after one week (recovery of the material).

Results for residual strain are presented in Figure 2.4-15. The presence of residual strain is highly dependent on temperature irrespective of the HNBR formulation; as temperature increases, the residual strain decreases. At room temperature, it is significant on average around 40% of global strain. For all temperatures during testing, one could observe this change in length of the specimens, where buckling occurred at the minimum machine actuator displacement. It is important to note that small compressive forces are recorded due to the use of thin specimens, whereas in massive specimens, such behavior would results in significant compressive forces. Finally, the largest drop in residual strain is observed for all blends except A24H96 from 100 °C to 120 °C.

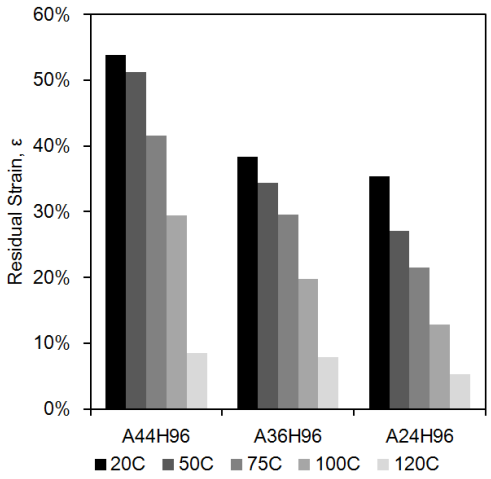

(a) Effect of ACN content.

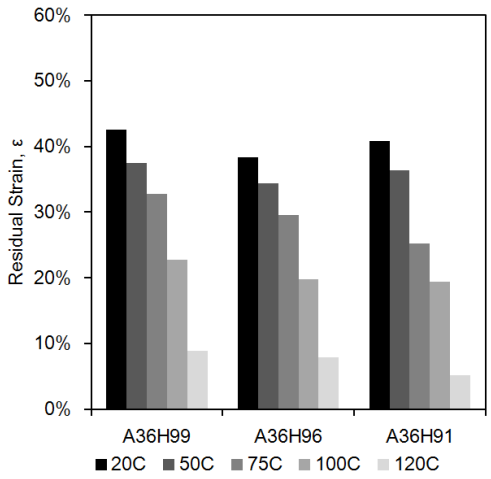

(b) Effect of hydrogenation.

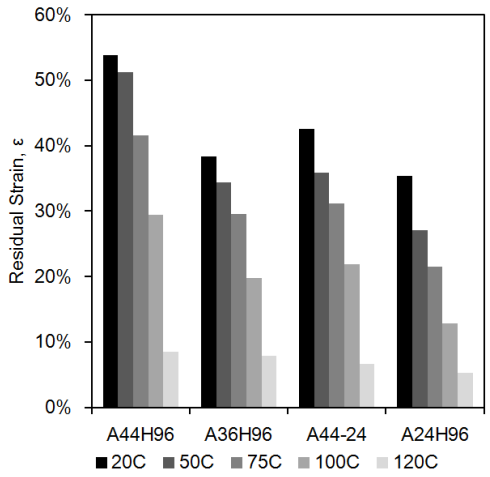

(c) Composite A44-24.

Figure 2.4-15 – Residual strain (ϵ_{res}) of HNBR blends measured after 10,000 cycles up to 120 °C.

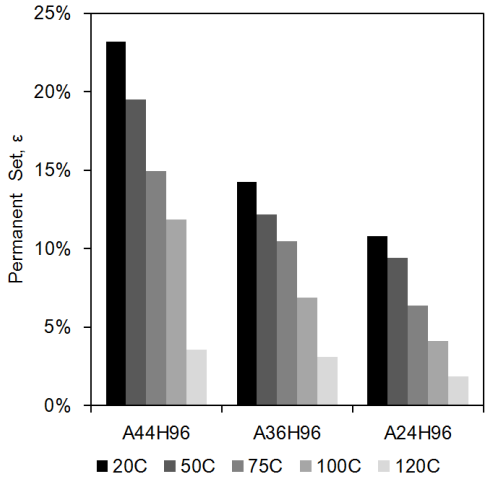

(a) Effect of ACN content.

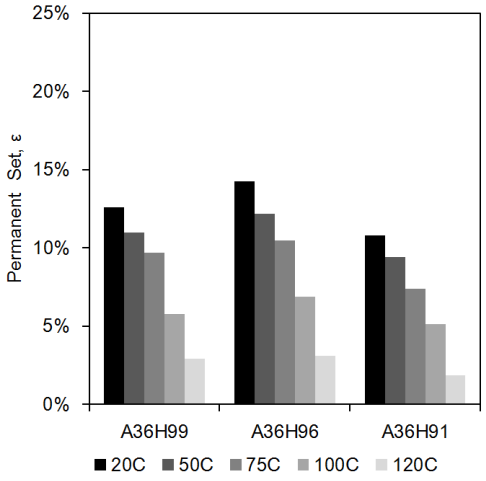

(b) Effect of hydrogenation.

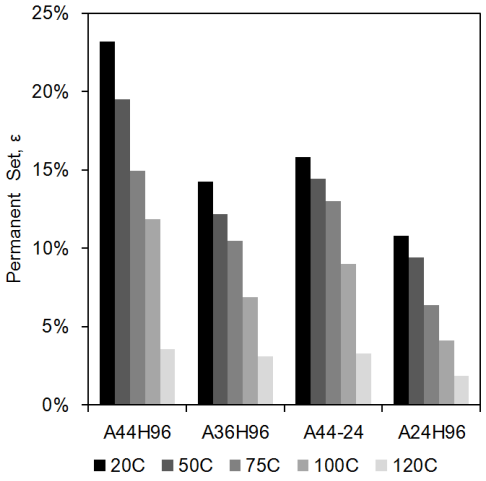

(c) Composite A44-24.

Figure 2.4-16 – Permanent set (ϵ_p) of HNBR blends measured after 10,000 cycles up to 120 °C.

Moreover, residual strain decreases with ACN content (Fig. 2.4-15(a) and does not seem to depend on the hydrogenation level (Fig. 2.4-15(b) at least for 36 wt.-% ACN. For the composite A44-24 (Fig. 2.4-15(c)), it again has median properties of A44H96 and A24H96. It is also interesting to note that these trends closely resemble to those highlighted by DMA as shown in Fig. 2.4-12, especially in the effects of ACN content and for the behavior of the composite A44-24. As mentioned earlier, it points out that presence of residual strain is closely related to the temperature difference with the glass transition temperature. More precisely, limiting the residual strain requires testing outside of the glass-to-rubber transition phase.

The results for permanent set are shown in Figure 2.4-16 And they tend to closely follow the trends for residual strain, but with a reduced magnitude by about a factor of 2 on average. This is a representation of a qualitative observation, where a specimen tends to slowly contract closer to its original length as time passes, *i.e.*

recovery. It should be noted here that the majority of the recovery occurs within the first hour after stopping of loading and, after one week, no change in specimen length is observed for all six blends.

As a concluding remark, both of these phenomena are representative of the highly inelastic behavior of HNBR, especially at low temperatures. They are manifestations of either the plastic or the viscoplastic nature of the material. For prescribed cyclic displacement loading conditions, presence of both residual strain and permanent set poses some problems: primarily, it is clear that the reference state of the specimen, *i.e.* its length, changes with each cycle. As a consequence, a question arises on how to treat measurements such as λ, the calculation of which varies with the choice of one out of the many possible reference states.

Hardness

The averages of three Shore-A hardness tests are presented in Table 2.4-5. The tensile modulus at 10 MPa and room temperature presented in Tab. 2.4-1 is added for comparison. Moreover, a widely used empirical correlation between hardness

Table 2.4-5 – Shore-A hardness of six HNBR blends; comparison with tensile modulus and estimated modulus (Gent 1958).

	Shore A Hardness	E_{10MPa} **(MPa)**	E_{Gent} **(MPa)**
A36H96	$66.77^{+0.63}_{-0.57}$	20.41	4.78
A44H96	$68.67^{+0.43}_{-0.27}$	21.77	5.19
A24H96	$60.83^{+0.67}_{-0.93}$	19.31	3.73
A36H99	$66.63^{+0.77}_{-0.43}$	18.05	4.75
A36H91	$68.83^{+0.27}_{-0.23}$	20.99	5.23
A44-24	$66.53^{+0.67}_{-0.83}$	22.80	4.73

and elastic modulus proposed by Gent (1958) is considered:

$$E_{\text{Gent}} = \frac{0.0981(56 + 7.62336\,S)}{0.137505(254 - 2.54\,S)}, \tag{2.4-4}$$

where S is the Shore-A hardness.

First, the measured Shore-A hardness of A36H96 with those presented in Fig. 2.1-12. *N774* carbon black (75 phr) from the figure is the closest to the *N772* carbon black (70 phr) used in the present study, and our measured hardness is lower and closer resembles the results obtained for 50 phr. The specifics of material formulation and of experimental protocol were not specified in Lanxess (n.d.[b]), hence no concrete conclusion can be drawn. Second, it is well-understood that the tensile modulus at large strain is not comparable with the one estimated from hardness measurements. However, it is useful to compare the general trends depicted in Figure 2.4-17, in which percent difference ($\Delta_{\%}$) is calculated similarly to Eq. (2.4-1), but with respect to the reference blend A36H96. Overall, the trends in hardness match the measured and estimated tensile moduli for all blends except for A44-24. The measured modulus of A44-24 is actually higher than the one of A36H96; however, both the hardness and the modulus calculated from it are lower. It is difficult to propose

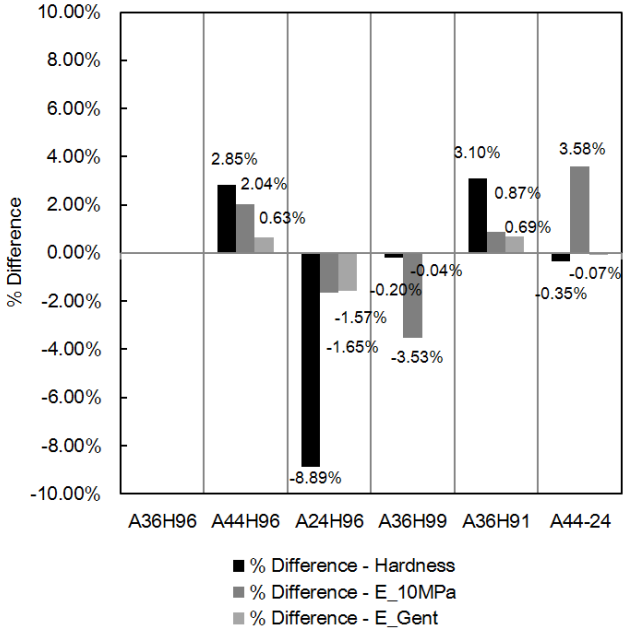

Figure 2.4-17 – Percent difference in Shore-A hardness, measured tensile modulus at 10 MPa ($E_{10\ \mathrm{MPa}}$), and estimated modulus (E_{Gent}), with reference to A36H96.

an explanation for this phenomenon; perhaps, the physical contribution of A24H96 is greater than of A44H96 in A44-24 at room temperature.

2.5 Strain-Induced Crystallization of HNBR

Strain-induced crystallization is a scientific subject of great interest for *LRCCP*, *GeM*, and myself included. It was initially planned to use the results obtained from study of SIC of HNBR in the subsequent wider investigation of fatigue (and aging) of HNBR. However, it should be noted that SIC will not be discussed in sections following this one. Fatigue testing is to be performed at 120 °C and, second, on carbon black filled specimens. As the results and discussions of this section will show, unfortunately, SIC and its beneficial impact on mechanical properties is absent in the context of fatigue studies of this thesis.

2.5.1 Qualitative observations

Before presenting the numerical results obtained on diffraction patterns, it is valuable to first discuss some qualitative observations in a manner similar to Obrecht et al. (1986) and Braun et al. (1992), among others. The X-ray diffraction patterns of filled A44H96, A36H96, A24H96 at room temperature and 90 °C and unfilled blends UF44 and UF36 at room temperature are shown in Figure 2.5-1. The corresponding prescribed stretch ratios are $\lambda = 4.2$ at room temperature, and $\lambda = 2.4$ at 90 °C due to fracture of specimens at larger stretches. Diffraction patterns for unfilled HNBR blends are more prominent compared to the filled. Moreover, there is an ACN effect: diffraction spots are much wider and the amorphous ring is much more distinguishable with decreasing ACN content for both filled and unfilled blends. These results are expected, since it has been reported that incidence of SIC increases with ACN content in HNBR (Sawada 1993). Furthermore, comparing filled and unfilled HNBR, diffraction patterns are less pronounced with decrease of carbon black fillers, similarly as in NR (Trabelsi et al. 2003). Moreover, there is a clear effect of temperature because disappearance of incidence of SIC is associated with temperatures above 50 °C (Braun et al. 1992). Consequently, the strongest diffraction patterns are observed for UF44 at room temperature. As an illustration, Figure 2.5-2 shows the stress-strain curve of UF44 with four diffraction patterns observed in the undeformed state, during loading and unloading at $\lambda = 3.5$, and for the maximum stretch. In the undeformed state, the amorphous ring is most prominent. As the specimen is stretched to $\lambda = 3.5$, diffraction spots form along horizontal and vertical axes. However, the amorphous ring is still present and it only disappears at the maximum stretch ratio, in which one can identify clear diffraction spots. With unloading back to $\lambda = 3.5$, the amorphous ring once again masks the diffraction spots, but to a lower extent - pointing that there is a higher percentage of crystallinity upon unloading and that the crystallization melting (λ_M) point is delayed with respect to crystallization onset (λ_C), *i.e.* $\lambda_M < \lambda_C$, as expected from many studies on NR.

2.5.2 Details of data processing

After performing an angular scan along the azimuthal angle ϕ, an intensity curve with two peaks can be observed as shown in Figure 2.5-3. Due to the mirror symme-

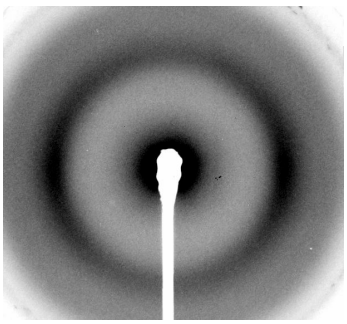

(a) A44H96 at 90 °C (λ = 2.4).

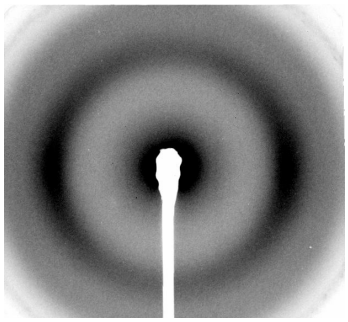

(b) A36H96 at 90 °C (λ = 2.4).

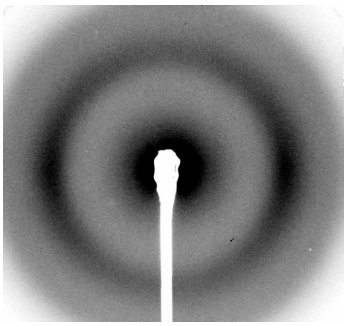

(c) A24H96 at 90 °C (λ = 2.4).

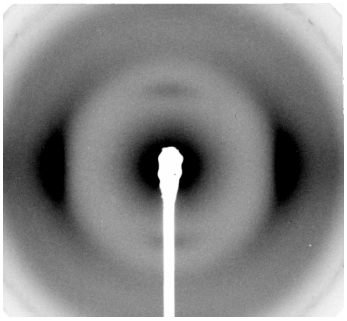

(d) A44H96 at room temperature ($\lambda = 4.2$).

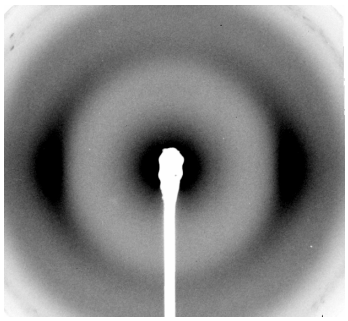

(e) A36H96 at room temperature ($\lambda = 4.2$).

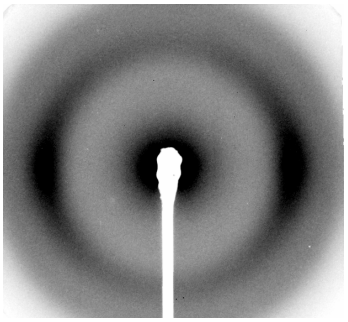

(f) A24H96 at room temperature ($\lambda = 4.2$).

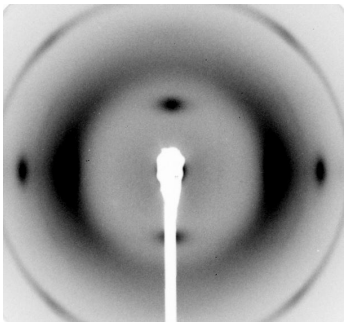

(g) UF44 at room temperature ($\lambda = 4.2$).

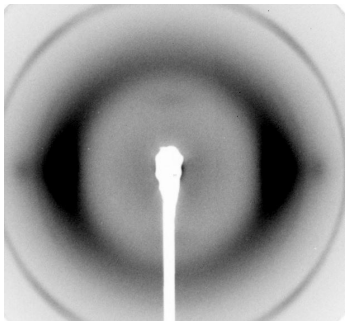

(h) UF36 at room temperature ($\lambda = 4.2$).

Figure 2.5-1 – Diffraction patterns of filled and unfilled (UF) HNBR with respect to temperature and ACN content.

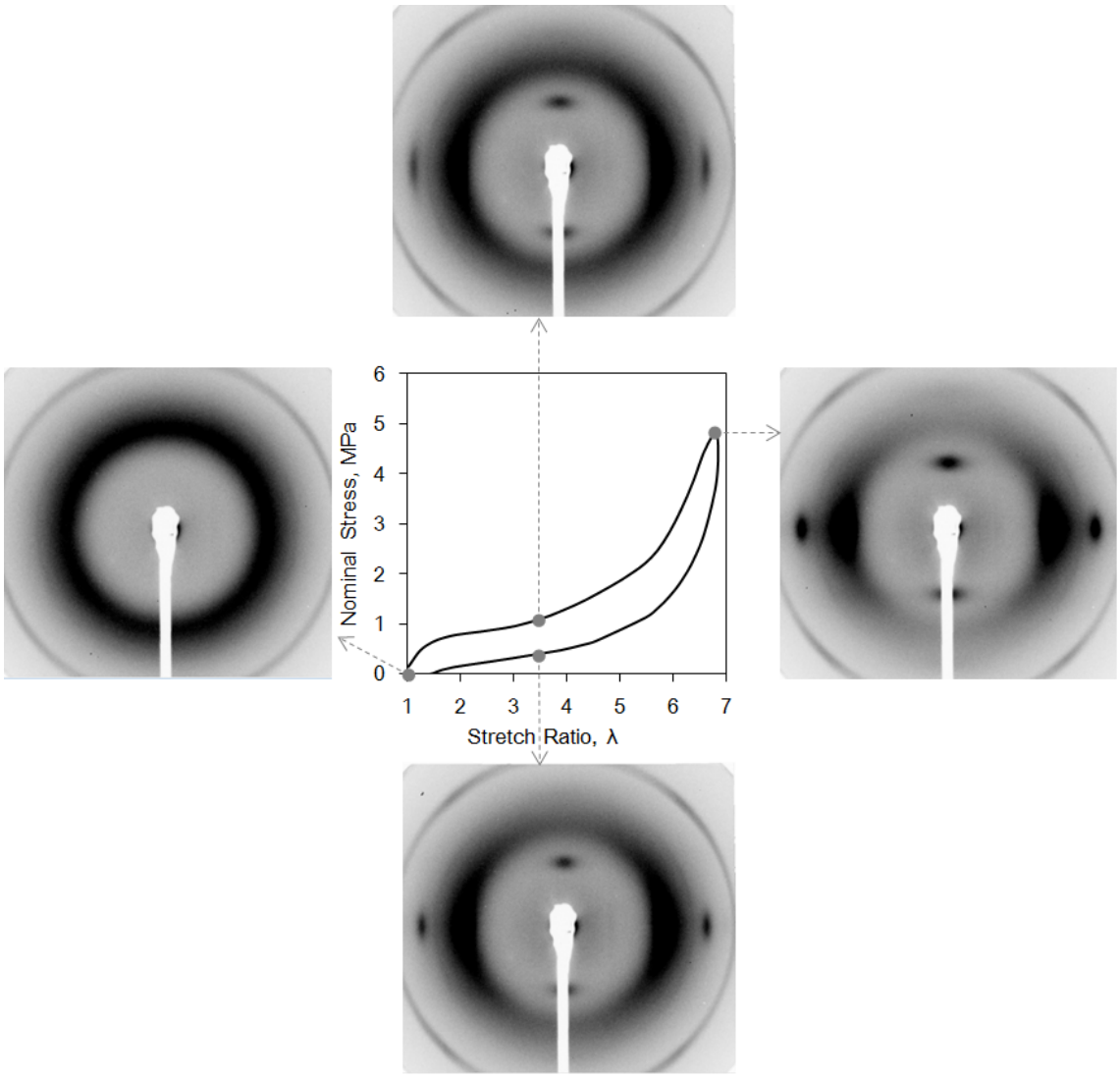

Figure 2.5-2 – Stress-strain curve of UF44 with four SIC diffraction patterns; vertical direction of loading.

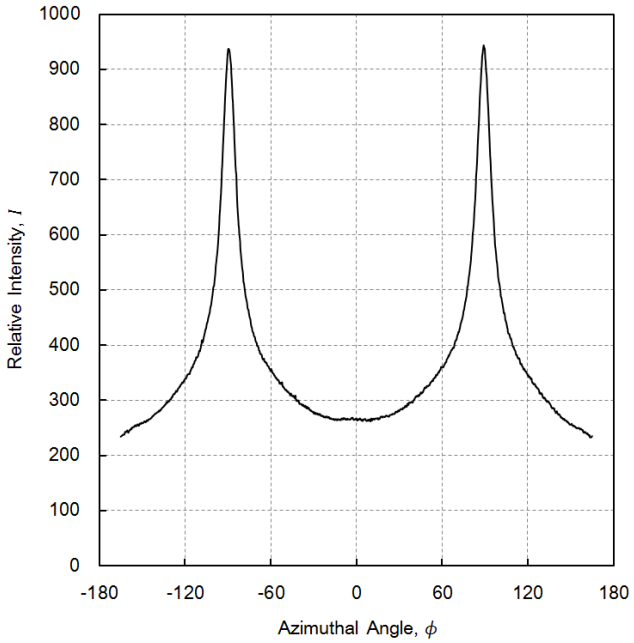

Figure 2.5-3 – Relative recorded intensity as a function of azimuthal angle ϕ after an angular scan of a diffraction pattern of UF36.

try of the diffraction pattern, it is sufficient to analyze one of the two peaks. Thus, the upper integration interval during the calculation of the index of crystallinity, given by Eq. (2.3-11), is reduced to π rad.

The deconvolution methods utilized by Albouy et al. (2012), Vieyres et al. (2013), and Zaghdoudi et al. (2015) has to be modified for HNBR because of the less pronounced diffraction patterns as compared to NR. As such, isolating the amorphous contribution in HNBR is of particular challenge. Thus, the methods are modified in the present study and a slightly different numerical approach is attempted. Since the computed index of crystallinity rather strongly depends on the peak deconvolution methodology, its details are described below:

- An intensity curve obtained by an angular scan is extracted from each X-ray diffraction image for a specific blend;
- For all extracted intensity curves, a method of least squares is utilized to minimize the residual of

$$R(\phi) = I_{\text{exp}}(\phi) - (I_{\text{am}}(\phi) + I_{\text{crys}}(\phi)), \tag{2.5-1}$$

  where $I_{\text{exp}}(\phi)$ stands for experimental intensity measurements, $I_{\text{am}}(\phi)$ is given by Eq. (2.3-8) from which parameters A, B, and C are fitted, and $I_{\text{crys}}(\phi)$ is given by Eq. (2.3-9) from which parameters I_{max}, w, ϕ_0, and μ are fitted. A starting estimated vector is carefully chosen from preliminary calculations to ensure convergence of the fit.
- The fitted parameters I_{max}, w, ϕ_0, and μ are analyzed, and coefficients that represent statistical outliers or do not make physical sense are discarded. For example: if I_{max} is negative because the intensity of crystalline phases cannot

be negative in this context; if the widths represented by w are larger than the domain of analysis (π rad); if the centers of the peak ϕ_0 are not about $\pi/2$ rad; or if μ, related to the shape of the distribution, is more than 2 stardard deviations away from the mean.

After filtering of parameter values, mean values of w, ϕ_0, and μ are considered in the next steps;

- A method of least squares is utilized once again, however the parameters obtained in the previous step are fixed. Hence, for every intensity curve, fitted values of $I_{\max}$, A, B, and C are computed.

- Finally for each diffraction pattern, I_{am} and I_{crys} are calculated with the fitted parameters and are numerically integrated to obtain index of crystallinity given by Eq (2.3-11).

This method is implemented in a custom script written in *Python* with the help of *NumPy* library.

An example of peak deconvolution for three different stretch ratios is shown in Figure 2.5-4. Up until the onset of crystallization at $\lambda = 1.5$, the experimental

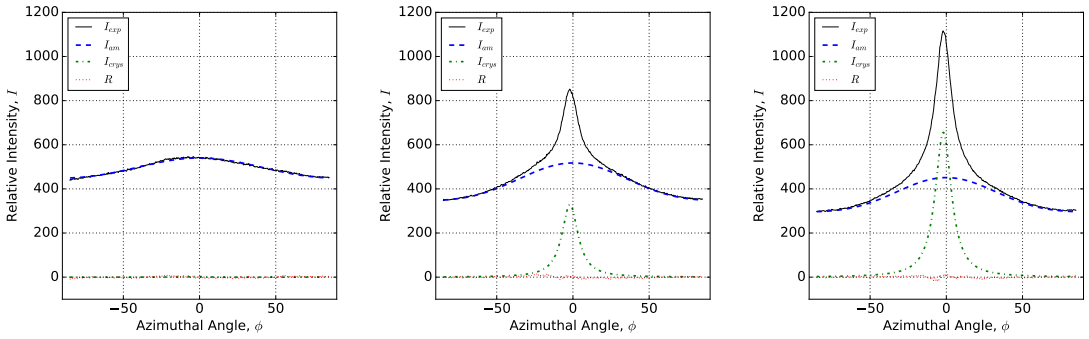

(a) $\lambda = 1.5$. **(b)** $\lambda = 4.9$. **(c)** $\lambda = 6.2$.

Figure 2.5-4 – Examples of intensity peak deconvolution obtained from an X-ray diffraction pattern for three different stretch ratios; experimental intensity (solid), amorphous contribution (dashed), crystalline contribution (point dashed), and residual (point) are presented.

intensity is completely modeled by I_{am} as shown in Fig. 2.5-4(a). As the stretch ratio increases to 4.9, the intensity peaks due to crystallization are more prominent; Fig. 2.5-4(b) shows both an amorphous contribution (which is smaller than the one at $\lambda = 1.5$) and a crystalline contribution. This crystalline contribution continues to grow and the amorphous one to decline at large stretch ratio as shown in Fig. 2.5-4(c). It should be noted that the choice for the amorphous contribution (Eq. (2.3-8)) and the numerical approach developed for this analysis perform quite well, because the residuals of the fit are quite small.

2.5.3 Unfilled HNBR

Figure 2.5-5 shows both stress-strain and crystallinity-strain curves at room temperature for unfilled blends of HNBR - UF44 and UF36. The unique characteristic

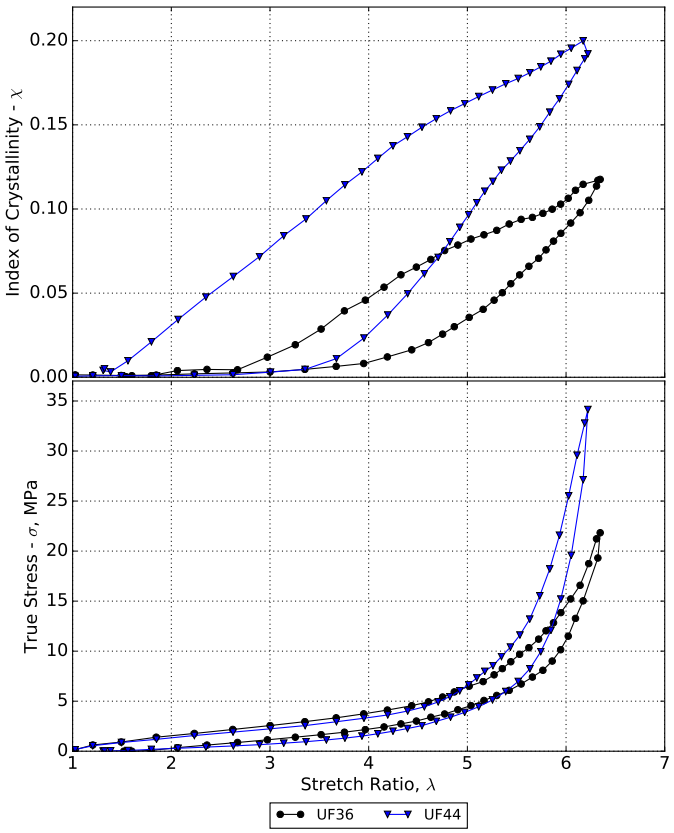

Figure 2.5-5 – Stress-strain and crystallinity-strain curves at room temperature for unfilled blends of HNBR - UF44 and UF36.

of SIC incidence is present in the crystallinity curve: a counter-clockwise hysteresis curve, similar to NR, where the crystallinity index for a given stretch ratio is higher during unloading than during loading. Moreover, crystallization onset (λ_C) occurs later during loading as compared to crystallization melting (λ_M) during unloading. The corresponding values for both blends are given in Table 2.5-1. Additionally, the

Table 2.5-1 – Crystallization onset and melting for two unfilled blends of HNBR at room temperature; additionally, the fitted parameter μ is presented.

	λ_C	λ_M	μ
UF36	3.9	2.6	1.08
UF44	3.5	1.4	1.08

fitted parameter μ is given; it indicates that the shape of the Pearson VII closely resembles a Lorentzian distribution, *i.e.* it equals close to one.

The figure also confirms the qualitative observations about the effects of ACN content. As compared with UF44, for the 36 wt.-% ACN unfilled HNBR blend, the overall degree of crystallinity is lower, and the crystallization onset occurs later while melting occurs earlier. These results agree with hypothesis of Braun et al.

(1992). Results obtained for UF44 are in accordance with the results obtained in a separate study on the SIC of HNBR outside of the scope of the present PhD project (Narynbek Ulu et al. 2017a). Specifically for UF44, λ_C is also around $\lambda \approx 3.5$ and λ_M around $\lambda \approx 1.3$ at 20 °C.

2.5.4 Effects of carbon black and temperature

Unfortunately, as shown in Figs 2.5-1(d)-2.5-1(f), presence of carbon black causes diffusion of X-rays, which in turn leads to the broadening of peaks and an increase to the amount of amorphous scattering. This complicates the analysis and the methodology utilized in this work is not suitable to analyze the data corresponding to carbon black filled HNBR blends. Other approaches have been tried; however, no appropriate solution has been found. Finally, at 90 °C, the presence of diffraction patterns is questionable and one can refer to the findings of Braun et al. (1992) in concluding that SIC cannot appear at high temperatures.

2.6 Summary and Conclusions

As presented in the *State of the Art* on HNBR, its resistance to heat, oil, solvents, and abrasion, complemented by exceptional mechanical properties, make it a highly attractive industrial elastomer. The general trends of its mechanical response has been reported in the literature; however, the specifics - especially for filled blends - are notably limited.

Furthermore, the experimental results of the chapter can be summarized:

- First, the mechanical characteristics of the six blends have been investigated in Section 2.4.1. Quasi-static uniaxial tensile testing at room temperature showed notable high strength and stiffness of HNBR blends; and, all things considered, the six blends exhibit moderately similar behavior. Additionally, some signs of plastic or viscoplastic deformation are observed in all blends at room temperature . However, for higher temperatures, higher ACN content in HNBR is associated with better preservation of elastic modulus, stretch and stress at break. As A24H96 showed signs of embrittlement at high temperatures, these point to the fact that low ACN HNBR grades are usually used in low temperature applications. Additionally, it appears that hydrogenation contributes to the preservation of mechanical properties as noted by its beneficial effect on heat resistance. For the composite blend A44-24, the general conclusion is that it offers higher stiffness at room temperature, but does not present additional benefits for high temperature applications.

- Second, DMA results were presented for all six blends in Section 2.4.2. All in all, ACN has a greater effect on the dynamic characteristics of HNBR (with respect to tested HNBR with varying percent hydrogenation). This is closely related to the glass transition temperature of HNBR, which is also highly affected by ACN content. Moreover, in accordance with the previous conclusions from performed quasi-static tests, A24H96 has the lowest T_g that makes it suitable for low temperature applications. Roughly speaking, there is a 10 °C increase from A24H96 (−39.9 °C) to A36H96 (−30.1 °C) and to A44H96 (−20.2 °C). Whereas the difference in T_g with varying percent hydrogenation is smaller: −20.9 °C for A36H99, −30.1 °C for A36H96, and −23.9 °C for A36H96. Moreover, T_g of all blends also depends on frequency. Additionally, it should be noted that the T_g of HNBR is high if compared to other elastomers such as natural rubber (−70 °C), polybutadiene rubber (−108 °C), or styrene-butadiene rubber (−61 °C); this possibly explains the plastic or viscoplastic nature of HNBR at room temperature, since it corresponds to the relative closeness to the glassy-to-rubbery transition region of the blends (near T_g).

- Third, in terms of hardness as presented in Section 2.4.3, the obtained results are lower than those reported in literature; however direct comparison cannot be made as the exact formulations of HNBR blends used in other studies are not known. All in all, with the exception of A44-24, the hardness trends fit the measured tensile modulus in uniaxial tension.

- Fourth, strain-induced crystallization of HNBR has been investigated in Sec-

tion 2.5. A modified approach for numerical analysis of X-ray diffraction intensity peaks has been proposed; it exhibits good performance in analyzing unfilled HNBR blends. This approach allowed to establish a quantitative trend between index of crystallinity, true stress, and stretch ratio. Moreover, for the first time quantiatively, the effects of increased acrylonitrile content from 36 wt.-% to 44 wt.-% on increased incidence of SIC in HNBR are highlighted. As ACN percentage increases, crystallization onset and melting occur at smaller stretch ratios. Overall, crystallization in HNBR occurs in a similar manner to the widely reported phenomena in natural rubber (NR): one can observe hysteresis and greater magnitude upon unloading for the index of crystallinity.

- Finally, as a transition to the next chapter on fatigue life testing of elastomers, it seems logical to conclude this chapter with the inelastic response of HNBR submitted to cyclic loading conditions (Section 2.1.2).

  First, the Mullins effect is observed. The level of stress-softening seems to rely more on the stretch rather than on the blend of HNBR. It is also worth mentioning that upon unloading, all blends exhibit inelastic strain, meaning the specimens do not recover to the original undeformed state.

  Similarly, residual strain and permanent set are observed for all blends during repeated cyclic loading with prescribed displacement ($R_u = 0$); they both decrease in magnitude as temperature increases from 20 °C to 120 °C. Thus, it appears that significant residual strain and permanent set are related to the difference between the testing and the glass transition temperatures. More precisely, in order to limit residual strain one has to operate outside of the glass-to-rubber transition phase.

  In HNBR, residual strain and permanent set are manifestations of the inelastic nature of the material, particularly at lower temperatures. And coming back to the context of prescribed displacement cyclic loading, the presence of both residual strain and permanent set leads to some difficulties: buckling occurs and/or compressive forces are recorded at the minimum machine actuator displacement. Moreover, it is well-established that the reference state of the specimens (unstressed geometry) alters with every new cycle. This poses new challenges, among them: how to treat measurements of quantities such as the stretch ratio, if their calculation depends on a choice of one out of many reference states at different cycles.

  These observations led to further investigations that are discussed in the next chapter.

Chapter 3

New Experimental Approaches for Fatigue Testing of Elastomers

Chapter Highlights

- Conventional fatigue life testing methods are not well adapted for inelastic elastomers: mechanical parameters (strain and stress) are not constant throughout an experiment;
- With displacement control testing, in the best case, mechanical parameters can be roughly approximated; in the worst, as for many engineering elastomers, this approximation is erroneous;
- A new experimental procedure in true stress control is developed;
- The procedure allows testing of specimens individually and in parallel; it is successfully validated;
- For the first time, a relevant Wöhler (S-N) curve is established for elastomers;
- Two statistical tools, borrowed from medical sciences, are applied to fatigue life results; it is shown how they can be applied to take into account scattering in both loading and fatigue life, as well as unbroken specimens.

Introduction

Analysis of fatigue resistance of materials, including elastomers, can be performed by two complementary approaches - fatigue crack propagation and fatigue life experiments - and the focus of the present chapter is on the latter. This chapter is divided into two parts.

During and even before proceeding to fatigue investigation of HNBR, several complexities were encountered in experimental approaches. Thus, first, the conventional testing approaches and their limitations, in the context of this work and in general for elastomers, are presented in the state of the art. More specifically, conventional approaches are not optimal in taking account inelastic response of elastomers. To solve and alleviate the encountered issues, secondly, a novel experimental approach in true stress control is presented. In particular, the experimental method allows testing of individual specimens, for which a machine control algorithm is presented. Furthermore, methods are developed for extension of true stress control testing of multiple specimens in parallel, for which a special grip setup is designed. Some parts have already been published in the *International Journal of Fatigue* (Narynbek Ulu et al. 2017b); their discussion is expanded here.

Second, a state of the art on the general approaches that are encountered in statistical analysis of fatigue results in elastomers is presented. Finally, novel application of two statistical approaches is presented within the context of experiments carried out in true stress control.

Contents

3.1 State of the Art on Fatigue Life Testing of Elastomers

3.1.1 Conventional testing approach

Fatigue life approach for investigation of fatigue resistance focuses on the two steps of fatigue failure: initiation of cracks and their growth. In the first step, one can observe after repeated loading formation of cracks in a region that was free, at least nominally, of observable cracks. In the second step, the crack (or cracks) grows increasing up to a critical stress concentration, after wich a specimen or a part fails. The main advantage of fatigue life approach is that it allows to use parameters, which are defined in a material point in the sense of continuum mechanics, rather than fracture mechanics concepts (Mars and Fatemi 2002). The basis for this arises from a continuum mechanics approach, where a history of repeated mechanical loading is said to predict duration until failure, *i.e.* fatigue life. Of course, in reality, parts are subjected to complex and varying loading, which can be difficult to be adequately represented or summarized (Mars and Fatemi 2004a). Thus, in experimental practice, the history of repeated mechanical loading is usually simplified to application of constant cyclic loading as shown in Figure 3.1-1. Here P is any mechanical load-

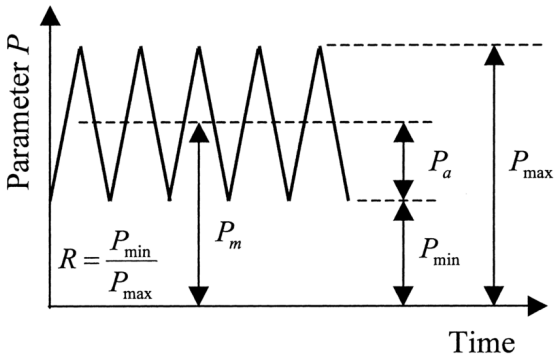

Figure 3.1-1 – Commonly used parameters for description of constant-amplitude history loading (Mars and Fatemi 2004a).

ing parameter and the mechanical loading history can be characterized by any two parameters: mean (P_m), maximum ($P_{\max}$), minimum ($P_{\min}$), and alternating loads (P_a). Moreover, as mentioned in the previous chapter, the R-ratio (R) of $P_{\min}$ to ($P_{\max}$) can also be used. Finally, a curve, similar to the first $S-N$ curve presented by Wöhler (Schütz 1996), is plotted with the loading parameter (depending on personal preference of either maximum, minimum or alternating value) as a function of fatigue life.

It should be noted that values of P are specifically of a mechanical parameter. These are differentiated from experimental state parameters. If one considers two important experimental parameters - displacement (u) and force (F) - they are related to both material properties and specimen geometry; if displacement is prescribed, then force is measured, and *vice versa*. Additionally, specimen cross-section area (S) is another experimental parameter that depends on the displacement. Correspondingly, strain (ϵ) and true (Cauchy) stress (σ) are the two mechanical parameters; the

importance of these parameters is that they are inherent only to the material itself. Globally speaking, the true stress is what is actually experienced by the material. The two categories of parameters are connected, in practice, by calculation of material parameters from measured experimental parameters. Strain can be represented as the stretch ratio (λ). As defined in the previous chapter, in case of simple uniaxial loading, $\lambda = l/l_0$, where l and l_0 are, respectively, the lengths in deformed and unstressed states (*i.e.* no loading is applied); the former is a function of the applied displacement, $l = l_0 + u$. Furthermore, true stress is defined as $\sigma = F/S$, where F is the applied force and S is the actual cross-section area. Figure 3.1-2 shows simplified relationships between the above-mentioned experimental and mechanical state parameters.

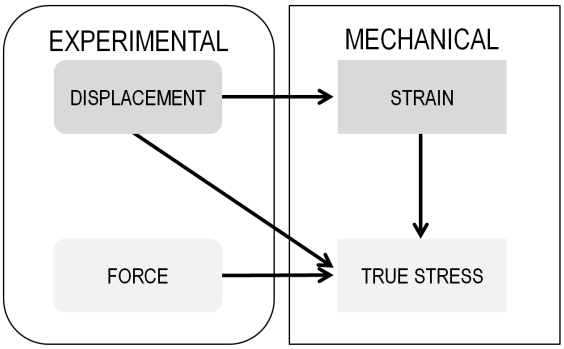

Figure 3.1-2 – Relationships between experimental and mechanical state parameters.

Coming back to the topic of loading parameters, these can be split into strain, stress, or energy related categories. In practice, using stress is suitable for rigid materials, where strain are small and force is prescribed experimentally, from which stress is subsequently calculated. For example, fatigue life in metals has been extensively investigated (Forrest 1962; Klesnil and Lukáš 1992; Stephens et al. 2001), where it is common to find measurements of applied force that is then used to calculate engineering stress by F/S_0, where S_0 is the initial cross-section area; the rigidity of metals allows to make an equivalence between true and engineering stress within the small strain assumption

$$\sigma = F/S \approx F/S_0 \tag{3.1-1}$$

Thus, for a given metal, one can find $S - N$ curves in databases; the analysis is then mostly straightforward due to a presence of a wide variety of fatigue initiation criteria based on stress parameters. On the other hand, conventionally, strain is used as the mechanical history parameter in fatigue experiments of elastomers and other soft and flexible materials. The experiments are conducted with displacement control. There are two principal reasons: first, it is simply much easier in practice to control displacement when material strain are large; second, due to the fact that determination of the stress state in rubber components is considerably difficult (Mars and Fatemi 2003).

Consequently, displacement control is widely utilized for elastomers within industry and in academic research, and there are international standards (Mars and Fatemi 2002; Mars and Fatemi 2003). One of the most commonly used is ASTM D4482

standard on "Standard Test Method for Rubber Property-Extension Cycling Fatigue" (ASTM International 2017). Here are some of the key characteristics of the standard:

- From the beginning it is stated that the procedure should be used for comparative evaluation and that no correlation should be implied with real-world service conditions;
- A constant displacement amplitude is applied at $R = 0$, from which stretch ratio is calculated; moreover, strain energy is calculated from stretch and engineering stress;
- Flat dumbbell specimens are used emphasizing the study of crack initiation (the cross-section area is relatively small, thus crack propagation is negligible); due to the geometry, compression is not possible;
- Fatigue life is considered as the complete failure of the specimen (again specimens are thin);
- The procedure accounts for presence of permanent set; to condition the material before actual fatigue testing, it is proposed to load the specimen for 1000 cycles; and then stop the testing machine and manually increase the distance between the grips so that there is no buckling/compressive forces at minimum position of the testing machine actuator; this is to be re-done after 10,000 cycles and every 24 h.

It seems that the basis for this procedure mostly likely rests on first experiments conducted by Cadwell et al. (1940), who explored the effect of maximum engineering strain on fatigue life for both uniaxial and shear tests of unfilled vulcanized NR. Similar experiments were carried out on various synthetic rubbers by Fielding (1943), who referred to fatigue life as "flex life".

In general, it can be said that the items listed above outline the general displacement control approach. Some modifications are made in other studies:

- massive specimen geometry is chosen to include the effects of fatigue crack propagation and also to allow testing in compression, *e.g.* Raoult (2005);
- consequently, different end of life criteria can be applied (not final failure), *e.g.* André et al. (1999), and Huneau et al. (2016);
- additionally, the effects of different R-ratios can be examined, *e.g.* Cadwell et al. (1940), Mars and Fatemi (2003), and Le Gac et al. (2015).

Lastly, the final fatigue life curve is usually plotted as $\epsilon - N$ or $\lambda - N$, replacing the classical $S - N$ curve.

Strain energy density (W), introduced by Beatty (1964), is another strain-based mechanical state parameter that is also used in fatigue. The principal advantage of this parameter is in its applicability during multiaxial loading. The ideas are borrowed from the concept of fracture mechanics of elastomers, where it is said that, under specific conditions, strain energy is a measure of the energy release rate of naturally occurring flaws. Early efforts reflect the work performed by Rivlin and Thomas (1953), Gent et al. (1964), and Lake and Lindley (1965) by integration of

fatigue crack growth rates and some more recent works are related to connection of experimental fatigue life results with finite element analysis (De Eskinazi et al. 1990; Zine et al. 2006). Moreover, several fatigue life criteria have been developed Mars (2001), Verron and Andriyana (2008), and Saintier et al. (2006b), among others. Experimentally, fatigue tests are controlled either by displacement or force, where strain energy is estimated from force and displacement measurements or calculated from a hyperelastic strain density function (Mars and Fatemi 2002; Gent et al. 1964). Subsequently, the $S - N$ curve is replaced by $W - N$ curve.

3.1.2 Conventional approach limitations

The applicability of displacement control testing is dependent on the assumption of elastic response of elastomers: an applied displacement always corresponds to unique mechanical state - either in terms of stress or strain. This is usually not the case. Thus, experimenters are forced to adopt several major assumptions to overcome the complexities faced in fatigue life testing, which arise from inelastic behavior. Moreover, this approach seems to represent a transfer of *force-to-stress* based testing methods utilized in fatigue investigations of metals and other rigid materials with an interchange it to *displacement-to-strain* due to practical simplicity in test control. As mentioned earlier, transition from force to (true) stress is straightforward in metals (Eq. (3.1-1)). In displacement control, determination of the mechanical parameters from the experimental ones is considerably more challenging. Primarily, the behavior of filled rubbers includes many complex phenomena where interactions between them are not well understood; these phenomena can be described as dissipative mechanical responses that emerge as hysteresis and stress-softening on a stress-strain curve of an elastomeric material (Bergström and Boyce 1998; Mars and Fatemi 2004b).

The inelastic behavior of elastomers can be characterized by two relaxation phenomena. First, as mentioned in the previous chapter (Section 2.1.2), the Mullins effect is responsible for significant stress-softening during initial cycles of a filled virgin material. As shown in Figure 2.1-13, the measured maximum stress decreases with each cycle as a constant displacement amplitude at $R = 0$ is applied. The magnitude of stress-softening decrease, unless the previous maximum loading is exceeded, upon which stress-softening magnitude once again increases (Mullins 1969). In addition to stress-softening, inelastic strain is observed after each successive unloading. When a specimen/part is unstressed (or measured $F = 0$), the measured strain does not equal to zero; therefore at that point a compressive force in massive specimens or buckling in thin specimens at zero displacement is measured in experimental practice. Moreover, if an elastomeric material is continued to be loaded at a constant displacement amplitude, one can measure stress-softening and decrease in material stiffness after the initial cycles commonly attributed to the Mullins effect (Figure 3.1-3).

Additionally, the softening also contributes to accumulation of inelastic strain during loading and/or in an unstressed state. This softening is classically attributed to the viscoelastic nature of elastomers, however the exact mechanisms are not well understood. Mars (2007) attributes this to micro-structural changes in the material such as chain scission and/or filler-matrix decohesion. Ayoub et al. (2011)

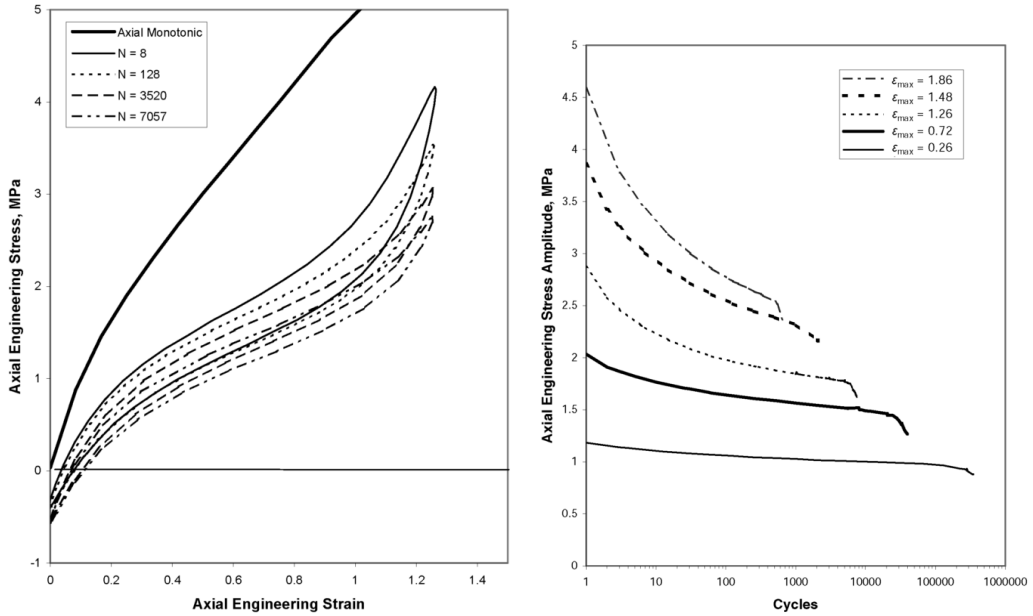

(a) Stress-strain cycles at intervals N. **(b)** Evolution of maximum stress.

Figure 3.1-3 – Example of long-term softening in displacement control (Mars 2007).

consider this phenomenon as a non-reversible damage process that is characterized by presence of residual strain and permanent rearrangement of the macromolecular network; on that scale, the authors hypothesize presence of longer chains, but on fewer of which stress is distributed. In literature, this phenomenon is referred to as "cyclic stress relaxation" (and as "cyclic creep" or "ratcheting" for tests carried out in force control) (Derham and Thomas 1977; Kingston and Muhr 2007; Mars and Fatemi 2004b; Mars 2007; Asare et al. 2009; Ayoub et al. 2011; Ayoub et al. 2014); hereinafter, this phenomenon is referred to as *long-term cyclic stress relaxation* (or for brevity as*long-term relaxation*), since its effects are only evident after a large number of cycles. Moreover, the magnitude of long-term stress relaxation is highly temperature dependent; *e.g.* as reported by Duan et al. (2015), stress-softening phenomenon increases in natural rubber as temperature is increased from 23 °C to 90 °C. However, even at room temperature, it is clear from Fig. 3.1-3(b) that the mechanical parameter applied on the material is not constant throughout the duration of an experiment. Thus, how can this **mechanical loading history** can be properly described?

The two relaxation phenomena, Mullins effect and long-term relaxation, are present in all elastomers. Although, their expression in magnitude during fatigue life testing of elastomers varies depending on both the material and testing conditions (loading level, temperature, etc.). For some elastomers, such as natural rubber (NR), the Mullins effect is present (for filled formulations), but long-term relaxation is considered as negligible by many. Conventional testing approaches can be made functional, but with some drawbacks. For some others, such as the HNBR blends investigated here, both relaxation phenomena are significant and have to be accounted for during fatigue life testing. To aid with the discussion of the limitations of the conventional approach, and, specifically, how these inelastic behaviors affect fatigue life testing, two simplified and idealized scenarios are presented.

Scenario 1 - Presence of mostly the Mullins effect

In this scenario, long-term cyclic stress is considered as insignificant. Natural rubber (NR) is chosen as a material of investigation, since in many studies it is assumed that its stress-strain response stabilizes after a certain amount of cycles, *e.g.* Mars and Fatemi (2002), Mars and Fatemi (2004b), Mars (2007), Zine et al. (2006), Le Gac et al. (2015), and Narynbek Ulu et al. (2016). If one plots the maximum force over number of cycles, this phenomenon is referred to as the "plateau" region, since the change per cycle is relatively low; however, over duration of long fatigue life experiments, these small changes tend to accumulate as seen in Figure 3.1-3(b). The choice of the starting point of the plateau region starts is rather arbitrary, since it can be highly dependent on the loading level, material (and its composition), temperature, specimen geometry, and many other factors. For example, André et al. (1999) carried out uniaxial and biaxial experiments in displacement control for NR. Since the tested material exhibited negligible viscoelastic response and the force seemed stabilized after 100 cycles, authors used a generalized Mooney-Rivlin model to calculate the true stress by finite element analysis and plot the results in terms of that mechanical parameter. Table 3.1-1 shows some of the experimental procedures undertaken to *accommodate* for the Mullins effect in NR and other materials. It is

Table 3.1-1 – Example of number of cycles for accommodation of the Mullins effect for various elastomers.

	Accommodation Cycles	**Material**
ASTM International (2017)	1,000	Various
Le Gac et al. (2015)	1,000	NR
Duan et al. (2015)	1,000	NR
André et al. (1999)	100	NR
Zine et al. (2006)	100	SBR
Narynbek Ulu et al. (2016)	50	NR
Mars and Fatemi (2004a)	10	NR
Cadwell et al. (1940)	0	NR
Fielding (1943)	0	Various
Minguez and Royo (1980)	0	Various
Svensson (1981)	0	NR
Ostoja-Kuczynski et al. (2003)	0	NR
Choi et al. (2005)	0	NR
Woo et al. (2009)	0	NR
Ayoub et al. (2011)	0	SBR
Weng et al. (2012)	0	NR
Huneau et al. (2016)	0	NR
Seichter et al. (2017)	$25\%N_f$	Various

clear that there exist a wide variety of academic and industrial testing protocols, which try to take into account the Mullins effect exhibited by the material before the actual fatigue life testing. In fact, there is no consensus on the best approach for the *accommodation* phase, which makes comparison between different studies somewhat problematic. Moreover, presence of this inelastic response in the tested materials is sometimes even acknowledged, but no action is taken, *e.g.* (Ostoja-Kuczynski et al. 2003; Huneau et al. 2016).

Another consequence of the Mullins effect and the inelastic response that it causes is not usually acknowledged, *i.e.* a specimen is in compression at zero displacement

after the initial cycles. For example, if one considers the R-ratio of $R = 0$ in terms of prescribed displacement

$$R_d = \frac{u^{\min}}{u^{\max}}, \tag{3.1-2}$$

and compares it to R-ratio in terms of stretch

$$R_\lambda = \frac{\lambda^{\min} - 1}{\lambda^{\max} - 1}, \tag{3.1-3}$$

or to true stress R-ratio in terms of true stress

$$R_\sigma = \frac{\sigma^{\min}}{\sigma^{\max}}, \tag{3.1-4}$$

R_d will always be greater than R_λ and R_σ, because these will be negative due to $\lambda^{\min}$ being less than one and $\sigma^{\min}$ also being negative. It should be mentioned that the R-ratio is important in fatigue testing of elastomers, especially in cases of presence of strain-induced crystallization (SIC) (Mars and Fatemi 2004a; Huneau 2011; Beurrot-Borgarino et al. 2013). In general, increased presence of SIC improves fatigue resistance of elastomers, and numerous studies have shown that the incidence of SIC is sensitive to the R-ratio (Mars and Fatemi 2004a; André et al. 1999; Le Gorju-Jago and Bathias 2002; Saintier et al. 2011).

Finally, it is common to find experiments carried out in displacement control and the "Wöhler" curve to be plotted with calculated engineering stress, determined after a certain number of cycles or averaged over the duration of the experiment (Le Gorju-Jago and Bathias 2002; Rausch et al. 2015). However, engineering stress is not a relevant representative quantity of the mechanical state of the material under loading due to large strain and inelastic behaviors (Charlton et al. 1994).

To ease the discussion of the aforementioned, an idealized case is presented for a specimen tested under constant amplitude cyclic uniaxial loading in displacement control. To visualize the case, Figure 3.1-4 is drawn upon the reference figure for the Mullins effect as shown previously in Figure 2.1-13. The case is divided into two steps

- Step 1 (cycle A to cycle B - A is the first loading cycle; afterwards, presence of the Mullins effect with stress-softening and inelastic strain;
- Step 2 (cycle B on-wards) - cycle B marks the end of the Mullins effect; negligible long-term cyclic stress relaxation after cycle B.

Displacement loading is from zero to $u^{\max}$. At both A and B, we can measure the maximum and minimum forces, $F^{\max}$ and $F^{\min}$ respectively. During cycle B, due to stress-softening, the specimen is compressed at zero displacement. Moreover, there is inelastic strain due to stress-softening: displacement u_{M} (M for Mullins) does not equal to zero when force is equal to zero. The maximum stretch ratio (λ) at $u^{\max}$ after loading A is

$$\lambda_{\mathrm{A}}^{\max} = \frac{l_0 + u^{\max}}{l_0} = \frac{l_{\max}}{l_0}. \tag{3.1-5}$$

However at B, the reference length is no longer l_0, but $l_0 + u_{\mathrm{M}}$. Thus, the maximum strain at B equals to

$$\lambda_{\mathrm{B}}^{\max} = \frac{l_{\max}}{l_0 + u_{\mathrm{M}}} = \frac{l_{\max}}{l_0}\frac{l_0}{l_0 + u_{\mathrm{M}}} = \frac{\lambda_{\mathrm{A}}^{\max}}{\lambda_{\mathrm{M}}}, \tag{3.1-6}$$

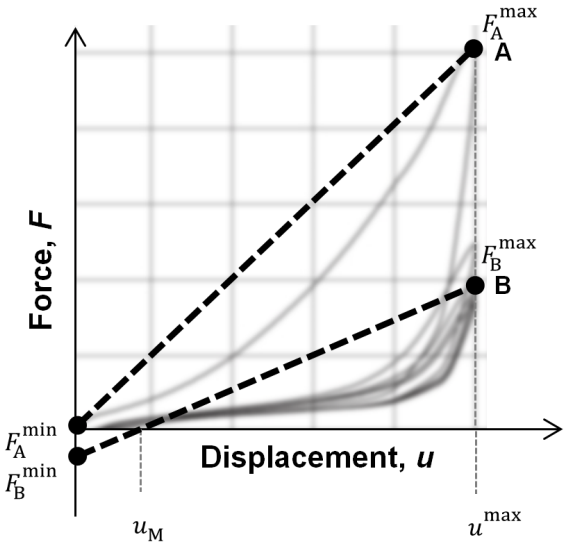

Figure 3.1-4 – Scenario 1 - Simplified representation of cyclic loading in displacement control with presence of the Mullins effect.

where λ_M is the reference stretch at B with respect to the original specimen length. Therefore, we can conclude that

$$\lambda_B^{max} < \lambda_A^{max}. \tag{3.1-7}$$

To calculate the true (Cauchy) stress (σ) at u^{max}, first the cross-section area (S) has to be known. Assuming incompressibility, $S = S_0/\lambda$, where S_0 is original specimen cross-section area. Thus, the cross-section area at A equals to

$$S_A^{max} = \frac{S_0}{\lambda_A^{max}}. \tag{3.1-8}$$

However at B, the original area is not S_0 anymore, but S_0/λ_M due to the inelastic strain and, thus, the area is

$$S_B^{max} = \frac{S_0/\lambda_M}{\lambda_B^{max}}. \tag{3.1-9}$$

From Eq. (3.1-6), it leads to

$$S_B^{max} = \frac{S_0}{\lambda_A^{max}} = S_A^{max}. \tag{3.1-10}$$

Finally, the maximum and minimum stresses can be calculated at A

$$\sigma_A^{max} = \frac{F_A^{max}}{S_A^{max}}, \tag{3.1-11}$$

$$\sigma_A^{min} = \frac{F_A^{min}}{S_0} = 0. \tag{3.1-12}$$

In similar fashion, we can deduce that the maximum and minimum stress at B are respectively smaller than at A

$$\sigma_B^{max} = \frac{F_B^{max}}{S_B^{max}} = \frac{F_B^{max}}{S_A^{max}} < \sigma_A^{max}, \tag{3.1-13}$$

$$\sigma_{\mathrm{B}}^{\min} = \frac{F_{\mathrm{B}}^{\min}}{S_0} < \sigma_{\mathrm{A}}^{\min}. \tag{3.1-14}$$

These derivations are summarized in Figure 3.1-5. This simplified schematic shows

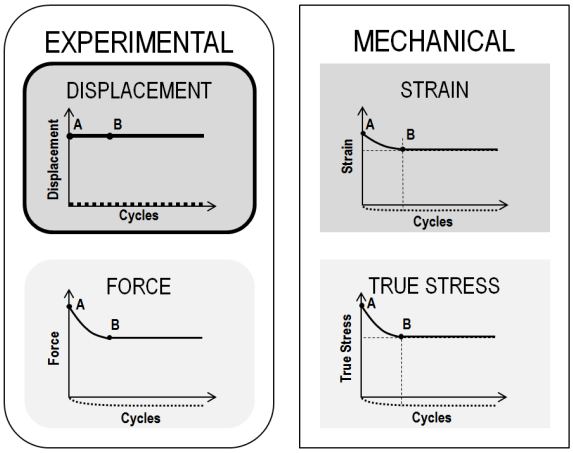

Figure 3.1-5 – Scenario 1 - Evolution of force, strain, and true stress under constant cyclic loading in displacement control (bold outline) with the Mullins effect.

the evolution of force, stretch, and true stress under constant cyclic loading in displacement control (bold outline) with the Mullins effect. After point B, both mechanical parameters are relatively constant and the material can be said to enter the *plateau* region as indicated by the dashed lines. A relationship between the prescribed displacement and the strain can be established; consequently, a hyperelastic model can be used to calculate true stress.

In case of natural rubber, these assumptions appear somewhat reasonable in some cases. For example, Raoult (2005) found that fatigue life tests carried out separately in displacement control and force control have comparable fatigue lives for equivalent strain and stress loading, if the testing is carried out under identical experimental conditions (material formulation, accommodation procedure, temperature, specimen geometry, *etc.*). However, Royo (1992) reports that for six different elastomers (type not reported) the overall ranking of fatigue resistances is inconsistent depending on whether the Wöhler is plotted with stress or strain. Additionally, as mentioned earlier, the real R-ratio, either in terms of stress or strain, is smaller in this particular case in the *plateau* region.

Finally, and most importantly, two remarks have to be made:

- Once again, not a single elastomeric material exhibits such idealized behavior;
- As some of the many experimental variables change, analysis of results becomes complicated.

  As an example, one can come back to a study carried out by Duan et al. (2015). Fatigue life has been tested in displacement control at two temperatures, 23 °C and 90 °C. At high engineering strain (calculated at 1000^{th} cycle), fatigue life is shorter at 90 °C than at 23 °C by about an order of magnitude (log-scale). However, at low engineering strain, fatigue life at 90 °C, compared with that

at 23 °C, is equal and even becomes longer as strain decreases. The authors attribute this, arguably *unexpected* result, to increased stress-softening at the higher temperature and concluded that the actual stress is lower with small strain loading at 90 °C as compared to 23 °C. So the question arises: is natural rubber better in fatigue at 90 °C considering that its operating ceiling is around 100 °C? One can say that, if in practical application the main applied load is in displacement, *e.g.* a load by a piston that moves until a certain distance, then perhaps that could be true. On the other hand, if these results are applied to finite element analysis, where the load to be applied is some force or stress (as the authors did to investigate fatigue life of a powertrain mount), then the result is obviously false (as mounts like these do not experience some specified displacement in operation).

Scenario 2 - Presence of the Mullins effect and long-term cyclic stress relaxation

In the second scenario, both stress relaxation phenomena are considered. We can extend the previous deductions for an additional third arbitrary cycle C, where there is long-term cyclic stress relaxation after the Mullins effect. Figure 3.1-6 shows

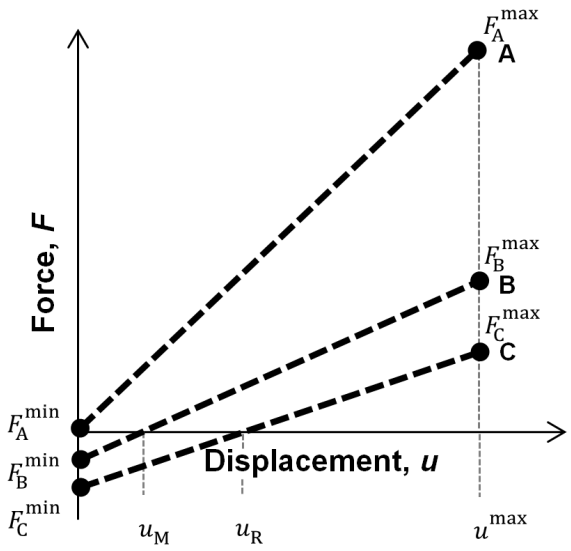

Figure 3.1-6 – Scenario 2 - Simplified representation of cyclic loading in displacement control with presence of the Mullins effect and long-term cyclic stress relaxation.

loading of cycle C along with measured maximum and minimum forces, in addition to inelastic stretch at u_R. Similar to Eq. (3.1-6), the maximum stretch ratio at C is

$$\lambda_C^{max} = \frac{l_{max}}{l_0 + u_R} = \frac{\lambda_A^{max}}{\lambda_R} < \lambda_B^{max} < \lambda_A^{max}, \tag{3.1-15}$$

where λ_R is the stretch corresponding to inelastic strain due to long-term relaxation. The cross-section area (S) at u^{max} also remains constant

$$S_C^{max} = \frac{S_0/\lambda_R}{\lambda_C^{max}} = \frac{S_0}{\lambda_A^{max}} = S_A^{max}, \tag{3.1-16}$$

and the maximum and minimum stress decrease with respect to B and A

$$\sigma_{\mathrm{C}}^{\max} = \frac{F_{\mathrm{C}}^{\max}}{S_{\mathrm{C}}^{\max}} = \frac{F_{\mathrm{C}}^{\max}}{S_{\mathrm{A}}^{\max}} < \sigma_{\mathrm{B}}^{\max} < \sigma_{\mathrm{A}}^{\max}, \tag{3.1-17}$$

$$\sigma_{\mathrm{C}}^{\min} = \frac{F_{\mathrm{C}}^{\min}}{S_0} < \sigma_{\mathrm{B}}^{\min} < \sigma_{\mathrm{A}}^{\min}. \tag{3.1-18}$$

These effects can be summarized in Figure 3.1-7. There is long-term stress relax-

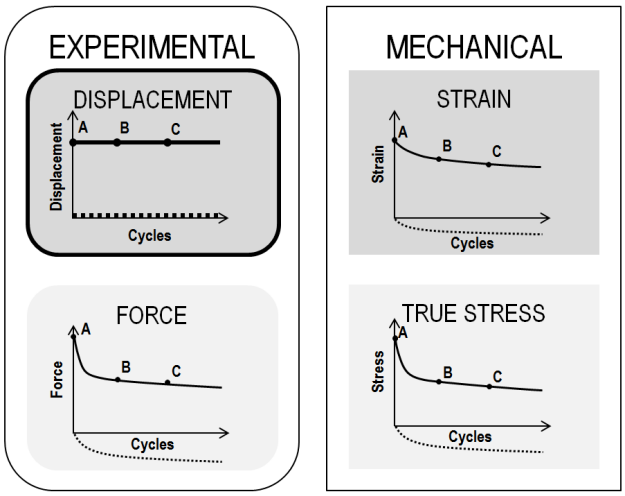

Figure 3.1-7 – Scenario 2 - Evolution of force, strain, and true stress under constant cyclic loading in displacement control (bold outline) with the Mullins effect and long-term cyclic stress relaxation.

ation: the maximum and minimum stress decrease over the duration of the experiment without a *plateau* region, *i.e.* there is no stabilization of stress. The maximum strain also varies under constant displacement loading. Therefore, experimentally, displacement control testing does not ensure constant mechanical state parameters over the duration of an experiment.

Scenario 2' - Presence of the Mullins effect and long-term cyclic creep

Finally, but less commonly, sometimes one can encounter studies performed in force control and use of massive specimens, *e.g.* Le Gorju-Jago and Bathias (2002) and Neuhaus et al. (2017). Force control does not alleviate the problems with inelastic response of the material. One can show this by extending a similar deduction for experiments carried out in force control. In force control, it is more proper to refer to the phenomena not as stress relaxation, but as creep. Thus, immediate (Mullins effect) and long-term cyclic creep are shown in Figure 3.1-8. The stretch ratio (λ) at A for $F^{\max}$ is:

$$\lambda_{\mathrm{A}}^{\max} = \frac{l_0 + u_{\mathrm{A}}^{\max}}{l_0}, \tag{3.1-19}$$

At B and C, the stretch are slightly different:

$$\lambda_{\mathrm{B}}^{\max} = \frac{l_0 + u_{\mathrm{B}}^{\max}}{l_0 + u_{\mathrm{M}}}, \tag{3.1-20}$$

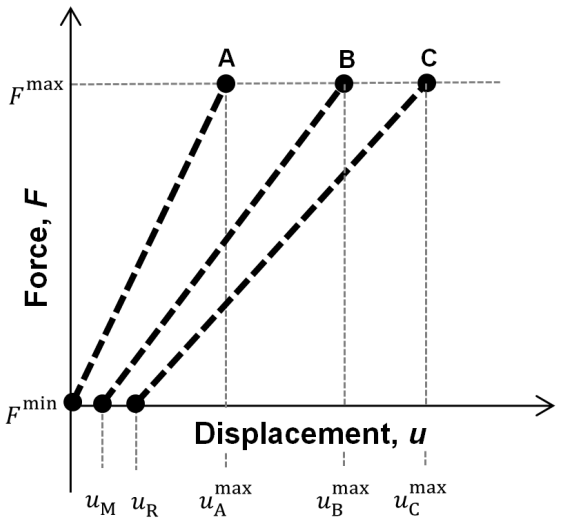

Figure 3.1-8 – Scenario 2b - Simplified representation of cyclic loading in displacement control with presence of the Mullins effect and long-term cyclic stress relaxation.

and

$$\lambda_{\mathrm{C}}^{\max} = \frac{l_0 + u_{\mathrm{C}}^{\max}}{l_0 + u_{\mathrm{R}}}. \tag{3.1-21}$$

Without experimental information, it is impossible to tell whether there is and to what extent stretch changes from A to C. There is no direct relationship between u_{M}, u_{R}, $u_{\mathrm{A}}^{\max}$, $u_{\mathrm{B}}^{\max}$, and $u_{\mathrm{C}}^{\max}$; these highly depend on material's inelastic response and specimen geometry. It is possible that stretch remains constant, if the condition

$$\frac{l_0 + u_{\mathrm{A}}^{\max}}{l_0} = \frac{l_0 + u_{\mathrm{B}}^{\max}}{l_0 + u_{\mathrm{M}}} = \frac{l_0 + u_{\mathrm{C}}^{\max}}{l_0 + u_{\mathrm{R}}} \tag{3.1-22}$$

is satisfied. However, it does not seem probable that all the different experimental parameters lead to such equivalence. Nevertheless, if one takes a simple strip-like specimen of length l_0, for example, the stretch could be constant from A to C only under one condition, where the general relationship between maximum and minimum displacements satisfies

$$\frac{u^{\max} + l_0}{u^{\min} + l_0} = \text{constant}. \tag{3.1-23}$$

Nonetheless, one can still calculate surface area, at A:

$$S_{\mathrm{A}}^{\max} = \frac{S_0}{\lambda_{\mathrm{A}}^{\max}}, \tag{3.1-24}$$

but at B, the surface area is:

$$S_{\mathrm{B}}^{\max} = \frac{S_0/\lambda_{\mathrm{M}}}{\lambda_{\mathrm{B}}^{\max}} = \frac{S_0}{\lambda_{\mathrm{M}}\lambda_{\mathrm{B}}^{\max}}. \tag{3.1-25}$$

One can show using Eq. (3.1-19) and Eq. (3.1-20) that the relationship between the denominators of Eq. (3.1-24) and Eq (3.1-25):

$$\lambda_{\mathrm{M}}\lambda_{\mathrm{B}}^{\max} = \left(\frac{l_0 + u_{\mathrm{M}}}{l_0}\right)\left(\frac{l_0 + u_{\mathrm{B}}^{\max}}{l_0 + u_{\mathrm{M}}}\right) = 1 + \frac{u_{\mathrm{B}}^{\max}}{l_0} > 1 + \frac{u_{\mathrm{A}}^{\max}}{l_0} \equiv \lambda_{\mathrm{A}}^{\max}. \tag{3.1-26}$$

Similarly, these deductions can be extended to point C. It becomes clear that the cross-section area at $F^{\max}$ decreases from A to C, where $S_{\mathrm{A}}^{\max} > S_{\mathrm{B}}^{\max} > S_{\mathrm{C}}^{\max}$. So finally from A to C, given that the applied force is constant, the maximum true stresses ($\sigma = F/S$)

$$\sigma_{\mathrm{A}}^{\max} < \sigma_{\mathrm{B}}^{\max} < \sigma_{\mathrm{C}}^{\max}. \tag{3.1-27}$$

The evolution of the experimental and mechanical parameters are summarized in Figure 3.1-9.

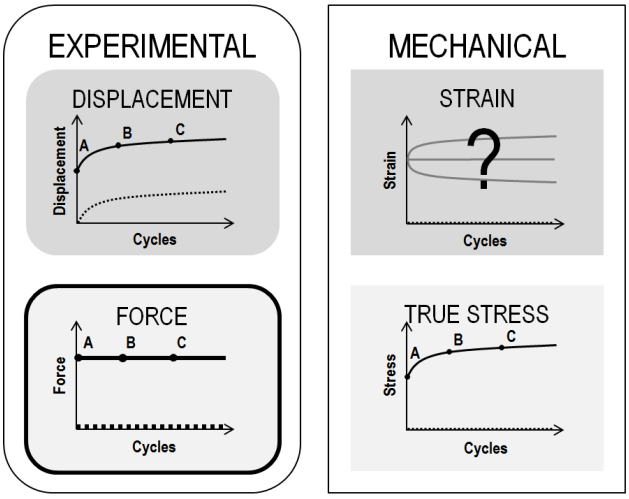

Figure 3.1-9 – Scenario 2' - Evolution of displacement, strain, and true stress under constant cyclic loading in force control (bold outline) with the Mullins effect and long-term cyclic creep.

Concluding remarks

Finally, it can be concluded that application of procedures based on displacement or force control on elastomers that exhibit these two prominent stress relaxation phenomena (the Mullins effect and long-term cyclic stress relaxation) is not valid given the fact that both mechanical parameters experienced by the material, strain and stress, appear to be never constant throughout the duration of the experiment. In reality, there is no stabilization of the stress-strain behavior under displacement or force control.

In best cases (Scenario 1), mechanical parameters - stretch ratio and true stress - can be roughly approximated with measurements after a certain number of cycles. In worst (and many) cases (such as Scenarios 2 and 2'), the choice of reference cycle, at which displacement and force are used to calculate stretch and stress, will skew the results plotted on the Wöhler curve (irrespective if plotted in terms of stress or stretch ratio). It should be emphasized once again, that the root of the problem is in displacement and force control. Hence, if the discussion is extended, for example, to the use of strain energy as a parameter on a Wöhler curve, it will be equally erroneous for inelastic elastomers in experiments carried out in displacement or force control; it is well established that strain energy is calculated *a posteriori* from force-displacement measurements or from finite element analysis, which in turn is based on the same force-displacement measurement. Therefore, the only solution

to this problem to carry out experiments, where either stretch, true stress, or strain energy are calculated in real time. The focus of the next chapter is on the first - true stress.

3.2 True Stress Fatigue Life Method

Control in true stress is chosen for several reasons. First and foremost, and coming from a more *philosophical perspective*, I strongly believe (under the guidance of my PhD advisors) that true stress is the mechanical parameter that is experienced by the material. Especially in uniaxial loading, its value can be easily calculated from two simple measurements - force and cross-section area. Second are of course the practical reasons for fatigue experiments. Control in strain is difficult to implement. Measuring local stretch ratio and controlling the loading imposed by the machine all in real-time is challenging, considering that experiments are carried out at high frequency (as a consequence of duration measured in several million cycles). Large strain are also added to this dynamic nature of testing, making it problematic irrespective of equipment utilized, *e.g.* mechanical or optical strain gauges.

Maintaining true stress throughout the whole duration of an experiment is also complex. Its adoption remains limited and has been only reported once by Johnson et al. (2013). The method, however, offers an alternative solution to the problems associated with conventional testing procedures. It allows to maintain at least one of the mechanical state parameters constant over the duration of the experiment. By controlling true stress, the procedure innately accounts for the Mullins effect and long-term cyclic stress relaxation.

Thus, the objective of the present procedure is to control, in uniaxial loading, the true stress amplitude for a given loading ratio R

$$\Delta\sigma = \sigma^{\max,i} - \sigma^{\min,i}, \tag{3.2-1}$$

where $\sigma^{\max,i} = \mathrm{Max}(F/S)$ and $\sigma^{\min,i} = \mathrm{Min}(F/S)$ for each cycle i; F is the real-time force measured by a load-cell and S is the real cross-section area in the gauge-length of the specimen. The procedure consists of two parts: first, for testing on a single specimen is presented; second, it is expanded to test multiple specimens in parallel.

3.2.1 Individual testing

Calculation/determination of cross-section area

The initial step consists in calculating the cross-section area of the specimen *a priori* as a function of imposed displacement. Initially, DIC measurements are performed on a sample at specific cycle intervals, *e.g.* every thousand cycles, to measure the cross-section area as a function of prescribed displacement $S(u)$. A sinusoidal waveform in displacement control is applied with a loading ratio $R = 0$. Assuming that the material is isotropic, transverse strain λ_2 is measured for different values of the maximum displacement and it can be considered that $\lambda_2 = \lambda_3$; for anisotropic materials, it is necessary to measure both λ_2 and λ_3. Thereafter, cross-section area is calculated from the specimen initial dimensions. To further complement the DIC measurements, a finite element analysis can be employed. Special care should be taken to properly take into account hyperelastic, viscoelastic, and/or plastic/viscoplastic responses of the material under cyclic loading.

Machine control algorithm

The next step is the definition of a machine control algorithm, which will be utilized to prescribe true stress amplitude on a specimen. The algorithm is run for simultaneous control of minimum and maximum true stresses as seen in Figure 3.2-1. It should be noted that the algorithm is cycle dependent, but independent of the

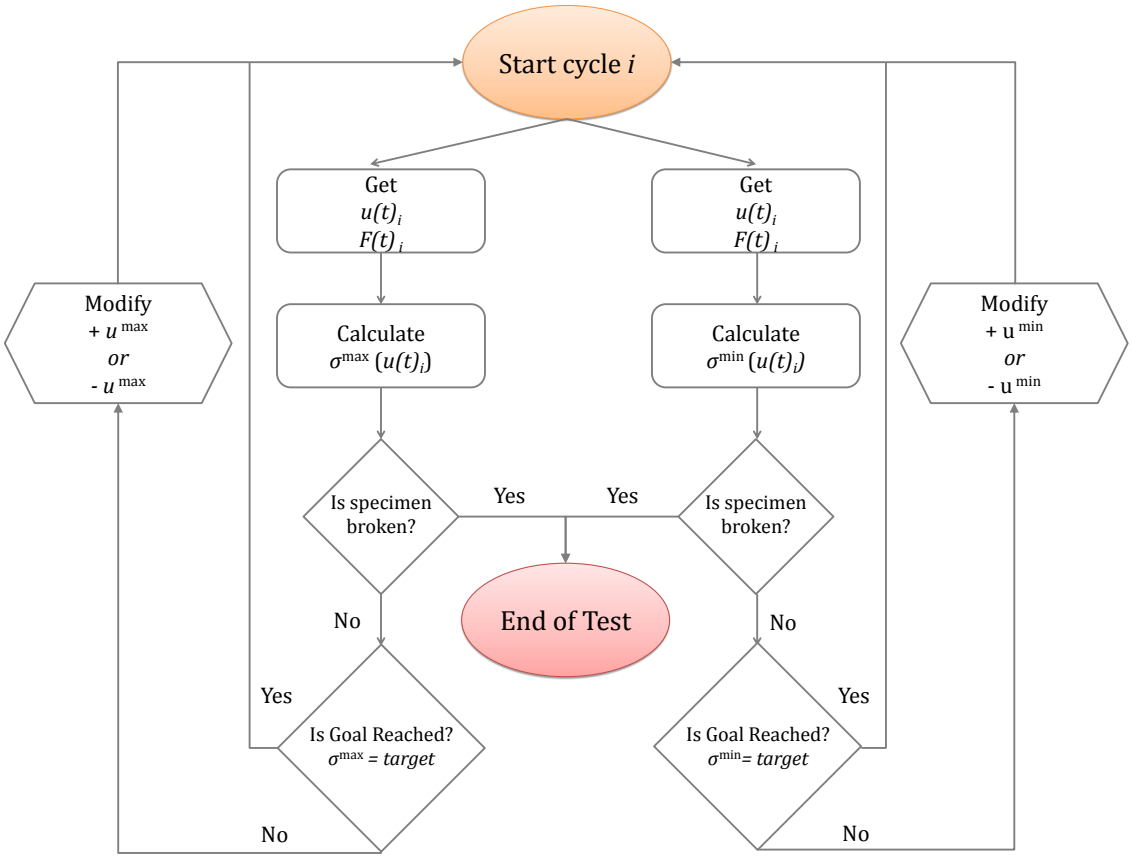

Figure 3.2-1 – Machine control algorithm for prescribing true stress on a specimen.

utilized testing frequency. At each cycle, upon defining a target true stress, the real-time readings of force and displacement are recorded. Subsequently, true stress amplitude is calculated by Eq. (3.2-1); maximum and minimum true stresses at each cycle are calculated respectively by:

$$\sigma^{\max,i} = \mathrm{Max}\left(\frac{F(t)}{S(u(t))}\right), \tag{3.2-2}$$

and

$$\sigma^{\min,i} = \mathrm{Min}\left(\frac{F(t)}{S(u(t))}\right), \tag{3.2-3}$$

where t is the time elapsed during each cycle i. After each cycle, the algorithm checks whether the specimen has broken. It does so by monitoring measured force with respect to prescribed displacement. If the specimen is broken, the test is terminated. If it is still intact, the actual true stress amplitude is compared with the target. The prescribed displacements - maximum ($u^{\max}$) and minimum values($u^{\max}$)

- are corrected by increasing or decreasing in small increments, depending on the value of the actual minimum and maximum true stress values. The magnitudes of displacement increments regulates the speed with which the machine control algorithm can reach the desired true stress loading. If it is too small, it might take too many cycles to achieve the target stress and, therefore, affect fatigue results. If the increment is large, it can induce an overshoot of the maximum or minimum target stress; in fatigue testing this is an undesired outcome, as it can negatively affect the results by damaging the material. It should be noted that the material, the specimen geometry, and the testing machine itself have a strong influence on the magnitude of the increment. The following cycle is then run under the newly altered displacement values and the procedure iterates.

On the practical side, such experimental setup has to conform to some basic requirements:

1. The ability to monitor and regulate the displacement of the testing machine actuator continuously and in real-time;
2. The experimental setup must be supplied with a load-cell of adequate accuracy (for dynamic loading), from which the measurements are to be imported into the algorithm;
3. The algorithm itself has to be carried out in a controller, which is normally included with the testing machine or on a personal computer of appropriate processing power.

In the described experimental setup, imposing displacement after calculations in real-time represents the biggest challenge. A setup can be either custom-built or acquired from several commercial manufacturers of fatigue testing equipment that offer this functionality.

3.2.2 Parallel testing

In fatigue life testing of any material, there is an inherent variance of measured fatigue lives. Unfortunately, this scattering is also present in elastomers, and especially so in synthetic elastomers. This is a separate subject of study and will be dealt in detail in the upcoming Section 3.5. At this point, it is sufficient to mention that, due to the scatter, a large number of specimens have to be tested to ensure statistically significant results. Therefore, to save machine time and overall testing time, it is advised to test several specimens at the same time.

The machine control algorithm cannot be applied to multiple specimen simultaneously, as it can only control true stress loading on one specimen at a time. Specifically, this algorithm is also unable to account for large cracks or complete breaks present in any of the specimens tested in parallel, because the effective specimen surface area drastically changes. This means that, with a single machine actuator, it is not theoretically possible to extend the true stress control to parallel testing.

This limitation is resolved by introducing master displacement curves that correspond to a specific true stress loading. The master displacement curves contain minimum and maximum prescribed displacement values at each cycle over duration

of an experiment for a specific loading level. When the effective surface area changes, this approach allows to keep the stress applied on other specimens constant. To create the master curves, the displacement values for each cycle are derived from the experiments run on single specimens at desired true stress targets as specified in the previous subsection. That is, preliminary individual testing is required *a priori* and real-time adjustments are not done during parallel testing. Hence, at each cycle, the positions of the machine actuator at the maximum and minimum displacements are registered and then used as reference points for the master displacement curves. Since individual specimens might have varied dimensions, processing defects (such as internal voids, material heterogeneity), as well as other contingent variables, the prescribed displacement for each individual specimen for the same true stress target may be affected. Thus, there is a need to test several specimens under the desired loading conditions to check whether these additional factors have a significant effect.

As experience shows, it is quite challenging to apply an exact true stress load on all specimens in parallel. Various experimental variables and conditions cannot be cancelled out entirely. Their presence will affect true stress experiences of each specimen to various degrees (introducing scattering in true stress values in addition to the fatigue life). The present procedure, however, allows to approximate the applied true stress load on specimens in parallel. To validate the extension to parallel testing, the true stress experienced by each specimen must be quasi-constant and close to the target.

Development of a parallel testing setup

A standard experimental setup has to have specimen grips in parallel with a failure-detecting apparatus, such as a camera. For this method, however, it is recommend to employ individual force sensors for each specimen grip. Not only does it allow to monitor loading on each specimen, it also detects specimen failure, as well as any other failure criteria.

In terms of arrangement of grips, several design iterations were explored - horizontal, grid, and circular arrangement. Circular arrangement was chosen due to ease of centering (alignment of top and bottom grips), symmetrical loading across the machine actuator, and optimization of used spaced in available space (constrained by a heating chamber). This type of experimental setup has been designed and utilized in the present work as shown in Figure 3.2-2. Each of the 8 individual specimen grips is equipped with a s-type load-cell (*HBM-500N*). The design allows manual adjustment of the distance between the bottom and top grips to ensure that the loading is uniform in all specimens. Additional details on the grip design are presented in Appendix D.

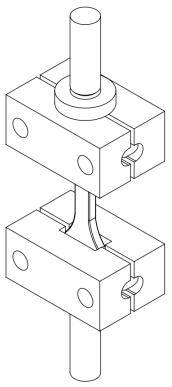

(a) Individual grips.

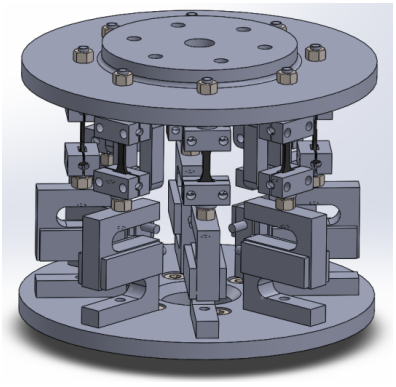

(b) Assembly with grips and load cells.

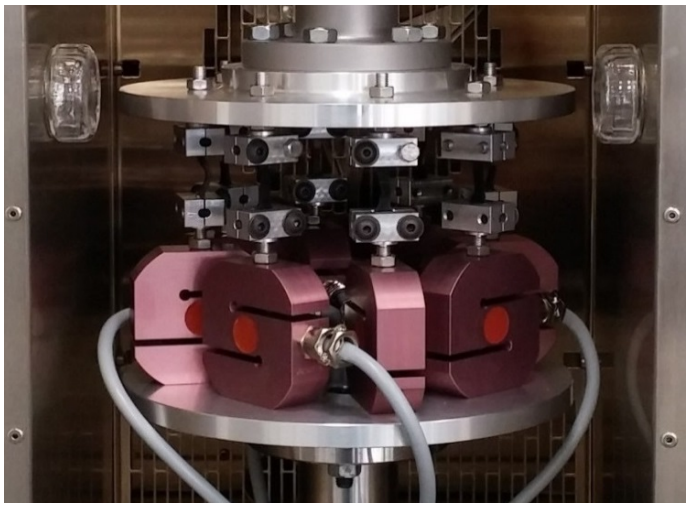

(c) Assembly installed on a machine with a heat chamber.

Figure 3.2-2 – Grip design utilized for parallel testing.

3.3 Experimental Implementation of the True Stress Method

The testing machine (*Instron E10000*) is equipped with a 1 kN load cell. It is also equipped with a heating chamber set at a temperature so that the surface of the specimen under loading, measured *in-situ* by a pyrometer, is at 120 °C; the testing temperature is specific to the service temperature of this grade of HNBR. It should be noted that due to thin geometry of specimens and high testing temperature, heat generation within the specimen is almost negligible and measured to be at most 0.5 °C. Variation of the heating chamber amounted to around ±0.9 °C. *Instron WaveMatrix*, the testing machine software used in the present experiment, allows to realize the algorithm (see Figure 3.2-1) by implementing a script in *C#* programming language. It both computes true stress amplitude and prescribes a sinusoidal waveform in displacement control.

For fatigue life tests, the same flat dumbbell specimen geometry, as specified in Figure 2.3-1, is utilized. There are several reasons for choice of this type of geometry:

- With use of cylindrical specimens, presence of problems with metal/rubber interface adhesion, especially at high temperatures;
- Economic considerations, considering the number of specimens to be tested for all six blends at four loading levels;
- Maximization of the travel of the machine actuator with grips and the heating chamber installed.

As mentioned earlier, this geometry only allows testing in tension because the specimens undergo buckling under compression. Moreover, due to the thin geometry of specimens, the number of cycles after complete failure is considered as the fatigue life, N_f.

3.3.1 DIC measurements

First, the digital image correlation (DIC) measurements are made for cyclic tests that are carried out in displacement control. Overall, the procedure is similar to that outlined in Section 2.3.1, except a high speed camera is used. Constant amplitudes of 30 mm, 45 mm, and 55 mm are applied with R-ratio of $R = 0$ at a frequency of 3 Hz (limitation imposed by camera speed, but within the same order of magnitude as for fatigue life testing). In order to calculate the evolution of the cross-section area in terms of the prescribed displacement, several cycles at 10; 10,000; and 100,000 cycles for each amplitude are analyzed. As before, both λ_2 and λ_3 are measured once for each blend up to 10,000 cycles to validate the assumption of isotropic response of the material; afterwards, only λ_2 is measured since $\lambda_2 = \lambda_3$ as shown in Figure 3.3-1.

A finite element analysis performed with commercial software *Abaqus*, for the given material and geometry, to confirm the results of DIC measurements. Hyperelastic behavior is modeled by the Arruda-Boyce model (Arruda and Boyce 1993) with the

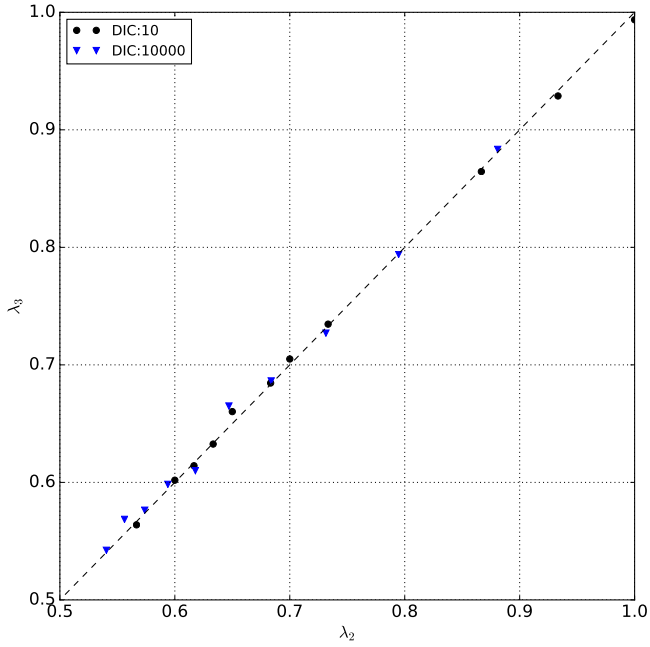

Figure 3.3-1 – Comparison of λ_2 and λ_3 measured by DIC after 10 and 10,000 cycles.

following coefficients: μ=1.57 MPa, λ_m=2.1, and D=10^{-4} MPa^{-1}; the coefficients are a best-fit of uniaxial tension results presented in Section 2.4.1. The viscoelastic behavior is considered elastic and is modeled with a 1-term Prony series and the following coefficient are used: g_1=0.398 MPa, k_1=0, and τ_1=0.347 s. Finally, cyclic loading up to 60 mm is prescribed at a frequency of 3 Hz.

The results of DIC measurements and FE analysis results are presented in Figure 3.3-2; a nominal area of 8 mm^2 is used to plot the results. As DIC measurements suggest, the relationship between the area and the prescribed displacement, for the given material, remains constant – at least up to 100,000 cycles for any amplitude. There is also a correlation between the FE analysis results and DIC measurements.

3.3.2 Individual testing

Then, individual specimens are tested at R=0 with four loading levels of stress amplitude - $\Delta\sigma$ = 10, 8, 6, and 4 MPa. As mentioned earlier, it is expected that some number of cycles will be required to achieve the target true stress amplitude, because of the nature of the algorithm. This number of cycles is omitted from the total fatigue life. At last, 2 million cycles mark the end of the experiments.

A constant average stress rate

$$\dot{\bar{\sigma}} = \frac{\text{Max}(\sigma) - \text{Min}(\sigma)}{\Delta t} \tag{3.3-1}$$

of 20 MPa/s is applied throughout the experiment. It should be noted that average stress rate is different from instantaneous stress rate

$$\dot{\sigma} = d\sigma/dt. \tag{3.3-2}$$

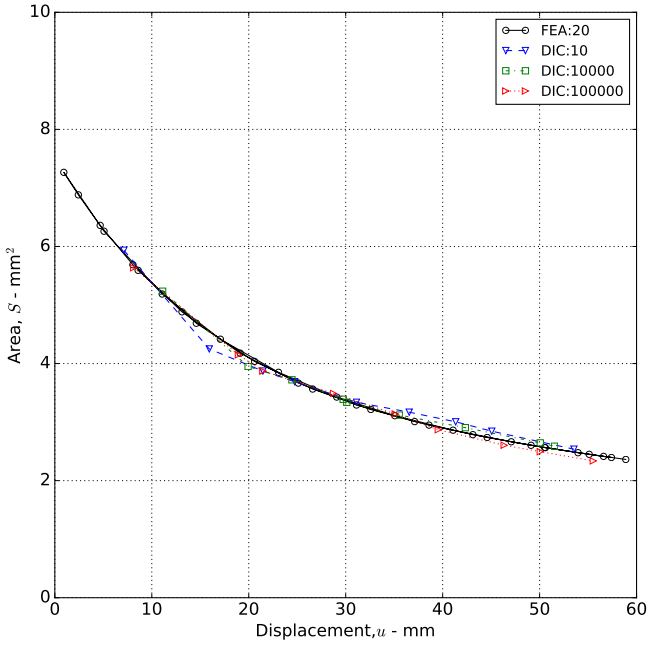

Figure 3.3-2 – Reference area of the specimen with respect to displacement prescribed by the testing machine. Average area is shown for DIC cycles 10; 10,000; and 100,000 and FE analysis at cycle 20.

The reason behind this choice lies in the fact that using a constant frequency is not ideal since the stress rate, which is a mechanical parameter that influences the behavior of the material, is not constant for different loading levels. The nominal frequencies that correspond to constant average stress rate of 20 MPa/s are calculated *a priori* to be 2.0 Hz, 2.5 Hz, 3.33 Hz, and 5 Hz for $\Delta\sigma = 10$, 8, 6, and 4 MPa, respectively.

3.3.3 Parallel testing

For parallel testing, master displacement curves for the three loading levels are created from the results of the tests performed on individual specimens. For repeatability, at least two to three individually tested specimens should be tested each loading level.

These master curves are calculated from average values at each loading level for both minimum and maximum prescribed displacement values. The technical limitations impose restrictions on recording the maximum and minimum displacements: instead of registering them for each cycle, it is done so only at specific intervals. Linear interpolation allows to fill the gaps by computing intermediate points between recorded values. Furthermore, during individual testing, it is assumed that large cracks occur and propagate at the end of the fatigue life. The specimens' geometry is thin and, consequently, data from the last 10% of cycles ($i \in [0.9N_f, N_f]$) are omitted in calculation of the master curve; in this case, cracks might achieve a significant size and, thus, reduce the real cross-section area. This, in turn, might lead to miscalculation of true stress. Additionally, at this stage, there is a particular need

to account for the statistical scattering inherent in fatigue life testing. This means that the two or three tests carried out on individual specimens at each loading level for the creation of a master curve, in most cases, do not represent a test with the longest fatigue lifetime. For longer testing, therefore, the minimum and maximum displacement values need to be extrapolated.

In the current work, the particularities of the material behavior and specimen geometry determined a function of best-fit, which is extrapolated up to 2 million cycles from the last 50% of cycles for both the maximum and the minimum prescribed displacements (after initially excluding the final 10% of cycles related to crack propagation, *i.e* best-fit within $i \in [0.5 * 0.9N_f, 0.9 * N_f]$).

3.3.4 Evaluation parameters

Finally, we introduce several parameters to evaluate, if the objective - prescribing constant true stress amplitude at a specific R-ratio - is satisfied. Some of these parameters are shown in the exaggerated schematic of Figure 3.3-3.

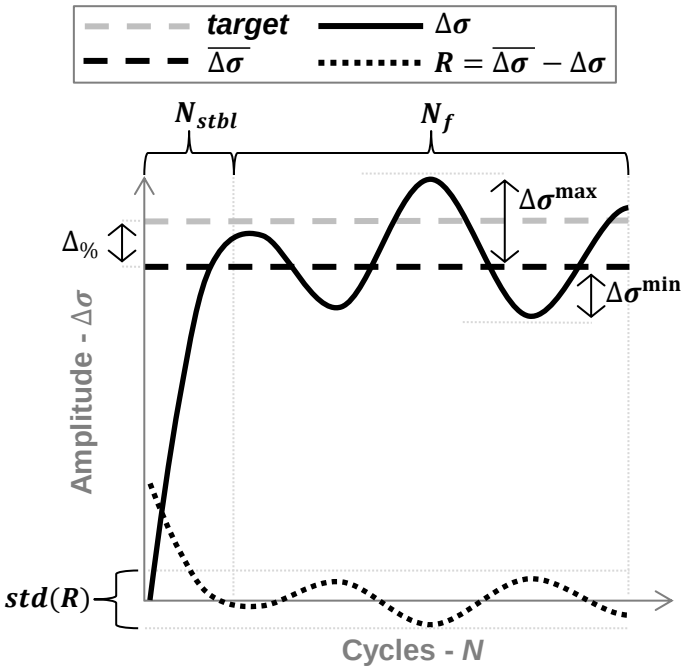

Figure 3.3-3 – Schematic of parameters used in evaluation of set objectives.

- Applied true stress amplitude ($\Delta\sigma$) - the actual true stress amplitude as applied by machine; calculated by Eq. (3.2-1);
- Average stress amplitude ($\overline{\Delta\sigma}$) - average true stress amplitude calculated for each cycle once target is reached;
- Stress range ($\Delta\sigma \in \left[\overline{\Delta\sigma}_{\min}, \overline{\Delta\sigma}_{\max}\right]$) - the range in average true stress amplitude values for all specimens tested at a particular target loading level;

- Percent difference to target ($\Delta_{\%}$) - percent difference calculated by

$$\Delta_{\%} = 100\% * \frac{\overline{\Delta\sigma} - \sigma_{\text{ref}}}{\sigma_{\text{ref}}}, \tag{3.3-3}$$

  of average amplitude ($\overline{\Delta\sigma}$) with target stress as the reference;

- Maximum amplitude ($\Delta\sigma^{\max}$) - difference between maximum measured true stress amplitude and average true stress amplitude ($\overline{\Delta\sigma}$);

- Minimum amplitude ($\Delta\sigma^{\min}$) - difference between minimum measured true stress amplitude and average true stress amplitude ($\overline{\Delta\sigma}$);

- R-ratio in terms of true stress (R_σ) - as defined in Eq. (3.1-4), R-ratio is calculated at each cycle, and then averaged;

- Average R-ratio in terms of true stress ($\overline{R_\sigma}$) - the average R_σ for all specimens tested at same target loading level.

- Stability of loading (std(R)) - a parameter to measure how constant (or *flat*) is the applied true stress amplitude for each experiment; it represents a measurement of the standard deviation of the residual with respect to the average amplitude ($\overline{\Delta\sigma}$)

$$\text{std}(R) = \sqrt{\frac{\sum(\overline{\Delta\sigma} - \Delta\sigma)^2}{N_f}}, \tag{3.3-4}$$

  where a value of std(R) = 0 indicates a perfect constant amplitude (or *flat* line);

- Number of cycles required to reach target stress (N_{stbl}) - due to the nature of the machine control algorithm, several cycles are required for the machine to attain the desired true stress amplitude;

- Fatigue life (N_f) - cycles until failure minus number of cycles required to reach target stress (N_{stbl}).

3.4 Validation of the True Stress Method

A44H96 HNBR blend is chosen for validation of the method. As investigated in the previous chapter, it displays the most significant Mullins effect (Section 2.4.3), permanent set and residual strain (Section 2.1.2) after cyclic loading.

3.4.1 Individual testing

For various loading levels, the procedure produces consistent results. As an example, Figure 3.4-1 shows minimum and maximum displacements prescribed by the testing

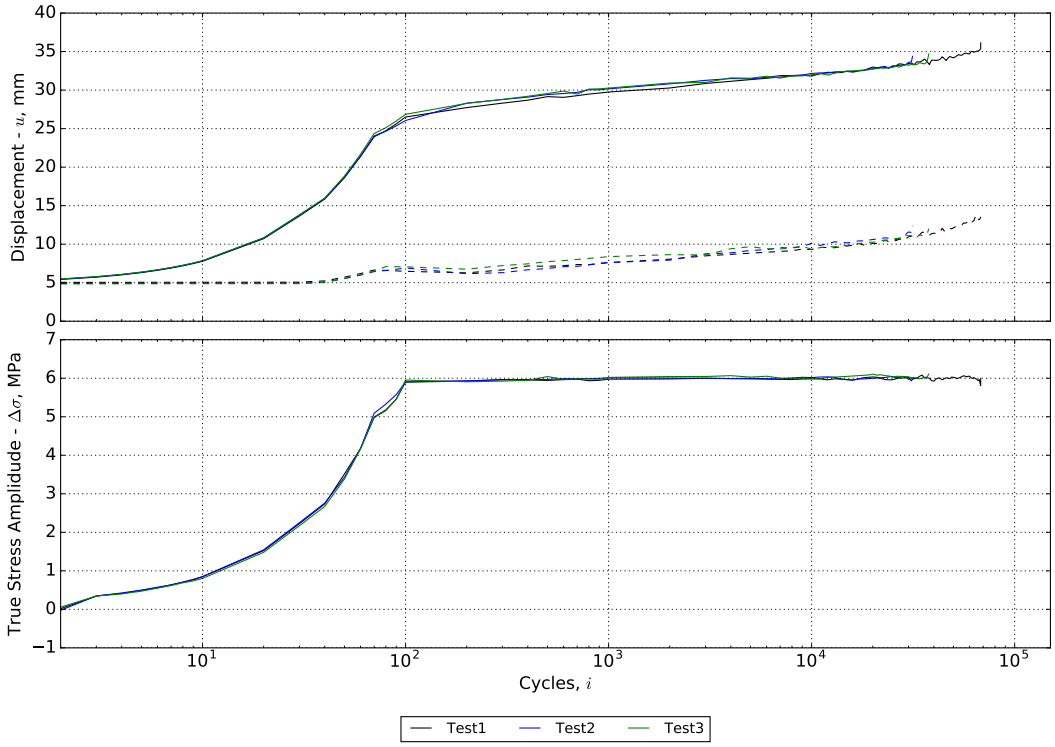

Figure 3.4-1 – Maximum and minimum imposed displacement (top) to attain constant true stress amplitude of 6MPa (bottom).

machine on three different individual specimens in order to reach a constant stress amplitude of $\Delta\sigma$=6 MPa. The evaluation parameters are presented in Table 3.4-1. There are two phases during stress control. The first phase, up to around 100 cycles,

Table 3.4-1 – Evaluated parameters for three tests at true stress amplitude of 6 MPa.

N_f **(Cycles)**	$\overline{\Delta\sigma}$ **(MPa)**	$\Delta_{\%}$	$\Delta\sigma^{\max}$ **(MPa)**	$\Delta\sigma^{\min}$ **(MPa)**	$\Delta\sigma$ **Range (MPa)**	R_σ	$\overline{R_\sigma}$	**std**(R) **(MPa)**
31 204	6.005	0.09	0.044	0.074		0.00054		0.03341
67 943	5.992	0.13	0.089	0.187	0.048	-0.00010	-0.00001	0.04681
37 386	6.041	0.68	0.068	0.069		-0.00048		0.03035

is comprised of machine stabilization (the imposed sinusoidal waveform increases gradually in its amplitude to a specified target), where the algorithm is reaching the target of 6 MPa. Upon completing 100 cycles, the target stress is achieved and

minimum and maximum prescribed displacements stabilize. There are no significant changes in displacement amplitude, but it still increases to maintain closely a true stress amplitude of 6 MPa. This is indicated by the average of true stress amplitude ($\overline{\Delta\sigma}$) over the duration of the three experiments and the percent difference ($\Delta_{\%}$). R-ratio, in terms of true stress, generally equals to zero over the duration of the three experiments. Moreover, we can comment on how constant the applied true stress amplitude is. In general, the values of std(R) are less than 0.1, *i.e.* the standard deviation of the applied true stress amplitude from the test-duration average ($\overline{\Delta\sigma}$) is less than 0.1 MPa. Moreover, the maximum ($\Delta\sigma^{\max}$) and the minimum ($\Delta\sigma^{\min}$) true stress amplitudes with respect to the average ($\overline{\Delta\sigma}$) are smaller than 0.1 MPa, except during test 2, where $\Delta\sigma^{\min} = .187$ MPa. This confirms the visual observations from Fig. 3.4-1, *i.e.* once the target amplitude is reached after 100 cycles, it can be said to be constant.

The number of cycles in the first phase will be different for other loading levels. As a rule, if the stabilization phase takes up under 2% of the average fatigue life at that particular loading level is considered generally acceptable. As mentioned earlier, those cycles are not counted in the fatigue life. There is another important aspect to be mentioned: in Fig. 3.4-1, all three specimens have different fatigue lives as shown in Table 3.4-1. With this in mind, the prescribed minimum and maximum displacement represent a good correlation and repeatability. Thus, a master displacement curve for this specific loading level can be created.

3.4.2 Testing in parallel

The master displacement curves in Figure 3.4-2 are derived from the individual tests

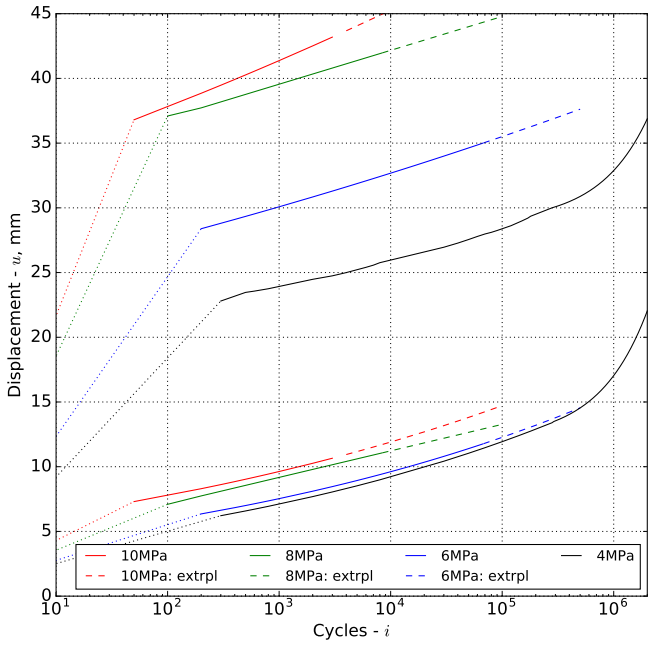

Figure 3.4-2 – Master displacement curves for prescribed constant true stress amplitude of 10, 8, 6, and 4 MPa and R=0.

for the four loading levels. The dashed lines represent the extrapolated maximum and minimum displacement values and the initial cycles (50 for 10 MPa, 100 for 8 MPa, 200 for 6 MPa, and 300 for 4 MPa) required for machine to stabilize and reach the target stress.

Figure 3.4-3 shows the evolution of the true stress amplitude for all tested specimens

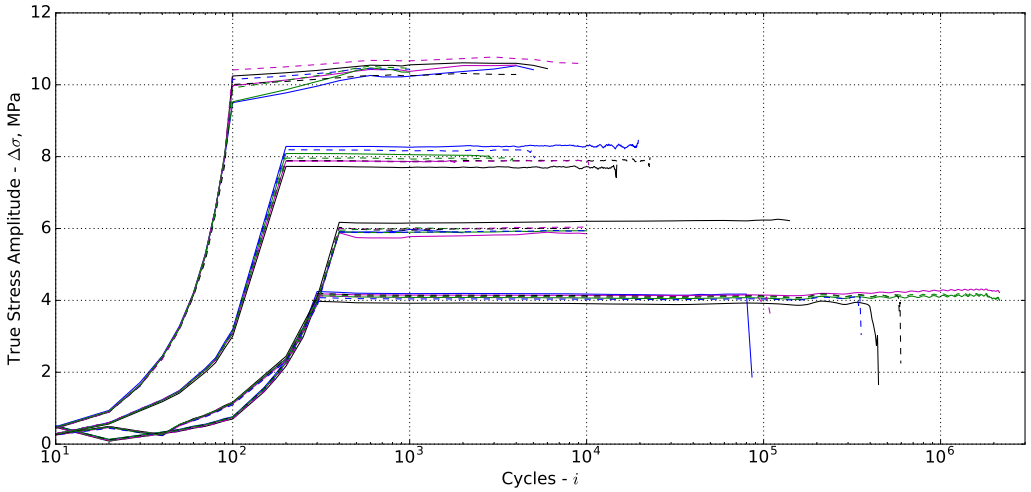

Figure 3.4-3 – Evolution of true stress amplitude under parallel loading of 10, 8, 6, and 4 MPa and R=0.

at each loading level. Moreover, the corresponding evaluation parameters are shown in Table 3.4-2.

It appears that the results of loading in parallel are highly dependent from one test to another, *i.e* at each target loading level of 10, 8, 6, or 4 MPa. Looking at each individual loading level, it turns out that the actual stress amplitude experienced by each specimen does not necessarily equal the target stress, as the percent difference indicates ($\Delta_{\%}$). It is the most significant for 10 MPa loading in general. This occurrence can be explained by the specimen installation and how it causes minute differences between different specimens. Despite additional precaution involved in setting up the specimens, some of them are slightly compressed or in tension with respect to one another. Thus, the average stress amplitude range measured for each specimen generally varies as shown in Table 3.4-2 - 0.39 MPa at 10 MPa, 0.60 MPa at 8 MPa, 0.38 MPa at 6 MPa, and 0.43 MPa at 4 MPa.

Moreover, all specimens tested at 10, 8, 6 MPa are overloaded as compared to the desired target stress amplitude; at 4 MPa loading level, there are two specimens whose average is below the desired target amplitude. In some situations, for example when there are several specimens tested at 4 MPa, cracks appear within the specimen that leads to a significant decrease in the measured force and calculated stress as a result. The presence of such cracks, however, complicates the identification of cross-section area of the specimen. Therefore, this stress value is not the actual true stress.

Additionally, the measured R-ratios are relatively close to the desired value of zero. The highest deviation from zero is observed for the 4 MPa loading level, where

Table 3.4-2 – Evaluated parameters for parallel tests at true stress amplitudes of 10, 8, 6, and 4 MPa and R=0.

Target Level	N_f **(Cycles)**	$\overline{\Delta\sigma}$ **(MPa)**	$\Delta_{\%}$	$\Delta\sigma^{\max}$ **(MPa)**	$\Delta\sigma^{\min}$ **(MPa)**	$\Delta\sigma$ **Range (MPa)**	R_σ	$\overline{R_\sigma}$	$std(R)$ **(MPa)**
10	5 133	10.38	3.814	0.149	0.607	0.39182	0.03264	0.00744	0.15752
	6 397	10.55	5.477	0.063	0.213		0.00217		0.04653
	4 479	10.49	4.924	0.054	0.361		0.01755		0.09201
	1 577	10.28	2.843	0.185	0.421		0.01838		0.14301
	1 397	10.39	3.918	0.057	0.146		-0.00243		0.05118
	4 770	10.28	2.787	0.037	0.185		0.00629		0.04320
	9 894	10.67	6.705	0.103	0.171		-0.01519		0.05517
	1 610	10.40	3.975	0.126	0.273		0.00007		0.09598
8	19 652	8.29	3.685	0.159	0.081	0.59662	0.01089	0.00302	0.02909
	14 969	7.70	3.772	0.063	0.202		-0.00619		0.03181
	1 692	7.87	1.614	0.020	0.016		0.00213		0.00629
	2 713	8.04	0.552	0.039	0.032		0.01188		0.01493
	4 951	8.17	2.084	0.036	0.053		0.00738		0.01697
	22 850	7.89	1.397	0.097	0.164		0.00598		0.02861
	10 241	7.88	1.542	0.026	0.031		-0.00950		0.01127
	3 884	7.94	0.757	0.026	0.051		0.00159		0.01730
6	2 037	5.90	1.722	0.081	0.002	0.37657	0.00364	0.00353	0.01109
	143 455	6.22	3.699	0.036	0.074		-0.00113		0.01442
	14 980	5.85	2.577	0.051	0.109		0.00388		0.04578
	12 397	5.92	1.296	0.016	0.035		0.00195		0.01547
	10 332	5.93	1.206	0.017	0.041		-0.00187		0.01720
	8 531	6.00	0.051	0.016	0.045		0.00584		0.01707
	11 280	6.02	0.401	0.021	0.036		0.00464		0.01558
	2 029	5.99	0.228	0.036	0.003		0.01128		0.00155
4	82 299	3.97	0.800	0.307	0.182	0.43596	0.08269	0.03490	0.01203
	443 971	3.82	4.565	0.180	0.046		0.02089		0.02934
	2 155 796	4.25	6.334	0.062	0.124		0.01098		0.03051
	2 155 796	4.10	2.510	0.062	0.075		0.05108		0.03538
	354 630	4.03	0.743	0.073	0.020		0.02980		0.02360
	595 017	4.10	2.561	0.116	0.024		0.05947		0.02432
	108 779	4.07	1.652	0.075	0.028		-0.00005		0.00479
	2 155 796	4.13	3.374	0.058	0.092		0.02436		0.03995

$\overline{R_\sigma}$ = 0.035 and is an order of magnitude larger compared to others. This could be explained that at 4 MPa loading, some variation in the minimum loading would result in a greater R-ratio calculated.

Finally, one can look at the standard deviation of the residual (std(R)). Its calculation can be confirmed by Fig. 3.4-3. For example, the true stress amplitude loading for several specimens at 10 MPa are not constant; the values for the standard deviation of the residual are quite large: specimen No.1 is std(R) = 0.16 MPa; and for specimen No.4 - std(R) = 0.14 MPa. For other tested specimens, this value does not exceed 0.1 MPa.

Overall, the magnitudes are deemed reasonable, and the objective for constant true stress control is reached.

3.4.3 S-N curve in true stress

Finally, the primary objective of plotting a Wöhler curve in true stress is achieved as presented in Figure 3.4-4. Since, for both individual and parallel testing, the

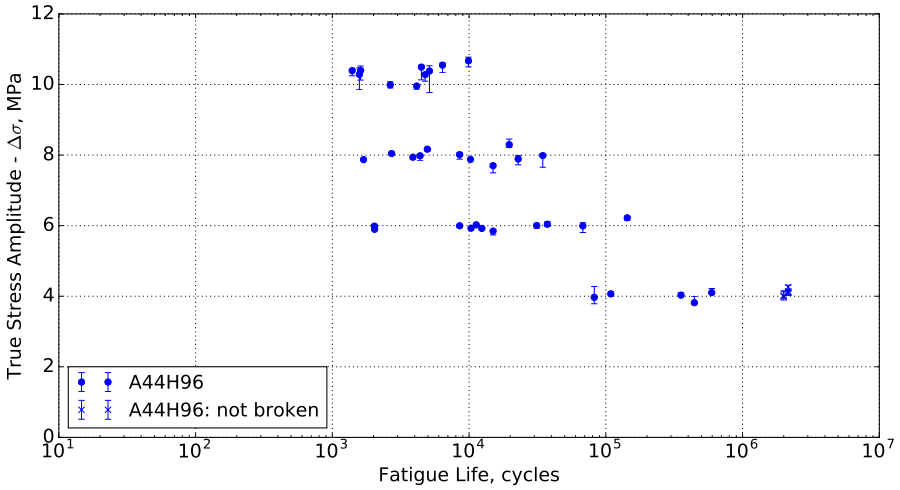

Figure 3.4-4 – Wöhler curve of HNBR blend A44H96, $R = 0$.

actual true stress experienced by the material is measured, the present procedure allows to plot the exact loading experienced by each specimen, which is useful for a future extensive statistical analysis. In this context such analysis is required due to large scattering of the results and also presence of data points at 4 MPa loading level, where specimens did not break. These statistical approaches are discussed in the next section.

3.5 Statistical Analysis

3.5.1 Need for Statistical Analysis in Elastomers

Generally, scattering is inherent to fatigue life testing of elastomers (and other materials), irrespective of the type of control. This is mainly due to material defects introduced during processing and their influence on crack initiation (Svensson 1981). Moreover, the statistical distributions of the results are mostly non-normal and tend to exhibit large standard deviation (ASTM International 2017).

The magnitude of scattering depends also on the material, *e.g.* natural rubber (NR) exhibiting smaller scattering as compared to synthetic rubbers as a consequence of its better resistance to fatigue crack propagation (Mars and Fatemi 2003); moreover, high scattering is observed for crystallizing rubbers at high R-ratios (caused by a phenomenon called "branching", where crack growth occurs in different directions than as classically expected) (Mars and Fatemi 2002). Figure 3.5-1 shows an example

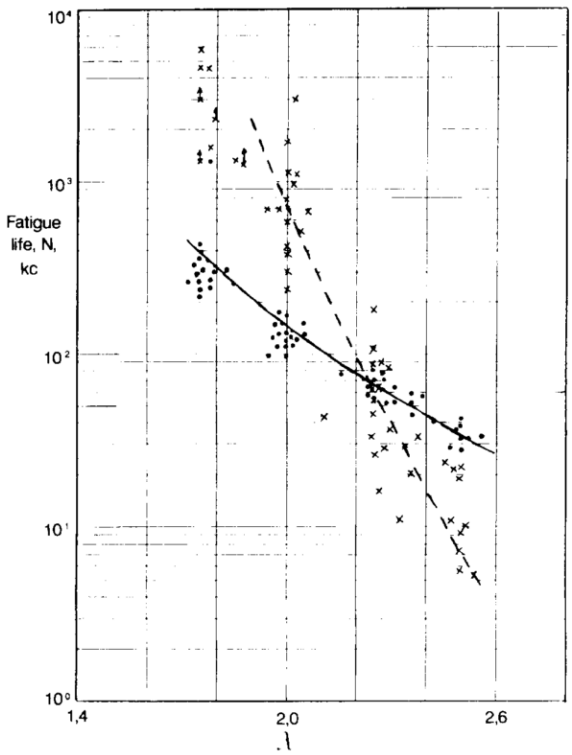

Figure 3.5-1 – Fatigue life (N) versus stretch ratio λ; each point is median of six specimens; solid line - NR, dashed - SBR/BR blend (Lake and Lewis 1978).

of generally observed scattering as well as material effect, where solid line refers to a NR vulcanizate and the dashed line to a SBR/BR blend. One can observe that the scattering for NR is smaller than for SBR/BR. Moreover, the scattering increases in magnitude with decreasing loading, and is largest at the smallest loads for SBR/BR blend as the material approaches its fatigue limit (Royo 1992).

3.5.2 Statistical methods

Basquin's law and regression analysis

Due to its simplicity and phenomenological significance, traditionally, the Basquin's law of fatigue is considered in analyzing fatigue life results in elastomers (Basquin 1910; Kun et al. 2008)

$$\Delta\sigma = C_B \left(N_f\right)^{a_B} , \tag{3.5-1}$$

where C_B and a_B are fitted values for a power law relationship. The wide use of the Basquin's law also leads to differences in its application on fatigue life data. In general, it can be summarized into two approaches: multiple linear regression is carried out all available fatigue loading levels; or it is carried out on average (arithmetic or geometric) at each separate loading level.

The Wöhler curve depicted in Fig. 3.4-4 (of blend A44H96) are used as example data for application of the Basquin's law (and other subsequent statistical analyses). It is important to recall the specific characteristics of these data: the presence of variation in average true stress amplitude values in additional to scattering in fatigue lives. Thus, multiple linear regression is applied for fitting of the Basquin's law. However, there are issues with the target loading level of 4 MPa; there are five unbroken specimens. As a remark, in statistical terminology, the life of unbroken specimens is referred to as "right censored" data, *i.e.* it is censored because the number of cycles to failure is not known. Thus, the present regression analysis is performed on two sets of data: where 4 MPa loading level results are excluded; and where unbroken specimens are excluded. A method of least squares is used to find coefficients of Eq. (3.5-1).

The corresponding results are shown in Figure 3.5-2 along with the coefficients in Table 3.5-1. It is obvious that the choice of a data set significantly influences the obtained results. For example, at the lowest loading level of 4 MPa there is a difference of a logarithmic order of magnitude. If the 4 MPa loading level is ignored

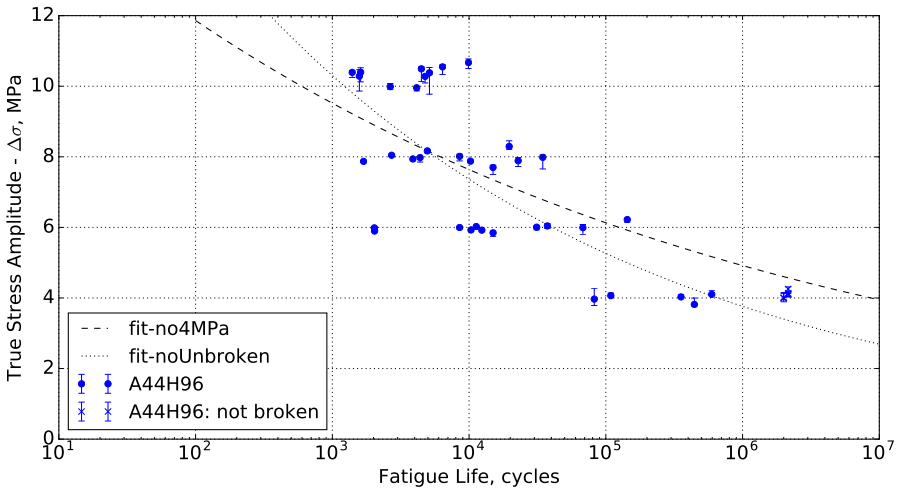

Figure 3.5-2 – Basquin's Law fit for two sets of data: 4 MPa loading level excluded and unbroken specimens excluded.

Table 3.5-1 – Coefficients of the Basquin's law for two sets of data.

Data set	C_B	a_B	r^2
4MPa excluded	18.421	-0.096	0.24
Unbroken excluded	28.201	-0.146	0.58

during fitting, the Basquin's law is a poor fit as indicated by its $r^2 = 0.24$; the influence of long fatigue life at 6 MPa loading is too important and the 10 MPa loading is completely misrepresented. If only the unbroken specimens at 4 MPa are excluded, the overall fit is better ($r^2 = 0.58$), however the fatigue life given by the Basquin's law is greatly underestimated. In both data sets, the unbroken specimens are not taken into account. Moreover, the linear extrapolation gives no indication of how much scattering is observed in data. Thus, there is a need for more advanced methods for analysis of fatigue life results presented in Fig. 3.4-4.

Parametric approach

In life sciences, the study of distribution of lifetimes is referred to as *survival analysis*, whilst in industrial setting the term *reliability analysis* is commonly encountered. Of the latter, the Weibull distribution is widely used for parametric statistical failure analysis in engineering and other fields (Klein and Moeschberger 2003). For example, it is the *de facto* method employed for the statistical discussion of fatigue of metals and metallic parts (Stephens et al. 2001). For elastomers, there are several explicit studies that consider Weibull analysis (Dizon et al. 1974; Minguez and Royo 1980; DeRudder 1981; Gargani and Bruzzone 1986; Derringer 1988; Hallett 1997), however recent investigations appear to be lacking. In an extensive study, Minguez and Royo (1980) tested fatigue life with around 6600 specimens of 10 different elastomers and investigated fitting of normal, log-normal, and Weibull distributions. It was found that only results of natural rubber fit a normal distribution and only results of SBR 1803 fit a log-normal distribution. On the other hand, a Weibull distribution was successfully fitted for almost all materials.

The Weibull probability density function (PDF - probability that a failure will occur at a certain cycle N) is defined as (Weibull 1951; Weibull 1961)

$$f(N) = \begin{cases} \frac{k}{\rho}\left(\frac{N-\gamma}{\rho}\right)^{k-1} e^{-\left(\frac{N-\gamma}{\rho}\right)^k}, & \text{if } N \geq \gamma \\ 0, & \text{otherwise,} \end{cases} \tag{3.5-2}$$

where k, ρ, and γ are the so-called shape, scale, and location parameters, respectively. By comparing the values of the shape parameter, it becomes clear that Weibull distributions are frequently used for their flexibility in fitting many different types of data. For special cases:

- $k = 1$ - the Weibull distribution is equivalent to the exponential distribution;
- $k = 2$ - it is equivalent to the Rayleigh distribution;
- $k = 2.5$ - it is a close approximation of the log-normal distribution;
- $k = 3.6$ - it is a close approximation of the normal distribution.

The scale parameter, ρ, determines how "wide" the distribution is and its value always corresponds to the number of cycles at which 63.2% of the specimen population fail. Moreover, the cumulative distribution function (CDF - total probability that specimen survives until cycle N) is

$$F(N) = 1 - e^{\left(\frac{N-\gamma}{\rho}\right)^k}. \tag{3.5-3}$$

The Weibull analysis is performed on only one variable, *i.e.* the fatigue life. Thus, in application of the Weibull analysis on fatigue data from Fig. 3.4-4, the variations around the true stress amplitude loading are assumed to be negligible. In practice, average values of $\Delta\sigma$ around 10, 8, 6, and 4 MPa are calculated for each loading level. These values are considered as the target loading levels, at which univariate statistical analysis is performed. Due to the small number of specimens per loading level and to the presence of right censored data, γ is set to 0 (Lockhart and Stephens 1994; Abernethy 1996; Cousineau 2009). Three parameter fit methods are relatively more complicated than required for two parameter fit and large sample populations ($N > 100$) are necessary for a correct fit. For a two parameter fit, Eq. (3.5-3) is reduced to

$$F(N) = 1 - e^{\left(\frac{N}{\rho}\right)^k}. \tag{3.5-4}$$

And the two parameter fit is classically performed considering the following "linearized" relationship

$$\ln\left[-\ln(1 - F(N))\right] = k\ln(N) - k\ln(\rho). \tag{3.5-5}$$

Practically, this statistical analysis is implemented in a custom *Python* script with the use of *NumPy* and *SciPy* libraries to calculate the Weibull coefficients, where linearization and the subsequent fit are performed with a method of maximum likelihood estimation. The probability of failure $F(N)$ is approximated by median rank tables (refer to the review of Genschel and Meeker (2010) for more information). Moreover, these can be estimated relatively quickly by Benard's approximation (Stapelberg 2009)

$$F_{\text{Benard}} = \frac{j - 0.3}{J + 0.4}, \tag{3.5-6}$$

where j is the ordered number of a specimen and J is the total number of tested specimens at a particular loading level. The use of median rank tables (or their approximation) is necessitated by a statistically small number of tested specimens; moreover, it allows to take into account unbroken specimens, where unbroken specimens still influence the total number J.

Figure 3.5-3 show the application of Eq. (3.5-5) applied to each loading level to determine k and ρ. An r^2 values of greater than 0.95 indicate the closeness of fit and, in general, it can be argued that the data is well-fitted. However, the 4 MPa loading presents some problems. It is hard to judge whether the Weibull distribution fits the data. With only five fatigue life measurements, the other specimens did not break up to 2 million cycles. Moreover, in general, with few specimens tested, it is difficult to discern whether concavity is present after "linearization" in Figure 3.5-3. Presence of such concavity is an indication that the third location parameter (γ) is required for the fit (Abernethy 1996). In general, presence of censored data brings

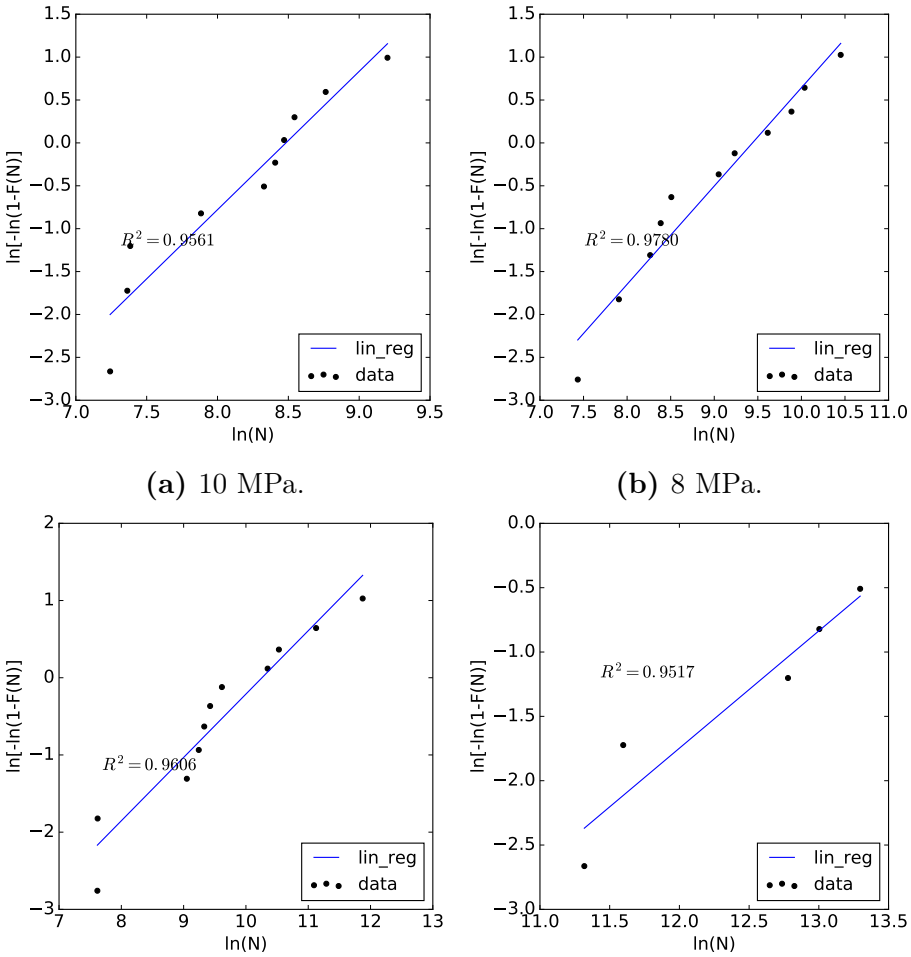

(a) 10 MPa. **(b)** 8 MPa.

(c) 6 MPa. **(d)** 4 MPa.

Figure 3.5-3 – Calculation of Weibull parameters for data presented in the Wöhler curve of Fig. 3.4-4.

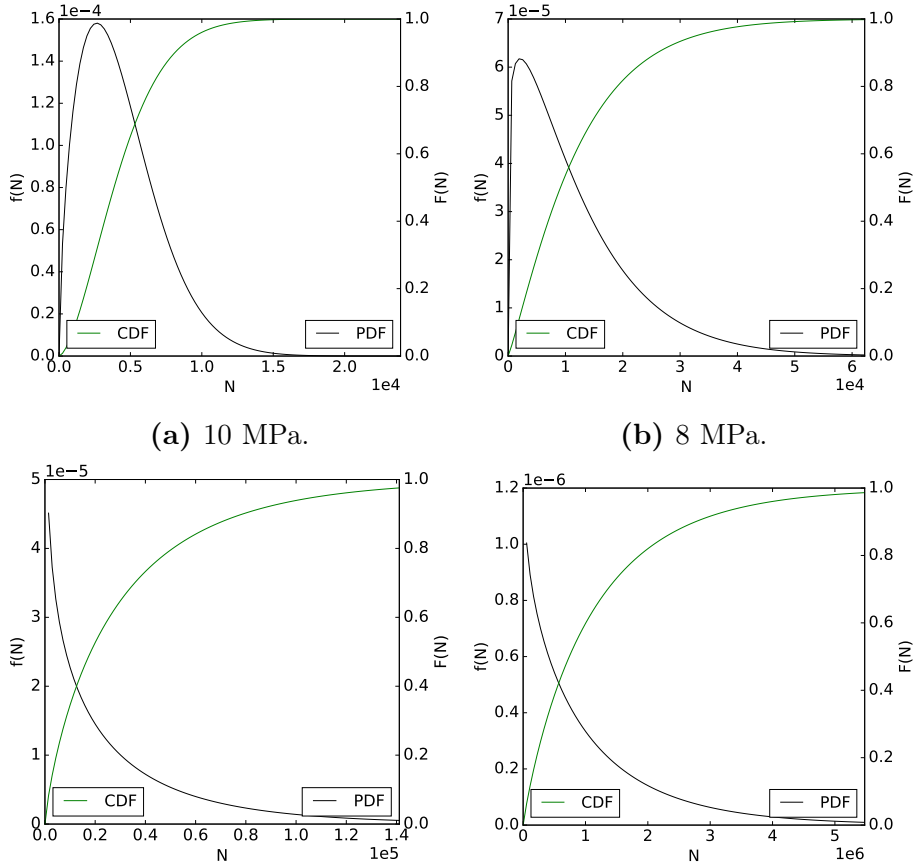

(a) 10 MPa. **(b)** 8 MPa.

(c) 6 MPa. **(d)** 4 MPa.

Figure 3.5-4 – Probability and cumulative distribution functions of fitted Weibull parameters for data presented in the Wöhler curve of Fig. 3.4-4.

a lot of uncertainty into the fit of the Weibull distribution with such small number of samples.

Figure 3.5-4 shows the probability and cumulative distribution functions for each loading level. The fitted probability density functions for 10 and 8 MPa loading levels (Figs. 3.5-4(a) and 3.5-4(b)) have increasing probability of observation of a failure up to a certain number of cycles and then this probability decreases. On the other, probability of observation of a failure decreases continuously for 6 and 4 MPa loading levels (Figs. 3.5-4(c) and 3.5-4(d)). This result, interpreted in terms of the Weibull fatigue analysis, would indicate that the failure rate of specimens is decreasing due to early failure of specimens with defects; thus, as a filtering mechanism, only specimens with least affecting flaws are left at 2 million cycles. The parameters are shown in Table 3.5-2 reflecting the distributions plotted in Fig. 3.5-4. In addition to the parameters, the average true stress amplitude at each target loading level ($\overline{\Delta\sigma}$), the mean ($\overline{N_w}$), and the minimum (N_w^{min}) and maximum (N_w^{max}) of 95% bounds of the distribution are calculated. The above-mentioned observations are explained by the values of the shape parameter $k < 1$ for 6 and 4 MPa. A value of less than 1 indicates that the instantaneous failure rate decreases with time (Jiang and Murthy 2011); when applied to fatigue, it can imply that the specimens with significant flaws are the first to fail early with short fatigue lives, while the remaining have a relatively long fatigue life. Moreover, these results confirm the qualitative

Table 3.5-2 – Weibull parameters with average true stress amplitude for a given target loading level, as well as mean, minimum (lower) and maximum (upper) 95% bounds of the distribution for data presented in the Wöhler curve of Fig. 3.4-4.

Target Load	k	ρ	$\overline{N_w}$	$N_w^{\min}$	$N_w^{\max}$	$\overline{\Delta\sigma}$ **(MPa)**
10 MPa	1.61	4 831	4 329	766	9 540	10.34
8 MPa	1.15	12 565	11 971	940	32 738	7.98
6 MPa	0.82	28 507	31 734	3 764	108 562	5.99
4 MPa	0.91	1 106 620	1 156 352	42 560	3 687 213	4.05

observations that can be made with respect to Fig. 3.4-4. Due to large scattering of fatigue lives, the minimum and maximum 95% bounds of the distribution are orders of magnitude apart. As expected. mean Weibull fatigue life ($\overline{N_w}$) decreases with increased loading. And, the obtained values can be compared with the Basquin's law estimate ($\overline{N_B}$) (Fig. 3.5-2), or the geometric mean given by (Mars and Fatemi 2003; ASTM International 2017)

$$\overline{N_G} = \left(\prod_{i=1}^{n} N_i \right)^{1/n} . \tag{3.5-7}$$

Table 3.5-3 shows these comparisons. If one recalls, there are two data sets: $\overline{N_{B1}}$

Table 3.5-3 – Comparison of Weibull mean with geometric mean and those derived from Basquin's law; unit - cycles.

Load	$\overline{N_w}$	$\overline{N_G}$	$\overline{N_{B1}}$	$\overline{N_{B2}}$	$\overline{\Delta\sigma}$
10 MPa	4 329	3 598	421	974	10.34
8 MPa	11 971	5 455	6 325	5 760	7.98
6 MPa	31 734	15 785	127 180	41 195	5.99
4 MPa	1 156 352	-	7 633 742	603 432	4.05

represents the data set without 4 MPa loading and $\overline{N_{B2}}$ represents the data set without the unbroken specimens. Additionally, the geometric average for 4 MPa loading level is not computed because of presence of unbroken specimens. Overall, there are large discrepancies between the 4 values for all loading levels (excluding absence of geometric mean at 4 MPa). Such variance in the obtained averages is a consequence of the large scatter. As a consequence, plotting a classical Wöhler curve with average values per loading level appears to be insufficient with the present data.

Non-parametric approach

In cases where data does not fit a particular distribution or if the number of samples is small, the fit of a Basquin's law or of a parametric distribution (such as Weibull) can be difficult and eventually provide erroneous conclusions. Then, a non-parametric fit can overcome this difficulty, because it assesses the relationships strictly in terms of available data (Rich et al. 2010).

For example, the Kaplan-Meier estimator is a non-parametric approach that is widely used in medical sciences to carry out survival analysis (or reliability analysis).

Its main advantage lies in being a great comparative tool when analysing time-to-event studies, especially those with incomplete observations (Rich et al. 2010). The data can be characterized by three variables:

- Time to an event - *i.e.* fatigue life or number of observed cycles;
- Status at the end of that time - *i.e.* failure or survival;
- Category or group - *i.e.* blend and loading level.

Such approach has been considered in fatigue studies of various metal alloys. However, the influence of its widespread use in medical sciences is evident as these metals are used for applications in prostheses or implants (Scherrer et al. 2011; Chan et al. 2013), medical equipment (Fitzgerald et al. 2001; Fišerová et al. 2015), *etc.*

It is used to estimate the survival function

$$S(N) = 1 - F(N) \tag{3.5-8}$$

where $F(N)$ is the cumulative distribution function, and is defined by (Kaplan and Meier 1958)

$$\widehat{S}(N) = \prod_{i:N_{(i)}<N} \left(1 - \frac{q_i}{r_i}\right), \tag{3.5-9}$$

where $N_{(1)} < N_{(2)} < ... < N_{(m)}$ is an ordered set of m distinct measurements of fatigue life in cycles at a particular target loading level (10, 8, 6, or 4 MPa), q_i is the number of failures at $N_{(i)}$, and r_i is the number of failures before $N_{(i)}$. Fatigue life results are analyzed at the four target loading levels in the *R*-software package using the *survival* library (Therneau and Lumley 2017).

Figure 3.5-5 shows Kaplan-Meier curves for four target loading levels. As a quick introduction to Kaplan-Meier curves, the line going along the x-axis represents a duration of survival; when a specimen fails, a drop occurs and there is a change in the cumulative probability. Increase in the negative slope (or steepness) of each curve indicates a decrease in survivability (increase in failure rate). The crosses on plotted lines indicate unbroken specimens. To note on the results of Figure 3.5-5, it is evident that as the loading level increases, the failure rate increases. As expected, $\widehat{S}(N) = 0.5$ corresponds to the medians of 4308 cycles for 10 MPa, 8524 cycles for 8 MPa, 12397 cycles for 6 MPa, and 595017 cycles for 4 MPa. Finally, a log-rank test can be performed to compare the statistical significance of the four curves. It is a non-parametric test that compares the observed events for each group, *i.e.* loading level, to what would be expected with a null hypothesis[1]. Fig. 3.5-5 shows the p-value of $p = 0.0001 < 0.05$ from the log-rank test, implying that survivability differs significantly (statistically) with varying loading level.

Multivariate and semi-parametric approach

Both Kaplan-Meier and Weibull analysis are univariate approaches, *i.e.* survivability is analyzed only on one variable at a time. Moreover, they cannot be used with

[1] null hypothesis, in this case, implies that there is no difference in survival with varying loading levels

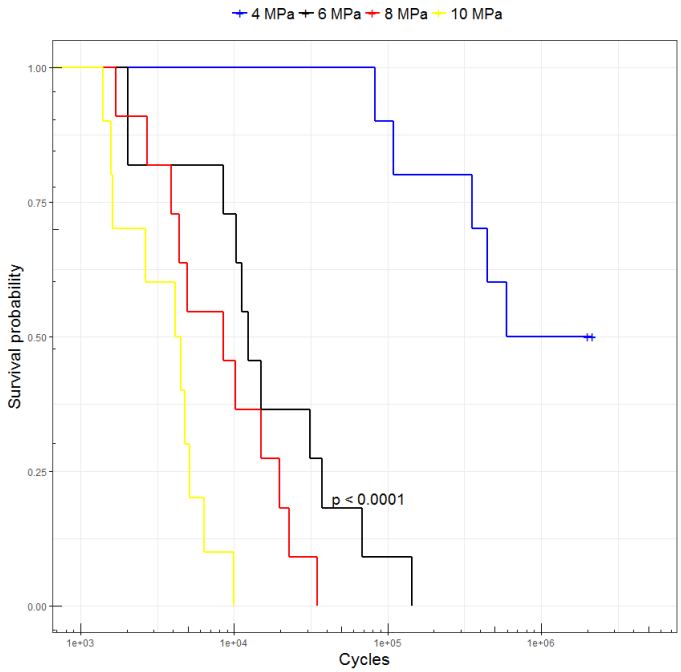

Figure 3.5-5 – Kaplan-Meier estimate of the survival function for data presented in the Wöhler curve of Fig. 3.4-4.

a continuous variable such as true stress amplitude. Thus, the Cox proportional hazards model can be introduced to investigate the influence of several variables (covariates) simultaneously and of continuous variables (Cox 1972). Interestingly, it appears that the Cox hazards model is rarely used in fatigue studies; there are few studies that focus on fatigue of prostheses (Tang et al. 2013) and medical equipment (Fišerová et al. 2015), as well as of oil pipelines (Farhangdoost and Siahpoosh 2006) and engine turbine blades (Zhang et al. 2012).

The Cox proportional hazards model is based on the hazards function

$$h(N) = \frac{f(N)}{S(N)}, \tag{3.5-10}$$

where $f(N)$ is the probability density function and $S(N)$ is the survival function. The practical meaning of the hazards function is that is represents the probability that a specimen at cycle N will undergo failure in the next instant; often, it is referred to as the hazard rate (in survival analysis) or as conditional (instantaneous) failure rate (in reliability analysis) (Klein and Moeschberger 2003). The hazard function of the Cox model is generalized to

$$h(N, \vec{x}) = h_0(N) \times \exp\left(\beta_1 x_1 + \beta_2 x_2 + \cdots + \beta_m x_m\right), \tag{3.5-11}$$

where N is the fatigue life, $\vec{x} = (x_1, x_2, \ldots, x_m)$ is a vector of m covariates, β_1, β_2, …, β_m are unknown regression coefficients that measure the impact of the covariates, and $h_0(N)$ is referred to as the baseline hazard and it corresponds to the hazard when $\vec{x} = 0$. Thus, the Cox model can be solved for by multiple linear regression of $\ln(h(N))$, where $h_0(N)$ becomes the intercept.

An exponent of a coefficient β_i is referred to as the hazard ratio (HR) as

$$\mathrm{HR} = \exp \beta_i, \tag{3.5-12}$$

and its value indicates the following:

- HR = 1 - no effect of covariate i;
- HR > 1 - as value of covariate i increases, *e.g.* stress amplitude, the event hazard increases and subsequently duration of survival decreases;
- HR < 1 - the opposite, as value of covariate i increases, *e.g.* stress amplitude, the event hazard decreases and duration of survival increases.

An important remark should be made: the *proportional* part of the Cox proportional hazards model name comes from the key assumption of the model - hazard curves are proportional for groups of observations - and, thus, the hazard ratio is independent of N and the baseline hazard; this is evident, where with Eq. (3.5-11), the hazard ratio can also be expressed for two observations j and j' as

$$\mathrm{HR} = \frac{h_j(N, \vec{x_j})}{h_{j'}(N, \vec{x_{j'}})} = \frac{h_0(N) \times \exp\left(\vec{x_j}\beta_j\right)}{h_0(N) \times \exp\left(\vec{x_{j'}}\beta_{j'}\right)} = \frac{\exp\left(\vec{x_j}\beta_j\right)}{\exp\left(\vec{x_{j'}}\beta_{j'}\right)}. \tag{3.5-13}$$

In other words, if applied on fatigue life data, the assumption implies that if one specimen (tested under one condition) has a risk of failure (hazard) that is, for example, 10 times higher than under some other condition at some time t - then the risk of failure remains 10 times higher at any other time. Thus, it is important to test for this assumption.

As mentioned earlier, Cox hazards model is useful for analyzing several variables that could be influencing the fatigue life; within the context of the present work, these could be variables such as true stress amplitude (continuous), blend type, or testing temperature. However, at this point, we can apply the Cox model on the data presented in the Wöhler curve of Fig. 3.4-4 to include the effects of scattering in the measured fatigue lives and the average true stress amplitudes. The analysis can also be implemented in the *R*-software environment using the *survival* package (Therneau and Lumley 2017).

The results of Cox regression analysis are shown in Table 3.5-4, where the regression

Table 3.5-4 – Cox hazards model results for one continuous variable: the average true stress amplitude.

Covariate	β	**HR**	**HR** $^{\min}$	**HR** $^{\max}$	p
$\overline{\Delta\sigma}$	0.599	1.821	1.475	2.248	2.65E-10

coefficient (β_i), the hazard ratio (HR) and its lower ($\mathrm{HR}^{\min}$) and upper ($\mathrm{HR}^{\max}$) 95% confidence intervals, as well as the log-rank test p-value are shown. First, the hazard ratio HR = 1.821 > 1 indicates a strong relationship between increase in true stress amplitude and increased risk of failure. In other words, this can be interpreted as: in most general terms, an additional increase in amplitude by 1 MPa induces the hazard of failure (at each respective cycle) by a factor of 1.81. The 95% confidence intervals are also greater than one. Of course, such trend is clear even from simple observations of Fig. 3.4-4 and, moreover, they are confirmed to be statistically significant from the p-value of the log-rank test, where $p = 2.65 \times 10^{-10} < 0.05$.

Additionally, it is useful to visualize the Cox hazards model as shown in the W Figure 3.5-6, similar to the Kaplan-Meier survival function estimate. Each curve

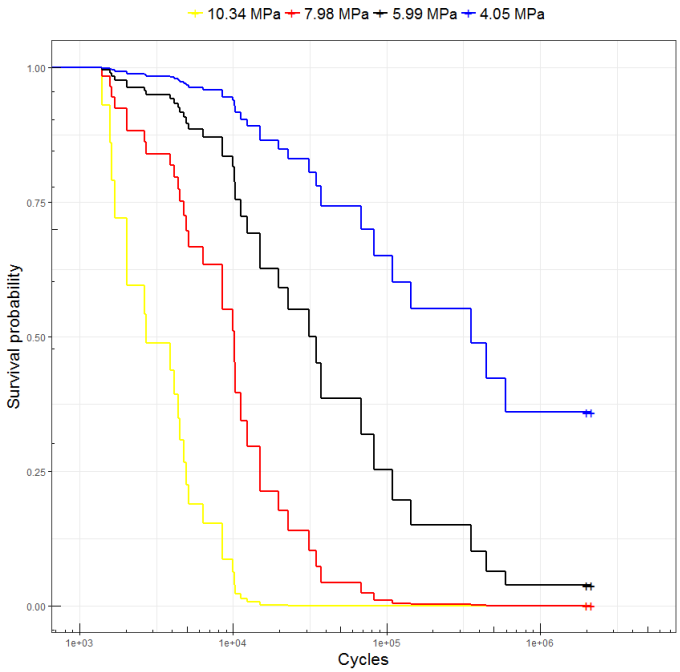

Figure 3.5-6 – Survival estimate of the Cox hazards model for data presented in the Wöhler curve of Figure 3.4-4.

is calculated around the average true stress amplitudes used for Weibull analysis (Tab. 3.5-3): 10.34, 7.98, 5.99, and 4.05 MPa. The overall trends are similar to those observed for the Kaplan-Meier estimate. However, with the Cox model, one is able to plot more continuous curves due to a nominally larger sample size. And notably, in addition to censored data, it takes into account the continuous nature of true stress amplitude values, *i.e.* scattering in the y-axis, which neither Weibull nor Kaplan-Meier analysis are able. Furthermore, one is able to extract the Cox statistical mean ($\overline{N_c}$ when $S(N) = 0.5$) and these are compared in addition to the values presented in Tab. 3.5-3. These are shown in Table 3.5-5.

Table 3.5-5 – Comparison of means from Weibull, geometric mean, Basquin's law (two data sets), Kaplan-Meier, Cox model; unit - cycles.

Target Load	$\overline{N_w}$	$\overline{N_G}$	$\overline{N_{B1}}$	$\overline{N_{B2}}$	$\overline{N_{KM}}$	$\overline{N_C}$	$\overline{\Delta\sigma}$
10 MPa	4 329	3 598	421	974	4 308	2 701	10.34
8 MPa	11 971	5 455	6 325	5 760	8 524	9 946	7.98
6 MPa	31 734	15 785	127 180	41 195	12 397	31 205	5.99
4 MPa	1 156 352	-	7 633 742	603 432	595 017	318 630	4.05

Finally, the validity of the proportional hazards assumption need to be tested. These can be checked by the commonly used statistical tests based on Schoenfield residuals (Grambsch and Therneau 1994). These are implemented by the *cox.zph()* function of the *suvival* package (Fox and Weisberg 2011; Therneau and Lumley 2017), which calculates tests for the proportionality for each covariate. A p-value is returned for each covariate, where high statistical significance, $p < 0.05$, indicates a strong evidence of non-proportionality of hazards of each covariate; the proportionality assumption is supported by a non-significant relationship, *i.e.* when $p > 0.05$. In the present case, the p-value for average true stress amplitude covariate is $p =$

$1.804 > 0.05$, indicating that one can assume proportional hazards.

3.6 Summary and Conclusions

In this chapter, the limitations of the widely used displacement control conditions in fatigue life testing of elastomers have been discussed. To overcome the limitations, a new testing procedure in true stress control has been presented, and it has been validated by plotting a Wöhler curve in true stress. Moreover, statistical tools for analysis of fatigue life results, have been presented and their utility discussed.

The basic idea behind fatigue life testing is that a history of applied **mechanical** loading can be used to predict fatigue lifetime of a material/part. As presented in Section 3.1, in some cases displacement control testing can be applied, but with significant drawbacks. However, it has been shown how it is inadequate for use in many cases, and especially for engineering elastomers. There are two main phenomena that such elastomers exhibit: the Mullins effect and long-term cyclic stress relaxation (or creep). Both are stress-softening phenomena and both are present in elastomers to various effect and degrees. It is these two phenomena that render irrelevant the use of displacement control. The methods used to accommodate for these effects are inconsistent from one study to another in the industry and/or academia.

Two simplified, straightforward scenarios have been discussed in this chapter that showed limitations of displacement control approach. In the best case, if material response permits, one can take into account the Mullins effect and then assume that long-term stress relaxation is negligible; with this approach in displacement control, the true stress and/or stretch ratio can be roughly approximated. In the worst case, that reflects the reality of the majority of elastomeric responses, long-term cyclic stress relaxation cannot be considered as insignificant. The choice of a reference cycle, at which researchers choose to calculate stretch ratio, true stress, or energy density, will provide erroneous values because **neither mechanical parameter is constant**. Moreover, these negative aspects have been also shown for force control and presence long-term cyclic creep. Therefore, the root of the problem lies in the fact that for many elastomers controlling tests in terms of experimental parameters (displacement, force) does not reflect the actual mechanical history that has been applied on a material.

To solve this problem, the next logical step is to control testing in term of mechanical parameters. A procedure for testing in true stress control has been developed as shown in Section 3.2. Tests in true stress control allow to keep at least one mechanical state parameter constant; thereby, it provides a more comprehensive approach to analysis, allowing to make valid comparisons between different materials and predictions in design. The procedure can be summarized as follows:

- First, specimen cross-section area is estimated by digital image correlation measurements and finite element analysis as a function of prescribed displacement;
- Then, a machine algorithm allows reaching a constant true stress amplitude target during testing of a single specimen;
- The procedure can also be extended to parallel testing by creation of master displacement curves; these curves contain the minimum and maximum prescribed displacement values for a specific loading level as a function of number

of cycles. Finally, they are used to carry out tests on multiple specimens in parallel using a special experimental setup.

Subsequently, this theoretical method has been implemented experimentally in Section 3.3, which was then successfully applied on HNBR blend A44H96 in Section 3.4. In individual testing of specimens, the procedure is able to accurately control true stress amplitude loading whilst respecting a specified R-ratio. In parallel loading, it is much more difficult to attain a specified target loading; there is range of different stresses measured per each loading level. However, the procedure can be said to be satisfactory, because the applied true stress amplitude is quasi-constant over the duration of the experiments. Finally, a Wöhler curve in true stress has been presented as a final result (Fig. 3.4-4).

As seen on the Wöhler curve, there is significant scattering in the observed results. This scattering is present in testing of all materials and irrespective of the control type. As discussed in Section 3.5, scattering is especially problematic in synthetic elastomers (such as HNBR) and at low loading levels. Consequently, application of the widely used Basquin's law has been presented and its limitations within the context of the present work have been described. Namely these are: presence of scattering in true stress amplitude and presence of right-censored data - where at the lowest loading level, specimens have not failed after a certain number of cycles. To account for these factors, different statistical tools have been introduced. The Weibull analysis, widely used for metals, has been initially applied. Afterwards, survival analysis approaches have been borrowed from medical sciences for statistical analysis of fatigue results. First, a non-parametric method, the Kaplan-Meier analysis, has been applied on the data and was shown to be statistically significant. Second, the widely used Cox proportional hazards model has been presented and the results from the Wöhler curve have been used to create a basic model describing the effects of true stress amplitude on fatigue life. The ability for multivariate assessment of different factors on fatigue life with the Cox model provides a good prospect. A well-defined model can be used to interpolate and extrapolate results based on base data; moreover, a probabilistic approach can be applied for creation of Wöhler curves. This tool will be applied in the next chapter, where one discusses the effects of formulation - ACN content, percent hydrogenation - on fatigue life of HNBR.

Chapter 4

Fatigue of HNBR: Effects of Formulation

Chapter Highlights

- Effect of acrylonitrile content: A36H96 has better fatigue resistance, followed by A44H96; A24H96 has significantly less resistance to fatigue as compared to the other two blends;
- Effect of percent hydrogenation: A36H96 has better fatigue resistance, followed by A36H99, then by A36H91;
- Composite A44-24, with average ACN content of 36%, has significantly lower fatigue resistance than A36H96.

Introduction

Building upon the experimental methods discussed in the previous chapter, the present focuses on the effects of HNBR formulation on fatigue resistance. Consequently, the developed method in true stress control is used to carry out fatigue life experiments and plot Wöhler curves for each HNBR blend. These are complemented by fatigue crack propagation experiments, where crack growth rates are conventionally plotted with respect to the tearing energy. These two experimental approaches are, finally, supplemented by fatigue damage analysis that is performed with aid of scanning electron microscopy. If one recalls, the formulation of the six HNBR blends contains different amount of acrylonitrile content (24, 36, and 44 wt.-%) and percent hydrogenation (91, 96, and 99 %); additionally, a composite of two blends of HNBR with 24 and 44 wt.-% ACN for an average of 36 wt.-% is compared to that with 36 wt.-%. To closely simulate the real world operating conditions of HNBR, the testing is carried out on carbon black filled blends of HNBR at a temperature of 120 °C, which is considered as a typical representation of an in-service temperature.

Contents

4.1 State of the Art

4.1.1 Study of Fatigue in Elastomers

The study of fatigue of elastomers is of great interest because, similar to other materials, their behavior under prolonged cyclic loading differs from their static response. Components tend to fracture under cyclic loads at much smaller loading levels than under static loading. Failure due to fatigue usually occurs in two steps. The first step is the initiation of cracks in a region that was free of observable cracks. In a subsequent phase, the crack grows until eventual failure. Therefore, the study of fatigue of elastomers is divided into two complementary approaches: investigation of crack initiation, *i.e.* prediction of crack initiation in a material without defects; and, investigation of crack propagation, *i.e.* observation of the growth of an existing crack (Mars and Fatemi 2002). These two approaches are then used to estimate the fatigue life.

An extensive overview of fatigue life testing of elastomers, which focuses on crack initiation and, to a lesser extent, propagation, has been presented in the previous Chapter 3, Section 3.1. Thus, discussions on fatigue crack propagation and fatigue damage analysis of elastomers are presented below.

Fatigue crack propagation

Fatigue crack propagation approach is based on the fracture properties of the material. Moreover, this approach has been more prevalent in the studies of fatigue behavior of elastomers. Due to the presence of existing flaws in the material, the introduction of a defect of known geometry leads to more reproducible results. Hence, crack propagation approach has been preferred, partly due to arguably greater elimination of external effects on fatigue testing.

The theory behind crack propagation approach is based on the Griffith failure theory, where the focus is put on investigation of a specific flaw. The work theorized that elastic energy stored under constant deformation is balanced by the surface energy that is used to create new surfaces during crack growth (Griffith 1921). Griffith's work was extended to rubber by Rivlin and Thomas (1953), where it was formulated that the elastic energy is balanced due to changes in the internal energy. The concept of tearing energy, an extension to large strain of the concept of energy release rate, was introduced, which could be calculated from experiments or be used to calculate the forces necessary to propagate the cracks in the specimen. Under assumption that rubber is perfectly elastic, the fracture of the specimen is determined by the strain energy release rate. The tearing energy is formulated as

$$T = -\frac{1}{t}\left(\frac{\delta U}{\delta c}\right)_u, \tag{4.1-1}$$

where t is the thickness the specimen, c is the crack length, and U is the energy stored elastically by a prescribed deformation; u is the deformed height of a specimen and its index indicates that integration is done at constant displacement.

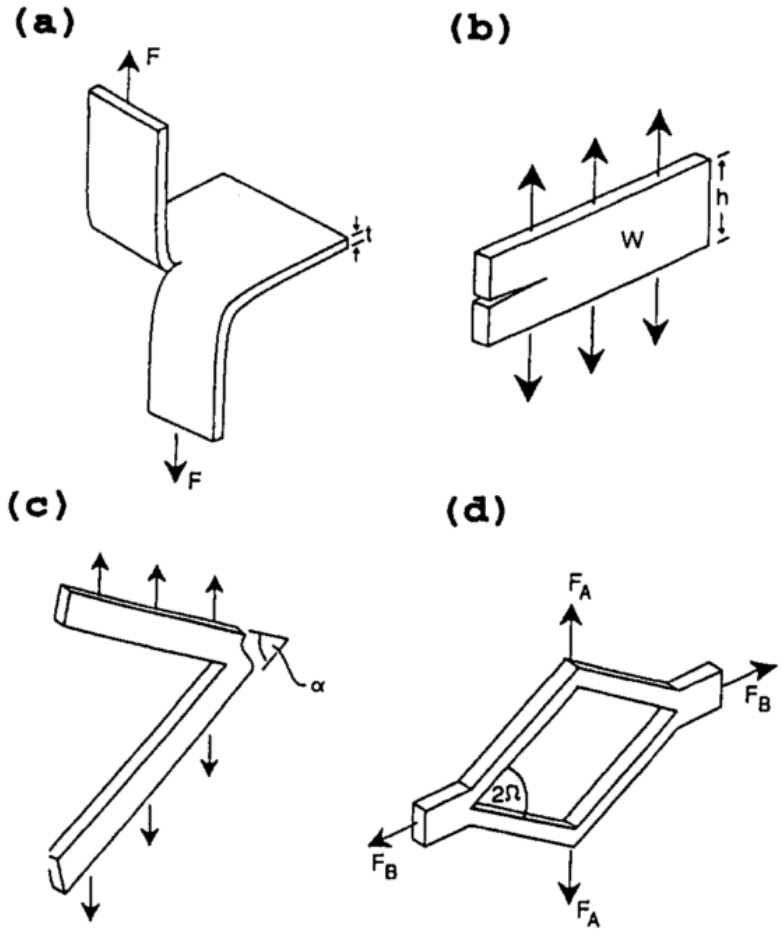

Figure 4.1-1 – Different specimens utilized for crack propagation experiments: a) "trouser", b) "pure-shear", c) "angled", and d) "split" (Lake 1995).

The practical calculation of T depends on the geometry of the specimen and type of loading applied on it. Figure 4.1-1 shows some of the more commonly used specimen types for crack propagation experiments.

If one considers the "pure-shear" specimen, its tearing energy has been first derived by Rivlin and Thomas (1953). First, the basic requirements for a pure-shear specimen is to have dimensions, such that its height is much smaller than its width, *i.e.* $w >> h$, and smaller than the initial crack length $c > h$. As such, the stretch ratios in the principal directions are $\lambda_1 = \lambda$, $\lambda_2 = 1$, and $\lambda_3 = 1/\lambda$, where λ_1 is the stretch in the direction of applied load. Under deformation, the specimen is divided into four different loading regions as shown in Figure 4.1-2. In Region A, stress and strain are free; B is under complicated strain regime; C is in pure-shear; and D can be said to be in a complex state. Rivlin and Thomas (1953) have noted that an increase in the crack length by dc causes region A to expand with regions B and C shifting in the direction parallel to the crack. Thus, a volume of $h_0 \times t \times dc$ undergoes a change from pure-shear to undeformed states. Thus, the change in elastic energy is given by

$$dU = -W\ h_0\ t\ dc, \tag{4.1-2}$$

where W is the strain energy density (per unit volume) in region C in pure-shear, h_0 is the undeformed height, t is the thickness, and dc is the increase in crack length.

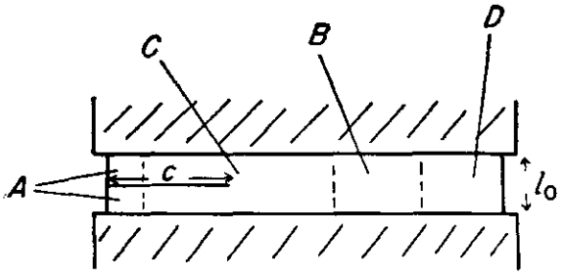

Figure 4.1-2 – Four regions of loading in a pure-shear specimen (l_0 indicates original specimen height - h_0) (Rivlin and Thomas 1953).

Finally, with Eq. (4.1-1), it can be shown that for a pure-shear specimen, the tearing energy is

$$T = Wh_0. \tag{4.1-3}$$

Thus, it is clear that the tearing energy does not depend on crack length c, which is one of the major advantages of pure-shear specimen geometry.

Such approach is then extended to fatigue (cyclic) loading, where cyclic crack propagation (growth) is generally represented by

$$\frac{dc}{dN} = f(T), \tag{4.1-4}$$

where T is measured over the duration of the cycle. Under fully relaxed cyclic loading ($R = 0$), the primary parameter determining the growth rate of a crack is the maximum tearing energy applied ($T^{\max}$) and there is almost no effect of how it was achieved (waveform) (Lake 1995).

In one of the first studies on unfilled natural rubber (NR), Thomas (1958) discovered that there is a square-law relationship between the tearing energy and the crack propagation rate under cyclic loading conditions. This phenomenon is similar to the Paris's law (Paris and Erdogan 1963), a power-law dependence that is observed for metals. Further experiments by Lake and Lindley (1965) identified four regimes of crack propagation for unfilled NR and SBR. The regimes are plotted in Figure 4.1-3 with crack propagation rate as a function of tearing energy, and the relationship between the two is the following

$$\frac{dc}{dN} = \begin{cases} r & T < T_0, \\ a\,(T - T_0) + r & T_0 < T < T_t, \\ bT^f & T_t < T_c, \\ \infty & T = T_c. \end{cases} \tag{4.1-5}$$

1. The first regime is below the fatigue threshold T_0, where the rate of crack growth per cycle (dc/dN) is constant (r) and affected only by the environmental factors independent of mechanical loading. Lake and Lindley stated that crack growth is driven by the presence of ozone below the threshold and, above the threshold, mechanic-oxidative crack growth occurs;
2. The second regime is a transition regime ($T_0 < T < T_t$);

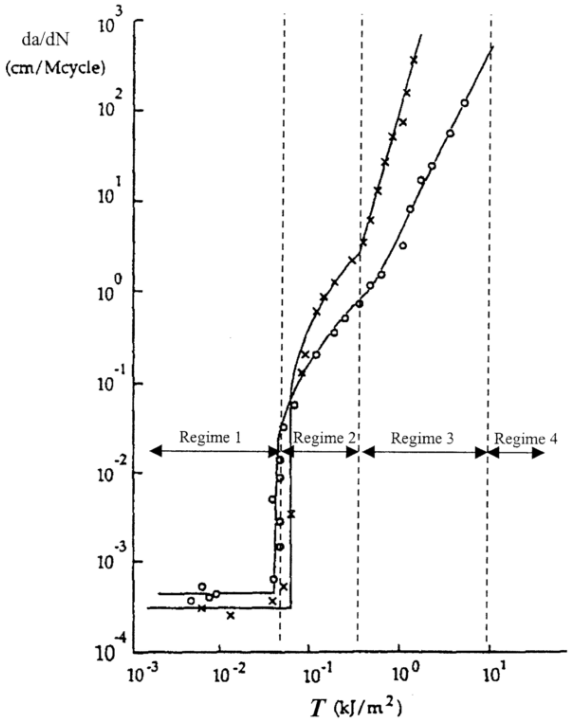

Figure 4.1-3 – Four regimes in fatigue crack propagation response of NR (×) and SBR (○); original figure from Lake and Lindley (1965) and modified by Mars and Fatemi (2002).

3. Afterwards, the crack propagation rate follows the power-law (with parameters b and f for tearing energy values between T_t and T_c;
4. Finally, in the last regime, the crack growth is unstable and the crack propagation rate is established to be essentially infinite. The tearing energy T_c corresponds to the fracture energy.

Fatigue damage analysis

The flaws and/or defects have a physical manifestation within the material. Thus, in addition to relatively macroscopic and quantitative measurements of fatigue life and crack propagation experiments, it is also useful to investigate how fatigue affects the material itself with its flaws. Fatigue damage mechanism analysis in elastomers is a broad and mostly qualitative subject. With respect to elastomers, two principal tools for investigation have been classical microscopic observations and X-ray computed microtomography.

Microscopic observations by optical microscopes or scanning electron microscopy (SEM) is a traditional approach to investigation of fatigue mechanisms (Bhowmick et al. 1980; Goldberg et al. 1989; Lee and Moet 1993). On the other hand, X-ray computed microtomography (or micro CT) is a tool where X-rays are applied from several directions and the projections are combined to create a 3-dimensional structure of a material (for more information, one can refer to a review by Le Gorju-Jago (2012)). As such, it allows for non-destructive internal observations with sizes ranging from 10 µm to 100 µm, whereas microscopic observations are limited to surface observation or destructive analysis with introduction of cuts (as in Le Cam et al.

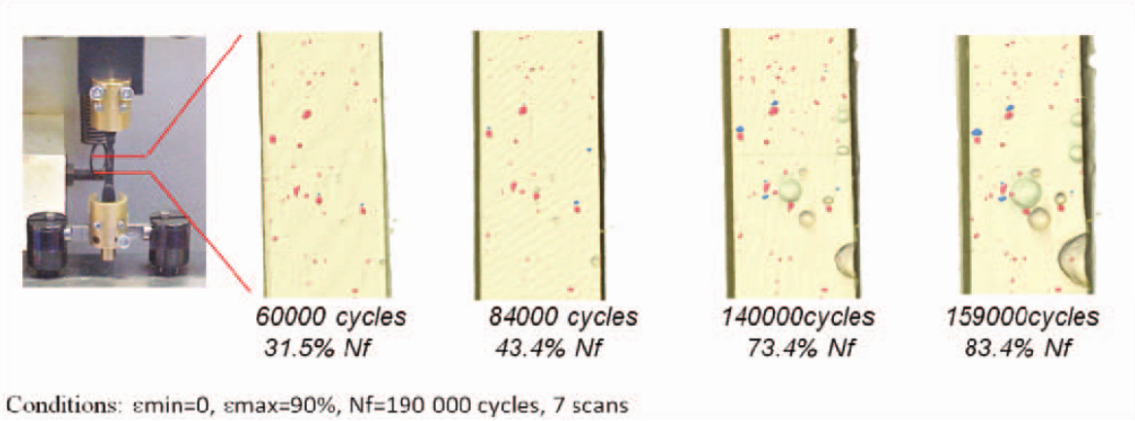

Figure 4.1-4 – Initiation and propagation of cracks inside a single specimen volume during fatigue testing (Le Gorju-Jago 2007).

(2004)). Figure 4.1-4 shows one of the earliest published investigations of fatigue damage of NR by micro CT. Projections were made at specific intervals (interrupted testing) up to fatigue life and crack initiation and propagation was observed. Micro CT was applied together with heat build-up measurements to develop a fatigue criterion (Le Saux et al. 2010; Marco et al. 2013). The methodology was also applied to chloroprene rubber (Le Saux et al. 2011) and used in conjunction with microscopic observations (Huneau et al. 2013).

As for the actual fatigue damage mechanisms, many investigations have been carried out, especially on natural rubber. There is a wide variety of flaws, majority of which constitute inhomogeneities within the material (Beatty 1964). Some of the flaws originate from inclusions, for example:

- Saintier et al. (2006a) found that such flaws were mostly silicon and calcium oxides, which are used in material manufacture, carbon black agglomerates (average size of 200 µm), and - to a lesser extent- by natural fibers or carbon-based inclusions, contained in the natural rubber gum itself;
- Le Saux et al. (2011) identified, in polychloroprene rubber, ZnO, silica and carbon black agglomerates by micro CT investigation;
- Le Cam et al. (2013) detected, in natural rubber, carbon black agglomerates (from 200 µm to 400 µm) and particles of oxygen, silicon, and magnesium, which make up talcum powder used in molding of natural rubber; there were also traces of aluminum oxide pointing to the origin of particles found in the ground;
- Huneau et al. (2013) identified, in natural rubber, carbon black agglomerates as the main cause in crack initiation; less frequently, various oxides (Si, Mg, Na, Ca, K) have been detected;
- Huneau et al. (2016) investigated crack initiation in natural rubber and divided the inclusions in four groups: carbon black agglomerates (which made up the majority of known causes of cracks), ZnO particles, talcum powder, and oxides (Si, Ca, Al).

It is clear that these inclusions are either agglomerates of substances used in the

formulation (*i.e* carbon black, ZnO), impurities in the ingredients or introduced during manufacturing (agent used in handling and processing of material, leftovers from previous mixing operations, *etc.*). Moreover, physical factors such as mold parting lines (Huneau et al. 2016) or stress concentrators (edges of specimen geometry) can act as initiation sites (Hainsworth 2007; Le Saux et al. 2011; Le Cam et al. 2013).

These flaws then act in initiation of cracks. Huneau et al. (2016) proposed a three-step initiation mechanism in NR due to a CB agglomerate. As shown in Figure 4.1-5, under cyclic loading, one can observe, first, debonding (or cavitation) at one of

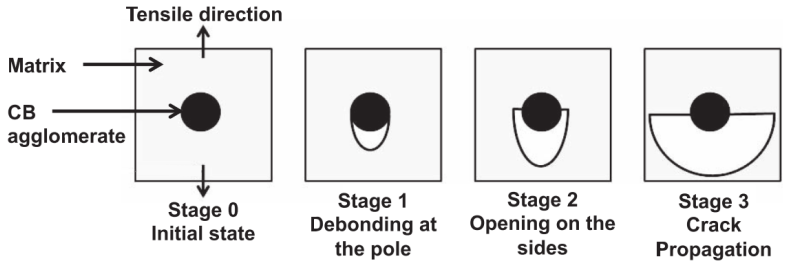

Figure 4.1-5 – Schematic representation of fatigue crack initiation mechanism around a CB agglomerate (Huneau et al. 2016).

the poles of an inclusion; afterwards, the crack (or cavity) growth in a direction perpendicular to the crack; finally, the crack grows both in surface area and in volume, which can be said to mark transition from initiation to propagation. Such mechanism is specific to CB with high internal cohesion; however, breaking of carbon blacks should not be ruled out (Le Cam et al. 2013). On the other hand, step 1 of the initiation mechanism for ZnO, having low internal cohesion and high adhesion to the matrix, can be debonding or fracture; however, there is usually no crack propagation for this type of flaw. Moreover, in addition to CB and ZnO, coalescence of cavities (300 µm in size) was also found to act as initiation sites (Le Cam et al. 2013). Using micro CT, Le Saux et al. (2011) identified in that majority of initiation and cavitation occurs within the first 10% of fatigue life and the number (or density) of initiation sites increases with larger prescribed loading. The authors also concluded, similar to Le Gorju-Jago (2007), that two cavitations between two inclusions, occurring in the direction of loading, generated the greatest damage. Finally, one can observe multi-cracking, *i.e.* initiation and propagation of several macro-cracks, in natural rubber (Saintier et al. 2011; Le Cam et al. 2013; Huneau et al. 2016; Narynbek Ulu et al. 2016); however, these were absent in silicone rubber (Hainsworth 2007).

Afterwards, Le Saux et al. (2011) note that the number and size of defects slowly increases with the number of cycles; there is no abrupt coalescence of cracks, but these occur locally to form first micro-cracks, once again "marking a transition" to crack propagation. Similar to crack initiation, the subsequent growth of these cracks is dependent on maximum loading. Hainsworth (2007) noted how crack growth processes were non-linear in NR and silicone rubber. In general, micro-cracks progress in a direction perpendicular to that of loading, at the same time combining with smaller cavities if these are on their path (Le Saux et al. 2011). The mechanism for crack growth was originally proposed by Le Cam et al. (2004)

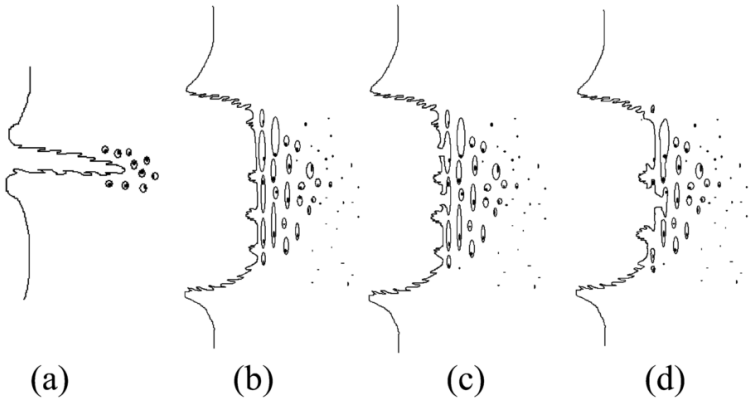

Figure 4.1-6 – Schematic representation of fatigue crack propagation mechanism (Le Cam et al. 2004).

and shown in Figure 4.1-6. And subsequently, this mechanism was later refined by Beurrot et al. (2010), where the presence of cavities behind the crack tip was downplayed. Moreover, the authors highlighted the importance of strain-induced crystallization in crack growth mechanisms, which is present in NR, as compared to SBR, which does not crystallize under strain: as a special case of presence of strain-induced crystallization, one can observe crack branching in natural rubber. On the other hand, cracks surfaces in SBR are smooth and no branching occurs.

Finally, if one investigates fracture surfaces due to fatigue, traditional three zones can be distinguished: initiation, propagation, and final failure (Hainsworth 2007; Le Cam et al. 2013). Figures 4.1-7(a) and 4.1-7(b) show a schematic of top and side

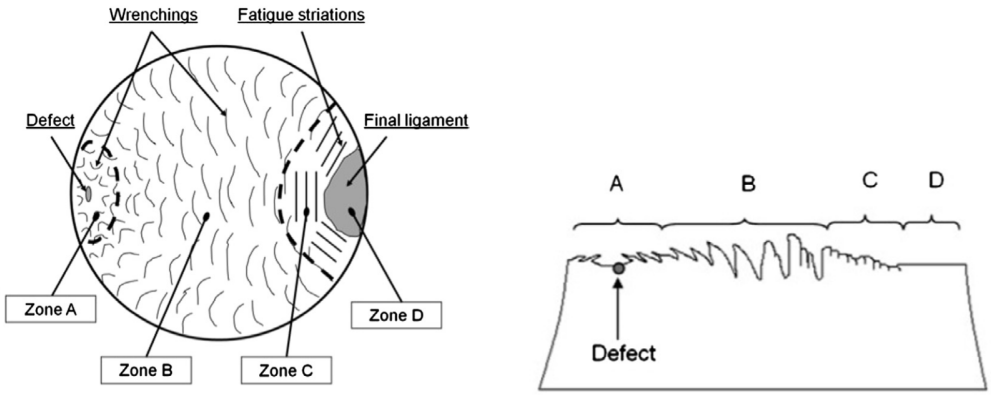

(a) Top view. **(b)** Side view.

Figure 4.1-7 – Schematic representation of fatigue fracture surface (Le Cam et al. 2013).

views, respectively, of the fracture surface observed in natural rubber. Zone A refers to the initiation phase. Zone B is the propagation phase, where one can discern the direction of propagation by the orientation of *ellipses* (or *leaves* (Beurrot et al. 2010), *tongues* (Poisson et al. 2016), or as originally referred - "wrenchings" (Le Cam et al. 2004)). Beurrot et al. (2010) proposed that occurrence of secondary cracks along a crack front is responsible for formation of these "leaves." Flamm et al. (2011) observed in natural rubber that at low strain amplitudes cause a narrow crack front, thereby decreasing size of these *ellipses* and increasing surface roughness; on the

other hand, large amplitudes lead to a wide crack front and thus form noticeable striations as indicated by Zone C. Finally, Zone D refers to the final brittle fracture of the specimen, similar to those observed in static fracture.

4.1.2 Fatigue Resistance of HNBR

One of the main interests in investigation of HNBR was the relative absence of studies on its fatigue resistance. Moreover, at present, there are no published studies on the effects of ACN content and percent hydrogenation on fatigue of HNBR. The few publicly available studies in the following sections are divided into three experimental approaches: fatigue life, fatigue crack propagation, and fatigue damage analysis.

Fatigue life of HNBR

An extensive study on the effect of carbon black fillers on fatigue damage of HNBR was carried out by Gauchet (2007). The primary focus of the work was to investigate the effects of different carbon blacks. The details of the study are listed below:

- The different types of carbon black used were N550, N990, and S6000 each with a specific surface area of 40 m^2/g, 8 m^2/g, and 21 m^2/g respectively; the amount of carbon blacks varies from 27 phr to 45 phr and to 34 phr for N550, N990, and S6000 respectively; such amounts of carbon black were chosen because they lead to an equal tensile modulus at 20% deformation and 20 °C;
- HNBR blend used in the study was a 70%/30% mixture of two types of HNBR of 34 wt.-% ACN with 99.1% hydrogenation (T_g of −25 °C) and 21 wt.-% ACN with 94.5% hydrogenation (T_g of −45 °C);
- For fatigue life tests, the specimens were of "mini-diabolo" type - corresponding to massive cylindrical specimens;
- Testing temperature was 120 °C;
- Fatigue life tests were carried out at 5 Hz with loading ratio of R=0.1 in displacement control; $u = 15$ mm, 12.5 mm, 12 mm, and 10 mm; five specimens tested per loading level and blend;
- Nominal stress was calculated around cycle 1050;
- End-of-life criterion was chosen as complete failure of a specimen;
- Fatigue life limit was chosen to be around 1 million cycles.

An example of a typical fatigue life curve obtained is shown in Figure 4.1-8. Overall, it can be said that the fatigue life results have very high scatter, especially at low loading levels. For example, at nominal stress range 1.2 MPa to 1.25 MPa, the minimum fatigue life is measured around 200 cycles and there is an unbroken specimen at 2 million cycles. Such dispersion is observed for other blends containing different carbon blacks and the author could not conclude with certainty on the relationship between carbon black type, loading, and fatigue life. Additional tests were carried

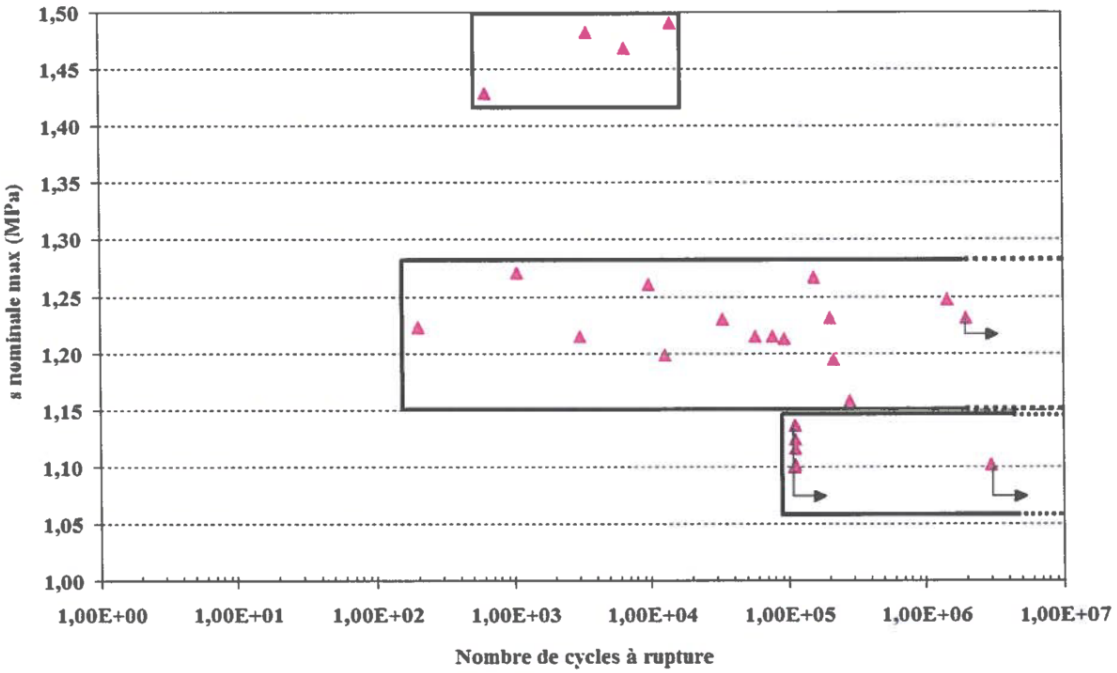

Figure 4.1-8 – Fatigue life of HNBR with S6000 carbon black; vertical axis - nominal stress, horizontal axis - number of cycles (Gauchet 2007).

out at the lowest displacement for blend containing S6000 carbon black up to 30 million cycles. These specimens did not break; thus, author concluded that this displacement corresponds to the fatigue life limit. From overall considerations, the author concluded that HNBR with N990 (smallest specific surface area) has the best fatigue resistance.

In another study, Lacroix et al. (2013) measured crack propagation of HNBR and polychloroprene (CR) elastomers using a dynamic mechanical analyzer (DMA). However, the primary objective of the work was not the study of the fatigue behavior of HNBR, but rather the development of a novel method for characterization of crack growth behavior in elastomers. The recipes for each elastomer were not specified, but their principal physical properties are shown in Table 4.1-1. Edge

Table 4.1-1 – Properties of materials investigated by (Lacroix et al. 2013).

Material	Young's Modulus (MPa)	Elongation at break (%)	Hardness (Shore A)
CR	3.8	680	54
HNBR	3.9	407	50

Cracked Simple Tension (ECST) specimens were used with thickness of 2 mm and width of 9 mm. The size of the initial crack varied from 0.35 mm to 2 mm. The applied dynamic strain amplitude was 10% at a frequency of 30 Hz and testing temperature was 80 °C.

Figure 4.1-9 presents is the fatigue life of HNBR and CR with respect to the initial crack surface area, where the end-of-life criterion is chosen as loss of 30% of stiffness. Primarily, it appears that HNBR has shorter fatigue life compared to CR under similar testing conditions. Moreover, the size of the initial crack has a significant effect on the fatigue life of HNBR: the fatigue life decreases with increase of the

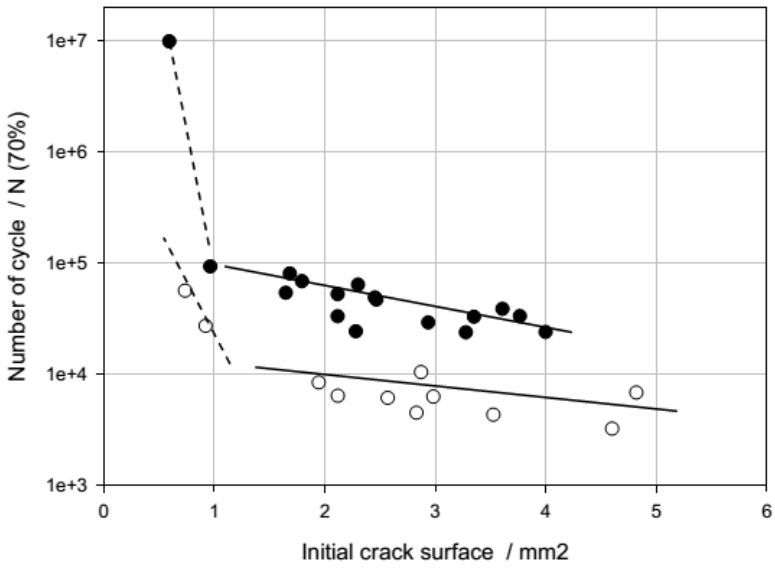

Figure 4.1-9 – Number of cycles at 70% stiffness of HNBR and CR with respect to initial crack surface; • – CR, ∘ – HNBR (Lacroix et al. 2013).

initial crack size. Additionally, there appears to be a threshold around 0.8-1.0 mm^2, after which the fatigue life significantly decreases for both elastomers.

Fatigue crack propagation in HNBR

Coming back to the study of Lacroix et al. (2013), crack propagation rates (note that it is measured as dE'/dT) as a function of initial crack surface are shown in Figure 4.1-10. The crack growth rate of HNBR is about 10 times greater compared to CR for a given initial crack size. These results support the difference in observed fatigue life results in Figure 4.1-9. The authors hypothesized that HNBR generates more viscous dissipation compared to CR, as indicated by loss modulus measurements; thus, it is concluded that greater damage occurs in HNBR during dynamic tests.

With respect to classical fatigue crack propagation studies, Kim et al. (2003) investigated fatigue crack propagation behavior, amongst other properties, of HNBR and HNBR/ZDMA blend (with comparison to natural rubber). The investigated materials are HNBR with 44 wt.-% ACN, 91% hydrogenation, and a HNBR/ZDMA [1] blend of HNBR with 36 wt.-% ACN, 91% hydrogenation and ZSC 2295 (Zeon Super Composite). Both types are carbon black filled at 30 phr. Carbon black filled (50 phr) natural rubber (NR) specimens were also considered for comparison. The geometry of the specimens was that of pure shear (150 mm × 25 mm × 1 mm with a 75 mm cut). The tests were carried out at room temperature at global elongations ranging from 25 to 200% with crack length measurements every 10,000 cycles.

Presented in Figure 4.1-11 is the fatigue crack propagation of HNBR, HNBR/ZDMA blend, and NR. During the experiments, neither fatigue threshold nor a regime with

[1] ZDMA (zinc dimethacrylate) is a polymer consisting of zinc oxide and methacrylic acid (Ikeda et al. 1999).

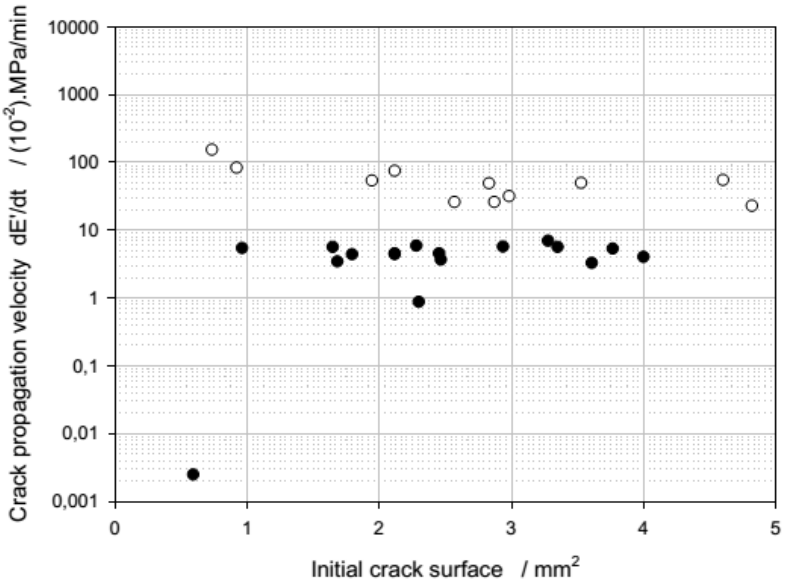

Figure 4.1-10 – Crack propagation rate of HNBR and CR with respect to initial crack surface; • – CR, ○ – HNBR (Lacroix et al. 2013).

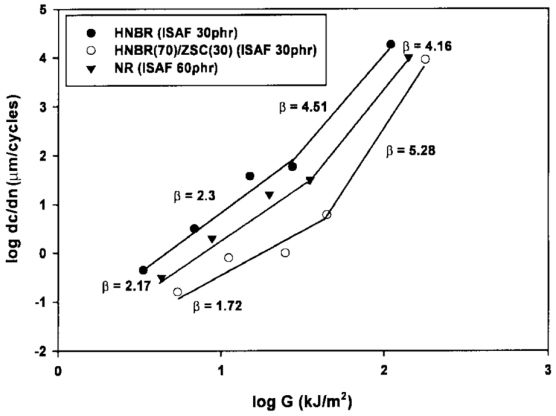

Figure 4.1-11 – Fatigue crack growth rate of HNBR (44 wt.-% ACN, 91% hydrogenation), HNBR70%/ZDMA30% blend (36 wt.-% ACN, 91% hydrogenation), and natural rubber (Kim et al. 2003).

rapidly increasing propagation rate were observed. For all tearing energies, the crack propagation is the slowest in HNBR/ZDMA blend followed by NR and, finally, HNBR. It is interesting that the blend of HNBR/ZMDA had slower crack propagation rate than natural rubber, which is known for its excellent resistance to fatigue crack propagation, also considering that the HNBR/ZDMA blend contained half of the carbon black amount than NR. The authors have attributed this to formation of crystalline regions in HNBR/ZDMA and to absence of such in "pure" HNBR. These claims are supported by increase in tensile modulus at 100% elongation with increasing ZDMA percentage; however, no measurements of crystallinity are made.

Another study has been carried out at LRCCP (Béranger et al. 2017) and it investigated the difference in crack propagation behavior by several criteria:

- Materials HNBR (36 wt.-% ACN and 96% hydrogenation), HNBR/ZDMA, and NBR; all materials are filled with carbon black N550, which is larger on

average than the N772 used in the present study; NBR and HNBR at 70 phr and HNBR/ZDMA at 10 phr;

- Effects of temperature - room and 120 °C.

The dimensions of pure-shear specimens are 40 mm×4 mm× 0.8 mm. First, the materials are compared at 120 °C. Figure 4.1-12 shows crack propagation of the

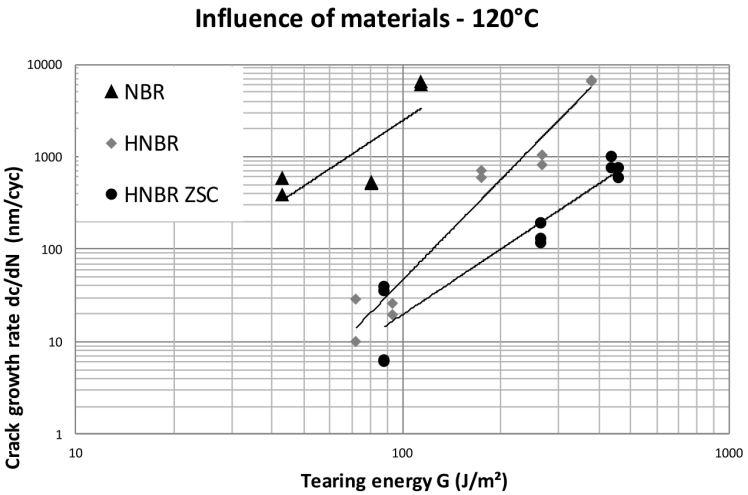

Figure 4.1-12 – Fatigue crack growth rate of NBR, HNBR (35 wt.-% ACN, 96% hydrogenation), and HNBR/ZDMA30 blend (Béranger et al. 2017).

three materials and it is evident that, in general, fatigue crack growth resistance is best in HNBR/ZDMA followed by HNBR and NBR. However, the differentiation between HNBR and HNBR/ZDMA are less clear (unlike in the study of Kim et al. (2003). And, as a note, the results for NBR are as expected since it has poor resistance to heat. Second, the effect of temperature is investigated and, as expected the crack growth rate significantly increases at high temperature. At low tearing energies ($T \approx 100$ J/m^2), crack growth rate increases from about 1 nm/cycle to about 15 nm/cycle. The change in crack growth rates at two temperatures increases with tearing energies: at $T \approx 400$ J/m^2, at room temperature the crack growth rate is around 20 nm/cycle as compared to around 1300 nm/cycle at 120 °C. The effects of pre-aging will be discussed in the next chapter.

Fatigue damage analysis of HNBR

In addition to fatigue life investigation of HNBR, Gauchet (2007) investigated effects of carbon black fillers on fatigue damage mechanismsin HNBR. Figure 4.1-13 show a fracture surface of HNBR with N550 carbon black. Similar to observations in other elastomers, the analysis of the fracture surfaces identified three distinct regions: initiation, propagation, and fracture. As for the inclusions discovered near initiation sites, there are two types: material heterogeneities with high carbon content, which occur symmetrically on two corresponding fracture surfaces; and other rigid inclusions, which are present only on one surface. Furthermore, the propagation region is of interest due to formation of "petal"-shaped cracks that, as the author argues, form a distinctive morphology in this region different to what is observed for other

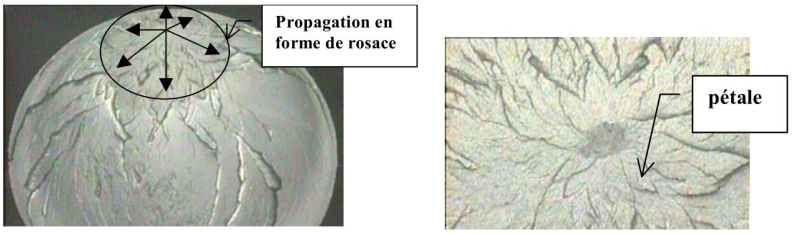

Figure 4.1-13 – Fracture surface of HNBR with N550 type of CB; left - ×25 magnification with arrows indicating the direction of propagation of the cracks; right) ×175 magnification of initiation and propagation regions with "petal" shaped cracks (Gauchet 2007).

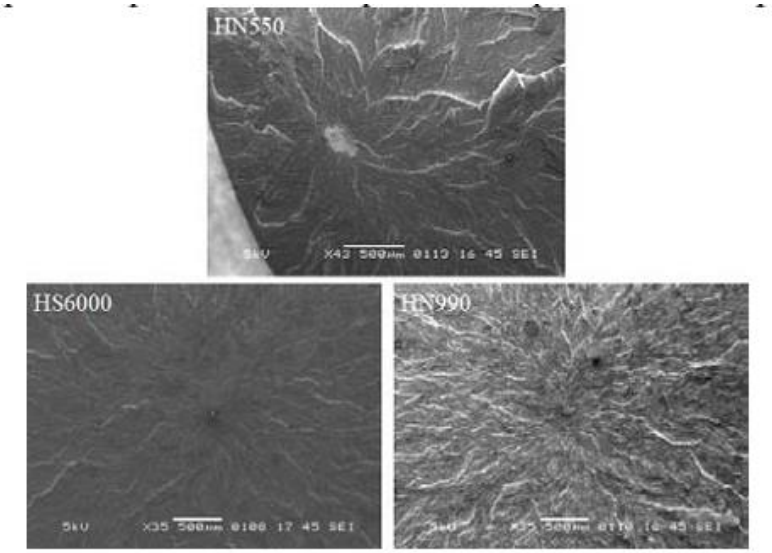

Figure 4.1-14 – Fracture surfaces of initiation and stable propagation regions of HNBR with N550, S6000, and N990 types of carbon black (Gauchet 2007).

elastomers. However, the fracture morphology appears to be similar to the one observed in another carbon black filled elastomer (SBR) by Le Cam et al. (2014).

Additionally, there is an influence of the carbon black type on the damage mechanisms (Figure 4.1-14). With decreasing specific surface of CB (N550>S6000>N990), the stable propagation region is extended and the number of "petal" shaped cracks increases while their size decreases. In general, increased crack growth rate is correlated with decreased roughness in this zone. Thus, these results are attributed to a mechanism that corresponds to the best fatigue resistance observed in N990 filled HNBR. Finally, in terms of macro-cracking, most occurred within the bulk of the specimen, whereas about 10% originated on mold parting lines and on the metal/rubber interface.

4.2 Experimental Methods

The formulation of the six HNBR blends utilized in the fatigue study are presented in detail in Chapter 2, Section 2.2. In summary, **A36H96** (36 wt.-% ACN and 96% hydrogenation) is chosen as the reference blend. First, hydrogenation is kept constant at 96% and ACN content is varied from 24 wt.-% - **A24H96** - to 44 wt.-% - **A44H96**. Second, ACN content is kept constant and percent hydrogenation is varied from 91% - **A36H91** - to 99% - **A36H99**. Finally, the composite blend of 24 and 44 wt.-% ACN for an average of 36 wt.-% - **A44-24**.

4.2.1 Fatigue life

The novel fatigue life procedure in true stress control, presented in the previous chapter and applied experimentally in Section 3.3, is utilized for fatigue life testing, which have been performed at GeM. In summary, the experiments are carried out on *Instron E10000* equipped with a 1 kN load cell and a heating chamber (Figure 4.2-1); moreover, a custom grip setup - detailed in Chapter 3 - is utilized for parallel experiments. There are three steps in the true tress control testing procedure:

1. DIC measurements and FE simulations are carried out to calculate the change in cross-section area with respect to the prescribed displacement. Then, a machine control algorithm is used to calculate the real-time true stress from displacement and force measurements.
2. For each blend and each loading level, two or three specimens are tested individually. It leads to the definition of displacement master curves that contain minimum and maximum displacement to maintain the target true stress amplitude.
3. The master curves are used to pilot the loading of eight specimens mounted in parallel with a custom-made system. In this system, each grip is attached to an independent load cell, that permits to monitor the force applied to each specimen.

The experimental conditions are the following:

- Surface temperature of the specimens is maintained at 120 °C (recorded by a pyrometer); due to heat generation within the specimens (the effect of which is less pronounced at 120 °C), the temperature of the heating chamber is adjusted (*i.e.* below 120 °C), with respect to applied loading and frequency, to maintain 120 °C on specimen surface;
- Four target loading levels are considered: 10, 8, 6, and 4 MPa. The loading ratio is $R = \sigma^{\min}/\sigma^{\max} = 0$;
- The nominal stress rate ($\dot{\bar{\sigma}} = \Delta\sigma/\Delta t_i = \Delta\sigma f$) is set to 20 MPa/s, corresponding to 2.0 Hz, 2.5 Hz, 3.33 Hz, and 5 Hz for $\Delta\sigma$ = 10, 8, 6, and 4 MPa respectively;
- Due to the geometry of specimens, the number of cycles at complete failure is considered as the fatigue life, N_f;

- The experiments were stopped at 2 million cycles assuming attainment of the fatigue limit. Additional experiments for the blend A36H96 until 5 million cycles are conducted to improve the estimation of fatigue life distribution;
- At least 10 specimens are tested per blend and loading level.

As a supplemental note, a comment should be made on the utilized specimens. As mentioned previously, the geometry is that of a flat dumbbell specimen as was shown in Figure 2.3-1. The specimens have been manufactured by compression molding and cut afterwards with a die. And thus, to reduce the negative impact on fatigue life tests, the mold surfaces and the edges of a cutting die have been finely polished to reduce surface roughness of the specimen edges.

4.2.2 Fatigue crack propagation

Fatigue crack propagation experiments are performed on *MetraVib DMA+300* at LRCCP. It is a specialized DMA testing machine equipped with binocular loupes with a digital measurement system for monitoring of crack growth rates (Figure 4.2-

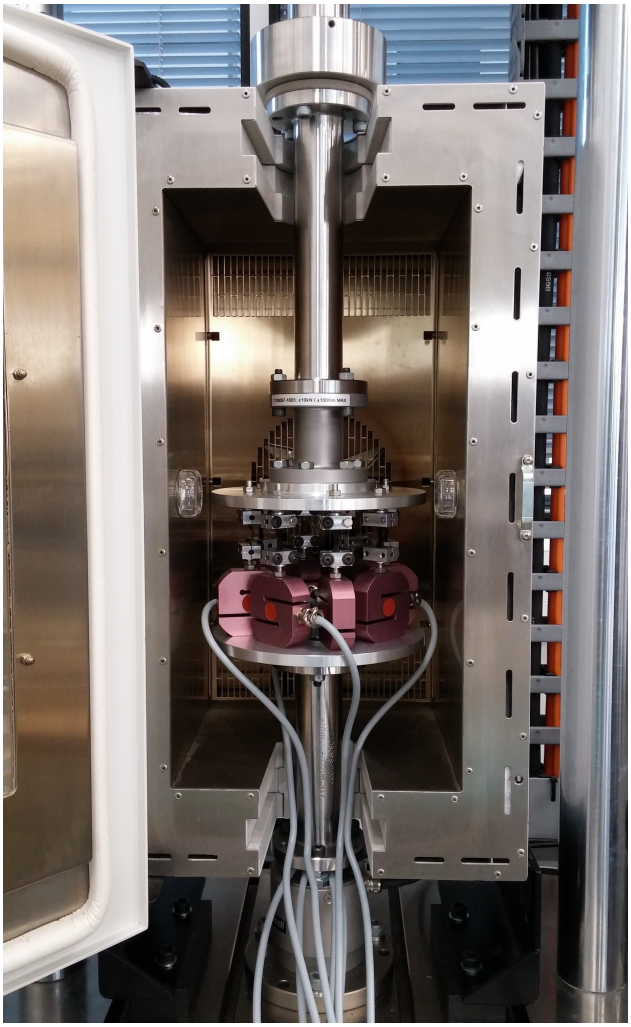

Figure 4.2-1 – *Instron E10000* machine utilized for fatigue life experiments, equipped with a heating chamber, 1 kN load cell, and custom grip setup.

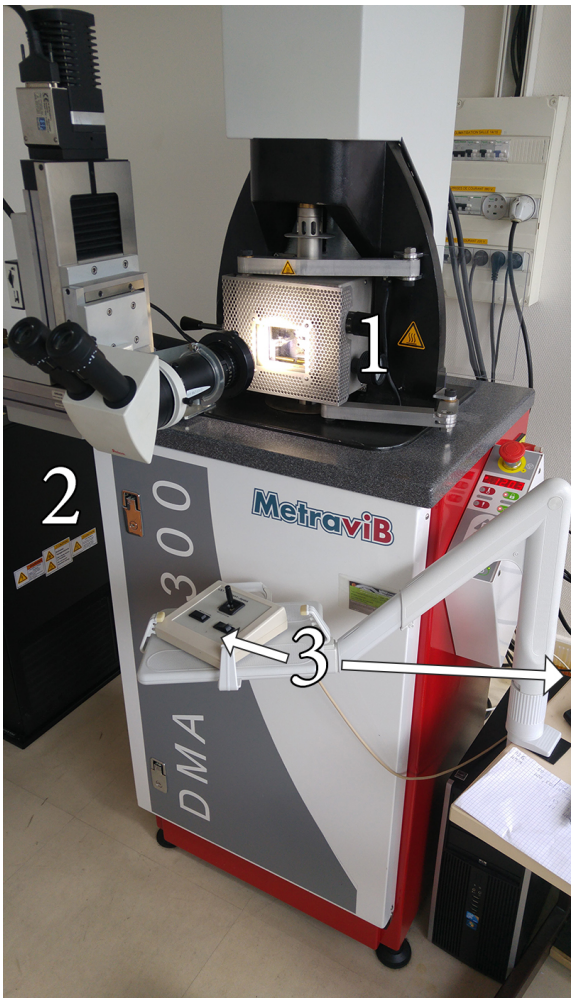

Figure 4.2-2 – *MetraVib DMA+300* machine utilized for fatigue crack propagation experiments, equipped with a 1) heating chamber, 2) binocular loupes, and 3) digital measurement system.

2). The thermal chamber of the DMA machine is set also to 120 °C, identical to the temperature used for fatigue life experiments. *Mini-PS* (PS for pure-shear) specimens are molded and cut for fatigue crack propagation experiments; the corresponding geometry is shown in Figure 4.2-3). As mentioned earlier by Eq. (4.1-3), this geometry leads to a simple analytical expression of the tearing energy that does not depend on the length of the crack (Rivlin and Thomas 1953):

$$T = W h_0, \tag{4.2-1}$$

where W is the strain energy density (per unit of undeformed volume) and h_0 is the undeformed height of the specimen. At least six crack growth rate measurements are performed per tearing energy per blend. Tearing energies vary from 50 to 1000 J/m^2. Finally, fatigue crack growth rate per cycle (dc/dN) is plotted with respect to the tearing energy, T.

Practically, there are four steps in the testing procedure of a given specimen. The testing protocol is one that is utilized at LRCCP, except with minor changes to the accommodation step.

1. The material is accommodated for the Mullins effect before energetic charac-

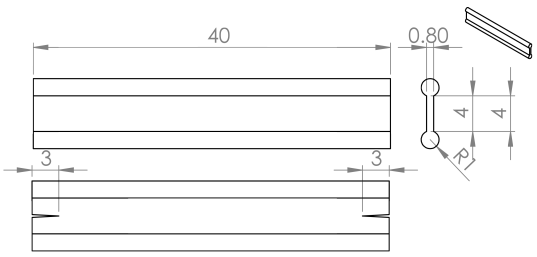

Figure 4.2-3 – Dimensions (in mm) of the mini-PS specimens; both notched and unnotched specimens are shown.

terization of the blends. Additionally, other long-term stress-softening phenomena need to be taken into account. Hence, the mini-PS specimen is loaded with a simple sinusoidal cyclic loading with a prescribed displacement amplitude of 2.5 mm and R=0 (in terms of displacement). The frequency during the accommodation phase is chosen to be 2.5 Hz.

The tearing energy is monitored at each cycle. Normalized tearing energy is calculated ($T_n = T/T^{\max}$) and the accommodation step is stopped after the normalized rate of change of the tearing energy per cycle is less than 1 %, *i.e.* the stress-strain response appears to stabilize. As an example, Figure 4.2-4 shows the negative, normalized rate of change of the tearing energy measured in A36H96; the number of accommodation cycles for the A36H96 blend is about 2500 cycles. For other blends, numbers of accommodation cycles are: A44H96 - 2300 cycles, A24H96 - 400 cycles, A36H99 - 2400 cycles, A36H91 - 1400 cycles, and A44-24 - 400 cycles.

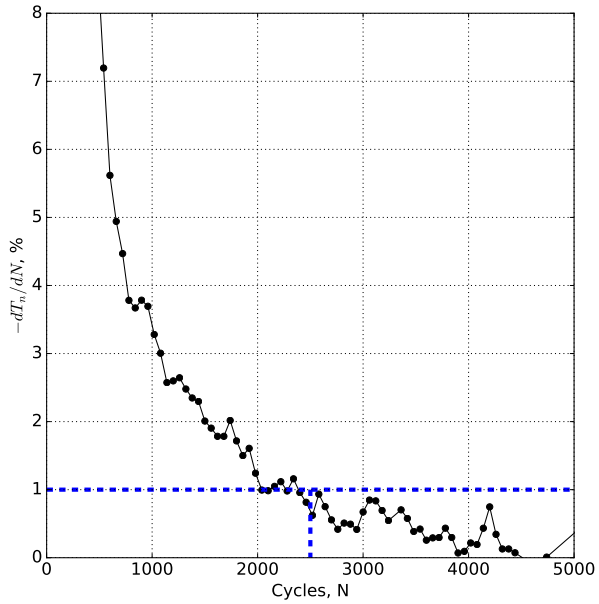

Figure 4.2-4 – Evolution of $-dT_n/dN$ of A36H96 with number of cycles.

2. The second step consists in the energetic characterization of the specimen as a function of the prescribed displacement amplitude; a condition is set so that

at minimum displacement the measured force equals to zero, *i.e* there are no compressive forces or buckling of the specimen. The amplitude is increased in equal increments from 0.2 mm to 2 mm and the tearing energy is calculated after 150 cycles by integration of the nominal stress vs. stretch ratio curve. The frequency is set to 2.5 Hz.

Subsequently, the relationship between the prescribed displacement amplitude and the tearing energy is established and can be fitted by a power law

$$T = A\,\Delta u^{C}, \tag{4.2-2}$$

where A and C are scalar constants, and Δu is the displacement amplitude. It should be noted that, due to slight variations in the specimen geometry, each tested specimen has a unique characterization curve. However, in order to present the general trend of this relationship, average curves of many specimens for all blends are shown in Figure 4.2-5.

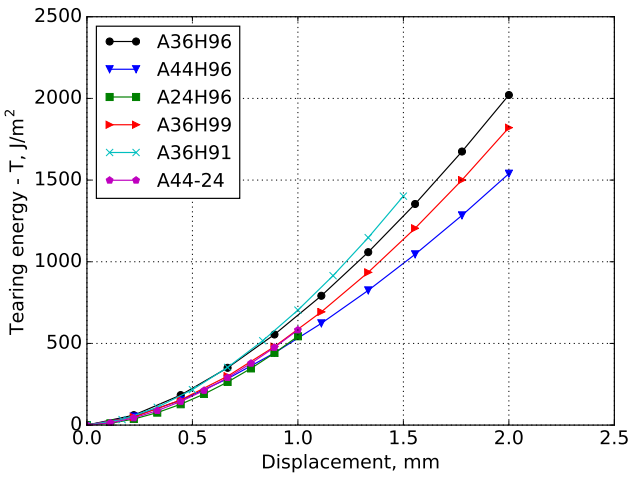

Figure 4.2-5 – Energetic characterization of different blends of HNBR at 120° C.

3. The third step entails introducing, *in-situ*, two notches of 3 mm at midpoint of both ends of a specimen as shown in Figure 4.2-3 (bottom).

4. Finally, a displacement amplitude for a specific tearing energy applied and fatigue crack growth rate is recorded after some number of cycles; similar to energy characterization, a special condition is imposed on minimum displacement, where at minimum amplitude there are no compressive forces on the specimen. To reduce the duration of experiments, the frequency of 24.5 Hz is chosen; preliminary tests showed that there is no significant effect of frequency (2.5, 10.0, and 24.5 Hz) on the measured crack growth rate.

   It should be noted that due to the nature of fatigue crack-tip blunting after initial introduction of a notch (Lindley 1973; Lake et al. 1991; Mars and Fatemi 2004a), stabilization of the crack growth rate is observed after several cycles and this value is recorded. As an example, Figure 4.2-6 presents the stabilization of crack growth rate for two tests on the A36H96 blend and for $T = 900$ J/m^2. First, around 2000 cycles were required by the machine to

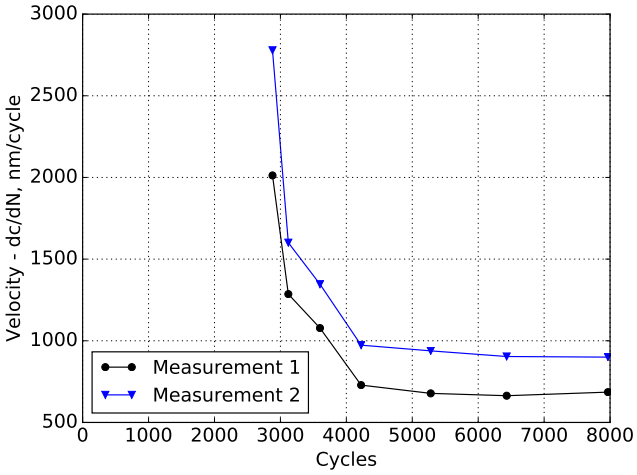

Figure 4.2-6 – Example of evolution of two fatigue crack growth rate measurements of A36H96.

attain the required loading condition. Up to around 4000 cycles, there is significant drop in the measured crack growth rate for both tests. Then, only the last three points of each test are considered to determine the average crack growth rate. Then, fatigue crack growth rates are plotted with respect to prescribed tearing energies. For clarity, averages of three crack growth rate measurements are plotted and error bars indicate the maximum and minimum variance.

For relatively high tearing energies, where crack growth is rapid, the specimen is discarded after testing at one tearing energy. Otherwise, the crack growth rate is measured for one specific tearing energy (after stabilization of the crack growth rate) and measurements are continued on the same specimen with decreasing the tearing energy. The specimen is discarded if the combined lengths of the cracks are greater than 50% (roughly 20 mm) of the width of the specimen (on average 40 mm).

Finally, the results are plotted on a traditional dc/dN vs. T curves, where T is the maximum prescribed tearing energy. Subsequently, a power law relationship is calculated from multiple linear regression by a method of least squares

$$\frac{dc}{dN} = b * T^f, \tag{4.2-3}$$

where b and f are fitted scalars.

4.2.3 Fatigue damage analysis

Finally, a *JEOL JSM-6060LA* scanning electron microscope (SEM), located at GeM, is used for microscopic analysis. An acceleration voltage of 20 kV, which is chosen due to the conductivity of carbon black filled HNBR blends, is used with capture of secondary electron signals. Fracture surfaces of fatigue life specimens are analyzed to identify the initiation site, the nature of possible flaws that are responsible

for initiation, and the propagation path. Depending on the specimen, up to 20 micrographs are taken with magnification ranging from $\times 20$ up to $\times 5000$. An X-ray energy dispersive spectroscopy (EDS) is used on selected areas of the fracture surfaces to determine the chemical composition of flaws. The classification and presentation of results is similar to the one used in Masquelier (2014) and Huneau et al. (2016). Moreover, some macroscopic observations are performed with an aid of an optical microscope.

4.3 Results

4.3.1 Fatigue life

Raw results

Fatigue life experiments have been carried out for the six blends and the four loading levels. Three Wöhler curves, plotted in true stress amplitude versus number of cycles to failure, are presented in this section corresponding to different acrylonitrile (ACN) content, percent hydrogenation, and for the composite HNBR blend. Where visible, error bars indicate absolute maximum and minimum amplitudes experienced by a particular specimen. Crosses represent specimens that did not break after 2 million cycles; additional specimens were tested for the reference blend **A36H96** up to 5 million cycles.

Figure 4.3-1 shows the fatigue life curves of **A36H96** - the reference blend, A44H96,

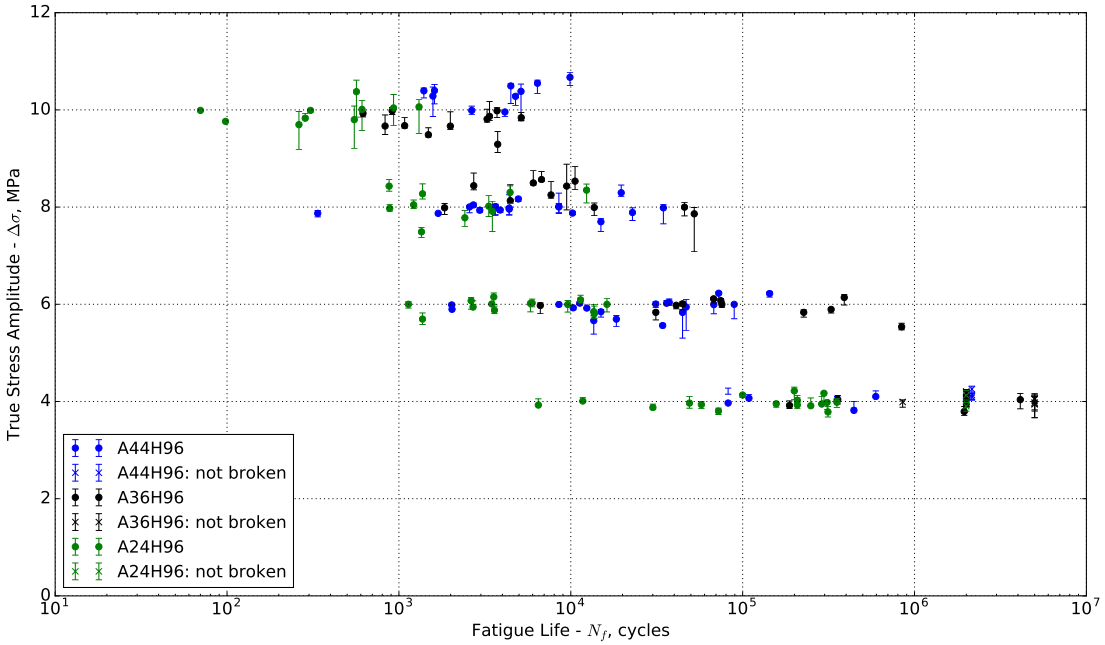

Figure 4.3-1 – Effect of ACN content on fatigue life of HNBR at 120 °C; R=0.

and A24H96 to investigate the effect of ACN content. Similarly, Figure 4.3-2 presents fatigue life results of **A36H96** with additional two HNBR blends with 91% (A36H91) and >99% (A36H99) hydrogenation. Finally, fatigue life results for the composite blend - A44-24 - are shown in Figure 4.3-3. The reference blend is also plotted for comparison.

From Figures 4.3-1 to 4.3-3, it is evident that there is significant scattering in the results. The statistical tools presented in Chapter 3, Section 3.5 have to be applied in order to make some concrete conclusions. Finally, it should be noted that some specimens broke at the grips; as damage analysis results will show in Section 4.3.3, the failure of these specimens is influenced by introduction of a cut by overtightening and roughness of the grip. The grips have been polished several times, but

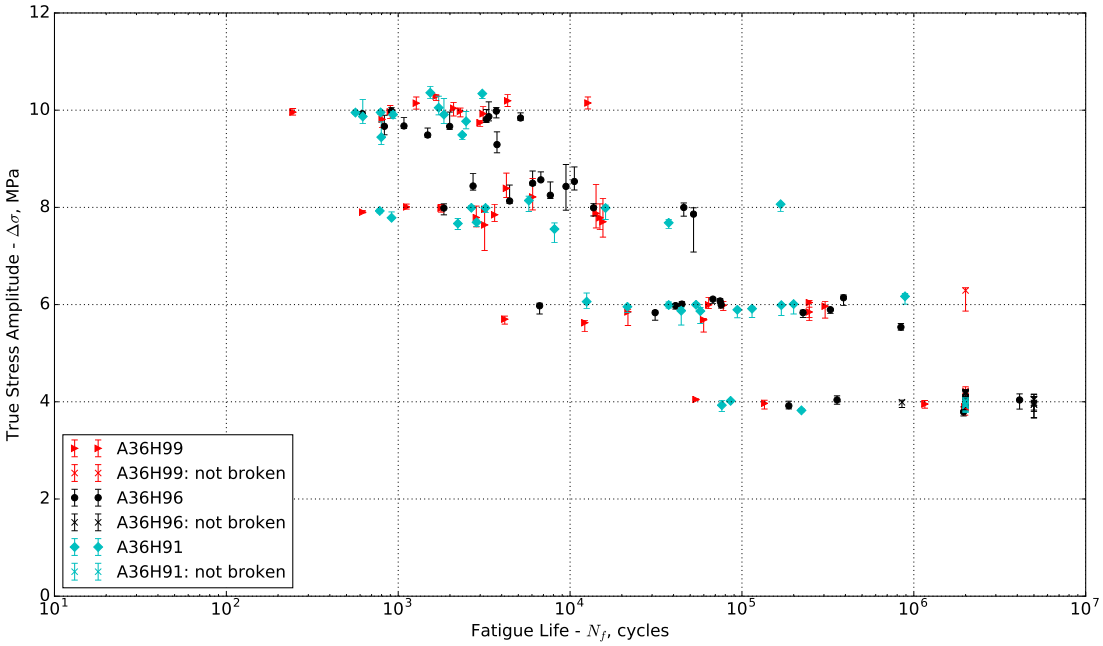

Figure 4.3-2 – Effect of hydrogenation on fatigue life of HNBR at 120 °C; R=0.

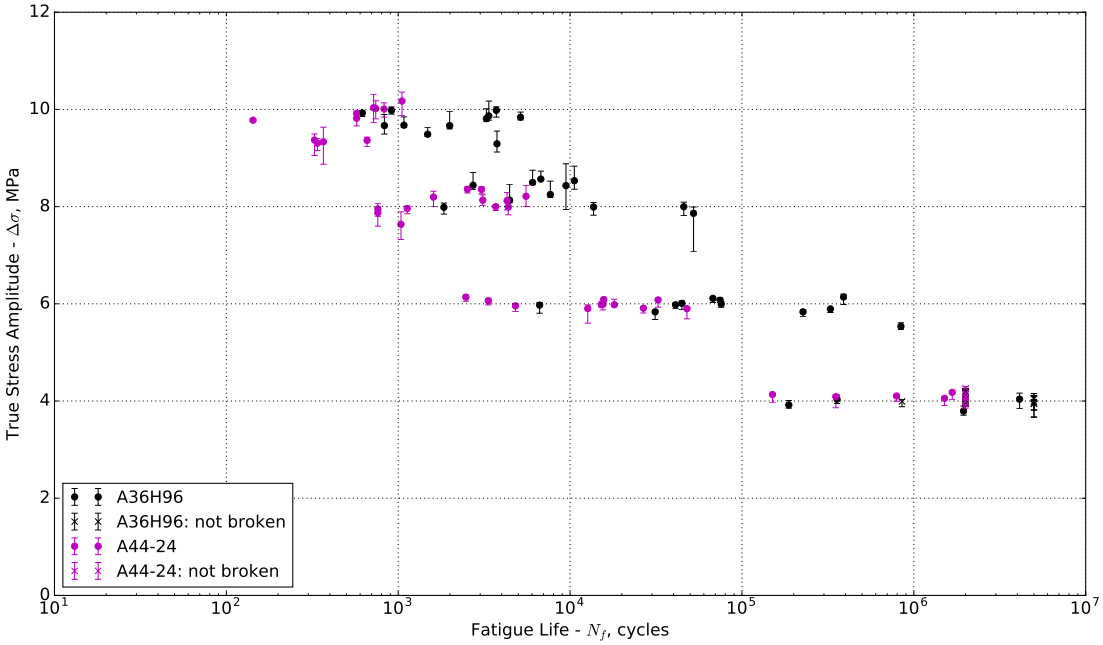

Figure 4.3-3 – Fatigue life of composite HNBR - A44-24 at 120 °C; R=0.

blends A24H96, A44-24, and A36H91 are especially sensitive to breaks at the grips. These specimens are excluded from statistical analyses; however, it should be noted that enough experiments have been carried out to ensure there are at least eight specimens per each target loading level and blend (10 on average) for a total 243 fatigue life measurements. Overall, this amounted to about 2434 h (101 days) of machine test time.

Univariate statistical analysis

First, a traditional Weibull univariate fit is applied on each blend and each target loading level (thus, univariate) allowing to estimate the distribution of the specimens and take into account unbroken specimens (right censored results). Two-parameter Weibull distributions are fitted identical to the method presented in Chapter 3, Section 3.5. For all blends at each target loading level of 10, 8, 6, and 4 MPa, the variations in stress are assumed negligible and the average true stress amplitude is calculated ($\overline{\Delta\sigma}$); the fitted coefficients (k and ρ) of the Weibull distributions correspond to this true stress amplitude. Table 4.3-1 shows these coefficients as well as the mean $\overline{N_w}$, the minimum $N_w^{\min}$ and the maximum $N_w^{\max}$ 95% bounds of the distribution for each blend and each loading level. The mean, the minimum and maximum 95% bounds are plotted in Figure 4.3-4 for all blends; please note that the lines are plotted for visual aid as no conclusion can be made between fatigue lives between the target loading levels. The results are grouped into three figures and can be summarized as follows:

- **Top** - effect of ACN: **A36H96**, A44H96, A24H96. In general, A36H96 has the best fatigue resistance at 120°C followed by A44H96 and A24H96, except at 10 MPa target loading level, where A44H96 has longer fatigue life than the reference blend. Moreover, A24H96 is by far the worse material, as its maximum 95% bound is shorter in duration than the mean fatigue lives of both A36H96 and A44H96.
- **Middle** - effect of hydrogenation: **A36H96**, A36H99, A36H91. The difference between fatigue lives is less pronounced for blends with different percent hydrogenation than for ACN content. However, it appears that A36H96 has in general the longest mean fatigue lives, except again at 10 MPa where A36H99 has a slightly longer fatigue life. The difference between the blends increases with decreased loading (longer experiments). At 4 MPa loading level, the maximum 95% bound of A36H91 is shorter than the mean fatigue lives of A36H96 and A36H99.
- **Bottom** - fatigue life of composite A44-24 with comparison to **A36H96**. It appears that fatigue life of A44-24 is affected by the applied loading. At high loading levels, fatigue lives are significantly shorter; however at 4 MPa target loading level, Weibull analysis shows that there is no difference between fatigue lives of A44-24 and A36H96.

As a general note, if one looks at the *widths* of distributions at each target loading level, that is minimum ($N_w^{\min}$) and maximum ($N_w^{\max}$) 95% bounds, the distributions are *wide* due to the scatter and the ranking of the materials in terms of fatigue resistance is the same. Moreover, the values of the Weibull shape parameter k are

Table 4.3-1 – Weibull distribution coefficients k and ρ; mean ($\overline{N_w}$), minimum ($N_w^{\min}$) and maximum ($N_w^{\max}$) 95% bounds calculated for each average target loading level $\overline{\Delta\sigma}$

Blend - Target Load	k	λ	$\overline{N_w}$	$N_w^{\min}$	$N_w^{\max}$	$\overline{\Delta\sigma}$
A36H96 - 10 MPa	1.52	2917.22	2 630	413	6 009	9.75
A36H96 - 8 MPa	1.11	11342.65	10 904	786	30 408	8.27
A36H96 - 6 MPa	0.79	176629.52	201 158	4 198	703 027	5.94
A36H96 - 4 MPa	0.96	5141525.25	5 223 516	236 688	16 030 522	4.03
A44H96 - 10 MPa	1.50	5087.82	4 592	704	10 564	10.38
A44H96 - 8 MPa	1.05	7519.42	7 367	748	21 314	8.02
A44H96 - 6 MPa	0.93	31954.92	33 104	1 297	104 380	5.93
A44H96 - 4 MPa	0.89	1574022.87	1 666 205	55 977	5 398 467	4.05
A24H96 - 10 MPa	1.16	487.18	463	37	1 258	9.94
A24H96 - 8 MPa	1.65	2289.20	2 047	380	4 445	8.04
A24H96 - 6 MPa	1.20	5249.42	4 942	438	13 135	5.95
A24H96 - 4 MPa	0.78	264918.05	305 836	5 876	1 081 709	3.95
A36H99 - 10 MPa	1.07	3044.62	2 966	190	8 490	10.02
A36H99 - 8 MPa	1.35	9475.67	8 684	1 057	21 301	7.93
A36H99 - 6 MPa	0.69	131052.31	168 492	1 757	644 439	5.90
A36H99 - 4 MPa	2.30	3358693.95	2 975 508	922 978	5 412 474	3.97
A36H91 - 10 MPa	1.54	1585.55	1 427	231	3 232	9.86
A36H91 - 8 MPa	0.87	7307.06	7 813	245	25 616	7.84
A36H91 - 6 MPa	1.28	71309.29	66 079	6 995	168 123	5.96
A36H91 - 4 MPa	1.05	662937.82	649 114	39 674	1 876 012	3.95
A44-24 - 10 MPa	1.99	538.90	478	121	935	9.62
A44-24 - 8 MPa	1.42	2370.50	2 157	291	5 145	7.97
A44-24 - 6 MPa	1.16	19984.95	18 951	1 560	51 266	6.01
A44-24 - 4 MPa	0.81	4010505.98	4 497 922	103 252	15 498 372	4.10

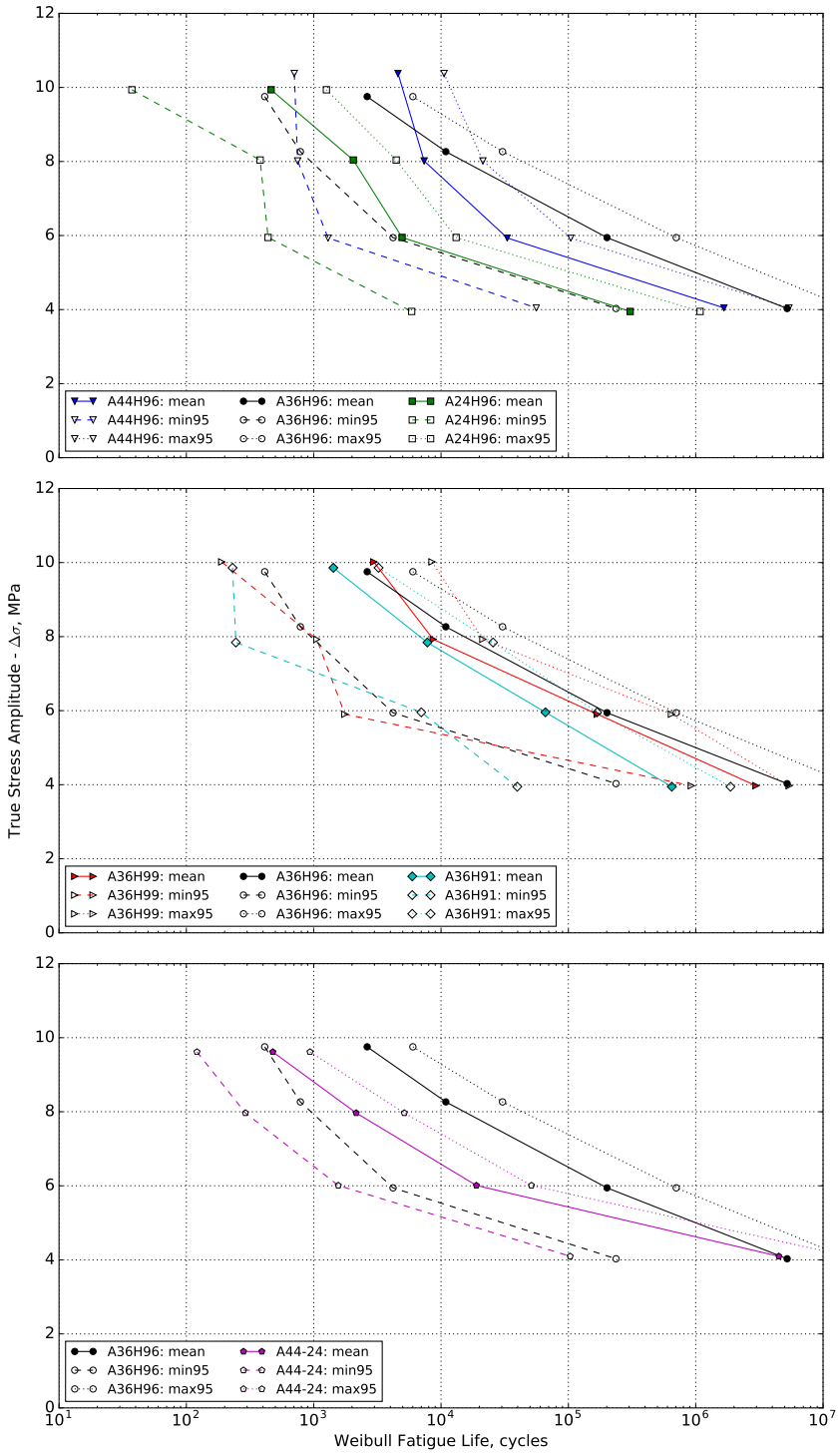

Figure 4.3-4 – Weibull distribution mean, minimum and maximum 95% bounds: effects of ACN content (top), percent hydrogenation (middle), and composite HNBR (bottom) on fatigue life of HNBR at 120° C; R=0. Solid and dashed lines are drawn for visual aid.

less than one at some target loading level for all six blends, thus indicating that failure rate decreases with time and that perhaps mechanical flaws have a greater effect on specimens that failed early.

Finally, one limitation of the Weibull analysis is that it is difficult to predict fatigue lives between target loading levels. Secondly, the confidence in the results at the 4 MPa level is questionable. The influence of unbroken specimens greatly affects the fit of the Weibull distribution. For example, for A44-24 only 11 specimens have been tested at 4 MPa, out of which 6 are unbroken at 2 million cycles. Weibull mean fatigue life is 4.01 million cycles. However, hypothetically speaking, if one additional test would have been carried out (7 unbroken, 12 total specimens), then a new Weibull mean would equal to 4.6 million cycles. On the other hand, if 1 fewer test would have been carried out and there were only 5 unbroken specimens out of 10, then Weibull mean would become 3.4 million cycles. For these two reasons, more advanced statistical analysis is necessary.

Multivariate statistical analysis

As discussed previously in Chapter 3, Section 3.5, application of univariate approach to the fatigue life results obtained in present work is unsatisfactory due to the presence of scatter in true stress amplitude (y-axis). Moreover, due to a statistically small number of specimens tested per material and presence of right-censored data, a Weibull fit could be proven to be inaccurate due to high sensitivity to these elements. Thus, the Cox proportional hazards model is also applied for multivariate analysis taking into account the scatter in both stress amplitude and fatigue life.

In the model, all blends are simultaneously considered and the model can be formally expressed from the general formulation of the Cox proportional hazards model in(Eq. (3.5-11). In the model, there is one categorical covariate - type of blend; as per model requirements, A36H96 is chosen as the reference. There is also a continuous covariate: the true stress amplitude. Thus the model can be formally expressed as

$$\begin{aligned} h(N,\vec{x}) = h_0(N) \times \exp(&\beta_{A24H96}x_{A24H96} + \beta_{A36H91}x_{A36H91} \\ &+\beta_{A36H91}x_{A36H91} + \beta_{A36H99}x_{A36H99} \\ &+\beta_{A44H96}x_{A44H96} + \beta_{A44-24}x_{A44-24} \\ &+\beta_{\Delta\sigma}x_{\Delta\sigma}), \end{aligned} \tag{4.3-1}$$

As previously in Chapter 3, Section 3.5, the model is implemented in the R-software environment using the *survival* package (Therneau and Lumley 2017). First and foremost, the model has to be verified for the validity of proportional hazards assumption. Similarly, *cox.zph()* function of the *survival* package (Fox and Weisberg 2011; Therneau and Lumley 2017) is used to calculate tests for the proportionality for each covariate. The return of the function is shown in Table 4.3-2. Since the statistical significance of the test on each covariate and globally is low, *i.e.* p-values are all greater than $p > 0.05$, proportionality assumption of the model is considered satisfactory (Fox and Weisberg 2011).

Table 4.3-3 presents the results of the fit of the model with the hazard ratios (HR

Table 4.3-2 – Return of the *cox.zph()* function.

Covariate	p
material_A24H96	0.126645
material_A36H91	0.381508
material_A36H99	0.934377
material_A44-24	0.101105
material_A44H96	0.109647
stress	0.760043
GLOBAL	0.105015

Table 4.3-3 – Cox hazards model results.

Covariate	β	HR	$HR^{\min}$	$HR^{\max}$	p
A24H96	1.99	7.33	4.41	12.17	1.47E-14
A36H91	0.61	1.84	1.11	3.05	1.72E-02
A36H99	0.11	1.12	0.68	1.86	6.57E-01
A44-24	1.37	3.93	2.36	6.54	1.45E-07
A44H96	0.23	1.26	0.78	2.04	3.39E-01
stress	0.87	2.40	2.15	2.67	2.00E-16

with lower $HR^{\min}$ and upper $HR^{\max}$ 95% confidence intervals) for each covariate along with a p-value indicating statistical significance of the hazard ratio. The hazard ratio ($HR = 2.40$) for `stress`, *i.e.* true stress amplitude, indicates in very general terms that for all blends an increase of 1 MPa induces a hazard of failure (at each cycle) by a factor of 2.4. The hazards for the materials indicate a similar factor of increased failure rate (at each cycle) with respect to the reference blend A36H96; for example, over the range of true stress amplitude from 4 to 10 MPa, A24H96 has an increased failure rate than A36H96 by a factor of 7.33. Of course, since there are not many observations (fatigue tests) in statistical terms, the 95% confidence intervals for each material are rather broad. Nevertheless, comparing HR values with their respective confidence intervals, a general fatigue life ranking of blends can be created:

- Effect of ACN content: A36H96 is better than A44H96 and the two are significantly better than A24H96;
- Effect of hydrogenation: A36H96 is better than A36H99, which in turn is better than A36H91;
- Composite blend: A36H96 is significantly better than A44-24.

However, this analysis can be extended further to create a probabilistic Wöhler curve based on the Cox hazards model. As an example, Figure 4.3-5 shows the survival estimate for A36H96 with respect to 4 target loading levels. However, the choice of these four loading levels is arbitrary with respect to the Cox hazards model; it allows modelling of continuous variables, such as true stress amplitude, and, thus, these probability curves can be extracted for any loading level from 4 to 10 MPa.

Thus, it has been decided to carry out post-treatment of Cox model results (in *Python* with *NumPy* package) to calculate the survival estimates from 4 to 10 MPa and "flatten" probability curves at some arbitrary loading level with application of a normalized color contour plot, where a single color represents a 5% range in survival probability. Moreover, the probabilistic model can be used to make predictions,

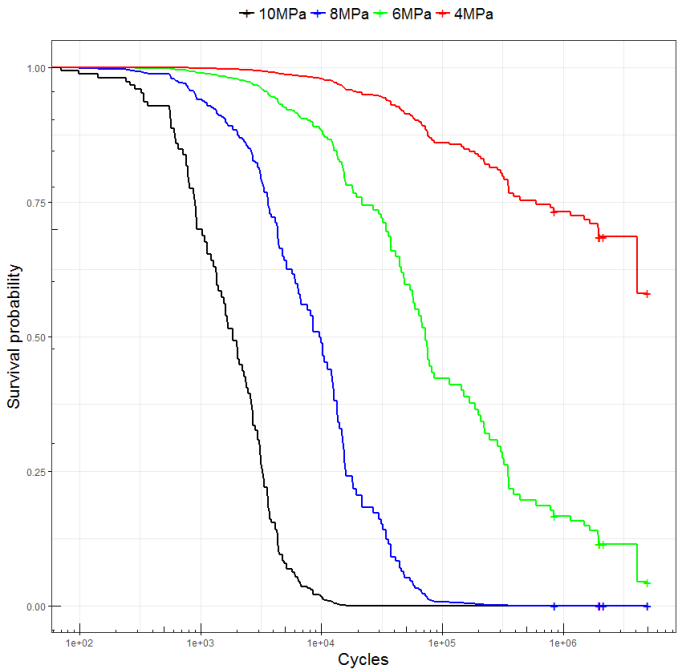

Figure 4.3-5 – Survival estimate of the Cox hazards model for A36H96 at four target loading levels.

and survival probabilities are extrapolated for true stress amplitudes outside of the tested range. In present case, the extrapolation is carried out up to 12 MPa and down to 2 MPa loading. However, since observations are made only up to 5 million cycles, the time domain (in cycles) is limited to this duration.

The results are shown in Figures 4.3-6 to 4.3-11 for all six blends. The solid lines indicate the mean probability, as well as near absolute survival and near absolute failure (as indicated by labels $\widehat{S}(N)$ =0.500, $\widehat{S}(N)$ =0.999, and $\widehat{S}(N)$ =0.001). The dashed lines are the maximum ($\widehat{S}(N) \approx 0.05$) and the minimum ($\widehat{S}(N) \approx 0.95$) 95% bounds of the survival estimates. The hatched regions from 2 to 4 MPa and from 10 to 12 MPa indicate the extrapolated survival estimates. In these figures, for example, it is clear from each figure up to which true stress amplitude a specimen can be subjected to ensure nearly full survival for example. Moreover, it can also be said that the choice to plot the mean and the 95% bounds is rather arbitrary and depends on the choice for analysis: depending on application of the Wöhler curve, lines for any probabilities of survival can be plotted.

To simplify the visualization of the results, the mean lines are compared for each formulation category. Additionally, Weibull means from univariate analysis are plotted for comparison. Figure 4.3-12 shows the results, where solid lines indicate the Cox mean ($\overline{N_c}$) and dotted lines represent the extrapolated values; moreover, the two-color large markers correspond to the Weibull mean values ($\overline{N_w}$), which were presented in Figure 4.3-4, and the dashed lines are plotted for visual aid. Furthermore, percent difference of the Weibull mean values with respect to Cox mean values at each target loading level is determined to asses the closeness of results; it is calculated for each average true stress of each blend ($\overline{\Delta\sigma}$ used earlier in Weibull

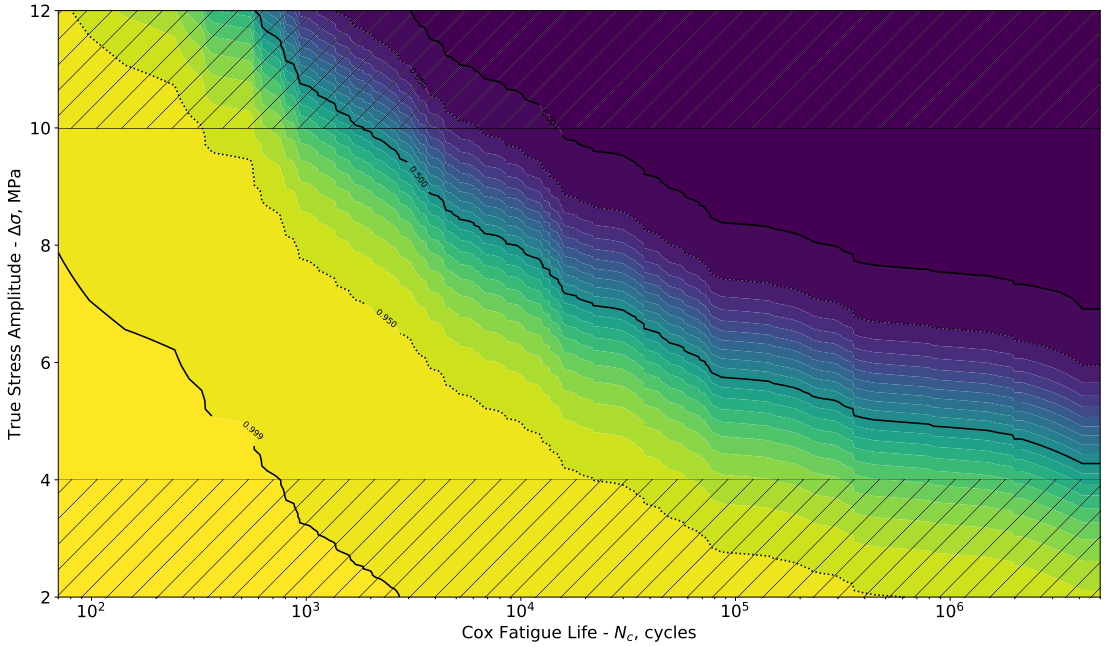

Figure 4.3-6 – Probabilistic Wöhler curve of A36H96 at 120 °C estimated by Cox model. Hatched regions indicate extrapolated data.

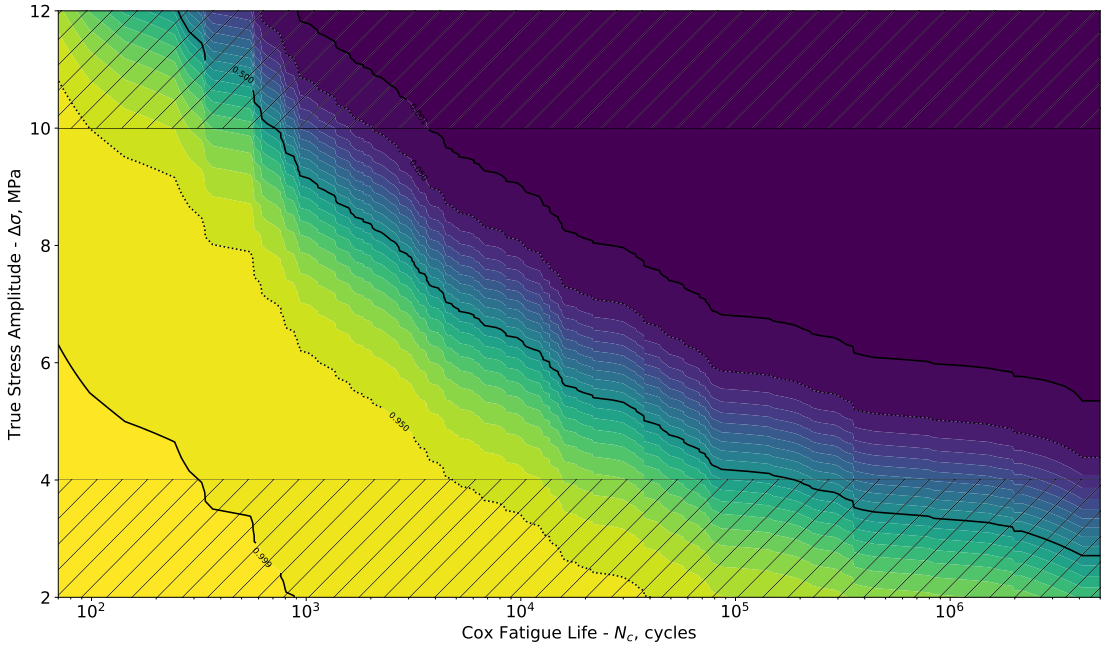

Figure 4.3-7 – Probabilistic Wöhler curve of composite A44-24 120 °C estimated by Cox model. Hatched regions indicate extrapolated data.

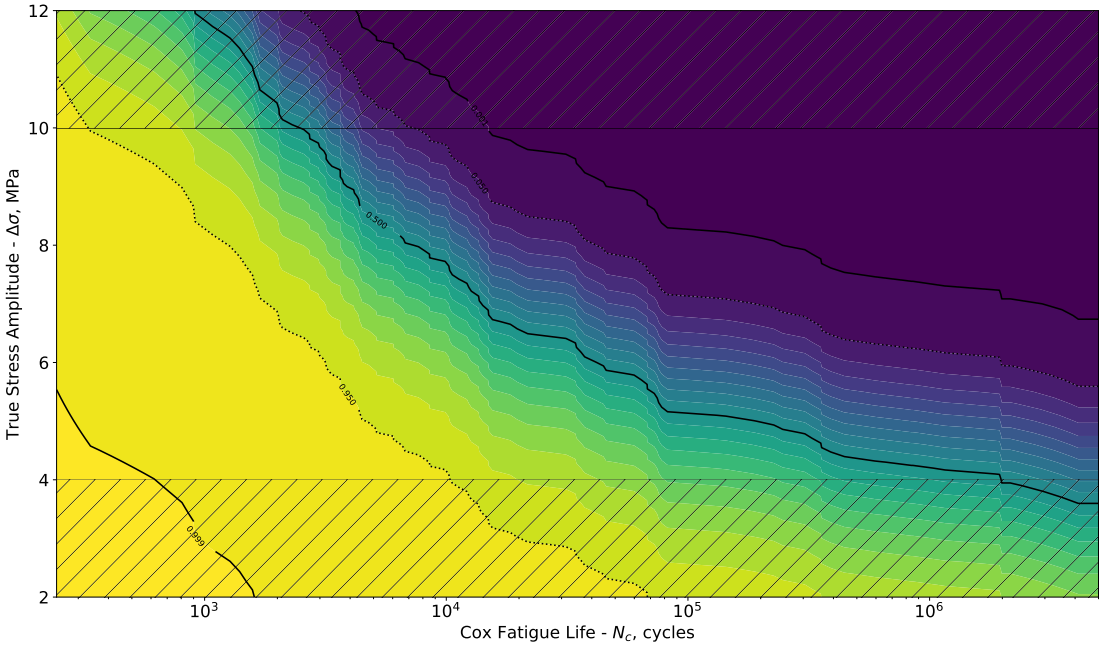

Figure 4.3-8 – Probabilistic Wöhler curve of A44H96 120 °C estimated by Cox model. Hatched regions indicate extrapolated data.

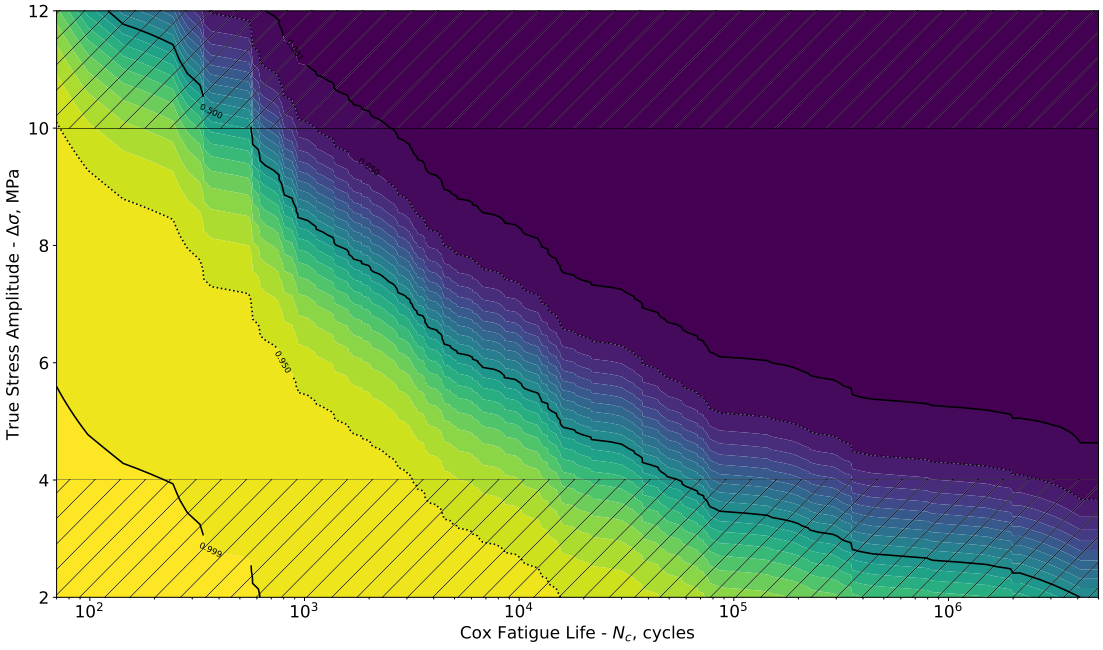

Figure 4.3-9 – Probabilistic Wöhler curve of A24H96 120 °C estimated by Cox model. Hatched regions indicate extrapolated data.

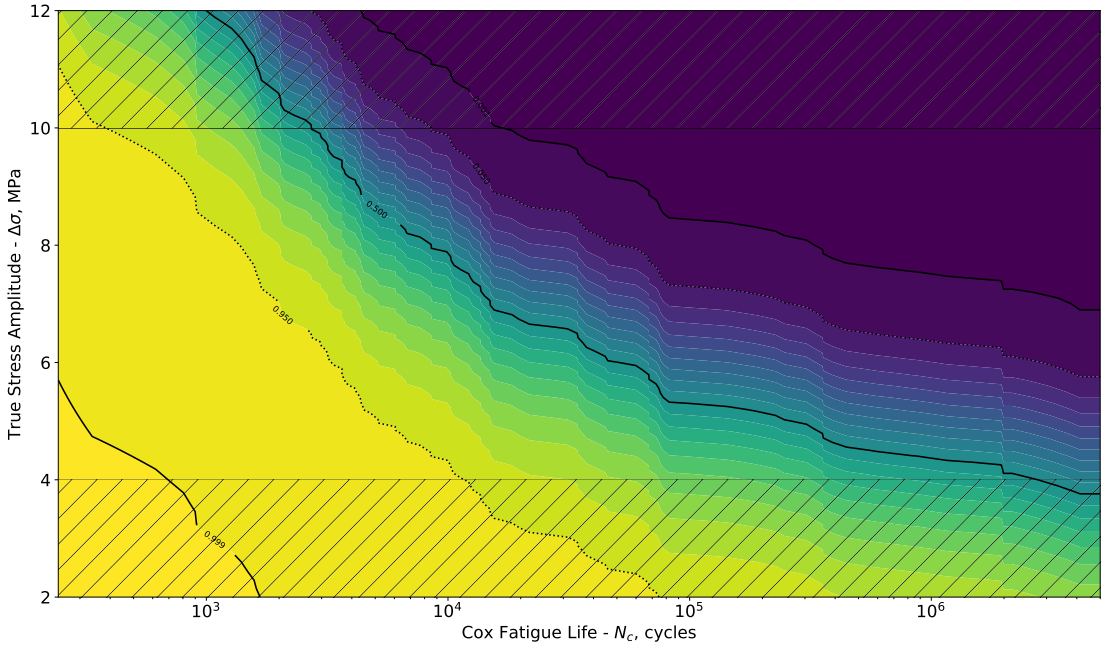

Figure 4.3-10 – Probabilistic Wöhler curve of A36H99 120 °C estimated by Cox model. Hatched regions indicate extrapolated data.

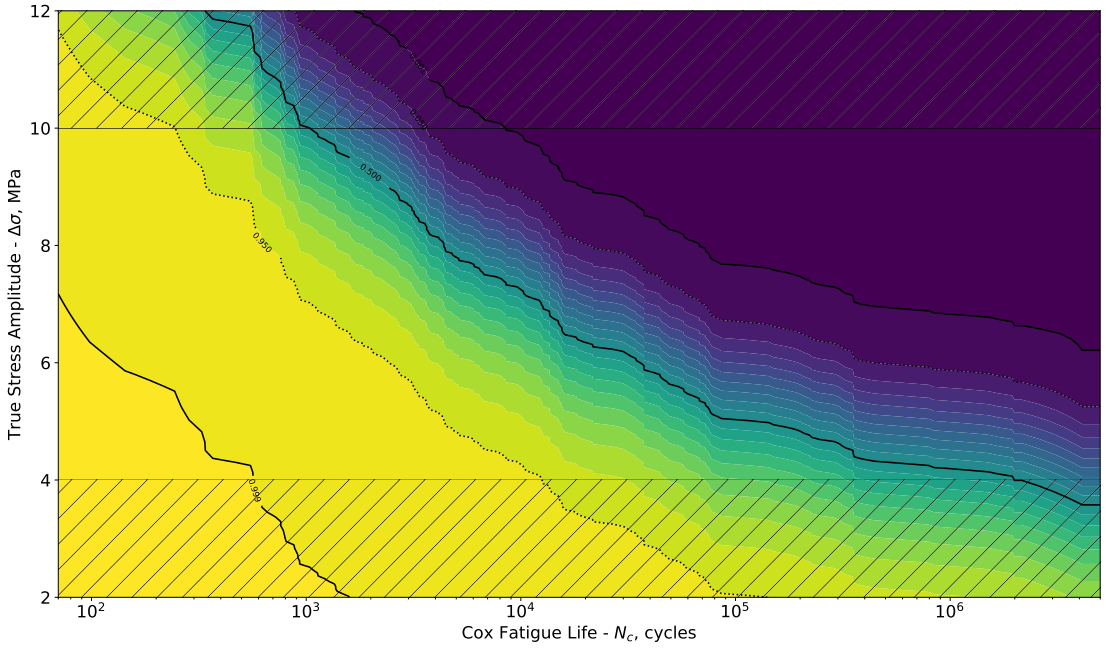

Figure 4.3-11 – Probabilistic Wöhler curve of A36H91 120 °C estimated by Cox model. Hatched regions indicate extrapolated data.

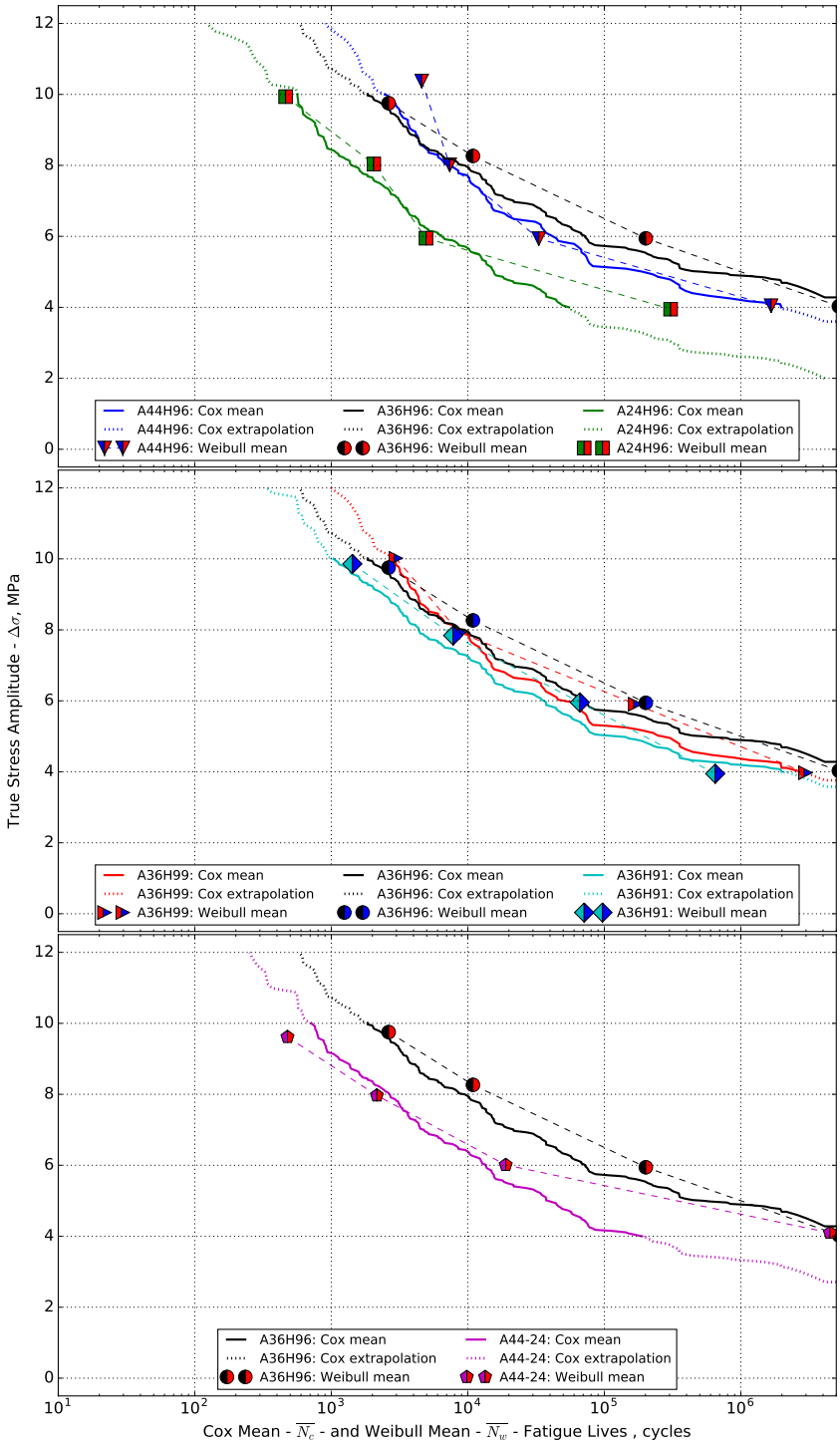

Figure 4.3-12 – Mean fatigue lives of the Cox model ($\overline{N_c}$) with comparison to univariate Weibull fit ($\overline{N_w}$); effect of ACN content, percent hydrogenation, and for composite A44-24.

analysis) and log-scale is used

$$\Delta_{\%} = 100\% * \frac{\log\left(\overline{N_w}\right) - \log\left(\overline{N_c}\right)}{\log\left(\overline{N_c}\right)}, \tag{4.3-2}$$

where $\overline{N_c}$ is the Cox mean and $\overline{N_w}$ is the Weibull mean. The results are shown in Table 4.3-4.

Table 4.3-4 – Percent difference between Weibull and Cox mean values.

Target $\Delta\sigma$	**A36H96**	A44H96	A24H96	A36H99	A36H91	A44-24
10 MPa	1.13%	10.71%	-3.14%	1.09%	3.33%	-7.76%
8 MPa	6.05%	0.09%	3.38%	-1.09%	5.27%	-2.67%
6 MPa	8.71%	-2.94%	-4.39%	9.00%	5.81%	3.48%
4 MPa	-1.33%	-0.76%	15.68%	0.51%	-7.71%	28.84%

The results are grouped into three categories and can be summarized as following:

- **Figure 4.3-12 - Top** - effect of ACN: **A36H96**, A44H96, A24H96.

  The general trend is identical to the one observed for the Weibull analysis. At 10 MPa, A44H96 is slightly better than A36H96, but A36H96 has longer fatigue lives for true stress amplitudes smaller than about 8.6 MPa. Similarly, A24H96 evidently has shorter fatigue lives; however, at 4 MPa, the Cox mean life is significantly shorter as compared to the Weibull fit, *i.e.* $\Delta_{\%} = -7.71\%$.

- **Figure 4.3-12 - Middle** - effect of hydrogenation: **A36H96**, A36H99, A36H91.

  The general trends are also identical, where the difference between fatigue lives is less pronounced for blends with different percent hydrogenation than for ACN content. Moreover, it is evident that A36H96 has in general longer mean fatigue lives, except, again, from about 8.3 MPa to 10 MPa, where A36H99 has a slightly longer fatigue life. On the other hand, A36H91 has consistently lower mean fatigue lives.

- **Figure 4.3-12 - Bottom** - fatigue life of composite A44-24 with comparison to **A36H96**.

  Similar to the trends observed after Weibull analysis, in general, fatigue life of the composite A44-24 is shorter than that of the reference A36H96. However, Cox analysis shows that the fatigue life of A44-24 is not affected by the applied loading, contrary to what was observed with Weibull analysis. At 4 MPa target loading level, percent difference of the Weibull mean is 28% pointing to overestimation of mean of Weibull analysis.

4.3.2 Fatigue crack propagation

Overall, an average of 10 specimens have been tested for each blend, with the machine testing time amounting to around 90 h. First, Figure 4.3-13 shows the effect

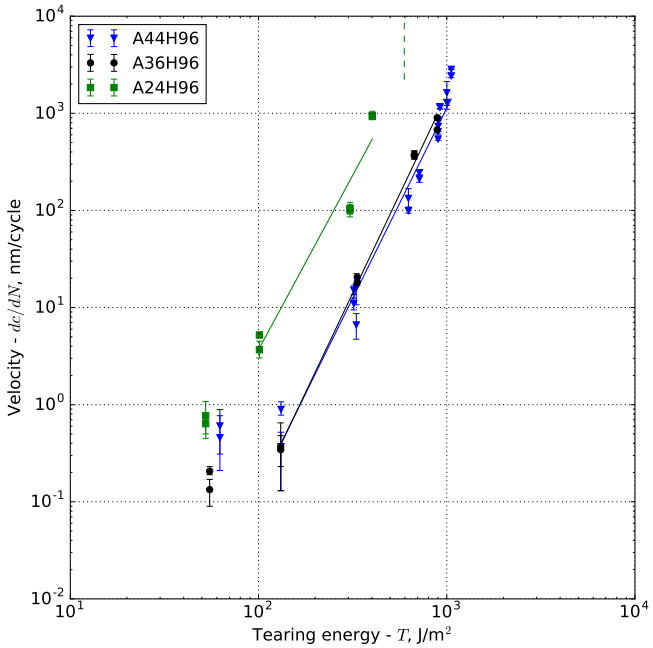

Figure 4.3-13 – Effect of ACN content on fatigue crack propagation of HNBR at 120°C.

of ACN content on fatigue crack propagation. In general, **A36H96** and A44H96 have similar resistance to fatigue crack growth as indicated by fitted coefficients given in Table 4.3-5. A decrease in ACN content to 24 wt.-%, significantly increases fatigue crack growth rates. With the data available, it is difficult to judge whether there are distinct regimes as originally proposed by Lake and Lindley (1965). However, it seems that around $T \approx 100$ J/m^2 there is a transition in regimes for A44H96 and **A36H96**, where the "slope" or f decreases. Hence, for consistency, the power-law fit only considers points above this tearing energy. At low energies

Table 4.3-5 – Power law fit coefficients characterizing fatigue crack propagation; effect of ACN.

	A36H96	**A44H96**	**A24H96**
b	8.53E-10	1.96E-09	2.43E-07
f	4.09	3.92	3.59

($T < 100$ J/m^2), cracks propagate faster in A44H96 (≈ 0.6 nm/cycle) than in **A36H96** (≈ 0.1 nm/cycle). Indeed, it seems that these low energy crack growth measurements point to existence of some value for r from Eq. (4.1-5) that corresponds to the environmental effect (in present case - temperature). Without direct measurements, it could be estimated that for these two blends the mechanical fatigue threshold T_0 is around 50 to 100 J/m^2. In case of A24H96, there is no apparent change in "slope" such that a regime transition occurs and it appears that there is no apparent fatigue threshold. The former conclusion can be supported by the fact

that A24H96 appears to have a low critical tearing energy T_c, which is referred to the fourth regime of infinite growth. At tearing energies equal to and higher than ≈ 600 J/m^2 (indicated by dashed line in Figure 4.3-13), complete failure occurs during the first loading cycle; hence, considering the "parallelism" of the three curves, the curve of A24H96 is roughly shifted to the left with respect to the two other blends.

Keeping the reference blend **A36H96**, the fatigue crack propagation results with respect to changing percent hydrogenation are shown in Figure 4.3-14. Once again,

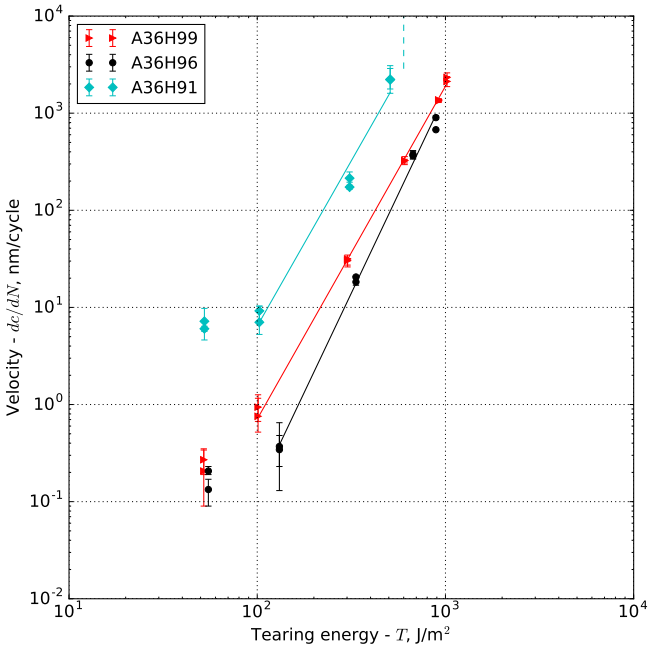

Figure 4.3-14 – Effect of hydrogenation on fatigue crack propagation of HNBR at 120°C.

in two blends, A36H91 and **A36H96**, two regimes are observed with a transition roughly around $T = 100$ J/m^2, and, for consistency, a power-law fit is plotted for energies greater than $T = 100$ J/m^2 with coefficients shown in Table 4.3-6. The

Table 4.3-6 – Power law fit coefficients characterizing fatigue crack propagation; effect of hydrogenation.

	A36H96	**A36H99**	**A36H91**
b	8.53E-10	9.91E-08	9.93E-07
f	4.09	3.43	3.41

reference HNBR blend with 96% hydrogenation, **A36H96**, has generally better resistance to fatigue crack propagation. At the lowest energies around 50 J/m^2, there is some overlap in crack growth rate measurements of blends with 99% and 96% hydrogenation. Moreover, there appears to be no drastic transition in a regime (change of "slope" f) in A36H99, which could indicate earlier fatigue threshold values for A36H99 than for **A36H96**, or that such threshold does not exist for A36H99. Additionally, propagation is similar for energies higher than 1000 J/m^2. Whereas the difference between **A36H96** and A36H99 is relatively insignificant, resistance to fatigue crack growth is greatly diminished as percent hydrogenation is reduced

to 91%: at low energies around 50 J/m^2, where environmental contribution is significant, the growth rate for A36H91 is around 7 nm/cycle and decreases to around 0.2 nm/cycle for the other two blends. At the other extreme of tearing energies, A36H91 (similar to A24H96) has a critical tearing energy T_c since it suffered instantaneous failure at tearing energies equaling and greater than $\approx$ 600 J/m^2, as indicated by dashed line in Fig. 4.3-14.

Finally, Figure 4.3-15 and coefficients in Table 4.3-7 show that fatigue crack prop-

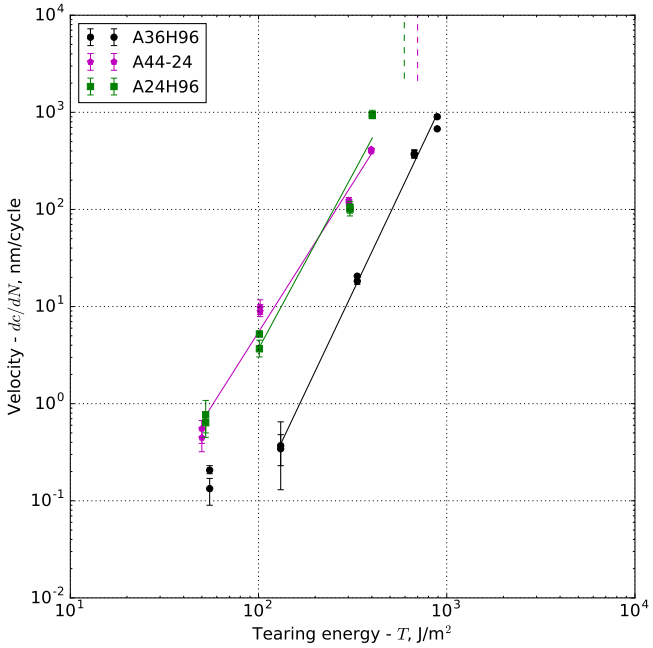

Figure 4.3-15 – Fatigue crack propagation of composite HNBR with 24 wt.-% and 44 wt.-% ACN for an average of 36 wt.-% at 120°C; compared with the reference **A36H96** and A24H96.

Table 4.3-7 – Power law fit coefficients of composite HNBR blend characterizing fatigue crack propagation.

	A36H96	**A44-24**	**A24H96**
b	8.53E-10	4.13E-06	2.43E-07
f	4.09	3.06	3.59

agation resistance of the composite HNBR is similar to the blend with 24 wt.-% ACN, the resistance of which is significantly lower than the one of the reference blend, **A36H96**. Moreover, similar to A36H91 and A24H96, cyclic loading at tearing energies of $\approx$ 700 J/m^2 and higher could not be applied due to failure of the specimens, thus indicating the existence of critical tearing energy T_c.

4.3.3 Fatigue damage analysis

In the present section, fatigue damage analysis is discussed for specimens failed during fatigue life experiments. All fatigue life specimens of the reference blend

A36H96 have been analyzed; for each other blend, a limited number of specimens have been sampled at random. Overall, at least 280 man-hours have been spent on analysis of specimens.

Failure at grips

First, a remark on one type of observed failure is made. As briefly mentioned in Section 4.3.1, some specimens broke at or near grips. Upon investigation of fracture surfaces, one can observe that the initiation of the crack is due to a physical damage caused by a grip on the surfaces of a specimen. Figure 4.3-16(a) shows a typical

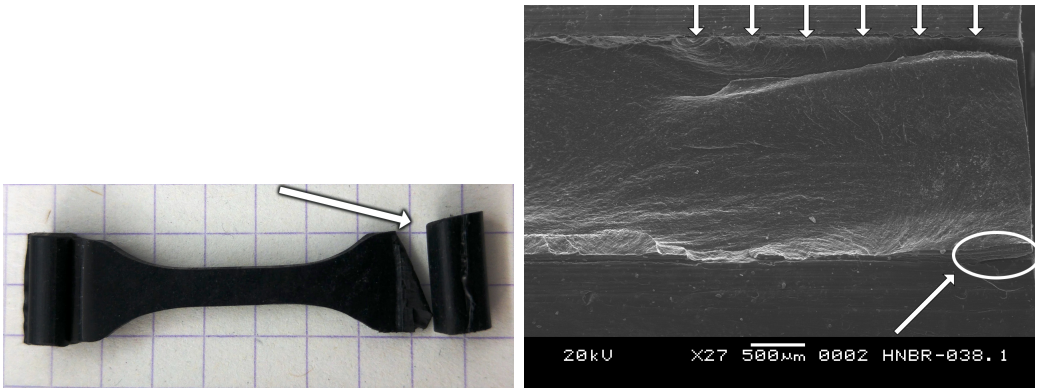

(a) Global view. **(b)** Micrograph of the fracture surface.

Figure 4.3-16 – Example of a specimen failing at the grip.

specimen broken at a grip. Upon investigation of the fracture surface as indicated by the arrow in Fig. 4.3-16(a), it is evident that in some cases the grips damage the surfaces of the specimen. Fig. 4.3-16(b) shows a micrograph of the fracture surface; the arrows on top indicate the damage caused by small incisions due to the grip and initiation of such incision can be seen in the lower right corner (circled). The cause is definitely overtightening or roughness of the grips. To overcome this, the grips have been re-polished multiple times and breaking at the grip reduced over time. However, blends A24H96, A44-24, and A36H91 remained especially sensitive to breaks at the grips. At this point, these specimens are excluded from further discussion as this phenomenon is caused by experimental contingencies and does not accurately reflect damage due to fatigue.

Macroscopic observations

Before investigation of fracture surfaces, some macroscopic observations, visually and with an optical microscope, have been made. First, the general nature of crack growth within the specimens has been investigated. For all tested specimens, this behavior can be split into two categories as shown in Figure 4.3-17:

- When initiation and propagation occur on a single plane perpendicular to the direction of loading;

- When initiation occurs on "plane 1" and brittle, smooth failure surface is observed on "plane 2" that is offset by some vertical distance (along the direction of loading).

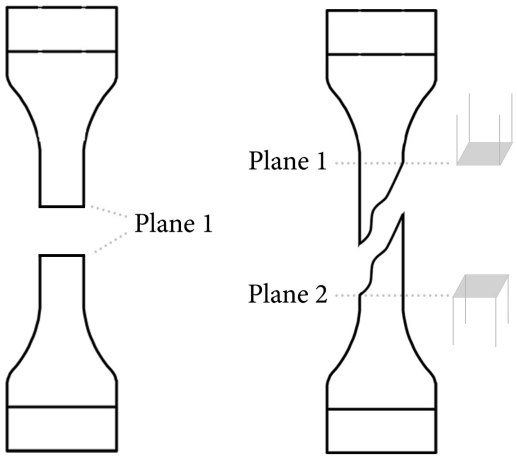

Figure 4.3-17 – Schematic for observed crack growth behavior.

Additionally, observations have been made to detect any signs of multiple cracks present on both failed and unbroken specimens after fatigue life testing. These are categorized into two groups:

- First, none of the unbroken specimens show signs of multi-cracking. As mentioned earlier, multi-cracking is observed for natural rubber, but not for some synthetic rubbers;
- On the other hand, multi-cracking has been observed in some failed specimens.

The observations of the nature of crack growth (on a plane or two planes) and the presence of multi-cracking in failed specimens are summarized in Figure 4.3-18.

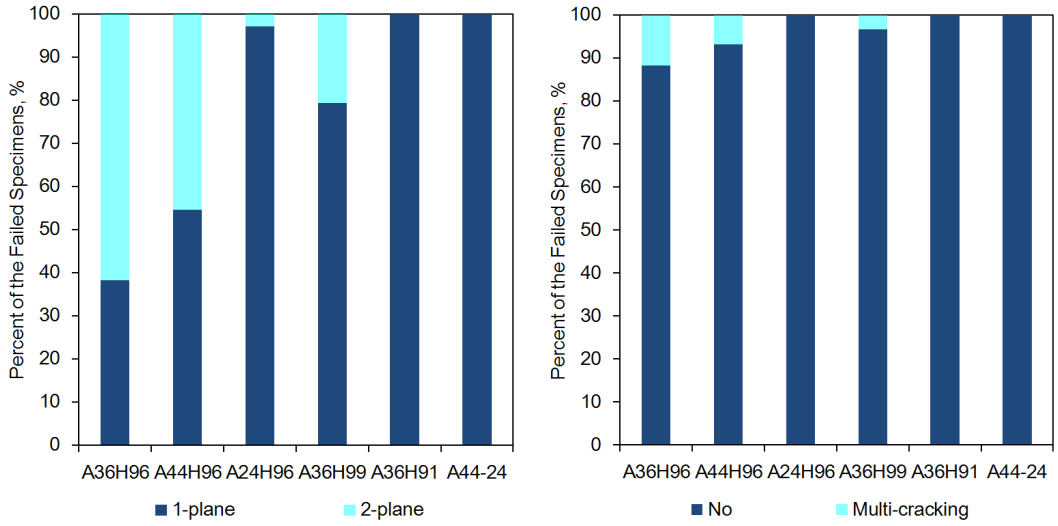

(a) Crack growth behavior. **(b)** Multi-crack appearance.

Figure 4.3-18 – Macroscopic observations of crack growth behavior and of appearance of multi-cracking in broken specimens.

Furthermore, measurements are made along the specimen length to record the length to initiation, L_I, and the vertical length of crack propagation, L_P, as shown in Figure 4.3-19. Figure 4.3-20 shows these two measurements grouped in intervals

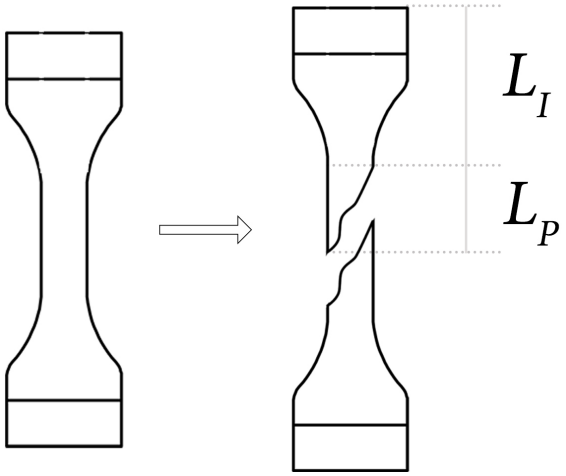

Figure 4.3-19 – Schematic for measurements of the length to initiation (L_I) and the vertical length of propagation (L_P) with respect to fractured specimen.

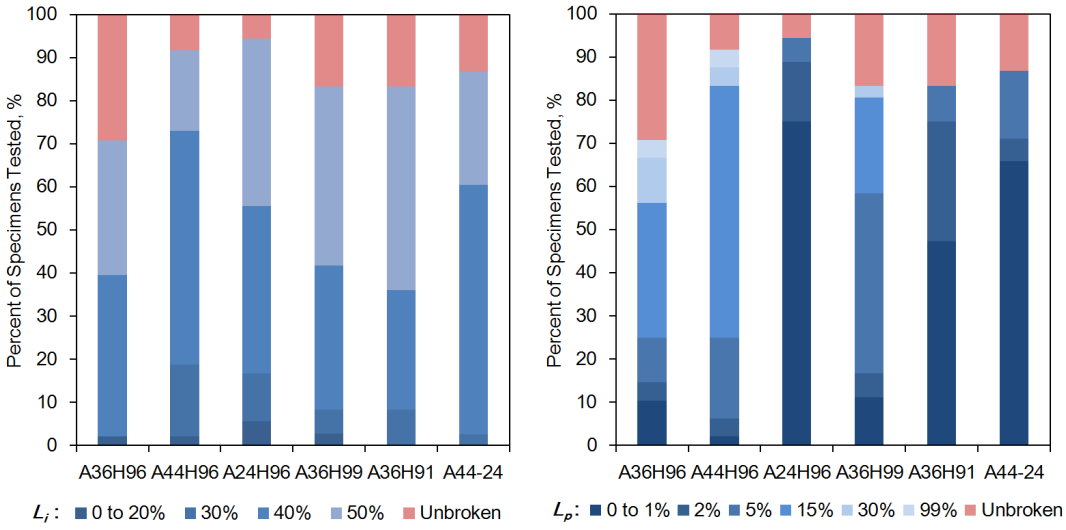

(a) Length to initiation (L_I). **(b)** Vertical length of propagation (L_P).

Figure 4.3-20 – Macroscopic measurements of the length to initiation and the vertical length of propagation; shown as percentages to the total length of the specimen.

of percentage to the total length of the specimen (*i.e* L_I/L_{specimen} or L_P/L_{specimen}, where $L_{\text{specimen}} = 36$ mm); on the figures, the percentage in the legend indicates the upper interval value. First, the length to initiation is shown in Figure 4.3-20(a). The vast majority of specimens fail from 30% to 50% as expected, since this corresponds to the middle section of the specimen that experiences most stress. Second, Figure 4.3-20(b) shows the measurements of the vertical crack propagation length, L_p; these are interesting results that seem to correlate to the results observed in .

A trend is clear from Figs. 4.3-18 and 4.3-20, where the six blends can be divided into two groups:

- **Group 1: A36H96, A44H96, and A36H99** are blends with longer vertical propagation lengths spanning in some cases two planes, and presence of some multi-cracking.

  The greatest number of failed specimens have vertical propagation lengths from 5% to 15% for A36H96 and A44H96 and from 2% to 15% for A36H99. All three blends also have some specimens breaking up to 30%. Moreover, vertical propagation lengths greater than 30% have been observed for blends A36H96 and A44H96. Thus, these blends have two macroscopic crack growth mechanisms. In some specimens (38% for A36H96, 55% for A44H96, 80% for A36H99), crack initiates on one plane and crack grows in the same plane, which is perpendicular to the loading direction. However, for the remaining failed specimens, crack growth behavior is best described by initiation on one plane, followed by vertical crack growth along the length of a specimen, and final failure on a second plane. Finally, multi-cracking is observed in some of the specimens with greatest amount in A36H96 (12%), followed by A44H96 (7%), and A36H99 (4%).

- **Group 2: A36H91, A24H96, and A44-24** are blends with short vertical propagation lengths with crack growth occurring on one plane, and absence of multi-cracking.

  In this case, vertical crack propagation lengths are less than 2% of the total specimen length for the vast majority of specimens. In none of the specimens, the vertical propagation lengths are greater than 5%. Thus the macroscopic crack growth mechanism of these blends is simple initiation, growth, and failure on one plane perpendicular to the loading direction. Finally, no multi-cracking occurs in these blends.

These results are compelling since, if one recalls the results of the previous sections, the blends in the group with long vertical propagation lengths had generally better resistance to fatigue (long lives, slow propagation) than the blends of the group with short vertical lengths.

Microscopic observations

Due to the time-consuming nature of microscopic analysis, only 103 specimens have been analyzed. All specimens of the reference blend A36H96 have been analyzed; for the remaining blends, specimens have been sampled in random for each four loading levels to get a generalized view of microscopic features. For more micrographs, please refer to Appendix C.

In general, the fracture surfaces can be categorized into three categories and examples are shown in Figure 4.3-21. These can be characterized as following:

1. As shown in Figure 4.3-21(a), classic surfaces with three regimes of initiation, propagation with high rugosity (roughness), and failure with low rugosity (smoothness); these are related to one-plane macroscopic observations and

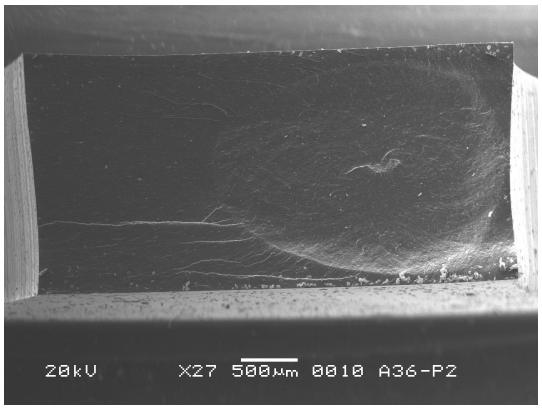

(a) Rough-smooth at ×27.

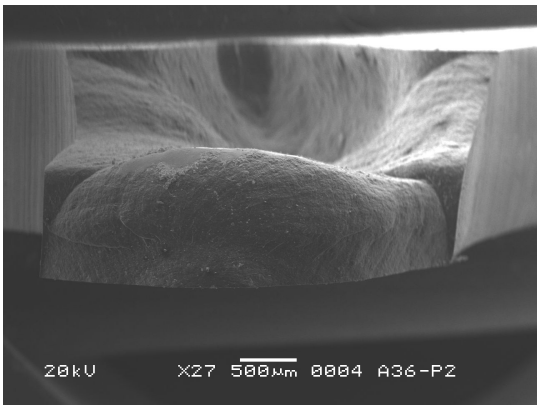

(b) Vertical rough-smooth at ×27.

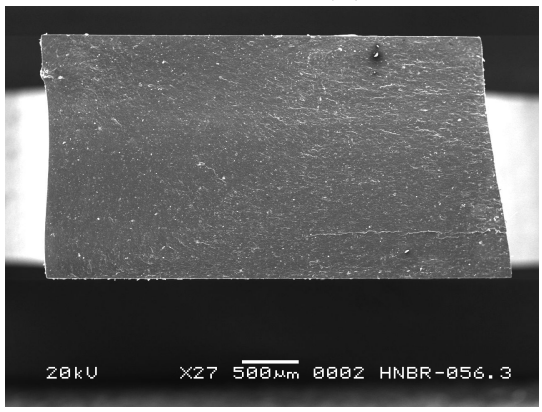

(c) Smooth at ×27.

Figure 4.3-21 – Micrographs of typical fracture surface categories.

will be referred to as *rough-smooth* surfaces;

2. As shown in Figure 4.3-21(b), similar surfaces except with the earlier mentioned vertical propagation; these are related to two-plane macroscopic observations and will be referred to as *vertical rough-smooth* surfaces;

3. Finally, as shown in Figure 4.3-21(c), almost completely smooth surfaces over the whole fracture surface of a specimen; these are related to one-plane macroscopic observations and will be referred to as *smooth* surfaces.

The number of observations for each category of fracture surfaces is shown in Figure 4.3-22; it should be noted that partial sampling is done for all blends except for A36H96 (for which all specimens have been observed) and, as such, are indicated by hatched fill. The results are very similar to those presented in Fig. 4.3-18 and Fig. 4.3-20(b); a parallel can be drawn that separates the materials into two groups: on one hand, A36H96, A44H96, and A36H99 with both *rough-smooth* and *vertical rough-smooth* fracture surfaces; on the other hand - A24H96, A36H91, and A44-24 with *rough-smooth* and *smooth* fracture surfaces.

First, an example of a *smooth* surface is shown in detail in Figure 4.3-23 for A36H91 tested at 6 MPa target loading level. The damage mechanism appears straightforward. There is an initiation site as shown in Figure 4.3-23(a). There is also an apparent propagation region, but the difference in the surface rugosities of the propagation and final fracture area is not visible at different magnifications. Moreover,

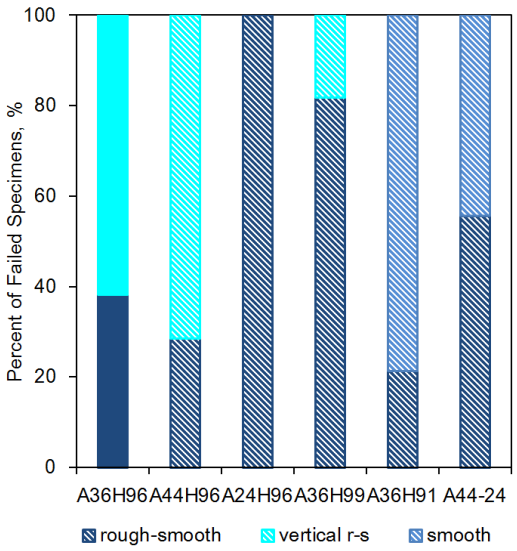

Figure 4.3-22 – Microscopic observations of fracture surfaces categories in broken specimens; hatched fill indicates partial sampling.

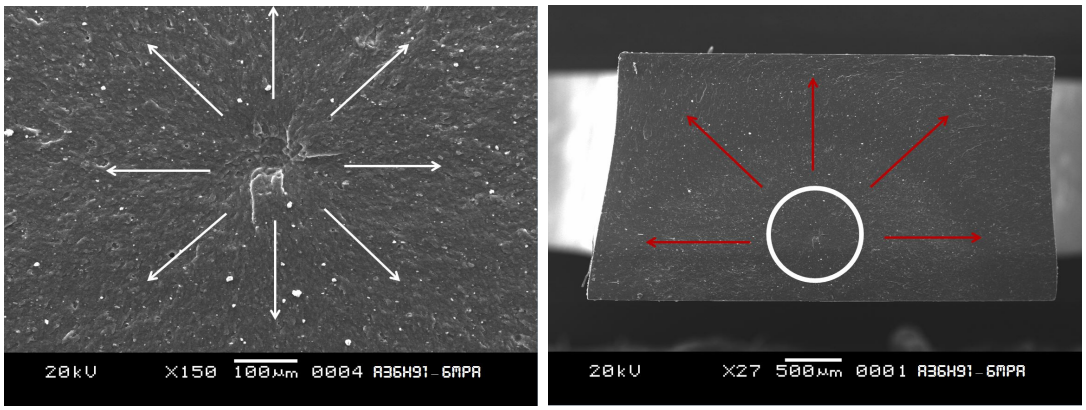

(a) Initiation site at ×150. **(b)** Propagation path ×27.

Figure 4.3-23 – Micrograph with an example of a *smooth* fracture surface; A36H91 tested at 6 MPa target loading level.

this category of a fracture surface is similar to the fracture surfaces of specimens failed in tensile loading, most likely indicating that fatigue crack propagation is very rapid for such *smooth* failures.

Analysis of fracture surfaces is continued with an example of a *rough-smooth* surface as shown in detail in Figure 4.3-24 for A36H96 tested at 10 MPa target loading level. The overall damage mechanism is classical. As expected, there is an initiation site due to a flaw, in this case within the body of the specimen, as shown in Fig. 4.3-24(a). Afterwards, the crack propagates outward in a circular manner as shown by white arrows in Fig. 4.3-24(b). White dashed line indicates a point at which final rapid fracture occurs. These results are similar to the HNBR fracture surfaces observed by Gauchet (2007), however the "petal" shapes are not as evident in this case. Moreover, these are similar to the fracture surfaces observed by Le Cam et al. (2014) in carbon black filled SBR, where it was concluded that "morphology of fracture surfaces only depends on [present] heterogeneities."

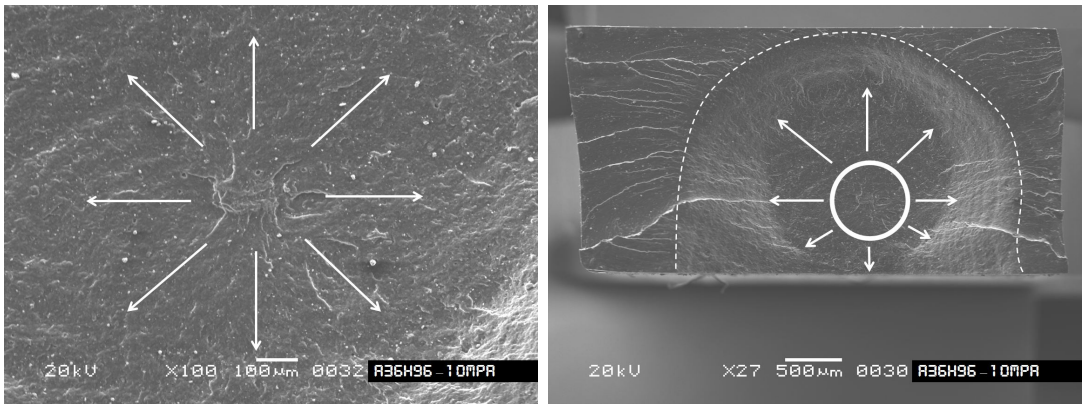

(a) Initiation site at ×100. **(b)** Propagation path ×27.

Figure 4.3-24 – Micrograph with an example of a *rough-smooth* fracture surface; A36H96 tested at 10 MPa target loading level.

Furthermore a detailed view of *vertical rough-smooth* fracture surface is shown in Figure 4.3-25. The initiation site is shown in Fig. 4.3-25(a), where the arrow points to a flaw on the surface of the specimen. One can observe the initial propagation in a semi-circular fashion with the so-called "fatigue rivers" radiating away from the initiation site. Subsequently, the propagation path is shown in Fig. 4.3-25(c). The circular region is the initiation site from Fig. 4.3-25(a), and the white arrows indicate the initial propagation within a plane away from the initiation site. Afterwards, the crack propagates in a vertical direction, as indicated by red lines. Finally, there is a rapid fracture as indicated by smooth surface in Fig. 4.3-25(b).

Moreover, different types of vertical crack propagation phenomena with respect to different target loading levels of A36H96 are shown in Figure 4.3-26. It appears that there is no influence of the loading level on characteristics of vertical propagation except for the appearance of fatigue striations (large ridges that appear along the crack front as shown by arrows in Fig. 4.3-26(b)) at true stress amplitudes of 6 MPa and higher, which is perhaps similar to the observations of Flamm et al. (2011).

It is interesting to observe the "side" of a specimen that has *vertical rough-smooth* surface, as technically these also make up the fracture surface. Figure 4.3-27 shows such view of A36H96 tested at 6 MPa; in fact, this is the same specimen as shown in Fig. 4.3-26(c). The arrows indicate presence of some flaws such as embedded particles or voids (it is unclear whether these are due to missing particles or material voids). Similar results have been observed for other specimens, which failed in such manner. Without possibility for additional interrupted testing or use of other tools such as micro CT, only a hypothetical damage mechanism for such failures can be proposed.

1. A crack initiates due to a critical flaw in the specimen;

1'. At the same time, other smaller cracks initiate within the specimen;

2. The critical flaw grows, but follows a stress path of "least resistance," leading to coalescence and absorption of smaller cracks. Thus, the propagation occurs not strictly on a plane.

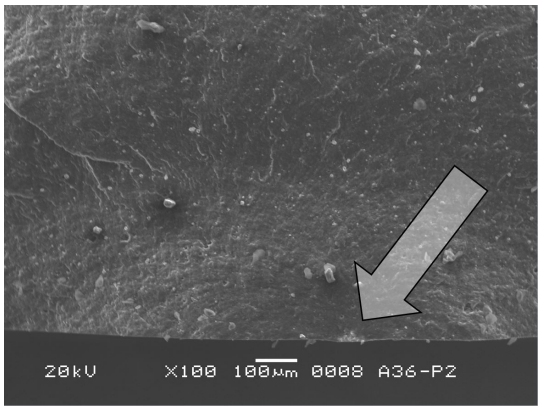

(a) Initiation site at ×100.

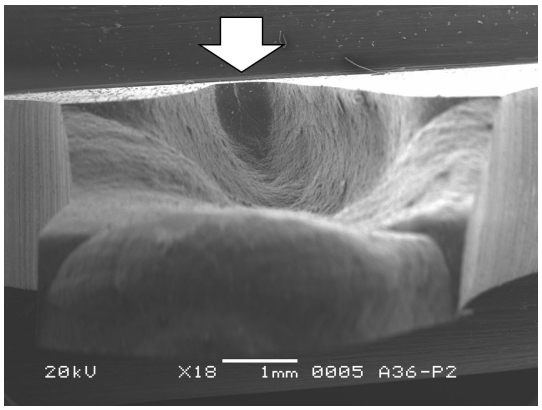

(b) Final fracture ×18.

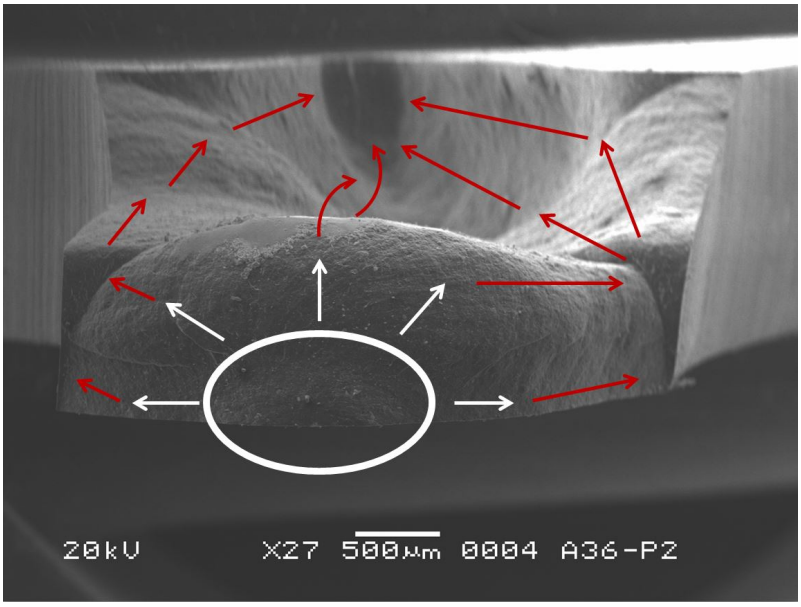

(c) Propagation path ×27.

Figure 4.3-25 – Micrograph with an example of a *vertical rough-smooth* fracture surface; A36H96 tested at 4 MPa target loading level.

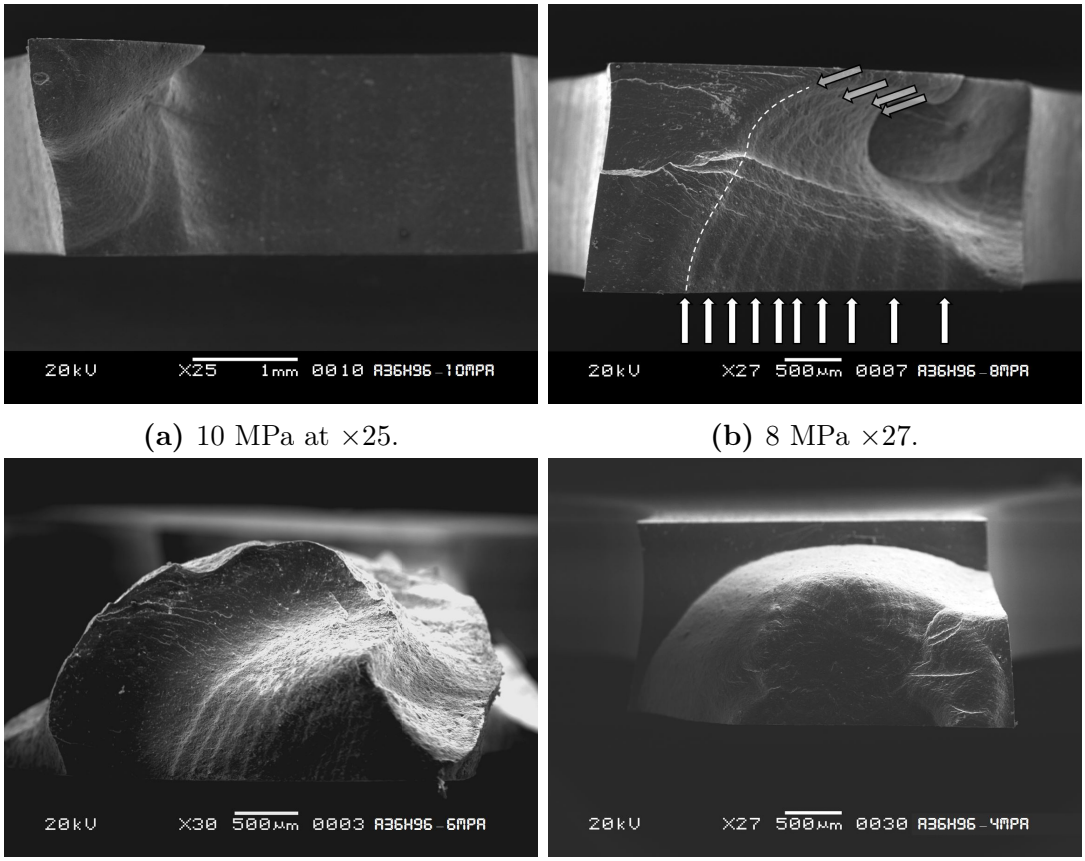

(a) 10 MPa at ×25.

(b) 8 MPa ×27.

(c) 6 MPa ×30.

(d) 4 MPa ×27.

Figure 4.3-26 – Micrograph with an examples of a *vertical rough-smooth* fracture surface; A36H96 tested at four loading levels.

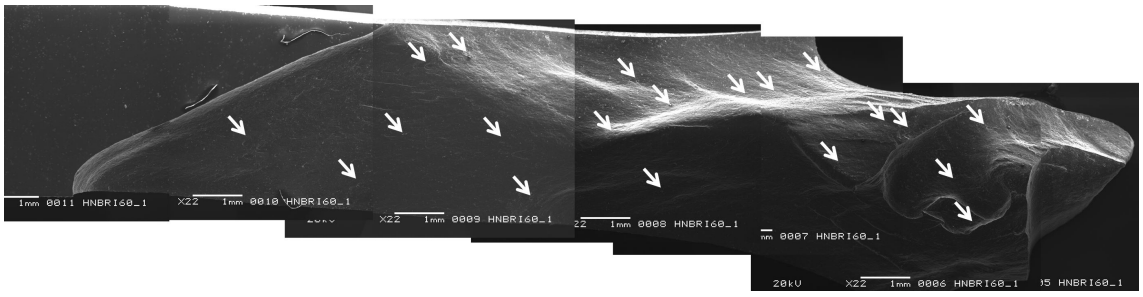

Figure 4.3-27 – "Side" composite micrograph of a *vertical rough-smooth* fracture surface; A36H96 tested at 6 MPa.

3. The crack reaches a critical size and there is a sudden, rapid failure.

Causes for initiation of flaws

The initiation sites have been analyzed with X-ray energy dispersive spectroscopy (EDS). All initiation sites of the reference blend A36H96 have been analyzed; as mentioned earlier, for the other five blends, random sampling has been used to get a general idea and to investigate whether it differed from those of A36H96. In many cases, an initiation site is clear, but EDS analysis did not show any difference with respect to the matrix formulation; in other cases, six different elements/particles have been detected. All seven are described as follows:

- **Matrix** - initiation site is clear, but EDS analysis of both fracture surfaces is identical to the matrix formulation. These could be due to some material heterogeneities, however the exact cause of these failures is unknown.
- **Voids** - Similar to the previous observation, EDS does not show any differences. However a very smooth semi-spherical surfaces can be observed on the two fracture surfaces.
- **Oxide** - EDS analysis of the initiation site shows presence of additional oxygen in combination with elements (with respect to the matrix) such as Ca, Si, Al and/or Mg. This seems to point to particles found in the ground or of talcum origin. Such categorization is made only in cases, where it is evident that the particle is embedded into the matrix to exclude any cases of contamination.
- **Carbon black** - EDS analysis showed relative increase in carbon and decrease of other elements. Moreover, fracture surfaces showed a specific morphology or presence of round carbon black agglomerates.
- **Large particles** - These are clearly foreign particles within the matrix, such as fibers. EDS analysis showed that there are made from metals or carbon-based elements.
- **Metals** - EDS analysis identified small metallic particles of either Fe, Ti, or Al (without high oxygen concentrations). On fracture surfaces, these are small particles embedded in the matrix.
- **ZnO** - EDS identified high concentrations of zinc and oxygen.

Flaws such as oxides, large particles, metals, and ZnO are mostly likely introduced during manufacturing. By comparing EDS spectra specific to these inclusions to a spectra of the matrix, it can be said that none of these appear to be used in the formulation.

Figure 4.3-28(a) shows the frequency of occurrence of these types of flaws in all observed specimens. The largest number of initiations are caused by an unknown/undetected particle or material heterogeneity (matrix). Out of the identified flaws, presence of oxides causes most initiations (31%). This is followed by initiation due to carbon black agglomerates (10%). Large particles, such as fibers, make up about 9% of flaws. Metal and ZnO particles and voids initiate about 4% each. On the other hand, Fig. 4.3-28(b) shows the percentages for each blend; please note

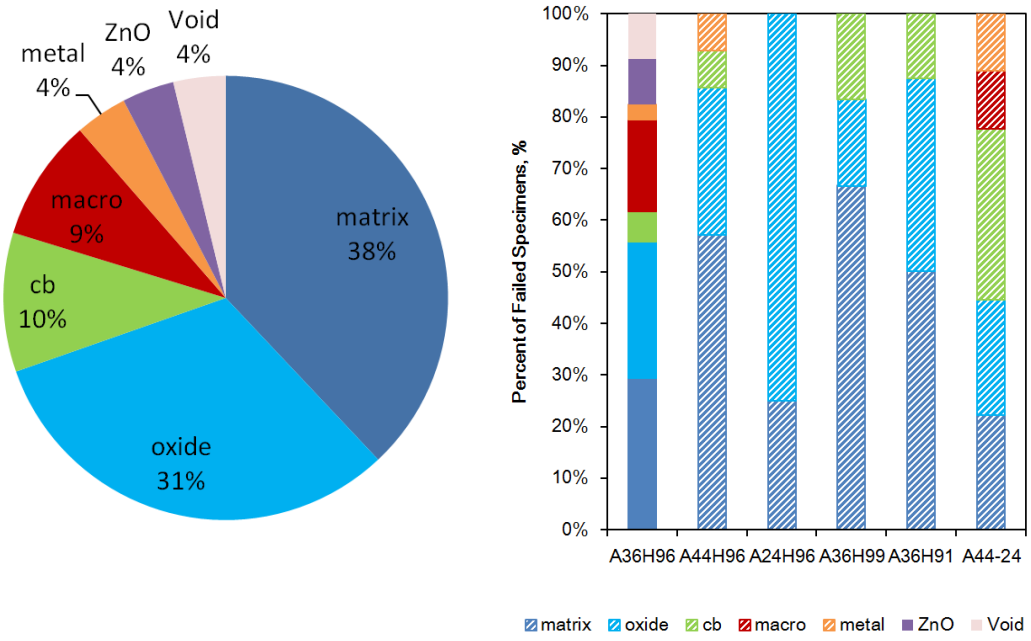

(a) All observations in all blends. **(b)** For each blend.

Figure 4.3-28 – Different causes of initiation in all analyzed blends; hatched fill indicates partial sampling.

that hatched fill indicates that not all specimens have been observed for all blends except for A36H96. Thus, it is hard to draw concrete conclusions on whether certain flaws are more frequent in one blend or another.

Furthermore, the location of these flaws is shown for all specimens in Figure 4.3-29. Fig. 4.3-29(a) shows the coordinate scheme used to record the location of the initiation sites, where the cross-section area of a specimen is divided into quadrants and all sites are recorded with respect to one quadrant due to the 2-axis symmetry of the specimen. Fig. 4.3-29(b) shows the distribution of the sites as a percentage of all observed sites. If one recalls from earlier, the specimens have been compression molded into sheets and then cut with a die. Correspondingly, first, we can categorize surface cracks:

- About 17% of initiation sites occur on the long surface (along the x-axis) that corresponds to the molded surface. EDS analysis of the initiation sites showed presence of various flaws: oxides, ZnO, metal, and large contaminants. About a third is categorized as matrix since EDS analysis did not show differentiation with respect to the matrix. However, it seems likely that these flaws are result of contaminants present on the mold surface.
- On the other hand, 9% of initiations formed on the short surface (along the y-axis) corresponding to the surfaces created by a cutting die. For these, all except one are flaw types are of type matrix; hence, it seems that the initiation site is caused by rough surface created from cutting. The other is due to presence of carbon black. This includes about 1% of initiation sites that occur in the corner of the specimen; for these, all flaw types are categorized as

matrix (similarly EDS showed no differentiation). Thus, these are also mostly likely caused by some initial damage due to cutting.

The remaining initiation sites (the majority) are located inside the specimen. All types of flaws are present and these occur near the surface. With respect to foreign particles, it appears that these are also introduced during mixing in addition to contamination during molding. Finally, the split of the location of the initiation sites - on the surface or internally - is shown for each blend in Figure 4.3-30; once again, hatched fill indicates that not all broken specimens have been observed. Thus, initiation occurs inside of the specimen in A36H96 and, it appears, in all other blends.

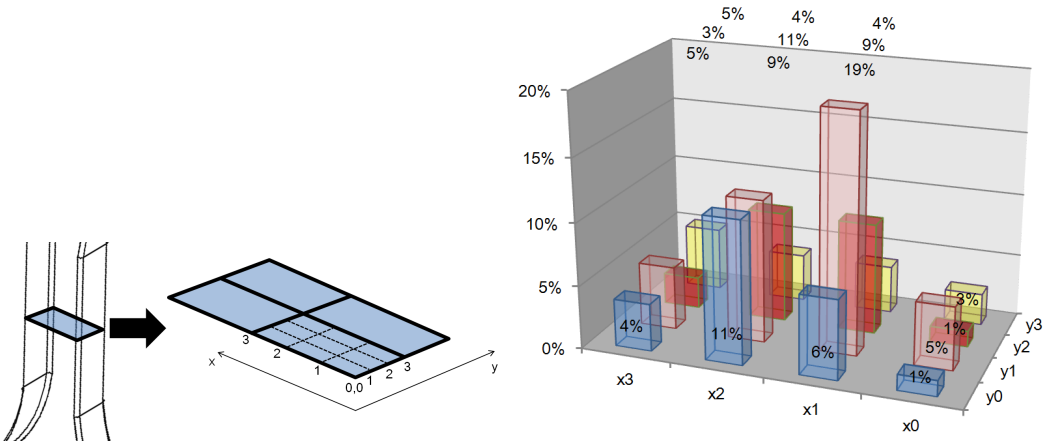

(a) Coordinate scheme. **(b)** Distribution per location in %.

Figure 4.3-29 – Initiation site location in all observed specimens.

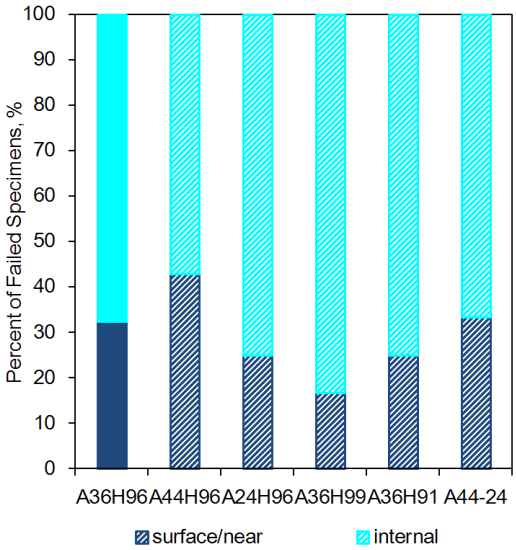

Figure 4.3-30 – Surface and internal initiation sites for all blends; hatched fill indicates partial sampling.

4.4 Summary and Conclusions

4.4.1 Effect of Acrylonitrile Content

The three experimental approaches lead to similar conclusions on the effect of ACN on fatigue resistance of HNBR at 120 °C: **A36H96 has better fatigue resistance, followed by A44H96, and A24H96 has significantly less resistance to fatigue compared to the other two blends.**

- Fatigue life experiments and subsequent statistical analysis showed that A36H96 has longer fatigue life, followed by A44H96, and A24H96 has significantly worse fatigue life; the results are shown in Fig. 4.3-12.
- Fatigue crack propagation experiments show similar growth rates for both A36H96 and A44H96; on the other hand, A24H96 has crack growth rates on an order of magnitude faster for same tearing energies; the results are shown in Fig. 4.3-13.
- Fatigue damage analysis is different in both macroscopic and microscopic scales; for all blends the differences can be grouped in two categories: A36H96 and A44H96 in one, and A24H96 in the other.

  Macroscopic observations have shown that A44H96 and A36H96 (to a greater extent) have a significant number of cracks growing vertically along the loading direction, whereas crack growth in A24H96 occurs on a single plane perpendicular to the loading direction.

  These results translate to microscopic observations of fracture surfaces. In A36H96 and A44H96, there are classic initiation-propagation-failure regimes of fracture surfaces on a single plane perpendicular to the direction of loading. However, there are also similar type of failures that have propagation regime occurring in the vertical direction corresponding to macroscopic observations. On the other hand, the propagation regime of A24H96 takes place on one plane. Finally, multi-cracking can be observed in about 12% of failed A36H96 specimens and in A44H96 specimens to a lesser extent, but this phenomenon is completely absent in A24H96 specimens.

Therefore, it appears that occurrence of crack growth in direction parallel to loading could be an indication of good resistance to fatigue crack propagation. Since in all three blends cracks initiated from flaws, it could be stated that longer fatigue lives are a result of slow crack propagation rates. However, this explanation is not all satisfactory because fatigue life specimens are thin, with the implication being that crack propagation phase of fatigue life is negligible; moreover, this is not sufficient to explain the large differences in fatigue lives at each target true stress levels for blends A36H96 and A44H96.

Perhaps, the difference between these blends (especially between A36H96/A44H96 and A24H96) could be discussed with respect to the results of Chapter 2. More specifically, one can compare the fatigue endurance limit (σ_e) to the stress at break (σ_f) as it is usually done for metals (*e.g.* Stephens et al. (2001)); this value is called the fatigue ratio (FR), which can be said to represent the efficiency of a material in

fatigue[2], and is given by

$$\mathrm{FR} = \frac{\sigma_e}{\sigma_f}, \tag{4.4-1}$$

where the fatigue endurance limit σ_e is chosen as the corresponding true stress amplitude for the Cox mean fatigue life at 2 million cycles. Cox mean is chosen because it appears to better estimate mean fatigue lives at low target loading levels (where there are censored data) and can be extrapolated for blends, such as A24H96, the mean of which is only around 50,000 cycles at the lowest loading level. The fatigue ratios are shown in Figure 4.4-1

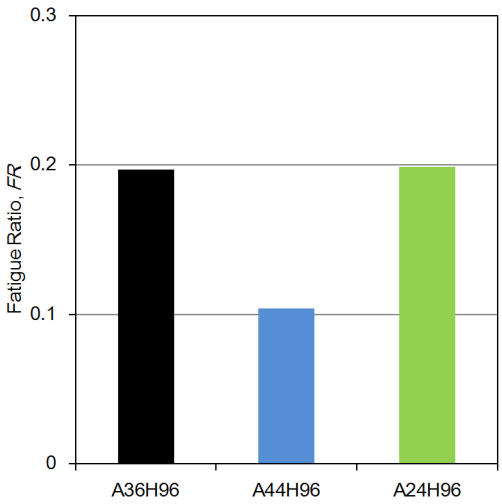

Figure 4.4-1 – Fatigue ratio of HNBR blends with different ACN content.

In fact, if one considers each material's efficiency in fatigue, A36H96 and A24H96 are identical, and A44H96 is almost twice less efficient. Thus, one can conclude that relatively poor fatigue life performance of A24H96 is due to its mechanical weakness as was shown in tensile test results: its stress at break is roughly around 12 MPa, which is very close to the maximum loading level of 10 MPa. Finally, as mentioned in Chapter 2, HNBR blends with low ACN content are mostly designed to be used at low temperatures (low T_g) and, **it seems obvious, that use of A24H96 for applications at 120 °C is not a good choice if good fatigue resistance is required.**

On the other hand, Fig. 4.4-1 does not answer a question on the difference between A36H96 and A44H96. In terms of applied loading, A44H96 has almost twice the stress at break than A36H96 (38.5 MPa vs. 23.8 MPa) and perhaps the load range from 4 to 8 MPa, thus, does not have significant influence on fatigue life. Moreover, if one recalls Fig. 4.3-12, A44H96 has and is extrapolated to have longer fatigue lives from around 8.5 MPa and higher. **Thus, it seems that in fatigue applications, where high loading is expected (on average or with "peak" loads), A44H96 is a good choice.**

In terms of damage mechanics, A36H96 did exhibit more frequently the more "favorable" damage mechanism with greater occurrence of vertical cracks and observation

[2]It equals to about 0.5 in steels for example.

of multi-cracking; one could assume that such phenomenon allows for dissipation of energy and delay of fracture. Perhaps A36H96 has a higher fatigue propagation threshold and, consequently, better resistance to initiation/propagation transition from existing flaws; however, a deeper investigation is required to fully answer this question. **Nonetheless, it is obvious that A36H96 is the best choice for general applications at 120 °C.**

4.4.2 Effect of Hydrogenation

Similar to the results on the effect of acrylonitrile, but with less pronounced differences, the results of the effect of hydrogenation from the three experimental approaches are also in accordance with each other: **A36H96 has better fatigue resistance, followed by A36H99, and followed by A36H91.** In the discussion of the results, a parallel can be drawn:

- Fatigue life experiments and subsequent statistical analysis showed that A36H96 has longer fatigue life, followed by A36H99, and A36H91; the results are shown in Fig. 4.3-12.
- Fatigue crack propagation experiments show that A36H96 has better resistance to fatigue than A36H99 (although these appear similar at very high tearing energies); on the other hand, A36H91 has crack growth rates on an order of magnitude faster for same tearing energies; the results are shown in Fig. 4.3-14.
- Fatigue damage analysis is similar in both macroscopic and microscopic scales and, once again, the blends can be grouped in two categories: A36H96 and A36H99 in one, and A36H91 in the other.

  Macroscopic observations have shown that A36H96, to a greater extent, and A36H99 have a number of cracks growing in a vertical direction along the direction of loading; A36H91, similar to A24H96, has cracks occurring on a single plane perpendicular to the direction of loading.

  Likewise, fracture surfaces of A36H96 and A36H99 present classic initiation-propagation-failure regimes on a single plane perpendicular to the direction of loading; but, once again, there are fracture surfaces that have propagation regime occurring in the vertical direction corresponding to the macroscopic observations. Such phenomenon was not observed for A36H91 and, moreover, some completely smooth fracture surfaces have been observed, which are similar to those of quasi-static tensile failure. Finally, in about 12% of failed A36H96 specimens multi-cracking can be observed and in about 4% of A36H99 specimens, but this phenomenon is completely absent in A36H91 specimens.

The fatigue ratio (FR) of the three blends with respect to hydrogenation is shown in Figure 4.4-2. A36H91 has very high efficiency in fatigue even though it has the lowest mean fatigue lives of the three blends, while A36H99 has the lowest of three.

Starting with A36H91, the results discussed above show that at 120 °C fatigue resistance of A36H91 is worse than of A36H96 and A36H99. **It seems likely that A36H91 is not an optimal material in fatigue resistance at 120 °C**, even though it has high fatigue efficiency relative to its ultimate stress.

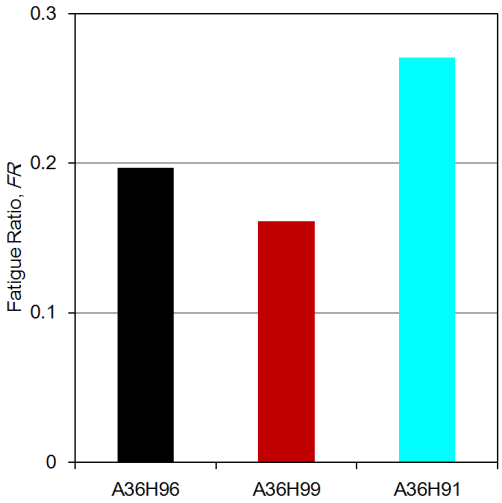

Figure 4.4-2 – Fatigue ratio of HNBR blends with different percent hydrogenation.

As for A36H99, it can be argued that this is a surprising result, considering that heat resistance increases with percent hydrogenation: thus, it would be expected to have an increase in fatigue efficiency with percent hydrogenation for fatigue tests carried out at 120 °C. Perhaps the expected better resistance is not sufficiently accounted for tests at 120 °C. **It seems likely that fatigue testing at higher temperatures, taking into account that the general application limit is around 150 °C, could show that A36H99 has better fatigue performance than A36H96.** This is an interesting result and a study on the influence of temperature is presented in the next chapter.

Nonetheless, for practical applications at 120 °C, where relatively high strength and fatigue resistance are required, A36H96 is once again the better choice.

4.4.3 Fatigue resistance of the composite blend - A44-24

Once again, three experimental approaches come to the same conclusion: **composite A44-24, with average ACN content of 36%, has significantly lower fatigue resistance than A36H96.**

- Fatigue life experiments and statistical analysis showed that composite A44-24 has significantly shorter fatigue life than the reference A36H96 as shown in Fig. 4.3-12.
- Fatigue crack propagation experiments show that A44-24 has significantly faster crack growth rates than A36H96; moreover, they seem to closely match the results obtained for A24H96. The results are shown in Fig. 4.3-15.
- Fatigue damage observed in A44-24 significantly differs from that in A36H96 and seems similar to the one observed in A24H96. On macroscopic scale, all cracks grow on a single plane parallel to the direction of loading. Fracture surfaces have classic initiation-propagation-failure regimes, but also completely

smooth surfaces such as those observed in quasi-static failures. Moreover, multi-cracking is not present.

The fatigue ratio (FR) of A44-24 with comparison to A36H96 is shown in Figure 4.4-3. Efficiency in fatigue of A44-24 is still close to A36H96; moreover, if one recalls Fig. 4.4-1, A24H96 also has a similar fatigue ratio. With all of the above information, it is clear that A44-24, even with average ACN content identical to A36H96, has worse fatigue resistance and it resembles closely the characteristics of A24H96. Perhaps, similar to A24H96, its fatigue resistance and efficiency is better at lower temperatures. **However, choice of A44-24 seems a poor one for use at 120°C.**

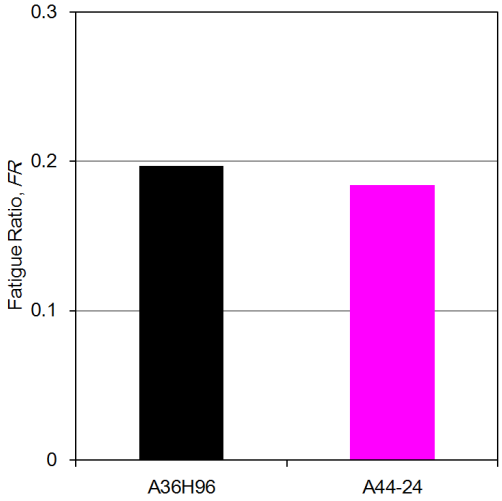

Figure 4.4-3 – Fatigue ratio of composite HNBR blend A44-24.

Chapter 5

Fatigue and Aging of HNBR

Chapter Highlights

- Increased percent hydrogenation plays a positive role in fatigue resistance as temperature is increased from 120 °C to 150 °C;
- Loss of fatigue resistance at high temperature: least for A36H99, and increasing for A36H96, followed by A36H91;
- A pre-aging time threshold seems to emerge, where pre-aging at 150 °C up to 42 h showed negligible effects on fatigue resistance;
- Almost uniform decrease in fatigue life at all loading levels is observed for pre-aging at 150 °C for 240 h;
- Loading conditions during pre-aging appear to have negligible effect on fatigue life.

Introduction

Continuing with the investigation of fatigue resistance of HNBR, this chapter presents the most recent results of this thesis: the effects of thermal aging on fatigue life of HNBR. The general characteristics of thermal aging of elastomers as well as its effects on fatigue are first discussed in the state of the art. From experimental perspective, two additional fatigue life tests are performed. In the first test, the effect of simultaneous aging and fatigue at high temperature (150 °C) is investigated in blends of varying percent hydrogenation (A36H99, A36H96, A36H91). The second test focuses on the reference blend A36H96, where fatigue testing is done on preliminary aged (pre-aged) specimens. The specimens are pre-aged at the same temperature (150 °C) to compare their responses with the results of the simultaneous aging and fatigue experiments. Moreover, two different pre-aging conditions are utilized: without and under load. Pre-aging under static load is considered to investigate whether there is a parallel with the simultaneous aging and fatigue experiments, in which specimens are subjected to cyclic loading.

Contents

5.1 State of the Art

5.1.1 Thermo-oxidative aging of elastomers

Thermal or thermo-oxidative aging of elastomers is a chemical aging process, *i.e.* it is an irreversible degenerative process causing change to the chemical structure of the material [1] (Johlitz 2012; Lion and Johlitz 2012). The chemical nature of the elastomer also affects heat resistance characteristics. Additionally, exposure to high temperatures and presence of oxygen in air causes a progressive change of their mechanical and chemical properties (Andrews et al. 1946; Shaw et al. 2005). In one of the earliest works on thermal aging, Tobolsky et al. (1944) confirmed that thermal stability of elastomers is highly dependent on presence of oxygen. Indeed, even a 2% increase in the concentration of oxygen significantly increases the deterioration of elastomers, more so at high temperatures; with respect to temperature, the rate of reaction of oxygen with elastomers doubles for each 10 °C increase in the temperature (Tao et al. 2005). Consequently, at high temperatures, greater thermo-oxidative degradation occurs.

Thermo-oxidative aging is driven by two different network processes: network degradation (polymer chain scission) and network reformation (additional chain crosslinking)(Tobolsky et al. 1944; Andrews et al. 1946; Ahagon et al. 1990; Johlitz 2012; Lion and Johlitz 2012). Tao et al. (2005) describe a cyclic thermo-oxidative process from a chemical perspective as shown in Figure 5.1-1. The mechanism is divided

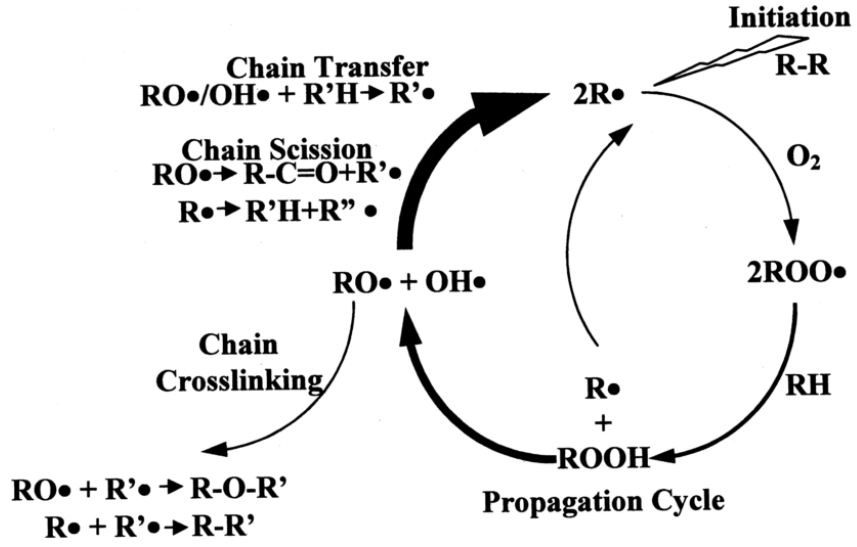

Figure 5.1-1 – Cyclic oxidation process in elastomers (Tao et al. 2005).

into three steps: initiation, propagation, and termination. Initially, the process takes place through radical reactions that are initiated by an increase in energy (it could be in any form such as heat, mechanical shear, radiation, *etc.*), or by other additives and contacting fluids. These cause a break in the covalent bonds of the polymer

[1] On the other hand, physical aging refers to changes in characteristics of a material in glassy region or near glass transition. These changes occur because of reorientation of macromolecules and this process accelerates with increased temperature (Johlitz 2012).

chains and produce unstable carbon radicals[2] (R*). In chemical terms, it is more favorable for the peroxy radical (-O_2-) to bond with hydrogen from the polymer to form hydroperoxide (ROOH) because O-H bond is more stable (higher bond energy) than C-H bonds; this in turn produces another carbon radical (R*) to propagate the cycle. The O-O bond is very weak and breaks down into two radicals: alkoxy (RO*) and hydroxyl (HO*) causing the process to become self-accelerating. From this point, chain scission can occur producing even more radicals; in the other case, two radicals combine (or a radical combines with a stabilizing agent such as anti-oxidant additives) and form a new cross-link leading to termination of the reaction.

From a mechanical perspective, the fundamentals have been described as early as 1940s by research group of Tobolsky *et al.* (Tobolsky et al. 1944; Andrews et al. 1946). The two aging processes exhibit different characteristics. Network degradation causes softening (reduction in tensile modulus) in specimens. On macromolecular scale, this is caused by chain scission; if a material is under loading, the broken chains create new cross-links at this new equilibrium, and stress relaxes. The stress decays to zero if material is loaded long enough. On the other hand, network reformation stiffens the material as cross-link density increases. In practice, differentiation of the two processes is complicated by the fact that both can occur simultaneously (Andrews et al. 1946).

To investigate the effects of thermo-oxidative aging, the following three experiments are usually performed: continuous and intermittent relaxation experiments, as well as measurement of permanent set (Andrews et al. 1946; Dunn et al. 1959; Johlitz 2012; Lion and Johlitz 2012; Johlitz et al. 2014). Continuous testing is performed to isolate the effects of network degradation or chain scission; in such tests, a constant strain is applied on a specimen and decrease in stress is measured. Network reformation (additional cross-linking) also occurs during continuous testing; however, since the specimen is deformed, the process of creation of additional cross-links does not produce additional stress and cannot be measured. Hence, intermittent relaxation tests are required since they account for the total rate of both network degradation and reformation; in these tests, specimens are isothermally aged in an unloaded state and are tested mechanically at specific time intervals. To measure permanent set, specimens are unloaded after a continuous relaxation test at a specific temperature and their length is recorded.

Finally, one should mention the presence of diffusion limited oxidation (DLO), which occurs in massive specimens/part. DLO occurs when the rate of oxygen consumption in thermo-oxidation is faster than the diffusion of oxygen within specimen/part (Shaw et al. 2005; Gent 2012); diffusion of oxygen depends on the elastomer type and its composition (Tao et al. 2005). This is referred to as heterogeneous aging, where only the surfaces exposed to the oxygen environment tend to undergo thermal aging; as a consequence, mechanical properties become different with respect to the distance away from the surface (Gillen et al. 1996). Under these conditions, therefore, thick specimens/parts are more resistant to thermo-oxidation because the outer layer becomes oxidized and the further absorption of oxygen is decreased (Tao et al. 2005).

[2]A radical is an atom or a molecule with an unpaired valence electron (IUPAC n.d.)

Thermal aging of HNBR

C=C bonds are more susceptible to heat than C-C bonds because the energy required to break them is relatively low (Tao et al. 2005). Therefore, elastomers such as IR, SBR, and NBR do not have good heat resistance characteristics. For HNBR, following the selective hydrogenation of the C=C bonds of NBR, the degree of unsaturation is significantly reduced. This, compared to NBR, improves the resistance of HNBR to high temperature oxidation and provides better thermal stability in air and other environments containing oxygen (Keller 2012). Thus, with increasing percent hydrogenation, heat resistance is improved. Sawada (1993) isothermally aged HNBR grades of different percent hydrogenation at 150 °C for 72 h and measured maximum elongation; as percent hydrogenation increases, elongation after aging increases especially for percent hydrogenation greater than 80%. Moreover, Bender and Campomizzi (2001) concluded that percent hydrogenation plays the dominant role in heat aging behavior of HNBR, whereas ACN content has a much smaller effect.

Bhattacharjee et al. (1991) investigated thermal degradation in air and nitrogen environments. Two types of HNBR have been utilized with 37 wt.-% ACN and 99.5% hydrogenation, and with 40 wt.-% ACN and 99.9% hydrogenation. From IR spectroscopy, the authors report that the oxidation degradation mechanism occurs by attack on the acrylonitrile groups of HNBR. In contrast, Bender and Campomizzi (2001) came to a conclusion that thermo-oxidative changes in HNBR are due to the oxidative reactions within the hydrocarbon parts of the polymer; there was no indication that chemical reactions occurred to the nitrile group. However, both studies agree that network reformation (additional cross-linking) is the predominant aging mechanism.

Of major interest is, of course, how aging affects mechanical properties of HNBR. Bender and Campomizzi (2001) measured modulus at 50% elongation of several blends of HNBR with different percent of hydrogenation after aging at 160 °C for 72 h and 120 h. As evident from Figure 5.1-2, the modulus is relatively constant for different percentages of hydrogenation (measurement RDB % used by the authors equals to 1-% hydroggenation) in unaged HNBR (blue line). After 72 hr of aging (red line), modulus increases for all % hydrogenation and to a greater extent as percent hydrogenation decreases (RDB % increases). Furthermore, there is a drastic increase of modulus for HNBR with % hydrogenation less than 98% after aging at 120 h (green line). Moreover, the change in stress-strain response in HNBR (95% hydrogenation) with respect to different aging times is shown in Figure 5.1-3. As expected, HNBR undergoes significant stiffening and elongation at break decreases with increased aging time due to increase in network reformation. Similar results have been obtained by Ohm (2002), who additionally tested the influence of two antioxidants, *Naugard 445* and *ZMTI*, and found no difference between them. Reincke et al. (2014) also explored the effect of prolonged thermal aging on physical properties of carbon black filled, cross-linked HNBR. The tensile strength of HNBR decreased and elongation at break remained constant for thermal aging at moderate temperature of 90 °C (Figure 5.1-4).

Kömmling et al. (2016) investigated the presence of DLO in HNBR (and EPDM) O-rings; specifically, HNBR blend with 36 wt.-% ACN and 96% hydrogenation is

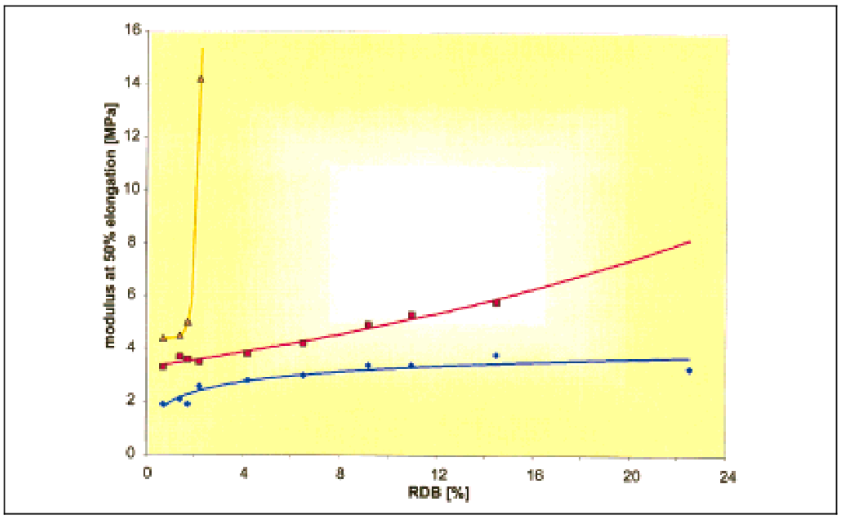

Figure 5.1-2 – Change in modulus at 50% of unaged HNBR (blue) with different % hydrogenation, and after aging at 160 °C for 72 h (red) and 120 h (green) (Bender and Campomizzi 2001).

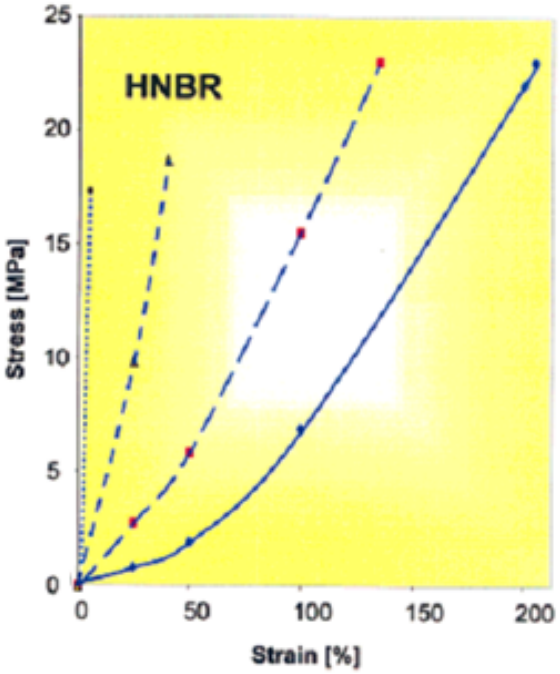

Figure 5.1-3 – Stress-strain behavior HNBR aged at 160 °C (- 0 h (unaged), - - 150 h, – – 475 h, ··· 1000 h) (Bender and Campomizzi 2001).

used. Aging is carried out on rings with 10 mm cord diameter in an unstressed state and in compression at four temperatures ranging from 75 °C to 150 °C and six durations ranging from 1 to 183 days. Figure 5.1-5 shows a cut cross-section of HNBR aged for 101 days at 150 °C in uncompressed state. There are two layers within the specimen: a hardened brittle outer layer, and a softer inner layer with less aging. Micro-hardness profiles (along the thickness of a ring) have been measured for each aging temperature and results are shown in Figure 5.1-6. Up to 100 °C, there is no apparent DLO effect and aging is uniform over 10 mm irrespective of

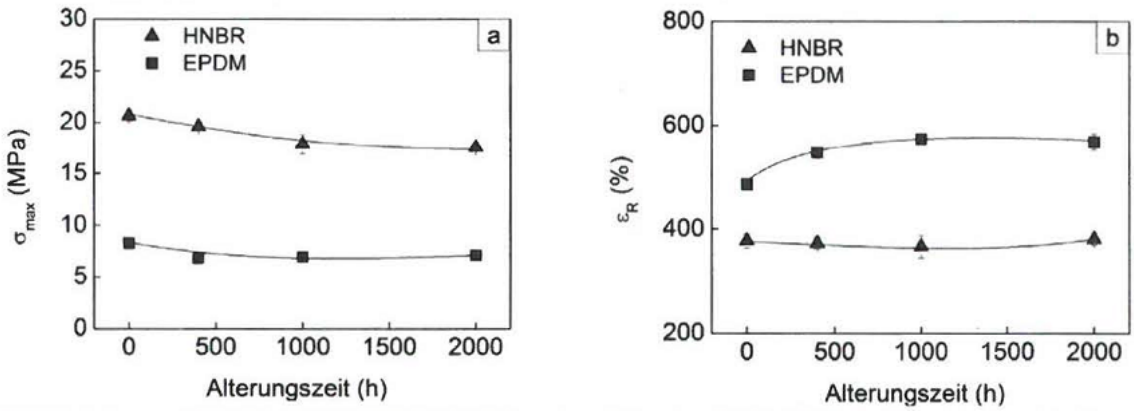

Figure 5.1-4 – Effect of thermal aging time (alterungszeit) at 90 °C on: left – tensile strength and right – elongation at break of carbon black filled, cross-linked HNBR and EPDM rubbers (Reincke et al. 2014).

Figure 5.1-5 – Photo of a cut cross-section of HNBR aged for 101 days at 150 °C in uncompressed state (Kömmling et al. 2016).

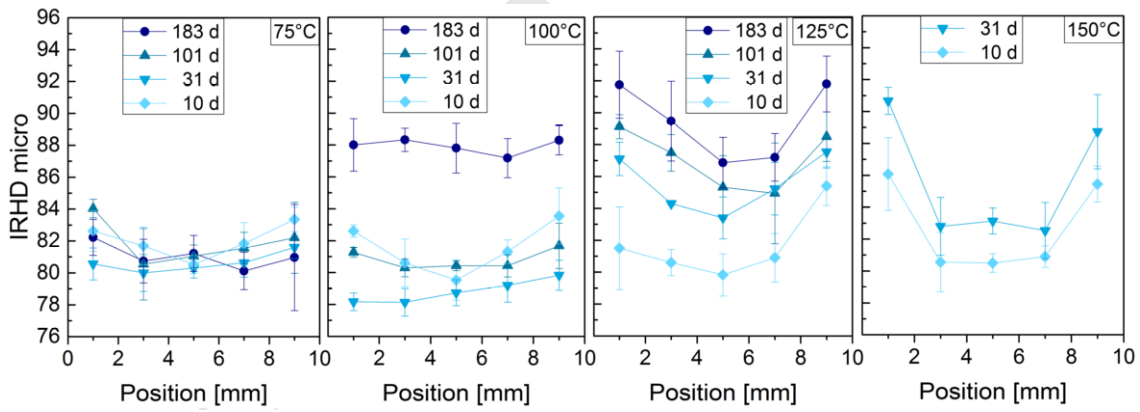

Figure 5.1-6 – Micro-hardness profiles of HNBR O-rings (10 mm diameter) aged in compression at specified temperatures and durations (Kömmling et al. 2016).

aging time. DLO effect is starting to appear at 125 °C over a thickness of about 3 mm after 10 days of aging. Moreover, at 150 °C, one can observe significant DLO effect after 10 days at a thickness of 3 mm.

5.1.2 Interaction between thermal aging and fatigue

For elastomers, effects of thermal aging on fatigue have not been studied extensively as the two topics have been generally investigated separately. This is primarily due to complicated interdependence between the two phenomena. However, taking into account both is required in order to test the full range of the operational conditions, under which materials are used in service; moreover, there is a need to determine the extent (if any) of coupling between the two phenomena.

Effects of high temperature on fatigue

However, before starting with investigation of thermal aging and fatigue, it is prudent to summarize the relationship between temperature and fatigue. In one of the earliest studies,Lake and Lindley (1964) examined the effect of increasing temperature (from 0 to 100 °C) on fatigue life of unfilled SBR and NR (Figure 5.1-7). The authors concluded that the effect of increased temperature is the greatest in

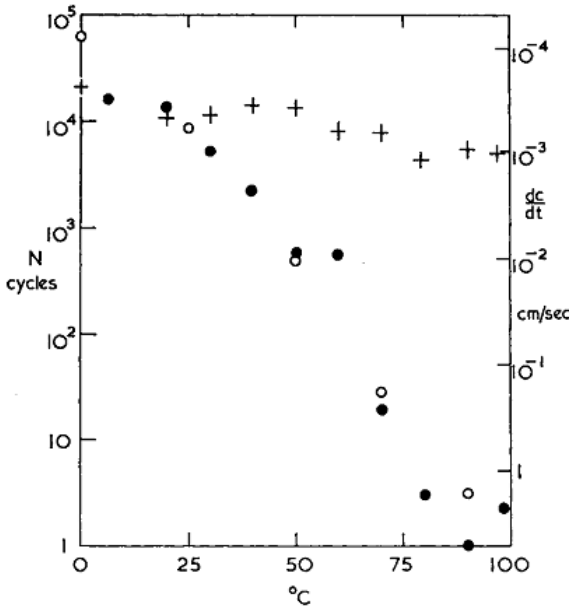

Figure 5.1-7 – Effect of temperature on fatigue life (left axis) of: • – SBR (at 175% maximum strain), and + – NR (at 250% maximum strain); ∘ – crack propagation rate of SBR (right axis) (Lake and Lindley 1964).

non-strain-crystallizing rubbers (SBR), where the decrease in fatigue life is in the order of 10,000; in strain-crystallizing natural rubber, the decrease is by a factor of 4. Duan et al. (2015) investigated fatigue life of filled natural rubber at 23 °C and 90 °C. The authors found that fatigue life is shorter at 90 °C for large engineering

strain, but the fatigue life is about equal at small engineering strain and even increases at the smallest engineering strain. The authors attributed this phenomenon to:

- Experiments are carried out in displacement control;
- Stress-softening under constant displacement loading is greater with higher temperatures. Thus, at small engineering strain, the actual applied stress is much smaller at 90 °C as compared with 23 °C.

Thus, it appears that these findings are questionable (see disucssion on limations of diplacement control in Chapter 3, Section 3.1.2). In another study, Charrier et al. (2011) observed a decrease in fatigue life with increased temperature in NR. For two materials, the shift of the fatigue life curve has been parallel. Similar results have been obtained by Woo et al. (2009) in natural rubber at 70 °C. Finally, in a more recent extensive work, Neuhaus et al. (2017) carried out experiments under force control on NR/BR blend at 70 °C, 85 °C, and 100 °C (additionally with pre-aging, the results of which will be presented later). Overall, there is a nearly parallel shift of power-law fitted fatigue life curves; as seen in Figure 5.1-8, fatigue life decreases as temperature increases. Moreover, the authors remark that the experiments are

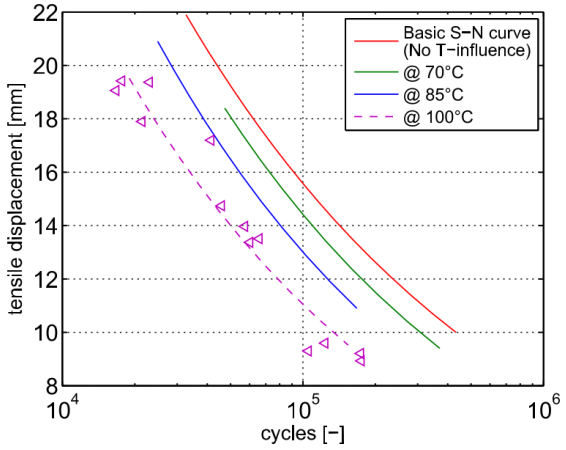

Figure 5.1-8 – Effect of temperature on fatigue life of NR/BR blend (Neuhaus et al. 2017).

short enough (maximum 27 h) to exclude effects of aging at high temperatures.

With respect to fatigue crack propagation, crack growth rate generally increases with temperature in NR, polybutadiene, and chlorobutyl rubbers (Young 1986; Young and Danik 1994). Le Gorju-Jago and Bathias (2002) also observed similar effects for high testing temperatures on fatigue crack propagation of natural rubber in air. The authors proposed that the reduction in the resistance to fatigue crack growth is due to increased mechanical and chemical damage, as well as reduced beneficial effects of strain-induced crystallization for crystallizing elastomers. The presence of oxygen on the fatigue behavior at elevated temperatures has been also highlighted. Experiments in water and nitrogen exhibited slower fatigue crack growth compared to air at all tested temperatures.

As for damage analysis, Weng et al. (2012) examined the fatigue initiation mechanisms of unfilled natural rubber at 85 °C. Scanning electron microscopy (SEM)

analysis has shown that the surface of high temperature tested samples is more rough compared to the ones tested at room temperature. The authors concluded that crack initiation is due to degradation of products of low molecular weight that are within NR (proteins, phospholipids, fatty acids, etc.). According to the authors, at high temperatures, such products concentrate in vapor and gas bubbles within the matrix; the dissolved vapor and gas bubbles act as nucleation sites for crack growth.

Effects of preliminary aging on fatigue

Another approach for investigating of both thermal aging and fatigue consists in testing preliminary aged (pre-aged) specimens. Choi et al. (2005) carried out fatigue experiments (in displacement control) on virgin and pre-aged natural rubber specimens at 90 °C for about 192 h. Figure 5.1-9 shows the corresponding results for pure-shear and hourglass specimens, from which it is evident that, for both types

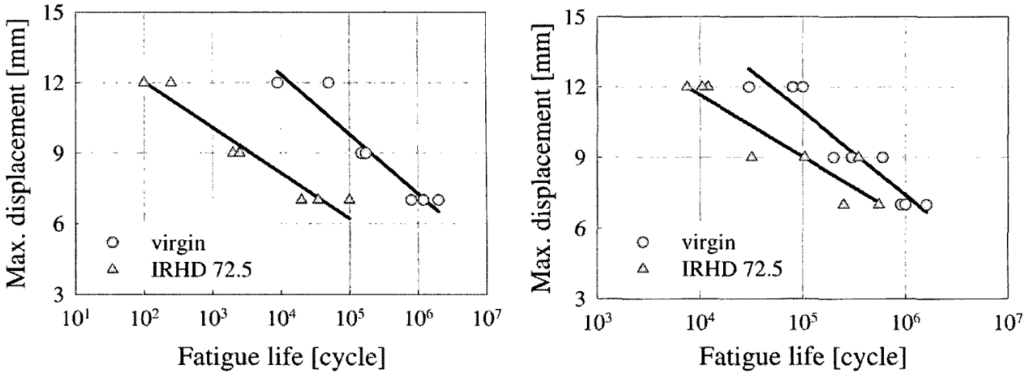

(a) Pure-shear specimen. **(b)** Hourglass specimen.

Figure 5.1-9 – Fatigue life of virgin and pre-aged (90 °C for about 192 h) natural rubber specimens (Choi et al. 2005).

of specimen geometries, fatigue life decreases with pre-aging with larger relative decrease (in log-scale) at high loading levels. In another study, Charrier et al. (2011) found a clear decrease in fatigue life with increasing pre-aging temperature and pre-aging duration in natural rubber (prescribed displacement); Figure 5.1-10 shows a 3D bar plot, where the vertical axis is the normalized fatigue life with respect to tests at room temperature. Similar response has been observed by Ngolemasango et al. (2008), who attribute decrease in fatigue life with aging temperature and duration to network reformation and stiffening of the material; due to this hardening, the authors argue, cracks form and serve as initiation sites for fatigue crack propagation.

In another extensive study, Broudin et al. (2015) also investigated effects of pre-aging in NR/IR blends on fatigue life (prescribed displacement). Figure 5.1-11(a) shows how fatigue life decreased with increased aging duration at 80 °C; the curve shifts are more or less parallel with respect to an unaged material, except after pre-aging for 42 days, where there is apparent impact of loading level. Figure 5.1-11(b) shows the evolution of fatigue lives with respect to both aging temperature and duration; the authors concluded that aging temperature is a more severe parameter than aging duration. Moreover, the authors tested pre-aged specimens in anaerobic

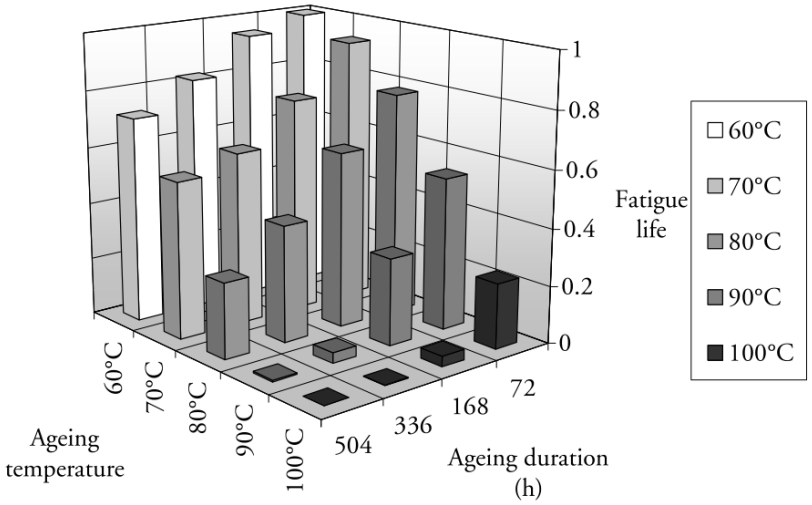

Figure 5.1-10 – Effect of pre-aging temperature and duration on fatigue life of natural rubber; fatigue life is normalized with respect to room temperature tests (Charrier et al. 2011).

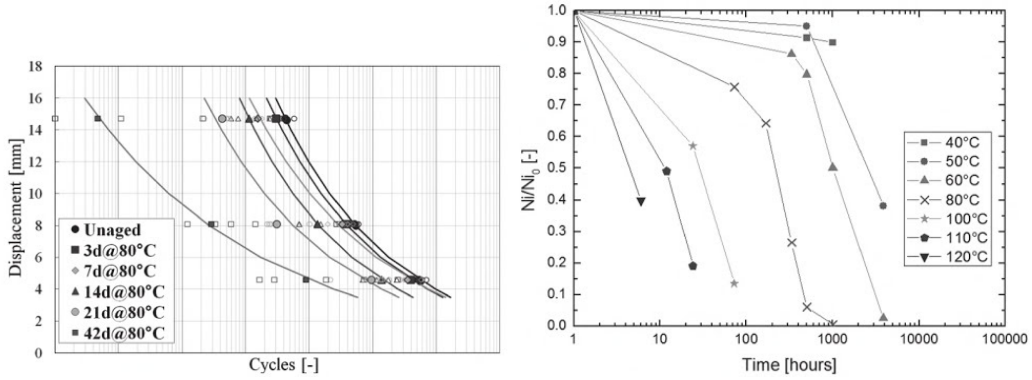

(a) Fatigue life with pre-aging from 3 to 42 days at 80 °C.

(b) Relative evolution of fatigue life with temperature and duration.

Figure 5.1-11 – Fatigue life of NR/IR pre-aged at different temperatures and durations (Broudin et al. 2015).

conditions (without oxygen) and observed only a slight decrease in fatigue lives, again confirming the importance of oxygen in thermo-oxidative aging.

Finally, coming back to the study of Neuhaus et al. (2017), specimens have been pre-aged from 70 °C to 120 °C, and fatigue experiments have been carried out at room temperature as well as at high temperatures (from 70 °C to 100 °C. First, Figure 5.1-12 shows the results obtained at room temperature for two different aging temperatures; in each figure, the lines indicate power-law fitted curves for a specific duration of pre-aging. Ignoring the short pre-ageing times, *i.e.* 36 h, where

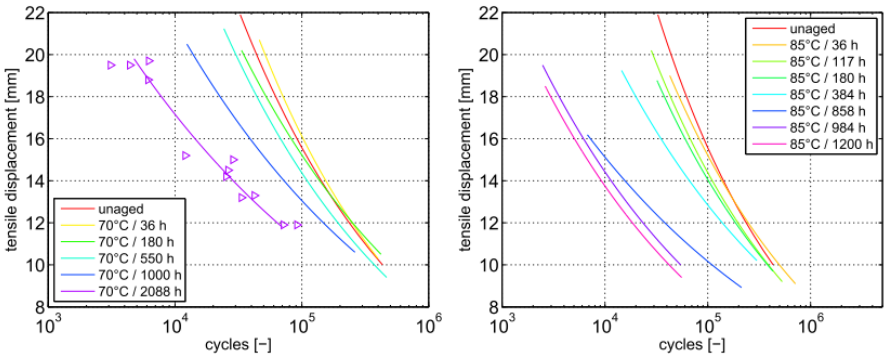

Figure 5.1-12 – Effect of pre-aging temperature and duration on fatigue life of NR/BR blend (Neuhaus et al. 2017).

fatigue lives appear to increase at small amplitudes to what the authors attribute to incomplete vulcanization process before aging, fatigue life decreases as expected with increasing pre-aging temperature and duration. However, there appears to be a dependence on loading levels: as loading decreases, the slope of the curves change and the difference in fatigue lives of pre-aged specimens at small loading levels decreases. Second, pre-aged specimens have been tested at different high temperatures as shown in Figure 5.1-13. Similar to the results obtained for unaged

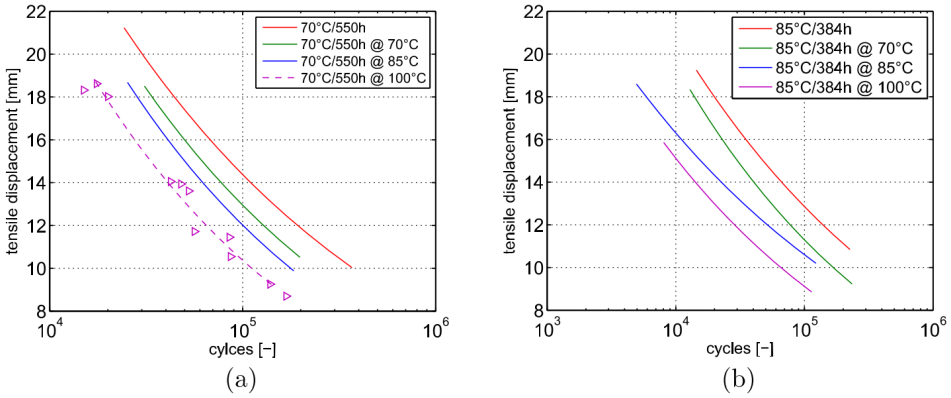

Figure 5.1-13 – Effect of pre-aging temperature and duration on fatigue life of NR/BR blend (Neuhaus et al. 2017).

specimens at high temperature (Fig. 5.1-8), there is roughly a parallel shift as testing temperature is increased. The authors introduce a parameter that measured the magnitude of this shift and found that there is no effect of pre-aging at 70 °C/550 h

with respect to unaged specimens, *i.e.* the magnitudes of the parallel shift are the same.

With respect to the effects of pre-aging on fatigue crack propagation, Kim and Lee (1994) reported an increase in crack growth rate for both unfilled and filled natural rubber after pre-aging for 72 h at 120 °C. Moreover, as expected, presence of oxygen is worse for fatigue resistance; pre-aging in nitrogen environment, did not show as large of an increase in crack growth rate. Finally, for filled natural rubber, crack propagation increased significantly at high tearing energies, *i.e.* the slopes are not parallel as shown in Figure 5.1-14.

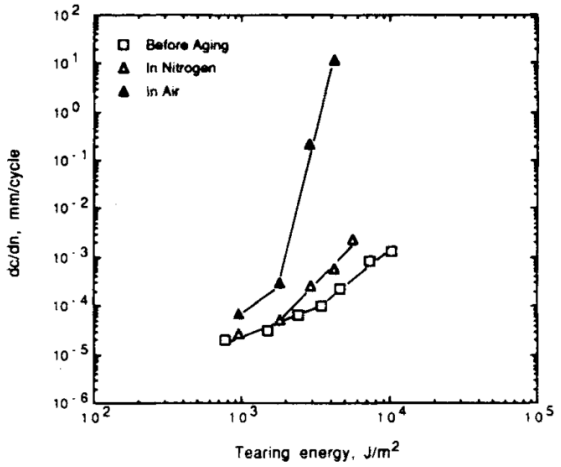

Figure 5.1-14 – Effect of pre-aging environment (air and nitrogen) at 100 °C for 72 h on fatigue crack propagation of natural rubber (Kim and Lee 1994).

5.1.3 Modelling approaches of thermal aging and fatigue

Practically all viable methods on modelling of fatigue after pre-aging are based on Arrhenius type approaches, the time temperature superposition (TTS) method developed by the research group of Gillen (Gillen et al. 1996; Gillen et al. 2000; Celina et al. 2005). Ngolemasango et al. (2008) first applied a TTS model to take into account the effects of pre-aging of natural rubber. The method is based on the assumption that degradation occurs proportionally to $\exp(E_a/RT)$, where E_a is the Arrhenius activation energy, R is the gas constant, and T is the absolute aging temperature. More specifically, there is a shift factor

$$a = A \exp\left(\frac{E_a}{RT}\right), \tag{5.1-1}$$

where A is a pre-exponential factor that is dependent on the reference temperature. Consequently, fatigue life (or, as a matter of fact, any other mechanical parameter) of a pre-aged material can then be estimated as

$$N_a = N_0 \exp(-t_a a), \tag{5.1-2}$$

where N_0 is fatigue life of an unaged material and t_a is the pre-aging time. In this study, Ngolemasango et al. (2008) calculated an activation energy (E_a) of about 60

kJ/mol. A similar approach is used by Broudin et al. (2015) and Neuhaus et al. (2017) for prediction of fatigue lives after pre-aging. Broudin et al. (2015) determined an activation energy of 93 kJ/mol for NR/IR blend; this is done by a best fit of fatigue lives at each loading level for variation of pre-aging temperature and duration. On the other hand, Neuhaus et al. (2017) showed that E_a is dependent on the magnitude of the applied load for temperatures lower than 100 °C; from 100 °C to 120 °C, activation energy is more or less constant. Their model is validated by choosing an aging spectrum, *i.e.* different pre-aging times and durations, that all correspond to similar reduction in fatigue life with respect to unaged fatigue life tests.

Furthermore, Neuhaus et al. (2017) modelled the effect of temperature on fatigue life. In general, S-N curves are modelled with a power-law relationship and, as mentioned earlier, authors obtained nearly parallel shifts in fatigue life curves, where fatigue life decreased with increased temperature. A parameter measuring the shift is introduced

$$C_T = N_0/N_T, \tag{5.1-3}$$

where C_T is modelled by

$$\begin{cases} 1 & \text{if } T \leq T_0, \\ 1 + K\left(\frac{T-T_0}{T_0}\right)^2 & \text{if } T > T_0. \end{cases} \tag{5.1-4}$$

where T_0 is a threshold temperature, below which there is no reduction in fatigue life, and K is a material constant representing temperature sensitivity of a material; in this particular investigation, value of K depends on both aging temperature and duration, and is determined with an Arrhenius-type approach. With this 3-variable approach (testing temperature, pre-aging temperature, and pre-aging duration), the model provides a value of C_T that fits measured results.

5.2 Experimental Methods

To investigate the effects of aging and fatigue of HNBR, in addition to fatigue life tests at 120 °C (which will be referred to as **Test 1**), two types of tests are carried out. A temperature of 150 °C is chosen as the reference aging temperature. It represents the upper operational limit of HNBR. The two tests are the following:

- **Test 2: Simultaneous aging and fatigue tests** refer to fatigue life tests carried out at 150 °C; the principle idea is that at lower loading levels, where tests are relatively long, one could observe effects of simultaneous aging and fatigue;

- **Test 3: Pre-aging and fatigue tests** refer to fatigue tests carried out at 120 °C, similar to regular fatigue tests, but on pre-aged specimens. The main objective of this test is to compare the results to those of Test 2. Traditional pre-aging is done at 150 °C in an unloaded state as well as on specimens that are under static load. The choice of the latter is based on the fact that it is not clear whether pre-aging under load changes the aging mechanism in the material, similar to perhaps how simultaneous fatigue (dynamic load) and aging of Test 2 could also change the aging mechanism.

Likewise to the regular fatigue life tests, these have been carried out at GeM. Experimental methods for Tests 2 and 3 are described in more detail below.

5.2.1 Test 2: Simultaneous aging and fatigue

Fatigue testing is performed on three blends with different percent hydrogenation: the reference A36H96, A36H99, and A36H91. The experimental method is identical to the true stress fatigue life testing procedure described in detail in Chapter 3, Section 3.3, except the temperature is set to 150 °C. All steps are carried out anew since the mechanical response of the material changes. More importantly, it should be noted that new DIC experiments are performed at 150 °C to calculate the relationship of cross-section area with respect to displacement. This step is required to account for thermal expansion of the material, since it changes the reference geometry of the specimen. The blends are tested at the same four nominal loading levels: $\Delta\sigma$ = 10, 8, 6, and 4 MPa at $R = 0$.

The heating chamber of the testing machine is set to a temperature so that the middle section surface of a specimen at different loading levels is 150 °C (measured *in-situ* by a pyrometer); the heating chamber equipped with a fan to provide a homogeneous temperature and circulation of air within the chamber. It should be noted that due to thin geometry of specimens and high testing temperature, heat generation within the specimen is almost negligible and measured to be at most 0.6 °C. Variation of the heating chamber amounted to around ±1.1 °C.

5.2.2 Test 3: Pre-aging and fatigue

This test is limited to the reference blend A36H96. Specimens have been subjected to preliminary aging at 150 °C and performed at LRCCP. The specimens are pre-aged in accordance with ISO norms on "Accelerated ageing and heat resistance tests" (ISO 188 2011). Pre-aging is carried out in two states: unloaded and loaded. In the unloaded state, the specimens are put in the oven as is. On the other hand, for the loaded state, the specimens are stretched and kept at a constant displacement (u) that corresponds to true stress loading of 4 MPa at cycle 200 for fatigue tests carried out at 150 °C (Test 2). Such loading state is chosen for the following reasons:

- Ideally, to compare the effects of aging under loading with simultaneous aging and fatigue, it would be prudent to load the specimen in constant stress, *i.e.* similar to creep experiments. However, this option has not been chosen due to absence of proper equipment and time constraints;
- Thus, the maximum displacement (u) is used as a compromise; 200 cycles corresponds to the time necessary for the machine to reach the target of 4 MPa during fatigue life testing of Test 2. An experimental setup is designed and manufactured to apply this constant displacement, onto which the specimens are loaded and then put into an oven for aging.

There are two aging durations. The first of 42 h corresponds roughly to mean fatigue life duration for Test 2 at 4 MPa. The second is a longer duration of 10 days (240 h).

Once again, the procedure for fatigue life tests on pre-aged specimens is identical to those performed at 120 °C. Subsequently, all of the steps of the true stress method are carried out because of the changes to the mechanical response and to the geometry of pre-aged specimens. The loading is limited to two loading levels: 10 and 4 MPa.

5.2.3 Fatigue damage analysis

Fatigue damage analysis of some of the broken specimens from Test 2 and Test 3 is carried out as described in Chapter 4, Section 4.2.3. In summary, optical microscopy and scanning electron microscopy (SEM) are used to examine fracture surfaces; moreover, energy dispersive spectroscopy (EDS) is used to chemically investigate initiation sites.

5.2.4 Supplementary investigation of aged material

To investigate the effects of aging on mechanical behavior of HNBR blends A36H96, A36H99, and A36H91, additional quasi-static tensile tests have been performed at *GeM* for specimens aged at 150 °C for a duration of 42 h, 72 h, 168 h, and 240 h (10 days). The procedure for tensile testing is identical to the one outlined in Chapter 2, Section 2.3.1. However, these studies are not complete and, thus, they are presented in Appendix B.

5.3 Results of Test 2: Simultaneous Aging and Fatigue

5.3.1 Fatigue life

The results of fatigue life tests carried out at 150 °C are plotted on Wöhler curves in terms of true stress amplitude with respect to fatigue tests at 120 °C. As in Chapter 4, Section 4.3.1, the average true stress amplitude of each specimen is plotted with respect to its fatigue life; where visible, error bars indicate absolute maximum and minimum amplitude experienced by a particular specimen. For ease of visualization, color-filled markers correspond to results at 150 °C and unfilled to 120 °C; additionally, *stars* represent specimens that did not break after 2 million cycles (for blends A36H99 and A36H91) and 5 million cycles (only for A36H96 at 120 °C). Finally, specimens that failed at the grip are excluded from these figures; 135 specimens were considered with an average of 11 specimens per loading level for each blend. This amounted to 978 h (41 days) of machine testing time.

Figures 5.3-1 to 5.3-3 show these results for **A36H96**, A36H99, and A36H91. Once again, there is significant scatter in fatigue lives. However, it is clear by visual inspection that an increase in temperature leads to a decrease in fatigue life for blend **A36H96** from 6 to 10 MPa, and especially for blend A36H91 at all loading levels; moreover, all tested specimens of A36H91 broke at the 4 MPa loading level. On the other hand, it appears that the effect of higher temperature is not as clear for A36H99.

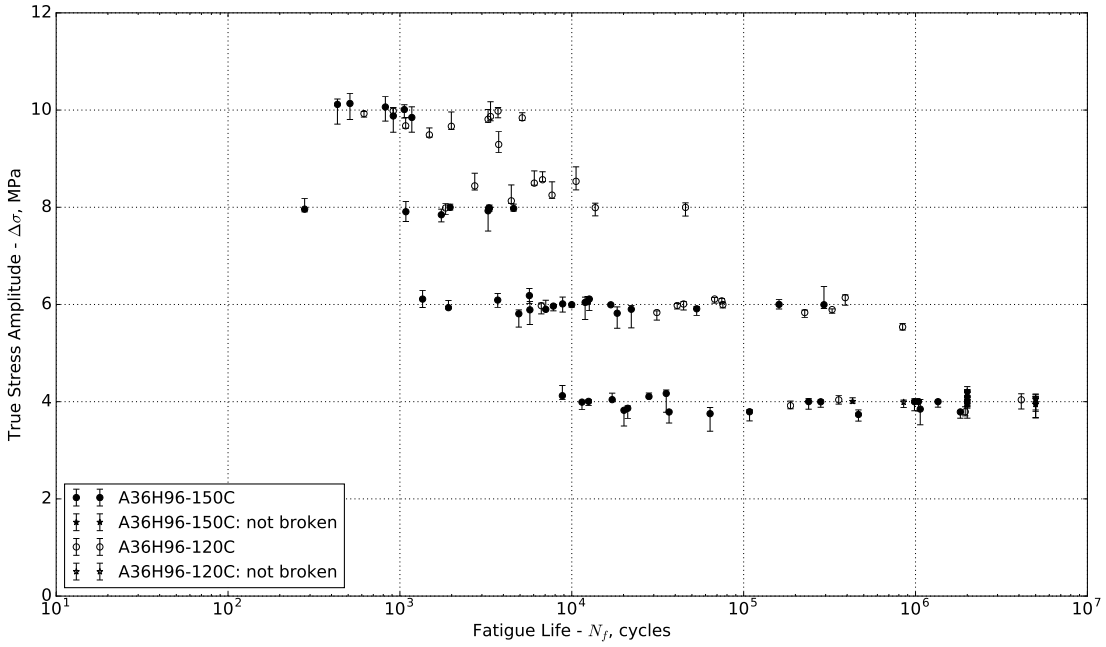

Figure 5.3-1 – Fatigue life of A36H96 at 150 °C as compared to 120 °C; R=0.

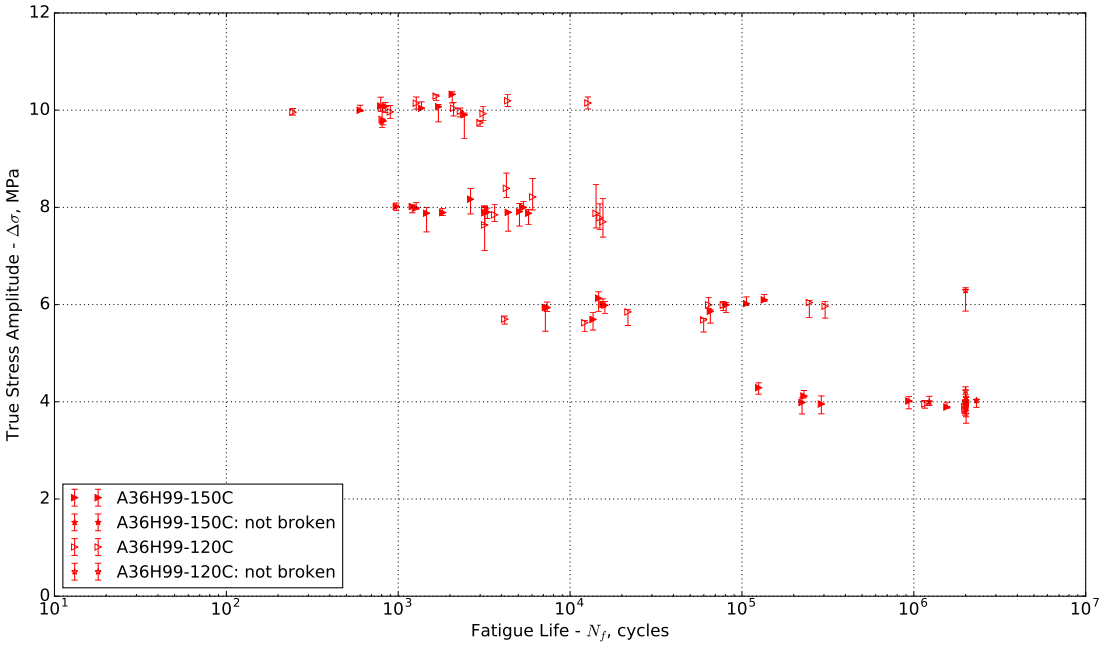

Figure 5.3-2 – Fatigue life of A36H99 at 150 °C as compared to 120 °C; R=0.

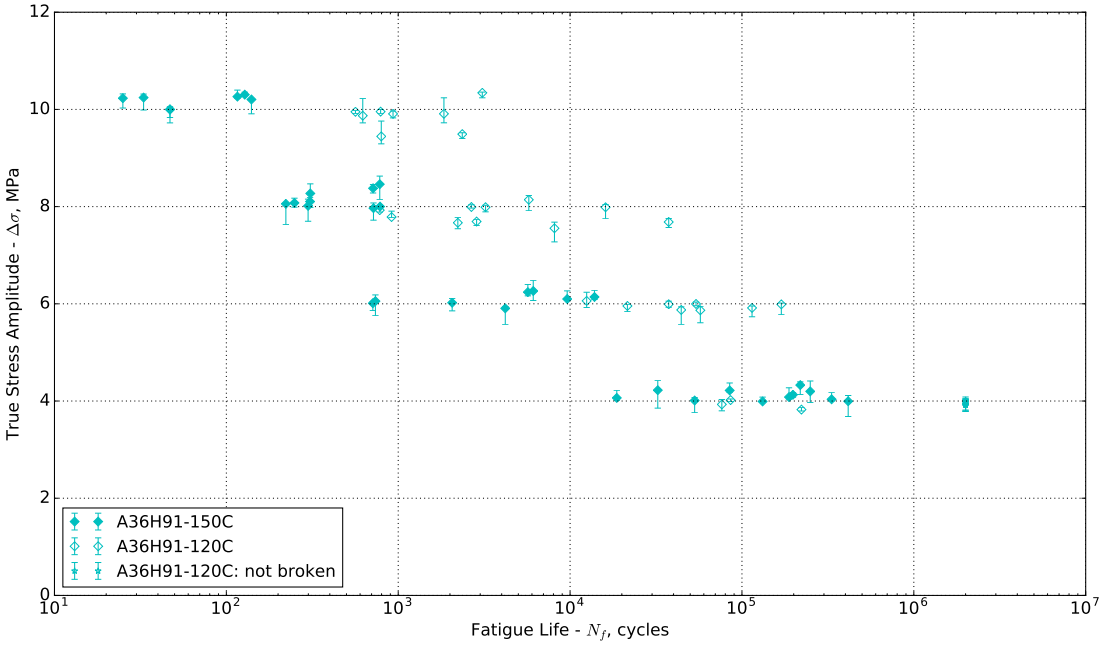

Figure 5.3-3 – Fatigue life of A36H91 at 150 °C as compared to 120 °C; R=0.

Multivariate statistical analysis

The same methodology for multivariate statistical analysis as presented in Chapter 4, Section 4.3.1 is applied to these results. Due to scatter in both axes and presence of right-censored results (unbroken specimens), Cox proportional hazards model is utilized. Initially, a global model including all three blends has been tried. However, such model does not satisfy the assumption of proportionality of the hazard functions; for whatever reasons, it appears that introduction of results at 150 °C violates this assumption. Therefore, a model is created for each blend, and each can be formally expressed as

$$h(N, \vec{x}) = h_0(N) \times \exp(\beta_{\Delta T} x_{\Delta T} + \beta_{\Delta\sigma} x_{\Delta\sigma}), \tag{5.3-1}$$

where, as before, $\Delta\sigma$ represents the continuous covariate true stress amplitude in MPa, and a new continuous covariate for change in temperature ΔT is added (for example, $\Delta T = 150-120 = 30$ °C or K). It should be noted that since there are three separate models for each blend, the results of these models at 120 °C will not match exactly the results of model presented in Chapter 4, Section 4.3.1, where all blends (including A24H96, A44H96, and A44-24) are included in the model. However, after comparing the results of these three models and the result of the *all-blends* model, it can be said that they closely match for a temperature of 120 °C.

Thus, for the three models, Table 5.3-1 presents the resulting values for each covariate hazard ratio (with lower HR^{min} and upper HR^{min} 95% confidence intervals) and corresponding p-value indicating statistical significance; moreover, the global p-value returned by the `cox.zh()` function is shown, whereby low statistical significance ($p > 0.05$) indicates a valid proportionality assumption of hazard functions. The hazard

Table 5.3-1 – Results of each Cox hazards models for blends A36H96, A36H99, and A36H91 tested at 150 °C.

Model 1: A36H96

Covariate	HR	HR^{min}	HR^{max}	p-value	`cox.zph()` p-value
$\Delta\sigma$	2.90	2.39	3.53	2.00E-16	0.204
ΔT	1.06	1.04	1.08	4.16E-11	

Model 2: A36H99

Covariate	HR	HR^{min}	HR^{max}	p-value	`cox.zph()` p-value
$\Delta\sigma$	2.58	2.10	3.17	2.00E-16	0.971
ΔT	1.03	1.02	1.05	3.85E-04	

Model 3: A36H91

Covariate	HR	HR^{min}	HR^{max}	p-value	`cox.zph()` p-value
$\Delta\sigma$	3.47	2.64	4.57	2.00E-16	0.293
ΔT	1.09	1.06	1.12	6.88E-11	

ratio for the covariate ΔT is of most interest here. These three hazard ratios of each blend are different even taking into account the 95% confidence intervals, and they can be ranked in the following order: $HR_{\Delta T,\ A36H91} > HR_{\Delta T,\ A36H96} > HR_{\Delta T,\ A36H99}$. Taking A36H91 as an example, the general interpretation is that an increase in temperature by 1 °C (or K) induces a hazard of failure by a factor of 1.09 ± 0.03 with high statistical significance ($p = 6.88\text{E-}11 << 0.05$). On the other hand, the effect of

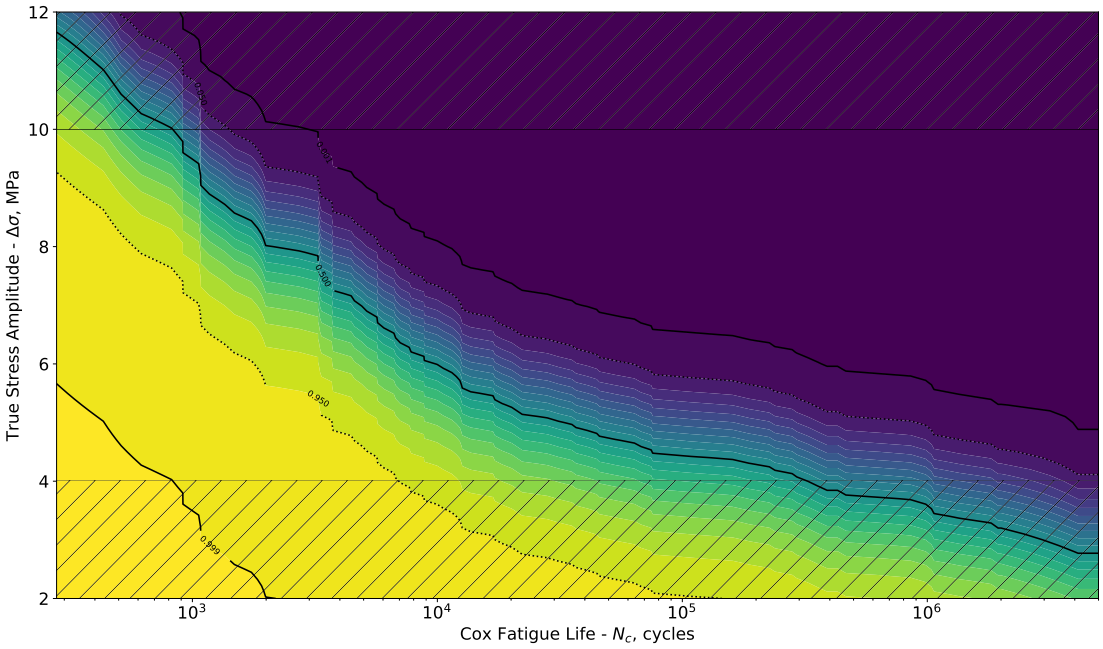

Figure 5.3-4 – Probabilistic Wöhler curve of A36H96 at 150 °C estimated by Cox model. Hatched regions indicate extrapolated data.

increased temperature is not as strong for A36H99 as indicated by HR $= 1.03 \pm 0.02$ and p-value of $p = 3.85\text{E-}4 << 0.05$. Thus, these results show that **the effect of increased temperature and, thus, aging is more significant as percent hydrogenation decreases**.

Consistent with the results of Chapter 4, Section 4.3.1, the results of the present models are plotted on probabilistic Wöhler curves of each blend as shown in Figures 5.3-4 to 5.3-6. The solid lines indicate the mean probability, as well as near absolute survival and near absolute failure (as indicated by labels $\widehat{S}(N)$ =0.500, $\widehat{S}(N)$ =0.999, and $\widehat{S}(N)$ =0.001). The dashed lines are the maximum ($\widehat{S}(N) \approx 0.05$) and the minimum ($\widehat{S}(N) \approx 0.95$) 95% bounds of the survival estimates. The hatched regions from 2 to 4 MPa and from 10 to 12 MPa indicate the extrapolated survival estimates.

Moreover, since the covariate ΔT is a continuous variable, one can use the model to predict the results of fatigue testing at various temperatures. A median temperature of 135 °C, corresponding to one in between 120 °C and 150 °C, is chosen. However, it should be noted, that the validity of the prediction is questionable without additional experiments; for this to hold true, one must assume that the physical mechanisms of thermal aging evolve is some uniform way between the two temperatures. For interpolation and extrapolation of the true stress amplitude covariate, there are four nominal loading levels from which predictions can be based; whereas, in this case, extrapolation is done only from tests at two temperatures. Nevertheless, the comparison of the mean values at three temperatures is shown in Figure 5.3-7 for all three blends, where the prediction at 135 °C is indicated by dashed lines and dotted lines indicate the extrapolated prediction for true stress. The results for three blends can be summarized as following:

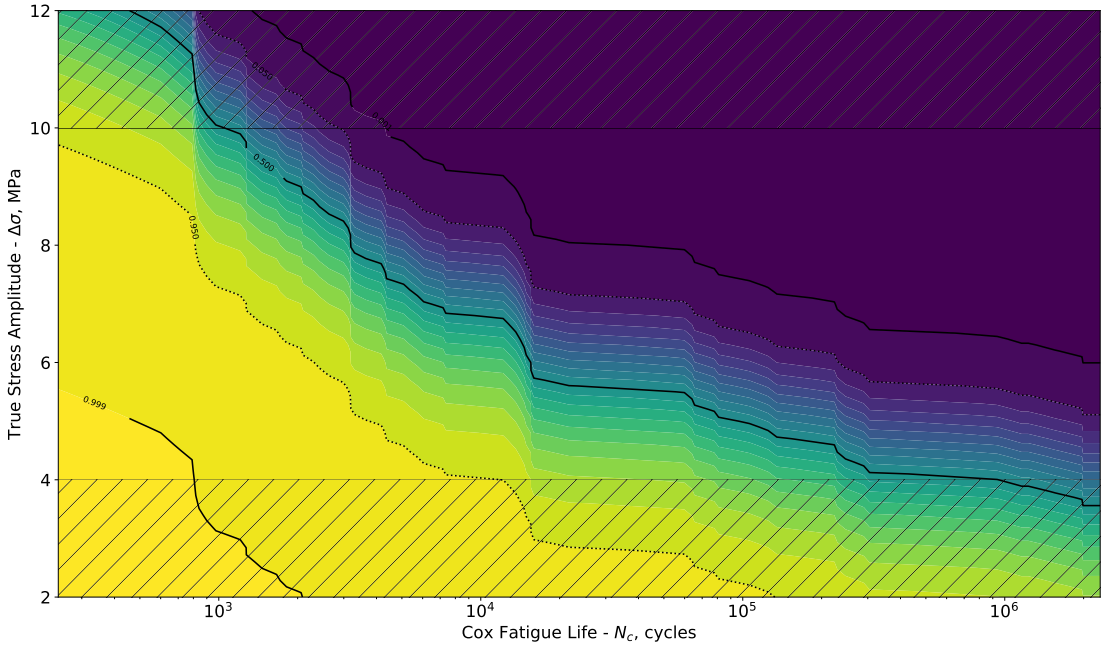

Figure 5.3-5 – Probabilistic Wöhler curve of A36H99 at 150 °C estimated by Cox model. Hatched regions indicate extrapolated data.

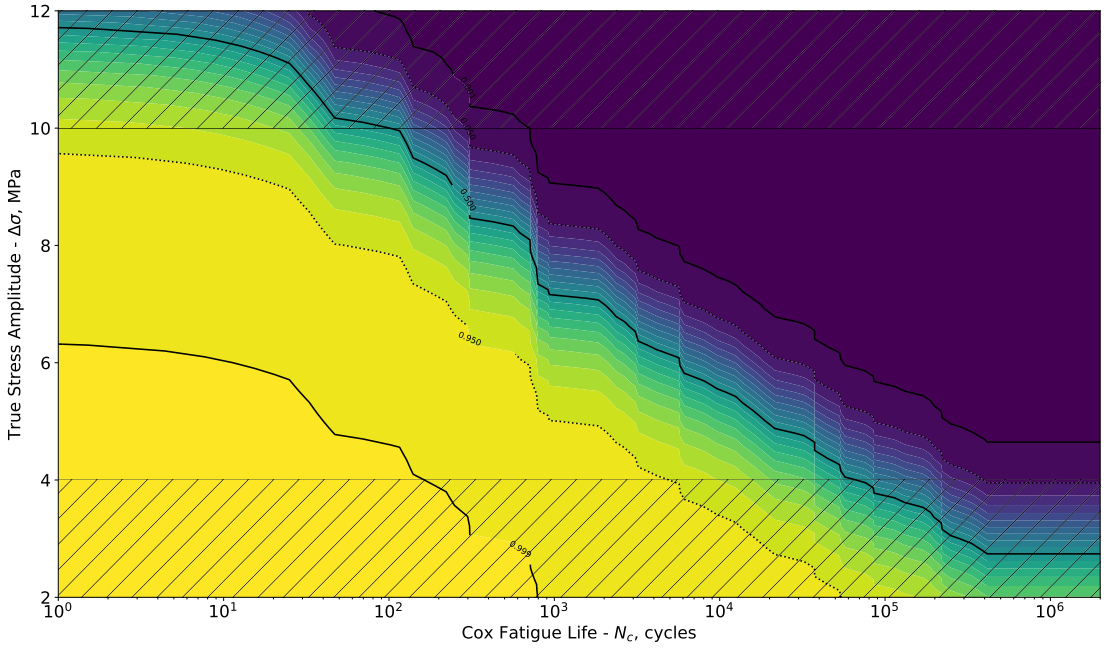

Figure 5.3-6 – Probabilistic Wöhler curve of A36H91 at 150 °C estimated by Cox model. Hatched regions indicate extrapolated data.

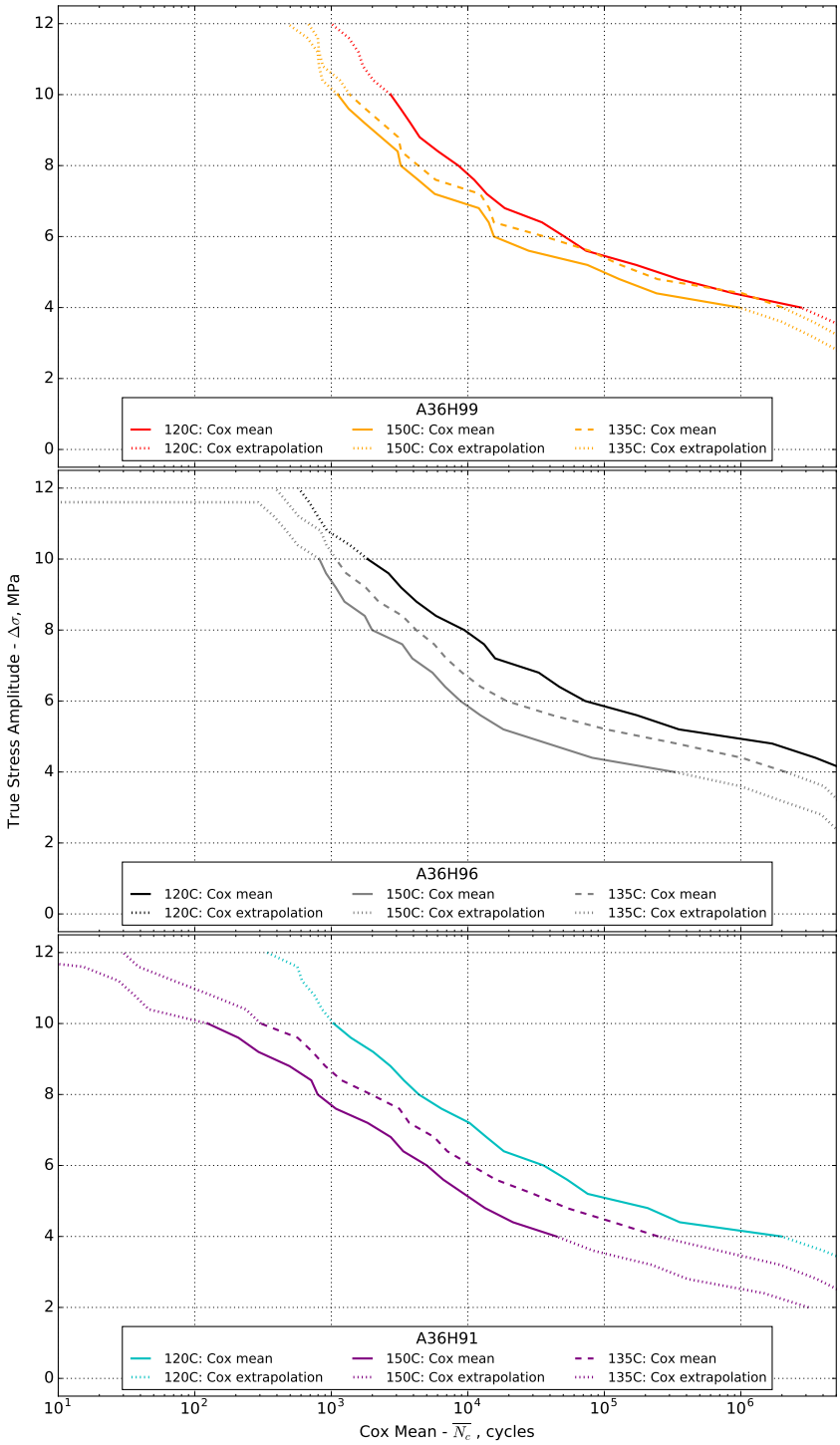

Figure 5.3-7 – Mean fatigue lives of blends A36H99, A36H96, and A36H91 from the Cox model at 120 °C and 150 °C, as well as prediction at 135 °C.

- **Fig. 5.3-7 - Top**: in A36H99, the effect of increased temperature is the smallest. Moreover, the shift does not appear to be parallel between 120 °C and 150 °C if compared on a log-scale. The model also predicts that the shift in the Wöhler curve is not parallel; for example from around 4 to 5 MPa at 135 °C, the mean values are similar to those at 120 °C. Perhaps this indicates that at low loading levels and long duration of experiments, the effects of aging are negligible for A36H99; on the other hand, the effect of only temperature is more pronounced at high loading levels, but not because of aging since tests are very short;
- **Fig. 5.3-7 - Middle**: A36H96 shows median response for tests at 150 °C. The shift between 120 °C and 150 °C is not parallel, as the difference appears to increase for smaller amplitudes. Perhaps this is indicative of larger aging effects at small true stress amplitude as the duration of tests increases; the mean at 4 MPa corresponds to a test duration of around 18 h.
- **Fig. 5.3-7 - Bottom**: A36H91 is most affected by testing at high temperature. This is as expected, since with higher degree of unsaturation, a material becomes less resistant to heat. Moreover, the shift between 120 °C and 150 °C is also not parallel with increase in difference for low loading levels and long tests. However, it is questionable if this is an effect of aging, because the mean at the 4 MPa loading level corresponds to a test duration of only around 2 h and 30 min.

5.3.2 Fatigue damage analysis

Macroscopic observations

Macroscopic observations have been made for all tested specimens. First, no multi-cracking is observed for all blends tested at 150 °C as shown in Figure 5.3-8(a); if one recalls the results of Chapter 4, Section 4.3.3, some multi-cracking has been observed for A36H96 and A36H99 at 120 °C. Second, in blends A36H96 and A36H99 at 120 °C, some of the cracks has initiated in one plane and the final brittle fracture occurred in another plane that is offset by some vertical distance along the direction of loading (schematic has been proposed in Figure 4.3-17). Figure 5.3-8(b) shows the frequency of such observations with respect to tests at 120 °C. With increased temperature, occurrence of two plane crack growth decreases for A36H96 and appears to not change in A36H99; and, there is no change in crack growth type in blend A36H91, where all crack growth occurs on one plane at both temperatures.

Furthermore, the vertical locations of initiation sites (L_I) and the vertical length of crack propagation (L_P) are measured as previously shown schematically in Figure 4.3-19. Figure 5.3-9(a) shows the lengths to initiation at 150 °C with respect to 120 °C for three blends. There is no apparent change in the location of initiation, where most occur between 30% to 50% of the specimen length; most notable difference, is absence of unbroken specimens for blend A36H91. However, there is a noticeable change in the vertical propagation lengths as shown in Figure 5.3-9(b). The greatest difference is observed for A36H96, where almost 80% of all specimens have a vertical propagation of up to 2% of the total specimen length at 150 °C as

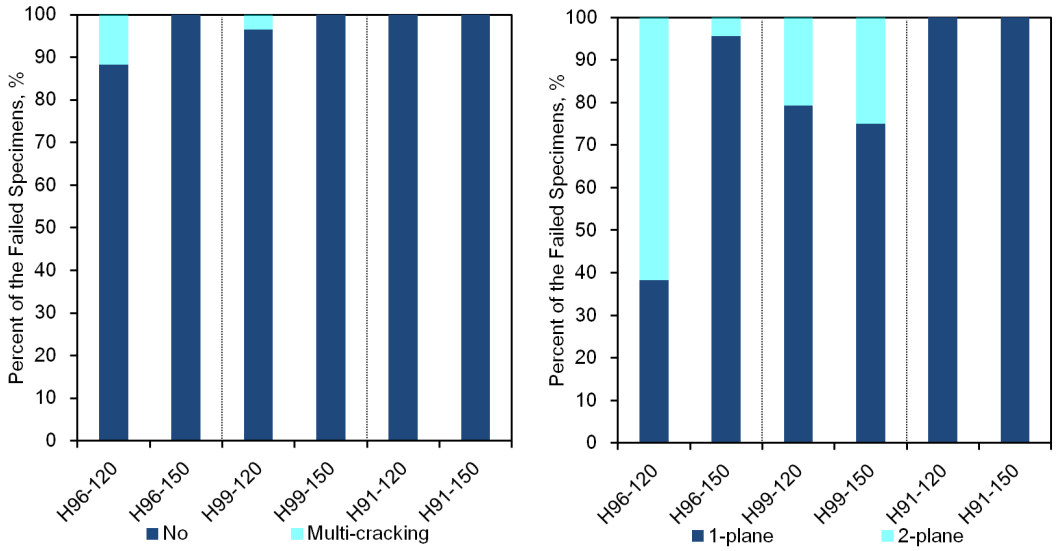

(a) Multi-crack appearance. **(b)** Crack growth behavior.

Figure 5.3-8 – Macroscopic observations of crack growth behavior and of appearance of multi-cracking in broken specimens at 150 °C.

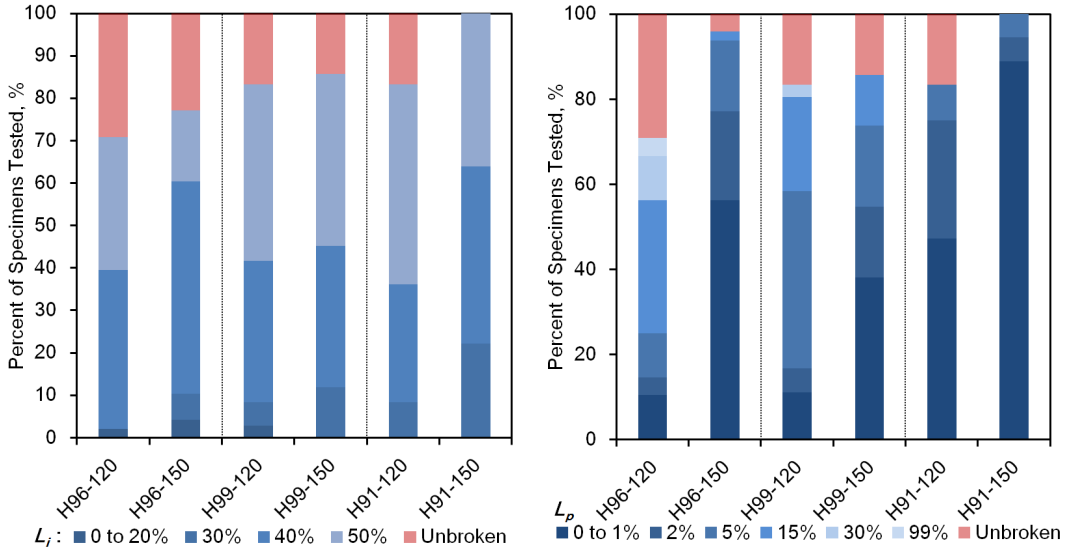

(a) Length to initiation (L_I). **(b)** Vertical length of propagation (L_P).

Figure 5.3-9 – Macroscopic measurements of the length to initiation and the vertical length of propagation; shown as percentages to the total length of the specimen.

compared to about 7% of all specimens at 120 °C. For A36H91, vertical propagation of up to 1% of the specimen length corresponds to about 90% at 150 °C as compared to about 50% at 120 °C. As for A36H99, the differences between two temperature are less pronounced, but one can observe an increase in number of vertical propagation lengths of 1% and less.

Microscopic observations

Microscopic observations with aid of scanning electron microscopy (SEM) and X-ray energy dispersive spectroscopy (EDS) have been carried out only on broken specimens of the reference blend A36H96 at 150 °C; roughly 70% of specimens have been analyzed starting from the lowest nominal loading level of 4 MPa. For more micrographs, please refer to Appendix C. First, no fractographic effects of diffusion limited oxidation (DLO) have been observed in all of the tested specimens. Furthermore, as outlined earlier in Chapter 4, Section 4.3.3, there are three types of fracture surfaces:

- **Rough-smooth** surface with classical initiation-propagation-fracture regimes as shown in Figure 5.3-10(a);
- **Vertical rough-smooth** surface similar to *rough-smooth*, but with a vertical component of propagation, as shown in Figure 5.3-10(b);
- **Smooth** surface with uniform rugosity as shown in Figure 5.3-10(c).

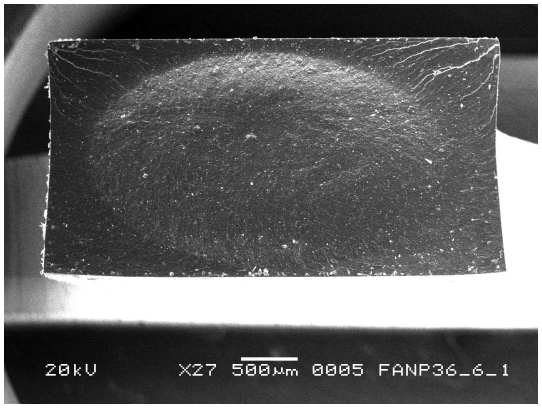

(a) Rough-smooth at ×27.

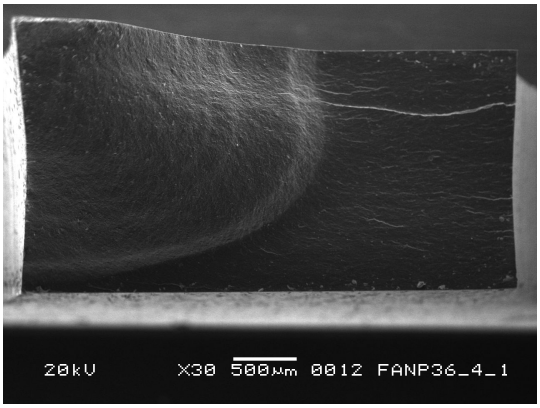

(b) Vertical rough-smooth at ×30.

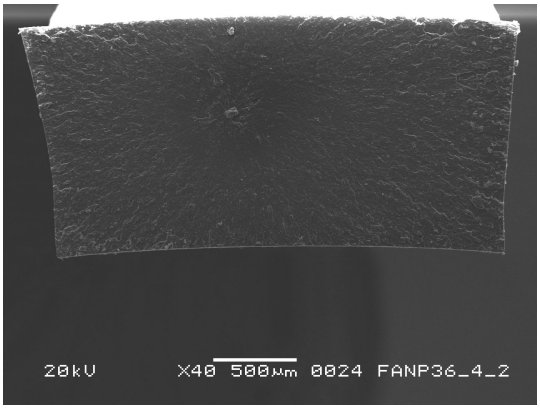

(c) Smooth at ×40.

Figure 5.3-10 – Micrographs of typical fracture surface categories tested at 150 °C.

The number of observations for each category of fracture surfaces is shown in Figure 5.3-11. As expected from macroscopic observations, the frequency of *vertical rough-smooth* fracture surfaces decreases at 150 °C. Moreover, *smooth* fracture surfaces are now present in A36H96 at this high temperature.

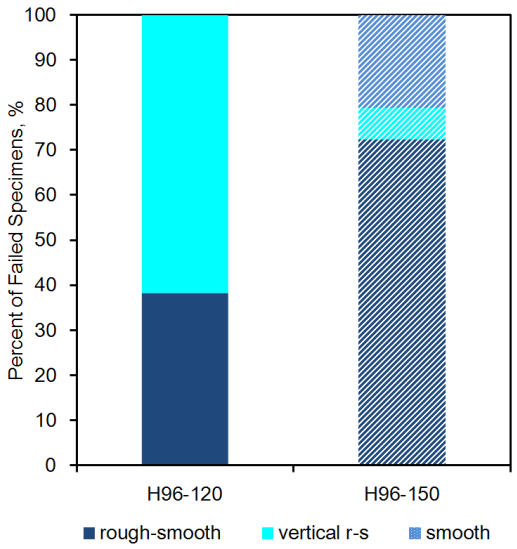

Figure 5.3-11 – Microscopic observations of fracture surfaces categories in broken specimens tested at 150 °C; hatched fill indicates partial sampling.

Initiation of flaws

Similar to the discussion in Chapter 4, Section 4.3.3, the initiation sites have been investigated by X-ray energy dispersive spectroscopy (EDS). As before, the cause of initiation at some sites is unknown; moreover, additional five types of flaws have been identified (all as in case of testing at 120 °C, except for voids). These are:

- **Matrix** - initiation site is identical to matrix; exact cause is not known;
- **Oxide** - additional presence of oxygen with respect to matrix, as well as elements such as Ca, Si, Al and/or Mg;
- **Carbon black** - relative increase in carbon with respect to matrix;
- **Macro particles** - large foreign particles of metallic of carbon origin;
- **Metals** - high concentration of metals such as Fe, Ti, or Al (without oxygen);
- **ZnO** - high concentration of zinc and oxygen.

Figure 5.3-12 shows the distribution of these flaws for A36H96 specimens tested at 150 °C with respect to those tested at 120 °C. Although, not all specimens have been analyzed at 150 °C, there is a significant increase in the failures associated to carbon black. Perhaps, carbon blacks are more sensitive to the high temperature, although no literature has been found to identify this effect. Moreover it should be noted that, since this blend has been manufactured in two different batches (batch 1 used in fatigue tests at 120 °C and batch 2 used at 150 °C), perhaps this is indicative of some difference in processing of the rubber.

Finally, the split of the location of the initiation sites - on the surface or internally - is shown for A36H96 specimens tested at 150 °C in Figure 5.3-13, and it appears that there is no significant difference in the location of initiation at high temperatures with respect to 120 °C. In terms of the surface cracks, 14% correspond to the surfaces

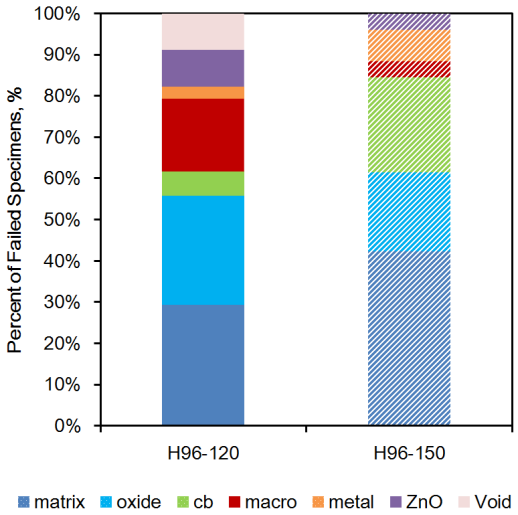

Figure 5.3-12 – Different causes of initiation in A36H96 tested at 150 °C; hatched fill indicates partial sampling.

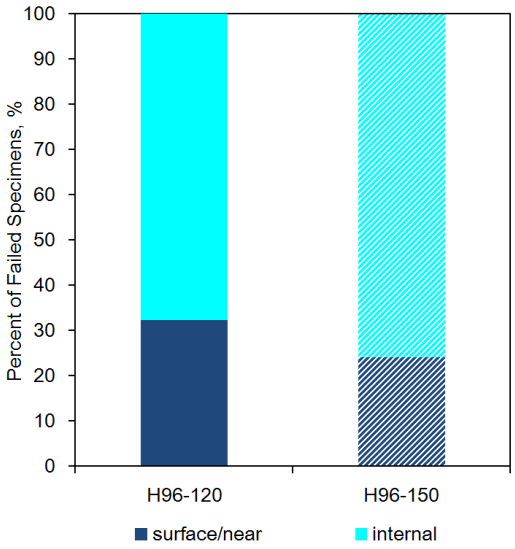

Figure 5.3-13 – Surface and internal initiation sites for A36H96 tested at 150 °C; hatched fill indicates partial sampling.

created during compression molding and 7% to those created during cutting with a die.

5.4 Results of Test 3: Pre-aging and Fatigue

5.4.1 Fatigue life

For blend A36H96, the results of fatigue life tests carried out at 120 °C on specimens pre-aged at 150 °C are plotted on Wöhler curves with true stress amplitude as a function of fatigue life with respect to fatigue tests on virgin specimens at 120 °C. Similar to the presentation of fatigue life results of the previous section, the average true stress amplitude of each specimen is plotted with respect to its fatigue life. In summary:

- Error bars indicate absolute maximum and minimum amplitude experienced by a particular specimen;
- Color-filled triangular markers correspond to pre-aged material at 150 °C and unfilled circular markers to virgin material tested at 120 °C;
- *stars* represent specimens that did not break after 2 million cycles and 5 million cycles (for virgin specimens at 120 °C only);
- Specimens that failed at the grip are excluded from these figures. In the end, 71 specimens are considered at two loading levels of 10 and 4 MPa, for two pre-aging durations of 42 h and 240 h, and two pre-aging loading conditions (unloaded and loaded), equalling to an average of eight specimens per each testing condition. Overall, this amounted to around 1040 h (43 days) of machine testing time.

Figures 5.4-1 and 5.4-2 show these results for pre-aging under no load and under load, respectively. One can observe significant scatter in fatigue lives and differentiation is difficult for 42 h pre-aged specimens and the virgin material. However, it is clear by visual inspection that an increase in pre-aging duration to 240 h decreases fatigue life at 10 MPa and 4 MPa with respect to virgin material; moreover, all tested specimens pre-aged for 240 h broke at the 4 MPa nominal loading level, irrespective of the pre-aging loading condition.

Multivariate statistical analysis

Once again, the Cox proportional hazards model is applied because of presence of scatter in both axes and presence of right-censored results (unbroken specimens) for specimens pre-aged for 42 h. To satisfy the assumption of proportional hazards, two models are created for blend A36H96 and separated by the type of pre-aging loading condition: with and without load; fatigue life data from fatigue tests on both virgin and pre-aged specimens under specific loading condition are used in the models. There are three continuous covariates: aging duration, aging temperature, and true stress amplitude. Model for each pre-aging loading condition can be formally expressed as

$$h(N, \vec{x}) = h_0(N) \times \exp(\beta_{\Delta T_a} x_{\Delta T_a} + \beta_{\Delta t_a} x_{\Delta t_a} + \beta_{\Delta\sigma} x_{\Delta\sigma}), \qquad (5.4\text{-}1)$$

where, $\Delta\sigma$ represents true stress amplitude in MPa, ΔT_a represents pre-aging temperature in K, and Δt_a represents pre-aging time in days.

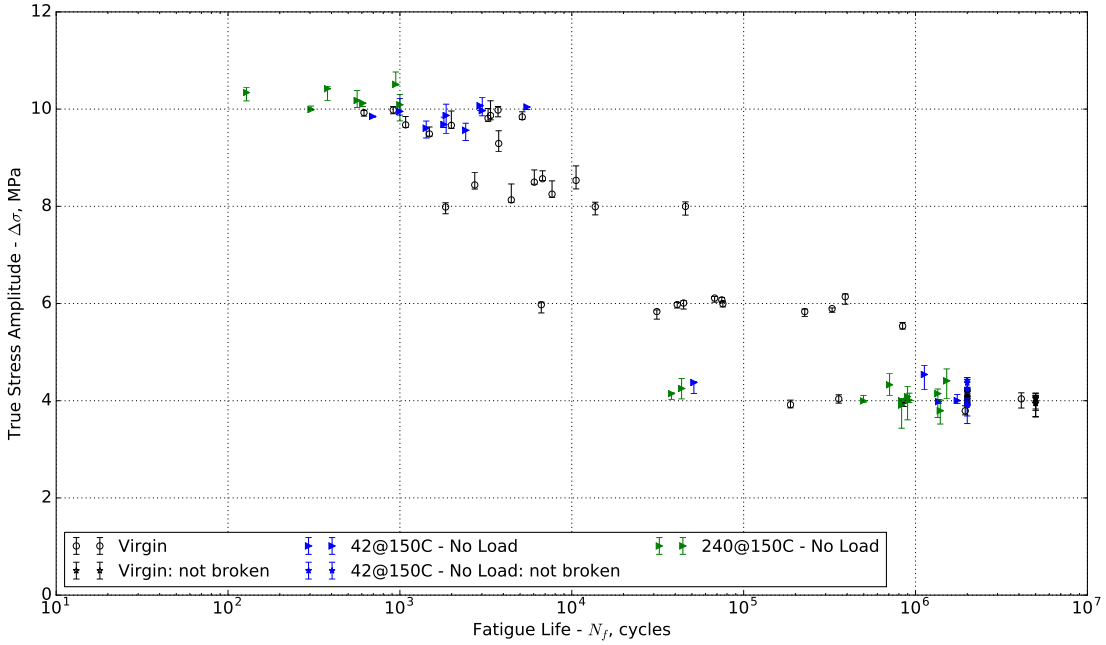

Figure 5.4-1 – Fatigue life of A36H96 at 120 °C after pre-aging under no load for 42 h and 240 h at 150 °C as compared to fatigue life of virgin material; R=0.

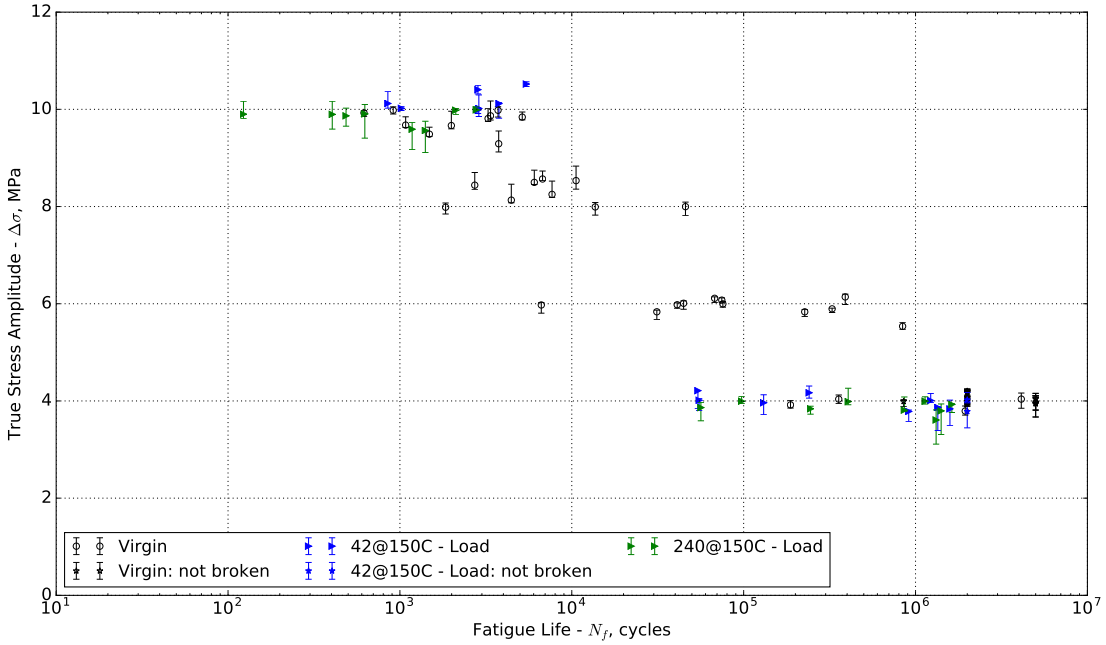

Figure 5.4-2 – Fatigue life of A36H96 at 120 °C after pre-aging under load for 42 h and 240 h at 150 °C as compared to fatigue life of virgin material; R=0.

For the two models, Table 5.4-1 presents the resulting values for each covariate hazard ratio (with lower HR^{min} and upper HR^{min} 95% confidence intervals) and corresponding p-value indicating statistical significance. Moreover, the global p-value returned by the `cox.zh()` function is given, whereby low statistical significance ($p > 0.05$) indicates a valid proportionality assumption of hazard functions. Con-

Table 5.4-1 – Results of two Cox hazards models on the effect of pre-aging on fatigue at 120 °C.

Model 1: Pre-aging with no load

Covariate	**HR**	**HR^{min}**	**HR^{max}**	**p-value**	`cox.zph()` **p-value**
$\Delta\sigma$	3.45	2.67	4.53	2.00E-16	0.906
Δt_a	1.20	1.09	1.31	2.16E-4	
ΔT_a	1.02	1.01	1.26	9.10E-3	

Model 2: Pre-aging under load

Covariate	**HR**	**HR^{min}**	**HR^{max}**	**p-value**	`cox.zph()` **p-value**
$\Delta\sigma$	2.93	2.29	3.75	2.00E-16	0.717
Δt_a	1.13	1.03	1.23	1.02E-2	
ΔT_a	1.013	1.000	1.188	2.29E-3	

sidering the hazard ratios and their 95% confidence intervals, their values for the covariates ΔT_a and Δt_a are somewhat similar for both models and it is difficult to draw a conclusion about how pre-aging loading condition affects fatigue life.

To visualize the results of the models for the two pre-aging loading conditions and two pre-aging durations, probabilistic Wöhler curves of each blend are plotted in Figures 5.4-3 to 5.4-6. The solid lines indicate the mean probability, as well as near absolute survival and near absolute failure (as indicated by labels $\widehat{S}(N)$ =0.500, $\widehat{S}(N)$ =0.999, and $\widehat{S}(N)$ =0.001). The dashed lines are the maximum ($\widehat{S}(N) \approx 0.05$) and the minimum ($\widehat{S}(N) \approx 0.95$) 95% bounds of the survival estimates. The hatched regions from 2 to 4 MPa and from 10 to 12 MPa indicate the extrapolated survival estimates.

Furthermore, the comparison of the mean values of the two pre-aging conditions and the two aging durations are shown in Figure 5.4-7; these are plotted in comparison with fatigue tests on virgin specimens and, also, fatigue life at 150 °C discussed in the previous section. Blue lines represent pre-aged specimen without a load and green - those under load; dashed line is the fatigue life at 150 °C and, as before, dotted lines are extrapolated true stress amplitudes. The results are grouped by pre-aging duration and can be summarized as following:

- **Fig. 5.4-7 - Top**: it appears that pre-aging for 42 h has little or no effect on fatigue life of A36H96 irrespective of the pre-aging loading conditions. The mean curves of pre-aged specimens tend to coincide with those of virgin specimens from around 6 to 9 MPa. As true stress decreases from 6 to 4 MPa, it appears that pre-aging under load slightly shortens fatigue life as compared to pre-aging without a load;
- **Fig. 5.4-7 - Bottom**: as pre-aging time increases from 42 h to 240 h (10 days), there is a significant decrease in fatigue life in a form of a almost parallel shift with respect to fatigue life curve of virgin material. Surprisingly, and most likely as a coincidence, pre-aged curves appear to be close to the fatigue life

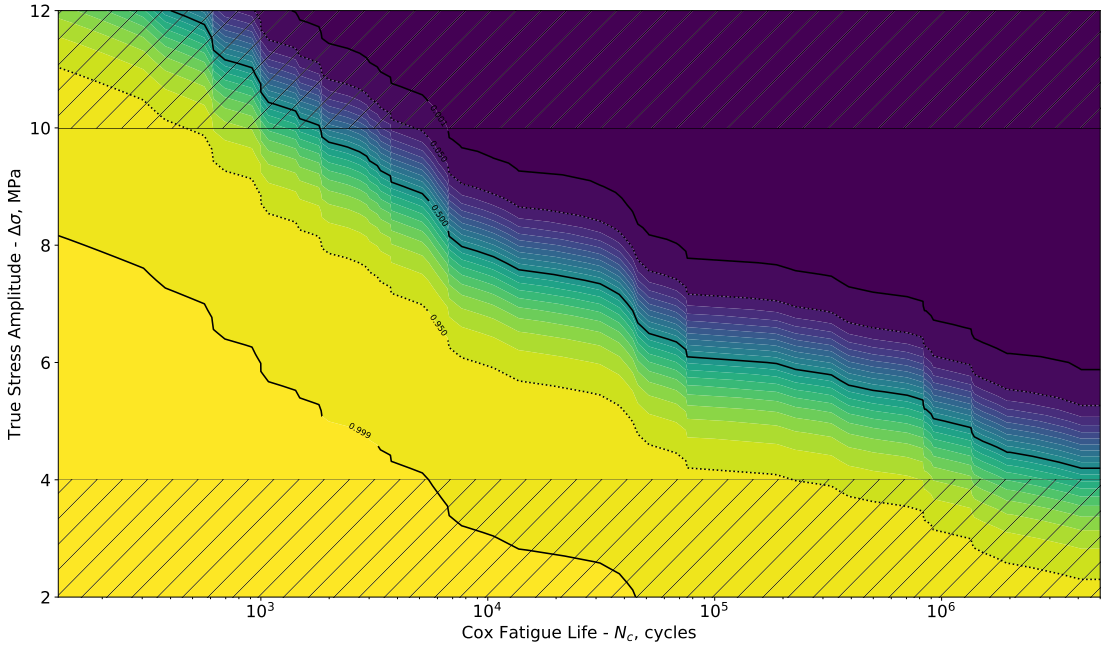

Figure 5.4-3 – Probabilistic Wöhler curve of A36H96 pre-aged at 150 °C under no load for a duration of 42 h. Hatched regions indicate extrapolated data.

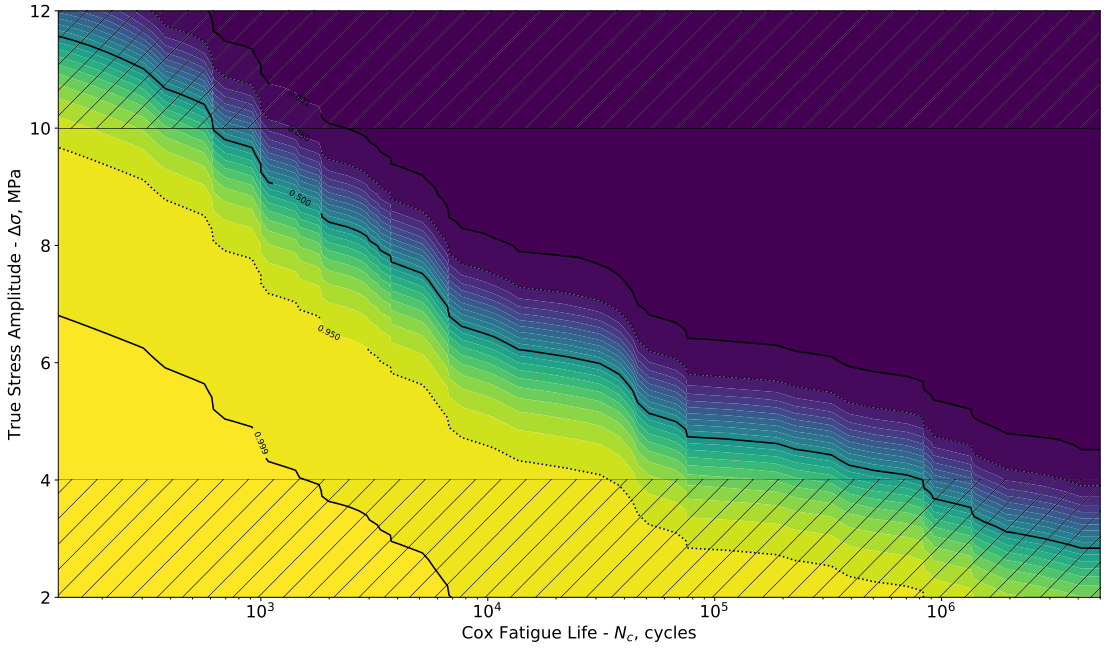

Figure 5.4-4 – Probabilistic Wöhler curve of A36H96 pre-aged at 150 °C under no load for a duration of 10 d. Hatched regions indicate extrapolated data.

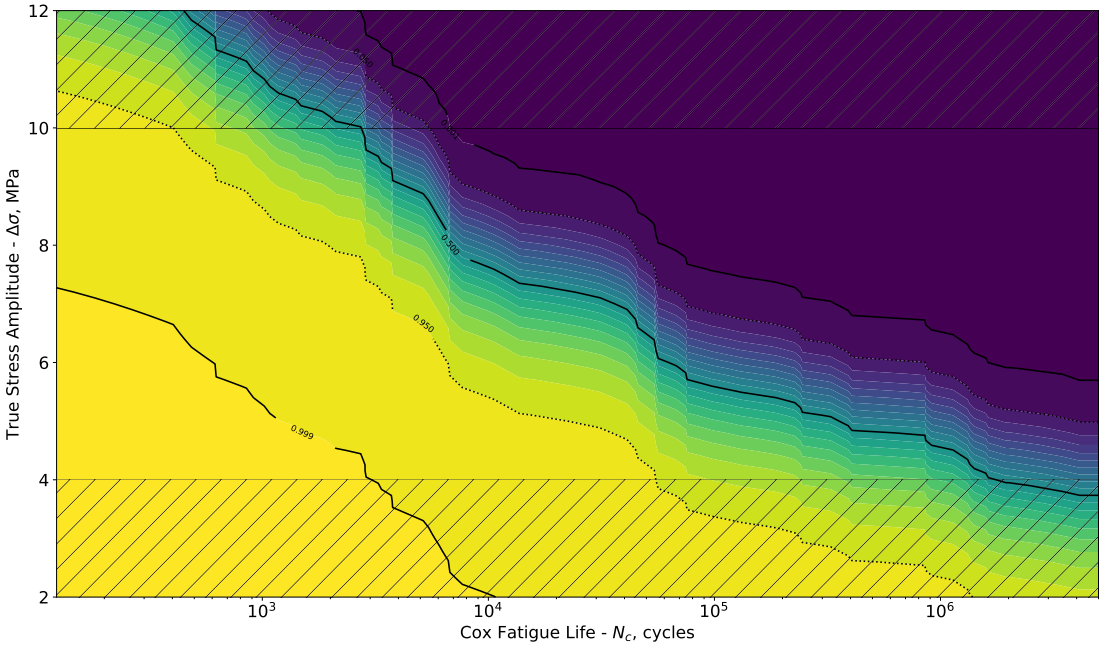

Figure 5.4-5 – Probabilistic Wöhler curve of A36H96 pre-aged at 150 °C under load for a duration of 42 h. Hatched regions indicate extrapolated data.

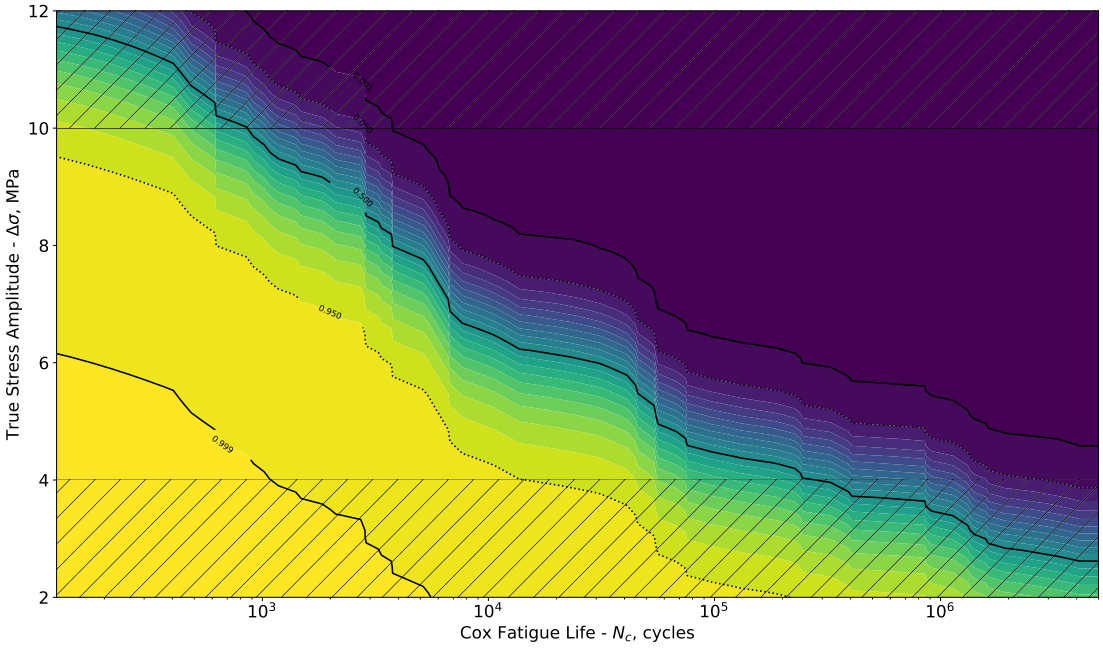

Figure 5.4-6 – Probabilistic Wöhler curve of A36H96 pre-aged at 150 °C under load for a duration of 10 d. Hatched regions indicate extrapolated data.

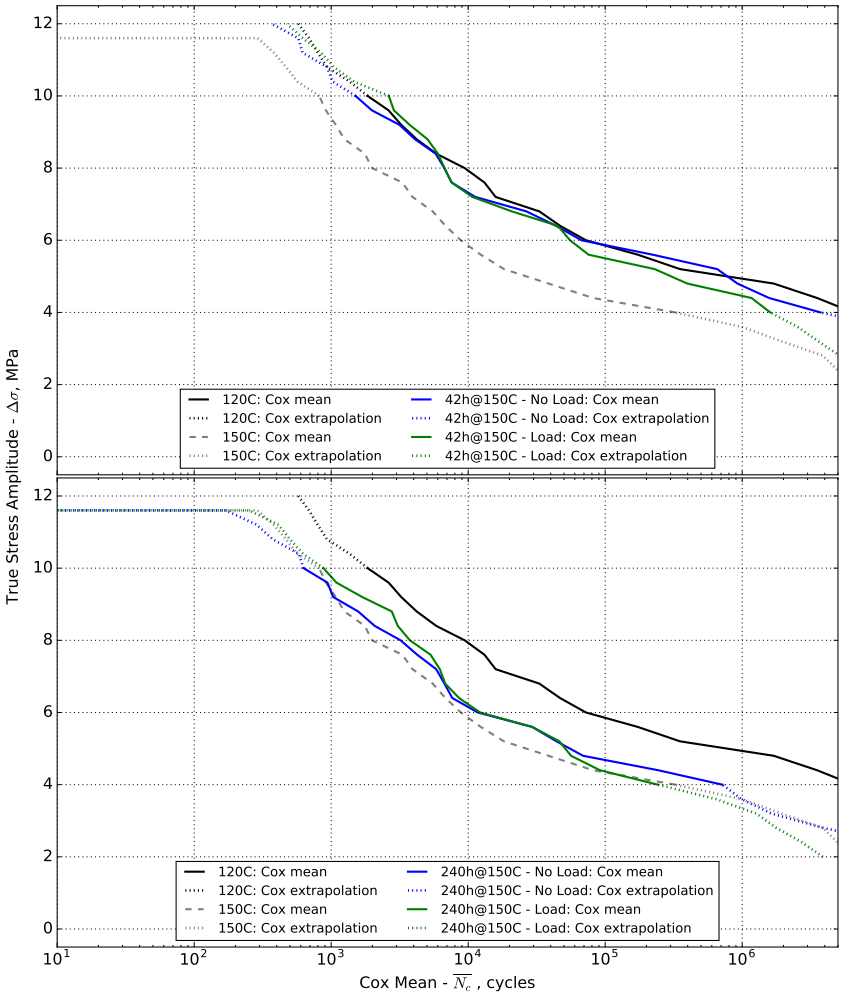

Figure 5.4-7 – Mean fatigue lives of blend A36H96 after pre-aging at 150 °C for two pre-aging loading conditions and two durations; comparison to fatigue lives of virgin specimens and fatigue lives tested at 150 °C.

tests carried out at 150 °C. Once again, there is only a slight difference in fatigue lives due to the two pre-aging loading conditions. At low true stress amplitudes, fatigue life is slightly longer for material pre-aged under load with respect to the one pre-aged without a load.

Application of the TTS approach

Using the predictive features of the Cox models, an approach identical to those use by Ngolemasango et al. (2008), Broudin et al. (2015), and Neuhaus et al. (2017) is applied for HNBR. *Model 2*, where pre-aging is carried out under load, is used as an example. A set of pre-aging temperatures and durations is chosen as shown in Table 5.4-2. The fatigue life means are predicted at loading level of 4 MPa at each

Table 5.4-2 – Pre-aging temperatures and durations to be predicted by the model.

Pre-aging Durations	**Pre-aging Temperatures**		
	140°C (413.15 K)	**150°C (423.15 K)**	**160°C (433.15 K)**
120 h	X	X	X
240 h	X	EXP	X
480 h	X	X	X
960 h	X	X	X

temperature and duration; the means are said to be equal to

$$N_a = N_0 \exp\left(-t_a a\right), \tag{5.4-2}$$

where N_0 is the mean fatigue life of a virgin material at 4 MPa, t_a is the pre-aging duration, and a is the shift factor. It is given by

$$a = A \exp\left(\frac{E_a}{RT_a}\right), \tag{5.4-3}$$

where A is a pre-exponential factor that is dependent on the reference temperature, E_a is the activation energy, R is the gas constant, and T_a is the pre-aging temperature.

First, the shift factor, a of Eq. (5.4-2) is fitted for predicted fatigue lives using maximum likelihood estimation (implemented in *Python* with the use of *NumPy* library). Subsequently, the natural log of the shift factor is plotted with respect to temperature. The results are shown in Figure 5.4-8, where the fit of fatigue lives is shown on the top and the fit of the shift factor on the bottom. The model predicts that the effect of aging duration is more important than the temperature; as such, fatigue lives are almost identical at 480 h and 960 h. The overall fit of mean fatigue lives is not completely satisfactory, but it provides with a value for activation energy of $E_a \approx 18$ kJ/mol. The reported value of the activation energy for HNBR varies from 48 to 72 kJ/mol (Le Huy and Evrard 1998; Lee et al. 2011; Kömmling et al. 2016). Even though the values of E_a change with respect to performed test (there are no E_a values for fatigue of HNBR), it appears that the derived value is strongly underestimated.

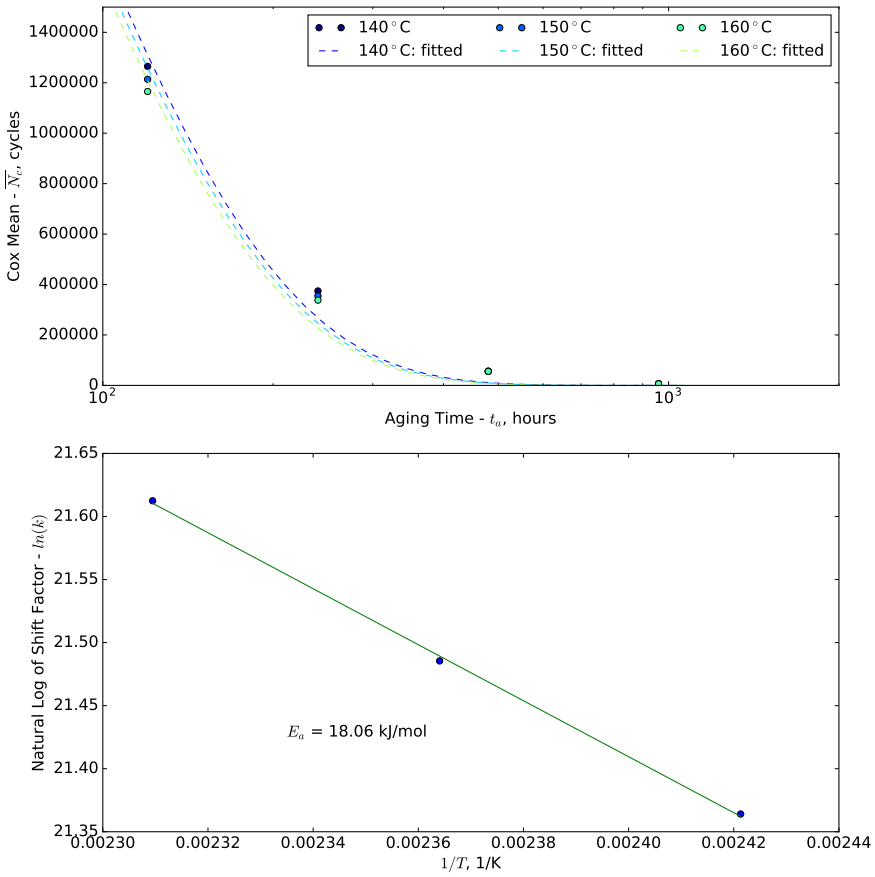

Figure 5.4-8 – Fitting of predicted mean fatigue lives (top) and shift factor (bottom).

However, if one recalls, actual experiments have been carried out on pre-aged specimens only at one temperature of 150 °C and at two durations of 42 h and 240 h; moreover, the actual maximum duration is extrapolated by 400% up to 960 h, which for all intents and purposes can be said to be optimistic. Nevertheless, since it is known that application of the TTS approach with actual experiments is time consuming, it appears that this probabilistic approach could be promising, if the actual pre-aging and fatigue experiments could be limited to two or three temperatures and durations. The model, then, can be used to predict the results by interpolation or extrapolation and, thereby, the actual experimentation time could be reduced. However, all of the above is possible only if the assumption of the uniform effect of increasing temperature on thermal degradation holds true.

5.4.2 Fatigue damage analysis

Only macroscopic analysis has been carried out for all tested specimens of blend A36H96. This is based on the fact that all fracture surfaces showed almost identical features:

- No micro-cracking has been observed irrespective of the pre-aging loading conditions and durations;
- Crack growth occurred on a single plane perpendicular to the direction of

loading in all failed specimens; no propagation in vertical direction has been observed;

- 95% of specimens failed specimens had a vertical propagation length of less than 1% of the specimen lengths for pre-aging under no load; the corresponding percentage for pre-aging under load is around 92%.

5.5 Initial Approach for Reconciliation of Simultaneous Testing and Pre-Aging Results

By chance, the fatigue lives of specimens pre-aged for 10 days at 150 °C and then subjected to fatigue life tests at 120 °C (Test 3) appear to roughly coincide with fatigue lives carried out at 150 °C on virgin specimens (Test 2). With the limited results presented in this chapter, it is difficult to make concrete conclusions about the connection between the two tests. However, the results do indicate that the fatigue testing temperature is the most significant factor affecting fatigue lives. For blend A36H96, pre-aging duration of 245 h is roughly equivalent to a fatigue life test at 150 °C, whose duration is only about 18 h.

Based on this coincidence, a link between the two tests is tried with the following phenomenological approach. The idea is, for a given fatigue life test at some high temperature (*e.g.* 150 °C), to find an equivalent fatigue test at reference temperature (*e.g.* 120 °C) that is carried out on specimens, pre-aged at that specific high temperature (*e.g.* 150 °C). In this case, the time required to pre-age the specimens (under no load) is to be determined. With the available results of Tests 2 and 3, such time is equal to around 245 h as mentioned earlier.

Ignoring the limitations of the models presented in Eq. (5.3-1) (Section 5.3.1) and Eq. (5.4-1) (Section 5.4.1), they can be used to predict mean fatigue lives at various high temperatures and with varying pre-aging duration. Model on the simultaneous test from Eq. (5.3-1) is used to predict fatigue lives of A36H96 at high temperatures ranging from 150 °C to 200 °C; model on pre-aging from Eq. (5.4-1) is used to predict fatigue lives with varying pre-aging temperatures, from 150 °C to 200 °C, and varying pre-aging durations. For example, simultaneous model is used to determine a mean fatigue life curve from 4 to 10 MPa at a temperature of 200 °C; pre-aging model is then used to predict the time required to pre-age the specimen at the same temperature of 200 °C. This model is implemented numerically in *Python* with the *NumPy* package. For a given temperature (T_f), first a mean fatigue life curve is extracted from the simultaneous test model. Subsequently, similar curves are extracted from the pre-aging model at T_f, but at different pre-aging times (t_a); the step for time intervals is 5 h. At each step, a fatigue life curve, corresponding to pre-aging of specific time, is compared to the fatigue life curve extracted from the simultaneous test model at the given temperature. Since the two curves are not exactly parallel in most cases, the closeness of the match between the curves is determined by calculating the standard deviation[3] of the difference between fatigue lives of two curves in log-scale; this standard deviation is calculated over the range of 4 to 10 MPa. The closest match is deemed for a pre-aging time that has corresponding lowest value of the standard deviation.

Figure 5.5-1 shows the calculated pre-aging times with respect to the pre-aging temperature; testing at the same temperature will provide a similar fatigue life curve. Various functions have been tried and an exponential fit provides the best fit

[3]If one recalls, this is the same approach used earlier in Chapter 3, Section 3.4, to determine how "flat" and constant applied true stress is; refer to Eq. 3.3-4

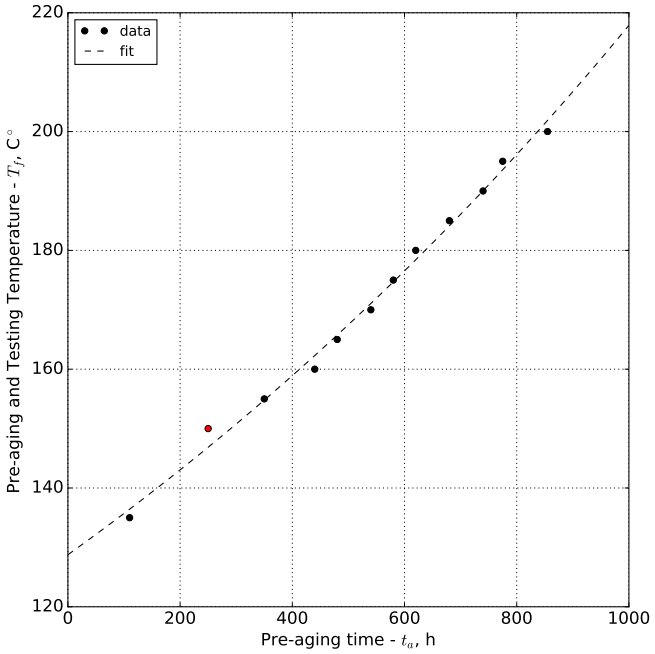

Figure 5.5-1 – Simulated pre-aging time (t_a) at pre-aging temperature (T_f), required to achieve similar fatigue life tested at T_f; red marker indicates the carried out experiment.

with a regression coefficient of $r^2 = 0.992$, and can be expressed as

$$T_f = T_{th} \exp\left(B t_a\right), \tag{5.5-1}$$

where t_a is the pre-aging duration, B is a fitted value, T_f is the testing and the pre-aging temperature, and T_{th} is a threshold temperature. This value equals to 128.7 °C and indicates that from 120 °C to this threshold no effects of high temperature will be observed during fatigue life testing. Thus, ideally, T_{th} should equal to 120 °C, and the difference can be perhaps explained by lack of wide-ranging source data for the models used to predict the effects of pre-aging and simultaneousing.

5.6 Summary and Conclusions

Simultaneous aging and fatigue

As percent hydrogenation increases, HNBR has higher resistance to heat; thus, percent hydrogenation plays an important role in fatigue resistance as temperature is increased from 120 °C to 150 °C. The decrease in fatigue life at high temperatures is the smallest for blend A36H99 with 99% of hydrogenation followed by A36H96 (96%); and finally, A36H91 (91%) has the largest decrease in fatigue life. For these two blends that have poorer resistance to heat (A36H96 and A36H91), first results point to the fact that testing for longer durations at low loading amplitudes, which are relatively longer as compared to short tests at high amplitudes, is more detrimental with respect to fatigue life. As a consequence, this points to an accumulation of damage due to high temperatures. As a perspective, tests could be carried out at adjusted frequencies so that the duration of tests at high temperatures are equal for all stress loading levels, which would allow to better isolate time effects.

From both microscopic and macroscopic analyses, it is evident that the fatigue damage mechanisms at 150 °C change with respect to those observed at 120 °C. Comparing the damage observed for blends A36H96 and A36H99 at 150 °C, it is clear that the HNBR with 99% hydrogenation retains to the greatest extent the damage mechanisms with vertical propagation of cracks, which are associated with longer fatigue lives and slower fatigue crack growth at 120 °C. Subsequently, the number of fracture surfaces, where initiation and propagation happens on a single plane perpendicular to the direction of loading, increases during testing at 150 °C. Moreover, there is a greater occurrence of "smooth" fracture surfaces with no indication of the propagation phase of fatigue crack growth. These two phenomena point to a faster and more "brittle" fracture at 150 °C.

Pre-aging and fatigue

Primarily, it is impossible to positively conclude whether there are any effects of pre-aging at 150 °C with or without load on HNBR blend A36H96. The first results indicate a very slight decrease in fatigue lives at low loading levels, if specimens have been pre-aged with load.

Additionally, there appears to be some pre-aging time threshold, where aging up to 42 h did not show significant differences with respect to virgin specimens. As pre-aging duration is increased to 240 h (10 days), there is an almost uniform decrease in fatigue lives at all loading levels for specimens pre-aged without load, which is illustrated by nearly parallel shift in fatigue live curves on a log-scale. For specimens pre-aged under load, there is a greater decrease in fatigue lives at low stress amplitudes as compared to high stress amplitudes. Pre-aging changes the fatigue damage mechanisms. Preliminary macroscopic analysis showed that, in all specimens, crack growth occurs on a single plane perpendicular to the direction of loading.

Finally, the previously presented probabilistic model (Chapter 4) has been tried to predict fatigue lives for different aging temperatures and durations, which are then modeled by an Arrhenius based time-temperature superposition (TTS) approach

that is widely encountered in the literature. This approach shows promising results, which could reduce the times required for fatigue life test on pre-aged specimens.

Chapter 6

General Conclusion

A considerable amount of results have been presented in this thesis. The focus on HNBR, with its relatively complex mechanical response and the lack of published literature, has caused some initial obstacles, the solution of which has allowed to highlight some new insights, develop new methodologies, and investigate the material itself as originally envisaged.

As such, the originality of this work corresponds to our initial industrial and scientific objectives set for this project; these can be roughly split into two major contributions:

- Improvement of fatigue life methods utilized for elastomers: from the basics of testing in true stress as foreseen initially by Wöhler to novel application of promising statistical tools;
- Knowledge of fatigue characteristics of HNBR with fatigue life tests, fatigue crack propagation experiments, and microscopic fatigue damage analysis, all the while taking into account the effects of formulation - acrylonitrile content, percent hydrogenation, and of a composite blend;

and two minor contributions:

- First results on the effects of the thermal aging: coupling between pre-aging, high temperature, and fatigue;
- A quantitative evaluation of the presence of strain-induced crystallization in unfilled HNBR, in consideration of ACN content.

As presented in Chapter 2, the mechanical investigation of HNBR has shown that the blends exhibit plastic or viscoplastic responses in tensile loading at room temperature. Presence of such inelastic behavior is attributed to the relatively high glass transition temperature of HNBR blends; the closer the testing temperature is to the glassy-rubbery transition phase, the more inelasticity is observed. As temperature is increased up to 120 °C, which is the median operating temperature of HNBR, the mechanical responses of the HNBR blends become less inelastic. However, at this temperature, the remaining inelastic effects are of great significance during cyclic loading. Specifically, this inelasticity is characterized by two stress-softening phenomena: the Mullins effect and long-term cyclic stress relaxation.

These two phenomena are closely linked to the discussion of conventional fatigue life testing methods utilized at present for elastomers and, specifically, to their limitations. As described in Chapter 3, dating back to the first studies of 1940s, these methods most often consist in application of a constant displacement cyclic loading. In the present work, it has been shown how this approach, at best, can be applied only to roughly approximate the history of mechanical loading (stretch, true stress, or energy); at worst, this approach is not valid. The root of the problem lies in the fact that controlling tests in terms of experimental parameters (displacement or force) does not reflect the actual mechanical history that has been endured by a material; calculation of mechanical parameters *a posteriori* could provide erroneous conclusions about fatigue resistance and, thus, complicate comparisons between different materials, testing conditions, *etc.* HNBR is a useful material to highlight these limitations.

In Chapter 3, a novel procedure for testing in true stress control has been developed and implemented experimentally: HNBR blend A44H96 has been used for the successful validation of the procedure. The procedure can be summarized as follows:

- First, *a priori* actual specimen cross-section area is predicted throughout the duration of an experiment;
- Then, a machine algorithm permits to reach a constant true stress amplitude target during testing of a single specimen;
- The procedure is also extended to parallel testing by creation of master displacement curves, which are considered to carry out tests on multiple specimens in parallel using a custom home-made experimental setup.

Another main drawback of fatigue testing has been tackled. Indeed, significant scattering is always observed in fatigue life experiments, irrespective of the material, but it is especially problematic for synthetic elastomers, such as HNBR. Standard statistical tools are reviewed and applied. However, of greater interest are statistical tools novel in their application to elastomers: these are the Kaplan-Meier estimate and the Cox proportional hazards model, which are borrowed from medical sciences and are applied here to fatigue results. The Cox model is especially useful in dealing with two issues encountered in the given fatigue results: scattering in both fatigue life measurements and applied true stress (multivariate analysis), and presence of right censored data that corresponds to unbroken specimens after a certain amount of cycles.

In Chapter 4, these new methods are then applied to investigate the effects of formulation - ACN content, percent hydrogenation, and of composite blend - on fatigue resistance at 120 °C. The fatigue life tests are supplemented by fatigue crack propagation tests. To obtain a comprehensive picture of the fatigue phenomenon in HNBR, optical and scanning electron microscopy is utilized to describe fatigue damage mechanisms. In general, the three experimental approaches show that A36H96 (36 wt.-% ACN and 96% hydrogenation) has the best fatigue resistance. The general effects of formulation can be summarized as follows:

- As ACN content is increased to 44 wt.-% (A44H96), fatigue resistance is slightly reduced, but seems to be better at high loading levels; as ACN content is decreased to 24 wt.-% (A24H96), fatigue resistance is greatly reduced;

- As percent hydrogenation is increased to 99% (A36H99), there is also a slight decrease in fatigue resistance; as it is reduced to 91% (A36H91), fatigue resistance, especially in terms of crack propagation, decreases to a greater extent;
- The composite blend (A44-24) of both 24 wt.-% (A24H96) and 44 wt.-% of ACN (A44H96) for an average of 36 wt.-% of ACN inherits the poor fatigue resistance characteristics of the blend with 24 wt.-% of ACN (A24H96).

Finally, Chapter 5 presents an initial study of both thermal aging and fatigue. A perspective approach for investigation of the two phenomena are discussed. First, simultaneous fatigue life tests are carried out at an elevated temperature of 150 °C. Results make it clear how percent hydrogenation has a beneficial effect on heat resistance. HNBR blend with the highest percent hydrogenation, A36H99, showed the least reduction in fatigue life durations; whereas, A36H91, the blend with the lowest percent hydrogenation, exhibited the greatest reduction in fatigue life. The second test involves classical preliminary aging at 150 °C with subsequent fatigue testing at 120 °C. The results of these tests are then compared to those obtained in Chapter 4 on virgin specimens and the simultaneous tests at 150 °C. Moreover, upon application of a statistical model, a promising procedure is proposed to reduce the duration of generally time-consuming pre-aging/fatigue experiments. As the last step, the three fatigue life tests are combined and a phenomenological relationship between them is established, which shows an exponential relationship between pre-aging times and tests at high temperatures.

Last, but not least, we return to Chapter 2, where the quantitative results of strain-induced crystallization (SIC) of HNBR have been given for two unfilled blends of HNBR with 44 wt.-% and 36 wt.-% ACN. As ACN content increases, the incidence of SIC also increases. Moreover, SIC onset and melting occur at lower stretch ratios for the higher ACN content HNBR blend.

The obtained results also pose some new questions. The perspectives are the following:

- It would be of great interest to investigate fatigue lives of the blends at different temperatures. It is well known that lower ACN content HNBR blends are utilized at low temperatures; therefore, it is interesting how the ranking of the blends evolves as temperature decreases, *i.e.* whether fatigue resistance of A24H96 improves.
- Moreover, it would also be of interest to differentiate between the three blends with similar fatigue crack propagation behaviors - A44H96, A36H96, and A36H99; more specifically, to determine whether fatigue thresholds exist for these materials and, if they do, how they differ.
- As discussed in Chapter 4, these blends (A44H96, A36H96, and A36H99) also exhibit interesting fatigue damage mechanisms, where crack growth occurs in parallel to the direction of loading. This could be further investigated with *in-situ* tests or interrupted fatigue life experiments.
- Complementary tests on the effects of pre-aging at 150 °C of blends A36H91 and A36H99 would be useful in obtaining a full picture of the effects of percent hydrogenation on fatigue resistance of HNBR.

- As for more long-term perspectives, a more comprehensive study on the effects of thermal aging and fatigue is to be carried out. A more detailed database of results is needed to validate the phenomenological predictions proposed in the present work.

Bibliography

[1] R. B. Abernethy. *The New Weibull Handbook*. R.B. Abernethy, 1996 (cit. on p. 91).

[2] A. Ahagon, M. Kida, and H. Kaidou. "Aging of tire parts during Service. I. Types of aging in heavy-duty tires." In: *Rubber Chemistry and Technology* 63.5 (Nov. 1990), pp. 683–697. DOI: 10.5254/1.3538282 (cit. on p. 161).

[3] P. A. Albouy, G. Guillier, D. Petermann, A. Vieyres, O. Sanseau, and P. Sotta. "A stroboscopic X-ray apparatus for the study of the kinetics of strain-induced crystallization in natural rubber." In: *Polymer (United Kingdom)* 53.15 (2012), pp. 3313–3324. DOI: 10.1016/j.polymer.2012.05.042 (cit. on pp. 17, 27, 28, 29, 51).

[4] P. A. Albouy, A. Vieyres, R. Pérez-Aparicio, O. Sanséau, and P. Sotta. "The impact of strain-induced crystallization on strain during mechanical cycling of cross-linked natural rubber." In: *Polymer (United Kingdom)* 55.16 (2014), pp. 4022–4031. DOI: 10.1016/j.polymer.2014.06.034 (cit. on p. 29).

[5] N. André, G. Cailletaud, and R. Piques. "Haigh diagram for fatigue crack initiation prediction of natural rubber components." eng. In: *KGK-Kautschuk und Gummi Kunststoffe* 52.2 (1999), pp. 120–123 (cit. on pp. 61, 64, 65).

[6] R. D. Andrews, A. V. Tobolsky, and E. E. Hanson. "The theory of permanent set at elevated temperatures in natural and synthetic rubber vulcanizates." In: *Journal of Applied Physics* 17.5 (May 1946), pp. 352–361. DOI: 10.1063/1.1707724 (cit. on pp. 161, 162).

[7] E. M. Arruda and M. C. Boyce. "A three-dimensional constitutive model for the large stretch behavior of rubber elastic materials." In: *Journal of the Mechanics and Physics of Solids* 41.2 (1993), pp. 389–412. DOI: 10.1016/0022-5096(93)90013-6 (cit. on p. 78).

[8] S. Asare, A. G. Thomas, and J. J. C. Busfield. "Cyclic stress relaxation (CSR) of filled rubber and rubber components." In: *Rubber Chemistry and Technology* 82.1 (Mar. 2009), pp. 104–112. DOI: 10.5254/1.3557000 (cit. on p. 63).

[9] ASTM International. *ASTM D4482 - 11: Standard Test Method for Rubber Property-Extension Cycling Fatigue*. 2017 (cit. on pp. 61, 64, 88, 94).

[10] G. Ayoub, F. Zaïri, M. Naït-Abdelaziz, and J. Gloaguen. "Modeling the low-cycle fatigue behavior of visco-hyperelastic elastomeric materials using a new network alteration theory: Application to styrene-butadiene rubber." In: *Journal of the Mechanics and Physics of Solids* 59.2 (2011), pp. 473–495. DOI: 10.1016/j.jmps.2010.09.016 (cit. on pp. 62, 63, 64).

[11] G. Ayoub, F. Zaïri, M. Naït-Abdelaziz, J. Gloaguen, and G. Kridli. "A visco-hyperelastic damage model for cyclic stress-softening, hysteresis and perma-

nent set in rubber using the network alteration theory." In: *International Journal of Plasticity* 54 (2014), pp. 19–33. DOI: 10.1016/j.ijplas.2013.08.001 (cit. on p. 63).

[12] O. H. Basquin. "The exponential law of endurance tests." In: *Proc Astm.* Vol. 10. 1910, pp. 625–630 (cit. on p. 89).

[13] J. R. Beatty. "Fatigue of rubber." In: *Rubber Chemistry and Technology* 37.5 (1964), pp. 1341–1364. DOI: 10.5254/1.3540402 (cit. on pp. 61, 109).

[14] H. Bender and E. Campomizzi. "Improving the heat resistance of hydrogenated nitrile rubber compounds Part 1: Aging mechanisms for high saturation rubber compounds." In: *Kautschuk Gummi Kunststoffe* 54.1-2 (2001), pp. 14–21 (cit. on pp. 163, 164).

[15] A.-S. Béranger, J. Qin, P. Heuillet, and H. Baurier. "Fatigue crack growth behavior of NBR , HNBR , HNBR ZSC compounds." In: *Fatigue Design 2017.* November. Senslis, 2017, pp. 29–30 (cit. on pp. 115, 116).

[16] J. S. Bergström and M. C. Boyce. "Constitutive modeling of the large strain time-dependent behavior of elastomers." In: *Journal of the Mechanics and Physics of Solids* 46.5 (1998), pp. 931–954. DOI: 10.1016/S0022-5096(97)00075-6 (cit. on p. 62).

[17] S. Beurrot, B. Huneau, and E. Verron. "In situ SEM study of fatigue crack growth mechanism in carbon black-filled natural rubber." In: *Journal of Applied Polymer Science* 117.3 (Aug. 2010), NA–NA. DOI: 10.1002/app.31707 (cit. on p. 111).

[18] S. Beurrot-Borgarino, B. Huneau, E. Verron, and P. Rublon. "Strain-induced crystallization of carbon black-filled natural rubber during fatigue measured by in situ synchrotron X-ray diffraction." In: *International Journal of Fatigue* 47 (2013), pp. 1–7. DOI: 10.1016/j.ijfatigue.2012.07.001 (cit. on pp. 17, 65).

[19] S. Bhattacharjee, A. K. Bhowmick, and B. N. Avasthi. "Degradation of hydrogenated nitrile rubber." In: *Polymer Degradation and Stability* 31.1 (1991), pp. 71–87. DOI: 10.1016/0141-3910(91)90097-B (cit. on p. 163).

[20] A. K. Bhowmick, G. B. Nando, S. Basu, and S. K. De. "Scanning electron microscopy studies of fractured natural rubber surfaces." In: *Rubber Chemistry and Technology* 53.2 (May 1980), pp. 327–334. DOI: 10.5254/1.3535045 (cit. on p. 108).

[21] D. M. Bielinski, L. Slusarski, A. Wlochowicz, and C. Slusarczyk. "Structure and mechanical properties of nitrile rubbers modified with iodine." In: *Journal of Applied Polymer Science* 67.3 (Jan. 1998), pp. 501–512 (cit. on p. 20).

[22] D. Braun, A. Haufe, D. Leiß, and G. P. Hellmann. "Strain-induced crystallisation and miscibility behaviour of hydrogenated nitrile rubbers." In: *Angewandte Makromolekulare Chemie* 202.1 (Dec. 1992), pp. 143–158. DOI: 10.1002/apmc.1992.052020109 (cit. on pp. 19, 20, 21, 48, 53, 54).

[23] M. Broudin, V. Le Saux, Y. Marco, P. Charrier, and W. Hervouet. "Investigation of thermal aging effects on the fatigue design of automotive anti-vibration parts." In: *Constitutive Models for Rubber IX.* Ed. by B. Marvalova and I. Petrikova. CRC Press, 2015, pp. 53–57 (cit. on pp. 168, 169, 172, 192).

[24] K. Brüning, K. Schneider, S. V. Roth, and G. Heinrich. "Kinetics of strain-induced crystallization in natural rubber studied by WAXD: Dynamic and

impact tensile experiments." In: *Macromolecules* 45.19 (2012), pp. 7914–7919. DOI: 10.1021/ma3011476 (cit. on p. 17).

[25] S. M. Cadwell, R. A. Merrill, C. M. Sloman, and F. L. Yost. "Dynamic fatigue life of rubber." In: *Industrial & Engineering Chemistry Analytical Edition* 12.1 (1940), pp. 19–23. DOI: 10.1021/ac50141a006 (cit. on pp. 61, 64).

[26] N. Candau, L. Chazeau, J. M. Chenal, C. Gauthier, J. Ferreira, E. Munch, and C. Rochas. "Characteristic time of strain induced crystallization of crosslinked natural rubber." In: *Polymer* 53.13 (2012), pp. 2540–2543. DOI: 10.1016/j.polymer.2012.04.027 (cit. on p. 17).

[27] N. Candau, L. Chazeau, J. M. Chenal, C. Gauthier, and E. Munch. "Compared abilities of filled and unfilled natural rubbers to crystallize in a large strain rate domain." In: *Composites Science and Technology* 108 (2015), pp. 9–15. DOI: 10.1016/j.compscitech.2014.12.014 (cit. on p. 17).

[28] N. Candau, R. Laghmach, L. Chazeau, J.-M. Chenal, C. Gauthier, T. Biben, and E. Munch. "Influence of strain rate and temperature on the onset of strain induced crystallization in natural rubber." In: *European Polymer Journal* 64 (2015), pp. 244–252. DOI: 10.1016/j.eurpolymj.2015.01.008 (cit. on p. 17).

[29] M. Celina, K. Gillen, and R. Assink. "Accelerated aging and lifetime prediction: Review of non-Arrhenius behaviour due to two competing processes." In: *Polymer Degradation and Stability* 90.3 (Dec. 2005), pp. 395–404. DOI: 10.1016/J.POLYMDEGRADSTAB.2005.05.004 (cit. on p. 171).

[30] G. Chagnon, E. Verron, L. Gornet, G. Marckmann, and P. Charrier. "On the relevance of Continuum Damage Mechanics as applied to the Mullins effect in elastomers." In: *Journal of the Mechanics and Physics of Solids* 52.7 (2004), pp. 1627–1650. DOI: 10.1016/j.jmps.2003.12.006 (cit. on p. 17).

[31] K. S. Chan, M. Koike, R. L. Mason, and T. Okabe. "Fatigue life of titanium alloys fabricated by additive layer manufacturing techniques for dental implants." In: *Metallurgical and Materials Transactions A: Physical Metallurgy and Materials Science* 44.2 (2013), pp. 1010–1022. DOI: 10.1007/s11661-012-1470-4 (cit. on p. 95).

[32] D. J. Charlton, J. Yang, and K. K. Teh. "A review of methods to characterize rubber elastic behavior for use in finite element analysis." In: *Rubber Chemistry and Technology* 67.3 (July 1994), pp. 481–503. DOI: 10.5254/1.3538686 (cit. on p. 65).

[33] P. Charrier, Y. Marco, V. L. Saux, and R. Ranaweera. *On the influence of heat ageing on filled NR for AVS automotive applications.* Ed. by S. Jerrams and N. Murphy. CRC Press, 2011 (cit. on pp. 167, 168, 169).

[34] J.-H. Choi, H. Jin Kang, H.-Y. Jeong, T.-S. Lee, and S.-J. Yoon. "Heat aging effects on the material property and the fatigue life of vulcanized natural rubber, and fatigue life prediction equations." In: *Journal of Mechanical Science and Technology* 19.6 (2005), pp. 1229–1242. DOI: 10.1007/BF02984044 (cit. on pp. 64, 168).

[35] D. Cousineau. "Fitting the three-parameter weibull distribution: review and evaluation of existing and new methods." In: *IEEE Transactions on Dielectrics and Electrical Insulation* 16.1 (Feb. 2009), pp. 281–288. DOI: 10.1109/TDEI.2009.4784578 (cit. on p. 91).

[36] D. R. Cox. "Regression models and life-tables." In: *Journal of the Royal Statistical Society. Series B (Methodological)*. Vol. 34. 2. 1972, pp. 187–220. DOI: 10.1007/978-1-4612-4380-9{_}37 (cit. on p. 96).

[37] J. De Eskinazi, K. Ishihara, H. Volk, and T. C. Warholic. "Towards predicting relative belt edge endurance with the finite element method." In: *Tire Science and Technology* 18.4 (1990), pp. 216–235. DOI: 10.2346/1.2141701 (cit. on p. 62).

[38] C. J. Derham and A. G. Thomas. "Creep of rubber under repeated stressing." In: *Rubber Chemistry and Technology* 50.2 (May 1977), pp. 397–402. DOI: 10.5254/1.3535153 (cit. on p. 63).

[39] G. C. Derringer. "Statistical methods in rubber research and development." In: *Rubber Chemistry and Technology* 61.3 (July 1988), pp. 377–421. DOI: 10.5254/1.3536194 (cit. on p. 90).

[40] J. L. DeRudder. "Statistical distribution analysis of rubber fatigue data." In: *Journal of Applied Physics* 52.10 (Oct. 1981), pp. 5887–5891. DOI: 10.1063/1.329825 (cit. on p. 90).

[41] J. Diani, B. Fayolle, and P. Gilormini. "A review on the Mullins effect." In: *European Polymer Journal* 45.3 (2009), pp. 601–612. DOI: 10.1016/j.eurpolymj.2008.11.017 (cit. on pp. 16, 41).

[42] E. S. Dizon, A. E. Hicks, and V. E. Chirico. "The effect of carbon black parameters on the fatigue life of filled rubber compounds." In: *Rubber Chemistry and Technology* 47.1 (Mar. 1974), pp. 231–249. DOI: 10.5254/1.3540429 (cit. on p. 90).

[43] X. Duan, W.-B. Shangguan, M. Li, and S. Rakheja. "Measurement and modelling of the fatigue life of rubber mounts for an automotive powertrain at high temperatures." In: *Proceedings of the Institution of Mechanical Engineers, Part D: Journal of Automobile Engineering* 230.7 (June 2015), pp. 942–954. DOI: 10.1177/0954407015597795 (cit. on pp. 63, 64, 67, 166).

[44] J. R. Dunn, J. Scanlan, and W. F. Watson. "Stress relaxation during the thermal oxidation of vulcanized natural rubber." In: *Transactions of the Faraday Society* 55.0 (Jan. 1959), p. 667. DOI: 10.1039/tf9595500667 (cit. on p. 162).

[45] K. Farhangdoost and M. Siahpoosh. "On the fatigue life prediction of die-marked drillpipes." In: *Design and Analysis*. Vol. 3. ASME, Jan. 2006, pp. 461–468. DOI: 10.1115/PVP2006-ICPVT-11-93181 (cit. on p. 96).

[46] J. D. Ferry. *Viscoelastic properties of polymers*. Wiley, 1980, p. 641 (cit. on p. 13).

[47] J. H. Fielding. "Flex life and crystallization of synthetic rubber." In: *Industrial and Engineering Chemistry* 35.12 (1943), pp. 1259–1261. DOI: 10.1021/ie50408a008 (cit. on pp. 61, 64).

[48] E. Fišerová, M. Chvosteková, B. Silvie, and M. Bumbálek. "Survival analysis of factors influencing cyclic fatigue of nickel-titanium endodontic instruments." In: 2015 (2015) (cit. on pp. 95, 96).

[49] S. G. Fitzgerald, R. A. Cooper, M. L. Boninger, and A. J. Rentschler. "Comparison of fatigue life for 3 types of manual wheelchairs." In: *Archives of Physical Medicine and Rehabilitation* 82.10 (2001), pp. 1484–1488. DOI: 10.1053/apmr.2001.26139 (cit. on p. 95).

[50] M. Flamm, J. Spreckels, T. Steinweger, and U. Weltin. "Effects of very high loads on fatigue life of NR elastomer materials." In: *International Journal*

of Fatigue 33.9 (Sept. 2011), pp. 1189–1198. DOI: 10.1016/J.IJFATIGUE.2011.03.008 (cit. on pp. 111, 147).

[51] P. Forrest. *Fatigue of Metals*. Oxford : Pergamon, 1962, p. 434. DOI: 10.1016/B978-0-08-009729-9.50003-8 (cit. on p. 60).

[52] J. Fox and S. Weisberg. "Cox proportional-hazards regression for survival data in R." In: *An R Companion to Applied Regression, Second Edition*. Sage Publications, 2011 (cit. on pp. 98, 130).

[53] L. Gargani and M. Bruzzone. "Fatigue resistance of polybutadienes and effect of microstructure." In: *Advances in elastomers and rubber elasticity*. Plenum Press, 1986, p. 242 (cit. on p. 90).

[54] S. Gauchet. "Etude de l'influence du type de noir de carbone sur la tenue en fatigue de caoutchouc HNBR." PhD thesis. Université Francois Rabelais, 2007 (cit. on pp. 112, 113, 116, 117, 146).

[55] U. Genschel and W. Q. Meeker. "A comparison of maximum likelihood and median-rank regression for weibull estimation." In: *Quality Engineering* 22.4 (Aug. 2010), pp. 236–255. DOI: 10.1080/08982112.2010.503447 (cit. on p. 91).

[56] A. N. Gent. "On the relation between indentation hardness and young's modulus." In: *Rubber Chemistry and Technology* 31.4 (Sept. 1958), pp. 896–906. DOI: 10.5254/1.3542351 (cit. on p. 46).

[57] A. N. Gent, P. B. Lindley, and A. G. Thomas. "Cut growth and fatigue of rubbers. I. The relationship between cut growth and fatigue." In: *Rubber Chemistry and Technology* 38 (1964), pp. 292–300. DOI: 10.5254/1.3535648 (cit. on pp. 61, 62).

[58] A. N. Gent and L.-Q. Zhang. "Strain-Induced Crystallization and Strength of Rubber." In: *Rubber Chemistry and Technology* 75.5 (Nov. 2002), pp. 923–934. DOI: 10.5254/1.3547692 (cit. on p. 17).

[59] A. N. Gent. *Engineering with Rubber*. 2012, pp. I–XVIII. DOI: 10.3139/9783446428713 (cit. on p. 162).

[60] K. T. Gillen, M. Celina, and M. R. Keenan. "Methods for predicting more confident lifetimes of seals in air environments." In: *Rubber Chemistry and Technology* 73.2 (May 2000), pp. 265–283. DOI: 10.5254/1.3547590 (cit. on p. 171).

[61] K. T. Gillen, R. L. Clough, and J. Wise. "Prediction of Elastomer Lifetimes from Accelerated Thermal-Aging Experiments." In: May 1996, pp. 557–575. DOI: 10.1021/ba-1996-0249.ch034 (cit. on pp. 162, 171).

[62] A. Goldberg, D. R. Lesuer, and J. Patt. "Fracture morphologies of carbon-black-loaded SBR subjected to low-cycle, high-stress fatigue." In: *Rubber Chemistry and Technology* 62.2 (May 1989), pp. 272–287. DOI: 10.5254/1.3536244 (cit. on p. 108).

[63] P. M. Grambsch and T. M. Therneau. "Proportional hazards tests and diagnostics based on weighted residuals." In: *Biometrika* 81.3 (Sept. 1994), pp. 515–526. DOI: 10.1093/biomet/81.3.515 (cit. on p. 98).

[64] A. A. Griffith. "The phenomena of rupture and flow in solids." In: *Philosophical Transactions of the Royal Society A: Mathematical, Physical and Engineering Sciences* 221.582-593 (1921), pp. 163–198. DOI: 10.1098/rsta.1921.0006 (cit. on p. 105).

[65] S. Hainsworth. "An environmental scanning electron microscopy investigation of fatigue crack initiation and propagation in elastomers." In: *Polymer Testing* 26.1 (Feb. 2007), pp. 60–70. DOI: 10.1016/J.POLYMERTESTING.2006.08.007 (cit. on pp. 110, 111).

[66] J. F. Hallett. "Multiaxial strength and fatigue of rubber compounds." PhD thesis. Loughborough University, 1997 (cit. on p. 90).

[67] K. Hashimoto, A. Maeda, K. Hosoya, and Y. Todani. "Specialty elastomers for automotive applications." In: *Rubber Chemistry and Technology* 71.3 (1998), pp. 449–519. DOI: 10.5254/1.3538491 (cit. on pp. 7, 8, 10).

[68] S. Hayashi, H. Sakakida, M. Oyama, and T. Nakagawa. "Low-temperature properties of Hydrogenated Nitrile Rubber (HNBR)." In: *Rubber Chemistry and Technology* 64.4 (Sept. 1991), pp. 534–544. DOI: 10.5254/1.3538571 (cit. on pp. 9, 10, 35).

[69] B. Huneau. "Strain-induced crystallization of natural rubber: a review of X-ray diffraction investigations." In: *Rubber Chemistry and Technology* 84.3 (2011), pp. 425–452. DOI: 10.5254/1.3601131 (cit. on pp. 17, 65).

[70] B. Huneau, I. Masquelier, Y. Marco, O. Brzokewicz, and P. Charrier. "Fatigue damage in carbon black filled natural rubber investigated by X-ray microtomography and scanning electron microscopy." In: *Constitutive Models for Rubber VIII*. Ed. by N. Gil-Negrete and A. Alonso. CRC Press, 2013 (cit. on p. 109).

[71] B. Huneau, I. Masquelier, Y. Marco, V. Le Saux, S. Noizet, C. Schiel, and P. Charrier. "Fatigue crack initiation in a carbon black–filled Natural Rubber." In: *Rubber Chemistry and Technology* 89.1 (2016), pp. 126–141. DOI: 10.5254/rct.15.84809 (cit. on pp. 61, 64, 109, 110, 124).

[72] T. Ikeda, B. Yamada, M. Tsuji, and S. Sakurai. "In situ copolymerization behaviour of zinc dimethacrylate and 2-(N-ethylperfluoro-octanesulphonamido)ethyl acrylate in hydrogenated nitrile-butadiene rubber during peroxide crosslinking." In: *Polymer International* 48.6 (June 1999), pp. 446–454. DOI: 10.1002/(SICI)1097-0126(199906)48:6<446::AID-PI159>3.0.CO;2-9 (cit. on p. 114).

[73] L. Imbernon, R. Pauchet, M. Pire, P. A. Albouy, S. Tenc-Girault, and S. Norvez. "Strain-induced crystallization in sustainably crosslinked epoxidized natural rubber." In: *Polymer (United Kingdom)* 93 (2016), pp. 189–197. DOI: 10.1016/j.polymer.2016.04.023 (cit. on p. 27).

[74] ISO 188. *Rubber, vulcanized or thermoplastic – Accelerated ageing and heat resistance tests*. 2011 (cit. on p. 174).

[75] ISO 7619-1. *Rubber, vulcanized or thermoplastic – Determination of indentation hardness – Part 1: Durometer method (Shore hardness)*. 2010 (cit. on p. 27).

[76] IUPAC. "radical (free radical)." In: *IUPAC Compendium of Chemical Terminology*. Research Triagle Park, NC: IUPAC. DOI: 10.1351/goldbook.R05066 (cit. on p. 162).

[77] R. Jiang and D. Murthy. "A study of Weibull shape parameter: Properties and significance." In: *Reliability Engineering & System Safety* 96.12 (Dec. 2011), pp. 1619–1626. DOI: 10.1016/J.RESS.2011.09.003 (cit. on p. 93).

[78] M. Johlitz. "On the representation of ageing phenomena." In: *The Journal of Adhesion* 88.7 (2012), pp. 620–648. DOI: 10.1080/00218464.2012.682905 (cit. on pp. 161, 162).

[79] M. Johlitz, N. Diercks, and A. Lion. "Thermo-oxidative ageing of elastomers: A modelling approach based on a finite strain theory." In: *International Journal of Plasticity* 63 (2014), pp. 138–151. DOI: 10.1016/j.ijplas.2014.01.012 (cit. on p. 162).

[80] M. Johnson, R. Ekins, N. Murphy, S. Jerrams, and J. Hanley. "The equibiaxial fatigue characteristics of EPDM under true (Cauchy) stress control conditions." In: *Constitutive Models for Rubber VIII*. Ed. by N. Gil-Negrete and A. Alonso. CRC Press, 2013 (cit. on p. 73).

[81] M. Kakudo and N. Kasai. "X-ray diffraction by polymers." In: *Kodansha Ltd.* (1972) (cit. on p. 28).

[82] E. L. Kaplan and P. Meier. "Nonparametric estimation from incomplete observations." In: *Journal of the American Statistical Association* 53.282 (1958), p. 457. DOI: 10.2307/2281868 (cit. on p. 95).

[83] J. Katz. "Rontgen spectographic testings on expanded rubber and its possible relevance for the problem of the extension characteristics of this substance." In: *Naturwissenschaften* 13 (1925), pp. 410–416 (cit. on p. 17).

[84] R. Keller. *Practical Guide to Hydrogenated Nitrile Butadiene Rubber Technology*. Smithers Rapra Technology Ltd, 2012 (cit. on pp. 7, 8, 9, 10, 12, 15, 35, 163).

[85] S. G. Kim and S.-H. Lee. "Effect of crosslink structures on the fatigue crack growth behavior of NR vulcanizates with various aging conditions." In: *Rubber Chemistry and Technology* 67.4 (Sept. 1994), pp. 649–661. DOI: 10.5254/1.3538700 (cit. on p. 171).

[86] W. Kim, M. Kim, Y.-W. Chang, J.-E. Shin, and J.-W. Bae. "Fatigue crack growth behavior of NR and HNBR based vulcanizates with potential application to track pad for heavy weight vehicles." In: *Macromolecular Research* 11.2 (Apr. 2003), pp. 73–79. DOI: 10.1007/BF03218333 (cit. on pp. 114, 115, 116).

[87] J. G. R. Kingston and A. H. Muhr. "Effects of strain crystallisation on cyclic fatigue of rubber." In: *6th Engineering Integrity Society International Conference on Durability and Fatigue* (2007) (cit. on p. 63).

[88] J. P. Klein and M. L. Moeschberger. *Survival Analysis : Techniques for Censored and Truncated Data*. Springer, 2003, p. 536 (cit. on pp. 90, 96).

[89] M. Klesnil and P. Lukáš. *Fatigue of Metallic Materials*. Elsevier, 1992, p. 270 (cit. on p. 60).

[90] R. C. Klingender. *Handbook of Specialty Elastomers*. Vol. 53. 1989, p. 160. DOI: 10.1017/CBO9781107415324.004 (cit. on pp. 9, 10).

[91] A. Kömmling, M. Jaunich, D. Wolff, A. Kimmling, M. Jaunich, and D. Wolff. "Effects of heterogeneous aging in compressed HNBR and EPDM O-ring seals." In: *Polymer Degradation and Stability* 126 (Apr. 2016), pp. 39–46. DOI: 10.1016/j.polymdegradstab.2016.01.012 (cit. on pp. 163, 165, 192).

[92] Y. Kubo, K. Hashimoto, and N. Watanbe. "Structure and properties of highly saturated nitrile elastomers." In: *Kautschuk Gummi Kunststoffe* 40.2 (1987), pp. 118–121 (cit. on p. 19).

[93] F. Kun, H. A. Carmona, J. S. Andrade, and H. J. Herrmann. "Universality behind Basquin's Law of Fatigue." In: *Physical Review Letters* 100.9 (Mar. 2008), p. 094301. DOI: 10.1103/PhysRevLett.100.094301 (cit. on p. 89).

[94] F. Lacroix, A. Tougut, N. Neelakantan, and N. Ranganathan. "A new approach for crack growth life of an elastomeric material." In: *ESIS -ECF 15 Sweden* (2013) (cit. on pp. 113, 114, 115).

[95] G. J. Lake and P. M. Lewis. *Interim report on ISO/TC 45/WG6 interlaboratory tests on tension fatigue resistance*. 1978 (cit. on p. 88).

[96] G. J. Lake and P. B. Lindley. "Cut growth and fatigue of rubbers. II. Experiments on a noncrystallizing rubber." In: *Journal of Polymer Science* 8 (1964), pp. 707–721 (cit. on p. 166).

[97] G. J. Lake and P. B. Lindley. "Mechanical fatigue limit for rubber." In: *Rubber Chemistry and Technology* 39.4 (Apr. 1965), pp. 348–364. DOI: 10.5254/1.3544847 (cit. on pp. 61, 107, 108, 138).

[98] G. J. Lake, A. Samsuri, S. C. Teo, and J. Vaja. "Time dependent fracture in vulcanized elastomers *." In: *Polymer* 32.16 (1991), pp. 2963–2975 (cit. on p. 122).

[99] G. Lake. "Fatigue and fracture of elastomers." In: *Rubber Chemistry and Technology* 68 (1995), pp. 435–460. DOI: 10.5254/1.3538750 (cit. on pp. 106, 107).

[100] Lanxess. *Therban 3446 Product Data Sheet*. 2010 (cit. on p. 10).

[101] Lanxess. *Zetpol HNBR Polymers - Carbon black study* (cit. on pp. 12, 15, 16).

[102] Lanxess. *Zetpol Technical Manual HNBR* (cit. on pp. 9, 35, 46).

[103] J.-B. Le Cam, B. Huneau, and E. Verron. "Failure analysis of carbon black filled styrene butadiene rubber under fatigue loading conditions." In: *Plastics, Rubber and Composites* 43.6 (2014), pp. 187–191. DOI: 10.1179/1743289814Y.0000000089 (cit. on pp. 117, 146).

[104] J.-B. Le Cam, B. Huneau, E. Verron, and L. Gornet. "Mechanism of fatigue crack growth in carbon black filled natural rubber." In: *Macromolecules* 37 (2004), pp. 5011–5017. DOI: 10.1021/ma0495386 (cit. on pp. 108, 110, 111).

[105] J.-B. Le Cam, B. Huneau, and E. Verron. "Fatigue damage in carbon black filled natural rubber under uni- and multiaxial loading conditions." In: *International Journal of Fatigue* 52 (July 2013), pp. 82–94. DOI: 10.1016/J.IJFATIGUE.2013.02.022 (cit. on pp. 109, 110, 111).

[106] P.-Y. Le Gac, M. Arhant, P. Davies, and A. Muhr. "Fatigue behavior of natural rubber in marine environment: Comparison between air and sea water." In: *Materials & Design* 65 (2015), pp. 462–467. DOI: 10.1016/j.matdes.2014.09.032 (cit. on pp. 61, 64).

[107] K. Le Gorju-Jago. "Fatigue life of rubber components: 3D damage evolution from X-ray computed microtomography." In: *Constitutive Models for Rubber V*. Ed. by A. Boukamel, L. Laiarinandrasana, S. Méo, and E. Verron. CRC Press, 2007, p. 173 (cit. on pp. 109, 110).

[108] K. Le Gorju-Jago. "X-ray computed microtomography of rubber." In: *Rubber Chemistry and Technology* 85.3 (Sept. 2012), pp. 387–407. DOI: 10.5254/rct.12.87985 (cit. on p. 108).

[109] K. Le Gorju-Jago and C. Bathias. "Fatigue initiation and propagation in natural and synthetic rubbers." In: *International Journal of Fatigue* 24.2-4

(2002), pp. 85–92. DOI: 10.1016/S0142-1123(01)00062-7 (cit. on pp. 65, 69, 167).

[110] M. Le Huy and G. Evrard. "Methodologies for lifetime predictions of rubber using Arrhenius and WLF models." In: *Die Angewandte Makromolekulare Chemie* 261-262.1 (Dec. 1998), pp. 135–142. DOI: 10.1002/(SICI)1522-9505(19981201)261-262:1<135::AID-APMC135>3.0.CO;2-W (cit. on p. 192).

[111] V. Le Saux, Y. Marco, S. Calloch, and P. Charrier. "Evaluation of the fatigue defect population in an elastomer using X-ray computed micro-tomography." In: *Polymer Engineering & Science* 51.7 (July 2011), pp. 1253–1263. DOI: 10.1002/pen.21872 (cit. on pp. 109, 110).

[112] V. Le Saux, Y. Marco, S. Calloch, C. Doudard, and P. Charrier. "Fast evaluation of the fatigue lifetime of rubber-like materials based on a heat build-up protocol and micro-tomography measurements." In: *International Journal of Fatigue* 32.10 (2010), pp. 1582–1590. DOI: 10.1016/j.ijfatigue.2010.02.014 (cit. on p. 109).

[113] J.-H. Lee, J.-W. Bae, J.-S. Kim, T.-J. Hwang, Y.-S. Choi, K.-S. Baek, and N.-J. Jo. "Effect of cure system on the life-time of hydrogenated NBR O-ring using intermittent compression stress relaxation (CSR)." In: *Elastomers and Composites* 46.2 (2011), pp. 144–151 (cit. on p. 192).

[114] M.-P. Lee and A. Moet. "Analysis of fatigue crack propagation in NR/BR rubber blend." In: *Rubber Chemistry and Technology* 66.2 (May 1993), pp. 304–316. DOI: 10.5254/1.3538314 (cit. on p. 108).

[115] P. B. Lindley. "Relation between hysteresis and the dynamic crack growth resistance of natural rubber." In: *International Journal of Fracture* 9.4 (1973), pp. 449–462. DOI: 10.1007/BF00036325 (cit. on pp. 17, 122).

[116] A. Lion and M. Johlitz. "On the representation of chemical ageing of rubber in continuum mechanics." In: *International Journal of Solids and Structures* 49.10 (May 2012), pp. 1227–1240. DOI: 10.1016/J.IJSOLSTR.2012.01.014 (cit. on pp. 161, 162).

[117] R. A. Lockhart and M. A. Stephens. "Estimation and tests of fit for the three-parameter Weibull distribution." In: *Journal of the Royal Statistical Society. Series B (Methodological)* (1994), pp. 491–500 (cit. on p. 91).

[118] Y. Marco, I. Masquelier, V. Le Saux, S. Calloch, B. Huneau, and P. Charrier. "Contributions of IR thermography and X-ray tomography to the fatigue characterization of elastomeric materials." In: *Constitutive Models for Rubber VIII*. Ed. by N. Gil-Negrete and A. Alonso. CRC Press, 2013. DOI: 10.1201/b14964-70 (cit. on p. 109).

[119] W. V. Mars. *Multiaxial fatigue of rubber*. ProQuest LLC, 2001 (cit. on p. 62).

[120] W. V. Mars. "Fatigue Life Prediction for Elastomeric Structures." In: *Rubber Chemistry and Technology* 80.3 (2007), pp. 481–503. DOI: 10.5254/1.3548175 (cit. on pp. 62, 63, 64).

[121] W. V. Mars and A. Fatemi. "A literature survey on fatigue analysis approaches for rubber." In: *International Journal of Fatigue* 24.9 (2002), pp. 949–961. DOI: 10.1016/S0142-1123(02)00008-7 (cit. on pp. 59, 60, 62, 64, 88, 105, 108).

[122] W. V. Mars and A. Fatemi. "Fatigue crack nucleation and growth in filled natural rubber." In: *Fatigue and Fracture of Engineering Materials and Struc-*

tures 26.9 (2003), pp. 779–789. DOI: 10.1046/j.1460-2695.2003.00678.x (cit. on pp. 60, 61, 88, 94).

[123] W. V. Mars and A. Fatemi. "Factors that affect the fatigue life of rubber: A literature survey." In: *Rubber Chemistry and Technology* 77.3 (2004), pp. 391–412. DOI: 10.5254/1.3547831 (cit. on pp. 59, 64, 65, 122).

[124] W. V. Mars and A. Fatemi. "Observations of the Constitutive Response and Characterization of Filled Natural Rubber Under Monotonic and Cyclic Multiaxial Stress States." In: *Journal of Engineering Materials and Technology* 126.1 (2004), p. 19. DOI: 10.1115/1.1631432 (cit. on pp. 41, 62, 63, 64).

[125] I. Masquelier. "Influence de la formulation sur les propriétés en fatigue d'élastomères industriels." PhD thesis. Université de Bretagne Occidentale, Dec. 2014 (cit. on p. 124).

[126] M. Minguez and J. Royo. "Evaluation of results of tension fatigue resistance tests on vulcanized rubber." In: *Polymer Testing* 1.4 (Oct. 1980), pp. 287–302. DOI: 10.1016/0142-9418(80)90012-4 (cit. on pp. 64, 90).

[127] L. Mullins. "Softening of rubber by deformation." In: *Rubber Chemistry and Technology* 42.1 (Mar. 1969), pp. 339–362. DOI: 10.5254/1.3539210 (cit. on pp. 16, 62).

[128] T. Nakagawa, T. Toya, and M. Oyama. "Ozone resistance of highly saturated nitrile rubber (HNBR)." In: *Journal of Elastomers & Plastics* 24.3 (July 1992), pp. 240–261. DOI: 10.1177/009524439202400307 (cit. on p. 9).

[129] K. Narynbek Ulu, M. Dragičević, P. A. Albouy, B. Huneau, A.-S. Béranger, and P. Heuillet. "Strain-induced crystallization ability of hydrogenated nitrile butadiene rubber." In: *Constitutive Models for Rubber X*. Ed. by A. Lion and M. Johlitz. CRC Press, 2017, pp. 279–282 (cit. on p. 54).

[130] K. Narynbek Ulu, B. Huneau, P.-Y. Le Gac, and E. Verron. "Fatigue resistance of natural rubber in seawater with comparison to air." In: *International Journal of Fatigue* 88 (July 2016), pp. 247–256. DOI: 10.1016/j.ijfatigue.2016.03.033 (cit. on pp. 64, 110).

[131] K. Narynbek Ulu, B. Huneau, E. Verron, A.-S. Béranger, and P. Heuillet. "True Stress Controlled Fatigue Life Experiments for Elastomers." In: *International Journal of Fatigue* 104 (2017), pp. 171–182. DOI: 10.1016/j.ijfatigue.2017.07.007 (cit. on pp. 58, 228).

[132] C. Neuhaus, A. Lion, M. Johlitz, P. Heuler, M. Barkhoff, and F. Duisen. "Fatigue behaviour of an elastomer under consideration of ageing effects." In: *International Journal of Fatigue* 104 (2017), pp. 72–80. DOI: 10.1016/j.ijfatigue.2017.07.010 (cit. on pp. 69, 167, 170, 172, 192).

[133] NF EN ISO 6721-1. *Plastiques: Détermination des propriétés mécaniques dynamiques*. 2011 (cit. on pp. 13, 26).

[134] F. E. Ngolemasango, M. Bennett, and J. Clarke. "Degradation and life prediction of a natural rubber engine mount compound." In: *Journal of applied polymer science* 110.1 (2008), pp. 348–355 (cit. on pp. 168, 171, 192).

[135] W. Obrecht, H. Buding, U. Eisele, Z. Szentivanyi, and J. Thörmer. "Hydrierter nitrilkautschuk ein werkstoff mit neuen eigenschaften." In: *Angewandte Makromolekulare Chemie* 145.1 (Nov. 1986), pp. 161–179. DOI: 10.1002/apmc.1986.051450109 (cit. on pp. 11, 12, 14, 15, 19, 21, 30, 48).

[136] B. Ohm. "Improving the heat resistance of HNBR, ACM and EAM by the use of antioxidants." In: Pittsburgh: Rubber Division, ACS, 2002 (cit. on p. 163).

[137] N. Osaka, M. Kato, and H. Saito. "Mechanical properties and network structure of phenol resin crosslinked hydrogenated acrylonitrile-butadiene rubber." In: *Journal of Applied Polymer Science* 129.6 (2013), pp. 3396–3403. DOI: 10.1002/app.39010 (cit. on pp. 8, 9, 12, 20, 21).

[138] E. Ostoja-Kuczynski, P. Charrier, E. Verron, G. Marckmann, L. Gornet, and G. Chagnon. "Crack initiation in filled natural rubber: experimental database and macroscopic observations." In: *Constitutive Models For Rubber III*. Ed. by J. Busfield and A. Muhr. CRC Press, 2003, pp. 41–47 (cit. on p. 64).

[139] P. Paris and F. Erdogan. "A critical analysis of crack propagation laws." In: *Journal of Basic Engineering* 85.4 (Dec. 1963), p. 528. DOI: 10.1115/1.3656900 (cit. on p. 107).

[140] J.-L. Poisson, F. Lacroix, S. Méo, G. Berton, and N. Ranganathan. "Rubber fatigue — the intrinsic Intricacies." In: *Fatigue of Materials II: Advances and Emergences in Understanding*. Ed. by T. S. Srivatsan, M. A. Imam, and R. Srinivasan. Cham: Springer International Publishing, 2016, pp. 181–192. DOI: 10.1007/978-3-319-48105-0{_}13 (cit. on p. 111).

[141] I. Raoult. "Structures elastomeres sous chargement cyclique : comportement, fatigue, duree de vie." PhD thesis. Ecole Polytechnique X, 2005 (cit. on pp. 61, 67).

[142] S. Rausch, M. Ruderer, W. Enke, A. Narváez, M. Ludwig, and T. Alshuth. "Lifetime prediction of elastomer components within gasoline engines." In: *Constitutive Models for Rubber IX*. Ed. by B. Marvalova and I. Petrikova. CRC Press, 2015, pp. 363–366. DOI: 10.1201/b18701-64 (cit. on p. 65).

[143] K. Reincke, B. Langer, S. Dohler, U. Heuert, Merseburg, W. Grellmann, and Halle. "Alterung und Beständigkeits- untersuchungen von Elastomerwerkstoffen." In: *Kautschuk Gummi Kunststoffe* 10 (2014), pp. 60–67 (cit. on pp. 163, 165).

[144] J. T. Rich, J. G. Neely, R. C. Paniello, C. C. J. Voelker, B. Nussenbaum, and E. W. Wang. "A practical guide to understanding Kaplan-Meier curves." In: *Otolaryngology–head and neck surgery : official journal of American Academy of Otolaryngology-Head and Neck Surgery* 143.3 (Sept. 2010), pp. 331–6. DOI: 10.1016/j.otohns.2010.05.007 (cit. on pp. 94, 95).

[145] R. S. Rivlin and A. G. Thomas. "Rupture of rubber. I. Characteristic energy for tearing." In: *Journal of Polymer Science* 10.3 (Mar. 1953), pp. 291–318. DOI: 10.1002/pol.1953.120100303 (cit. on pp. 61, 105, 106, 107, 120).

[146] J. Royo. "Fatigue testing of rubber materials and articles." In: *Polymer Testing* 11.5 (Jan. 1992), pp. 325–344. DOI: 10.1016/0142-9418(92)90002-S (cit. on pp. 67, 88).

[147] P. Rublon, B. Huneau, N. Saintier, S. Beurrot, A. Leygue, E. Verron, C. Mocuta, D. Thiaudire, and D. Berghezan. "In situ synchrotron wide-angle X-ray diffraction investigation of fatigue cracks in natural rubber." In: *Journal of Synchrotron Radiation* 20.1 (2013), pp. 105–109. DOI: 10.1107/S0909049512044457 (cit. on p. 17).

[148] P. Rublon, B. Huneau, E. Verron, N. Saintier, S. Beurrot, A. Leygue, C. Mocuta, D. Thiaudiere, and D. Berghezan. "Multiaxial deformation and strain-induced crystallization around a fatigue crack in natural rubber." In: *Engineering Fracture Mechanics* 123 (2014), pp. 59–69. DOI: 10.1016/j.engfracmech.2014.04.003 (cit. on p. 17).

[149] N. Saintier, G. Cailletaud, and R. Piques. "Crack initiation and propagation under multiaxial fatigue in a natural rubber." In: *International Journal of Fatigue* 28.1 (2006), pp. 61–72. DOI: 10.1016/j.ijfatigue.2005.03.006 (cit. on p. 109).

[150] N. Saintier, G. Cailletaud, and R. Piques. "Multiaxial fatigue life prediction for a natural rubber." In: *International Journal of Fatigue* 28.5 (2006), pp. 530–539. DOI: 10.1016/j.ijfatigue.2005.05.011 (cit. on p. 62).

[151] N. Saintier, G. Cailletaud, and R. Piques. "Cyclic loadings and crystallization of natural rubber: An explanation of fatigue crack propagation reinforcement under a positive loading ratio." In: *Materials Science and Engineering A* 528.3 (2011), pp. 1078–1086. DOI: 10.1016/j.msea.2010.09.079 (cit. on pp. 17, 65, 110).

[152] H. Sawada. "Hydrogenated Nitrile Rubber." In: *Nippon Gomu Kyokaishu* 9 (1993), p. 653 (cit. on pp. 8, 9, 10, 11, 15, 19, 21, 32, 38, 48, 163).

[153] S. S. Scherrer, M. Cattani-Lorente, E. Vittecoq, F. De Mestral, J. A. Griggs, and H. W. Wiskott. "Fatigue behavior in water of Y-TZP zirconia ceramics after abrasion with 30 μm silica-coated alumina particles." In: *Dental Materials* 27.2 (Feb. 2011), pp. 28–42. DOI: 10.1016/j.dental.2010.10.003 (cit. on p. 95).

[154] W. Schütz. "A history of fatigue." In: *Engineering Fracture Mechanics* 54.2 (1996), pp. 263–300. DOI: 10.1016/0013-7944(95)00178-6 (cit. on p. 59).

[155] S. Seichter, V. M. Archodoulaki, T. Koch, A. Holzner, and A. Wondracek. "Investigation of different influences on the fatigue behaviour of industrial rubbers." In: *Polymer Testing* 59 (May 2017), pp. 99–106. DOI: 10.1016/j.polymertesting.2017.01.018 (cit. on p. 64).

[156] G. Severe and J. L. White. "Physical properties and blend miscibility of hydrogenated acrylonitrile-butadiene rubber." In: *Journal of Applied Polymer Science* 78.8 (2000), pp. 1521–1529. DOI: 10.1002/1097-4628(20001121)78:8<1521::AID-APP90>3.0.CO;2-Z (cit. on pp. 19, 20, 21).

[157] J. A. Shaw, A. S. Jones, and A. S. Wineman. "Chemorheological response of elastomers at elevated temperatures: Experiments and simulations." In: *Journal of the Mechanics and Physics of Solids* 53.12 (Dec. 2005), pp. 2758–2793. DOI: 10.1016/J.JMPS.2005.07.004 (cit. on pp. 161, 162).

[158] R. F. Stapelberg. *Handbook of Reliability, Availability, Maintainability and Safety in Engineering Design*. Springer, 2009, p. 827 (cit. on p. 91).

[159] R. I. Stephens, A. Fatemi, S. Robert, and H. O. Fuchs. *Metal Fatigue in Engineering*. Wiley, 2001, p. 472 (cit. on pp. 60, 90, 154).

[160] S. Svensson. "Testing methods for fatigue properties of rubber materials and vibration isolators." In: *Polymer Testing* 2.3 (1981), pp. 161–174. DOI: 10.1016/0142-9418(81)90002-7 (cit. on pp. 64, 88).

[161] J. A. Tang, J. M. Leasure, J. S. Smith, J. M. Buckley, D. Kondrashov, and C. P. Ames. "Effect of severity of rod contour on posterior rod failure in the setting of lumbar pedicle subtraction osteotomy (PSO)." In: *Neurosurgery* 72.2 (Feb. 2013), pp. 276–283. DOI: 10.1227/NEU.0b013e31827ba066 (cit. on p. 96).

[162] Z. Tao, N. Viriyabanthorn, B. Ghuman, C. Barry, and J. Mead. "Heat resistant elastomers." In: *Rubber Chemistry and Technology* 78.3 (2005), pp. 489–515. DOI: 10.5254/1.3547893 (cit. on pp. 7, 8, 9, 10, 161, 162, 163).

[163] P. Thavamani and A. K. Bhowmick. "Dynamic mechanical properties of hydrogenated nitrile rubber: effect of cross-link density, curing system, filler and resin." In: *Journal of Materials Science* 27.12 (1992), pp. 3243–3253. DOI: 10.1007/BF01116020 (cit. on pp. 12, 13, 14, 38).

[164] T. M. Therneau and T. Lumley. *Survival Analysis Guide*. 2017. DOI: 10.1016/j.jhydrol.2011.07.022. (cit. on pp. 95, 97, 98, 130).

[165] A. G. Thomas. "Rupture of rubber. V. Cut growth in natural rubber vulcanizates." In: *Journal of Polymer Science* 31.123 (Sept. 1958), pp. 467–480. DOI: 10.1002/pol.1958.1203112324 (cit. on p. 107).

[166] A. Thomas. "Fats and fatty oils." In: *Ullmann's Encyclopedia of Industrial Chemistry*. Weinheim, Germany: Wiley-VCH Verlag GmbH & Co. KGaA, June 2000. DOI: 10.1002/14356007.a10{_}173 (cit. on p. 10).

[167] A. V. Tobolsky, I. B. Prettyman, and J. H. Dillon. "Stress relaxation of natural and synthetic rubber stocks." In: *Journal of Applied Physics* 15.4 (Apr. 1944), pp. 380–395. DOI: 10.1063/1.1707442 (cit. on pp. 161, 162).

[168] M. Tosaka. "Strain-induced crystallization of crosslinked Natural Rubber as revealed by X-ray diffraction using synchrotron radiation." In: *Polymer Journal* 39.12 (2007), pp. 1207–1220. DOI: 10.1295/polymj.PJ2007059 (cit. on p. 17).

[169] M. Tosaka, S. Kohjiya, S. Murakami, S. Poompradub, Y. Ikeda, S. Toki, I. Sics, and B. S. Hsiao. "Effect of network-chain length on strain-induced crystallization of NR and IR vulcanizates." In: *Rubber Chemistry and Technology* 77.4 (2004), pp. 711–723. DOI: 10.5254/1.3547846 (cit. on pp. 17, 18).

[170] S. Trabelsi, P. A. Albouy, and J. Rault. "Effective local deformation in stretched filled rubber." In: *Macromolecules* 36.24 (2003), pp. 9093–9099. DOI: 10.1021/ma0303566 (cit. on pp. 17, 18, 48).

[171] E. Verron and A. Andriyana. "Definition of a new predictor for multiaxial fatigue crack nucleation in rubber." In: *Journal of the Mechanics and Physics of Solids* 56.2 (Feb. 2008), pp. 417–443. DOI: 10.1016/j.jmps.2007.05.019 (cit. on p. 62).

[172] A. Vieyres, R. Pérez-Aparicio, P. A. Albouy, O. Sanseau, K. Saalwächter, D. R. Long, and P. Sotta. "Sulfur-cured natural rubber elastomer networks: Correlating cross-link density, chain orientation, and mechanical response by combined techniques." In: *Macromolecules* 46.3 (2013), pp. 889–899. DOI: 10.1021/ma302563z (cit. on pp. 27, 28, 51).

[173] C. S. Wang and G. S. Y. Yeh. "DRDF analysis of wide-angle x-ray scattering of natural rubber." In: *Journal of Macromolecular Science, Part B* 15.1 (Feb. 1978), pp. 107–118. DOI: 10.1080/00222347808212248 (cit. on p. 28).

[174] W. Weibull. "A statistical distribution function of wide applicability." In: *Journal of Applied Mechanics* 18 (1951) (cit. on p. 90).

[175] W. Weibull. "Fatigue testing and analysis of results." In: Published for Advisory Group for Aeronautical Research and development, North Atlantic Treaty Organization, by Pergamon Press, 1961, p. 305 (cit. on p. 90).

[176] G. S. Weng, G. S. Huang, H. X. Lei, L. L. Qu, P. Zhang, Y. J. Nie, and J. R. Wu. "Crack initiation of natural rubber under high temperature fatigue loading." In: *Journal of Applied Polymer Science* 124.5 (2012), pp. 4274–4280. DOI: Doi10.1002/App.35408 (cit. on pp. 64, 167).

[177] C. S. Woo, W. D. Kim, S. H. Lee, B. I. Choi, and H. S. Park. "Fatigue life prediction of vulcanized natural rubber subjected to heat-aging." In: *Procedia Engineering* 1.1 (2009), pp. 9–12. DOI: 10.1016/j.proeng.2009.06.004 (cit. on pp. 64, 167).

[178] C. Wrana, K. Reinartz, and H. Winkelbach. "Therban (R) - The high performance elastomer for the new millennium." In: *Macromolecular Materials and Engineering* 286.11 (2001), pp. 657–662. DOI: Doi10.1002/1439-2054 (cit. on pp. 7, 9).

[179] D. G. Young. "Fatigue crack propagation in elastomer compounds: effects of strain rate, temperature, strain level, and oxidation." In: *Rubber chemistry and technology* 59.5 (1986), pp. 809–825 (cit. on pp. 17, 167).

[180] D. G. Young and J. A. Danik. "Effects of temperature on fatigue and fracture." In: 67.1 (1994), pp. 137–147 (cit. on p. 167).

[181] M. Zaghdoudi, P. A. Albouy, Z. Tourki, A. Vieyres, and P. Sotta. "Relation between stress and segmental orientation during mechanical cycling of a natural rubber-based compound." In: *Journal of Polymer Science, Part B: Polymer Physics* 53.13 (2015), pp. 943–950. DOI: 10.1002/polb.23723 (cit. on pp. 27, 28, 51).

[182] J. Zhang, J. Lin, G. Zhang, and H. Liu. "High cycle fatigue life prediction and reliability analysis of aeroengine blades." In: *Transactions of Tianjin University* 18.6 (Dec. 2012), pp. 456–464. DOI: 10.1007/s12209-012-1785-7 (cit. on p. 96).

[183] A. Zine, N. Benseddiq, M. Nait Andelaziz, N. Ait Hocine, and D. Bouami. "Prediction of rubber fatigue life under multiaxial loading." In: *Fatigue & Fracture of Engineering Materials & Structures* 29.3 (2006), pp. 267–278 (cit. on pp. 62, 64).

Annexe A

Résumé étendu en français

A.1 Introduction

Les polymères butadiène-acrylonitrile hydrogénés (sigle HNBR - *hydrogenated nitrile butadiene rubber* en anglais) sont des élastomères de haute performance de plus en plus utilisés dans divers domaines industriels, de par leur propriétés remarquables. En effet, ils présentent une bonne résistance chimique aux hydrocarbures (huiles, essences) ainsi qu'une excellente tenue aux hautes températures. Les HNBR sont utilisés dans l'industrie automobile principalement pour la production des courroies, des tuyaux, d'amortisseurs de vibrations et de joints (toriques, d'étanchéité) ; ils sont aussi utilisés pour des applications pétrolières, militaires, aérospatiales, navales et d'autres industries de haute technologie. Dans ce contexte, il existe un fort besoin industriel pour la prédiction de la durée de vie en fatigue des produits en HNBR ; toutefois très peu d'études approfondies sur leur résistance à la fatigue sont disponibles. De plus, comme ces matériaux sont soumis à des hautes températures, il est important de considérer les effets du vieillissement thermo-oxydant sur la fatigue. Il convient de noter que l'interaction entre fatigue et vieillissement dans les élastomères en général est une thématique de recherche récente pour laquelle peu d'études ont été réalisées.

La présente thèse de doctorat, réalisée dans le cadre d'un financement CIFRE, est une collaboration entre le l'Institut de Recherche en Génie Civil et Mécanique (GeM, UMR CNRS 6183) de l'École Centrale de Nantes et le Laboratoire de Recherches et de Contrôle du Caoutchouc (LRCCP), un centre de transfert spécialisé dans la recherche, les essais et le conseil dans le domaine des caoutchoucs et polymères.

Ce projet collaboratif a deux objectifs principaux :

I. Étudier les effets de la formulation chimique des HNBR, spécifiquement les taux d'acrylonitrile et d'hydrogénation, sur leur résistance à la fatigue ;

II. Étudier l'interaction entre vieillissement thermique et fatigue dans les HNBR ;

et un objectif secondaire :

III. Qualifier la présence d'une cristallisation sous tension dans les HNBR et quantifier ses effets sur leurs propriétés mécaniques.

En pratique, six mélanges différents sont étudiés. Ils sont tous réticulés au peroxyde et chargés au noir de carbone (N772, 70 phr). Notre mélange de référence appelé A36H96 admet un taux d'acrylonitrile (ACN) de 36% et un pourcentage d'hydrogénation de 96%. L'influence du taux d'ACN est étudiée en considérant tout d'abord les deux mélanges A24H96 et A44H96, contenant respectivement 24% et 44% d'ACN. L'influence de l'hydrogénation est étudiée grâce aux mélanges A36H99 et A36H91 dont les taux d'hydrogénation sont 99% et 91%, respectivement. A cela s'ajoute le mélange composite A44-24, qui contient 60% / 40% de chacun des mélanges A24H96 et A44H96 avec un taux moyen d'ACN équivalent à celui du A36H96.

Dans le mémoire de thèse, les travaux menés sont présentés dans quatre chapitres dont les résumés étendus en français sont proposés dans les sections suivantes.

A.2 Propriétés mécaniques du HNBR (Chap. 2)

Le chapitre 2 se concentre sur l'étude des propriétés mécaniques des HNBR et des effets de la formulation sur celles-ci. L'étude des propriétés mécaniques des HNBR n'est pas seulement nécessaire pour la fatigue et le vieillissement abordés dans la présente thèse, mais est également motivée par le manque d'informations accessibles au public. Les résultats expérimentaux sont présentés ; ils concernent la réponse en traction uniaxiale quasi-statique, la viscoélasticité en petites déformations (DMA), l'effet Mullins, la dureté, la déformation résiduelle et la déformation permanente. De plus, ce chapitre s'intéresse également au phénomène de cristallisation sous tension (sigle SIC - *strain-induced crystallization* en anglais) et ses effets sur les propriétés mécaniques précédentes.

A.2.1 Traction uniaxiale

Les résultats des essais de traction uniaxiale quasi-statique sur les mélanges de HNBR à température ambiante et à 120 °C sont représentés sur les Figures A.2-1-A.2-3. En général, certains signes de plasticité et/ou viscoplasticité sont observés

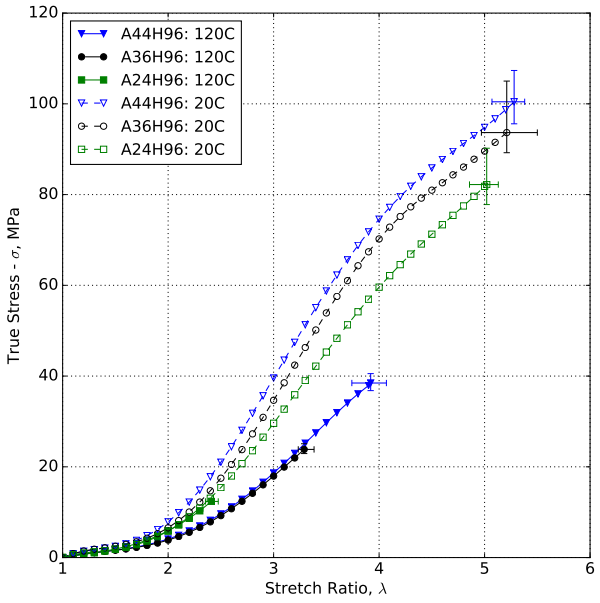

Figure A.2-1 – Effet de la température et du taux d'ACN sur la réponse uniaxiale du HNBR.

dans tous les mélanges à température ambiante.

À température ambiante, la figure A.2-1 illustre une tendance claire : lorsque le taux d'ACN augmente, la contrainte à rupture (σ_f), l'élongation à rupture (λ_f) et la rigidité à 10 MPa ($E_{10\ \mathrm{MPa}}$) augmentent aussi, même si les réponses mécaniques des mélanges A36H96 et A44H96 diffèrent peu puisque les courbes se chevauchent. Pour des températures plus élevées, un taux d'ACN élevé se traduit par de meilleures

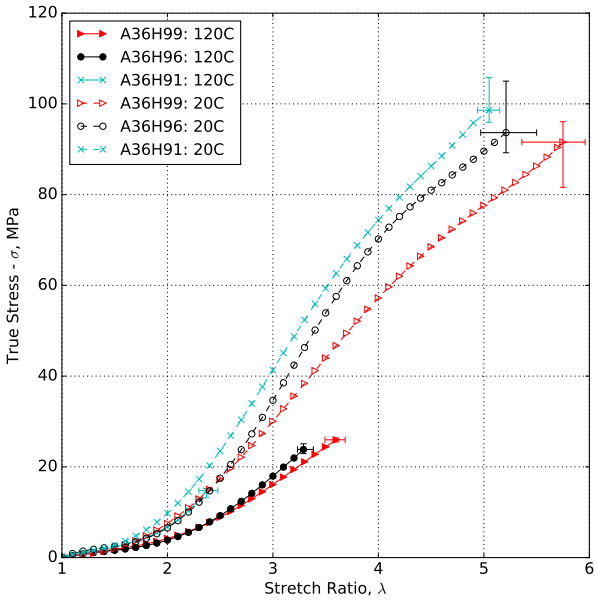

Figure A.2-2 – Effet de la température et du taux d'hydrogenation sur la réponse uniaxiale du HNBR.

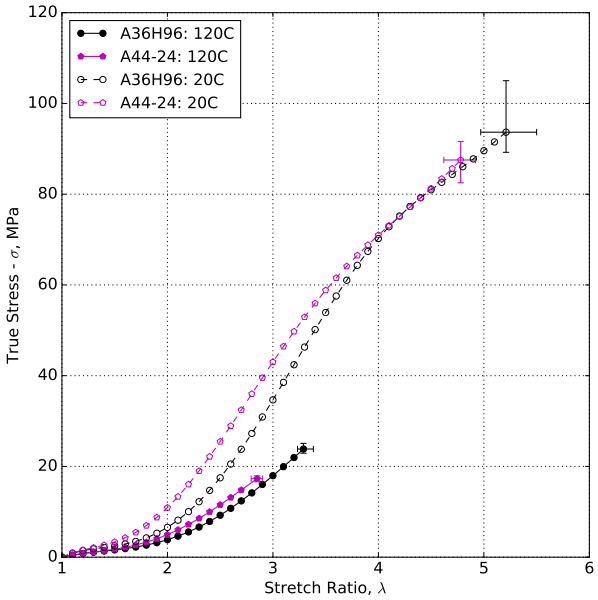

Figure A.2-3 – Effet de la température sur la réponse uniaxiale du mélange composite du HNBR.

rigidités, et élongation et contrainte à rupture. En particulier, le mélange A24H96 montre des signes de fragilisation à des températures élevées ; c'est pourquoi les grades de HNBR avec des taux d'ACN faibles sont généralement utilisés pour des applications à basse température.

Avec l'augmentation du taux d'hydrogénation, le HNBR devient plus « ductile »,

puisque λ_f augmente alors que σ_f et $E_{10\,\mathrm{MPa}}$ diminuent (fig. A.2-2). Avec l'augmentation de la température à 120 °C, il semble que l'hydrogénation contribue à la préservation des propriétés mécaniques, résultat compatible avec l'effet bénéfique bien connu de l'hydrogénation sur la résistance à la chaleur.

Pour le mélange composite A44-24 à température ambiante, la contrainte à rupture se situe approximativement entre celles des mélanges A44H96 et A24H96, mais se révèle inférieure à celle du A36H96. Cependant, ce mélange composite admet une plus grande rigidité à 10 MPa. En termes de performances à haute température, les propriétés du composite se situe à peu près entre celles des deux mélanges qui le composent.

Pour tous les mélanges, les différences de propriétés entre la température ambiante et 120 °C sont résumés dans le Tableau A.2-1.

Tableau A.2-1 – Pourcentage de différence des contrainte et déformation à la rupture et de la rigidité pour les six mélanges HNBR à 120 °C par rapport à la température ambiante.

	$\Delta_{\%}$ (%)		
Mélange	λ_f	σ_f **(MPa)**	$E_{\mathbf{10\ MPa}}$ **(MPa)**
A36H96	-44,61%	-74,55%	-23,06%
A44H96	-31,78%	-61,70%	-29,02%
A24H96	-64,93%	-84,95%	-2,69%
A36H99	-45,26%	-71,65%	-27,39%
A36H91	-66,17%	-85,03%	15,28%
A44-24	-51,06%	-80,25%	-32,17%

A.2.2 Analyse mécanique dynamique (DMA)

Une analyse mécanique dynamique est effectuée pour les six mélanges. En général, le taux d'ACN a un effet plus important sur les caractéristiques dynamiques du HNBR que le taux d'hydrogénation. Ce résultat est étroitement lié à la température de transition vitreuse (T_g) du HNBR, qui est elle-même fortement affectée par la teneur en ACN. T_g est extraite des pics des courbes tan(δ) pour chaque mélange, tel que résumé sur la Figure A.2-4. Le mélange A24H96 admet la plus basse T_g, ce qui en fait un matériau approprié pour les applications à basse température. Globalement, 10 °C sépare les températures de transition vitreuse du mélange A24H96 (−39.9 °C) au mélange A36H96, et de ce dernier (−30.1 °C) au mélange A44H96 (−20.2 °C). Alors que la différence des T_g est plus faible lorque le taux d'hydrogénation varie. De plus, T_g dépend de la fréquence pour tous les mélanges. Finalement, il convient de noter que T_g pour le HNBR est élevée en comparaison à d'autres élastomères tels que le caoutchouc naturel (−70 °C), le polybutadiène (−108 °C), ou le styrène-butadiène (−61 °C). Cette différence explique sans doute la réponse plastique ou viscoplastique du HNBR à température ambiante, puisque celle-ci se trouve à proximité de la zone de transition vitreuse des mélanges (voisinage de T_g).

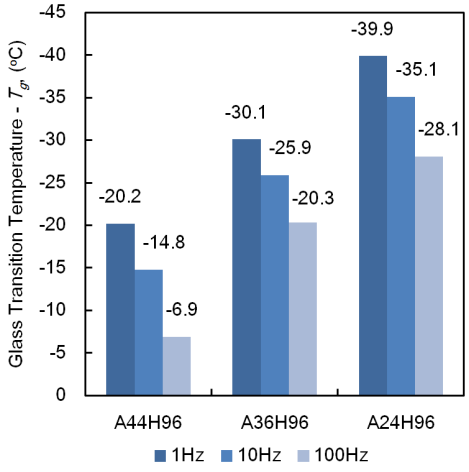

(a) Effet du taux d'ACN.

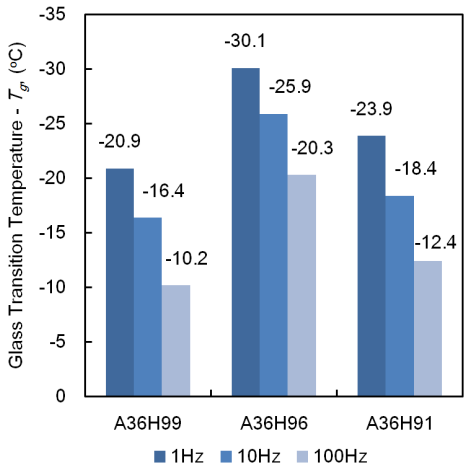

(b) Effet du taux d'hydrogénation.

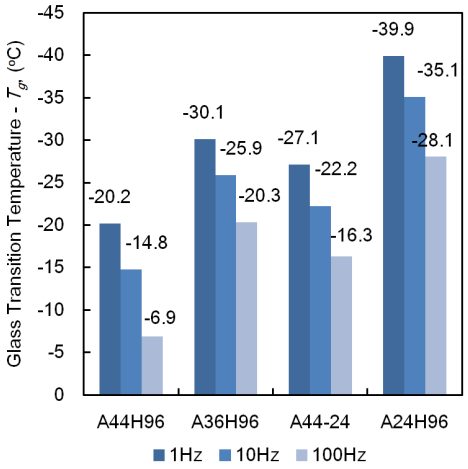

(c) Composite A44-24.

Figure A.2-4 – Température de transition vitreuse (T_g) des mélanges du HNBR mesurée par les pics tan(δ) avec effet de la fréquence.

A.2.3 Dureté

Les moyennes de trois mesures de dureté Shore-A sont présentées dans le Tableau A.2-2. Ces résultats sont en général conformes à celles rencontrées dans la

Tableau A.2-2 – Dureté Shore-A de six mélanges HNBR.

	Dureté Shore A
A36H96	$66,77^{+0,63}_{-0,57}$
A44H96	$68,67^{+0,43}_{-0,27}$
A24H96	$60,83^{+0,67}_{-0,93}$
A36H99	$66,63^{+0,77}_{-0,43}$
A36H91	$68,83^{+0,27}_{-0,23}$
A44-24	$66,53^{+0,67}_{-0,83}$

littérature.

A.2.4 Cristallisation sous tension

La cristallisation sous tension (SIC en anglais) du HNBR a été étudiée avec une approche modifiée pour l'analyse numérique des pics de diffraction des rayons X ; cette méthode s'avère efficace pour l'analyse des mélanges HNBR non chargés (différents des mélanges de l'étude présentés plus haut). Cette approche permet de construire les courbes classiques de l'évolution de l'indice de cristallinité et de la contrainte vraie en fonction de l'élongation lors d'un cycle de charge-décharge, comme montré sur la Figure A.2-5 pour des mélanges non chargés de HNBR - UF44 et UF36. Les courbes de cristallinité présentent les caractéristiques bien connues pour les élastomères (le caoutchouc naturel notamment) : une boucle d'hystérésis parcourue dans le sens direct, c'est-à-dire que l'indice de cristallinité pour une élongation donnée est plus élevée pendant la décharge que pendant la charge. De plus, le début de cristallisation apparaît pour une élongation plus élevée (lors de la charge) que celle de la fusion (lors de la décharge).

De plus, nous avons pour la première fois mis en évidence les effets d'une augmentation du taux d'ACN (de 36% à 44%) sur l'augmentation de l'incidence de la SIC dans le HNBR : lorsque le taux d'ACN augmente, le début de la cristallisation et la fusion se produisent à des élongations plus faibles.

A.2.5 Effet Mullins, déformations résiduelle et permanente

Sous chargement cyclique, c'est-à-dire pour une suite de charges-décharges, l'effet Mullins est observé dans tous les mélanges. La réponse cyclique est caractérisée par des boucles d'hystérésis, dont la plus grande est celle relative au premier cycle. Le niveau d'adoucissement de la contrainte semble dépendre plus de l'élongation que du type de HNBR comme montré sur la Figure A.2-6. Ainsi, il existe une relation linéaire entre l'élongation maximale atteinte et le degré d'adoucissement observé

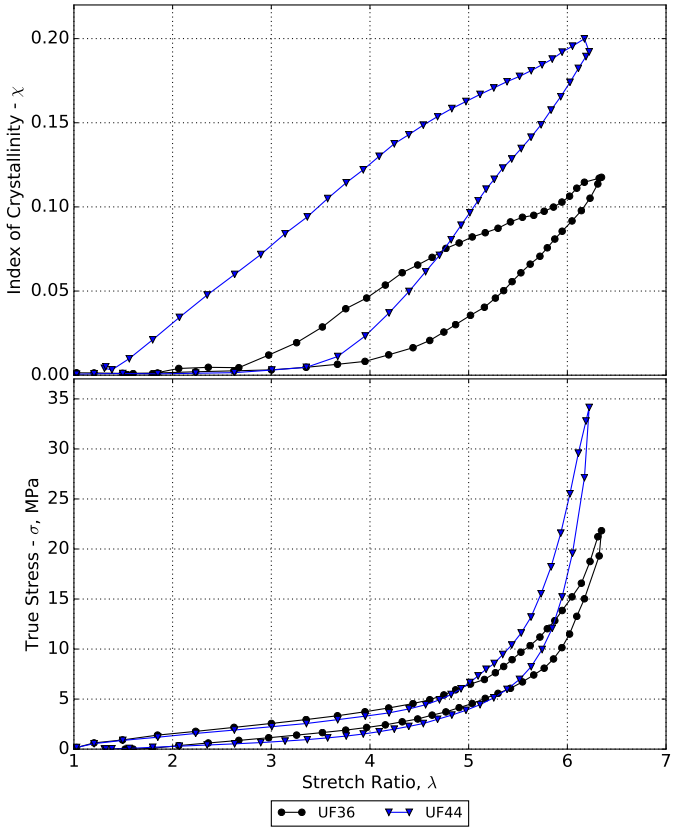

Figure A.2-5 – Courbes cristallinité-élongation et contrainte vraie-élongation à température ambiante pour les mélanges non chargés de HNBR - UF44 et UF36.

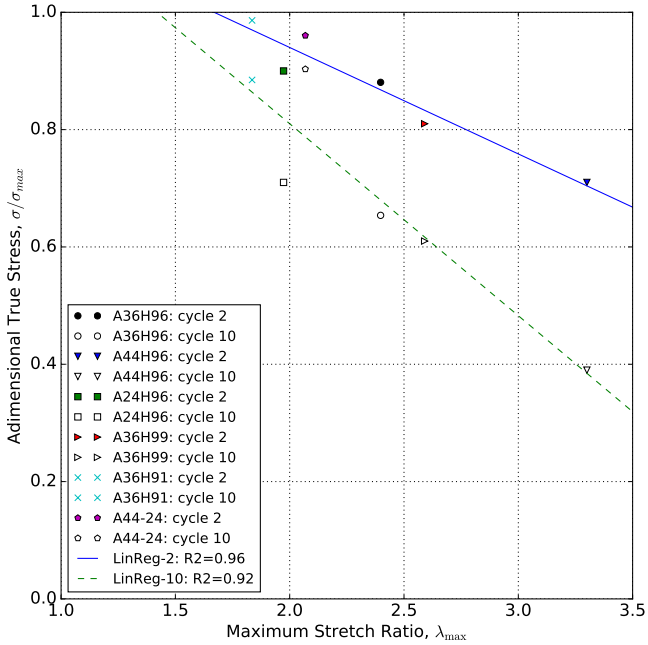

Figure A.2-6 – Relation entre l'effet Mullins et l'élongation maximale atteinte au cours d'un cycle de chargement.

après 2 et 10 cycles. Après déchargement complet, tous les mélanges présentent une déformation inélastique rémanente, qu'on appelle « déformation résiduelle ».

Cette déformation résiduelle ainsi que la déformation permanente (la déformation rémanente après une semaine de recouvrement) sont mesurées pour tous les mélanges après un chargement cyclique à déplacement imposé comme le montre les Figures A.2-7 et A.2-8 ; leurs amplitudes diminuent de façon monotone lorsque la température augmente de 20 °C à 120 °C. À la lumière des résultats précédents, il semble que les déformations résiduelle et permanente sont liées à la différence entre la température d'essai et T_g. Ainsi, pour diminuer ces deux déformations inélastiques, il convient d'utiliser le matériau dans des conditions de température éloignées de la zone de transition vitreuse.

Pour conclure, les déformations résiduelle et permanente du HNBR sont des manifestations du caractère inélastique du matériau, en particulier aux températures basses (par rapport à T_g). Pour revenir au cas du chargement cyclique à déplacement imposé, l'existence de déformation résiduelle et permanente significatives induit plusieurs difficultés. En premier lieu, les éprouvettes flambent et/ou des forces de compression non nulles sont enregistrées pour le déplacement minimal imposé par la machine d'essai. De plus, il est bien établi que l'état de référence des éprouvettes (état non déformé et non contraint) change à chaque nouveau cycle. Cela pose de nouveaux défis, parmi lesquels : comment traiter des mesures d'élongation, si leur calcul dépend du choix d'un état de référence, qui varie d'un cycle de chargement à l'autre.

Ces observations nous ont conduit à d'autres investigations expérimentales, présentées dans la section suivante.

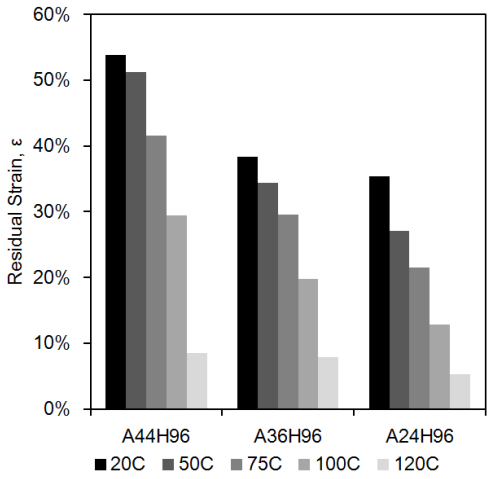

(a) Effet du taux d'ACN.

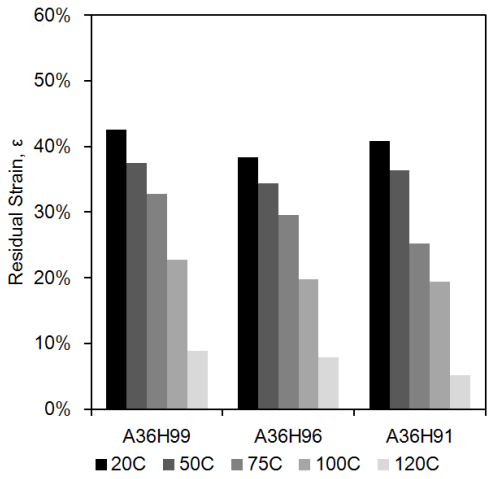

(b) Effet du taux d'hydrogénation.

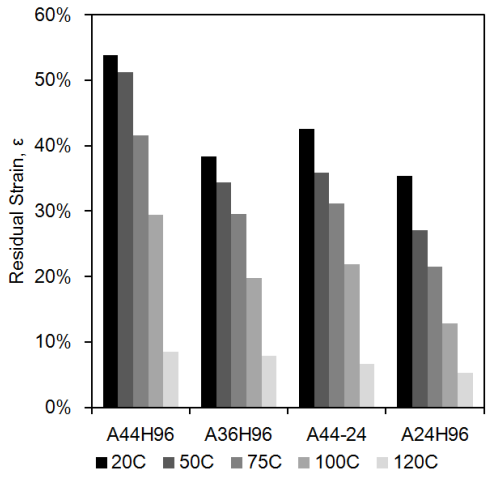

(c) Composite A44-24.

Figure A.2-7 – Déformation résiduelle (ϵ_{res}) des mélanges HNBR, mesurée après 10 000 cycles de 20 °C à 120 °C.

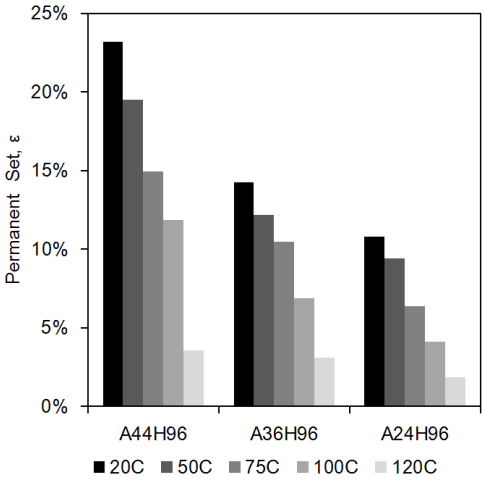

(a) Effet du taux d'ACN.

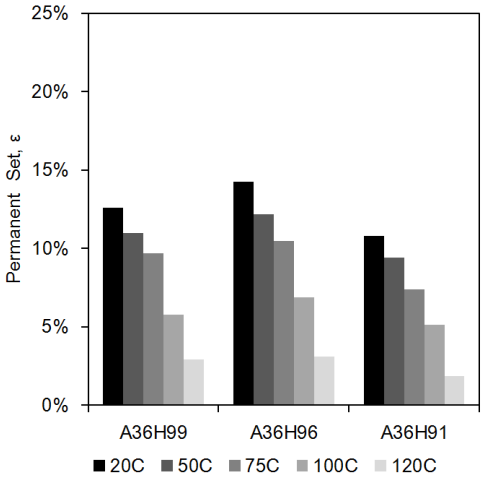

(b) Effet du taux d'hydrogénation.

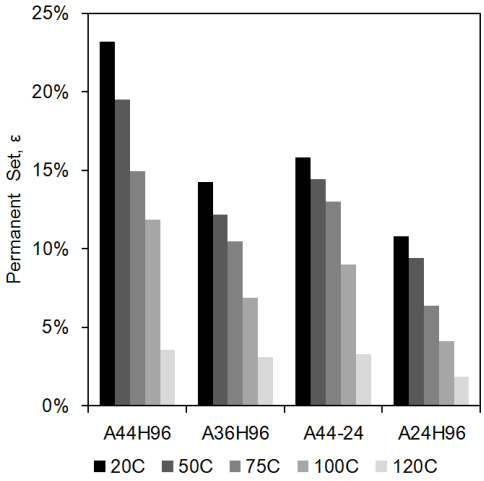

(c) Composite A44-24.

Figure A.2-8 – Déformation permanente (ϵ_p) des mélanges HNBR mesurée après 10 000 cycles de 20 °C à 120 °C.

A.3 Nouvelles approches expérimentales pour la fatigue des élastomères (Chap. 3)

Le chapitre 3 présente les méthodes expérimentales utilisées pour les essais permettant de mesurer la durée de vie en fatigue des élastomères. L'analyse de la résistance à la fatigue des matériaux, y compris les élastomères, peut être effectuée par deux approches complémentaires - la première dite en « propagation des fissures » de fatigue et la seconde en « durée de vie » en fatigue. Le présent chapitre est entièrement dédié à cette dernière. Une partie de la discussion présentée dans le chapitre 3 a été publiée dans *International Journal of Fatigue* (Narynbek Ulu et al. 2017b).

A.3.1 Approches conventionnelles et leurs limites

Avant de mettre en œuvre nos essais de fatigue sur le HNBR, plusieurs difficultés ont été analysées dans les approches expérimentales classiques. Comme souligné précédemment, des essais de fatigue pilotés en déplacement présentent des inconvénients importants. Ainsi, leur utilisation est inadaptée dans de nombreux cas, et en particulier pour les élastomères à cause de la nature inélastique de leur réponse cyclique. Plus précisément, les élastomères présentent deux phénomènes inélastiques lors de chargements à déplacement imposé : l'effet Mullins et la relaxation cyclique de la contrainte à long terme. Tous deux sont des phénomènes d'adoucissement des contraintes. Ces deux phénomènes rendent inadéquate l'utilisation du pilotage en déplacement pour des essais de fatigue, puisque les contraintes au sein de l'éprouvette varient tout au long d'un essai. Les méthodes utilisées pour tenir compte de ces effets diffèrent d'une étude à l'autre, aussi bien dans les travaux industriels qu'académiques. Pour illustrer les limitations du pilotage en déplacement des essais de fatigue, deux scénarios simplifiés sont présentés dans la suite.

Scénario 1

Dans le meilleur des cas, si la réponse du matériau le permet, on peut prendre en compte l'effet Mullins et supposer que la relaxation des contraintes à long terme est négligeable. Ce scénario peut être résumé par la Figure A.3-1, où l'évolution de la force, de la déformation et de la contrainte vraie (contrainte de Cauchy) sous un chargement cyclique piloté en déplacement (contour en gras) sont présentées. La relaxation de la contrainte dû à l'effet Mullins se produit du point A au point B. Après le point B, les deux paramètres mécaniques, déformation et contrainte vraie, sont à peu près constants ; les déformation et contrainte ne varient plus comme indiqué par les lignes pointillées, et des relations liant déplacement imposé, force mesurée, déformation et contrainte peuvent être établies. Ainsi, dans ce cas, les paramètres mécaniques, la contrainte vraie et/ou la déformation, peuvent être grossièrement calculés.

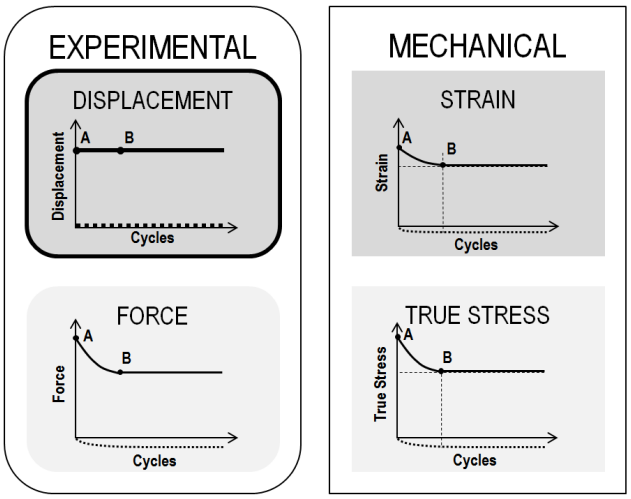

Figure A.3-1 – Scénario 1 - Évolution de la force, de la déformation et de la contrainte vraie sous chargement cyclique piloté en déplacement (contour en gras) avec effet Mullins.

Scénario 2

Dans le cas le plus défavorable, qui reflète toutefois la réponse réelle de la majorité des élastomères, la relaxation de la contrainte cyclique à long terme ne peut pas être négligée comme le montre la Figure A.3-2. La contrainte relaxe sur toute la durée de

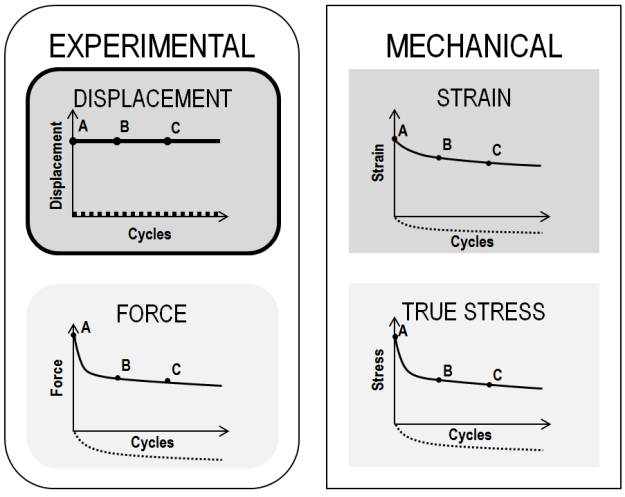

Figure A.3-2 – Scénario 2 - Évolution de la force, de la déformation et de la contrainte vraie sous chargement cyclique piloté en déplacement (contour en gras) avec effet Mullins et relaxation cyclique de la contrainte à long terme.

l'essai : les contraintes maximales et minimales diminuent sans atteindre de plateau, c'est-à-dire qu'il n'y a pas stabilisation de la contrainte. La déformation maximale varie également. Par conséquent, les essais expérimentaux pilotés en déplacement ne conduisent pas à des paramètres mécaniques constants pendant la durée de l'expérience. En pratique, le choix d'un cycle particulier considéré comme représentatif de l'état mécanique de l'essai, au cours duquel sont calculées l'élongation, la contrainte vraie (ou la densité d'énergie stockée ou dissipée), fournira des valeurs erronées car **aucun paramètre mécanique n'est constant tout au long de l'essai**.

De plus, ces difficultés expérimentales apparaissent également pour des essais pilotés en force, pour lesquels le fluage cyclique se substitue à la relaxation précédente, comme le montre la Figure A.3-3.

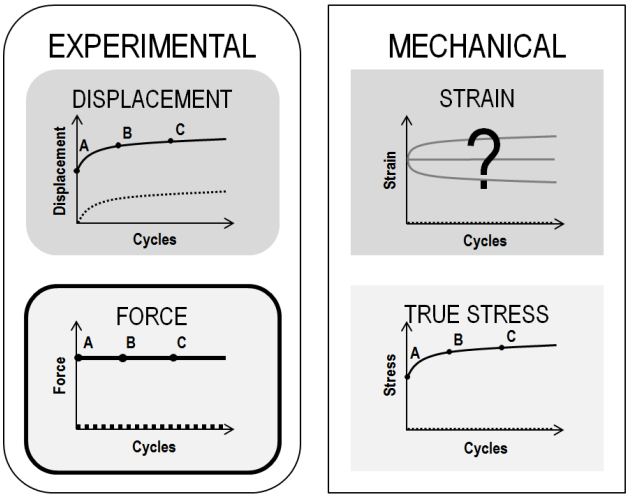

Figure A.3-3 – Scénario 2bis - Évolution de la force, de la déformation et de la contrainte vraie sous chargement cyclique piloté en force (contour en gras) avec effet Mullins et fluage cyclique de l'élongation à long terme.

Pour conclure, et ce pour de nombreux élastomères, le pilotage des essais par des paramètres dits expérimentaux (déplacement ou force) ne permettent pas de connaître l'histoire des grandeurs dites mécaniques (élongation et contrainte) appliquées au matériau.

A.3.2 Essais de fatigue pilotés en contrainte vraie

Pour résoudre les difficultés précédentes, une approche expérimentale originale permettant le pilotage des essais par la contrainte vraie est présentée. Les essais pilotés en contrainte vraie permettent de conserver au moins un paramètre d'état mécanique constant ; ainsi la méthode permettra une analyse plus pertinente des résultats, assurera la validité des comparaisons entre différents matériaux et fiabilisera les prévisions en cours de conception. Cette procédure peut être résumée comme suit :

- En premier lieu, l'évolution de l'aire de la section médiane de l'échantillon en fonction de l'allongement imposé est évaluée par des mesures de corrélation d'images numériques (sigle *digital image correlation* - DIC en anglais) et par une analyse par éléments finis ;
- Ensuite, un algorithme développé pour piloter la machine permet d'atteindre la cible d'amplitude de contrainte vraie pendant tout un essai mené sur un seul échantillon ;
- La méthode est étendue aux essais permettant de solliciter plusieurs éprouvettes (ici huit) en parallèle afin de créer des courbes maîtresses en déplacement. Ces courbes représentent les valeurs minimales et maximales de déplacement imposé pour un niveau imposé de contrainte vraie en fonction du nombre

de cycles. Enfin, ces courbes maîtresses sont utilisées pour effectuer des essais sur plusieurs échantillons en parallèle en utilisant un montage expérimental développé à cet effet.

A.3.3 Validation de la méthode

Dans la suite, la procédure est mise en œuvre et appliquée avec succès au mélange A44H96.

Essais sur des échantillons individuels

Pour les essais sur des échantillons individuels, la procédure contrôle avec précision le chargement en amplitude de contrainte vraie tout en respectant la valeur du rapport de charge spécifié. Pour différents niveaux de chargement, la procédure fournit des résultats cohérents. Par exemple, la Figure A.3-4 montre les déplacements minimal et maximal prescrits par la machine sur trois échantillons individuels différents afin d'atteindre une amplitude de contrainte constante $\Delta\sigma$=6 MPa. Sur les

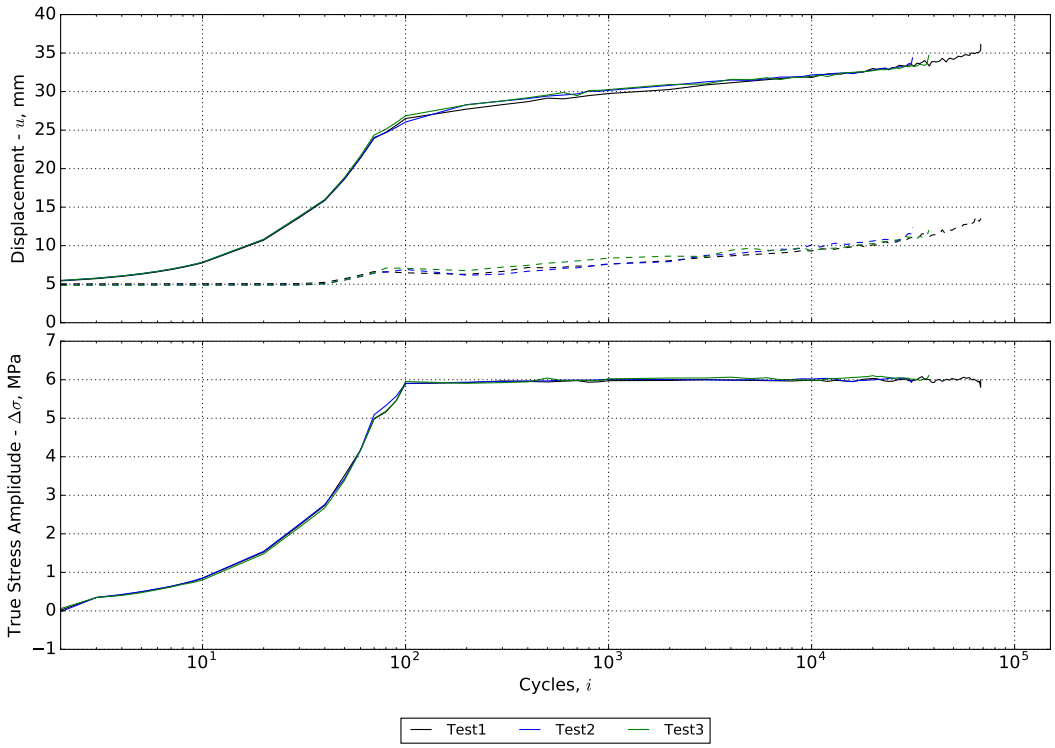

Figure A.3-4 – Déplacement imposé minimal et maximal (en haut) pour appliquer une amplitude de contrainte vraie égale à 6 MPa (en bas).

courbes de cette figure, deux phases apparaissent. La première phase, jusqu'à environ 100 cycles, comprend la stabilisation de la machine (l'amplitude de l'onde sinusoïdale imposée augmente progressivement jusqu'à une cible spécifiée), où l'algorithme atteint la cible de 6 MPa. Après 100 cycles, la cible étant atteinte, les déplacements minimal et maximal imposés par la machine se stabilisent. Il n'y a pas de changement significatif de l'amplitude en déplacement, mais celle-ci augmente

encore pour maintenir une amplitude de contrainte réelle de 6 MPa. Il convient de noter que sur la figure A.3-4, les trois éprouvettes ont des durées de vie en fatigue très différentes mais ont des courbes de pilotage identiques, ce qui valide la méthode. En effet, les déplacements minimaux et maximaux obtenus sont répétables et une courbe de référence en déplacement pour ce niveau de chargement spécifique peut ainsi être créée.

Essais à plusieurs éprouvettes montées en parallèle

Pour le chargement parallèle de plusieurs éprouvettes, il est beaucoup plus difficile d'atteindre uns cible de contrainte vraie spécifiée.

La Figure A.3-5 montre l'amplitude de contrainte vraie pour tous les échantillons testés à quatre niveaux de chargement (cible de 10, 8, 6 et 4 MPa). Pour chaque

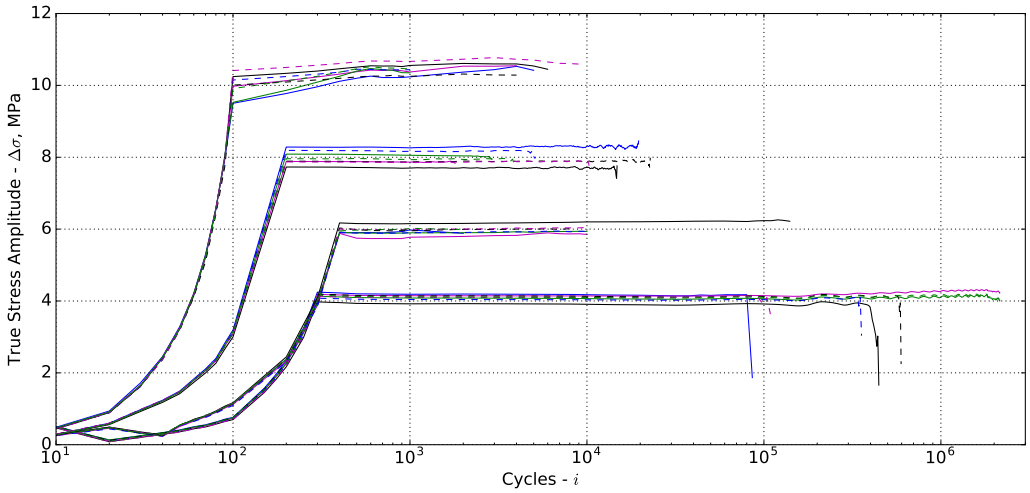

Figure A.3-5 – Évolution de l'amplitude en contrainte vraie des huit éprouvettes montées en parallèle à 10, 8, 6 et 4 MPa et R=0.

niveau de contrainte visé, différentes contraintes sont mesurées. Cependant, on peut dire que la procédure est satisfaisante, car l'amplitude appliquée en contrainte vraie est quasi constante pendant la durée des expériences.

Courbe Wöhler

Finalement, avec cette procédure, nous sommes capables d'établir la première courbe Wöhler (tracée en contrainte vraie) pour des élastomères ; cette courbe est montrée sur la Figure A.3-6. Il convient de noter que même si la consigne de contrainte vraie n'est pas parfaitement appliquée, la contrainte vraie dans le matériau est mesurée exactement aussi bien pour les essais individuels que les essais en parallèle. Ces mesures précises seront utilisées dans l'analyse statistique qui suit. En effet, une telle analyse s'avère ici nécessaire en raison de la grande dispersion des résultats et d'échantillons non rompus. Ces approches statistiques sont discutées dans la section suivante.

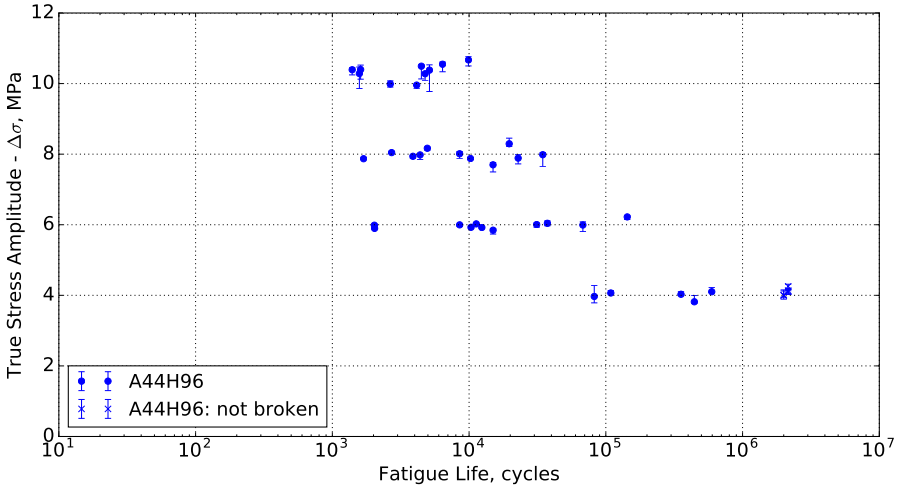

Figure A.3-6 – Courbe de Wöhler pour le mélange A44H96, $R = 0$.

A.3.4 Analyses statistiques

Comme le montre la courbe de Wöhler de la figure A.3-6, il y a une dispersion significative dans les résultats observés. Cette dispersion existe pour tous les matériaux et quel que soit le mode de pilotage. Un tel niveau de dispersion n'est pas particulièrement inconnu : il a déjà été observé pour d'autres élastomères synthétiques sollicités à de faibles niveaux de chargement.

Dans le corps du mémoire, la loi Basquin, largement utilisée par ailleurs, a été utilisée et ses limites dans le contexte du présent travail ont été mises en évidence, notamment une dispersion dans les valeurs de la contrainte vraie et l'existence d'échantillons non rompus à un très grand nombre de cycles, pour une amplitude de contrainte vraie égale à 4 MPa, échantillons dont la durée de vie n'est finalement pas connue. Pour tenir compte de ces facteurs, différents outils statistiques ont été introduits. Tout d'abord, l'analyse de Weibull, largement utilisée pour les métaux, a été initialement appliquée ; elle s'est avérée peu efficace. Par la suite, des approches de type « analyse de survie » ont été empruntées à la médecine pour l'analyse statistique des résultats de fatigue. Ainsi, une méthode non paramétrique, l'analyse de Kaplan-Meier, a été appliquée aux données et s'est révélée statistiquement significative. Ensuite, le modèle à risques proportionnels de Cox a été étudié en détails et la courbe de Wöhler a été utilisée pour créer un modèle de base décrivant les effets de l'amplitude en contrainte vraie sur la durée de vie en fatigue. En effet, en utilisant les résultats de la figure A.3-6, on détermine les moyennes statistiques du modèle de Cox (N_C) pour chaque niveaux de chargement et les comparer aux résultats issus de l'analyse Weibull (N_w), de celle de Kaplan-Meier (N_{KM}), de la loi de Basquin (N_B) et finalement de la moyenne géométrique (N_G) ; tous ces résultats sont présentés dans le Tableau A.3-1.

Pour conclure sur cette utilisation originale de méthodes statistiques, la capacité d'évaluation multivariée de différents facteurs affectant la durée de vie en fatigue avec le modèle de Cox offre de bonnes perspectives. En effet, un modèle bien défini peut être utilisé pour interpoler et extrapoler des résultats construits à partir de

Tableau A.3-1 – Valeurs moyennes à quatre niveaux de chargement ; unités - cycles.

Load	$\overline{N_w}$	$\overline{N_G}$	$\overline{N_B}$	$\overline{N_{KM}}$	$\overline{N_C}$	$\overline{\Delta\sigma}$
10 MPa	4 329	3 598	421	4 308	2 701	10.34
8 MPa	11 971	5 455	6 325	8 524	9 946	7.98
6 MPa	31 734	15 785	127 180	12 397	31 205	5.99
4 MPa	1 156 352	-	7 633 742	595 017	318 630	4.05

données de base ; de plus, une approche probabiliste peut être appliquée pour la création de courbes Wöhler.

A.4 Fatigue du HNBR (Chap. 4)

Le chapitre 4 se concentre sur les effets de la formulation sur la vie en fatigue de HNBR. La méthode du pilotage en contrainte vraie et les outils statistiques précédents sont utilisés pour étudier les effets du taux d'acrylonitrile et d'hydrogénation sur la durée de vie en fatigue du HNBR. Ensuite, ces résultats sont complétés par des expériences de propagation des fissures de fatigue. Les essais sont effectués à 120 °C, puisqu'il s'agit d'une température médiane d'utilisation du HNBR. Enfin, l'analyse de l'endommagement par microscopie optique et microscopie électronique à balayage est réalisée pour comprendre les mécanismes d'endommagement de fatigue du HNBR.

A.4.1 Effet du taux d'acrylonitrile

Les trois approches expérimentales conduisent à des conclusions similaires sur l'effet de l'ACN sur la résistance à la fatigue du HNBR à 120 °C : **le mélange A36H96 admet une meilleure résistance à la fatigue, suivie par le mélange A44H96, et le mélange A24H96 a significativement moins de résistance à la fatigue par rapport aux deux autres mélanges.**

- Les essais de durée de vie en fatigue et les analyses statistiques ont montré que le mélange A36H96 a une durée de vie en fatigue plus longue, suivie par le mélange A44H96, et le mélange A24H96 a une durée de vie en fatigue significativement plus courte. Les résultats sont présentés sur la Figure A.4-1.

- Les essais de propagation de fissures de fatigue fournissent des vitesses de propagation de fissures similaires pour les mélanges A36H96 et A44H96. D'autre part, le mélange A24H96 admet des vitesses de propagation supérieures d'un ordre de grandeur pour les mêmes énergies de déchirement. Les résultats sont présentés sur la Figure A.4-2.

- L'endommagement causé par la fatigue diffère suivant l'échelle d'observation : macroscopique ou microscopique. Apparaissent ainsi deux catégories de mélanges : les mélanges A36H96 et A44H96 d'une part, et le mélange A24H96 d'autre part.

  Les observations macroscopiques ont montré que les mélanges A44H96 et A36H96 (dans une plus grande mesure) présentent un nombre important des fissures qui se développent verticalement, c'est-à-dire dans la direction de chargement, alors que la croissance des fissures dans le mélange A24H96 a lieu sur un seul plan, perpendiculaire à la direction de chargement.

  Ces résultats sont corrélés avec les observations microscopiques des surfaces de rupture. Dans les mélanges A36H96 et A44H96, il apparaît des régimes d'initiation-propagation-rupture classiques sur un seul plan perpendiculaire à la direction de chargement. Toutefois, des modes de propagation dans la direction verticale, correspondant aux observations macroscopiques, apparaissent

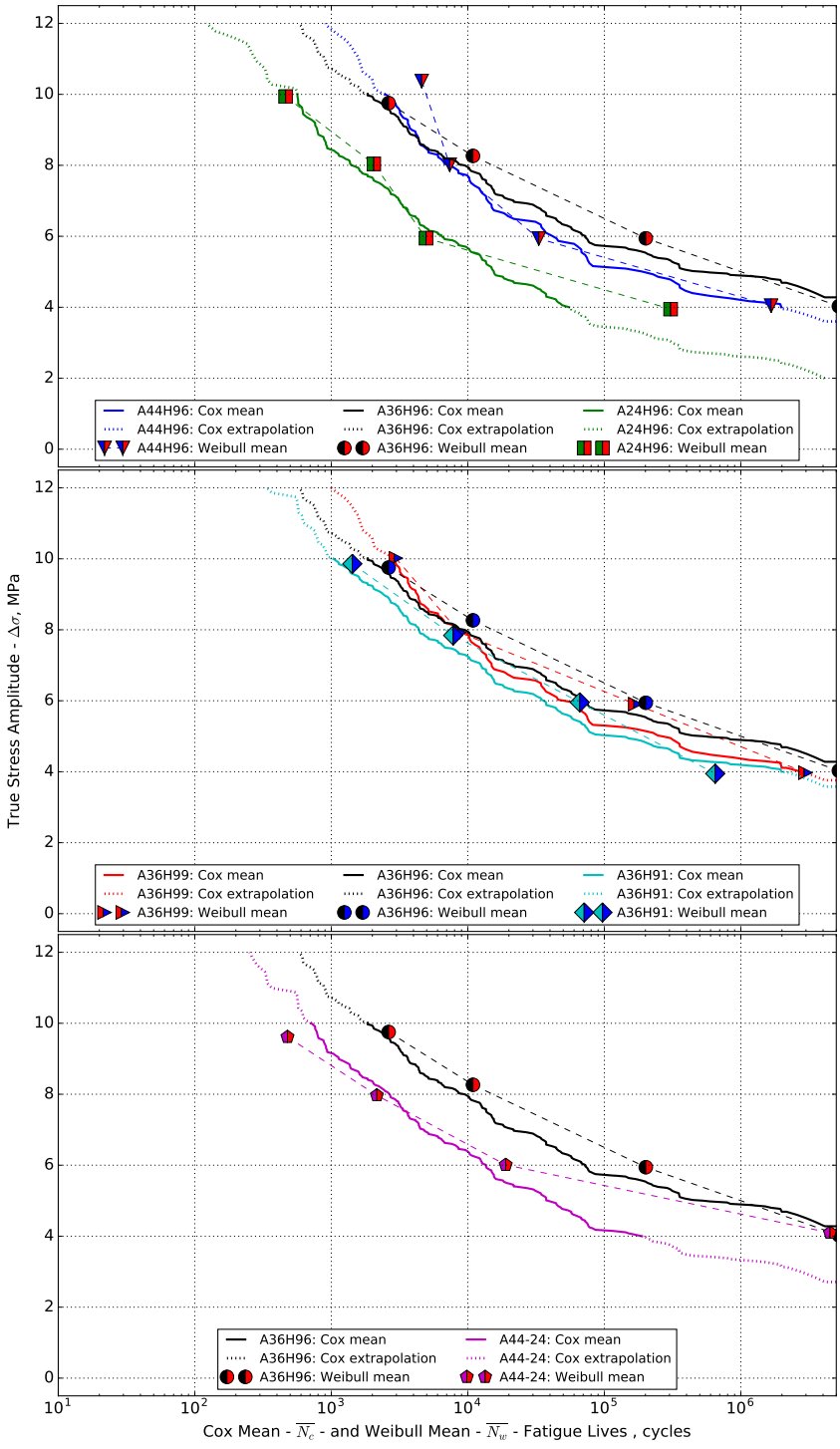

Figure A.4-1 – Durées moyennes du modèle de Cox ($\overline{N_c}$) avec comparaison avec l'analyse de Weibull ($\overline{N_w}$) ; effet du taux d'ACN, du taux d'hydrogénation et pour le composite A44-24.

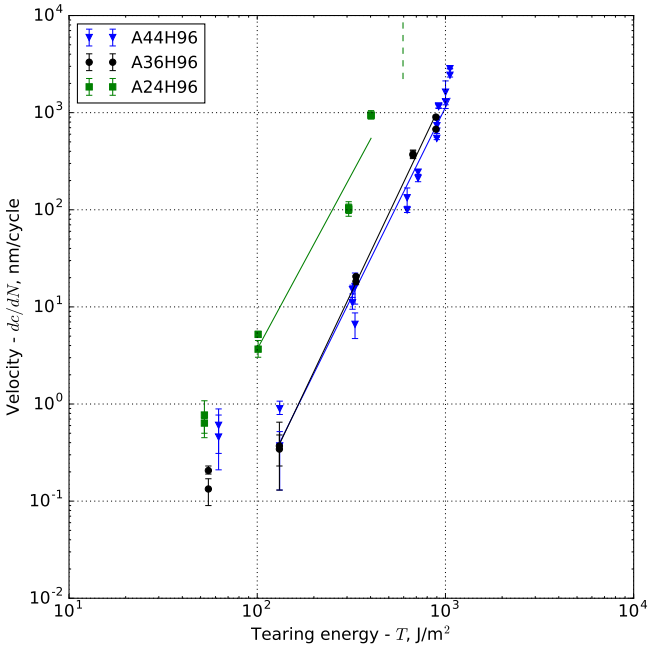

Figure A.4-2 – Effet du taux d'ACN sur la propagation des fissures de fatigue dans le HNBR à 120°C.

aussi à l'échelle microscopique. D'autre part, la propagation dans le mélange A24H96 a lieu dans un seul plan.

Enfin, de la multi-fissuration est observée dans environ 12% des échantillons du mélange A36H96 rompus et dans les échantillons du mélange A44H96 dans une moindre mesure. Cependant, ce phénomène est absent des échantillons du mélange A24H96.

À partir de ces résultats, on conclut que la résistance en fatigue relativement médiocre de l'A24H96 est due à sa faiblesse mécanique, comme l'ont montré les résultats des essais de traction : la contrainte à la rupture est de l'ordre de 12 MPa, ce qui est très proche du niveau de chargement maximal en fatigue (10 MPa). Les mélanges HNBR à faible taux d'ACN sont principalement conçus pour être utilisés aux basses températures (en raison d'une T_g plus basse) et **il est donc évident que l'utilisation du mélange A24H96 pour les applications à 120°C n'est pas un bon choix, si une bonne résistance à la fatigue est requise.** En termes de résistance mécanique, la contrainte à rupture du mélange A44H96 est presque deux fois celle du mélange A36H96 (38,5 MPa contre 23,8 MPa) ; ainsi, il se peut que la plage de contraintes de 4 à 8 MPa n'a pas d'influence significative sur la fatigue. De plus, si l'on rappelle la figure A.4-1, le mélange A44H96 a et est extrapolée pour avoir des durées de vie en fatigue plus longues pour les valeurs d'environ 8,5 MPa et plus. **Ainsi, pour des applications en fatigue, où un chargement important est attendu (en moyenne ou pour des pointes de charges), le mélange A44H96 est un bon choix. D'autre part, il est évident que le mélange A36H96 est en général le meilleur choix.**

A.4.2 Effet du taux d'hydrogénation

Comme les résultats sur l'effet de l'ACN, mais avec des différences moins prononcées, les résultats sur l'effet du taux d'hydrogénation à partir des trois approches expérimentales sont également en accord les uns avec les autres : **le mélange A36H96 admet une meilleure résistance à la fatigue, suivi par les mélanges A36H99 et A36H91.** Dans la discussion des résultats, un parallèle peut être établi :

- Des expériences de durée de vie en fatigue et des analyses statistiques ont montré que le mélange A36H96 a une durée de vie plus longue, suivi par les mélanges A36H99 et A36H91 ; les résultats sont présentés sur la figure A.4-1.
- Les expériences de propagation des fissures de fatigue montrent que le mélange A36H96 admet une meilleure résistance à la propagation des fissures de fatigue que le mélange A36H99 (sauf aux énergies de déchirement plus élevées). D'autre part, les vitesses de propagation des fissures du mélange A36H91 sont supérieures d'un ordre de grandeur les mêmes énergies de déchirement. Les résultats sont présentés sur la figure A.4-3.

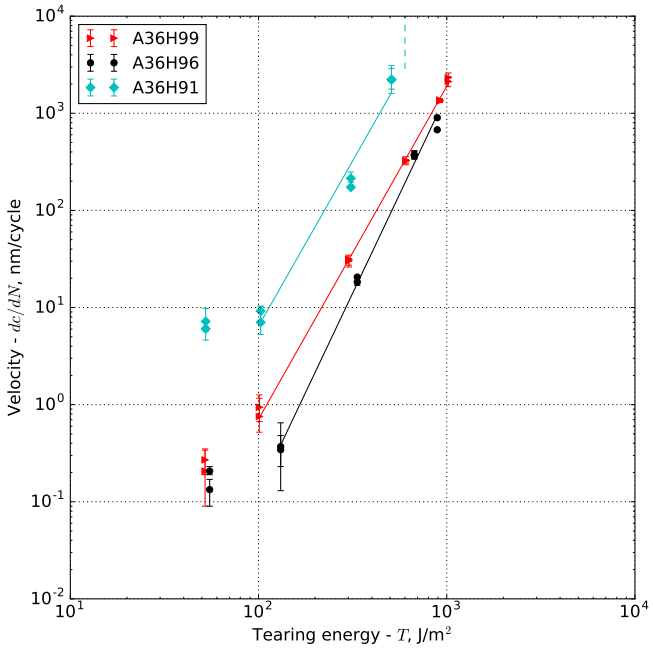

Figure A.4-3 – Effet du taux d'hydrogénation sur la propagation des fissures de fatigue dans le HNBR à 120°C.

- L'analyse de l'endommagement est similaire à l'échelle macroscopique et microscopique et, encore une fois, les mélanges peuvent être regroupés en deux catégories : les mélanges A36H96 et A36H99 d'une part, et le mélange A36H91 d'autre part.

  Les observations macroscopiques montrent que le mélange A36H96 et le mélange A36H99, dans une moindre mesure, admettent de nombreuses fissures qui croissent verticalement dans la direction de chargement. Le mélange A36H91, ainsi que le mélange A24H96, présentent des fissures sur un seul plan, perpendiculaire à la direction de chargement.

De même, les surfaces de rupture des mélanges A36H96 et A36H99 montrent des régimes d'initiation-propagation-rupture classiques, c'est-à-dire sur un seul plan perpendiculaire à la direction de chargement ; mais encore une fois, il apparaît des surfaces de rupture correspondant à un régime de propagation dans la direction verticale, en accord avec les observations macroscopiques. Un tel phénomène n'est pas observé pour le mélange A36H91 et, de plus, celui-ci présente certaines surfaces de rupture complètement lisses, similaires à celles issues d'une rupture en traction quasi-statique.

Enfin, dans environ 12% des échantillons du mélange A36H96 rompus, on observe le phénomène de multi-fissuration, tout comme dans environ 4% des échantillons du mélange A36H99 ; toutefois ce phénomène est complètement absent des échantillons du mélange A36H91.

Finalement, les conclusions suivantes peuvent être proposées. **Dans les applications pratiques, où une résistance à la fatigue relativement élevées est nécessaire, le mélange A36H96 est le meilleur choix.** Avec le mélange A36H99, les meilleures propriétés de résistance thermique attendues ne sont peut-être pas suffisamment sollicitées lors des tests à 120 °C. **Il semble probable que les essais de durée de vie en fatigue à des températures plus élevées, considérant que la limite supérieur d'utilisation du HNBR est environ 150°C, pourraient montrer que le mélange A36H99 a de meilleures performances en fatigue que le mélange A36H96.** Finalement, les résultats discutés ci-dessus montrent qu'à 120 °C la résistance à la fatigue du mélange A36H91 est moins bonne que celle des mélanges A36H96 et A36H99. **Il semble probable que le matériau A36H91 ne soit pas adapté pour des utilisations à 120°C.**

A.4.3 Résistance à la fatigue du mélange composite A44-24

Encore une fois, les trois approches expérimentales conduisent à la même conclusion : **le composite A44-24, avec des taux d'ACN de 24% et 44% pour une valeur moyenne de 36%, a une résistance à la fatigue significativement plus faible que le mélange A36H96.**

- Les expériences de durée de vie en fatigue et les analyses statistiques ont montré que le composite A44-24 a une durée de vie significativement plus courte que le mélange de référence A36H96, comme le montre la figure A.4-1.
- Les expériences de propagation des fissures de fatigue montrent que le mélange A44-24 admet des vitesses de propagation de fissure significativement plus rapides que celles du mélange A36H96 ; de plus, ces résultats correspondent parfaitement à ceux obtenus pour le mélange A24H96. Ces résultats sont présentés sur la figure A.4-4.
- L'endommagement en fatigue observé dans le mélange A44-24 diffèrent significativement de ceux du mélange A36H96 et sont similaires à ceux observés dans le mélange A24H96. À l'échelle macroscopique, toutes les fissures se développent dans un seul plan parallèle à la direction de chargement. Les surfaces de de rupture présentent des régimes d'initiation-propagation-rupture classiques,

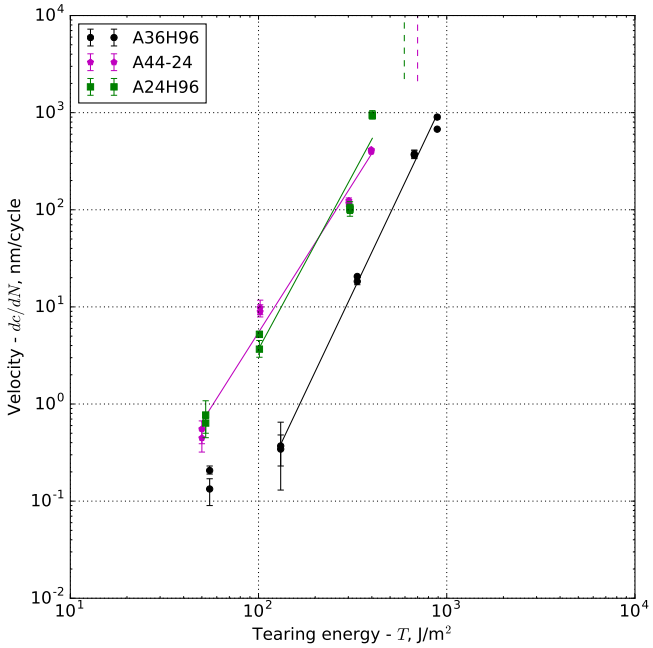

Figure A.4-4 – Propagation des fissures de fatigue dans le composite A44-24 à 120°C ; par rapport au mélange de référence A36H96 et au mélange A24H96.

mais aussi des surfaces complètement lisses telles que celles observées dans les essais de traction quasi-statiques. De plus, la multi-fissuration est absente.

Avec toutes les informations ci-dessus, il est clair que le mélange A44-24, même avec un taux moyen d'ACN identique à celui du mélange A36H96, admet une résistance en fatigue plus faible et qui ressemble étroitement aux caractéristiques du mélange A24H96. On peut penser que, tout comme le mélange A24H96, sa résistance à la fatigue est meilleure à des températures plus basses. **Le choix du mélange composite A44-24 n'est pas adapté à une utilisation à 120°C.**

A.5 Vieillissement et fatigue du HNBR (Chap. 5)

Le chapitre 5 se concentre sur les derniers résultats de la thèse, où les effets du vieillissement thermique sur la durée de vie en fatigue du HNBR sont étudiés. En plus des essais de la durée de vie en fatigue à 120 °C déjà effectués (appelés **Test 1** dans la suite, voir Figure A.5-1(a)), deux nouveaux essais sont mis en œuvre. 150 °C est choisie comme température de référence pour vieillissement ; elle représente la limite supérieure d'usage du HNBR. Ces deux types d'essais, dont les résultats seront comparés, sont les suivants :

- **Test 2 : essais simultanés de vieillissement et de fatigue** qui se réfère à des essais de durée de vie en fatigue effectués à 150 °C (Figure A.5-1(b)). L'idée principale motivant ces essais est qu'à bas niveau de chargement où les essais sont relativement longs, on peut observer les effets simultanés du vieillissement et de la fatigue ;
- **Test 3 : essais de pré-vieillissement puis de fatigue** qui se réfère à des essais de fatigue effectués à 120 °C mais sur des échantillons préalablement vieillis. Comme le montre la Figure A.5-1(c), un pré-vieillissement classique est fait à 150 °C, aussi bien sur des éprouvettes au repos que sur des échantillons sous chargement statique. Ces deux conditions de pré-vieillissement vise à déterminer si les sollicitations mécaniques affectent le mécanisme de vieillissement dans le matériau.

A.5.1 Vieillissement et fatigue simultanés

Lorsque le taux d'hydrogénation augmente, la résistance thermique du HNBR augmente ; ainsi, ce taux joue un rôle important dans la résistance à la fatigue lorsque la température augmente de 120 °C à 150 °C. Comme le montre la Figure A.5-2, la diminution de la durée de vie en fatigue à haute température est la plus faible pour le mélange A36H99, suivi par le mélange A36H96 (96%), enfin le mélange A36H91 (91%) admet la plus grande diminution de la durée de vie en fatigue. Pour les deux mélanges ayant une résistance thermique faible (A36H96 et A36H91), les premiers résultats semblent indiquer une accumulation d'endommagement dus aux températures élevées. De plus, pour les expériences de durées plus longues à faibles amplitudes de chargement (qui sont relativement plus longues que les courts expériences à haute amplitude) sont plus pires pour les durées de vie en fatigue.

D'après les analyses d'observations macroscopiques et microscopiques, il apparaît que les mécanismes d'endommagement en fatigue à 150 °C diffèrent de ceux observés à 120 °C. En comparant les types d'endommagement des mélanges A36H96 et A36H99 à 150 °C, il est clair que le HNBR avec 99% taux d'hydrogénation présente beaucoup plus fréquemment les mécanismes d'endommagement avec propagation verticale des fissures, qui correspondent à des durées de vie en fatigue plus longues ainsi qu'à des vitesses de propagation des fissures de fatigue plus faibles à 120 °C. D'autre part, le nombre de surfaces de rupture sur lesquelles l'initiation et la propagation ont lieu sur un seul plan perpendiculaire à la direction de chargement augmente pour les essais à 150 °C. De plus, il apparaît beaucoup de surfaces de rup-

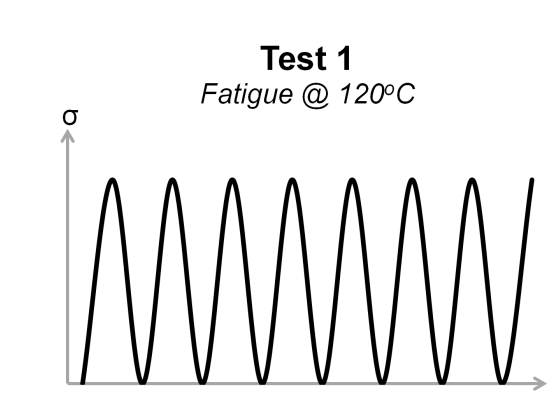

(a) Test 1 : Fatigue.

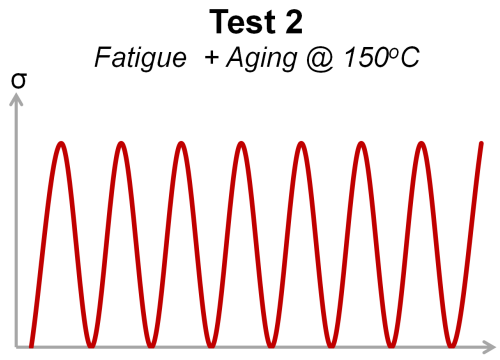

(b) Test 2 : Vieillissement et fatigue simultanés.

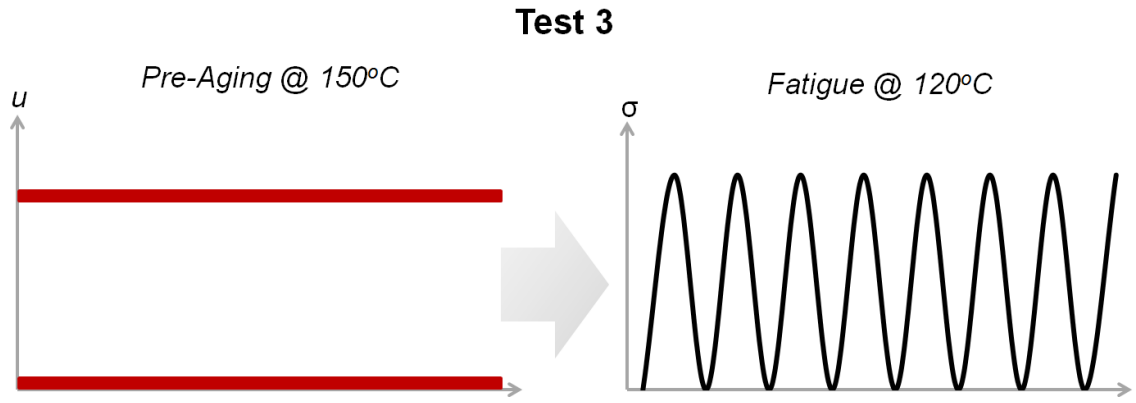

(c) Test 3 : Pré-vieillissement puis fatigue.

Figure A.5-1 – Représentation schématique des trois types d'essais utilisés pour étudier le vieillissement et la fatigue du HNBR.

ture « lisses » sans indication de la phase de propagation de la fissure de fatigue. Ces deux phénomènes indiquent une rupture plus rapide et plus « fragile » à 150 °C.

A.5.2 Pré-vieillissement puis fatigue

La Figure A.5-3 illustre qu'il est impossible de conclure sur l'existence des effets de pré-vieillissement avec ou sans chargement à 150 °C sur le mélange A36H96. Les premiers résultats indiquent une légère diminution de la durée de vie en fatigue à des niveaux de chargement faibles, si les spécimens ont été pré-vieillis sous charge. En outre, il semble y avoir un seuil de durée de pré-vieillissement, puisqu'un vieillissement de 42 h n'a pas induit de différences significatives sur la durée de vie par rapport à celle des échantillons vierges. Lorsque la durée du pré-vieillissement est de 240 h (10 jours), il y a une diminution quasi-uniforme des durées de vie en fatigue à tous les niveaux de chargement pour les échantillons pré-vieillis sans charge, comme le montre le décalage (quasi-)parallèle des courbes de durée de vie sur une échelle logarithmique. Pour les échantillons pré-vieillis sous charge, la durée de vie en fatigue diminue plus pour les faibles amplitudes de contrainte que pour les amplitudes élevées. De plus, le pré-vieillissement modifie les mécanismes de dégradation de la fatigue. Une analyse macroscopique préliminaire a montré que, dans tous les échantillons, la propagation des fissures n'a lieu que sur un seul plan perpendiculaire à la

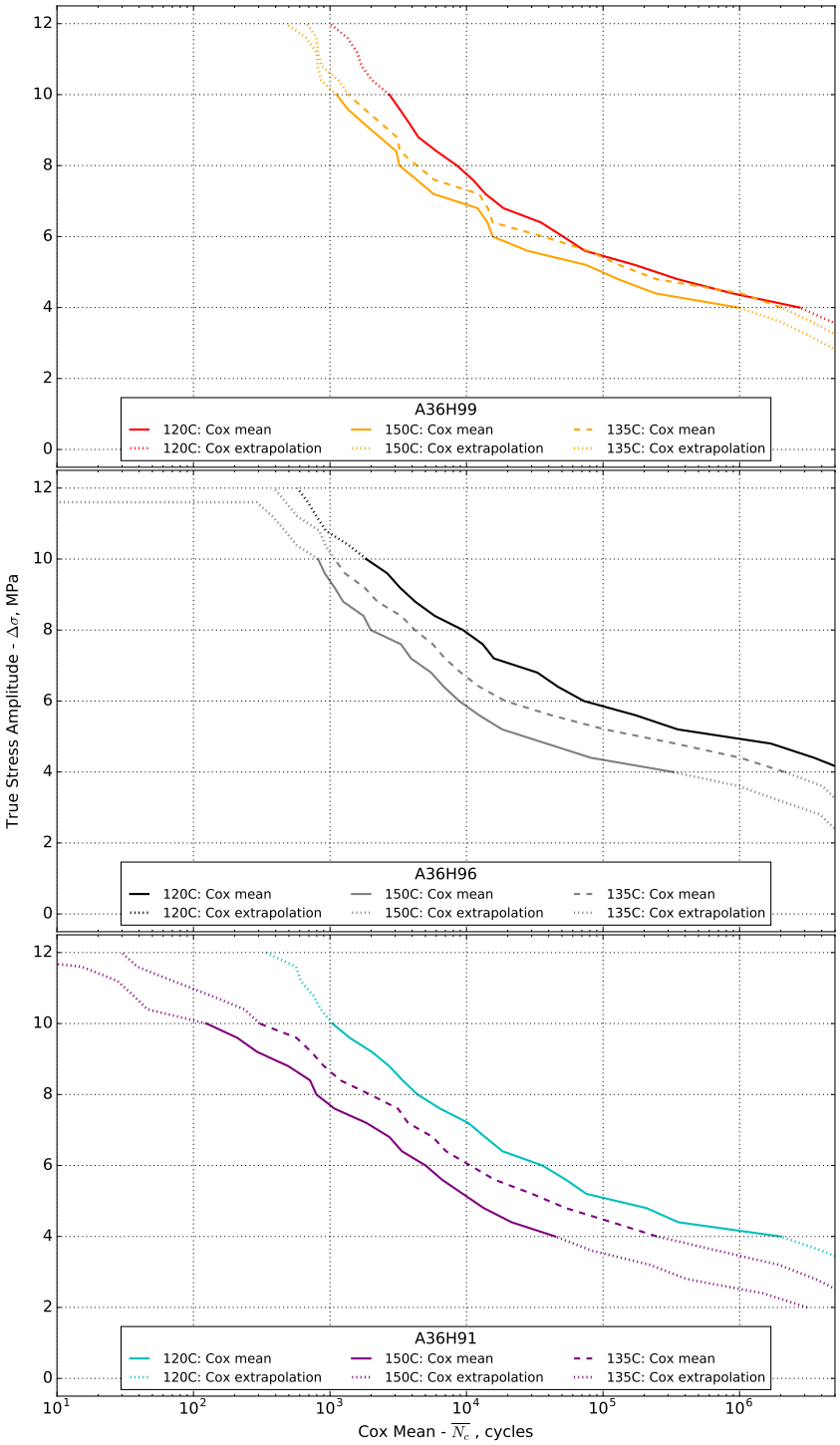

Figure A.5-2 – Durée de vie moyenne en fatigue des mélanges A36H99, A36H96 et A36H91 du modèle Cox à 120 °C et 150 °C, ainsi que la prédiction à 135 °C.

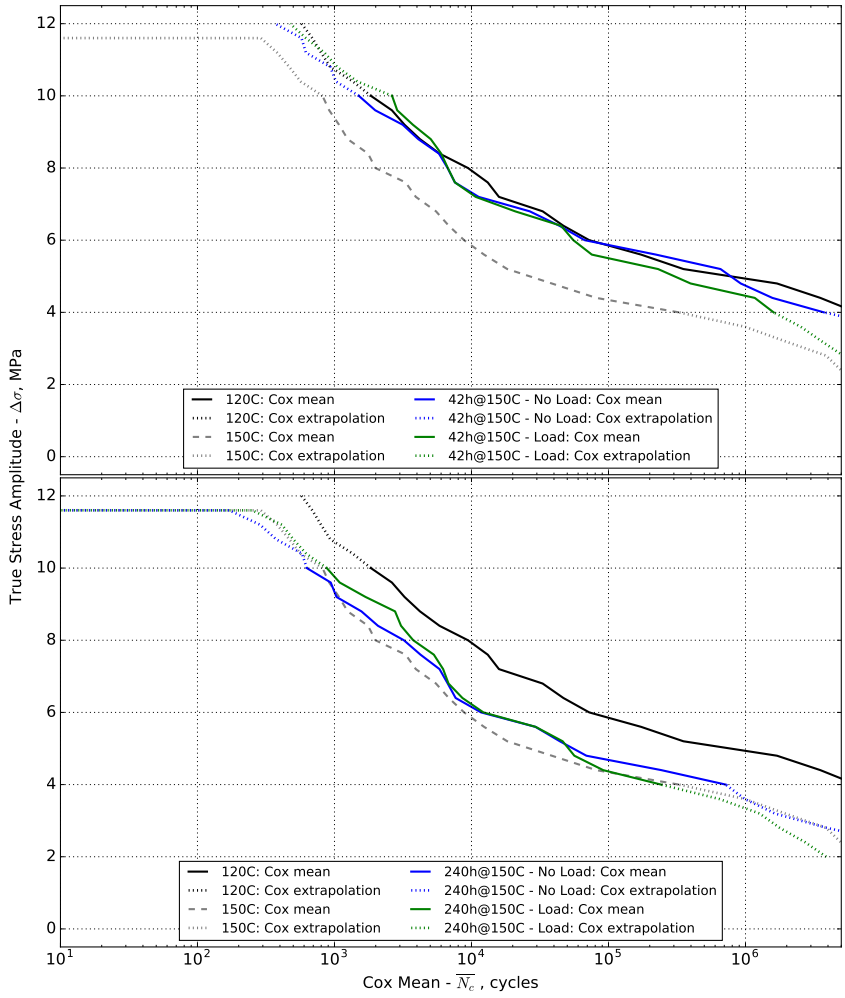

Figure A.5-3 – Durée de vie moyenne en fatigue du mélange A36H96 après pré-vieillissement à 150 °C sous deux conditions de chargement et deux durées de pré-vieillissement ; comparaison avec les durées de vie en fatigue des éprouvettes vierges et de celles testées à 150 °C.

direction de chargement.

Finalement, le modèle probabiliste développé précédemment a été appliqué afin de prédire les durées de vie en fatigue pour différentes températures et durées de vieillissement. Ces durées de vie sont ensuite approchées par un modèle d'Arrhenius de superposition temps-température (sigle TTS - *time-temperature superposition* en anglais) largement rencontré dans la littérature. Cette approche conduit à des résultats prometteurs qui pourraient réduire la durée des essais de fatigue sur échantillons pré-vieillis.

A.5.3 Différenciation entre les tests simultanés et les tests sur matériaux pré-vieillis

Une première tentative est faite pour réconcilier les résultats obtenus des deux tests. Les durées de vie en fatigue des échantillons pré-vieillis durant 10 jours à 150 °C et soumis ensuite à des essais de fatigue à 120 °C (Test 3) semblent coïncider avec celles issues des essais effectués à 150 °C sur des échantillons vierges (Test 2). Avec seulement ces quelques résultats, il est hasardeux de tirer des conclusions définitives sur le lien entre deux essais. Cependant, ces résultats indiquent que la température d'essai de fatigue est le facteur le plus influent sur la durée de vie en fatigue. Ainsi, pour le mélange A36H96, la durée de vie après un pré-vieillissement de 245 h est à peu près équivalente à celle issue d'un essai à 150 °C dont la durée n'est que d'environ 18 h.

Sur la base de cette observation, nous avons essayé de lier les deux essais par un modèle phénoménologique. Le principe consiste à déterminer un essai de fatigue équivalent à haute température, par. ex. à 150 °C, dont la durée de vie correspond à celle issue d'un essai équivalent à la température de référence, par ex. 120 °C, effectué sur des échantillons pré-vieillis à la haute température initiale, c.-à-d. 150 °C. Dans ce cas, le temps nécessaire pour pré-vieillir les échantillons (sans charge) doit être déterminé. Avec les résultats disponibles, issues des Tests 2 et 3, ce temps est égal à environ 245 h comme mentionné précédemment. Les durées de vie en fatigue sont prédites pour différentes températures, et différentes durées et températures de pré-vieillissement.

La Figure A.5-4 présente en abscisse le temps de pré-vieillissement t_a qui correspond à la température de pré-vieillissement T_f à appliquer à un échantillon (en ordonnée) avant un essai à 120 °C. Ainsi, un essai sur éprouvette vierge à T_f fournira une courbe de durée de vie en fatigue similaire à l'essai effectué à 120 °C sur un échantillon pré-vieilli à T_f durant t_a. Diverses fonctions ont été évaluées ; la fonction exponentielle fournit le meilleur ajustement avec un coefficient de régression de $r^2 = 0,992$:

$$T_f = T_{th} \exp\left(B t_a\right), \tag{A.5-1}$$

où B est une valeur ajustée et T_{th} est un seuil de température. Ici, $T_{th} = 128.7$ °C, ce qui indique qu'entre 120 °C et 128.7 °C aucun effet de température élevée ne sera observé pendant les essais de durée de vie en fatigue. Idéalement, T_{th} devrait être égal à 120 °C ; la différence s'explique sans doute par une quantité de données

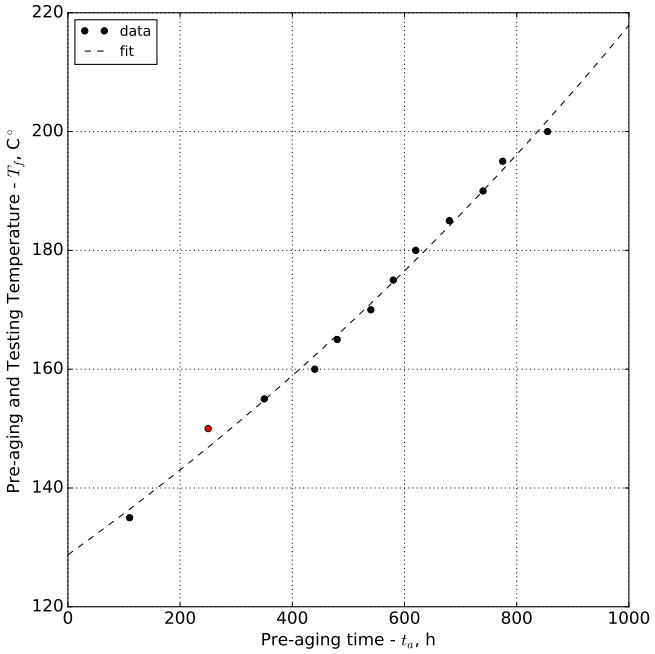

Figure A.5-4 – Temps (t_a) et température (T_f) de pré-vieillissement simulés, nécessaire pour atteindre la durée de vie en fatigue similaire testé à T_f.

insuffisante pour le recalage des modèles. Toutefois, cette approche ouvre des perspectives intéressantes pour l'étude du couplage entre vieillissement et fatigue dans les élastomères.

A.6 Conclusion générale

Une quantité considérable de résultats a été obtenue au cours de ce doctorat. Le choix du HNBR, caractérisé par une réponse mécanique relativement complexe et peu de littérature publiée, a induit des difficultés initiales, notamment lors de la mise en œuvre des premiers essais. Une fois ces obstacles franchis, les objectifs de départ ont en grande partie été atteints.

- Les méthodes expérimentales pour mesurer la durée de vie en fatigue des élastomères ont été grandement améliorées : la méthode permettant de conduire un essai de fatigue piloté par la contrainte vraie, tel qu'envisagé initialement par Wöhler, a été développé, et l'utilisation d'outils statistiques issus de la recherche médicale a permis de rationaliser les résultats.
- Les caractéristiques en fatigue du HNBR à la température de service de 120 °C ont été étudiées de manière exhaustive grâce à des expériences de durée de vie et de propagation de fissure de fatigue, et des analyses microscopiques d'endommagement. Ces travaux ont permis de discuter les effets de la formulation chimique des mélanges, plus particulièrement les effets du taux d'acrylonitrile et du pourcentage d'hydrogénation.

De plus, des études connexes ont été conduites :

- Une première étude sur les effets du vieillissement thermique et son couplage avec la fatigue a été proposée ;
- L'analyse quantitative de la présence de la cristallisation sous tension dans le HNBR non chargé, avec prise en compte du taux d'acrylonitrile.

Comme présenté dans le chapitre 2, l'étude mécanique du HNBR a montré que les mélanges présentent des réponses plastiques ou viscoplastiques en traction à température ambiante. Ce comportement inélastique est attribué à la température de transition vitreuse relativement élevée pour les mélanges de HNBR : plus la température d'essai est proche de la transition vitreuse, plus on observe d'inélasticité. Ainsi, lorsque la température augmente jusqu'à 120 °C, la réponse mécanique des mélanges du HNBR devient moins inélastique. Cependant, à cette température, même loin de la transition vitreuse, les effets inélastiques restent importants lors du chargement cyclique. Plus précisément, cette inélasticité se caractérise par deux phénomènes d'adoucissement des contraintes : l'effet Mullins et la relaxation cyclique des contraintes à long terme.

Ces deux phénomènes sont étroitement liés à la discussion des méthodes classiques d'essai de durée de vie en fatigue pour les élastomères et, en particulier, de leurs limites. Comme décrit dans le chapitre 3, ces méthodes remontent aux premières études des années 1940 et consistent le plus souvent en l'application d'un chargement cyclique à déplacement imposé. Dans le présent travail, nous avons montré pourquoi cette approche ne peut être appliquée, au mieux, qu'au prix d'une approximation du chargement mécanique ; toutefois, pour de nombreux élastomères industriels cette approximation n'est pas valide. En fait, le contrôle des essais par des paramètres expérimentaux (déplacement, force) ne reflète pas l'histoire mécanique réelle qui est appliquée au matériau : le calcul des paramètres mécaniques

(déformation, contrainte) *a posteriori* peut conduire à des conclusions erronées sur la résistance en fatigue du matériau, mais aussi rendre difficile les comparaisons entre différents matériaux, différentes conditions d'essai, *etc.* De plus, l'un des principaux inconvénients des essais de fatigue a été abordé : une dispersion significative est toujours observée dans les expériences de la durée de vie, quel que soit le matériau, mais celle-ci est particulièrement importante pour les élastomères synthétiques tels que HNBR. Les outils statistiques standards ont été étudiés et appliqués. Cependant, leur efficacité peu probante nous a conduit à nous intéresser à des outils statistiques peu ou pas utilisés pour les élastomères ; il s'agit de l'estimation de Kaplan-Meier et du modèle à hasards proportionnels de Cox issus de la recherche médicale et appliqués pour la première fois à la fatigue des élastomères. Le modèle de Cox est particulièrement adapté au traitement de deux problèmes rencontrés en fatigue : la dispersion des mesures de durée de vie et de la contrainte vraie appliquée (analyse multivariée), et la présence de données censurées à droite qui traduisent l'existence de spécimens non rompus après un certain nombre de cycles.

Dans le Chapitre 4, ces nouvelles méthodes sont été appliquées au HNBR afin d'étudier les effets de la formulation - taux d'ACN et pourcentage d'hydrogénation, ainsi qu'un mélange composite - sur la résistance à la fatigue à 120 °C, qui est la température de service médiane du HNBR. Les essais de durée de vie en fatigue ont été complétés par des essais de propagation des fissures de fatigue. Pour obtenir une image complète du phénomène, la microscopie optique et électronique à balayage permet de décrire les mécanismes d'endommagement en fatigue. En général, les trois approches expérimentales montrent que le mélange A36H96 (36% en poids d'ACN et 96% d'hydrogénation) a la meilleure résistance à la fatigue. Les effets de la formulation sur les performances peuvent être résumés comme suit :

- Si le taux d'ACN est augmenté à 44% (A44H96), la résistance en fatigue est légèrement réduite, mais semble être meilleure pour des chargements élevés ; si le taux d'ACN est réduit à 24% (A24H96), la résistance en fatigue est fortement réduite ;
- Si le pourcentage d'hydrogénation est augmenté à 99% (A36H99), il y a également une légère diminution de la résistance en fatigue ; lorsqu'il est réduit à 91% (A36H91), la résistance en fatigue, notamment en termes de propagation de fissure, diminue dans une plus large mesure ;
- Un mélange composite (A44-24) de 24% (A24H96) et de 44% (A44H96) d'ACN pour une moyenne de 36% d'ACN semble hériter de la mauvaise résistance en fatigue du mélange à 24% d'ACN (A24H96).

Enfin, le Chapitre 5 présente une première étude du couplage entre vieillissement thermique et fatigue. Premièrement, des expériences de fatigue-vieillissement simultanés sont effectuées à 150 °C. Les résultats obtenus montrent clairement comment le taux d'hydrogénation a un effet bénéfique sur la résistance à la température. Le mélange de HNBR avec le taux d'hydrogénation le plus élevé, A36H99, admet la plus faible réduction de durée de vie en fatigue, tandis que le mélange A36H91, mélange ayant le plus faible taux d'hydrogénation, admet la plus grande réduction de la durée de vie en fatigue. La seconde expérience consiste en un vieillissement préliminaire classique à 150 °C suivi d'un essai de fatigue à 120 °C. Les résultats de ces tests sont ensuite comparés à ceux obtenus au Chapitre 4 sur des spécimens

vierges et à ceux des tests simultanés à 150 °C. L'application d'un modèle statistique conduit à une procédure prometteuse qui peut être utilisée pour réduire la durée des expériences de pré-vieillissement/fatigue. La dernière étape de cette partie consiste à combiner les trois types des expériences de résistance à la fatigue afin d'établir une relation phénoménologique qui relie, par une simple exponentielle, les temps de pré-vieillissement et les essais de la durée de vie en fatigue à haute température.

En marge de ces travaux qui constituent le coeur de la thèse, revenons au Chapitre 2 où des résultats quantitatifs de cristallisation sous tension (SIC) du HNBR ont été établis pour deux mélanges non chargés avec 44% et 36% d'ACN. À mesure que le taux d'ACN augmente, l'incidence de la SIC augmente. De plus, le début de la cristallisation et la fusion se produisent à des taux d'étirement plus faibles pour le mélange de HNBR avec le taux d'ACN plus élevé.

Les résultats obtenus posent également de nouvelles questions. Les perspectives à ce travail sont notamment les suivantes :

- Il conviendrait de mesurer la durée de vie en fatigue des mélanges à différentes températures. Il est bien connu que les mélanges HNBR à faible taux d'ACN sont utilisés à basse température ; par conséquent, il serait intéressant de voir comment le classement des mélanges évolue lorsque la température diminue, *i.e.* si la résistance à la fatigue du mélange A24H96 s'améliore.
- De plus, il faudrait également différencier les trois mélanges ayant des comportements en propagation de fissures de fatigue similaires, c.-à-d. les mélanges A44H96, A36H96 et A36H99, afin de déterminer notamment s'il existe des seuils de fatigue pour ces matériaux et, le cas échéant, en quoi ceux-ci diffèrent.
- Comme discuté dans le Chapitre 4, ces mélanges (A44H96, A36H96 et A36H99) présentent également des mécanismes d'endommagement de fatigue intéressants : les fissures croissent parallèlement à la direction de chargement. Ceci pourrait être étudié plus en détails avec des tests *in situ* ou des essais interrompus.
- En ce qui concerne les perspectives à plus long terme, une étude plus complète sur les effets du vieillissement thermique et de la fatigue doit être réalisée. Une base de données plus détaillée des résultats est nécessaire pour valider les prédictions phénoménologiques faites dans le présent travail.

Appendix B

Raw Results of Pre-Aging Experiments

B.1 Quasi-static Tensile Response

Figure B.1-1 shows incomplete tensile tests carried out on blends with different percent hydrogenation. Tests are carried out at 120 °C on virgin and pre-aged specimens at 150 °C for different durations.

Table B.1-1 shows percent difference of stretch at break (λ_f), stress at break (σ_f), and tensile modulus at 10 MPa ($E_{10\,\mathrm{MPa}}$) of pre-aged specimens for 168 h with respect to virgin specimens. It is evident that A36H99 has the best resistance to

Table B.1-1 – Percent difference of virgin specimens versus those pre-aged for 168 h.

	Percent Difference (%)		
Blend	**Stretch at Break, λ_f**	**Stress at Break, σ_f**	**Tensile modulus at 10 MPa, $E_{10\mathrm{MPa}}$**
A36H96	-5.31%	23.92%	13.91%
A36H99	-9.22%	14.52%	4.11%
A36H91	-22.90%	4.95%	14.62%

thermal aging (at this duration). It has the lowest stiffening as indicated by values of the modulus at 10 MPa and stress at break. A36H91 has by far the worst resistance to heat, as indicated by its drastic decrease in stretch at break and increase in tensile modulus.

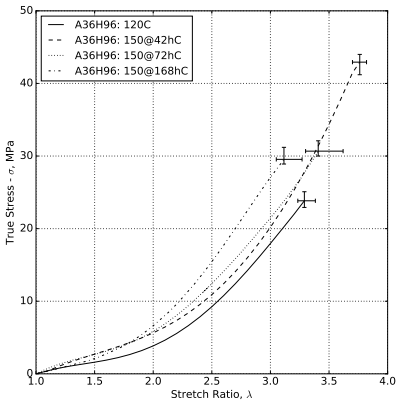

(a) A36H96.

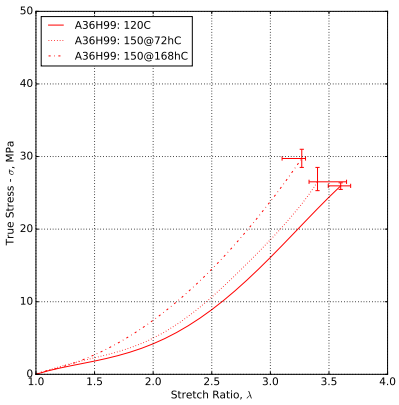

(b) A36H99.

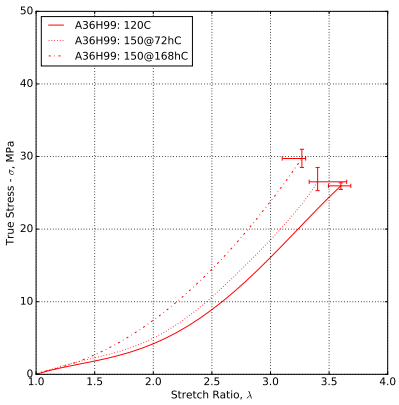

(c) A36H91.

Figure B.1-1 – Stress-strain response of pre-aged HNBR blends.

Appendix C

Fatigue Damage Analysis Micrographs

In the following Annex, the raw micrographs of specimen fracture surfaces obtained by scanning electron microscopy are presented. These are grouped by the type of test: regular fatigue life tests at 120 °C and simultaneous fatigue and aging tests at 150 °C. Furthermore, these are grouped into target loading levels. Due to a large number of examined specimens, only one fracture surface of a specimen at two different magnification levels will be shown for brevity. For more micrographs, please contact at kubat.narynbek-ulu [at] ec-nantes.fr

C.1 Fatigue

C.1.1 A36H96

10 MPa

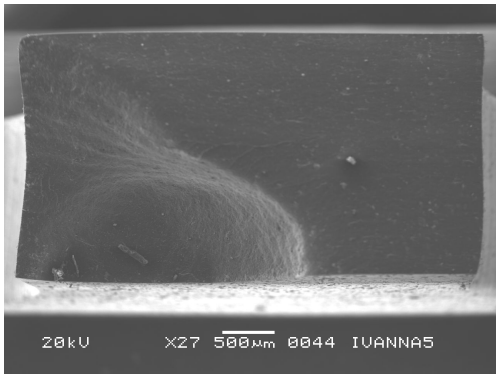

(a) Specimen 1 at x23.

(b) Specimen 1 at x100.

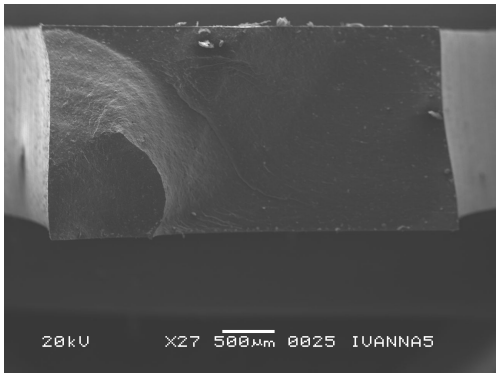

(c) Specimen 2 at x27.

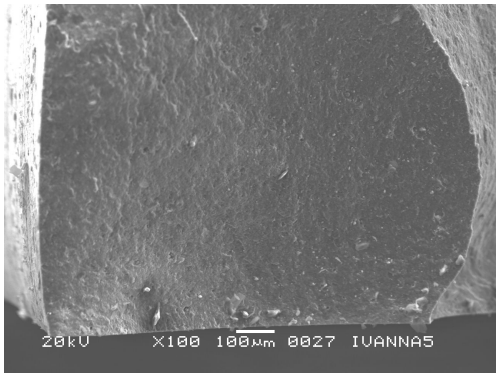

(d) Specimen 2 at x100.

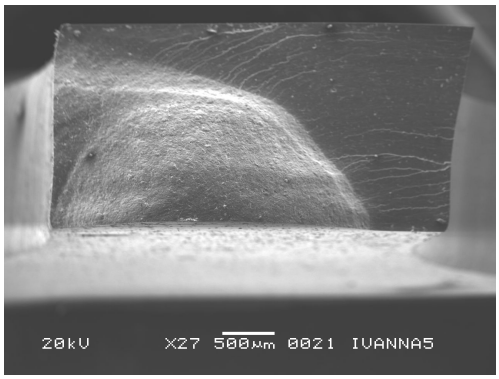

(e) Specimen 3 at x27.

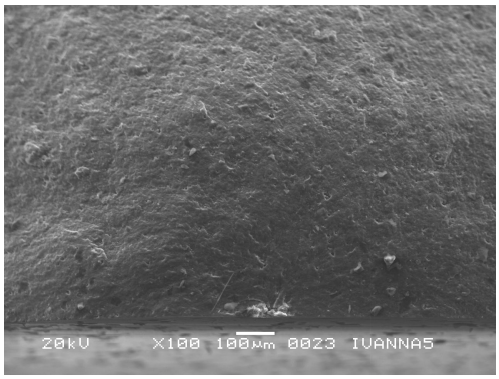

(f) Specimen 3 at x100.

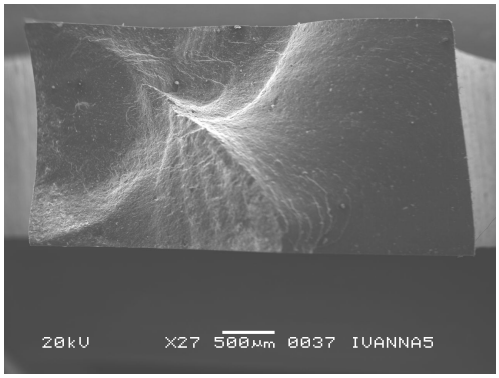

(g) Specimen 4 at x27.

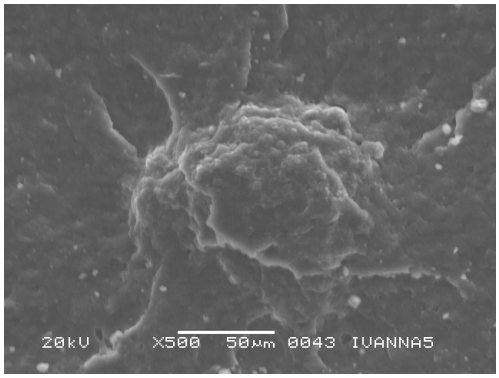

(h) Specimen 4 at x500.

Figure C.1-1 – A36H96 at 10 MPa.

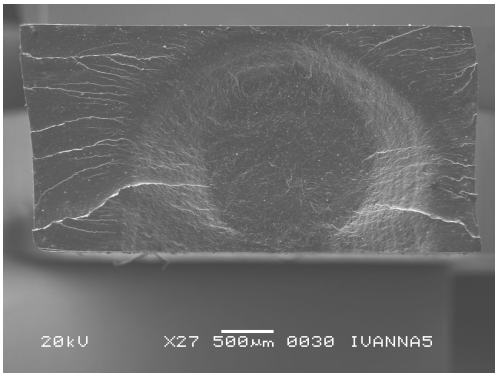

(a) Specimen 5 at x27.

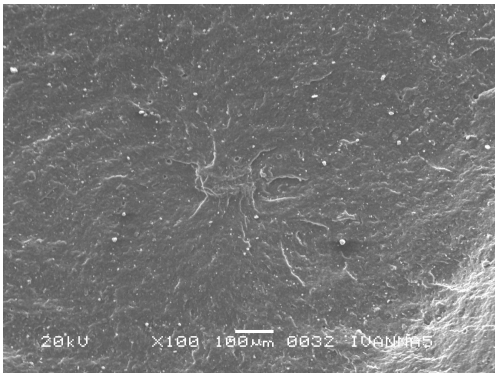

(b) Specimen 5 at x100.

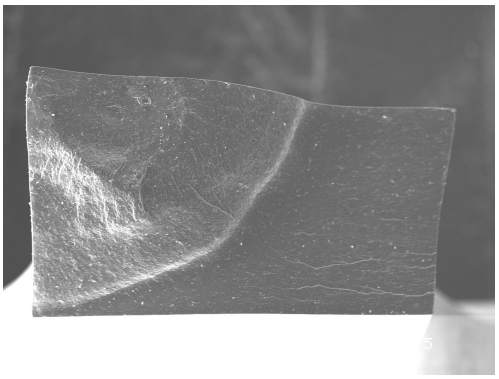

(c) Specimen 6 at x27.

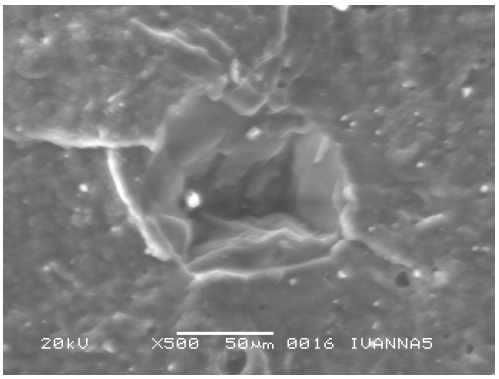

(d) Specimen 6 at x500.

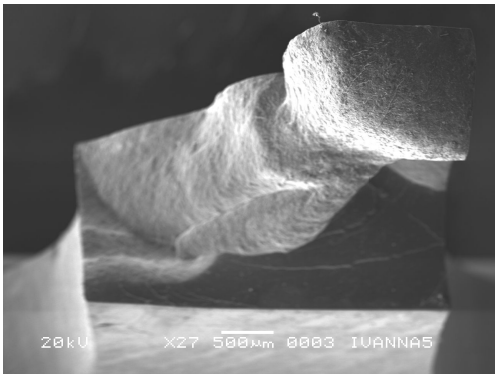

(e) Specimen 7 at x27.

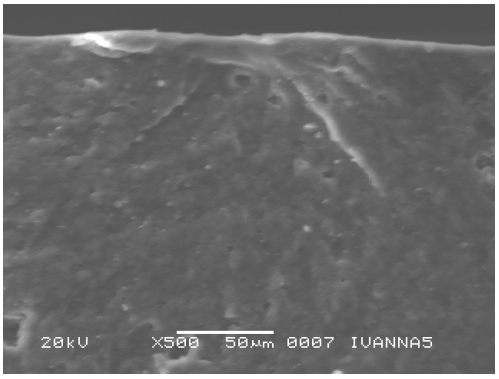

(f) Specimen 7 at x500.

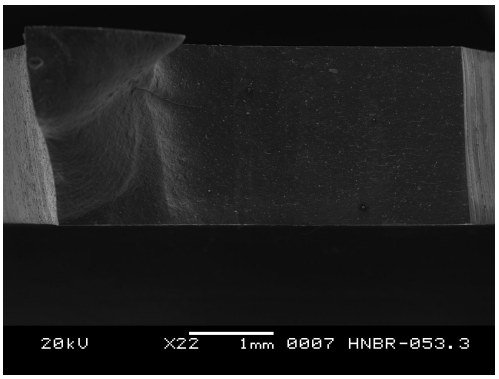

(g) Specimen 8 at x22.

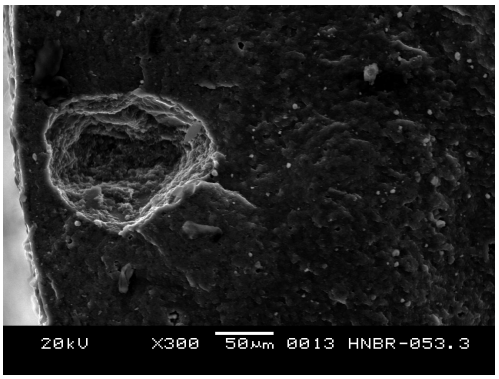

(h) Specimen 8 at x300.

Figure C.1-2 – A36H96 at 10 MPa.

8 MPa

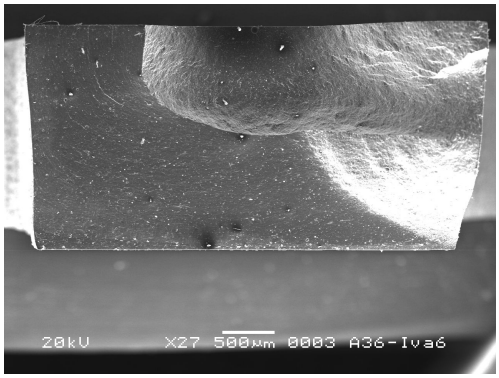

(a) Specimen 1 at x27.

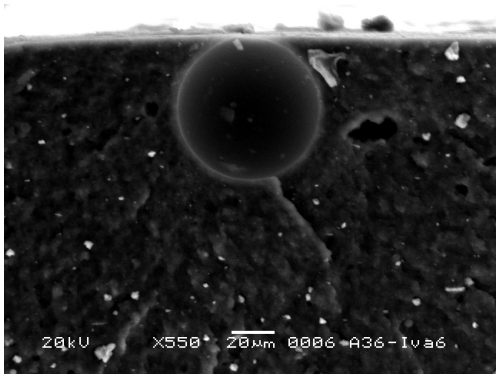

(b) Specimen 1 at x550.

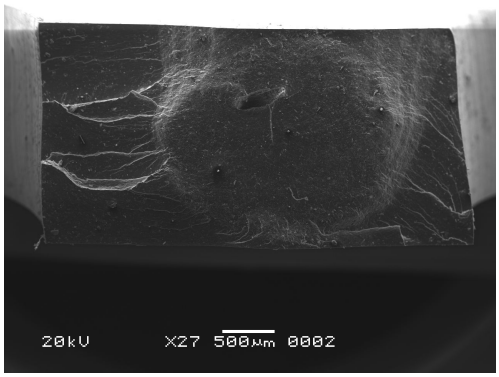

(c) Specimen 2 at x27.

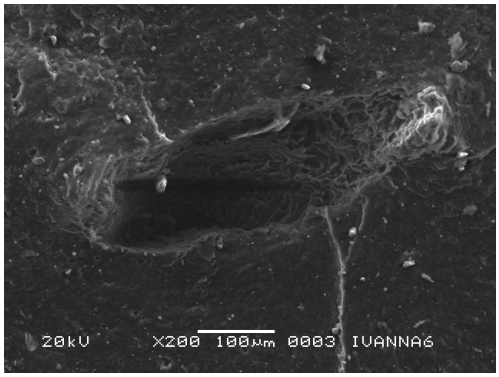

(d) Specimen 2 at x200.

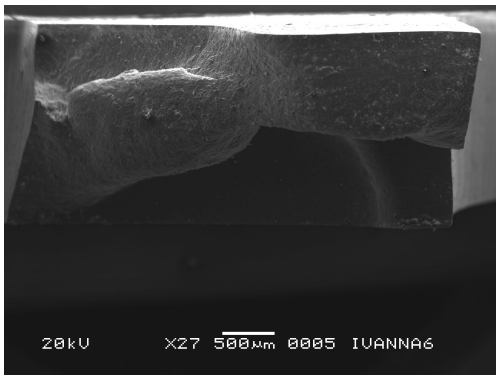

(e) Specimen 3 at x27.

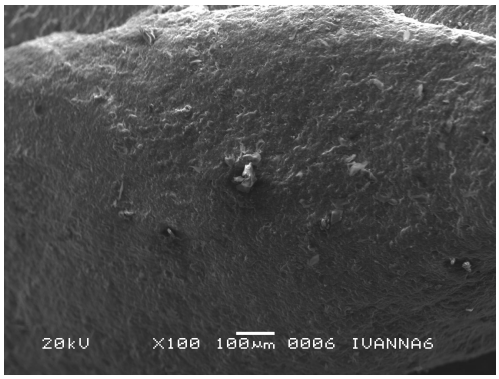

(f) Specimen 3 at x100.

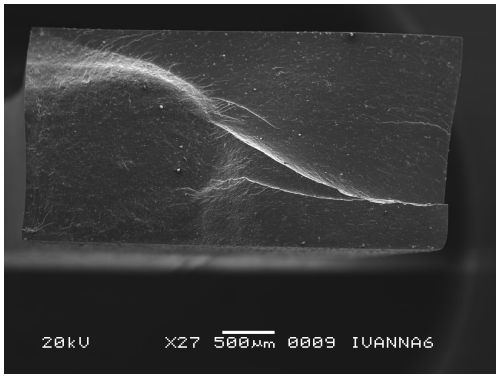

(g) Specimen 4 at x27.

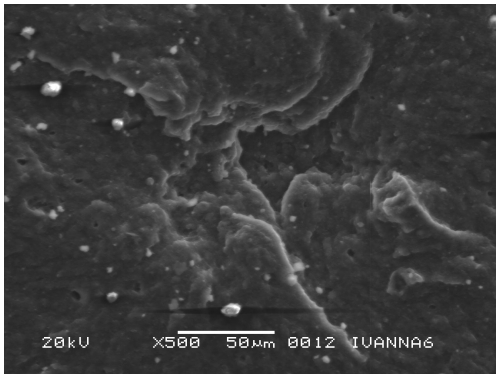

(h) Specimen 4 at x500.

Figure C.1-3 – A36H96 at 8 MPa.

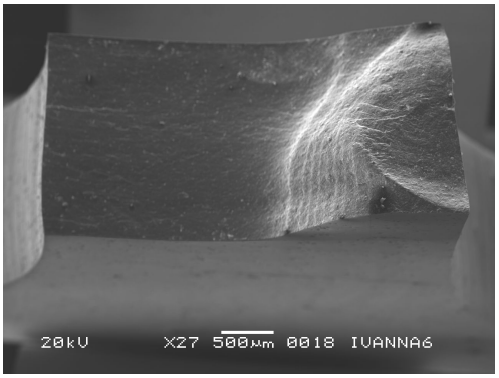

(a) Specimen 6 at x27.

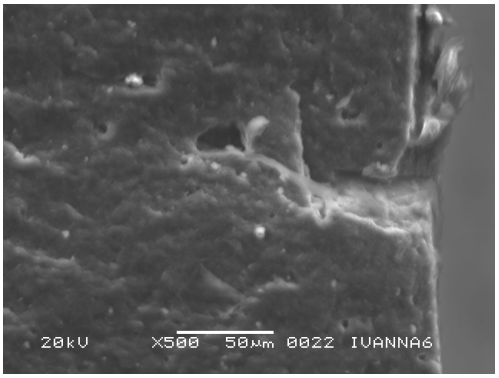

(b) Specimen 6 at x500.

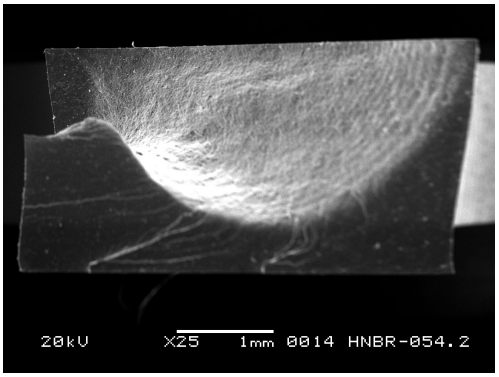

(c) Specimen 7 at x25.

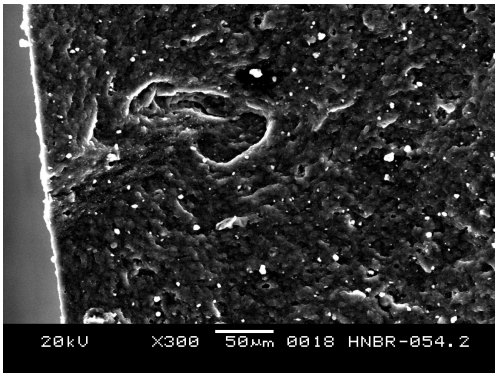

(d) Specimen 7 at x300.

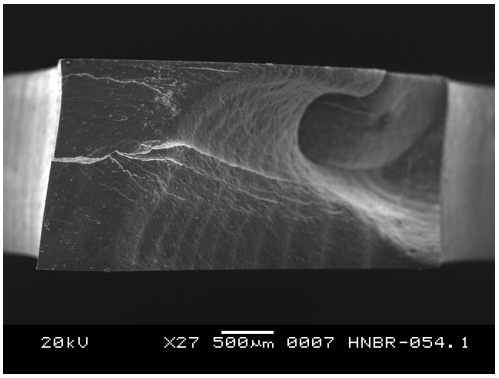

(e) Specimen 8 at x27.

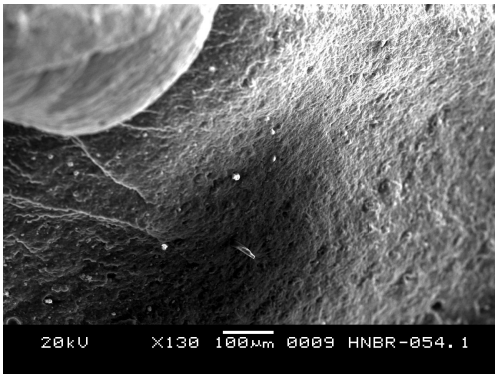

(f) Specimen 8 at x130.

Figure C.1-4 – A36H96 at 8 MPa.

6 MPa

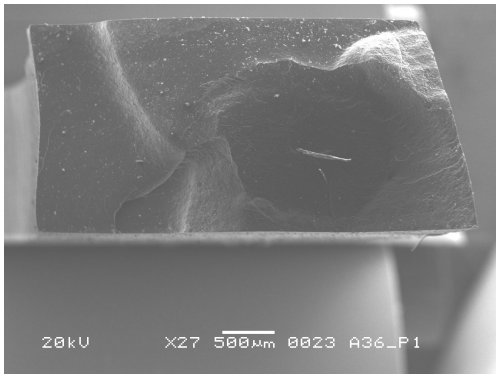

(a) Specimen 1 at x27.

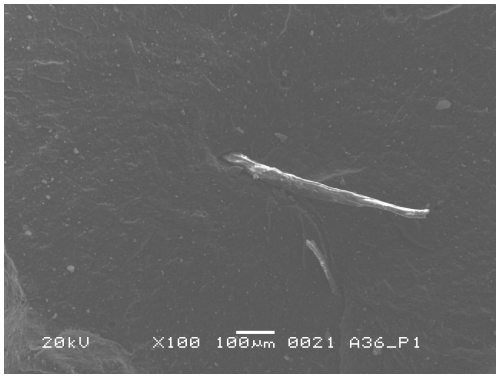

(b) Specimen 1 at x100.

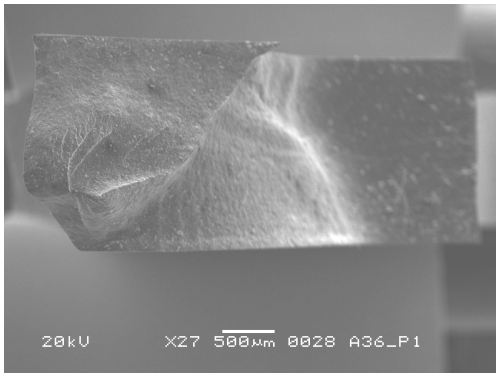

(c) Specimen 2 at x27.

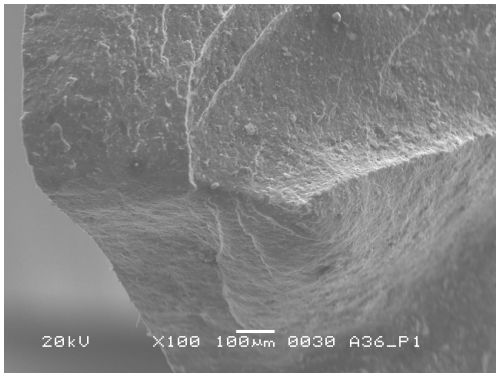

(d) Specimen 2 at x100.

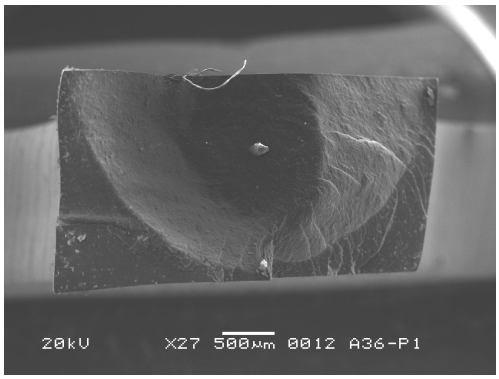

(e) Specimen 3 at x27.

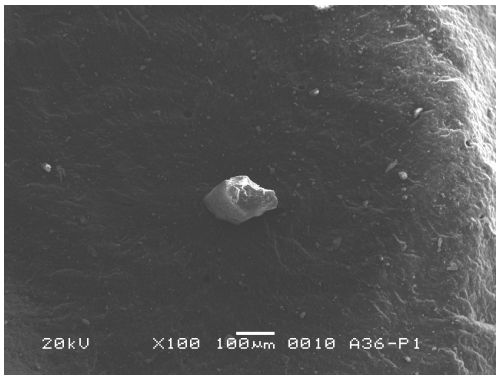

(f) Specimen 3 at x100.

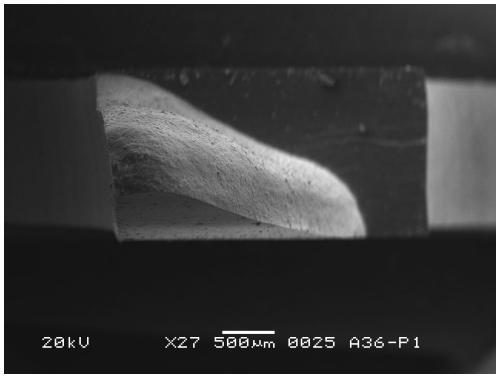

(g) Specimen 4 at x27.

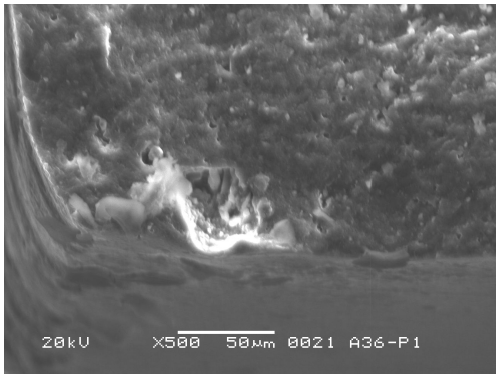

(h) Specimen 4 at x500.

Figure C.1-5 – A36H96 at 6 MPa.

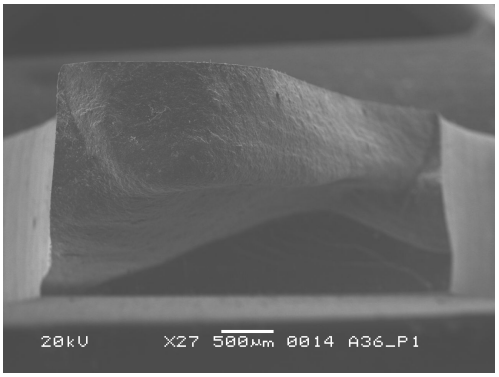

(a) Specimen 5 at x27.

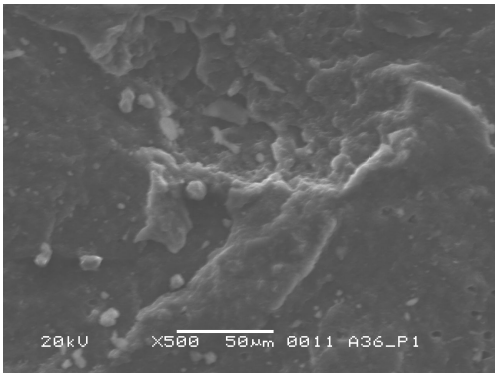

(b) Specimen 5 at x500.

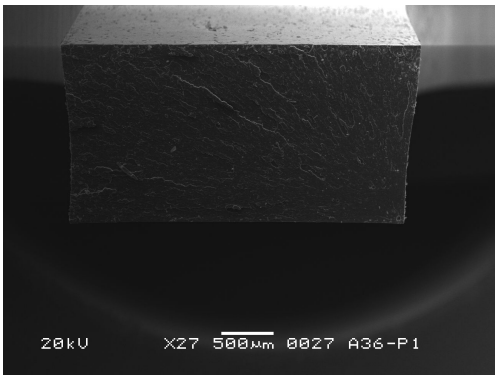

(c) Specimen 6 at x27.

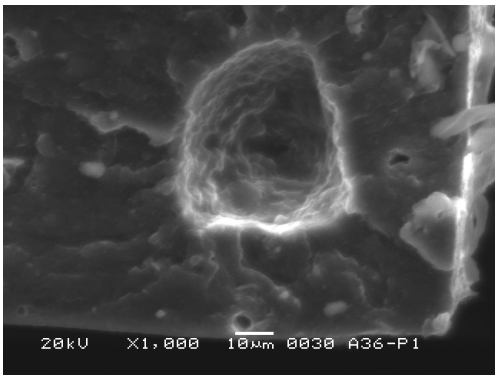

(d) Specimen 6 at x1000.

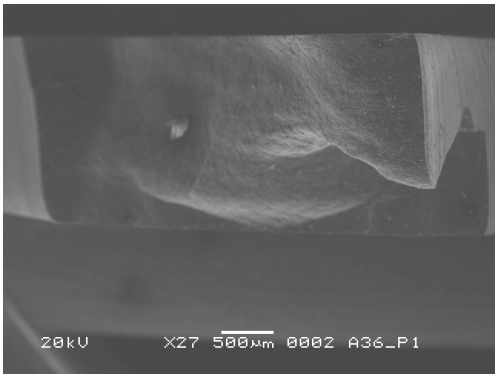

(e) Specimen 7 at x27.

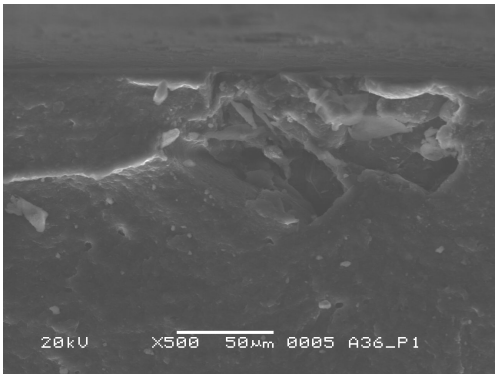

(f) Specimen 7 at x500.

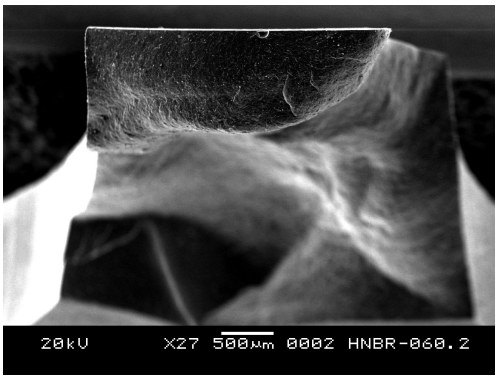

(g) Specimen 8 at x27.

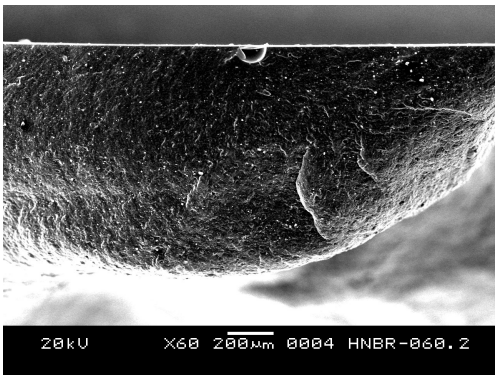

(h) Specimen 8 at x90.

Figure C.1-6 – A36H96 at 6 MPa.

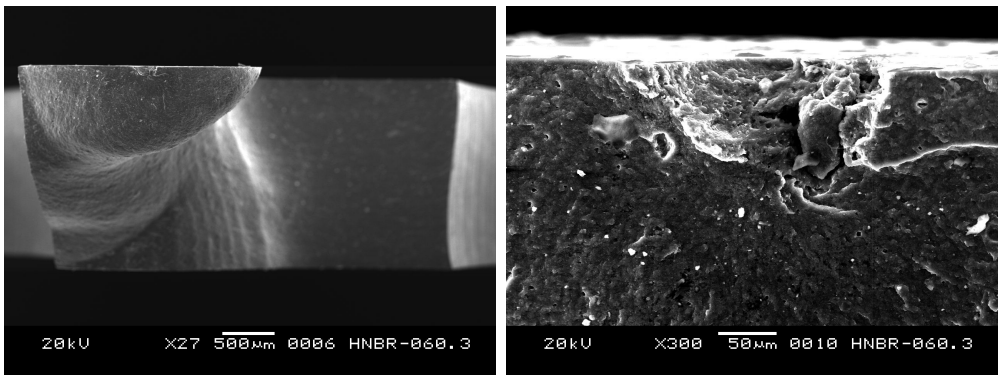

(a) Specimen 9 at x27. **(b)** Specimen 9 at x300.

Figure C.1-7 – A36H96 at 6 MPa.

4 MPa

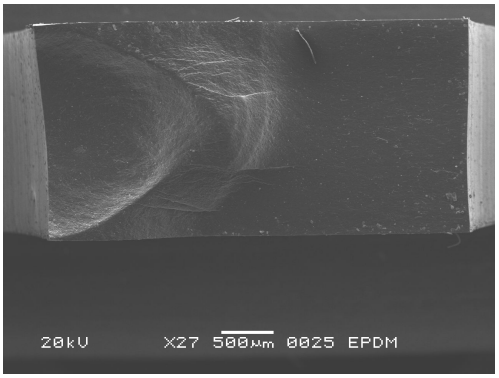

(a) Specimen 1 at x27.

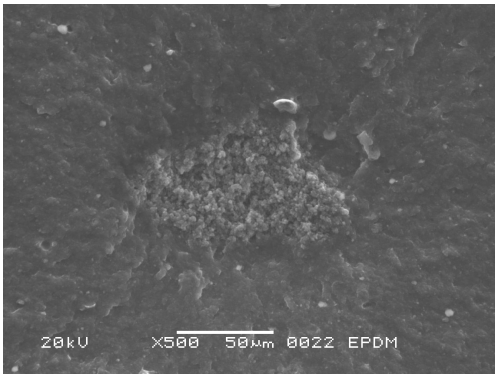

(b) Specimen 1 at x500.

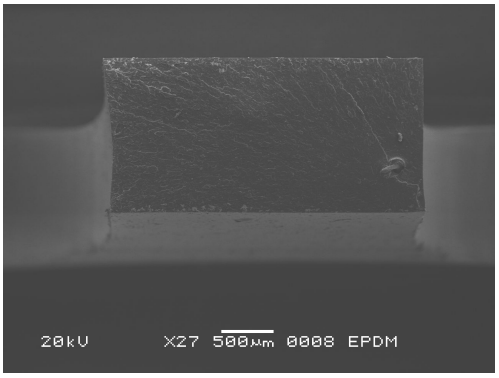

(c) Specimen 2 at x27.

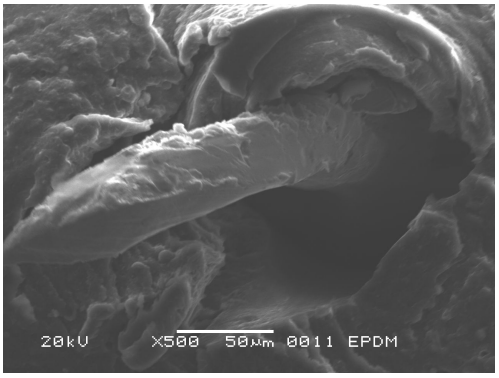

(d) Specimen 2 at x500.

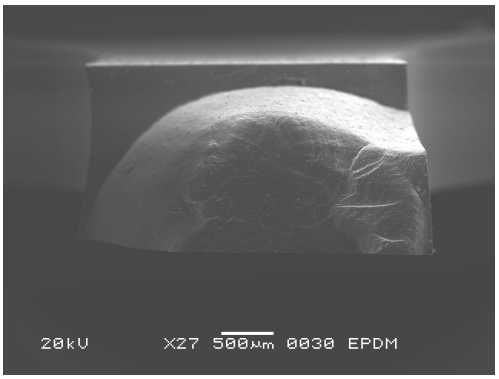

(e) Specimen 3 at x27.

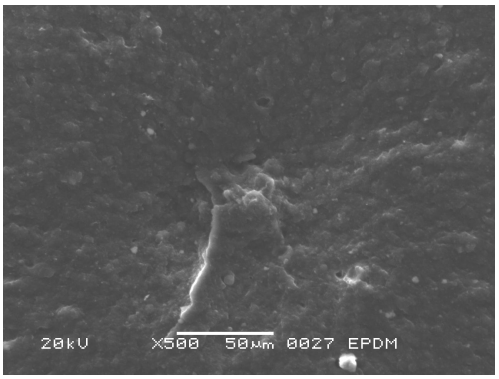

(f) Specimen 3 at x100.

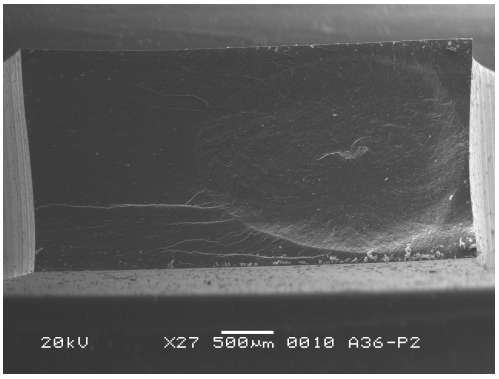

(g) Specimen 4 at x27.

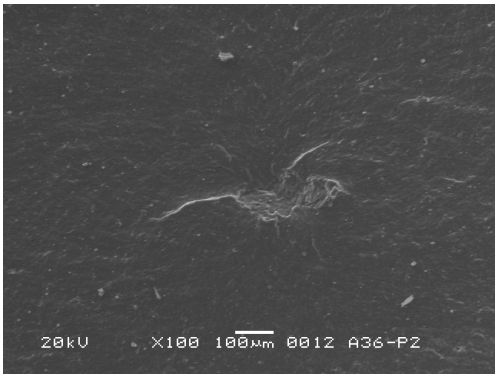

(h) Specimen 4 at x100.

Figure C.1-8 – A36H96 at 4 MPa.

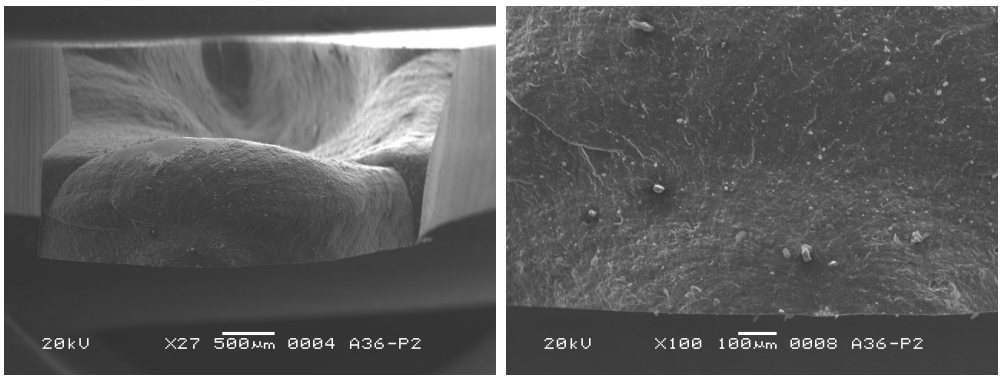

(a) Specimen 5 at x27. **(b)** Specimen 5 at x100.

Figure C.1-9 – A36H96 at 4 MPa.

C.1.2 A44H96

10 MPa

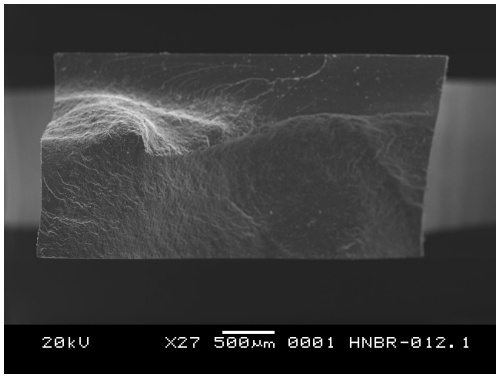

(a) Specimen 1 at x27.

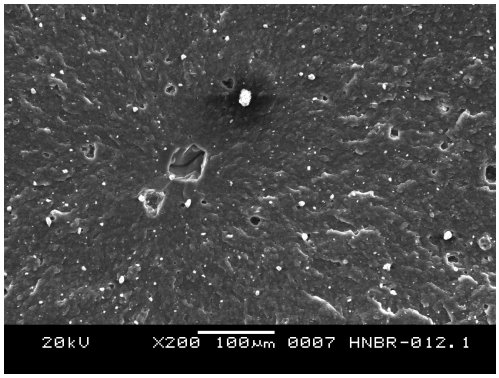

(b) Specimen 1 at x200.

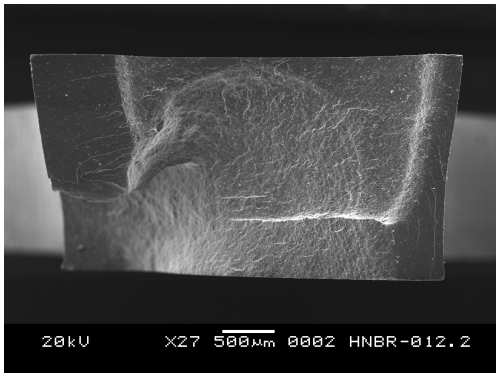

(c) Specimen 2 at x27.

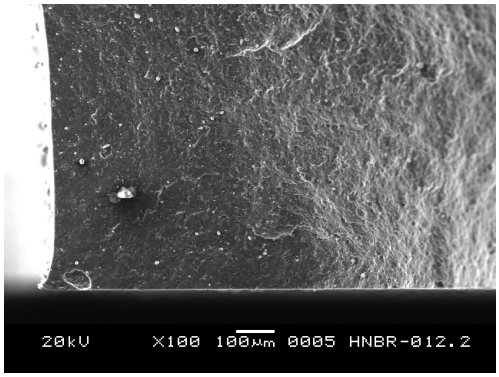

(d) Specimen 2 at x100.

Figure C.1-10 – A44H96 at 10 MPa.

8 MPa

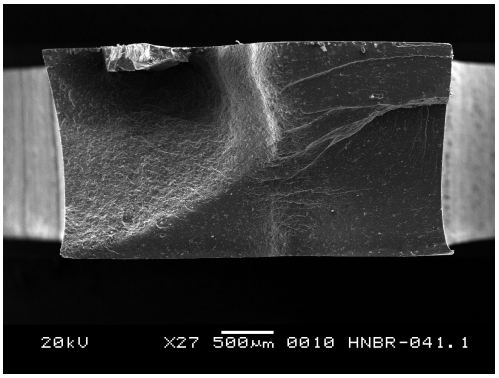

(a) Specimen 1 at x27.

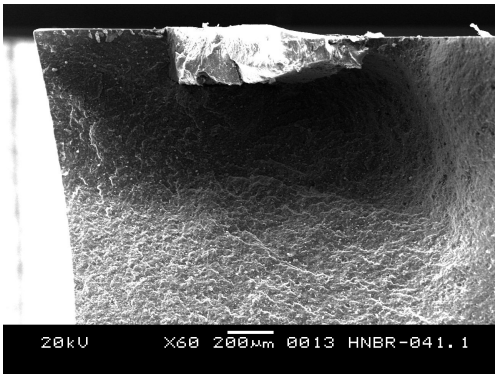

(b) Specimen 1 at x60.

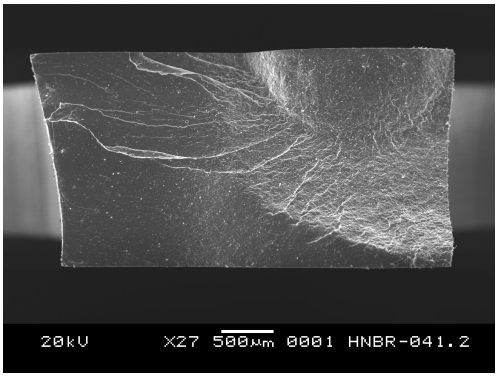

(c) Specimen 2 at x27.

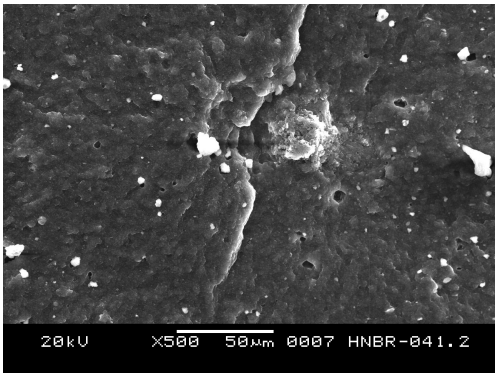

(d) Specimen 2 at x500.

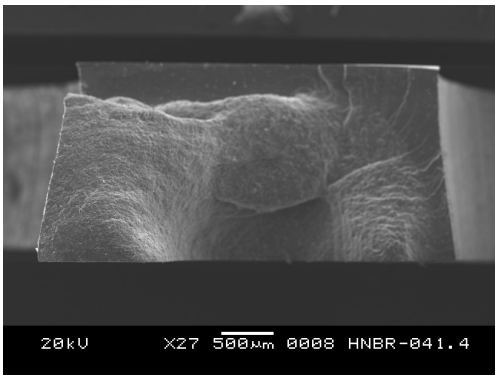

(e) Specimen 3 at x27.

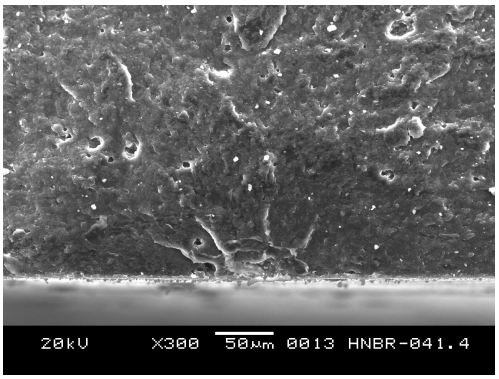

(f) Specimen 3 at x300.

Figure C.1-11 – A44H96 at 8 MPa.

6 MPa

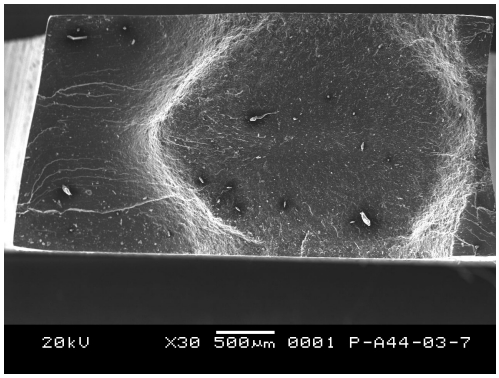

(a) Specimen 1 at x30.

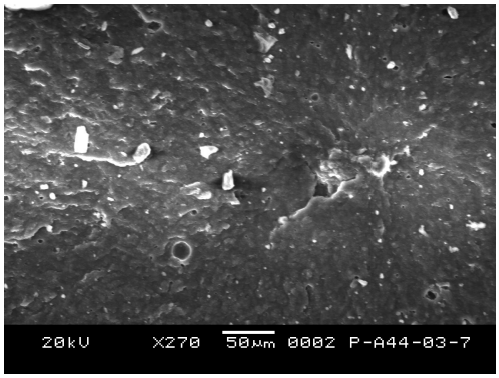

(b) Specimen 1 at x270.

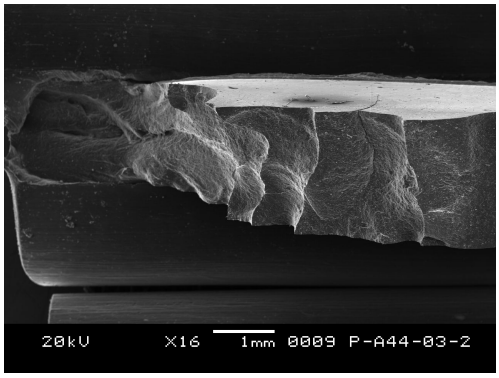

(c) Specimen 2 at x16.

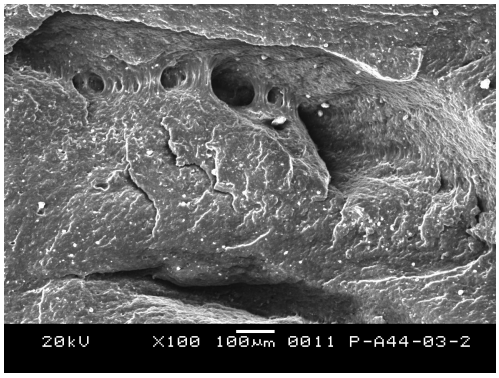

(d) Specimen 2 at x100.

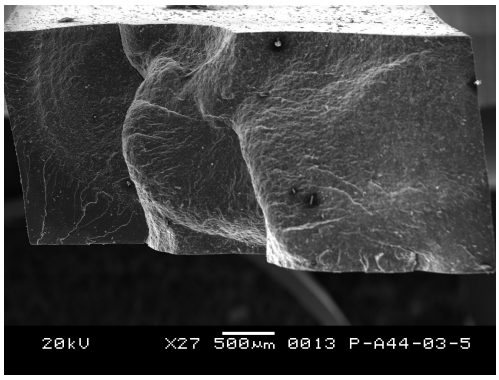

(e) Specimen 3 at x27.

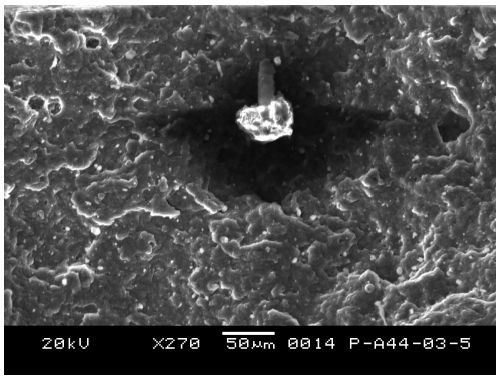

(f) Specimen 3 at x270.

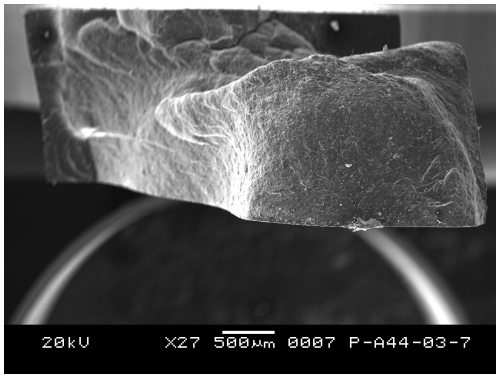

(g) Specimen 4 at x27.

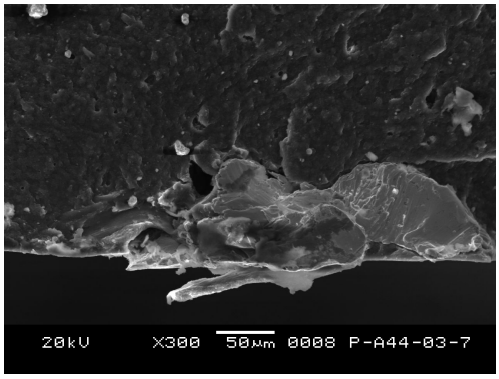

(h) Specimen 4 at x300.

Figure C.1-12 – A44H96 at 6 MPa.

4 MPa

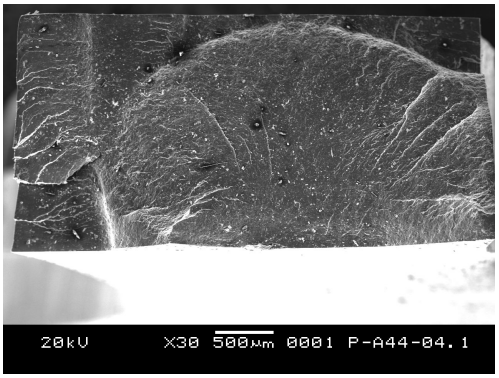

(a) Specimen 1 at x30.

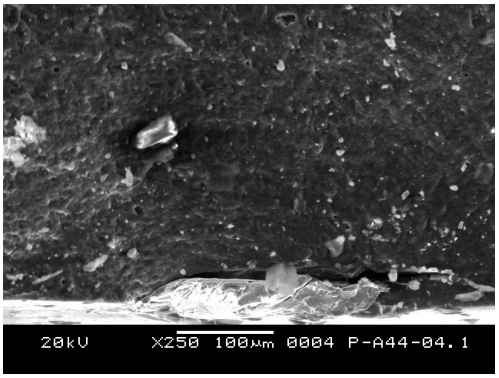

(b) Specimen 1 at x250.

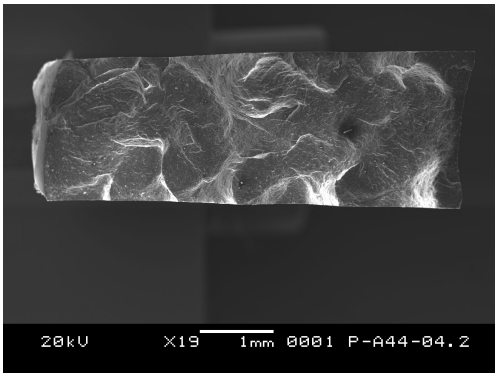

(c) Specimen 2 at x19.

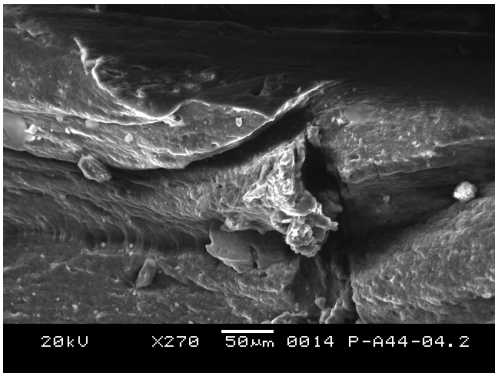

(d) Specimen 2 at x270.

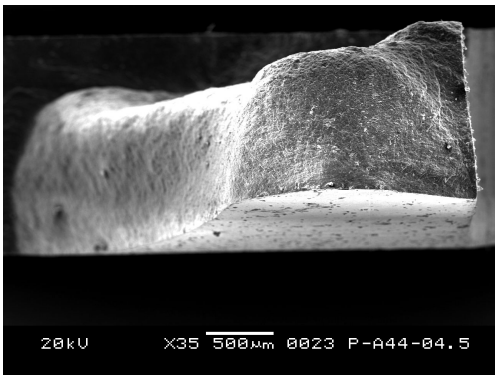

(e) Specimen 3 at x35.

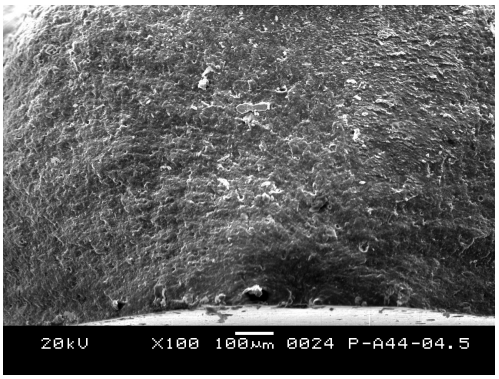

(f) Specimen 3 at x100.

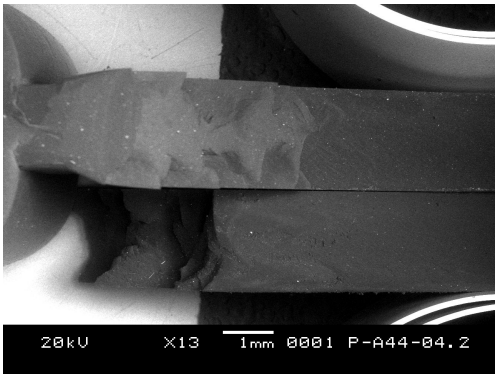

(g) Specimen 4 at x13.

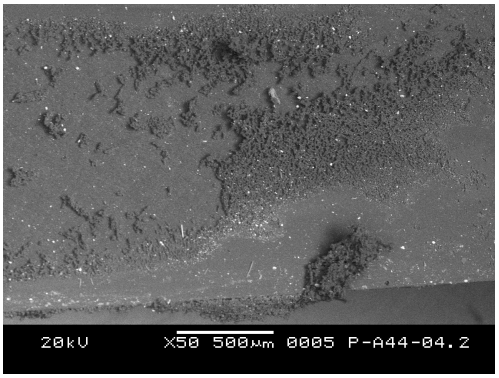

(h) Specimen 4 at x50.

Figure C.1-13 – A44H96 at 6 MPa.

C.1.3 A24H96

10 MPa

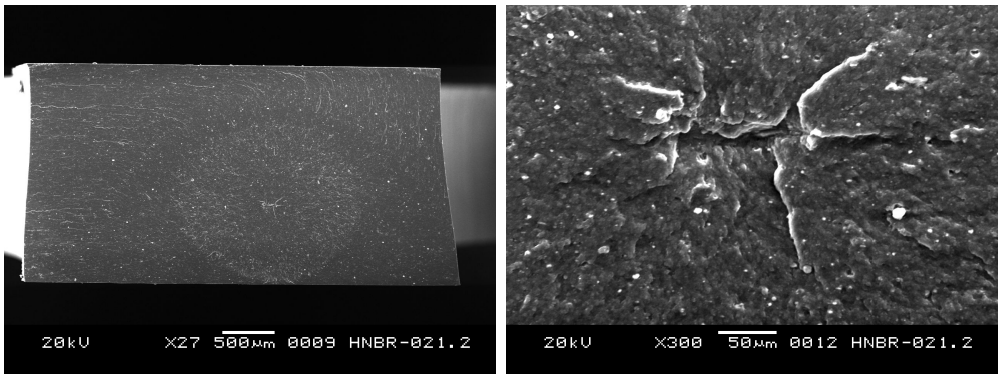

(a) Specimen 1 at x27. **(b)** Specimen 1 at x300.

Figure C.1-14 – A24H96 at 10 MPa.

8 MPa

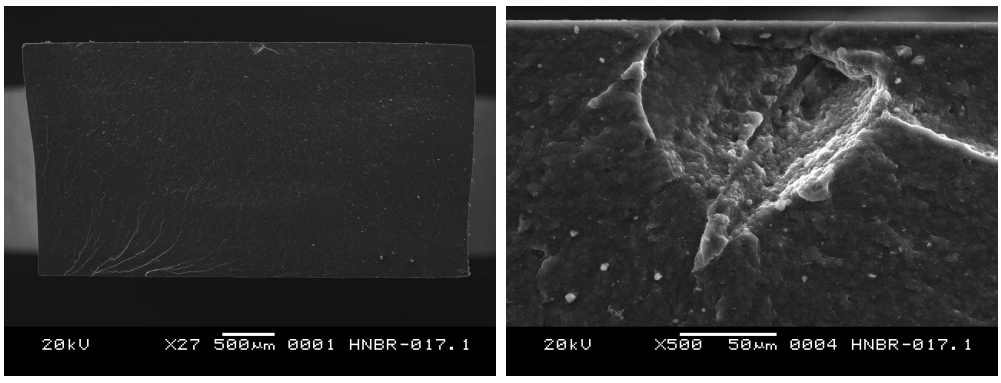

(a) Specimen 1 at x27. **(b)** Specimen 1 at x500.

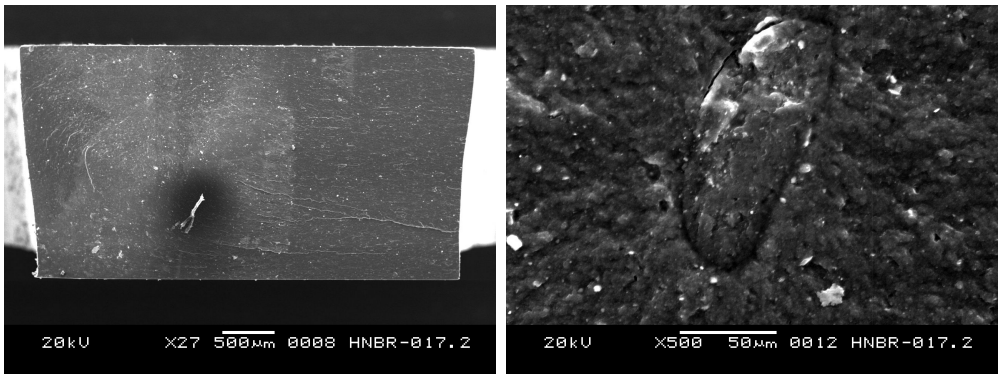

(c) Specimen 2 at x27. **(d)** Specimen 2 at x500.

Figure C.1-15 – A24H96 at 8 MPa.

6 MPa

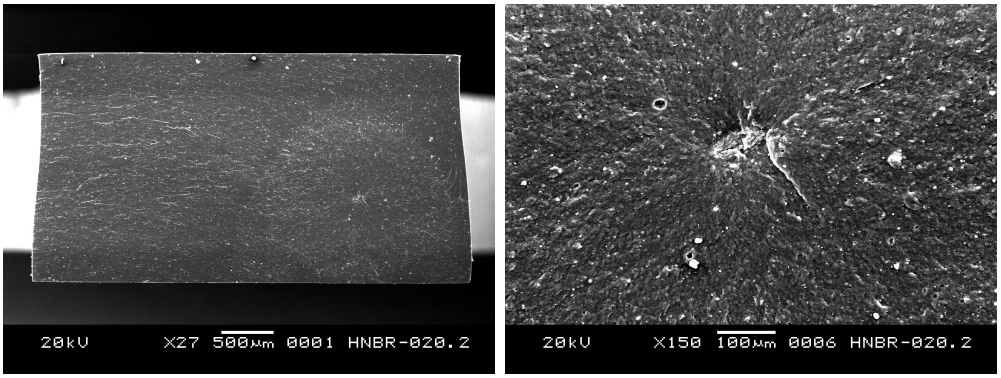

(a) Specimen 1 at x27. **(b)** Specimen 1 at x150.

Figure C.1-16 – A24H96 at 6 MPa.

4 MPa

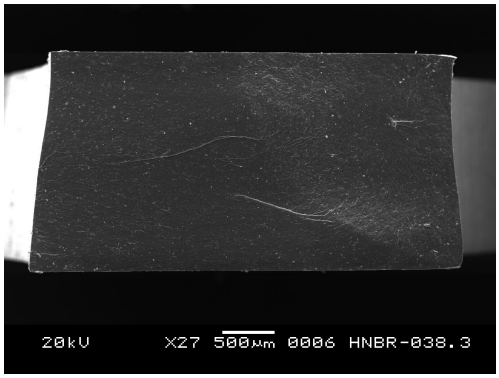

(a) Specimen 1 at x27.

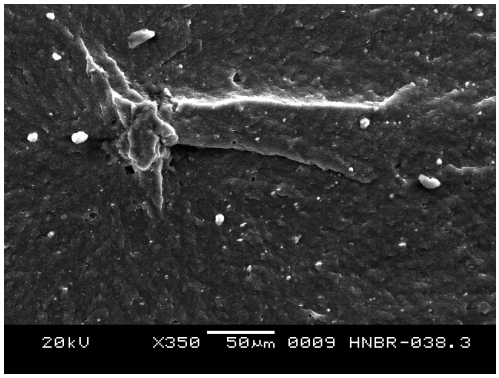

(b) Specimen 1 at x350.

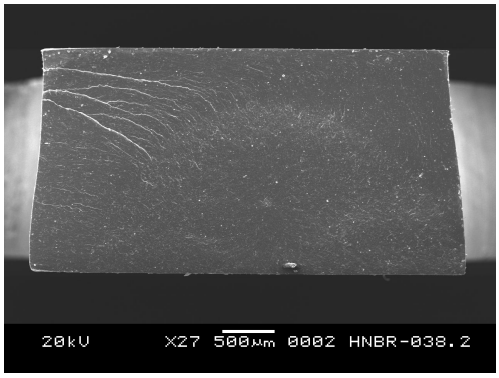

(c) Specimen 2 at x27.

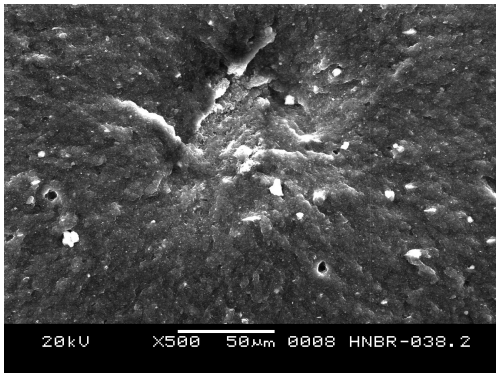

(d) Specimen 2 at x500.

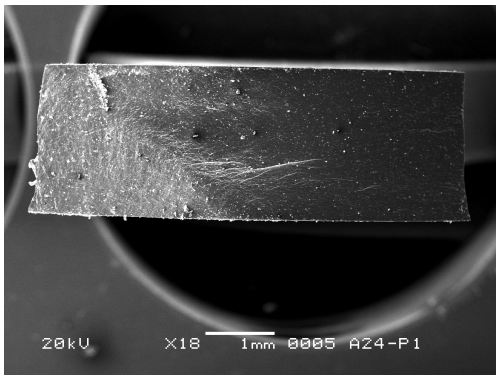

(e) Specimen 3 at x18.

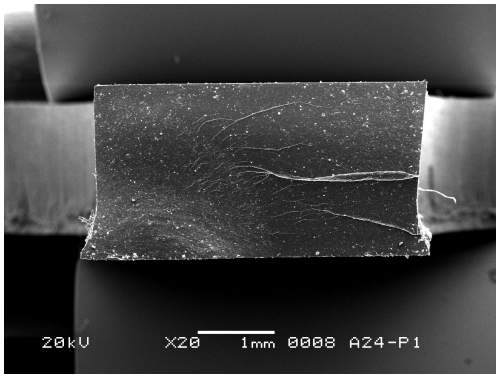

(f) Specimen 4 at x20.

Figure C.1-17 – A24H96 at 4 MPa.

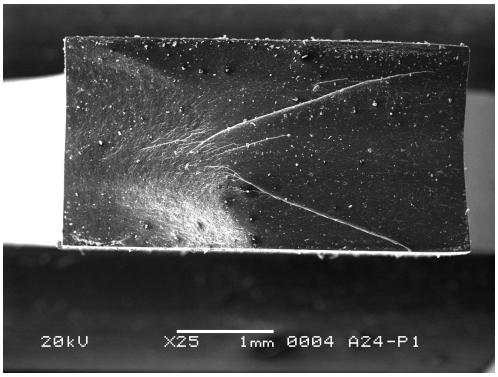

(a) Specimen 5 at x25.

Figure C.1-18 – A24H96 at 4 MPa.

C.1.4 A36H99

10 MPa

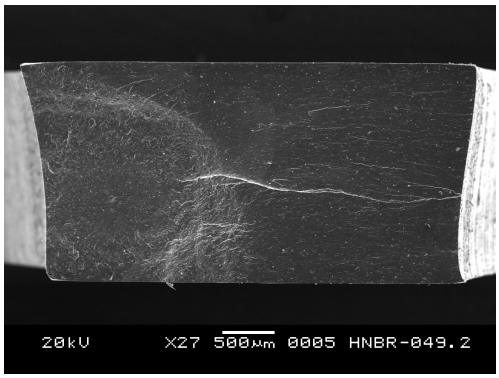

(a) Specimen 1 at x27.

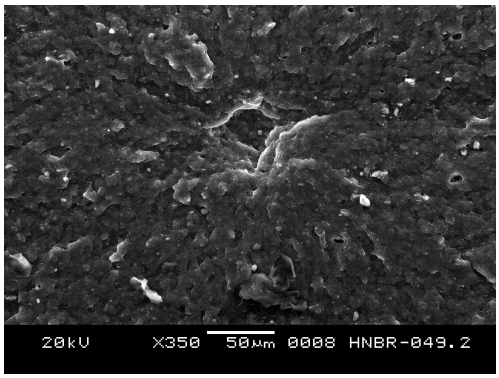

(b) Specimen 1 at x350.

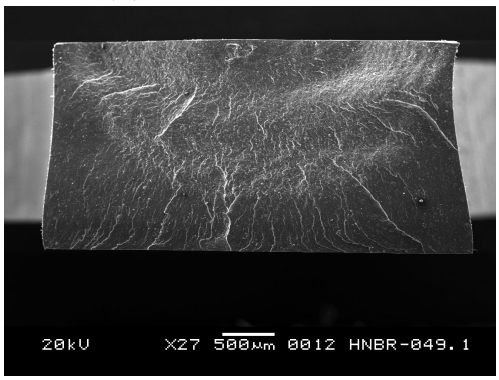

(c) Specimen 2 at x27.

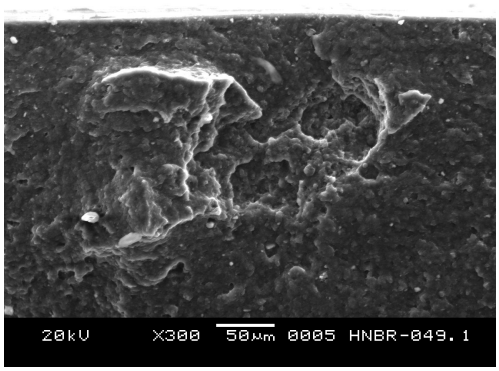

(d) Specimen 2 at x300.

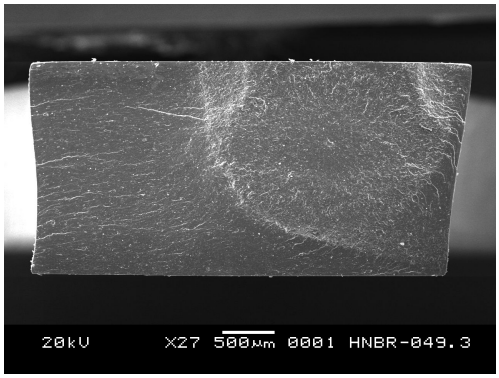

(e) Specimen 3 at x27.

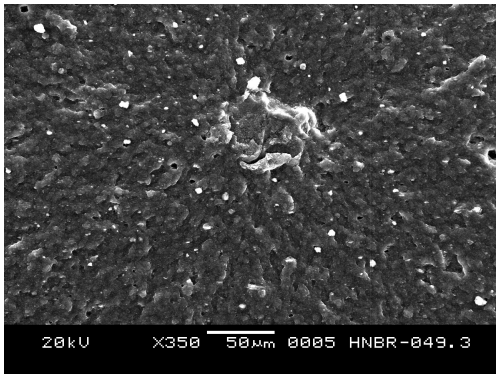

(f) Specimen 3 at x350.

Figure C.1-19 – A36H99 at 10 MPa.

8 MPa

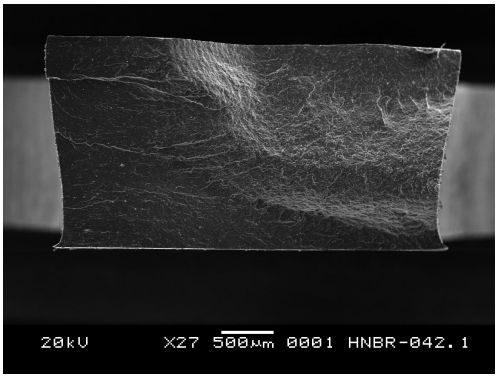

(a) Specimen 1 at x27.

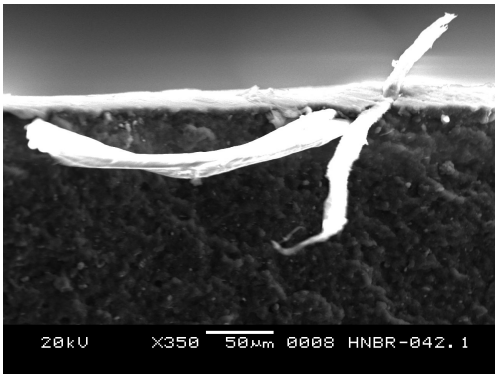

(b) Specimen 1 at x350.

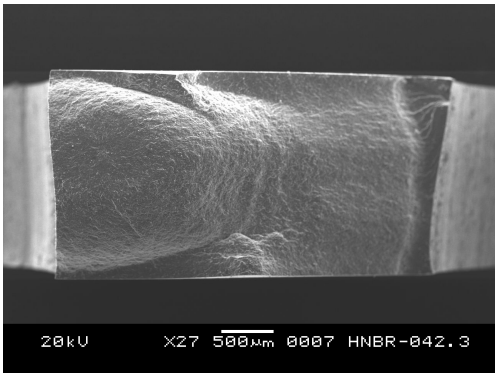

(c) Specimen 2 at x27.

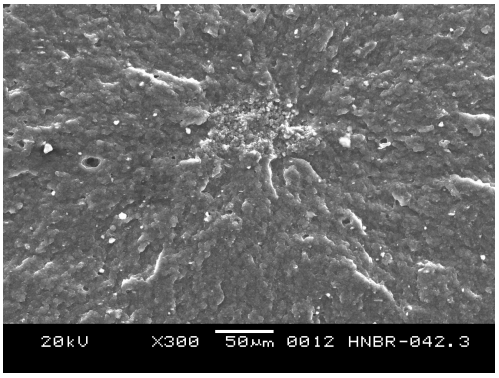

(d) Specimen 2 at x300.

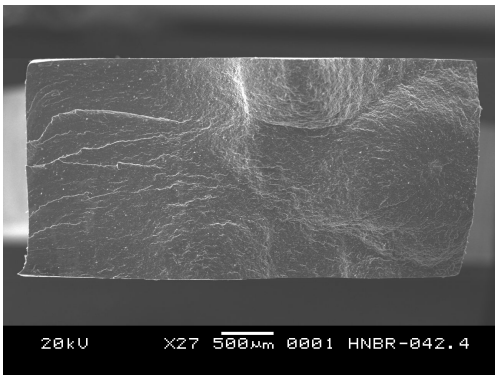

(e) Specimen 3 at x27.

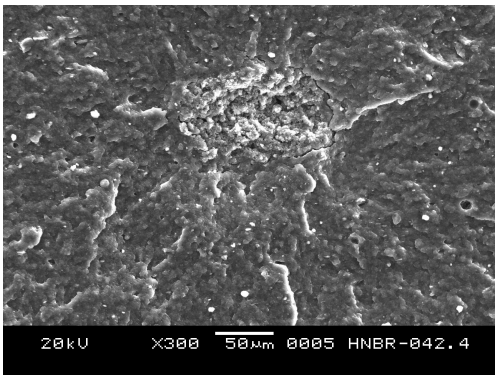

(f) Specimen 3 at x300.

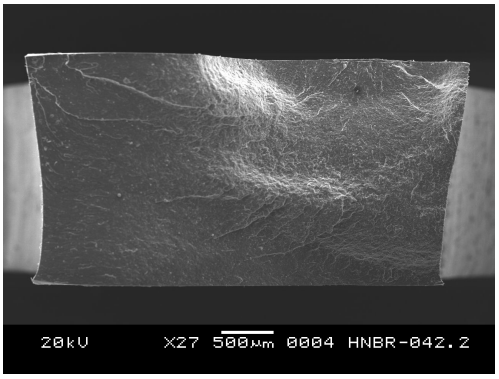

(g) Specimen 3 at x27.

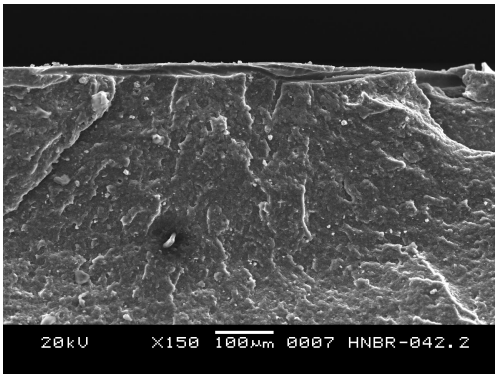

(h) Specimen 3 at x150.

Figure C.1-20 – A36H99 at 8 MPa.

6 MPa

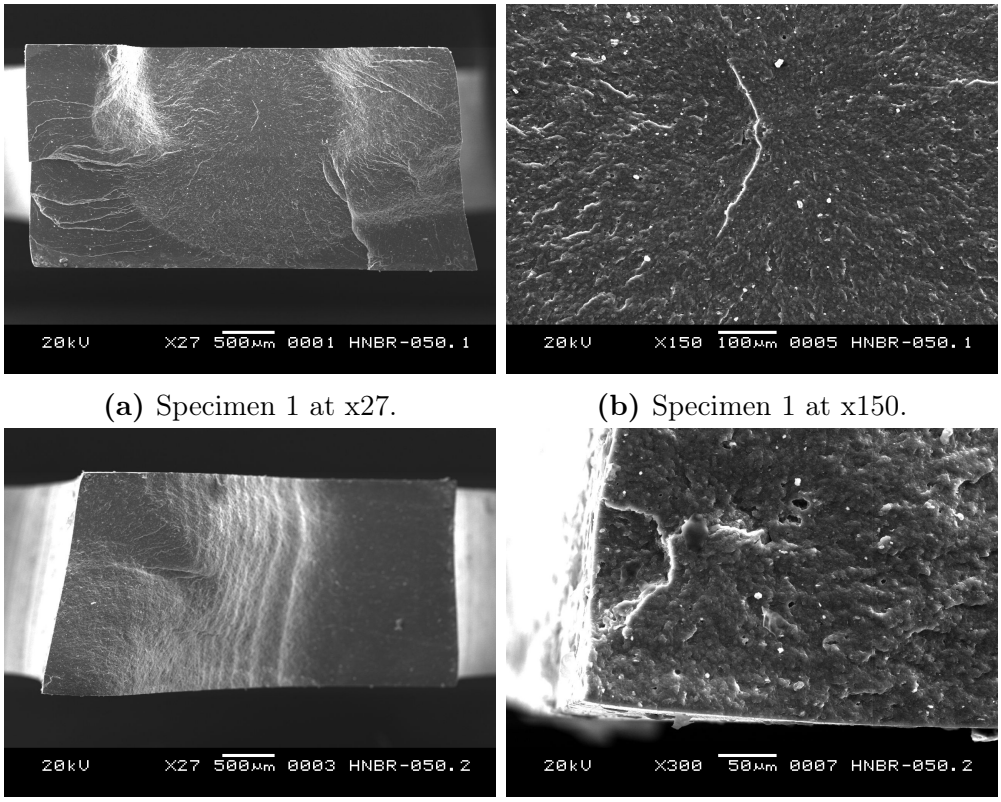

(a) Specimen 1 at x27.

(b) Specimen 1 at x150.

(c) Specimen 2 at x27.

(d) Specimen 2 at x300.

Figure C.1-21 – A36H99 at 6 MPa.

4 MPa

C.1.5 A36H91

10 MPa

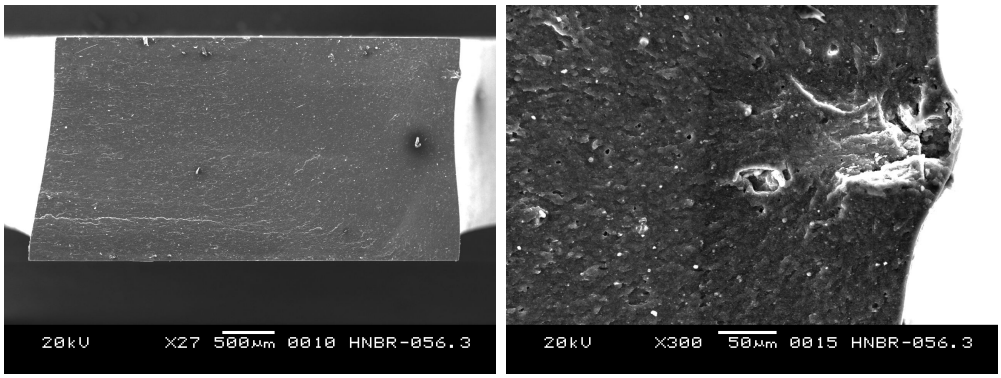

(a) Specimen 1 at x27. **(b)** Specimen 1 at x300.

(c) Specimen 2 at x27. **(d)** Specimen 2 at x300.

Figure C.1-22 – A36H91 at 10 MPa.

8 MPa

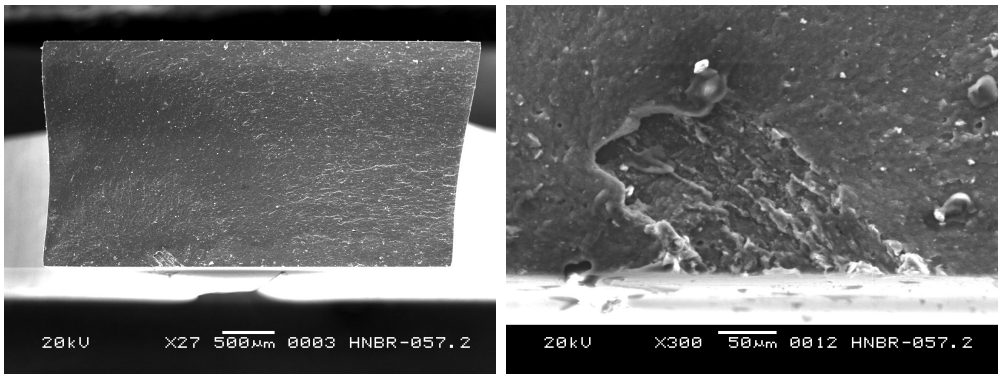

(a) Specimen 1 at x27. **(b)** Specimen 1 at x300.

Figure C.1-23 – A36H91 at 8 MPa.

6 MPa

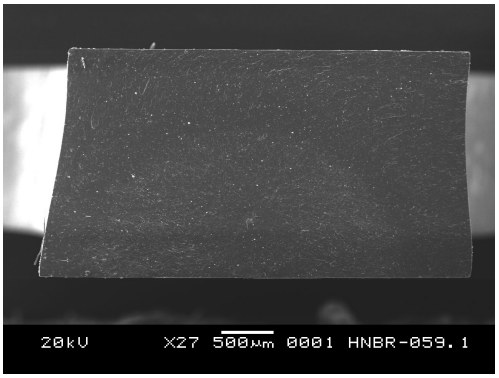

(a) Specimen 1 at x27.

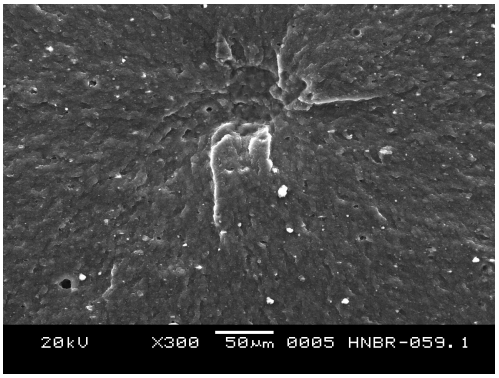

(b) Specimen 1 at x300.

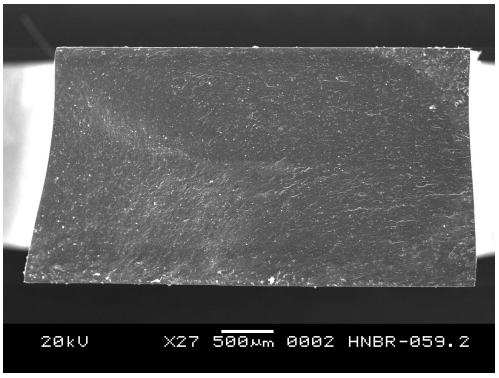

(c) Specimen 2 at x27.

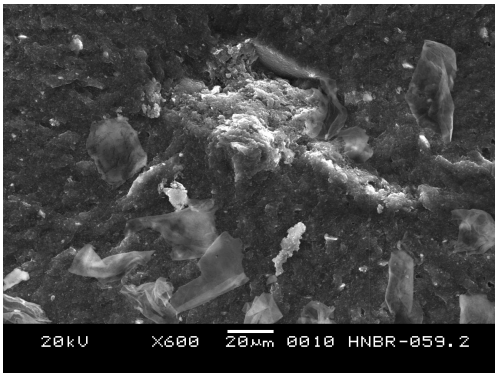

(d) Specimen 2 at x600.

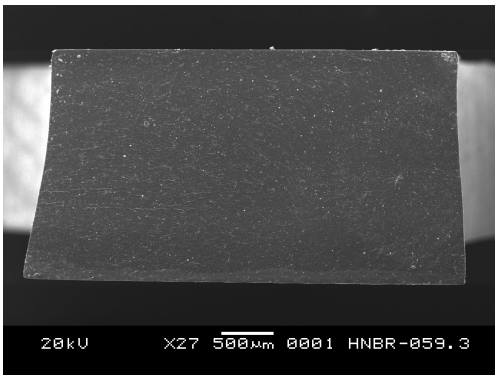

(e) Specimen 3 at x27.

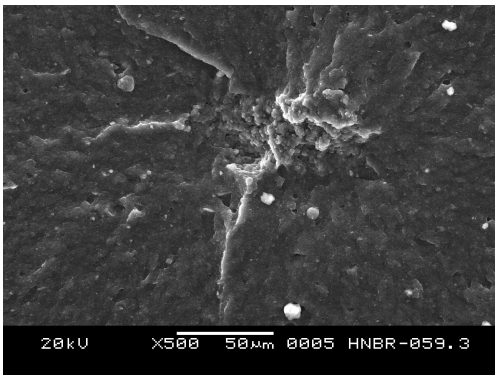

(f) Specimen 3 at x500.

Figure C.1-24 – A36H91 at 6 MPa.

4 MPa

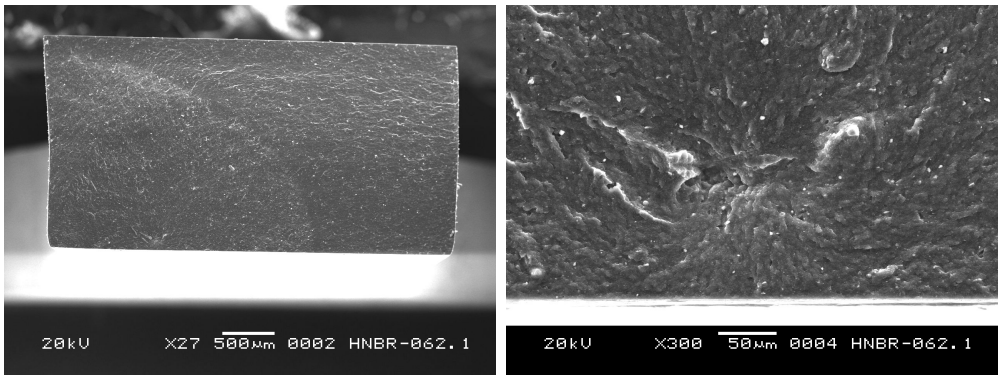

(a) Specimen 1 at x27. **(b)** Specimen 1 at x300.

Figure C.1-25 – A36H91 at 4 MPa.

C.1.6 A44-24

10 MPa

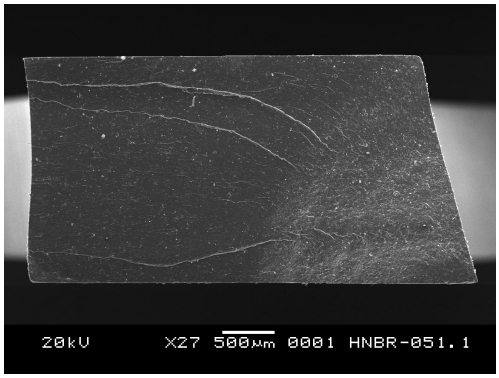

(a) Specimen 1 at x27.

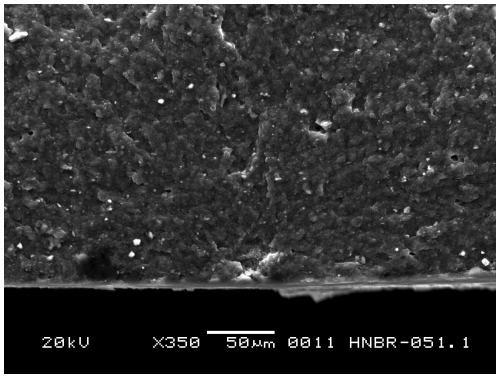

(b) Specimen 1 at x350.

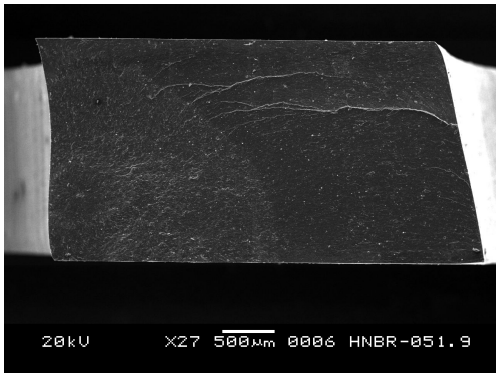

(c) Specimen 2 at x27.

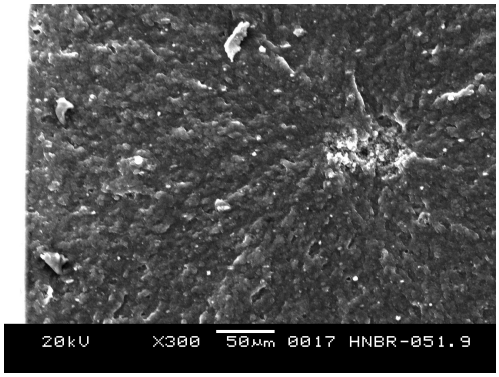

(d) Specimen 2 at x300.

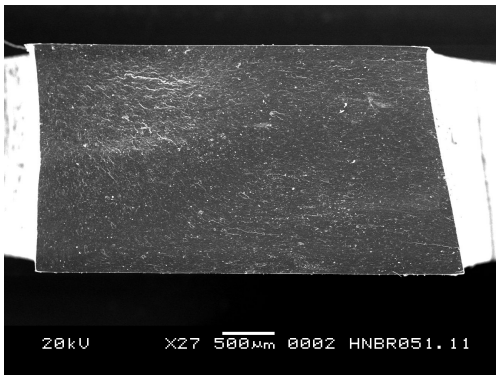

(e) Specimen 3 at x27.

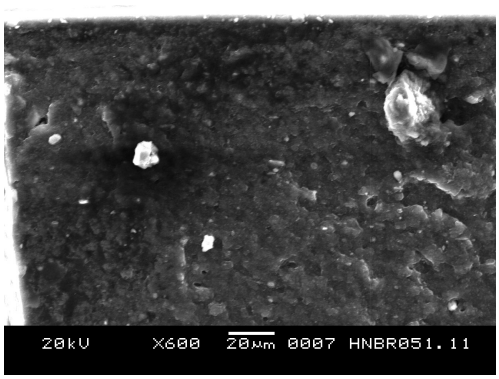

(f) Specimen 3 at x600.

Figure C.1-26 – A44-24 at 10 MPa.

8 MPa

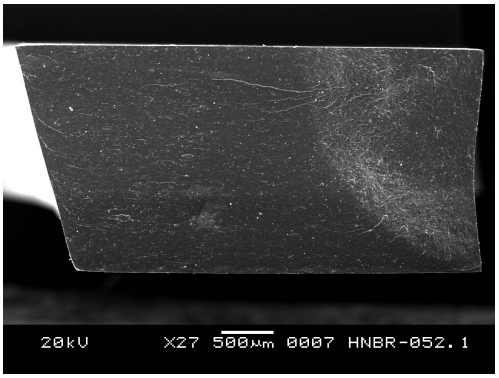

(a) Specimen 1 at x27.

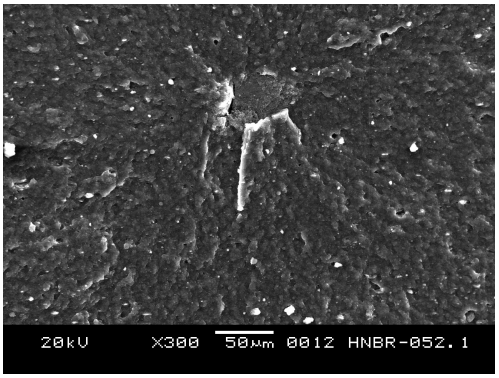

(b) Specimen 1 at x300.

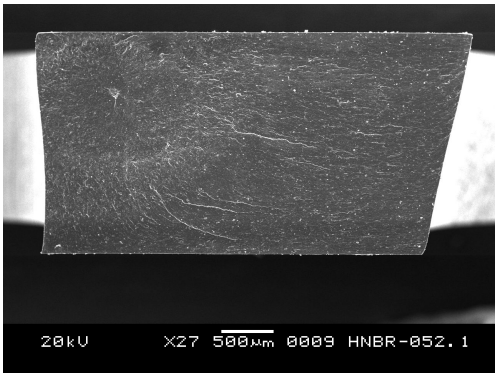

(c) Specimen 2 at x27.

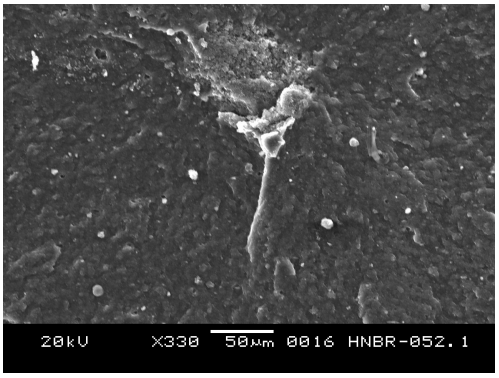

(d) Specimen 2 at x330.

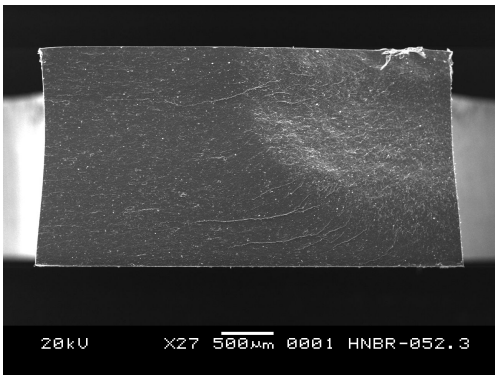

(e) Specimen 3 at x27.

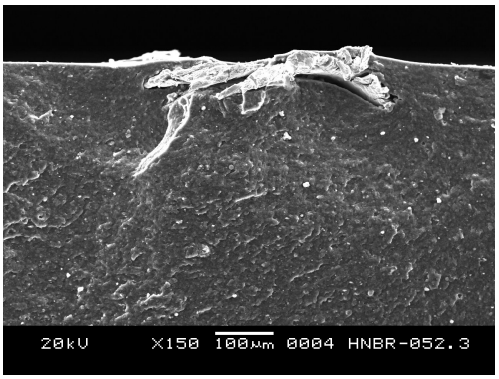

(f) Specimen 3 at x150.

Figure C.1-27 – A44-24 at 8 MPa.

6 MPa

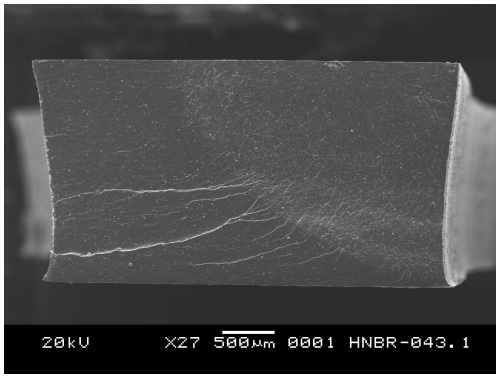

(a) Specimen 1 at x27.

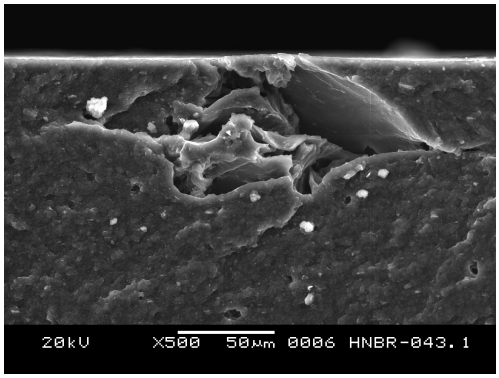

(b) Specimen 1 at x500.

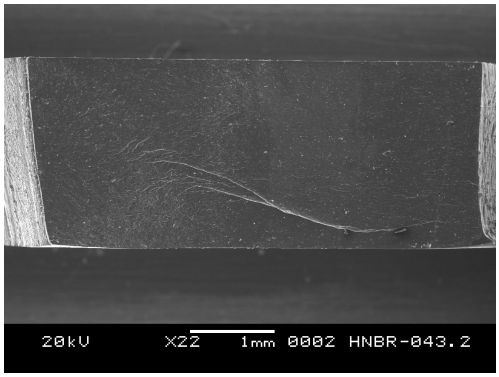

(c) Specimen 2 at x27.

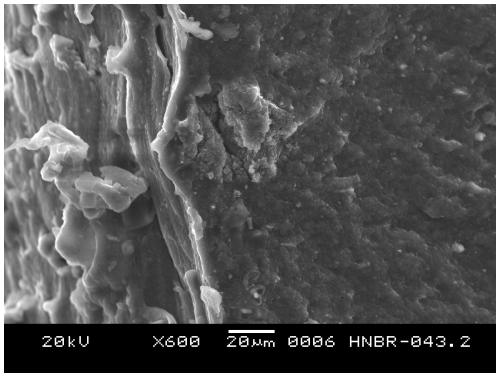

(d) Specimen 2 at x600.

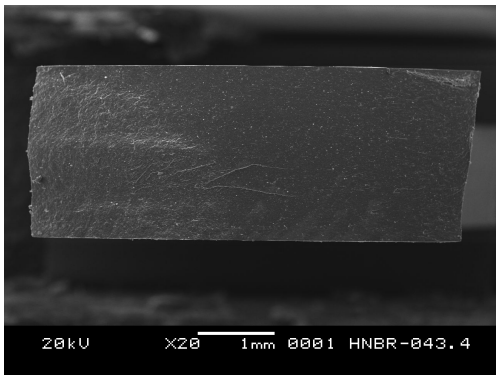

(e) Specimen 3 at x27.

Figure C.1-28 – A44-24 at 6 MPa.

4 MPa

C.2 Simultaneous Fatigue and Aging

C.2.1 A36H96

10 MPa

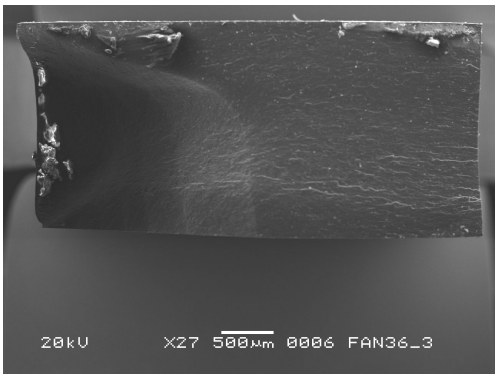

(a) Specimen 1 at x27.

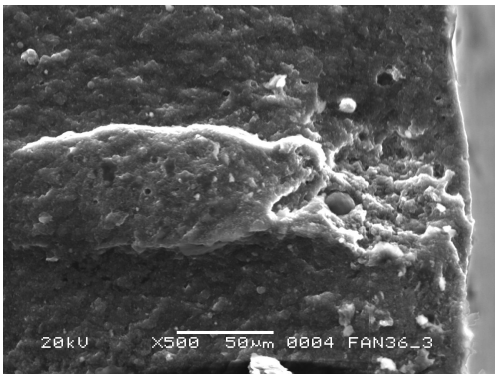

(b) Specimen 1 at x500.

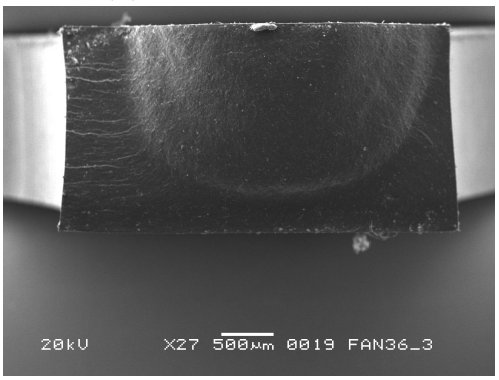

(c) Specimen 2 at x27.

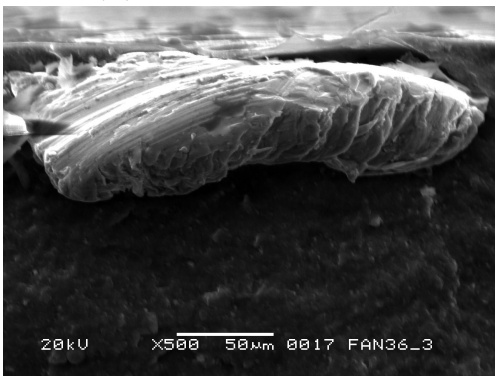

(d) Specimen 2 at x500.

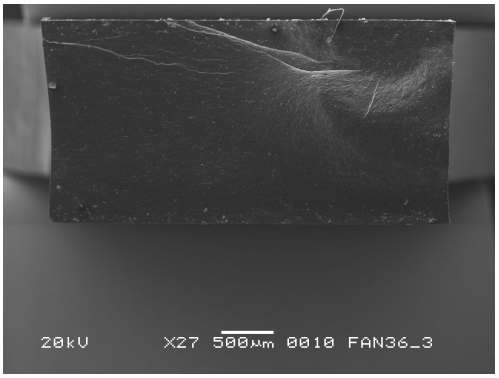

(e) Specimen 3 at x27.

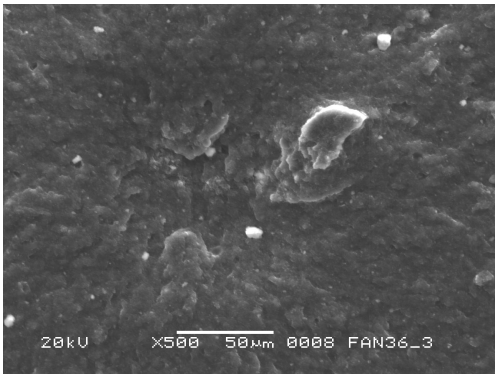

(f) Specimen 3 at x500.

Figure C.2-1 – A36h96 at 10 MPa; simultaneous fatigue and aging.

8 MPa

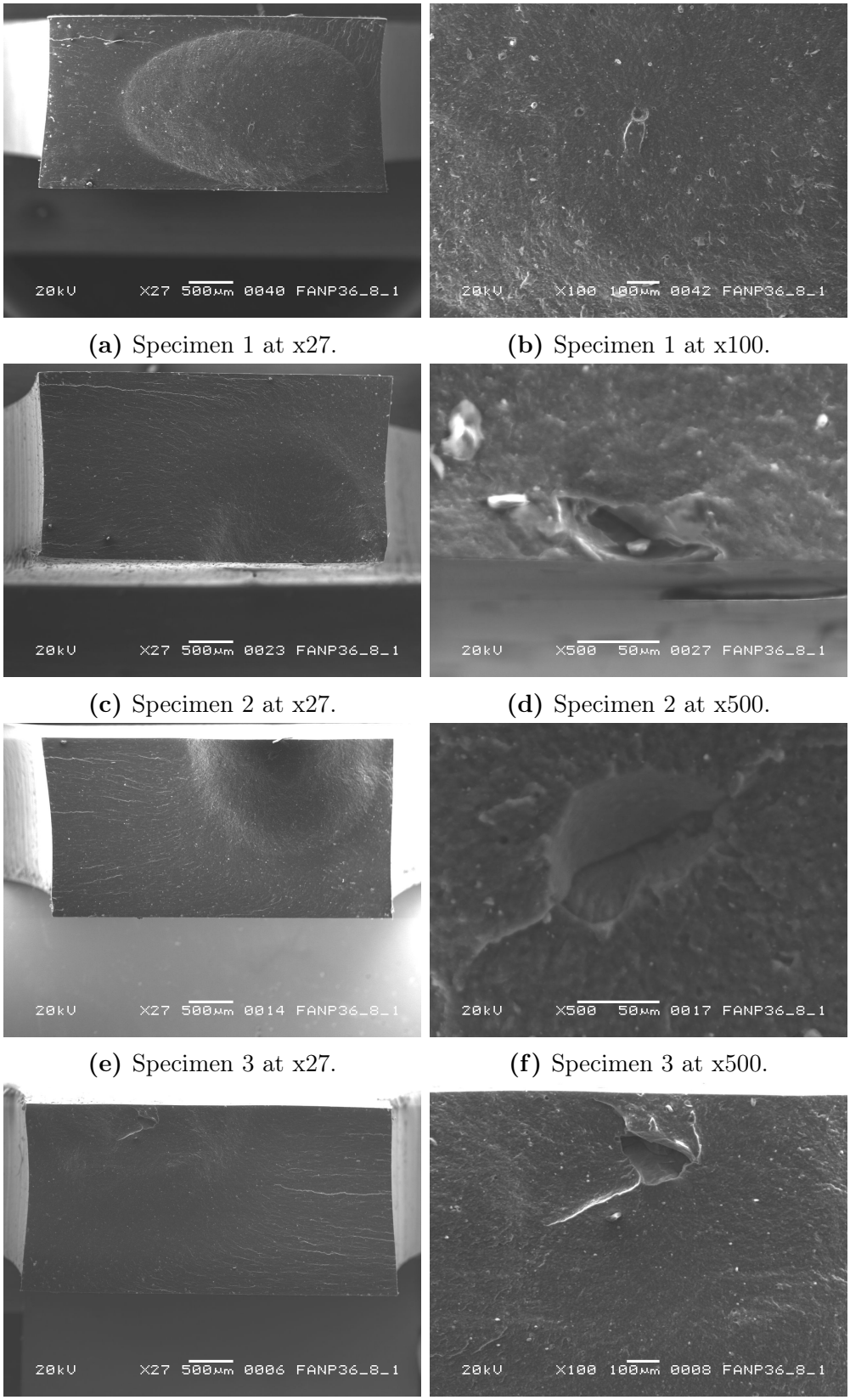

(a) Specimen 1 at x27. **(b)** Specimen 1 at x100.

(c) Specimen 2 at x27. **(d)** Specimen 2 at x500.

(e) Specimen 3 at x27. **(f)** Specimen 3 at x500.

(g) Specimen 4 at x30. **(h)** Specimen 4 at x500.

Figure C.2-2 – A36h96 at 8 MPa; simultaneous fatigue and aging.

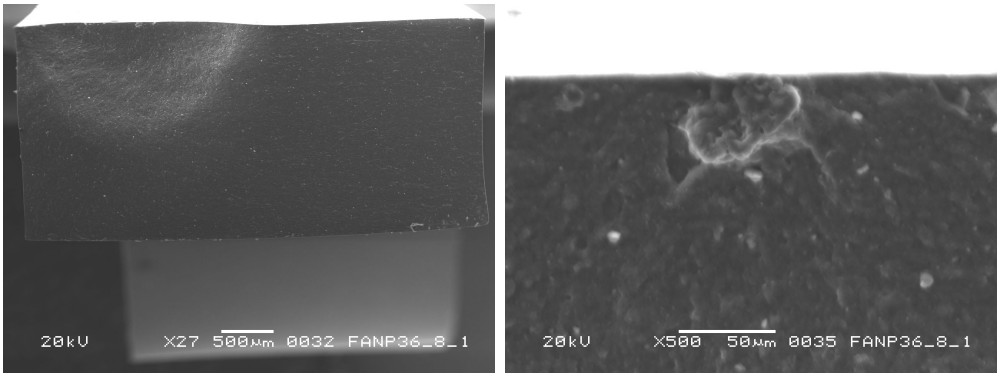

(a) Specimen 5 at x27. **(b)** Specimen 5 at x500.

Figure C.2-3 – A36h96 at 8 MPa.

6 MPa

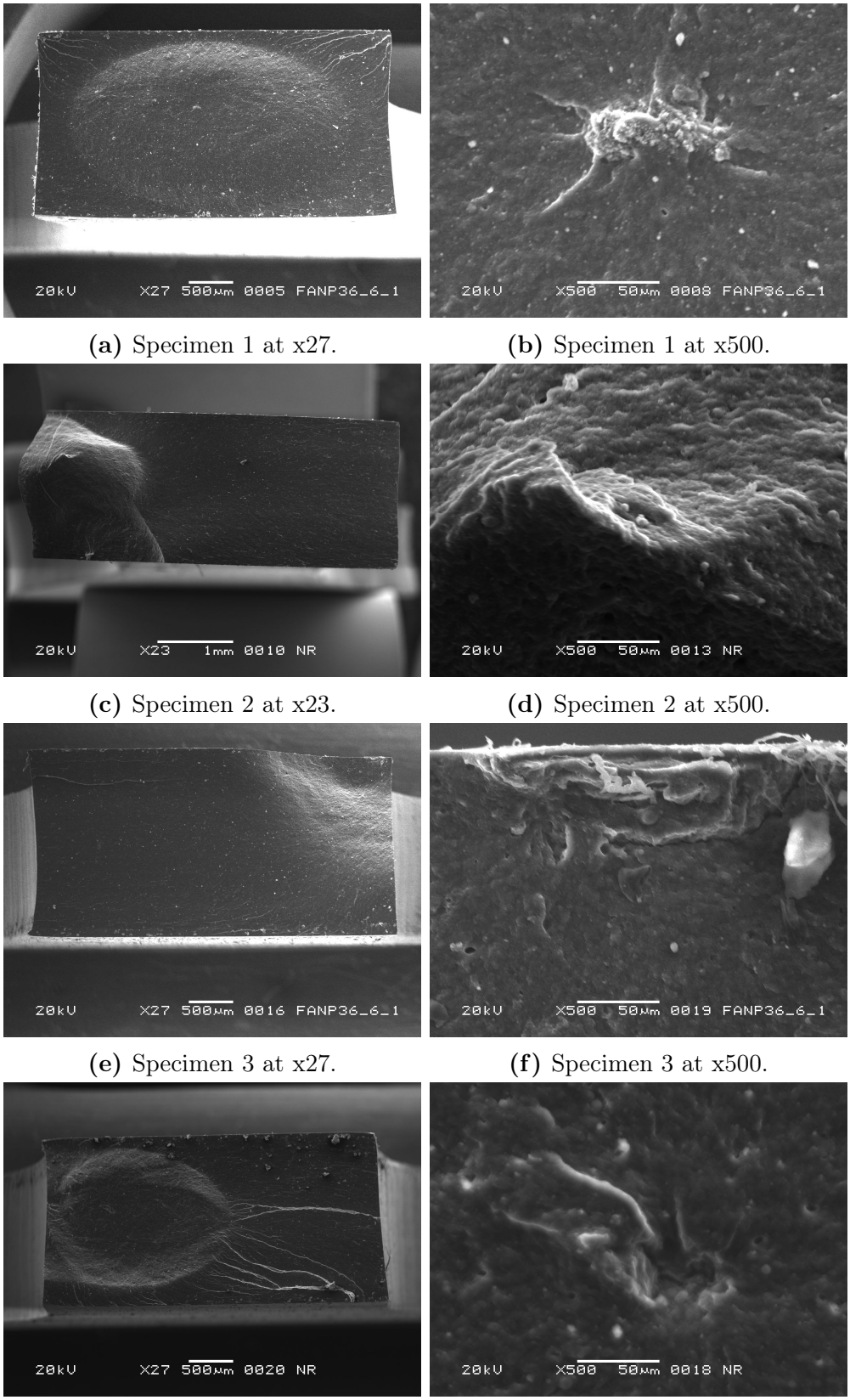

(a) Specimen 1 at x27. **(b)** Specimen 1 at x500.

(c) Specimen 2 at x23. **(d)** Specimen 2 at x500.

(e) Specimen 3 at x27. **(f)** Specimen 3 at x500.

(g) Specimen 4 at x27. **(h)** Specimen 4 at x500.

Figure C.2-4 – A36h96 at 6 MPa; simultaneous fatigue and aging.

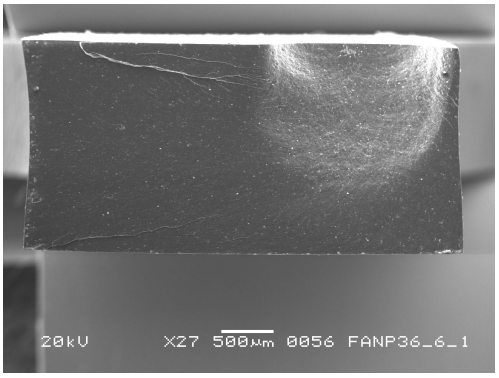

(a) Specimen 5 at x27.

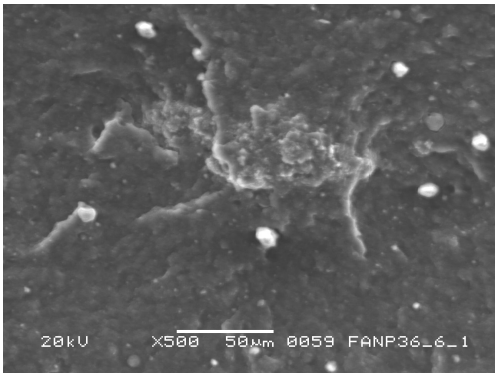

(b) Specimen 5 at x500.

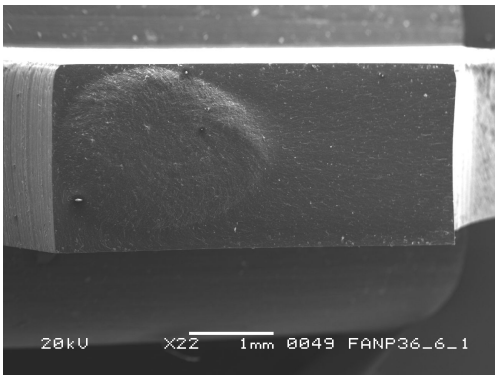

(c) Specimen 6 at x22.

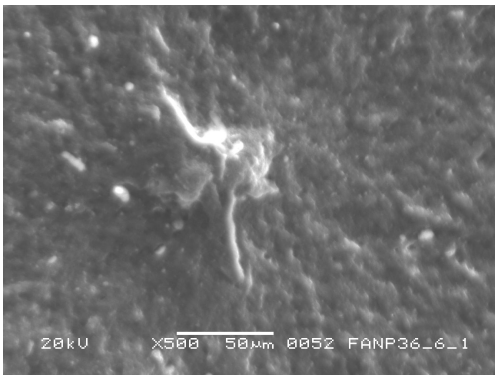

(d) Specimen 6 at x500.

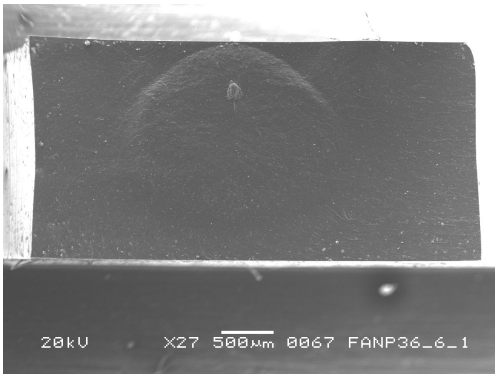

(e) Specimen 7 at x27.

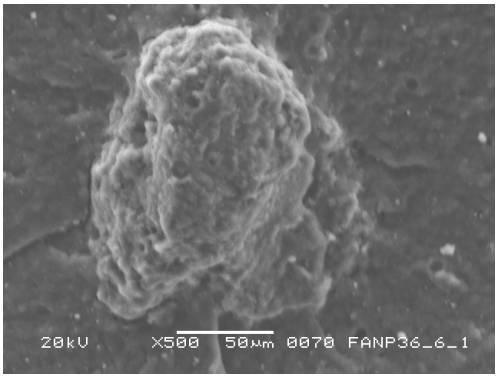

(f) Specimen 7 at x500.

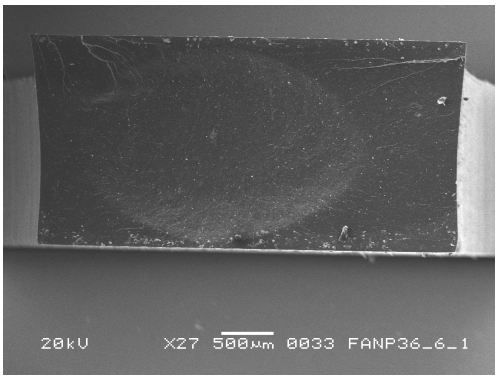

(g) Specimen 8 at x27.

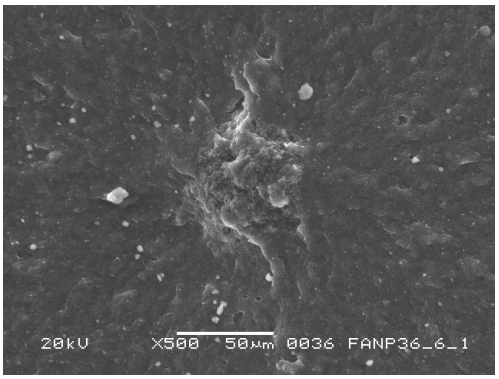

(h) Specimen 8 at x500.

Figure C.2-5 – A36h96 at 6 MPa; simultaneous fatigue and aging.

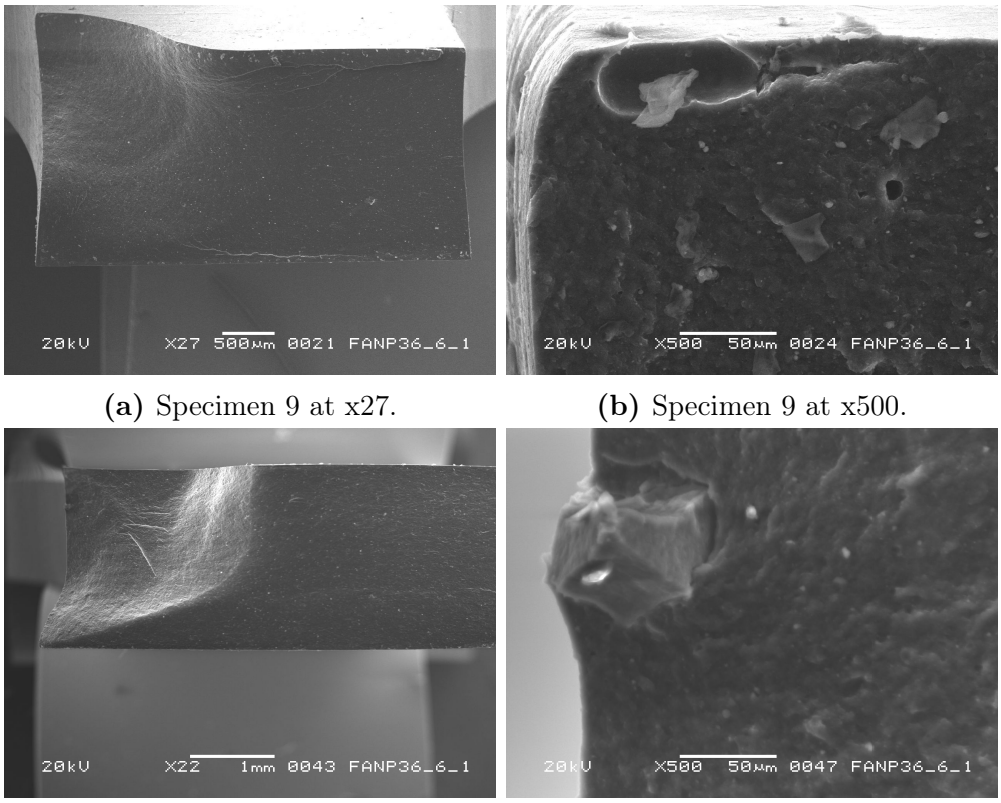

(a) Specimen 9 at x27.

(b) Specimen 9 at x500.

(c) Specimen 10 at x22.

(d) Specimen 10 at x500.

Figure C.2-6 – A36h96 at 6 MPa; simultaneous fatigue and aging.

4 MPa

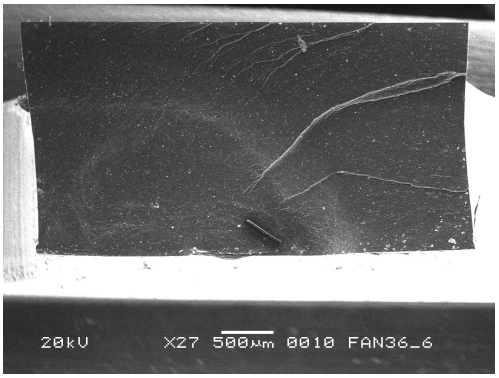

(a) Specimen 1 at x27.

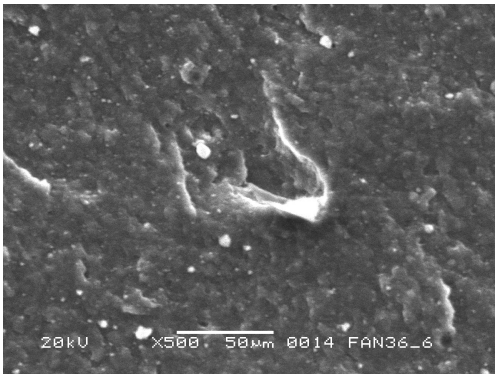

(b) Specimen 1 at x500.

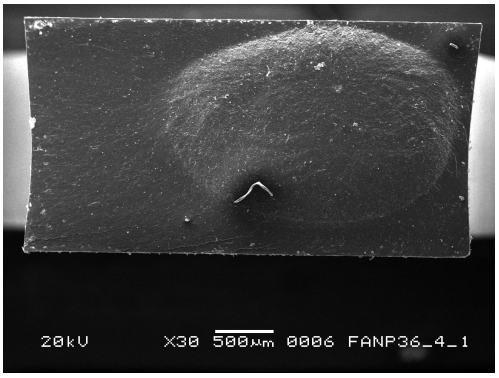

(c) Specimen 2 at x30.

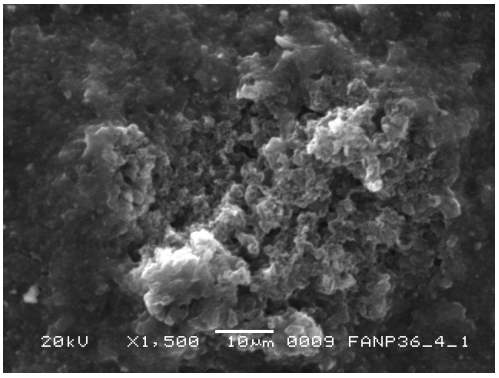

(d) Specimen 2 at x1500.

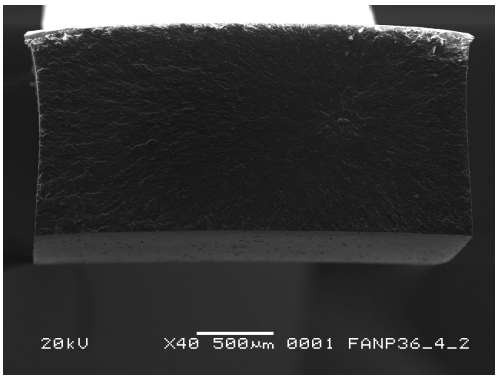

(e) Specimen 3 at x40.

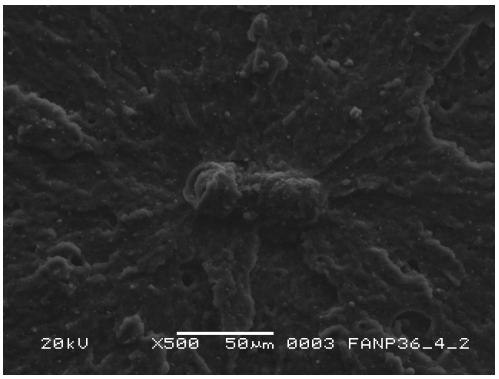

(f) Specimen 3 at x500.

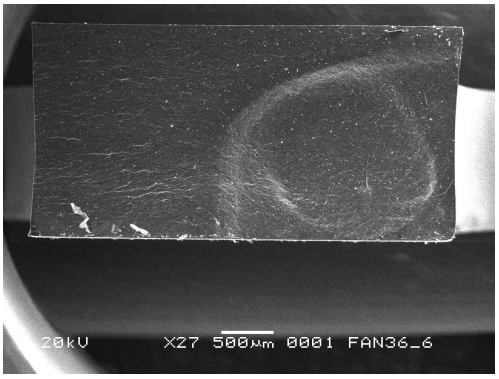

(g) Specimen 4 at x27.

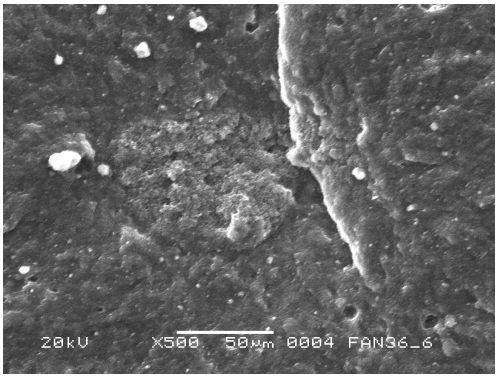

(h) Specimen 4 at x500.

Figure C.2-7 – A36h96 at 4 MPa; simultaneous fatigue and aging.

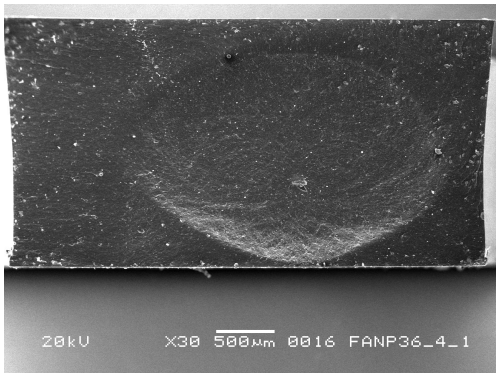

(a) Specimen 5 at x30.

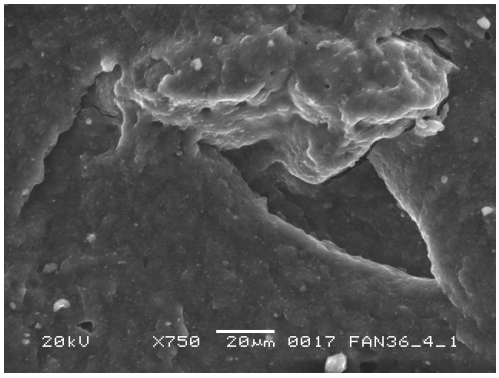

(b) Specimen 5 at x750.

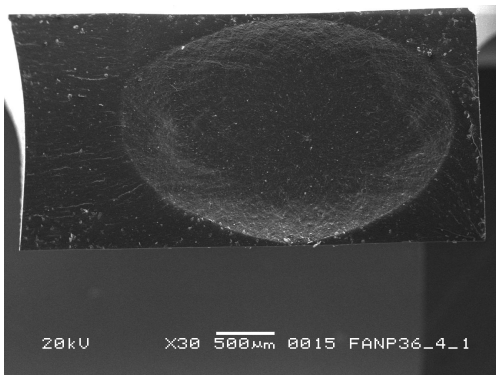

(c) Specimen 6 at x30.

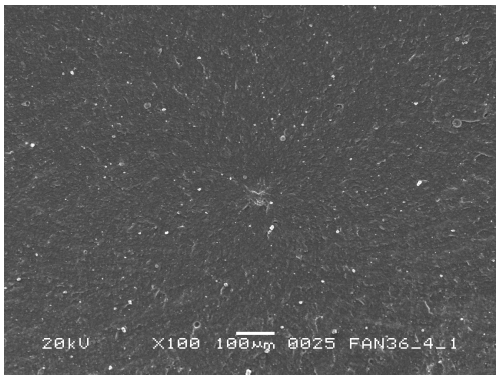

(d) Specimen 6 at x100.

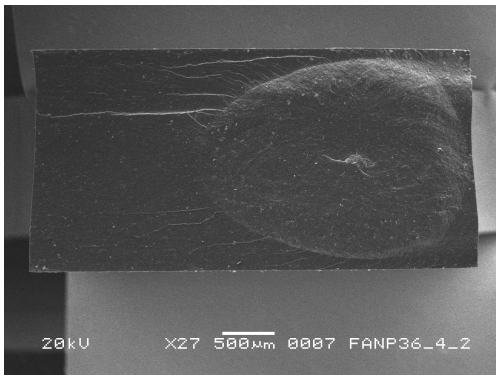

(e) Specimen 7 at x27.

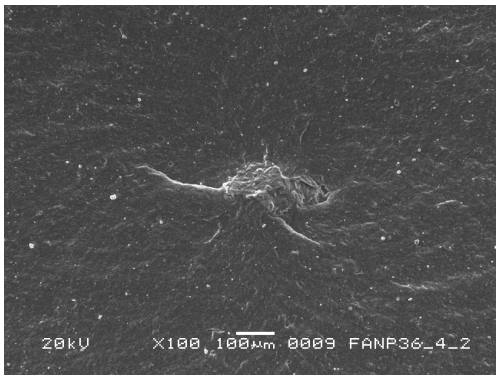

(f) Specimen 7 at x100.

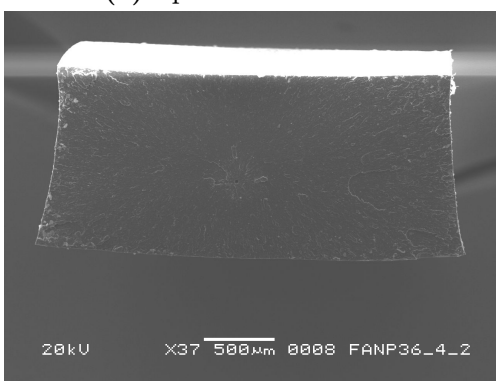

(g) Specimen 8 at x37.

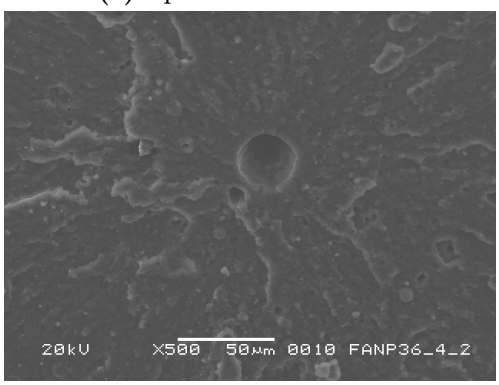

(h) Specimen 8 at x500.

Figure C.2-8 – A36h96 at 4 MPa; simultaneous fatigue and aging.

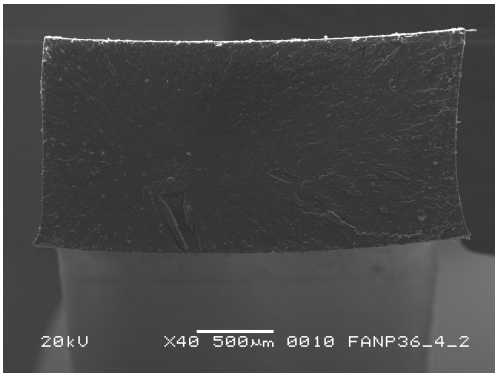

(a) Specimen 9 at x27.

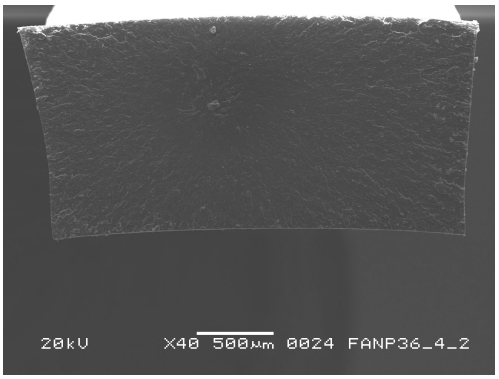

(b) Specimen 10 at x40.

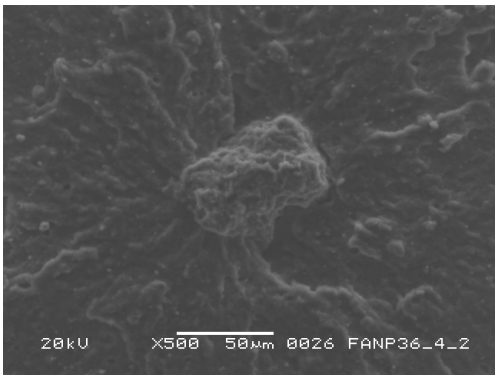

(c) Specimen 10 at x2000.

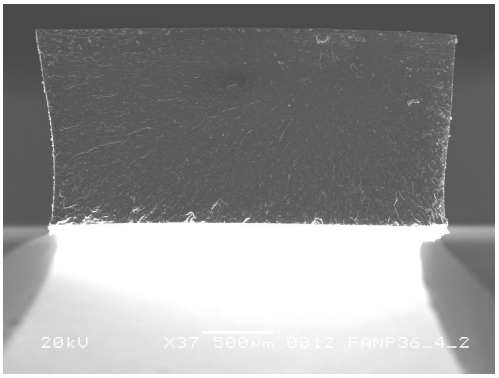

(d) Specimen 11 at x37.

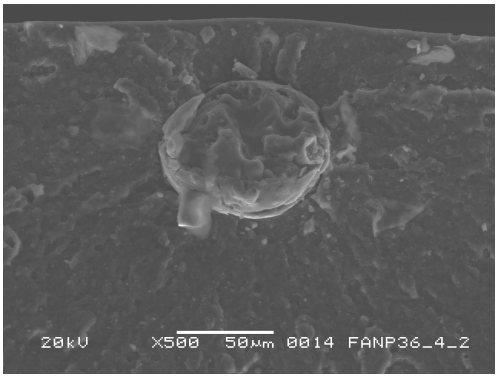

(e) Specimen 11 at x500.

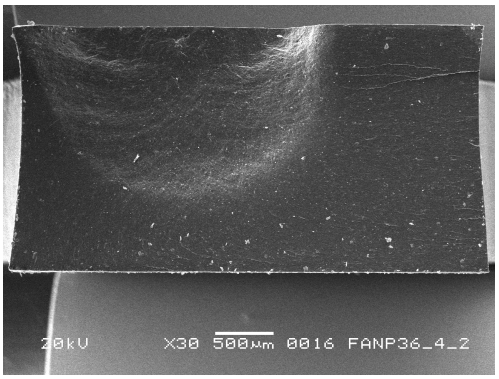

(f) Specimen 12 at x30.

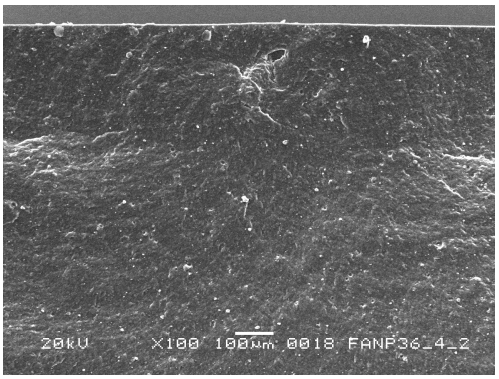

(g) Specimen 12 at x100.

Figure C.2-9 – A36h96 at 4 MPa; simultaneous fatigue and aging.

Appendix D

Grip Design for Parallel Testing

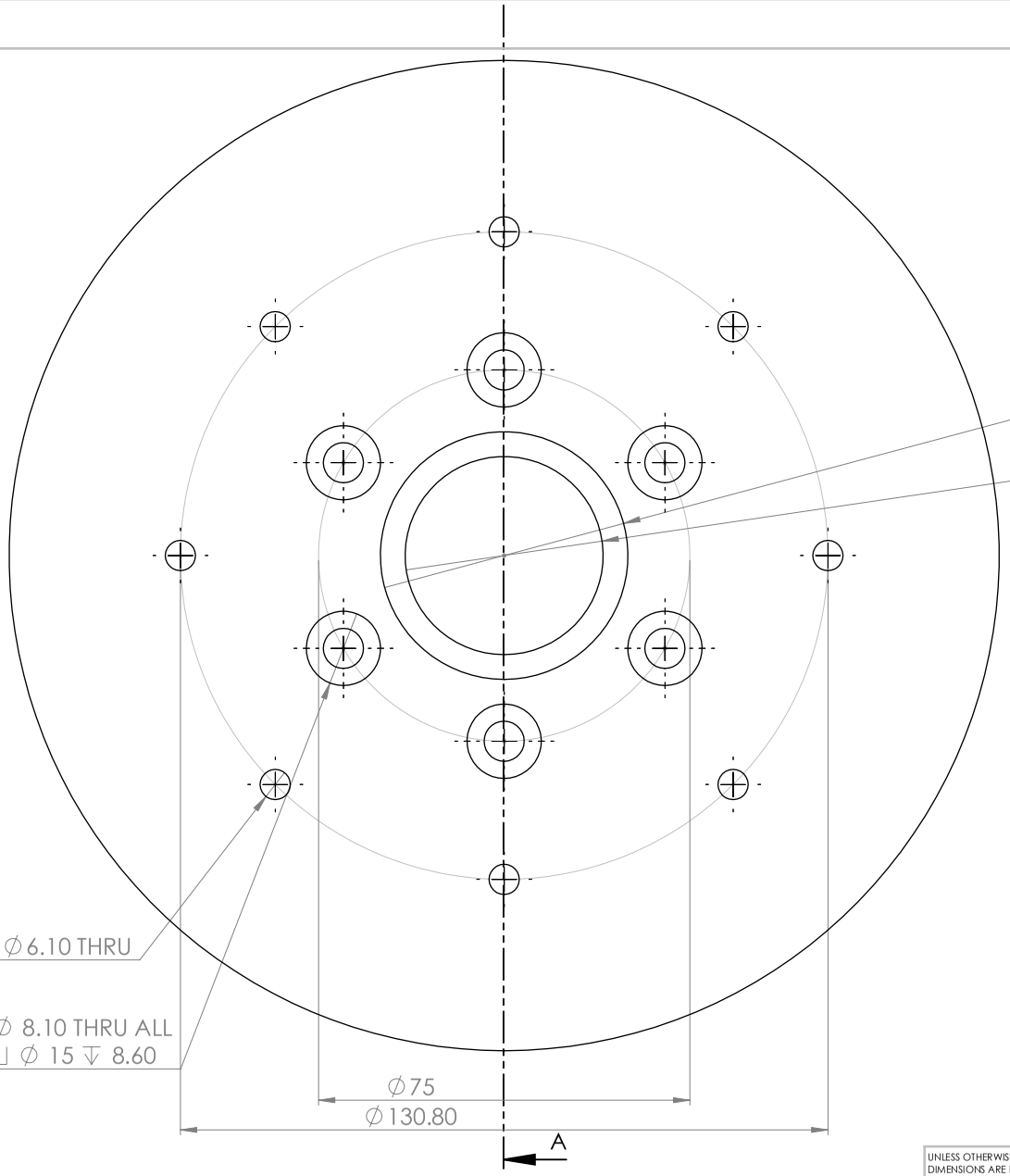

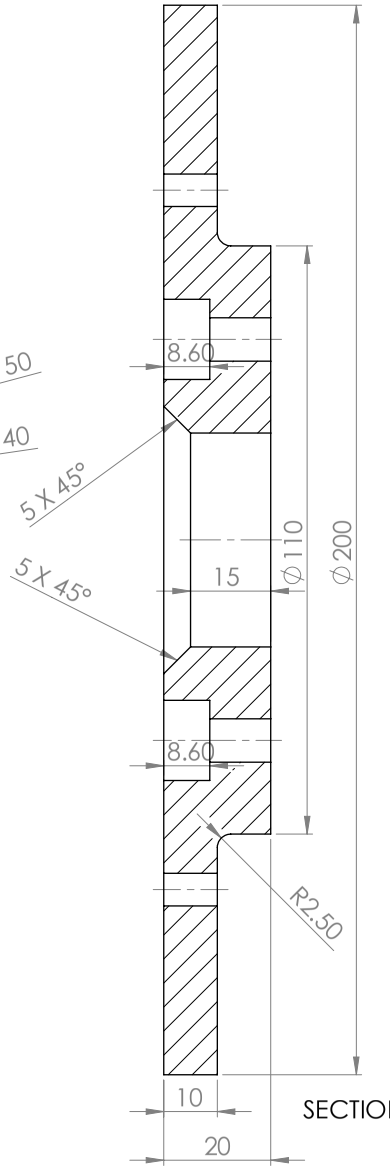

SECTION A-A

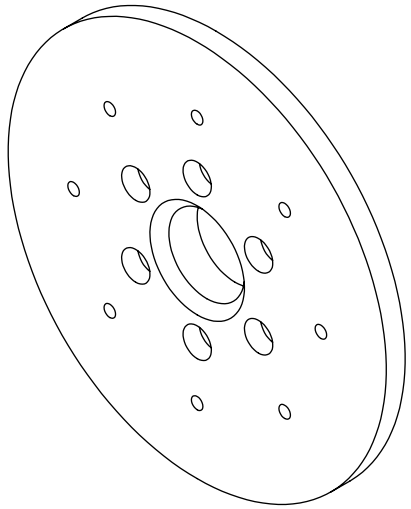

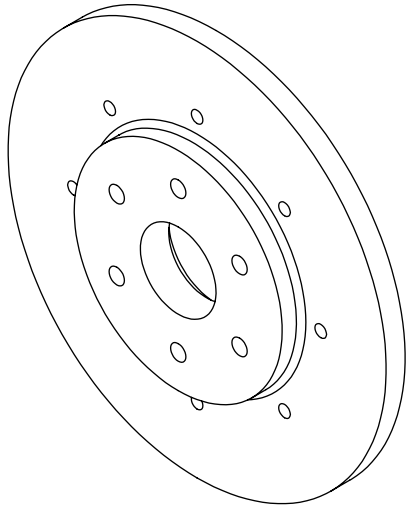

GENERAL TOLERANCE: 0.1 MM

UNLESS OTHERWISE SPECIFIED: DIMENSIONS ARE IN MILLIMETERS SURFACE FINISH: TOLERANCES: LINEAR: ANGULAR:	FINISH:		DEBUR AND BREAK SHARP EDGES	DO NOT SCALE DRAWING	REVISION	
				QUANTITY: 1		
	NAME	SIGNATURE	DATE	TITLE: BOTTOM SUPPORT PLATE		
DRAWN						
CHK'D						
APPV'D						
MFG						
Q.A				MATERIAL: AL 2014 T4	DWG NO. 1	A3
				WEIGHT:	SCALE:1:1	SHEET 1 OF 6

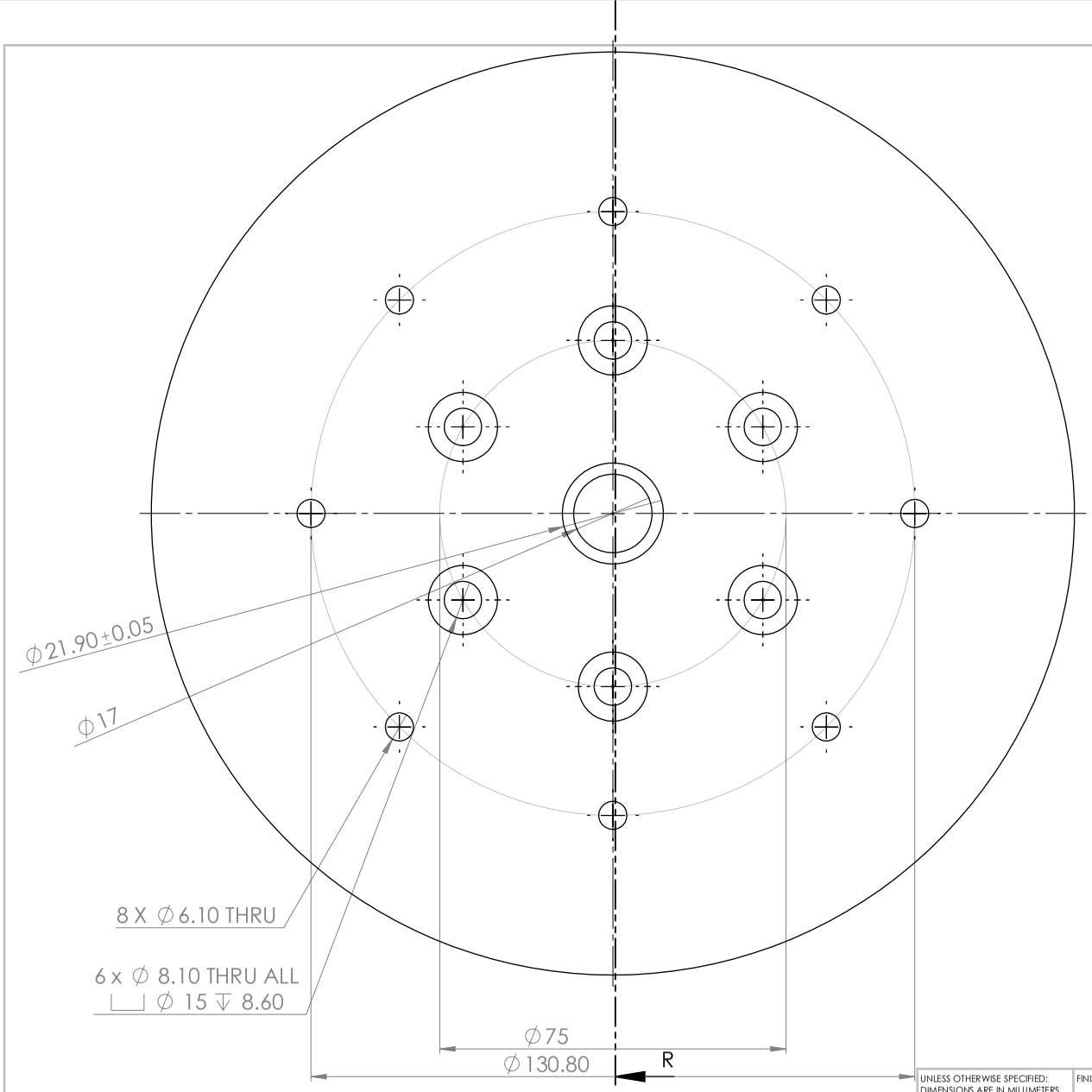

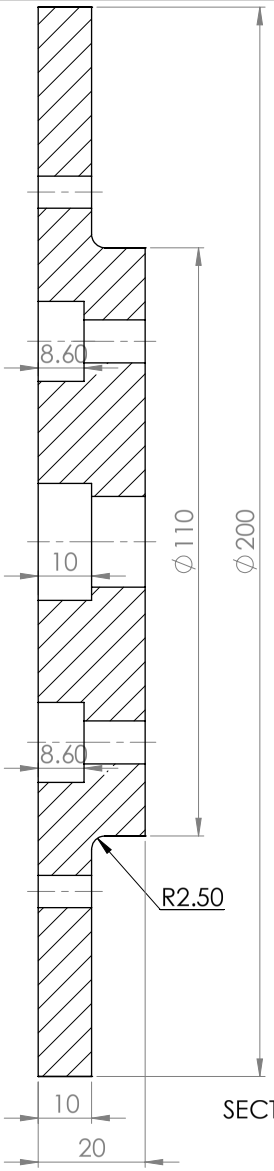

SECTION R-R

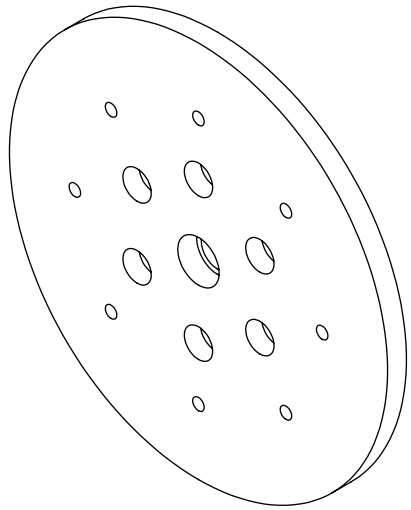

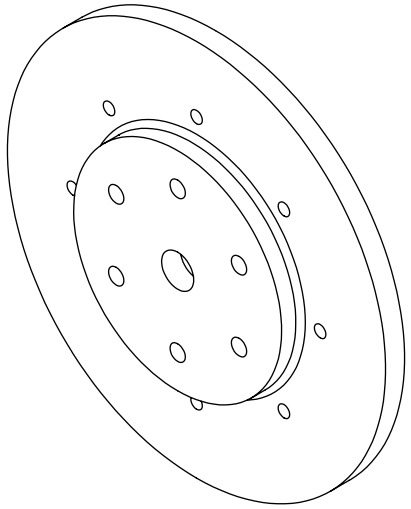

GENERAL TOLERANCE: 0.1 MM

UNLESS OTHERWISE SPECIFIED: DIMENSIONS ARE IN MILLIMETERS SURFACE FINISH: TOLERANCES: LINEAR: ANGULAR:	FINISH:	DEBUR AND BREAK SHARP EDGES	DO NOT SCALE DRAWING	REVISION		
			QUANTITY: 1			
	NAME	SIGNATURE	DATE	TITLE:		
DRAWN				TOP SUPPORT PLATE		
CHK'D						
APPV'D						
MFG						
Q.A						
			MATERIAL: AL 2014 T4	DWG NO. 2		A3
			WEIGHT:	SCALE:1:1	SHEET 2 OF 6	

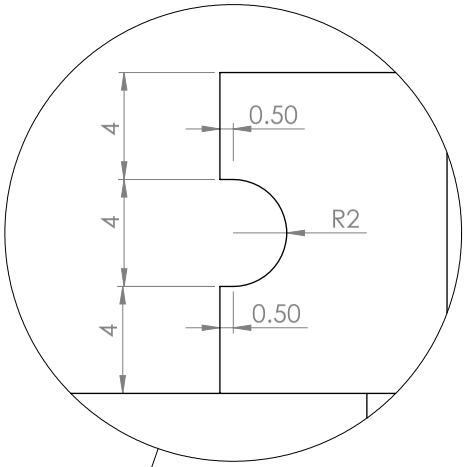

DETAIL F
SCALE 5 : 1

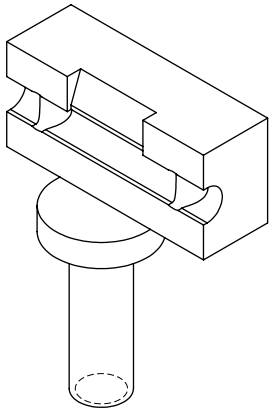

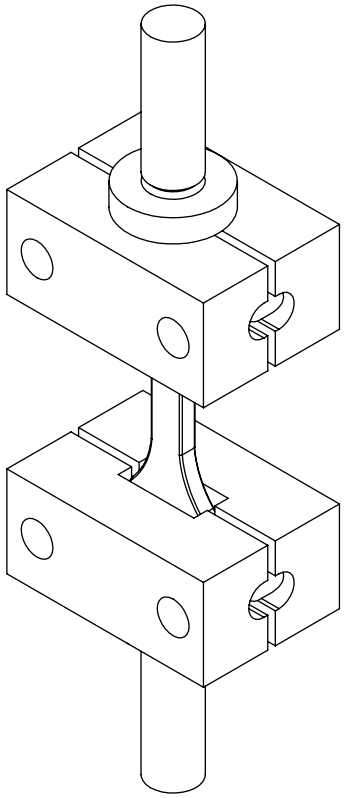

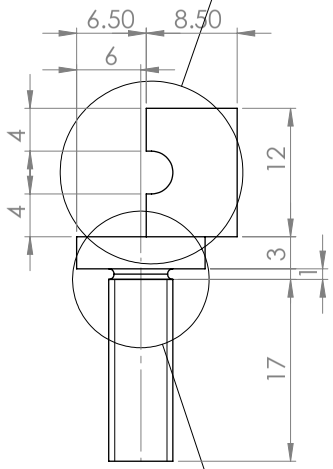

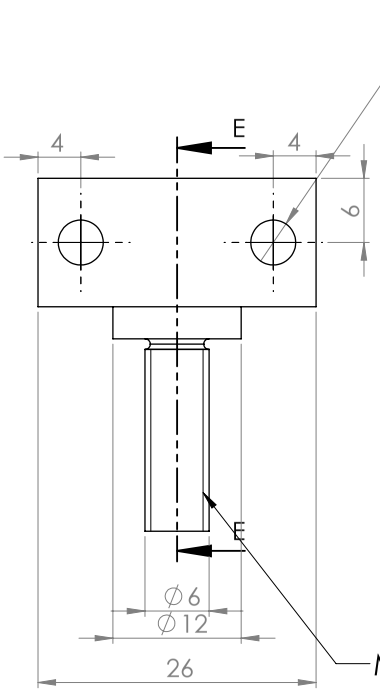

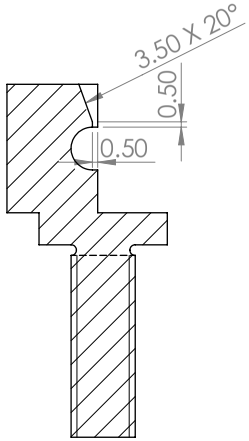

SECTION E-E

DETAIL Q
SCALE 4 : 1

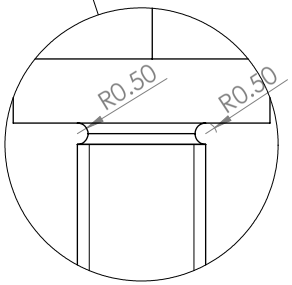

GENERAL TOLERANCE: 0.1 MM

UNLESS OTHERWISE SPECIFIED: DIMENSIONS ARE IN MILLIMETERS SURFACE FINISH: TOLERANCES: LINEAR: ANGULAR:	FINISH:		DEBUR AND BREAK SHARP EDGES	DO NOT SCALE DRAWING	REVISION	
				QUANTITY: 8		
	NAME	SIGNATURE	DATE	TITLE:		
DRAWN				GRIP MAIN BOTTOM		
CHK'D						
APPV'D						
MFG						
Q.A				MATERIAL:	DWG NO.	A3
				AL 2014 T4	3	
				WEIGHT:	SCALE:2:1	SHEET 3 OF 6

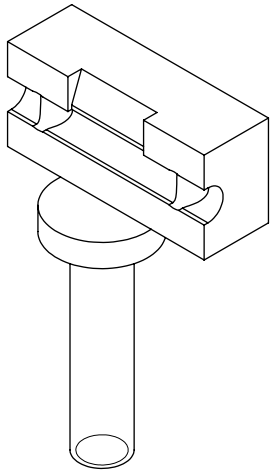

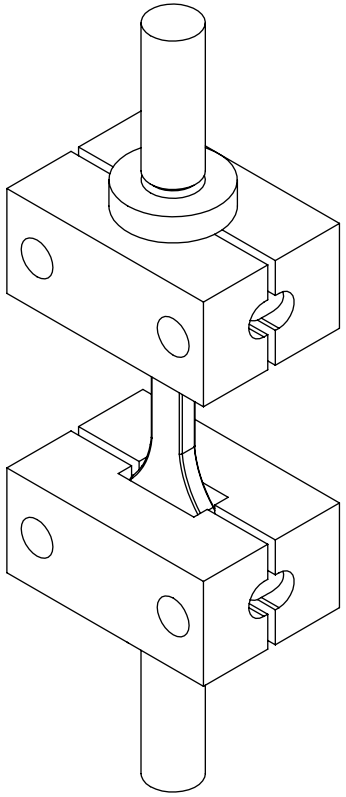

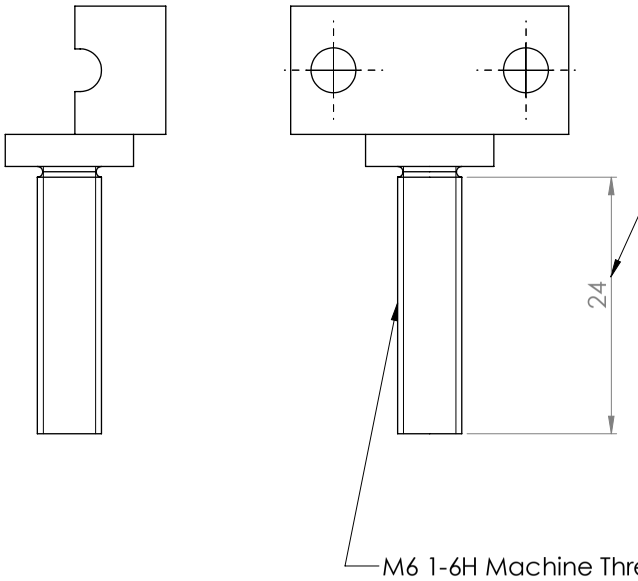

SAME DIMENSIONS AS DRAWING NO.3
EXCEPT FOR ROD LENGTH

GENERAL TOLERANCE: 0.1 MM

UNLESS OTHERWISE SPECIFIED: DIMENSIONS ARE IN MILLIMETERS SURFACE FINISH: TOLERANCES: LINEAR: ANGULAR:	FINISH:		DEBUR AND BREAK SHARP EDGES	DO NOT SCALE DRAWING	REVISION	
				QUANTITY: 8		
	NAME	SIGNATURE	DATE	TITLE:		
DRAWN				GRIP MAIN TOP		
CHK'D						
APPV'D						
MFG						
Q.A				MATERIAL:	DWG NO.	A3
				AL 2014 T4	4	
				WEIGHT:	SCALE:2:1	SHEET 4 OF 6

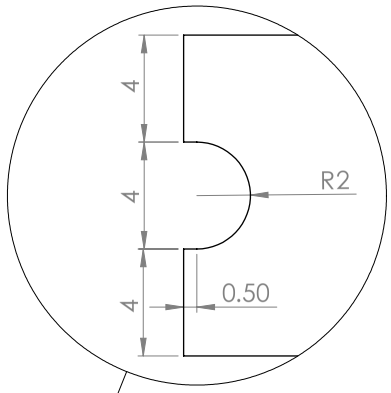

DETAIL I
SCALE 5 : 1

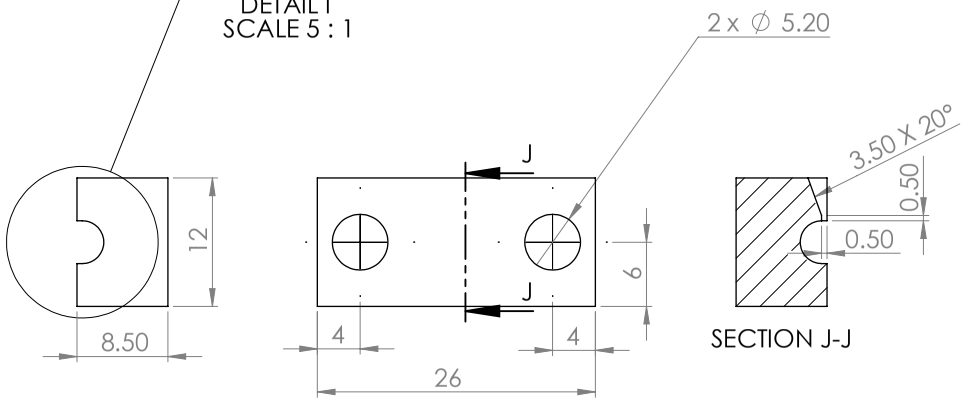

SECTION J-J

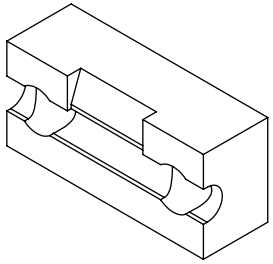

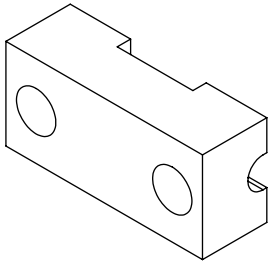

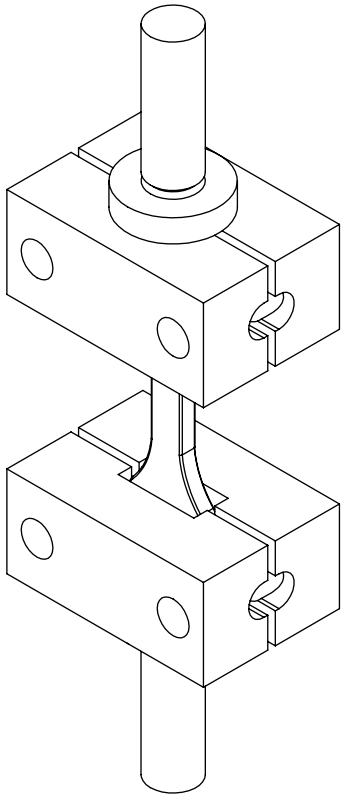

GENERAL TOLERANCE: 0.1 MM

UNLESS OTHERWISE SPECIFIED: DIMENSIONS ARE IN MILLIMETERS SURFACE FINISH: TOLERANCES: LINEAR: ANGULAR:	FINISH:		DEBUR AND BREAK SHARP EDGES	DO NOT SCALE DRAWING	REVISION	
				QUANTITY: 16		
	NAME	SIGNATURE	DATE	TITLE:		
DRAWN				GRIP SECONDARY		
CHK'D						
APPV'D						
MFG						
Q.A				MATERIAL:	DWG NO.	A3
				AL 2014 T4	5	
				WEIGHT:	SCALE:2:1	SHEET 5 OF 6

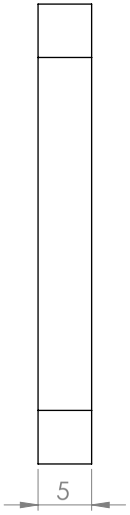

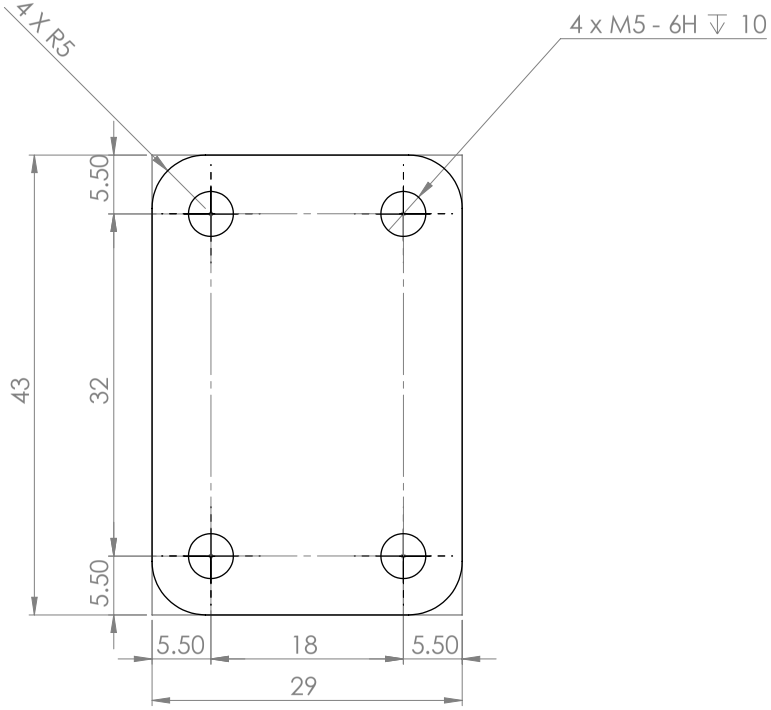

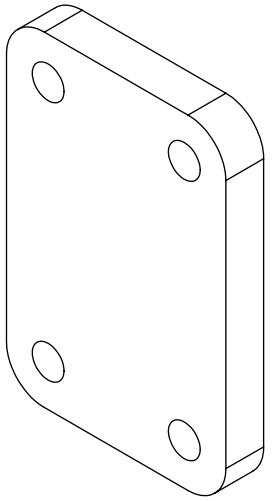

GENERAL TOLERANCE: 0.1 MM

UNLESS OTHERWISE SPECIFIED: DIMENSIONS ARE IN MILLIMETERS SURFACE FINISH: TOLERANCES: LINEAR: ANGULAR:	FINISH:		DEBUR AND BREAK SHARP EDGES	DO NOT SCALE DRAWING	REVISION	
				QUANTITY: 4		
	NAME	SIGNATURE	DATE	TITLE:		
DRAWN				GUIDE		
CHK'D						
APPV'D						
MFG						
Q.A				MATERIAL:	DWG NO.	A3
				AL 2014 T4	6	
				WEIGHT:	SCALE:2:1	SHEET 6 OF 6

Symbols and Acronyms

C_B Basquin's law fit coefficient. 89

E^* dynamic elastic modulus. 13

$E_{\mathbf{10\ MPa}}$ tensile modulus at 10 MPa. 30, 32, 251

F force. 59

$F(N)$ cumulative distribution function. 91, 95

$F_{\mathbf{Benard}}$ Benard's approximation. 91

G^* dynamic shear modulus. 13, 26

$I_{\mathbf{am}}$ amorphous contribution. 29

$I_{\mathbf{crys}}$ crystalline contribution. 29

$I_{\mathbf{tot}}$ total intensity. 29

L_0 reference specimen length. 27

$L_{t=0}$ specimen length upon unloading. 27

N_f fatigue life. 78, 82

N_{stbl} number of cycles required to reach target stress. 82

R R-ratio. 26, 59, 65

R_u R-ratio in terms of displacement. 26

R_λ R-ratio in terms of stretch. 65

R_σ R-ratio in terms of true stress. 65, 82

S specimen cross-section area. 59, 66, 68

$S(N)$ survival function. 95, 96

S_0 original specimen cross-section area. 66

T_g glass transition temperature. 10, 13, 38

W strain energy density. 61

$\Delta\sigma$ true stress amplitude. 73, 79–81

$\Delta\sigma^{\max}$ maximum amplitude. 82, 84

$\Delta\sigma^{\min}$ minimum amplitude. 82, 84

$\Delta_{\%}$ percent difference. 33, 46, 82

$\bar{\sigma}$ instantaneous stress rate. 79

β_i cox regression coefficients. 96, 97

χ_C index of crystallinity. 29

$\dot{\bar{\sigma}}$ average stress rate. 79

$\epsilon_{\mathbf{p}}$ global permanent strain. 27, 43

$\epsilon_{\mathbf{res}}$ global residual strain. 27, 43

γ Weibull location parameter. 90

λ stretch ratio. 60, 65, 68, 69

λ_C crystallization onset. 17, 21, 48, 53, 54

λ_M crystallization melting. 17, 48, 53, 54

λ_{M} stretch corresponding to inelastic strain due to the Mullins effect. 66

λ_{R} stretch corresponding to inelastic strain due to long-term relaxation. 68

λ_f stretch at break. 30, 32, 251

$\overline{N_B}$ Basquin's law estimate. 94

$\overline{N_G}$ geometric mean. 94

$\overline{N_c}$ Cox mean. 98, 132

$\overline{N_w}$ Weibull mean. 127

$\overline{R_\sigma}$ Average R-ratio in terms of true stress. 82

$\overline{\Delta\sigma}$ average stress amplitude. 81

ρ Weibull scale parameter. 90, 127

σ true (Cauchy) stress. 24, 59, 66

σ_e fatigue endurance limit. 154

σ_f stress at break. 11, 30, 32, 154, 251

HR hazard ratio. 96, 97, 130, 177, 188

$\mathbf{HR}^{\max}$ upper bound of the hazard ratio. 97, 131

$\mathbf{HR}^{\min}$ lower bound of the hazard ratio. 97, 131

$\mathbf{std}(R)$ stability of loading. 82

a_B Basquin's law fit coefficient. 89

$f(N)$ probability density function. 90, 96

$h(N)$ hazards function. 96

k Weibull shape parameter. 90, 127

r^2 coefficient of determination. 41, 90, 91

u displacement. 59

u_{M} displacement corresponding to inelastic strain due to the Mullins effect. 65, 70

u_{R} displacement corresponding to inelastic strain due to long-term relaxation. 70

ACN acrylonitrile. 9

CB carbon black. 12

DIC digital image correlation. 24, 73, 78, 173

DLO diffusion limited oxidation. 162, 163, 183

DMA dynamic mechanical analysis. 13, 26

EDS energy dispersive spectroscopy. 124, 174, 183, 184

FR fatigue ratio. 154, 156, 158

HNBR hydrogenated nitrile butadiene rubber. 1, 7

NBR nitrile butadiene rubber. 7

NR natural rubber. 64

SEM scanning electron microscopy. 123, 167, 174, 183

SIC strain-induced crystallization. 1, 10, 17, 27

TTS time temperature superposition. 171

WAXD wide angle X-ray diffraction. 17

UNIVERSITE BRETAGNE SCIENCES LOIRE POUR L'INGENIEUR

CENTRALE NANTES

Titre : Fatigue du HNBR - effet de la formulation et du vieillissement thermique

Mots clés : caoutchoucs nitrile hydrogénés (HNBR) ; fatigue ; vieillissement thermique ; techniques expérimentales ; analyses statistiques.

Résumé : Cette thèse de doctorat s'intéresse à la fatigue des élastomères, et plus particulièrement des caoutchoucs nitrile hydrogénés (sigle HNBR en anglais). Les HNBR sont des élastomères de haute performance, classiquement utilisés pour des applications industrielles à haute température où une bonne résistance chimique aux hydrocarbures est également requise.

La thèse est divisée en trois parties principales.

En premier lieu, des améliorations majeures pour les expériences de durée de vie en fatigue des élastomères sont proposées. Une approche expérimentale originale permettant le pilotage des essais en contrainte vraie est détaillée. Grâce à cette méthode, la première « vraie » courbe de Wöhler (contrainte vraie en fonction du nombre de cycles) pour des élastomères est tracée. Ensuite, des outils statistiques, issus de la recherche médicale, permettent une analyse probabiliste des résultats présentant une grande dispersion et des durées de vie censurées.

Dans un second temps, ces nouveaux outils sont utilisés pour étudier l'effet de la formulation chimique – les taux d'acrylonitrile et d'hydrogénation notamment - sur la résistance en fatigue du HNBR à 120 ^{o}C. Ces résultats sont complétés par des expériences de propagation de fissure de fatigue et par une analyse de l'endommagement.

Finalement, l'influence du vieillissement thermique sur la résistance en fatigue du HNBR est étudiée ; deux nouveaux essais sont développés : des essais simultanés de vieillissement et de fatigue, et des expériences de fatigue sur des échantillons préalablement vieillis.

De plus, la cristallisation sous tension dans le HNBR est pour la première fois étudiée de manière quantitative.

Title : Fatigue of HNBR - effects of formulation and thermal aging

Keywords: hydrogenated nitrile butadiene rubber (HNBR); fatigue; thermal aging; experimental techniques; statistical analysis.

Abstract : The present PhD thesis is devoted to investigation of fatigue in elastomers, and more particularly of carbon black-filled hydrogenated nitrile butadiene rubber (HNBR).

HNBR is a high performance elastomer classically used for high temperature industrial applications, where high resistance to industrial solvents is also required.

The thesis is divided into three main parts.

First, major improvements of testing procedures utilized in fatigue life testing of elastomers are proposed. An original method to prescribe the true stress throughout fatigue experiments is developed; it permits to plot the first "true" Wöhler curve, i.e. true stress vs. number of cycles, for elastomers. Then, statistical tools, widely applied in medical research, are adopted for a comprehensive probabilistic analysis of fatigue life results that exhibit high scatter and censored lifetimes.

Second, these novel tools are used to investigate the effect of chemical formulation - acrylonitrile content, percent hydrogenation, and of a composite blend - on fatigue resistance of HNBR at the service temperature of 120 ^{o}C. In addition to these fatigue life tests, fatigue crack propagation experiments and microscopic fatigue damage analysis are carried out.

Third, the influence of thermal aging on fatigue performances of HNBR is investigated. To this end, two additional fatigue life tests are carried out: simultaneous aging and fatigue experiments, and fatigue experiments on pre-aged samples.

Additionally, strain-induced crystallization in HNBR is studied; for the first time, quantitative relationships between crystallization, strain, and stress are established for unfilled HNBR blends.